University of Florida
Civil and Coastal Engineering

Final Report   May, 2022

Flexural Capacity of Concrete Elements with Unbonded and Bonded Prestressing

Principal investigator:
Gary R. Consolazio, Ph.D.

Co-Principal investigator:
H.R. Trey Hamilton, Ph.D., P.E.

Graduate research assistant:
Seaska I. Pérez-Avilés, Ph.D.

Department of Civil and Coastal Engineering
University of Florida
P.O. Box 116580
Gainesville, Florida 32611

DISCLAIMER

The opinions, findings, and conclusions expressed in this publication are those of the authors and not necessarily those of the State of Florida Department of Transportation.

SI (MODERN METRIC) CONVERSION FACTORS
*APPROXIMATE CONVERSIONS **TO** SI UNITS*

SYMBOL	WHEN YOU KNOW	MULTIPLY BY	TO FIND	SYMBOL
LENGTH				
in	inches	25.4	millimeters	mm
ft	feet	0.305	meters	m
yd	yards	0.914	meters	m
mi	miles	1.61	kilometers	km
AREA				
in^2	square inches	645.2	square millimeters	mm^2
ft^2	square feet	0.093	square meters	m^2
yd^2	square yard	0.836	square meters	m^2
ac	acres	0.405	hectares	ha
mi^2	square miles	2.59	square kilometers	km^2
VOLUME				
fl oz	fluid ounces	29.57	milliliters	mL
gal	gallons	3.785	liters	L
ft^3	cubic feet	0.028	cubic meters	m^3
yd^3	cubic yards	0.765	cubic meters	m^3
NOTE: volumes greater than 1000 L shall be shown in m^3				
MASS				
oz	ounces	28.35	grams	g
lb	pounds	0.454	kilograms	kg
T	short tons (2,000 lb)	0.907	Megagrams	Mg (or "t")
TEMPERATURE (exact degrees)				
ºF	Fahrenheit	5(F-32)/9 or (F-32)/1.8	Celsius	ºC
FORCE and PRESSURE or STRESS				
kip	1,000 pound force	4.45	kilonewtons	kN
lbf	pound force	4.45	newtons	N
lbf/in^2	pound force per square inch	6.89	kilopascals	kPa
ksi	kips force per square inch	6.89	Megapascals	MPa

TECHNICAL REPORT DOCUMENTATION PAGE

1. Report No.	2. Government Accession No.	3. Recipient's Catalog No.

4. Title and Subtitle	5. Report Date
Flexural Capacity of Concrete Elements with Unbonded and Bonded Prestressing	May 2022
	6. Performing Organization Code
	8. Performing Organization Report No.

7. Author(s)	
Gary R. Consolazio, H. R. Trey Hamilton, Seaska I. Pérez-Avilés	2022/P0071623-P0071624

9. Performing Organization Name and Address	10. Work Unit No. (TRAIS)
University of Florida Department of Civil and Coastal Engineering 365 Weil Hall, P.O. Box 116580 Gainesville, FL 32611-6580	
	11. Contract or Grant No.
	BDV31-977-93

12. Sponsoring Agency Name and Address	13. Type of Report and Period Covered
Florida Department of Transportation Research Management Center 605 Suwannee Street, MS 30 Tallahassee, FL 32399-0450	Final Report Jan 2018 – May 2022
	14. Sponsoring Agency Code

15. Supplementary Notes

16. Abstract

Prestressed concrete is widely used in bridge construction and is considered a cost-effective and efficient method of construction. However, durability issues have arisen which have been attributed to poor grouting practice or material performance. To improve durability and facilitate replacement of tendons, bridge construction projects in Florida may now incorporate flexible fillers in lieu of cementitious grout. These structures utilize concrete components with a combination of unbonded tendons and bonded prestressing and/or mild steel reinforcement. Although this is a new design approach in the United States, it has been widely used in European countries. However, the use of mixed reinforcement conditions (i.e., the simultaneous use of unbonded and bonded prestressed reinforcement) in concrete members has structural implications.

The flexural behavior of prestressed beams is affected by the presence of unbonded tendons. In the present research, this parameter was characterized by U/T, which is the ratio of unbonded tendon force to total tendon force at flexural capacity; this parameter varies between 0 for fully unbonded sections to 1.0 for fully bonded sections. Strains in unbonded tendons are not compatible with adjacent concrete strains, which makes the strain compatibility approach of capacity calculation non-applicable. In an unbonded tendon, stresses are dependent on the deformation of the entire member as well as tendon geometry. At the ultimate section strength condition, stress for unbonded tendons is lower than for bonded tendons. Current design guidance for prestressed concrete members with mixed reinforcement conditions is based on conservative underestimation of flexural capacity. A major component of this study was therefore the development of improved guidelines for computing the flexural capacity of members with mixed reinforcement conditions.

Full-scale experimental tests were conducted on positive and negative bending specimens to investigate the flexural behavior of concrete beams with mixed reinforcement conditions. Complementary nonlinear finite element analyses were also conducted. Finite element modeling and analysis procedures were validated against the collected experimental data and then used to conduct parametric studies that encompassed greater variations of system parameters than was feasible to investigate experimentally.

Results from this study revealed that the flexural capacity of concrete elements with mixed reinforcement is reduced as U/T increases. Based on the collected experimental data and finite element results, an empirical method for computing the flexural strength of beams with mixed reinforcement and a linear transition in resistance factor were proposed, which involved adjustments to current simplified provisions in AASHTO-LRFD (2020). Additionally, this study found that bonded strand rupture occurred in full-scale laboratory specimens with U/T of 0.4 and 0.7. A new requirement for a minimum amount of bonded prestressing reinforcement has been developed to reduce the possibility of strand rupture when ultimate strength is reached.

17. Key Words	18. Distribution Statement
Post-tensioned concrete, mixed reinforcement conditions, bonded reinforcement, unbonded reinforcement, flexure	No restrictions.

19. Security Classif. (of this report)	20. Security Classif. (of this page)	21. No. of Pages	22. Price
Unclassified	Unclassified	482	

Form DOT F 1700.7 (8-72). Reproduction of completed page authorized

ACKNOWLEDGEMENTS

EXECUTIVE SUMMARY

Prestressed concrete is widely used in bridge construction and is considered a cost-effective and efficient method of construction. However, durability issues have arisen which have been attributed to poor grouting practice or material performance. To improve durability and facilitate replacement of tendons, bridge construction projects in Florida may now incorporate flexible fillers in lieu of cementitious grout. These structures utilize concrete components with a combination of unbonded tendons and bonded prestressing and/or mild steel reinforcement. Although this is a new design approach in the United States, it has been widely used in European countries. However, the use of mixed reinforcement conditions (i.e., the simultaneous use of unbonded and bonded prestressed reinforcement) in concrete members has structural implications.

The flexural behavior of prestressed beams is affected by the presence of unbonded tendons. In the present research, this parameter was characterized by U/T, which is the ratio of unbonded tendon force to total tendon force at flexural capacity; this parameter varies between 0 for fully unbonded sections to 1.0 for fully bonded sections. Strains in unbonded tendons are not compatible with adjacent concrete strains, which makes the strain compatibility approach of capacity calculation non-applicable. In an unbonded tendon, stresses are dependent on the deformation of the entire member as well as tendon geometry. At the ultimate section strength condition, stress for unbonded tendons is lower than for bonded tendons. Current design guidance for prestressed concrete members with mixed reinforcement conditions is based on conservative underestimation of flexural capacity. A major component of this study was therefore the development of improved guidelines for computing the flexural capacity of members with mixed reinforcement conditions.

Full-scale experimental tests were conducted on positive and negative bending specimens to investigate the flexural behavior of concrete beams with mixed reinforcement conditions. Complementary nonlinear finite element analyses were also conducted. Finite element modeling and analysis procedures were validated against the collected experimental data and then used to conduct parametric studies that encompassed greater variations of system parameters than was feasible to investigate experimentally.

Results from this study revealed that the flexural capacity of concrete elements with mixed reinforcement is reduced as U/T increases. Based on the collected experimental data and finite element results, an empirical method for computing the flexural strength of beams with mixed reinforcement and a linear transition in resistance factor were proposed, which involved adjustments to current simplified provisions in AASHTO-LRFD (2020). Additionally, this study found that bonded strand rupture occurred in full-scale laboratory specimens with U/T of 0.4 and 0.7. A new requirement for a minimum amount of bonded prestressing reinforcement has been developed to reduce the possibility of strand rupture when ultimate strength is reached.

TABLE OF CONTENTS

LIST OF FIGURES

xvii

LIST OF TABLES

CHAPTER 1
INTRODUCTION

Prestressed concrete is widely used as a cost-effective and efficient method of bridge construction and offers a number of unique advantages over other systems. Prestressed concrete may be either pretensioned, post-tensioned, or both. Pretensioned concrete requires the stressing of prestressing strands prior to placement of concrete and is typically facilitated by constructing in a fixed location, where abutments have been constructed, to hold the pretensioning force. Precast, prestressed concrete bridge girders are commonly constructed using this method. Post-tensioned concrete is constructed by first casting concrete in place with anchorages and embedded ducts that hold bundles of individual strands; such an assembly is denoted as a post-tensioning (PT) tendon. PT tendons are stressed after the concrete strength has reached a level at which it can effectively resist the prestressing forces. Multi-strand post-tensioning tendons have typically been the primary method of prestressing long-span spliced-girder and box-girder bridges in Florida.

Post-tensioning tendons may be either bonded or unbonded. To be considered bonded, a tendon duct must be cast into the concrete and cementitious grout must be injected into the duct. The hardened grout provides bond transfer and corrosion protection to the prestressing steel. In contrast, in an unbonded tendon, bond transfer between the tendon and the surrounding material does not occur. Unbonded tendons have historically been used in single-strand post-tensioning tendons primarily used in building construction. In recent years, however, this approach has been applied to multi-strand tendons in which a flexible filler, in lieu of grout, is injected into the duct of the post-tensioning tendon. The filler provides corrosion protection for the prestressing strands, but does not provide bond, which results in a reduction in moment strength in the section. An advantage of an unbonded tendon is that it is more easily replaced than its bonded counterpart. Additionally, bonded tendons must be cast into a surrounding concrete element whereas this is not a requirement for unbonded tendons.

In recent years, durability issues have arisen in bonded construction due to poor grouting practice or poor material performance. These issues have prompted the Florida Department of Transportation (FDOT) to move toward the use of unbonded tendons with flexible fillers in lieu of cementitious grout to improve tendon durability and to facilitate possible future replacement of damaged or corroded tendons, having concrete components with mixed reinforcement conditions. The 'mixed conditions' concept refers to the use of a combination of unbonded tendons with bonded prestress and/or mild steel reinforcement.

The use of unbonded tendons with flexible fillers is not a wholly new idea; they have been in regular use in the nuclear industry for many years and have more recently been used in post-tensioning tendons for bridges in Europe. However, the decision to use flexible filler has structural implications, thus motivating a reevaluation of the current AASHTO LRFD Bridge Design Specifications (AASHTO, 2020) for post-tensioned structures with unbonded tendons and mixed reinforcement conditions. Research conducted by Brenkus (2016) suggested the use of mixed reinforcement conditions results in members with lower ductility and ultimate flexural strength when compared to fully-bonded members. Furthermore, experimental tests indicated potential for bonded strand rupture on beams with mixed reinforcement conditions (Brenkus et al. 2017a).

The study described in this report focused on evaluating the flexural behavior of prestressed concrete beams with bonded and unbonded tendons, with particular emphasis on determining how mixed conditions influence post-tensioned system behavior. Guidelines for design and analysis of concrete members with mixed reinforcement conditions were developed based on results obtained from experimental tests of full-scale beam specimens and parametric studies conducted using finite element analyses (FEA).

CHAPTER 2
LITERATURE REVIEW

The following sections summarize a review of related literature for the present study. The literature review was conducted with a focus on the flexural behavior of post-tensioned systems with a combination of bonded and unbonded tendons.

2.1 Post-tensioning tendons

Post-tensioning tendons typically consist of single or bundled seven-wire prestressing strands (Figure 2.1). Less commonly, tendons may be composed of bars or bundled wire. Post-tensioning tendons are used extensively in segmental and I-girder bridge construction. To house the post-tensioning tendons, ducts are placed in the concrete during casting. When the concrete surrounding the duct has reached the specified strength, prestressing strands are pushed or pulled through these ducts and are anchored to the concrete at each end of the tendon.
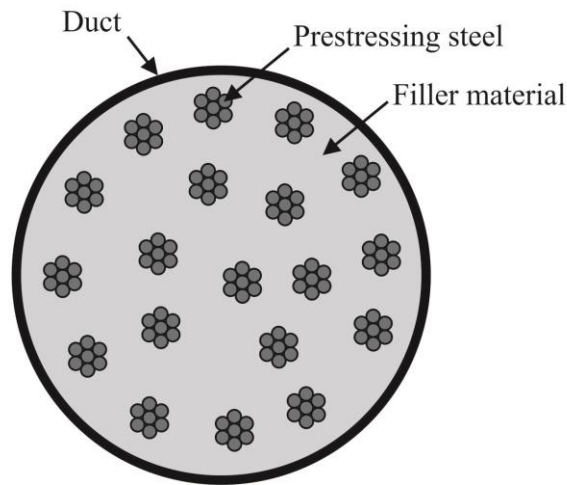
Figure 2.1 Components of a typical post-tensioning tendon

Structural members can be prestressed utilizing either bonded or unbonded tendons, combinations of bonded and unbonded prestress, or with mild reinforcement and unbonded tendons. Each prestressing approach can be categorized based on the contact of the tendon with the surrounding concrete. After installation and stressing of the tendon, the space in the duct is typically injected with a filler material, either flexible filler (unbonded) or cementitious grout (bonded).

Although cementitious grout is the most common filler used in the United States, inspections have revealed corrosion and durability issues that have motivated the transition to flexible fillers. The latter option provides an alternative to cementitious grout in unbonded tendons but is not capable of transferring force from the tendon to the surrounding concrete through bond stresses. Currently, there is limited experience using flexible fillers in the United States and the only flexible fillers currently approved by FDOT are microcrystalline petroleum-based waxes (Cox, 2017). These waxes are heated until they liquefy and are then injected to fill the post-tensioning tendon duct.

Wax fillers possess hydrophobic and metal adhering properties (PTI, 2015) which serve to protect the prestressing tendons from exposure to water. Additionally, one of the main advantages of flexible filler is that its use makes it easier to replace tendons, should the need arise. Use of flexible filler also allows tendons to be re-stressed later during the service life of a bridge structure (PTI, 2015). While there is not currently a national standard specification for these materials, and

their use in bridge construction is not typical in the United States, grease has previously been used in nuclear containment structures (PTI, 2015). However, outside the US, the use of flexible fillers in bridge applications has been increasing since the 1970s, most notably in France (Brenkus et al., 2018).

2.1.1 Bonded tendons

Bonded PT tendons are injected with cementitious grout, which, ideally, provides both bond and corrosion protection to the prestressing steel (Figures 2.2 and 2.3). To be considered bonded, the tendon must be cast inside the concrete element. Hence, this situation is also classified as an internal tendon. These two conditions ensure that bond transfer occurs between the prestressing steel and the surrounding concrete section. Tendons surrounded by cementitious grout but placed outside the concrete cross-section are known as external tendons and are considered unbonded.
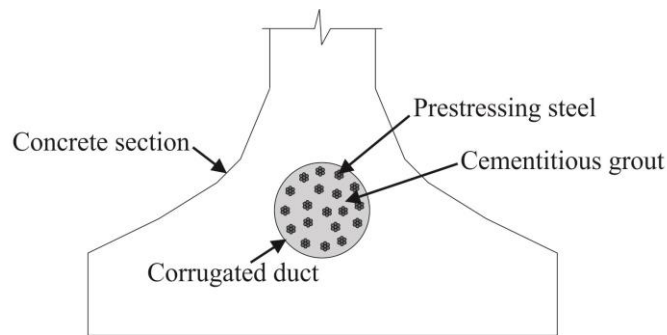
Figure 2.2 Components of bonded tendons

(a)

(b)   (c)

Figure 2.3 Cementitious grout: (a) inspection of a post-tensioned tendon (Vector Corrosion Technologies, 2014) and sections of a dissected mock-up at (b) anchorage and (c) at an intermediate location (DSI, 2000)

3

2.1.2 Unbonded tendons

Some unbonded tendons make use of non-cementitious materials that provide protection against corrosion without bond. In general, three non-cementitious pliable filler materials can be used for corrosion protection: petroleum wax, grease, and gel. Currently, FDOT allows the use of petroleum wax, but not grease or gel. An unbonded tendon is not bonded with the concrete cross-section at any location, but instead imparts prestressing force to the concrete over the tendon profile or at deviators and anchorages.

<u>Internal tendons</u>

Prestressing tendons located within the concrete cross-section are known as internal tendons. These are placed inside ducts cast within the concrete elements. In the U.S., internal unbonded tendons are found primarily in building construction. For instance, individually sheathed prestressing strands are widely used in post-tensioned flat slabs.

<u>External tendons</u>

Tendons placed outside of the concrete section are known as external tendons (Figure 2.4). In recent years, the use of unbonded external tendons in bridge repair and maintenance has increased, particularly for segmental box girders bridges (Brenkus et al., 2017a). External tendons are most commonly placed inside segmental box girders and impart prestressing at anchor points and transverse forces at deviation saddles (hereinafter referred to as deviators). External tendons combine characteristics of both bonded and unbonded tendons. In the U.S., external tendons are typically enclosed in a high-density polyethylene (HDPE) duct and injected with high-performance cementitious grout. At deviators, however, embedded steel pipes are used to facilitate the transfer of force between the tendon and concrete as the tendon angle changes. In lieu of steel pipes, FDOT also allows the use of diabolo deviators, which improve the replaceability of the tendons. Diabolos are openings formed in the deviator that flare open at the ends allowing the tendons to enter or exit the deviator over a range of angles in plan view and elevation. However, as depicted in Figure 2.5, diabolos are structurally different from individual pre-bent pipes that bear evenly over a uniform radius and the actual contact length in diabolos varies depending on the minimum radius of the flare (FDOT, 2002).

| (a) | (b) |

Figure 2.4 External tendons: (a) East Tsing Yi Viaduct, Hong Kong, (b) Gautrain Rapid Rail Link, South Africa (VSL International Ltd., 2009)
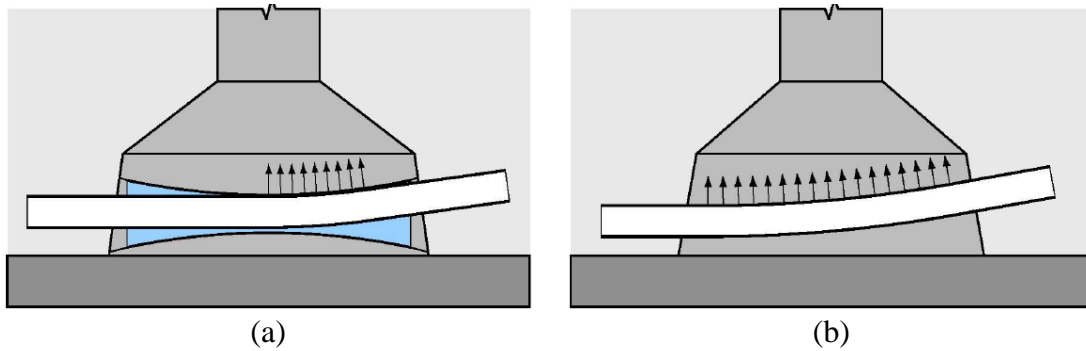
Figure 2.5 Comparison of (a) diabolo deviator and (b) deviator with curved pipe pre-bent to radius (FDOT, 2002)

2.2 Flexural behavior

This section addresses the flexural behavior for different conditions of prestressing in concrete members. This includes bonded tendons, unbonded tendons, and the combination of both bonded and unbonded tendons as well as the use of mild reinforcement in members with prestressing steel. Generally, design specifications recommend the use of strain compatibility analyses for members with bonded reinforcement (prestressed or non-prestressed). However, this approach is not valid for members with unbonded tendons. Therefore, empirical methods have typically been used by design specifications to allow computation of the stress in unbonded tendons at nominal flexural resistance.

2.2.1 Bonded tendons

The stress in a bonded tendon at ultimate flexural resistance can be evaluated through basic principles. The fundamental assumption that the prestressing steel is perfectly bonded to the concrete is a prerequisite for this approach and allows the flexural resistance to be computed at a chosen section. When tendons are fully bonded, tendon strains are the same as the concrete section strains at corresponding locations.

When the stress on the tension side of the prestressed concrete member exceeds the tensile strength of the concrete, the section will crack. As the applied load is increased, stress increases markedly in the bonded steel near the crack. If the section is tension-controlled, then the tendon will yield. Nominal resistance is signaled by either the concrete in the compression zone reaching the maximum useable compressive strain, or prestressing steel reaching the rupture strain. Steel rupture is not a typical failure mode and would occur only in sections with small amounts of prestressing steel.

If the section is compression-controlled, then the concrete will reach the maximum useable compressive strain signaling that the nominal resistance has been reached. Section behavior beyond nominal resistance depends on the ductility of the section. Under-reinforced sections typically have more displacement capacity than over-reinforced sections; they are able to undergo continued deformation while maintaining a majority of the peak strength. Selected details relating to the flexural behavior of bonded prestressed concrete members are presented in Figure 2.6 (Naaman, 2012). Additionally, Figure 2.7 illustrates how stresses and strains in the bonded prestressed tendon and concrete vary with applied load.

5
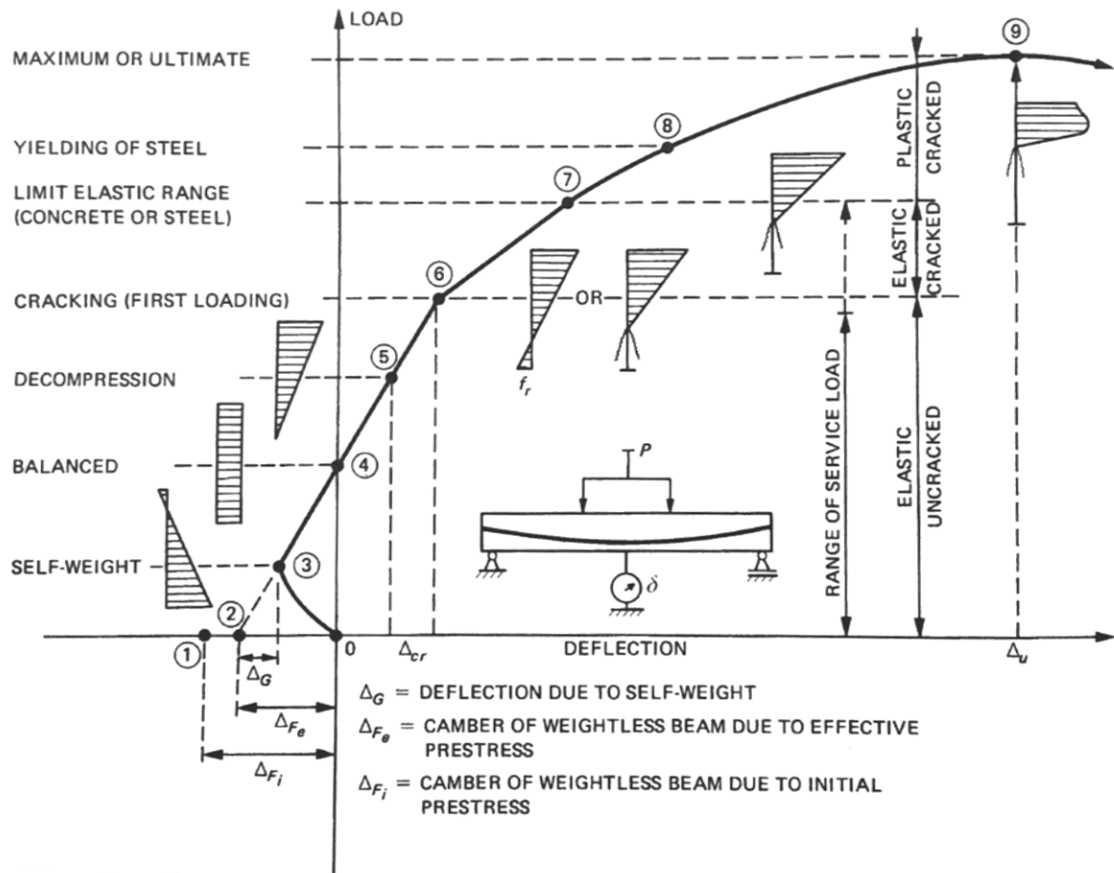
Figure 2.6 Load deflection curve of under-reinforced prestressed concrete beam with bonded tendons (Naaman, 2012)

As the relationship between the strain of concrete at the extreme compressive fiber and the strain of reinforcing steel at ultimate flexural capacity determines the type of failure for the section, one of the following flexural behaviors at ultimate could be expected depending on the amount of reinforcing steel used in the section:

- If the amount of reinforcement is small enough relative to the area of concrete (reinforcement ratio) such that the steel yields before the extreme compression fiber on the concrete reaches ultimate strain ($\varepsilon_c = 0.003$), the section is considered under-reinforced. Under-reinforced beams present a ductile behavior and such sections are defined as "tension-controlled". This type of behavior is recommended and can be observed in bonded tendons.

- A balanced strain condition in the section is achieved when the reinforcement ratio in the section allows the steel to reach yielding simultaneously when the concrete in the extreme compressive fiber reaches the ultimate strain.

- If the reinforcement ratio is large enough that the strain in the concrete extreme compressive fiber reaches the ultimate condition before yielding of the reinforcing steel, the section is considered over-reinforced and is typically defined as "compression-controlled".

6
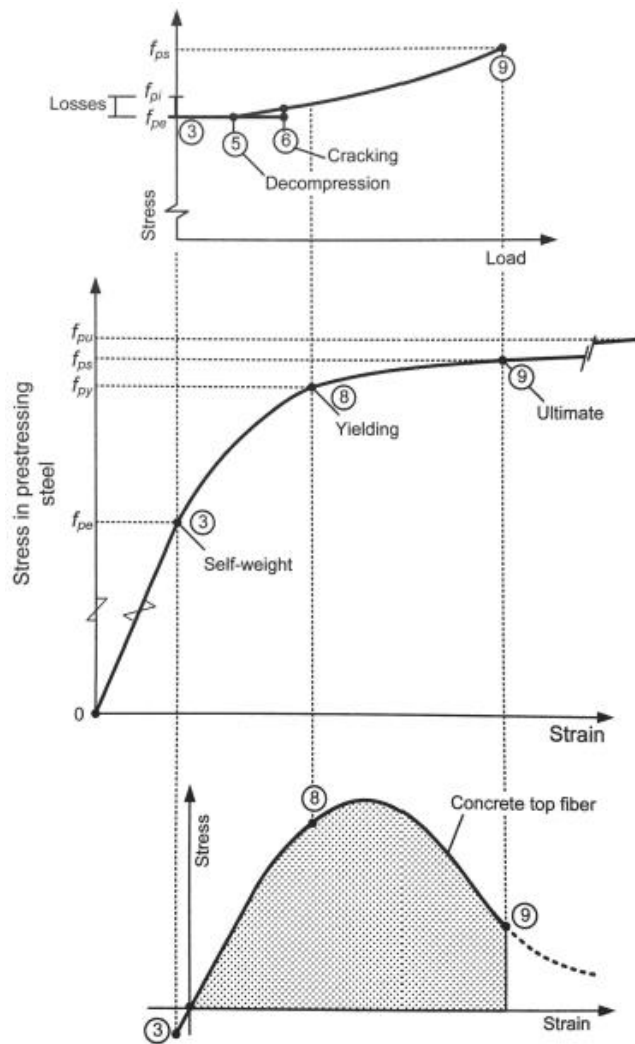
Figure 2.7 Variation of stress and strain of bonded prestressed tendon and concrete
with applied load (Naaman, 2012)

2.2.2 Unbonded tendons

For unbonded tendons, strain in the steel and strain in the adjacent concrete develop independently. Figure 2.8 shows a simply supported beam with a single unbonded tendon. As load is increased, the flexural tension in the bottom of the beam eventually exceeds the precompression and tensile strength of the concrete, typically resulting in a single crack at midspan. Prior to cracking, the stress along the length of the tendon is nearly constant. After cracking, a mechanism forms in which the crack width continues to grow as further displacement is imposed. Strain caused by the crack opening is distributed over the full length of the tendon. Though cracks may be relatively wide (compared with those seen in bonded members), the resulting increase in overall tendon force is comparatively small, which results in a modest increase in load following cracking (Figure 2.9). This difference results in higher ultimate flexural resistances at smaller deflections for bonded tendon members versus larger crack opening and lower ultimate strength for unbonded tendon members (Gerber and Burns, 1971). For unbonded tendons, tendon stress at ultimate section flexural capacity is most likely to remain below yielding. To obtain unbonded flexural resistance equal to that of an identically sized section using a bonded tendon system, additional unbonded tendons or mild steel (or both) are necessary.
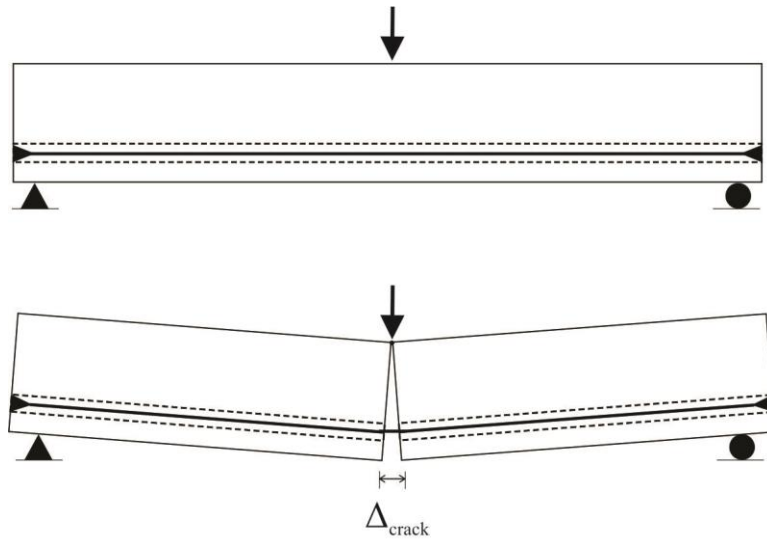
Figure 2.8 Crack opening in simply supported beam with unbonded tendon
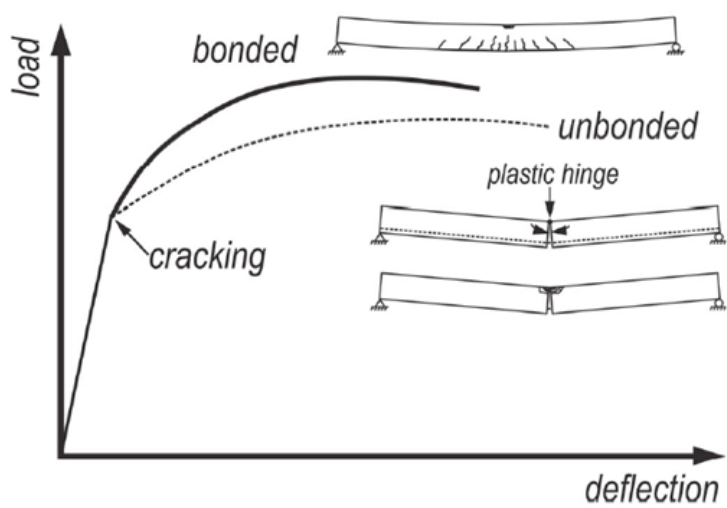
Figure 2.9 Theoretical bonded and unbonded behavior (Brenkus et al., 2017b)

Since unbonded tendons transfer stress only at anchorages and deviation points, consideration must be given to tendon profile, load pattern, friction, and member geometry. The tendon stress, in other words, is dependent on the deformation of the entire member and assumptions concerning friction and tendon contact within the member.

The behaviors of internal and external unbonded tendons are conceptually similar to each other. The principal difference between both configurations relates to the deflected shape of the beam and the tendon. Internal unbonded tendons are forced to deflect in the same manner as the concrete beam within which the tendon is embedded. In contrast, the deflected shape of external unbonded tendons is restricted only at the deviator locations (Alkhairi and Naaman, 1993). It is important to note that external tendons are not necessarily completely unbonded since they may be bonded at the deviators. In externally prestressed members, the profile of the external tendon and that of the deformed beam may differ, consequently there may be a reduction of effective depth of reinforcement (Gauvreau, 1993). In contrast to systems that use unbonded internal prestressed tendons, second-order effects influence the flexural resistance of externally prestressed

8

members and become particularly significant when no deviators are used in the critical region of the member (Harajli et al., 2002).

2.2.3 Mixed reinforcement conditions

Though much research has been done on members with either bonded or unbonded tendons, members with mixtures of bonded and unbonded tendons have received comparatively less consideration in the literature or in experimental testing. Structural components containing both bonded and unbonded tendons have not yet been adequately addressed by code writing bodies, nor has a model for determining the ultimate strength of sections with mixed reinforcement been adopted.

<u>Structural components with bonded and unbonded tendons</u>

In concrete sections reinforced with mixed bonded and unbonded tendons, full bond is assumed between bonded tendons and surrounding concrete and the ultimate stress in the bonded tendons are calculated using section analysis. However, analysis based on overall deformation of the structural system is required to determine the ultimate stress in unbonded tendons (Roberts-Wollmann et al., 2005).

Compared to bonded tendons, the average stress in prestressing steel at the time for which the nominal resistance of the structural component is required (f_{ps}) is smaller in unbonded tendons. As a result, to resist the same moment, the required area of steel will be larger in components with mixed reinforcement. In addition, the stresses in the unbonded tendons are most likely to remain below yield while the bonded tendons exceed yield (Naaman, 2012). This can be clearly seen in the load-deflection curve depicted in Figure 2.9 as the unbonded curve falls below the bonded one.

Seismic (cyclic) tests by Megally et al. (2001) conducted on precast segmental bridge superstructures with different post-tensioning systems (internal, external, and mixed) showed greater moment strength with internal bonded tendons versus those with either external tendons or those with a mixture of external and internal tendons. Internal tendons were grouted, but external tendons were left ungrouted to observe behavior during testing, to protect strain gages, and to inspect for wire failures; the tested specimens could, consequently, be considered fully unbonded. The specimen with unbonded external tendons exhibited increased ductility relative to the specimen with internal, fully bonded tendons. However, Megally et al. (2001) suggested that a combination of internal bonded tendons and external tendons should not be used in high seismic areas as the combination neither improves the strength, nor the ductility when compared to members with only bonded internal tendons.

Brenkus et al. (2017b) conducted experiments on prestressed concrete beams with pretensioned and post-tensioned tendons (bonded and unbonded). The post-tensioned tendon of one of the beams was fully bonded to serve as a control specimen (IGS); this was subjected to ultimate flexural testing using a three-point bending setup. Initially, the specimen developed a flexural crack near midspan. However, as loading progressed, cracks were noted to be uniformly distributed beneath the load point as shown in Figure 2.10a. The specimen exhibited ductile failure with the strand yielding prior to deck crushing. Figure 2.11a presents the stress increase in the fully bonded specimen. In the same study, Brenkus et al. (2017b) computed the flexural resistance of the grouted member in accordance with the AASHTO-LRFD (AASHTO, 2016) provisions for bonded tendons. The experimentally determined specimen strength was found to slightly exceed the flexural resistance calculated using AASHTO-LRFD by approximately 5%.

Brenkus et al. (2017b) also performed experiments on beams with unbonded post-tensioned tendons. One of the specimens (IWS) was loaded using a three-point bending setup while the other (IWC) was tested in four-point bending (constant moment). The specimens initially

developed a flexural crack near midspan, but as loading progressed the specimens exhibited a behavior more typical of unbonded beams: fewer cracks developed overall, and those cracks opened widely as the loading progressed (2.10 b and c). The strain of the bonded reinforcement was concentrated near the primary crack leading to strand rupture when ultimate flexural section resistance was reached. The relatively limited crack distribution is attributed to the low levels of bonded reinforcement. Beams with unbonded tendons mixed with lightly bonded pretensioned steel were found to exhibit lower ductility and flexural resistance when compared to fully bonded members. Figure 2.11 (b and c) shows the increase of stress in both specimens. When tested under a single point load, the specimen reached the maximum load before the tendon stress reached yield strength. Conversely, the beam under constant moment developed a wider distribution of cracks. The constant moment region was found to create a longer hinge length than a single concentrated load and the tendon in that specimen yielded. It was found that the hinge length, which affects the rotational capacity of the hinge, has implications for the flexural behavior and deflection of members with mixed tendons. Under mixed conditions, the hinge length was less than that assumed in the formulation of the unbonded tendon stress equation given in AASHTO-LRFD (Equation 5.7.3.1.2-1 in AASHTO, 2016; Equation 5.6.3.1.2-1 in AASHTO, 2020), especially for members with low quantities of bonded prestressing steel. Erroneous overestimation of the plastic hinge length could lead to a lower estimate of the unbonded tendon stress in calculations of nominal flexural resistance.

(a)

(b)

(c)
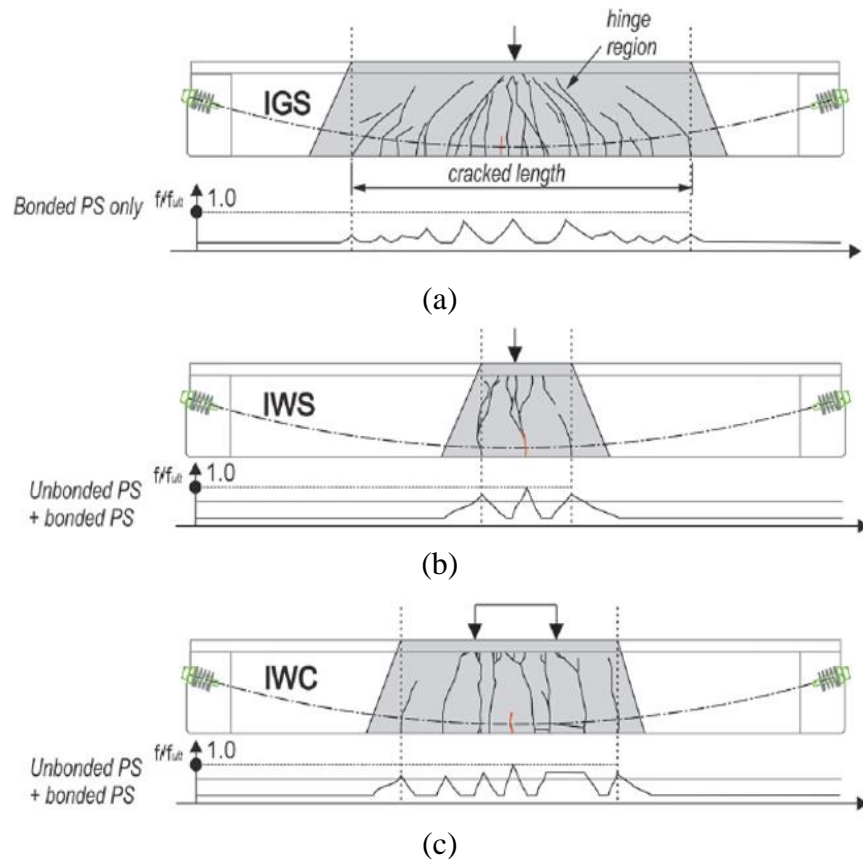
Figure 2.10 Crack distribution and plastic hinge region for beam specimens with bonded and unbonded tendons: (a) IGS, (b) IWS, and (c) IWC (Brenkus et al., 2017b)
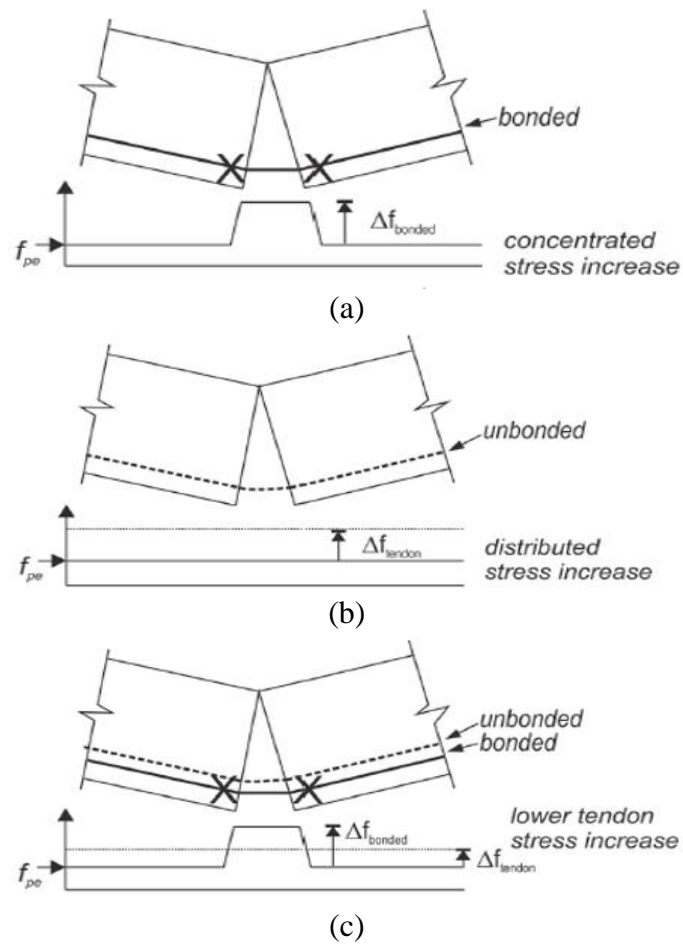
Figure 2.11 Stress increase in members with bonded and unbonded tendons: (a) IGS, (b) IWS, and (c) IWC (Brenkus et al., 2017b)

Structural components with prestressed and mild reinforcing steel

Mild steel (bonded) bars are typically added to prestressed concrete, composed mainly of unbonded tendons, to improve both cracking behavior and reserve capacity—defined as the ability to carry load after concrete failure, also referred to as primary failure. This approach has been evaluated by several researchers. Gerber and Burns (1971) observed that sections with bonded tendons have an increased maximum reserve capacity when compared to sections with only unbonded tendons. Harajli et al. 2002 conducted experimental testing of specimens with external unbonded tendons and mild reinforcement. Improved crack distribution was observed with an increase in the area of mild steel reinforcement. Using higher ratios of mild steel also resulted in an improved spread of plasticity. The mild reinforcement of all the test specimens yielded before flexural failure was reached, and all failures were ductile in nature. Conversely, increasing the area of external unbonded tendons lead to a reduction in ultimate load carrying capacity, due to cracks being relatively more concentrated.

In 1971, Mattock et al. also conducted a comparative study of grouted and unbonded (ungrouted) post-tensioned concrete beams, with the primary aim of investigating the effect of varying the amount of non-prestressed bonded reinforcement (in the form of prestressing steel). In addition to the presence (or lack) of bond, other variables in the study included span type (simple-span and continuous) and cross-section (rectangular and T-shape). It was found that unbonded post-tensioned beams with the minimum recommended non-prestressed bonded reinforcement had serviceability characteristics, strength, and ductility equal to—or better than—

11

those of comparable bonded PT beams. One of the intents of the study was to confirm the effectiveness of using prestressing strand as auxiliary bonded reinforcement, thus unbonded tendons were combined with bonded strands that were not prestressed (Mattock et al., 1971).

2.3 Approaches to determine nominal flexural resistance

This section outlines empirical design approaches to evaluate ultimate flexural resistance of prestressed concrete beam elements with bonded, unbonded, and mixed reinforcement conditions.

2.3.1 Bonded tendons

For a given prestressed beam (with bonded tendons) of known material properties, cross sectional dimensions, and area of reinforcement, the nominal flexural resistance of the section may be determined using strain compatibility. Two basic assumptions are made: (1) there is a perfect bond between the reinforcing steel and the surrounding concrete, and (2) plane sections remain plane. In addition to these, equilibrium of forces must be satisfied. When computing the resistance of sections with mild steel reinforcement using strain compatibility, the stress-strain relationship is assumed elastic-perfectly plastic. The reinforcement stress remains constant at the yield stress for under-reinforced sections, which simplifies the calculation to a closed-form equation. For materials with nonlinear post-yield behavior, however, the use of strain compatibility requires iteration. As part of the strain compatibility approach, the cumulative strain in the reinforcement due to prestressing, self-weight, and external loads is computed using the geometric relationships within the strain profile.

The concrete stress-strain relationship is typically represented by an equivalent rectangular stress block (Figure 2.12) while the stress-strain curve for the prestressing tendons can be obtained from Equations 2.1 and 2.2.

$$f_{ps} = E_p \varepsilon_{ps} \qquad \text{if } \varepsilon_{ps} \leq \varepsilon_{py} \qquad (2.1)$$

$$f_{ps} = f_{pu} - \frac{0.04}{\varepsilon_{ps} - 0.007} \quad \text{if } \varepsilon_{ps} > \varepsilon_{py} \qquad (2.2)$$

Where:

f_{ps} = stress in prestressing steel

E_p = modulus of elasticity of prestressing steel (28,500 ksi)

ε_{ps} = total strain in prestressing steel

ε_{py} = yield strain of prestressing steel (0.0086 in/in)

f_{pu} = ultimate tensile strength of prestressing steel (270 ksi)

Strain in the prestressing steel can be decomposed into three components: effective strain in the tendon after losses (ε_{pe}), decompression strain (ε_d), and flexural strain (ε_f) caused by applied load. Therefore, the total strain in the tendon is determined as presented in Equations 2.3 to 2.6.
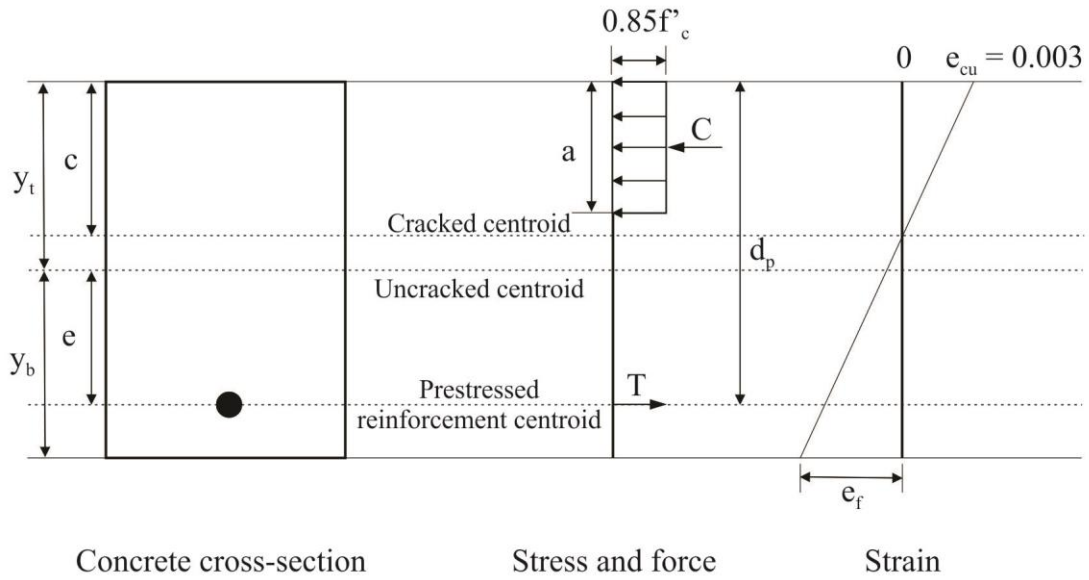
Figure 2.12 Concrete equivalent stress block

$$\varepsilon_{ps} = \varepsilon_{pe} + \varepsilon_d + \varepsilon_f \tag{2.3}$$

$$\varepsilon_{pe} = \frac{f_{pe}}{E_p} \tag{2.4}$$

$$\varepsilon_d = \frac{P_e}{A_p E_c} + \frac{P_e e^2}{I_g E_c} \tag{2.5}$$

$$\varepsilon_f = \varepsilon_{cu} \left(\frac{d_p - c}{c} \right) \tag{2.6}$$

Where:

f_{pe} = effective prestress in tendon (after all losses)

P_e = effective prestress force

A_p = area of prestressing steel

E_c = modulus of elasticity of concrete

e = eccentricity of prestressing tendon

I_g = gross moment of inertia of concrete section

ε_{cu} = concrete strain at nominal resistance (0.003)

d_p = distance from the compression face to the centroid of prestressed reinforcement

c = distance from the compression face to the cracked section centroid

The forces in each component are then calculated using constitutive relationships (Equations 2.7 and 2.8). Equating the tensile and compressive forces to satisfy equilibrium, the stress in the prestressing steel can be calculated using Equation 2.9.

$$T = A_p f_{ps} \tag{2.7}$$

$$C = 0.85 f_c' b a \tag{2.8}$$

13

$$f_{ps} = \frac{0.85 f_c' b a}{A_p} \qquad (2.9)$$

$$a = \frac{A_p f_{ps}}{0.85 f_c' b} \qquad (2.10)$$

$$c = \frac{a}{\beta_1} \qquad (2.11)$$

Where:

b = width of compression zone

a = depth of equivalent rectangular stress block

β_1 = characteristic value of equivalent rectangular stress block (Article 5.6.2.2; AASHTO, 2020)

$$\beta_1 = 0.85 \text{ for } f_c' \leq 4ksi \qquad (2.12)$$

$$\beta_1 = 0.65 \text{ for } f_c' \geq 8ksi \qquad (2.13)$$

$$\beta_1 = 0.85 - 0.05(f_c' - 4) \text{ for } 4ksi \leq f_c' \leq 8ksi \qquad (2.14)$$

Finally, the nominal flexural resistance can be obtained through the use of Equation 2.15.

$$M_n = A_p f_{ps} \left(d_p - \frac{a}{2} \right) \qquad (2.15)$$

2.3.2 Unbonded tendons

Numerous models of varying levels of complexity have been proposed for estimating tendon stress at the ultimate strength condition of members with unbonded tendons, as reviewed by Naaman and Alkhairi (1991a), Roberts-Wollmann et al. (2005), and by Harajli (2006). A recommendation for the calculation of ultimate stresses in unbonded prestressing tendons was made by ACI Subcommittee 423 in 2002 (Naaman et al., 2002) and was proposed as a modification for the ACI Code. A further modification/clarification regarding continuous members was proposed by Harajli (2012). For a comprehensive review of the numerous equations in use for the prediction of f_{ps} at nominal flexural resistance for members with unbonded tendons, the reader is referred to Naaman and Alkhairi (1991b) and Alqam et al. (2020).

To compute the flexural resistance of a beam, the magnitude and position of the resultant concrete compressive force must be known along with the magnitude of the force resultants in the other reinforcement present. Equations have been proposed to predict the maximum tensile stress in unbonded tendons. Harajli (2006) evaluated the proposed equations and found that they differ in the way they account for the main parameters that affect the stress at ultimate. The increase in the tendon stress induced by loading (Δf_{ps}) is influenced by the use of a linear elastic relationship between the stress and strain of the tendon, and the difficulty of quantifying both the plastic region length and the concrete compression strain at ultimate. One of the most important factors that makes the evaluation of stresses in unbonded tendons challenging is that it must be done at the member level rather than at the section level. The problem becomes more complex for multi-span members since the stress at ultimate becomes dependent on the collapse mechanism and the number of developed plastic regions.

<u>Internal unbonded tendons</u>

Naaman and Alkhairi (1991b) proposed that Equation 2.16 be used for unbonded internal tendons. This equation is based on deflection compatibility analysis which is then reduced to a section compatibility analysis using Ω_u and was derived assuming the tendon does not reach yielding.

$$f_{ps} = f_{pe} + \Omega_u E_p \varepsilon_{cu} \left(\frac{d_p}{c} - 1\right)\frac{L_1}{L_2} \leq 0.94 \, f_{py} \tag{2.16}$$

Where:

E_p = modulus elasticity of prestressed reinforcement.

ε_{cu} = failure strain of concrete in compression = 0.003

Ω_u = strain reduction factor

L_1 = sum of lengths of spans loaded with live load and containing tendons (L if one span is loaded)

L_2 = total length of tendons between anchors

The strain reduction factor at ultimate reflects the ratio of average strain increase in the unbonded tendon to the strain increase in the equivalent bonded tendon at the section of maximum moment and depends on the type of loading and the span-to-depth ratio, where:

$$\Omega_u = \frac{5.4}{L/dp}; \text{ for uniform or third point loading} \tag{2.17}$$

$$\Omega_u = \frac{2.6}{L/dp}; \text{ for one point midspan loading} \tag{2.18}$$

For design purposes, the numerators in Equations 2.17 and 2.18 are reduced to 3.0 and 1.5, respectively. This equation was adopted in the first draft of the AASHTO-LRFD (AASHTO, 1994). Although Equation 2.16 was later removed from the AASHTO code, the main advantage was that it accounts for the continuity of members, load conditions, and span-to-depth ratio. Also, it takes into consideration the presence of mild steel reinforcement and the bonded prestressed tendons.

Alqam et al. (2020) created a database using experimental data. This database was then used to test the accuracy of existing equations to predict f_{ps}. Alqam et al. (2020) proposed an equation (2.19) for Ω_u that takes into account the span-to-depth ratio and type of loading.

$$\Omega_u = \alpha \left(\frac{d_{ps} - h/2}{0.25d_{ps}}\right)\left(\mu + \frac{18}{L/d_{ps}}\right) \tag{2.19}$$

For code implementation purposes, Alqam et al. (2020) proposed the coefficients:

$\alpha = 0.05, \mu = 0.10$ for one-point midspan loading

$\alpha = 0.09, \mu = 0.80$ for uniform or third point loading

The stress in prestressing steel can be obtained using Equation 2.16. However, Alqam et al. (2020) proposed an upper bound of 0.86 f_{py} and lower bound as shown in Equation 2.20.

$$f_{ps} \geq f_{pe} + 0.30 f_{py}\bar{\omega}_{pe} \tag{2.20}$$

$$\bar{\omega}_{pe} = \frac{A_{ps}f_{pe} + A_s f_y}{f'_c b d_{ps}} \tag{2.21}$$

<u>External tendons</u>

MacGregor et al. (1989) developed an equation for determining the prestressing steel stress at ultimate flexural capacity based on experimental work. In their approach, strength design of members with unbonded tendons is based on the effective length of the tendons between deviators. The developed equation also included a factor developed by Tam and Pannell (1976) and incorporated the maximum allowable concrete strain allowed by ACI 318 (ACI, 2019). Roberts-Wollmann et al. (2005) confirmed this approach and proposed equations with further verification using more recently collected experimental data. Figure 2.13 shows the failure mechanism and geometry for unbonded tendons at ultimate.
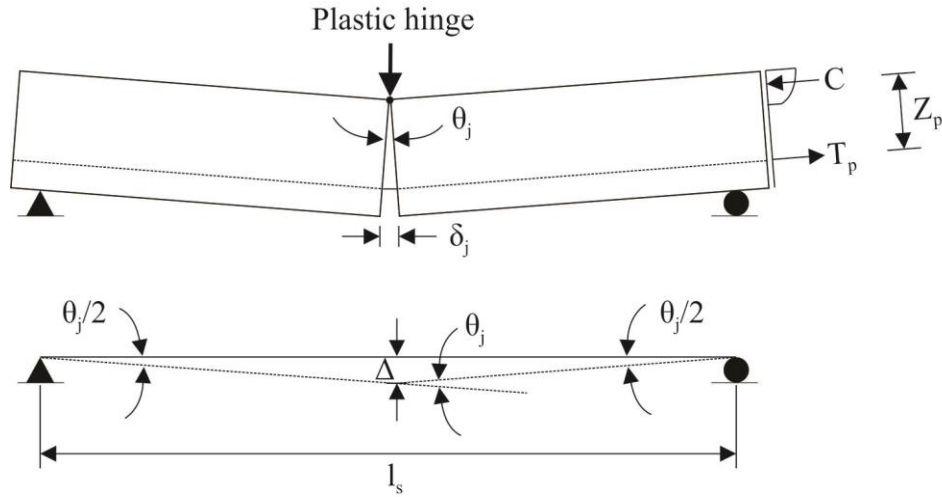
Figure 2.13 Joint mechanism for unbonded tendons

Maximum tendon elongation δ_j (and thereby tendons stress) is related to the ultimate curvature (related to the crushing strength of the concrete), length of plastic hinge, and the depth of the tendon in the system. A derivation of tendon stress follows.

From the rigid body displacement in Figure 2.13, tendon elongation δ_j is

$$\delta_j = \frac{4\Delta}{l_s} Z_p \qquad (2.22)$$

where Z_p is the distance from the compressive force resultant to prestressing tendons; l_s is the length of the tendon segment, and Δ is the vertical displacement at the joint.

From mechanism geometry (Figure 2.13), the angle of joint opening θ_j can be described:

$$\theta_j = \frac{4\Delta}{l_s} \qquad (2.23)$$

Assuming the tendon behaves in elastic-plastic manner, the decompression moment M_d and the plastic moment capacity of the tendon M are defined:

$$M_d = A_{ps} f_{pe} Z_p \qquad (2.24)$$

$$M = A_{ps} f_{pp} Z_p \qquad (2.25)$$

where A_{ps} is the area of the prestressing steel, f_{pe} is the steel stress corresponding to decompression of the section, and f_{pp} is the steel stress corresponding to plasticization of tendon.

Incorporating plastic hinge behavior, the change in tendon force at a plastic hinge is shown in Figure 2.14 (MacGregor et al., 1989). Equation 2.26 describes ΔT_j, the difference in the tendon

16

force between decompression and plasticization. Equation 2.27 describes T_e, the force in the tendon at decompression (also the effective tendon force due to prestressing of the tendon).
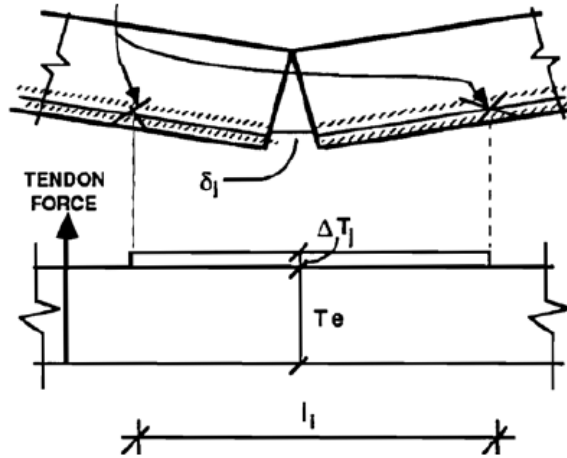
Figure 2.14 Tendon force versus curve length (MacGregor at al., 1989)

$$\Delta T_j = \frac{M - M_d}{Z_p} \tag{2.26}$$

$$T_e = A_{ps} f_{pe} \tag{2.27}$$

Assuming small deflection for conditions where the tendon force exceeds that required for decompression, from Figure 2.14 the tendon elongation can be written:

$$\delta_j = \frac{\Delta T_j l_i}{A_{ps} E_p} \tag{2.28}$$

Equating Equations 2.22 and 2.28:

$$\frac{\Delta T_j l_i}{A_{ps} E_p} = \frac{4\Delta}{l_s} Z_p \tag{2.29}$$

Replacing ΔT_j from Equation 2.26 and rearranging:

$$\Delta = \frac{l_i l_s}{4 A_{ps} E_p Z_p^2} (M - M_d) \tag{2.30}$$

Incorporating Equations 2.25 and 2.24, the vertical deflection is written:

$$\Delta = \frac{l_i l_s}{4 E_p Z_p} \left(f_{pp} - f_{pe} \right) \tag{2.31}$$

Virlogeux considered concentrated rotations to be distributed over a plastic hinge length equal to twice the distance from the resultant compressive force to the center of passive reinforcement in the tension side of the segment (Virlogeux, 1983; Figure 2.15); this corresponds to a diffusion of the compressive force by 45 degree angles. The curvature is assumed to be constant over the hinge length. Ultimate curvature is determined by limiting the maximum concrete compressive strain to the concrete crushing strain. The elongation at the plastic hinge δ_h can be expressed in terms of maximum curvature φ_m, the distance between the compressive force resultant and prestressing tendons Z_p, and the distance to the passive segment reinforcement Z_s.
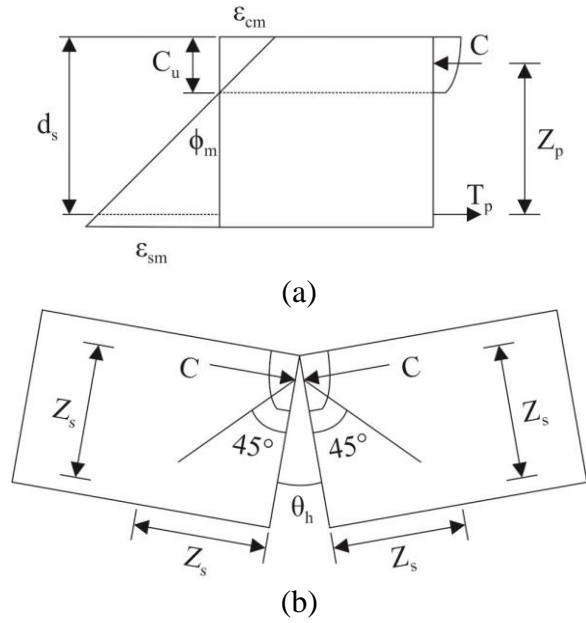
Figure 2.15 Unbonded diagram of (a) strain and force, and (b) joint opening

Calculating the tendon elongation along the hinge portion:

$$\delta_h = \int_{-Z_s}^{Z_s} \phi_m Z_p(x) \left(\frac{x}{Z_s}\right) \partial x \qquad (2.32)$$

Assuming constant eccentricity along the hinge length, therefore $Z_p(x)$=constant.

$$\delta_h = \frac{2\phi_m Z_p}{Z_s} \int_0^{Z_s}(x)\, \partial x = \phi_m Z_p Z_s \qquad (2.33)$$

From the rigid body plastic mechanism, the limiting mid-span deflection shall be

$$\Delta_m = \frac{\phi_m Z_s l_s}{4} \qquad (2.34)$$

Combining Equations 2.31 and 2.34:

$$\frac{\phi_m Z_s l_s}{4} = \frac{l_i l_s}{4 E_p Z_p}\left(f_{pp} - f_{pe}\right) \qquad (2.35)$$

Therefore, the steel stress corresponding to plasticization of tendon:

$$f_{pp} = f_{pe} + \frac{\phi_m Z_s E_p Z_p}{l_i} \qquad (2.36)$$

Where the maximum curvature:

$$\phi_m = \frac{\varepsilon_{cm} + \varepsilon_{sm}}{d_s} \qquad (2.37)$$

Where ε_{cm} is the concrete strain and ε_{sm} is the strain in prestressing steel. The strain in the steel is much greater than the strain in the concrete and hence Equation 2.37 can be simplified:

$$\phi_m = \frac{\varepsilon_{sm}}{d_s} \qquad (2.38)$$

Substituting Equation 2.38 into Equation 2.36, and assuming $d_s = Z_s$:

$$f_{pp} = f_{pe} + \frac{\varepsilon_{sm} E_p Z_p}{l_i} \qquad (2.39)$$

From the strain diagram Figure 2.15 (a):

18

$$\varepsilon_{sm} = \frac{\varepsilon_{cm}}{C_u}(d_s - C_u) \tag{2.40}$$

The tendon stress equation then reduces to

$$f_{pp} = f_{pe} + \frac{Z_p}{C_u}\varepsilon_{cm}E_p\frac{d_s - C_u}{l_i} \tag{2.41}$$

Tam and Pannell (1976) modified Equation 2.41 and presented an equation based on maximum concrete compressive strain and the neutral axis depth, assuming the tendons have yielded. The equation is given by

$$f_{ps} = f_{pe} + \psi\varepsilon_{cu}E_p\frac{d_p - C_y}{l_i} \tag{2.42}$$

where d_p is depth of prestressing steel, c_y is the neutral axis depth considering the tendons have yielded. Considering ψ=10.5 (found experimentally by Tam and Pannell, 1976), ε_{cu}=0.003 (limiting concrete compressive strain), E_p is the modulus of elasticity of prestressing steel (28,000 ksi):

$$f_{ps} = f_{pe} + 882\frac{d_p - C_y}{l_i} \tag{2.43}$$

2.3.3 Mixed reinforcement conditions

<u>Components with bonded and unbonded tendons</u>

Although limited, experimental investigations incorporating the use of prestressed concrete members with both bonded and unbonded tendons have typically been conducted as a counterpoint to the primary condition under investigation.

MacGregor et al. (1989) conducted flexural testing of quarter-scale, precast segmental concrete box girder continuous span specimens to assess flexural resistance in specimens with external tendons and in specimens with mixed internal and external tendons (MacGregor et al., 1989; Roberts-Wollmann et al. 2005). Based on this work, a prediction equation was developed for estimating tendon stresses at ultimate in members with only unbonded tendons. This prediction equation was later adopted into the AASHTO Guide Specification for the Design and Construction of Segmental Concrete Bridges (AASHTO, 2014a) and into the AASHTO-LRFD Bridge Design Specifications (AASHTO, 2014b; Roberts-Wollmann et al., 2005).

MacGregor et al. (1989) compared the moment-deflection response for three tested girders versus the theoretical response of a girder with only internal tendons, as shown in Figure 2.16. Prior to cracking, the stiffness of each system was comparable; after cracking, the behavior differed as the stiffness changed. The differences in stiffness, however, were slight until the specimens neared the ultimate strength. A section with both external and internal tendons had marginally greater flexural resistance and increased ductility compared to the specimens with only external tendons. For sections with external tendons only, the ultimate moment strength of the section with unbonded (greased) external tendons was slightly less than that of the section with only bonded external tendons. MacGregor noted that members with both external and internal tendons did not offer significant improvements to either ultimate strength or deflection.

Gauvreau (1993) proposed a model for the rational calculation of tendon stress at ultimate for components with bonded reinforcement, unbonded tendons, or both, based on a truss model with explicit consideration of the angle of inclination of the internal concrete compression chords. The approach relates the global structural deformations (used to calculate the elongation of the unbonded prestressing steel) to the strain state corresponding to the internal forces in the truss at any given section. The proposed method was compared with experimental load tests of eight

19

simply-supported concrete girders. The rational approach from Gauvreau has not been incorporated into code bodies.
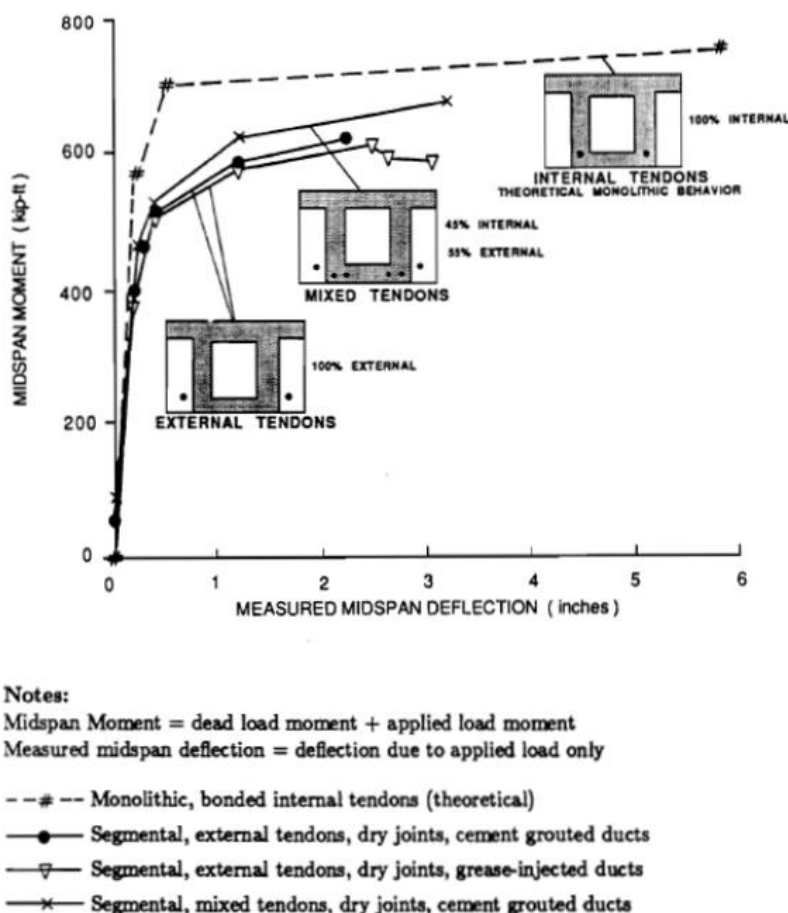
Figure 2.16 Moment-deflection response for testing specimens (MacGregor et al., 1989)

Components with prestressed and mild reinforcing steel

Gerber and Burns (1971) recommended the use of supplementary reinforcement to increase the maximum reserve capacity of unbonded systems, as well as to control cracking. Burns and Hemakom (1985) recommended a minimum percentage of mild reinforcement; this recommendation has since been incorporated into ACI 318 (ACI, 2019). It was found that providing the minimum bonded reinforcement helps to achieve an adequate performance of the member and to control the widths and spacing of cracks due to overload, shrinkage and/or temperature.

In the case of having both unbonded and mild steel reinforcement in the section, the moment arm $\left(d_p - \frac{c}{2}\right)$ can be evaluated using force equilibrium after f_{ps} is evaluated using the proposed design equations. The arm is then used to evaluate the flexural resistance at ultimate.

Several recent investigations have provided models or inspection techniques for predicting tendon stress at ultimate for cases with non-prestressed reinforcing (mild) steel and unbonded tendons, a condition which is similar to the one considered in the present study. For example, Ozkul et al. (2008) presented a rational approach for predicting unbonded tendon stress, considering cases with non-prestressed reinforcing steel (mild) with unbonded tendons. The methodology proposed by Ozkul et al. (2008) considers both the beam and the tendon as a truss-beam system, which allows for the use of equilibrium and compatibility equations, and the law of

20

conservation of energy. The described model can be used to calculate the stress in an unbonded tendon, including when bonded tendons are present.

2.4 Design specifications for tendon stress at nominal flexural resistance

In the United States, post-tensioning systems have been used with either bonded or unbonded tendons for decades. However, for future construction projects, the FDOT intends to use concrete components with a mixture of unbonded tendons and bonded prestress and/or mild steel reinforcement. A provision for components with bonded and unbonded tendons was recently added to the AASHTO-LRFD Bridge Design Specifications (AASHTO, 2014b). In spite of this, the mixed design situation has not yet been common in practice and has not been investigated in depth.

This section presents a review of the current code or standard provisions regarding the use of bonded and unbonded tendons and, particularly, mixed conditions. Both the AASHTO-LRFD Bridge Design Specifications and ACI 318-14 were considered. The review also encompassed provisions available in countries other than the United States where the use of mixed tendons has been increasing significantly during the past decades. These included the Canadian Code, the Eurocode, the Australian Standard, and Japanese Guidelines.

2.4.1 AASHTO-LRFD 2020

The AASHTO-LRFD Bridge Design Specifications (AASHTO, 2020) include separate provisions for members with bonded prestressing, with unbonded tendons, or with mixed bonded and unbonded tendons. For members with bonded tendons, tendon stress is estimated when the effective prestressing is at least $0.5 f_{pu}$ using the provisions from Article 5.6.3.1.1:

$$f_{ps} = f_{pu}\left[1 - k\left(\frac{c}{d_p}\right)\right] \tag{2.44}$$

$$k = 2\left[1.04 - \frac{f_{py}}{f_{pu}}\right] \tag{2.45}$$

where f_{pu} is the specified tensile strength of prestressing steel (ksi) and f_{py} is the yield strength of the prestressing steel (ksi).

However, the strain compatibility approach may be used when more precise calculations are required (Article 5.6.3.2.5; AASHTO, 2020).

The current AASHTO-LRFD design provisions (AASHTO, 2020) for unbonded tendons are based on equations developed by MacGregor et al. (1989). For members with unbonded tendons, AASHTO-LRFD design guidance considers the global deformation of the flexural member, assuming the formation of a single hinge (Article 5.6.3.1.2; AASHTO, 2020). The derivation of the design equation for flexural resistance of members with unbonded tendons considers the global displacement of the member but does not consider bonded reinforcement (AASHTO, 2020). Equation 2.43 was modified into 2.46 and presented by MacGregor et al. (1989). The latter provides the tendon stress at ultimate strength for an unbonded tendon.

$$f_{ps} = f_{pe} + 900\left(\frac{d_p - c}{l_e}\right) \tag{2.46}$$

where f_{pe} is the effective stress in the prestressing steel at the section under consideration after all losses (ksi); d_p is the depth of the prestressing strand (in.); c is the distance from extreme compression fiber to the neutral axis assuming the tendon prestressing steel has yielded (in.); and l_e is the effective tendon length (in.), which is given by Equation 2.47:

$$l_e = \frac{l_i}{1 + \frac{N_s}{2}} \tag{2.47}$$

where l_i is the length of tendon between anchorages, and N_s is the number of plastic hinges at supports (in an assumed failure mechanism) that are crossed by a tendon.

The mixed condition of components with both bonded and unbonded tendons is treated only briefly in the current AASHTO-LRFD code (AASHTO, 2020), without expressly described justification. Section 5.6.3.1.3 states that either a "simplified" or a "detailed" approach may be undertaken by the designer to assess the unbonded and bonded steel stress. The guidance given for the detailed analysis consists of a statement that the designer "consider both the strain compatibility of the bonded strand and the global displacement compatibility between bonded sections of the unbonded tendon when considering the stress in the unbonded tendon". Bonded sections of unbonded tendons may be anchorage points and any bonded section, such as deviators. A second provision allows for a "conservative" simplified estimation with the following method: 1) estimate the strength contribution from the unbonded tendon as the effective prestress after losses f_{pe}, and 2) determine the force in the combined tendons by replacing the term $A_{ps}f_{pu}$ in Equations 5.6.3.1.1-3 and 5.6.3.1.1-4 with $A_{psb}f_{pu} + A_{psu}f_{pe}$.

Parsons Brinckerhoff (2015) evaluated the stress in unbonded tendons at ultimate limit state comparing code provisions to non-linear finite element analyses and recommended the use of AASHTO-LRFD equations as they take into account the mode of failure of the overall system. However, for beams with both bonded and unbonded tendons, Parsons Brinckerhoff (2015) made use of $\Delta f_{psu} \neq 0$ in calculations for the depth of the neutral axis (c) and moment capacity (M_n) instead of just using $f_{ps} = f_{pe}$ as specified by AASHTO-LRFD.

2.4.2 FDOT Structures Manual

As part of the FDOT Structures Manual (FDOT Topic No. 625-020-018), the Structures Design Guidelines (SDG, 2021) provide technical design criteria, engineering standards, and guidelines for structures designed for the Florida Department of Transportation. SDG (2021) also includes additions or modifications to the requirements of the AASHTO LRFD Bridge Design Specifications.

General requirements for post-tensioned structures are comprised in Sections 1.11 and 4.5 of the SDG (2021). Meanwhile, Sections 4.6, 4.7, and 4.8 include provisions specific to segmental box girders, pretensioned and post-tensioned I-Beams and U-Girders respectively. Elements of post-tensioned superstructures are required to comply with minimum dimensions in accordance with SDG Table 4.5.1-1. Per SDG 1.11.1 B, all tendons that utilize flexible filler shall be designed and detailed to be unbonded, fully replaceable, meet anchorage clearance requirements (as specified in SDG Table 1.11.1-1), and have clearance at the anchorages for jacking and tendon replacement operations (SDG Table 1.11.1-2). SDG (2021) does not allow strand couplers (described in Article 5.4.5 of AASHTO, 2020) and strand anchorages to be cast into concrete structures. In addition, dry joints are not allowed. Instead, SDG (2021) provides alternative methods for the design and detailing of joints between precast elements.

Provision of corrosion protection is required by AASHTO (2020). Furthermore, SDG (2021) specifies several strategies to protect post-tensioned structures against corrosion. These strategies include: (1) completely sealed ducts and permanent anchorage caps, (2) ducts and anchorage caps completely filled with approved filler, (3) multi-level anchorage system, (4) watertight bridges, and (5) multiple tendon paths. Multiple levels of protection are required for the tendons as well as for the anchorages. The use of external tendons is not permitted in I-beam or girder superstructures except for repair or retrofit scenarios.

The FDOT provides design values for post-tensioned members, which includes concrete strengths, steel grades, and wobble and friction coefficients. These guidelines also contain specifications for design and detailing of ducts and tendons. All tendons other than those listed in Table 2.1 shall be designed to be unbonded and incorporate the use of flexible filler. The unbonded post-tensioning ultimate average stress (f_{ps}), shall be calculated using the equations from Article 5.6.3.1.2 (AASHTO, 2020) along with Figure 1.11.5-1 (SDG, 2021). The external tendon unsupported length shall be limited to 100 ft or hangers shall be provided to restrain the tendon laterally and vertically.

Table 2.1 Bonded and/or unbonded tendons

Tendon	Type
Internal strand tendons: • Top slab cantilever longitudinal tendons in segmental box girders • Top slab transverse tendons in segmental box girders • Tendons that are draped 2'-0" or less in post-tensioned slab type superstructures	Bonded
Other: • Straight strand or parallel wire tendons other than continuity tendons in U-beams and girders • Bar tendons	Bonded or Unbonded

A minimum number of tendons shall be satisfied for post-tensioned superstructure elements as specified in SDG Table 4.5.2-1. The tendons shall be designed in such a way that unbonded tendons can be removed and replaced one at a time using the Service I load combination (Table 3.4.1-1; AASHTO, 2020) with the live load placed only in the striped lanes. The tension stresses shall be limited as specified in Table 2.2 (Section 4.5.2; SDG, 2021).

Table 2.2 Tension stresses

Concrete elements	Tension stress limit (ksi)
Precast superstructure elements with match cast joints	$0.0948\sqrt{f'_c}$
All other concrete superstructure elements	$0.19\sqrt{f'_c}$

In the absence of more information, as per the Structures Design Bulletin 17-08 (SDB; FDOT 2017), Section 4.7 and 4.8 of the SDG (2021) specifies the use of strain compatibility to determine section capacities utilizing bonded and unbonded post-tensioning tendons, mild reinforcing steel, and pretensioning strands for pretensioned/post-tensioned I-Beams and U-Girders.

2.4.3 ACI 318-19

The ACI 318-19 (ACI, 2019) does not provide specific guidance for mixed conditions of reinforcement. It does, however, provide equations for the tendon stress in members with unbonded tendons. These equations were developed with building members in mind, not bridge members, and are empirical. Equation 2.48 gives the prestressing steel stress for members with span-to-depth ratios less than 35 and is based on experimental tests by Mattock et al. (1971). Equation 2.49 gives the prestressing steel stress for members with span-to-depth ratios greater than 35 and is based on tests conducted by Mojtahedi and Gamble (1978).

$$f_{ps} = f_{se} + 10000 + \frac{f'_c}{100\rho_p} \tag{2.48}$$

$$f_{ps} = f_{se} + 10000 + \frac{f'_c}{300\rho_p} \tag{2.49}$$

In the above, f_{se} is the effective stress in prestressed reinforcement after losses, f'_c is the specified 28-day concrete strength and ρ_p is the steel reinforcement ratio (area of prestressing steel to the effective area of the concrete).

In lieu of strain compatibility, ACI 318-19 allows the use of Equation 2.50 to evaluate f_{ps}:

$$f_{ps} = f_{pu}\left\{1 - \frac{\gamma_p}{\beta_1}\left[\rho_p \frac{f_{pu}}{f'_c} + \frac{d}{d_p}\frac{f_y}{f'_c}(\rho - \rho')\right]\right\}; f_{se} \geq 0.5f_{pu} \tag{2.50}$$

where f_{pu} is the ultimate strength of the prestressing steel, ρ_p is the reinforcement ratio of the prestressing steel and d is the distance from extreme compression fiber to centroid of tensile force in nonprestressed steel.

If compression steel is used, then:

$$\rho_p \frac{f_{pu}}{f'_c} + \frac{d}{d_p}\frac{f_y}{f'_c}(\rho - \rho') \geq 0.17 \tag{2.51}$$

$$d' \leq 0.15d_p \tag{2.52}$$

where:

$$\gamma_p = 0.28 \text{ for } f_{py} \geq 0.90f_{pu} \tag{2.53}$$

$$\gamma_p = 0.40 \text{ for } 0.85f_{pu} \leq f_{py} \leq 0.90f_{pu} \tag{2.54}$$

$$\gamma_p = 0.55 \text{ for } 0.80f_{pu} \leq f_{py} \leq 0.85f_{pu} \tag{2.55}$$

and

$$\rho_p = \frac{A_{ps}}{bd_p} \tag{2.56}$$

$$\rho_s = \frac{A_s}{bd} \tag{2.57}$$

$$\rho' = \frac{A'_s}{bd} \tag{2.58}$$

2.4.4 Canadian Code

The Canadian Highway Bridge Design Code (CSA-S6-14 2014) does not provide specific guidance for mixed conditions of reinforcement. It does, however, state that the effective prestress (of the post-tensioning tendon) be conservatively used as the unbonded tendon stress at ultimate, unless a detailed analysis is used to determine tendon stress, considering global member deformation.

2.4.5 Eurocode

The Structural Eurocodes are reference design codes divided into packages for each of the main materials: concrete, steel, composite concrete and steel, timber, masonry and aluminum. The Eurocode 2, *Design of concrete structures*, applies to the design of buildings and other civil engineering works in plain, reinforced, and prestressed concrete using either normal or light weight aggregates. Eurocode 2 is further divided into three parts: Part 1-1: *General rules and rules for buildings* (EN 1992-1-1:2004), Part 1-2: *General rules – Structural fire design* (EN 1992-1-

2:2004), Part 2: *Concrete bridges - Design and detailing rules* (EN 1992-2:2005), and Part 4: *Liquid retaining and containment structures* (EN 1992-3:2006).

Although the Eurocode provides guidance for the design of both internal and external prestressing systems, it does not include provisions for mixed conditions of reinforcement.

The Eurocode suggests the use of the partial factor (γ) method. Partial factors are values that provide an acceptable level of reliability; these are selected assuming that an appropriate level of workmanship and of quality applies. Part 1-1 of the Eurocode 2 (EN 1992-1-1:2004, 2004) states that the design value of the prestressing force should be determined by Equation 2.59.

$$P_{d,t}(x) = \gamma_p P_{m,t}(x) \tag{2.59}$$

Where the mean value of prestress force, $P_{m,t}(x)$, should be determined with respect to the prestressing method, and γ_p is the partial factor for actions associated with prestressing. Prestress is considered to be favorable in most situations. Hence, a value of $\gamma_{p,fav}$ should be used for the ultimate limit state verification. However, when using external tendons, an increase of the value of prestress can be unfavorable and $\gamma_{p,unfav}$ should instead be used. Recommended values of $\gamma_{p,fav}$ and $\gamma_{p,unfav}$ are 1.0 and 1.3 respectively, but values for each country may be found on their National Annex.

Part 1-1 includes additional considerations for prestress in structural analysis. It is specified that external tendons may be assumed to be straight between deviators. The use of this type of tendons can give rise to second order moments. Primary and secondary effects of prestressing should be applied before considering any redistribution of forces and moments when performing a linear analysis. In plastic and non-linear analyses, secondary effects may be treated as additional plastic rotations. A non-linear analysis should be used when the stress increase in external tendons is calculated using the deformation state of the overall member (EN 1992-2:2005, 2005).

2.4.6 Australian Standard

The Australian Standard for Bridge Design (AS 5100.5-2004), also known as the Bridge Code, includes individual provisions for bonded or unbonded prestressing reinforcement. However, no guidance is provided for concrete members with mixed reinforcement conditions.

Similar to the AASHTO-LRFD provisions, the Australian Standard (AS 5100.5-2004, 2004) states that the minimum effective prestress in bonded tendons be at least half of the tensile strength of the tendons ($0.5 f_p$). The maximum stress in bonded tendons at the ultimate limit state (σ_{pu}) may be calculated using Equations 2.60 to 2.63.

$$\sigma_{pu} = f_p \left(1 - \frac{k_1 k_2}{\gamma}\right) \tag{2.60}$$

$$\gamma = \left[0.85 - 0.007(f'_c - 28)\right]; \ 0.65 \leq \gamma \leq 0.85 \tag{2.61}$$

$$k_1 = 0.4; \text{ or}$$
$$k_1 = 0.28 \text{ if } f_{py}/f_p \geq 0.9 \tag{2.62}$$

$$k_2 = \frac{1}{b_{ef} d_p f'_c} \left[A_{pt} f_p + (A_{st} - A_{sc}) f_{sy}\right] \tag{2.63}$$

where:

f_{py} = yield strength of the tendons
f_{sy} = yield strength of mild steel

b_{ef} = effective width of a compression face or flange of a member

d_p = distance from the extreme compressive fiber of the concrete to the centroid of the tendons

A_{pt} = cross-sectional area of the tendons in the zone that will be in tension under ultimate load conditions

A_{st} = cross-sectional area of reinforcement in the tensile zone

A_{sc} = cross-sectional area of compressive reinforcement

For unbonded tendons, the stress at the ultimate limit state shall be determined using Equation 2.64.

$$\sigma_{pu} = \sigma_{p.ef} + 6200 + \frac{d_p k_u d}{L_{pe}} \qquad (2.64)$$

Where $\sigma_{p.ef}$ is the effective stress in the tendon and $k_u d$ is the neutral axis depth.

$$k_u d = \frac{[A_p f_{py} + (A_{st} - A_{sc})f_{sy} - 0.85\gamma(b-b_w)d_f f'_c]}{0.85\gamma b_w f'_c} \quad \text{for a T-section}$$

$$k_u d = \frac{k_2 d_p}{0.85\gamma} \quad \text{for a rectangular section} \qquad (2.65)$$

where A_p is the cross-sectional area of prestressing steel, d_f is the thickness of the compression flange, b is the width of the cross-section, and b_w is the width of the web.

The effective length of the tendons, L_{pe}, can be calculated as:

$$L_{pe} = \frac{L_{pa}}{1 + (n_s/2)} \qquad (2.66)$$

where L_{pa} is the length of the tendons and n_s is the number of support hinges crossed by the tendon.

2.4.7 Japanese Guidelines

The Japanese Standard Specifications for Concrete Structures (JSCE, 2007) classifies prestressed concrete structures into two categories: prestressed concrete (PC) and prestressed and reinforced concrete (PRC) structures. PC structures do not permit cracking in serviceability-related conditions and are structurally designed to control the 'edge stress' (extreme fiber stress) in concrete by inducing prestress. PRC structures permit cracking in serviceability-related conditions and are structurally designed to control crack width by utilizing deformed mild steel bars and introducing prestress.

According to the Japanese guidelines, the prestressing force on the cross-section, $P(x)$, shall be calculated using Equation 2.67.

$$P(x) = P_i - [\Delta P_i(x) + \Delta P_t(x)] \qquad (2.67)$$

Where:
P_i = initial prestress force at the tensioning end of the tendon
$\Delta P_i(x)$ = loss of prestressing force immediately after prestressing
$\Delta P_t(x)$ = time dependent variation of prestressing force

When calculating the loss in the prestressing force, one must consider the prestressing method as well as the tendon type (bonded, unbonded, external). Stresses in the concrete and the tendon under variable load should be considered in addition to those calculated under permanent loads (JSCE, 2007). Stresses are calculated considering the effects of relaxation of the tendon, creep and shrinkage of the concrete, and restraint due to mild steel bars.

The specifications provide equations that describe the decrease over time in tensile stress in the prestressing tendons. These equations can be applied to concrete members that use only internal tendons (both PC and PRC structures, Section 15.4.2). Moreover, if unbonded or external tendons are used, the strain variation at the centroid of the tendons due to deformation of the concrete member can be calculated and then one can determine the decrease over time in tensile stress from the average strain. When only external tendons are used, the decrease in tensile stress may be calculated in accordance to Section 15.3 of the Standard Specifications (JSCE, 2007). However, if unbonded and/or external tendons are used in conjunction with internal tendons, the decrease in the tensile stress may be calculated using the methods provided in Section 15.4.2 for the reasons listed below:

- Calculation by theoretical method would be very complex and laborious

- Under normal service conditions, the deformation of a member is very small and, consequently, the influence of strain variations at the tendon location is thought to be small

- The decrease in the tensile stress in external tendons due to creep and shrinkage of concrete is smaller than when internal tendons are used

2.5 Reliability of flexural resistance for elements with bonded and unbonded tendons

The resistance factor (ϕ) is a statistically based value that accounts for the variability of material properties, structural dimensions and workmanship, and uncertainties in the prediction of resistance. Article 5.5.4.2 (AASHTO, 2020) is dedicated to resistance factors. For tension-controlled prestressed concrete sections with bonded strand or tendons (as specified in Article 5.4.3.3), the resistance factor is to be taken as 1.00. Meanwhile, for concrete sections with unbonded strand or tendons, the resistance factor is to be taken as 0.9. Article 5.5.4.2 (AASHTO, 2020) specifies that the resistance factor for concrete sections where the post-tensioning is a combination of bonded and unbonded tendons shall be based on the bonding conditions of the tendons that provides the majority of the prestressing force at the section. For prestressed members where the net tensile strain in the extreme tension steel at nominal resistance (ε_t) is between the compression-controlled strain limit (ε_{cl}) and tension-controlled strain limit (ε_{tl}), the resistance factor may be obtained by the linear interpolation as described by Equation 2.68.

$$0.75 \leq \phi = 0.75 + \frac{0.25(\varepsilon_t - \varepsilon_{cl})}{\varepsilon_{tl} - \varepsilon_{cl}} \leq 1.0 \tag{2.68}$$

The previous AASHTO-LRFD Specifications (AASHTO, 2014b) addressed segmental construction in Article 5.5.4.2.2. It was stated that the resistance factors for the strength limit state shall be taken as provided in Table 5.5.4.2.2-1 (Table 2.3 in this report) according to the degree of bonding of the post-tensioning. The maximum value for the resistance factor was based on observations from limited test data. This provision was not, however, preserved in the current AASHTO-LRFD Specifications (AASHTO, 2020). Instead, a resistance factor for the unbonded condition was included in Article 5.5.4.2.

Nowak and Iatsko (2017) revised the original calibration presented in the 1999 National Cooperative Highway Research report 368, *Calibration of LRFD Bridge Design Code*. The load and resistance factors were recalculated for selected representative bridge components as resistance and load coordinates of the design point for the Strength I limit state. The strength limit state considers the stability or yielding of any element to resist the specified statistically significant load combinations to be experienced during the design life. Particularly, Strength I limit state considers basic load combinations related to the normal vehicular use of a bridge without wind. The original calibration considered a design life of 75 years for the Strength I limit state.

The statistical parameters used in the calibration of the resistance factor are a bias factor (λ) and a coefficient of variation (COV). According to Nowak and Iatsko (2017), the statistical parameters have been reduced as presented in Table 2.4 based on a considerable amount of research that has been conducted since the original calibration. Although they estimated the mean load-carrying capacity of bridge girders to be 5% to 10% higher than was indicated by the original calibration, the reliability analysis was conducted using the original parameters. It was stated that additional analyses are necessary in order to develop updated statistical parameters for resistance.

Table 2.3 Resistance factor for joints in segmental construction
per the 2014 AASHTO-LRFD Specifications

	ϕ_f Flexure	ϕ_v Shear
Normal Weight Concrete		
Fully Bonded Tendons	0.95	0.90
Unbonded or Partially Bonded Tendons	0.90	0.85
Sand-Lightweight Concrete		
Fully Bonded Tendons	0.90	0.70
Unbonded or Partially Bonded Tendons	0.85	0.65

Table 2.4 Statistical parameters of resistance for prestressed concrete
(Nowak and Iatsko, 2017)

Source	Moment	
	λ	COV
1999 NCHRP Report 368	1.05	0.075
New database	1.04	0.015

After obtaining the reliability indices (β) for the same cases considered on the original calibration, Nowak and Iatsko (2017) calculated the parameters of the design point using Equations 2.69 and 2.70.

$$R^* = \mu_R - \frac{\beta\sigma_R^2}{\sqrt{\sigma_R^2+\sigma_Q^2}} \qquad (2.69)$$

$$Q^* = \mu_Q + \frac{\beta\sigma_Q^2}{\sqrt{\sigma_R^2+\sigma_Q^2}} \qquad (2.70)$$

Where R^* and Q^* are the coordinates of the design points for the resistance (R) and load (Q) respectively; μ_R and μ_Q are the mean values of R and Q; and σ_R and σ_Q are the standard deviations of Q and R when Q and R are normal random variables. The resistance factor was then calculated using Equation 2.71.

$$\phi = \frac{\lambda_R R^*}{\mu_R} \qquad (2.71)$$

where λ_R is the bias factor of R.

The recommended resistance factors corresponding to the coordinates of the design point were about 10% to 15% lower than the values recommended by the current AASHTO-LRFD Code (Nowak and Iatsko, 2017). Table 2.5 compares the resistance factors in current specifications with the calculated and recommended values for flexure. However, these suggested values are applicable for bonded tendons; no recommendations were provided for unbonded tendons.

Table 2.5 Recommended values of resistance factor for prestressed concrete
(Nowak and Iatsko, 2017)

Material	Resistance factor in current AASHTO LRFD specifications ϕ	Calculated resistance factor ϕ	Recommended resistance factor ϕ
Steel	1.00	0.85	0.90
Prestressed concrete	1.00	0.85	0.90
Reinforced concrete	0.90	0.75	0.80

2.6 Finite element modeling

Experimental testing of prestressed concrete systems requires a significant investment of resources and time. Computational tools such as finite element (FE) models can produce detailed and accurate results in a less expensive way. The finite element modeling of prestressed concrete members typically requires representation of the bond condition between the concrete and the prestressing steel. Bonded tendons can be modeled using the strain compatibility between the tendons and the surrounding concrete. However, unbonded tendons require additional considerations. This section focuses on previous research studies that used finite element models and analyses to represent prestressed concrete beams with either bonded or unbonded tendons, or both. Several modeling approaches and assumptions are presented, including materials, element types, and bond between reinforcement and concrete.

A nonlinear finite element procedure was proposed by Kang and Scordelis (1980) to analyze prestressed concrete frames with bonded or unbonded tendons taking into account material and geometric nonlinearities. Also considered were the load and temperature history; creep, shrinkage, and aging of the concrete; and relaxation of the prestress. Bonded prestressed tendons were assumed to have perfect bond with the concrete, but the strain of the unbonded prestressing tendons was determined by the deformed geometry of the tendons. The simulations were in good agreement with results from previous experiments. Other researchers such as Van Greunen and Scordelis (1983), El-Mezaini and Citipitioglu (1991), and Nikolic and Mihanovic (1997) have also presented formulations and models capable of analyzing prestressed members with bonded and/or unbonded systems.

A series of finite element models for a post-tensioning strand and anchorage assembly were developed as depicted in Figure 2.17 (Abdullah et al., 2016; Brenkus et al., 2017a). These were conducted to support the development of a wire break location algorithm. A finite element model was prepared and calibrated using experimental results to estimate friction coefficients at the wedge-anchor head, anchor head-spacer plate, and spacer plate-end plate interfaces. A challenge when modeling the interaction between the wires composing a strand was to account for contact nonlinearities. The selection of appropriate contact parameters for post-tensioning anchorage interfaces is discussed by Brenkus et al. (2017a) and the mathematical formulations can be found in Johnson (1987). The contact condition at the interfaces was treated with a penalty method using Coulomb friction model while a master-slave approach was implemented for contact detection. The method used by Abdullah et al. (2016) only considered the variation of strains in the axial direction at the external surface of the anchor head. However, the model was capable of detecting and locating wire breakage with a limited number of strain monitoring locations.

Nikolic and Mihanovic (1997) performed finite element analyses for post-tensioned structures embedding the reinforcement into the concrete with perfect bonding. The simulation procedures typically consisted in three phases: (1) application of dead load, (2) prestressing, and (3) addition of remaining dead load and live load. Vecchio et al. (2006) modeled post-tensioned concrete beams with unbonded tendons, considering friction effects. The bond stress model was used to represent frictional shear stresses acting on unbonded tendons. Link elements consisting

29

of orthogonal springs (Figure 2.18) were defined between the unbonded tendon and the concrete to represent bond slip and bond stresses, and normal displacements. While a tangential spring was defined to describe the frictional stresses, the normal spring was assumed infinitely stiff such that no relative normal displacements were permitted. The analyses carried out by Vecchio et al. (2006) consisted in two phases: (1) application of a temperature field to the anchorage system and (2) application of an external load. Although the research was focused on shear strength, results from previous flexural tests were also considered. The finite element analyses and predicted crack patterns were in good agreement with previous test observations.
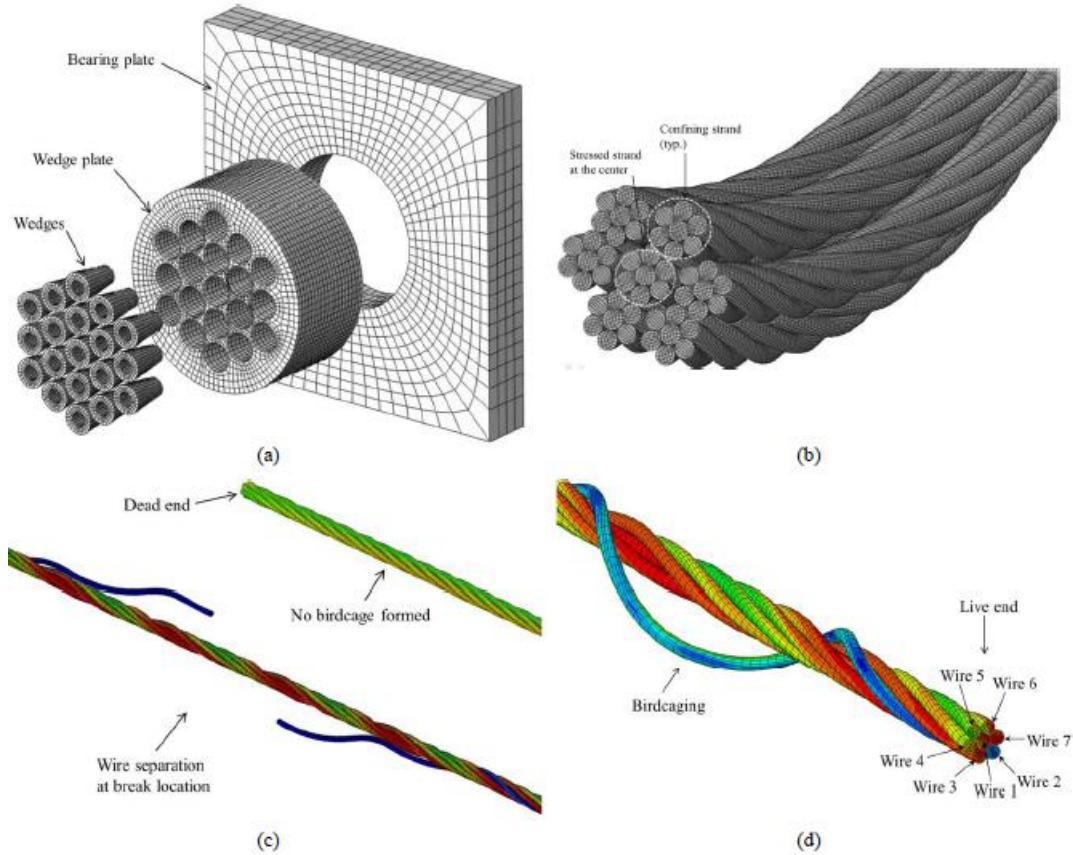
Figure 2.17 FE model: (a) anchorage, (b) multi-strand tendon, (c) wire break, (d) birdcaging (Abdullah et al., 2016; Brenkus et al., 2017a)
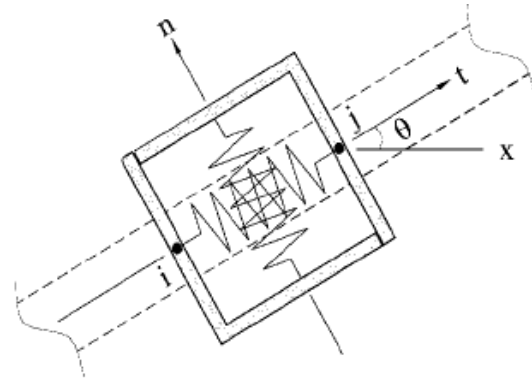
Figure 2.18 Representation of bond-link element (Vecchio et al. 2006)

Two modeling schemes were proposed by Huang (2012) for a post-tensioned concrete structure with bonded and unbonded tendons. The first consisted of the spring system method while the second incorporated a direct contact formulation. The anchorage system was simplified through the use of nodal constraints. The spring system was modeled as presented in Figure 2.19 (a) and the results for different amounts of springs were then compared to results of specimens tested by Foutch et al. (1990). Huang (2012) determined that neither the quantity nor length of springs influenced the results significantly. However, the length was limited by the concrete cover for the tendon. Although this method provided good estimates, it only models perfectly unbonded tendons which yields to a uniformly distributed strain field for the tendon. However, contact formulations allow the definition of different contact constitutive models (Figure 2.19b). The assumption of a frictionless tangential behavior of contact allowed the tendon to slip at the prestressing stage. A subsequent change in friction ensured perfect bond between the tendon and the sheathing after prestressing.

(a)   (b)
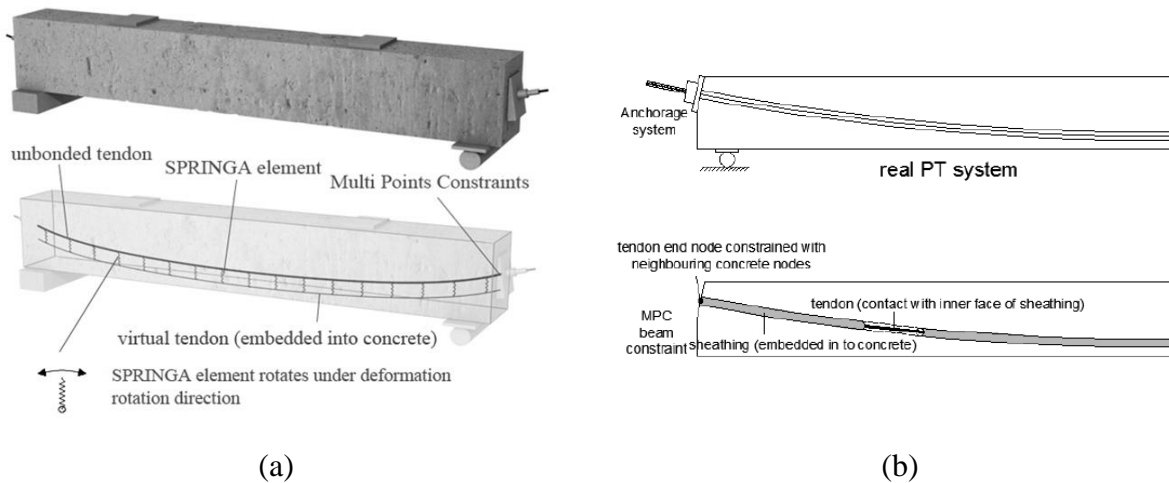
Figure 2.19 Modeling of unbonded post-tensioning system using:
(a) spring system method, (b) contact formulation (Huang 2012)

Later, Brenkus (2016) developed a finite element model for a beam specimen with mixed conditions of bonded and unbonded tendons (Figure 2.20a). An additional model only including bonded tendons was developed for comparison (Figure 2.20b). The modeling of the contact

31

conditions of the post-tensioned tendons was approached in two ways as described by Huang (2012). However, although previous investigations made use of solid elements to describe the concrete sections, Brenkus (2016) simplified the geometry of the model and used beam elements to represent the concrete. An I-shaped beam was represented by building up rectangular beam 'layer' elements; the beam layers were connected to each other by rigid body tie multiple point constraints. The prestressing tendons were represented by truss elements and the unbonded post-tensioning tendon was composed of a "real tendon" and a "virtual tendon". The real tendon was used in order to introduce the post-tensioning force at the anchorages. The virtual tendon was included only to transfer the post-tensioning load to the beam and enforce global displacement compatibility. As described by Brenkus (2016), the "real tendon" represented the prestressing strands while the "virtual tendon" represented the plastic duct.

(a)   (b)
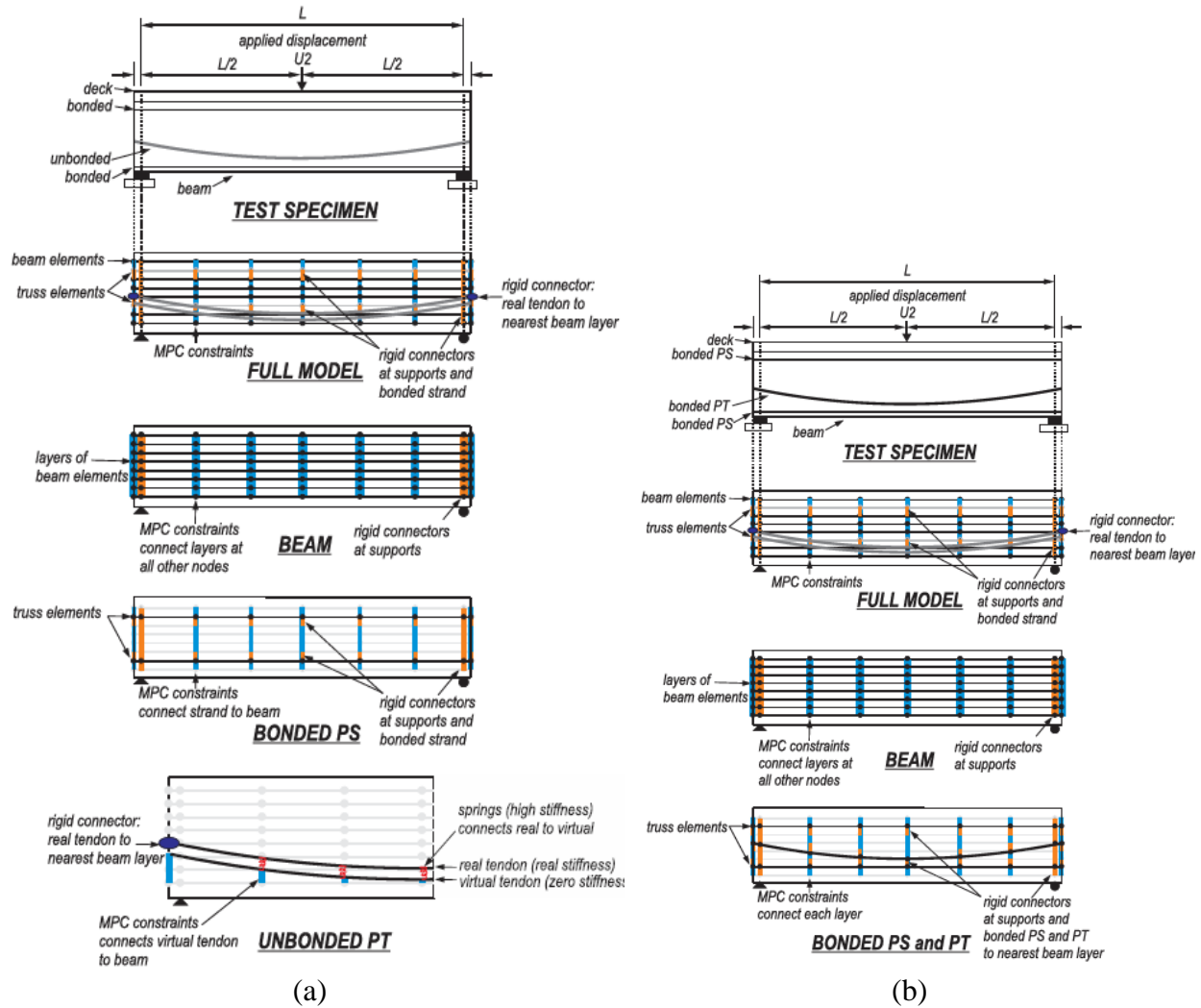
Figure 2.20 Finite element models: (a) unbonded model, (b) bonded model (Brenkus, 2016)

Some of the assumptions considered by Brenkus (2016) were: (1) effective prestress force was prescribed, (2) the condition that plane sections remain plane is applicable to bonded tendons but not to unbonded tendons, (3) perfect bond existed between bonded steel and surrounding concrete, (4) pre- and post-tensioning definitions introduced a prestrain to the prestressed parts, and (5) unbonded components were free to slide along the beam length, but followed the global deformation of the beam. The analyses were conducted using four steps:
- Step 1 – Girder self-weight was defined

- Step 2 – Deck was added

- Step 3 – Post-tensioning was applied (introduced as a thermal change to the "real tendon")

- Step 4 – Displacement was applied

The developed finite element models were validated using test data from experiments also conducted by Brenkus (2016). In general, it was found that the finite element models were in good agreement with the test data with regard to ultimate moment strength, rate of tendon stress increase, and tendon stress at ultimate. However, girder displacements were under-predicted by the finite element models.

Ayoub and Filippou (2010) developed a nonlinear model for pretensioned prestressed concrete girders implementing a mixed formulation where both forces and deformations were approximated within the element. The model consisted of three components: (1) a beam-column element, (2) a truss element, and (3) a bond element. The first two components were intended to describe the behavior of the concrete and prestressing tendons, respectively. The last component described the transfer of stresses between the prestressing tendons and concrete. Although the authors used experimental data to demonstrate the accuracy and efficiency of their model, Yapar et al. (2015) states that this study includes assumptions that may have questionable validity. For instance, the 1-D representation of the tendons ignores the Hoyer effect and the model does not adequately account for cracking and tension stiffening effects. Yapar et al. (2015) argued that results from prior finite element analyses were not reliable in the critical regions. For better prediction of the state of stress and the nature of damage in the critical regions of pretensioned concrete beams, Yapar et al. (2015) focused on determining the state of stress in the end-zone of beams.

Separately, Arab et al. (2011) and Okumus et al. (2012) used the Concrete Damaged Plasticity (CDP) in the commercial software Abaqus to model the interaction between the prestressing strands and concrete. While Arab et al. (2011) assumed strain compatibility at the steel and concrete interface (which does not allow for slippage due to bond failure), Okumus et al. (2012) ignored the presence of prestressing strands and applied the prestressing force directly to the concrete. According to Yapar et al. 2015, however, both made "unreasonable" assumptions that resulted in models failing to simulate the real behavior.

Yapar et al. (2015) took advantage of symmetry and modeled half of the beam length; strands and reinforcement were modeled using equivalent a rectangular cross section, but stirrups were ignored. Modeling was carried out in three steps (Figure 2.21):
- Step 1 – Initial prestressing of strands before pouring of concrete

- Step 2 – Mutual transfer of forces through the interface

- Step 3 – External loads (service condition)

The behavior of concrete was represented using a Plasticity-Damage (PD) model. The main mechanisms involved in transferring forces were identified as adhesion, friction, and mechanical interlock action. All rebar and prestressing strands were modeled with 3-D solid elements and the constitutive properties were represented by nonlinear elasto-plastic material models. The bond between concrete and the prestressing strands was modeled using hard contact normal behavior coupled with friction-governed tangential behavior, cohesive behavior, and damage behavior. Modeling results were compared to data from experimental studies showing good agreement up to the collapse load. In addition to this, the structures presented by Ayoub and Filippou (2010), Arab et al. (2011), and Okumus et al. (2012) were simulated using the proposed finite element model showing excellent agreement with the relevant experimental data.

Parsons Brinckerhoff (2015) evaluated the stress in unbonded tendons at ultimate limit state comparing non-linear finite element analyses to experimental data and provisions from AASHTO-LRFD, ACI-318, proposed modifications by Harajli (2012), and the Canadian Code. Non-linear finite element analyses were performed using Brigade Plus software, which includes an integrated Abaqus solver and non-linear concrete damage plasticity material from Simulia. Four of the seven beam cases considered were experimentally tested. Good agreement was found between the analytical and empirical results while the AASHTO-LRFD and Harajli equations seemed best suited to accurately predict tendon stress at ultimate.

(a)

(b)

(c)
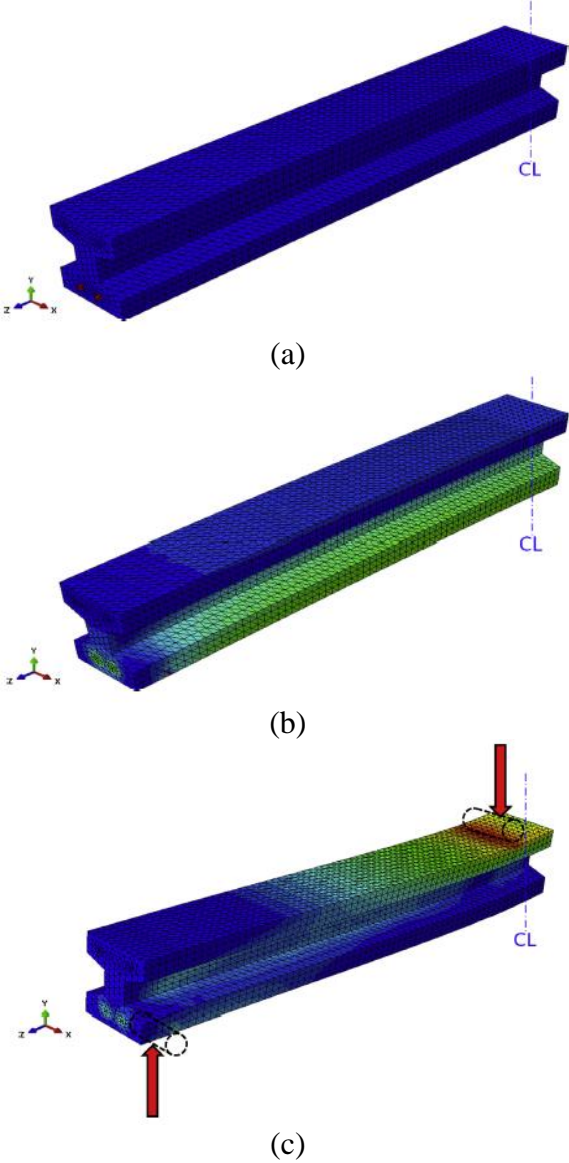
Figure 2.21 Modeling steps: (a) unbonded strands are stretched, (b) strands are bonded to concrete followed by releasing of strand, and (c) external load application (Yapar et al., 2015)

CHAPTER 3
RESEARCH APPROACH

This research project focused on the flexural strength behavior of prestressed concrete elements with a combination of bonded and unbonded reinforcement, with particular emphasis on determining how mixed conditions influence post-tensioned system behavior. The primary objective of this research was to develop analysis procedures that can be used to determine the flexural design capacity of beams with mixed reinforcement. The efforts towards accomplishing this goal were divided into two components:

1. Experimental study of flexural strength behavior, which included experimental tests on full-scale prestressed concrete beam specimens.
2. Numerical parametric studies consisting of finite element modeling of full-scale prestressed concrete beams with varying ratios of unbonded reinforcement.

Prior to performing the experimental study, a literature review was conducted and beam specimens were designed based on typical characteristics of representative bridges located in Florida. Finite element analyses simulating certain types of beams with similar characteristics (e.g. span-to-depth ratio, unbonded reinforcement ratio, and sectional stresses) to representative bridges were used to plan experimental tests. As explained later in Chapter 4, for practical reasons it was not feasible to test full-scale Florida I-beams (FIBs). Instead, an AASHTO section still available from precast producers was selected for the experimental tests.

Experimental test data were utilized to validate numerical modeling techniques. Then, those modeling techniques were used to further analyze a series of FIBs and investigate appropriate design processes. Proposed analysis procedures for determining the flexural design capacity of prestressed concrete elements with mixed bonded and unbonded reinforcement were based on a combination of experimental testing, and subsequent numerical parametric studies, conducted using validated numerical modeling techniques and classical methods like sectional analyses.

CHAPTER 4
DESIGN OF EXPERIMENTAL STUDY

4.1 Introduction

Experimental beam specimens were designed based on typical characteristics of representative bridges located in Florida. Bridge projects that were reviewed included State Road 55 (US 19/US 98) in Citrus County, the Gateway Expressway in Pinellas County, and the Wonderwood Connector in Duval County. These bridges were evaluated in terms of span-to-depth ratio, unbonded reinforcement ratio, and sectional stresses. Two types of beams were selected for the experimental study: (1) precast I-shape sections intended to simulate spliced girders and (2) a cast-in-place (CIP) specimen intended to simulate straddle bent arrangements. The experimental test plan included both configurations: positive and negative bending moment scenarios. As shown in Figure 4.1, simply-supported beams were considered to evaluate positive bending while continuous beams were considered to evaluate negative bending moments over the interior support. With the exception of straddle bents, representative bridges had typical parabolic PT tendon profiles with low points at midspan and high points at the supports. The post-tensioned tendons in straddle bent arrangements typically consisted of tendons with a double-harped profile. Stresses at the bottom of the beam section and the top of the precast concrete section were estimated for each of the representative bridges. Computed bottom-of-beam stresses were used to guide the design of simply-supported (SS) specimens tested in this study. Similarly, computed top-of-precast stresses were used to guide the design of negative bending (NB) specimens.

(a)

(b)
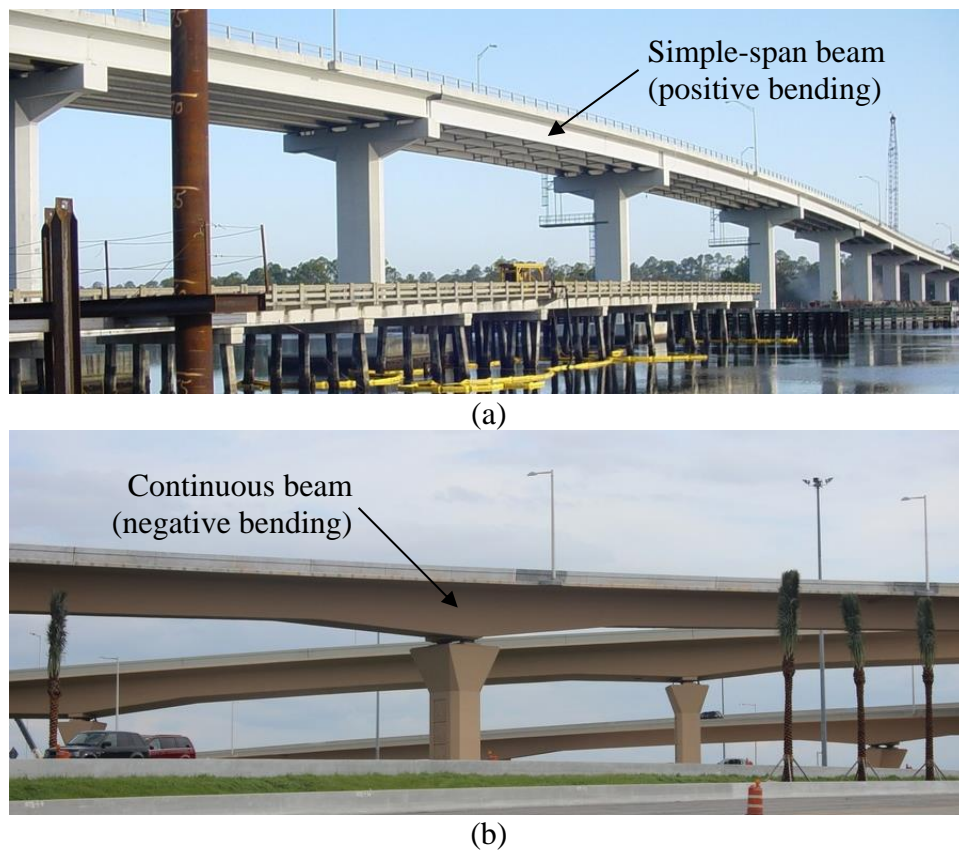
Figure 4.1 Beam configurations considered for design of experimental specimens:
(a) positive bending (Finley Engineering Group, 2008) and
(b) negative bending (Finley Engineering Group, 2015)

Additionally, a preliminary parametric study conducted using finite element analyses indicated that moment capacities were generally not sensitive to friction coefficients for the range of values that would be reasonably expected in design. Therefore, for purposes of experimental testing, the unbonded tendons in the beam specimens were not injected with flexible fillers but were left empty during testing. Preliminary parametric study results also indicated that the flexural behavior and capacity of prestressed concrete beams with mixed bonded and unbonded reinforcement are sensitive to the relative amounts of each reinforcement that is present in the system. Hence, U/T (ratio of unbonded reinforcement to total reinforcement) was established as a principal parameter of the experimental study. All beam specimens were tested in flexure, applying a concentrated static load.

4.2 Specimen design

This section describes the design of three types of experimental beam specimens. The first two types are precast concrete I-shaped sections that were intended to simulate spliced girder arrangements in positive and negative bending. These beams have parabolically draped unbonded post-tensioned tendon(s) along with bonded pretensioned strands. In addition, a custom cast-in-place specimen with a double-harped unbonded post-tensioned tendon and mild steel bonded reinforcement was used to simulate a straddle bent arrangement under positive bending. The principal parameter of the experimental study was the ratio of unbonded reinforcement to total reinforcement (U/T). For purposes of experimental testing, the unbonded tendons in the specimens were not injected with flexible fillers nor grout.

Specimen cross-section

Concrete I-girder bridges in Florida typically consist of Florida I-beams, Florida Bulb Tees, or AASHTO beam sections. However, the Florida I-beams and the AASHTO Type II beam are the FDOT standard prestressed concrete I-shaped beams and will be used in the design of all new bridges and bridge widenings in Florida (SDG, 2021).

Span-to-depth ratios from representative bridges were used to determine the length of beam specimens according to the height of the section. For instance, for a span-to depth ratio of 25, an FIB-72 will have a span length of 150 ft whereas an FIB-36 or AASHTO Type II will have a span length of 75 ft. Due to limitations of space in the FDOT Structures Research Center, the design span length was restricted to 95 ft. In addition to that, the capacity of the load actuator used for experimental tests and the amount of pretensioned strands and post-tensioned tendons that could be fitted in the cross-section played an important role when choosing the specimen cross-section.

Initially, different FIB sections were considered for the design of the experimental specimens (e.g. FIB-36, FIB-45, and FIB-54). It was determined to use a beam section with a height no greater than 45 in. so that span-to-depth ratios would be relevant to those from representative bridges while not exceeding a length of 95 ft. The use of AASHTO Type II sections would allow the fabrication of more beam specimens due to fabrication costs. AASHTO Type II sections satisfy the design characteristics from the representative bridges and finite element analyses demonstrated that these type of beams result in similar flexural behavior to FIBs.

The chosen precast cross-section, shown in Figure 4.2a, was a modified AASHTO shape using the side forms of an AASHTO Type II with the bottom form of an AASHTO Type III. The typical AASHTO Type II section had to be modified in order to fit HDPE ducts for internal post-tensioned tendons. When using multi-strand tendons, the cross-sectional area of the duct shall be at least 2.5 times the area of the post-tensioning steel, but maximum dimensions shall not exceed the limits specified by SDG (2021). In order to accommodate a maximum of 12 PT strands (0.6-in. diameter) per tendon, 3-in. diameter HDPE DR-17 ducts (outer diameter = 3.5 in.) were used. The

width of the web was widened to 10 in. to comply with the minimum concrete cover. However, the top flange conserved the original dimensions from a typical AASHTO Type II section, which caused some problems later discussed in Section 7.1 during fabrication of NB specimens.

Rectangular cast-in-place end blocks (Figure 4.2b) accommodated post-tensioning anchorage hardware and additional reinforcement. Strut-and tie calculations were performed to check the adequacy of transverse and through-thickness mild steel reinforcement in the end blocks.

All precast beam specimens were topped with an 8-in. thick concrete slab to simulate the bridge deck. The amount and spacing of deck steel was selected in accordance to AASHTO-LRFD Articles 5.10.3 and 5.10.6 (AASHTO, 2020); details are shown in Figure 4.3.

(a)   (b)
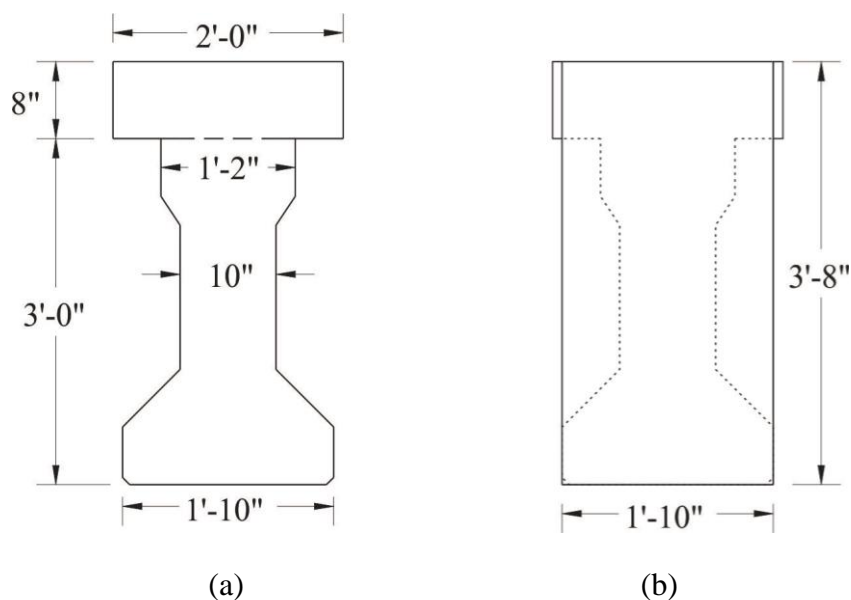
Figure 4.2 Modified AASHTO Type II girder:
(a) cross-section with concrete deck; (b) cast-in-place end block
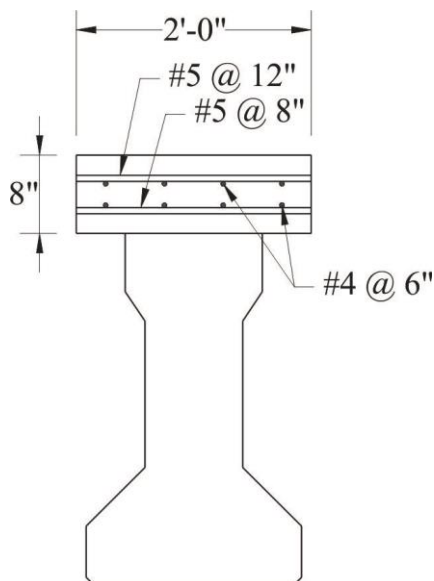
Figure 4.3 Reinforcement steel in concrete deck

A cast-in-place specimen was chosen to represent a straddle bent arrangement. Straddle bent arrangements from representative bridges generally consisted on rectangular sections with

38

smaller span-to-depth ratios than spliced I-girders. The experimental CIP beam section was selected using a span-to-depth ratio of 15. The chosen section is a rectangular cross-section (20 in. x 24 in.) as depicted in Figure 4.4 and accommodates one post-tensioned tendon within a 3-in. diameter HDPE DR-17 duct.
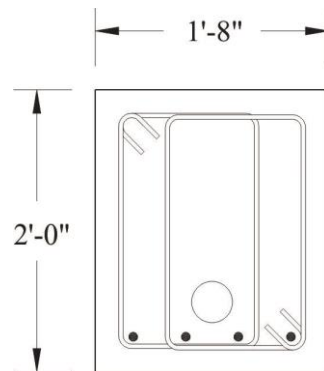
Figure 4.4 Cross-sectional view of cast-in-place specimen

PT tendon profile

PT tendon profiles commonly used in FDOT bridge structures were considered for the fabrication of experimental beam specimens. Typical internal post-tensioned tendon profiles from FDOT standard detail sheets (FDOT Index 21801) were selected according to the specimen type and arrangement (Figure 4.5).
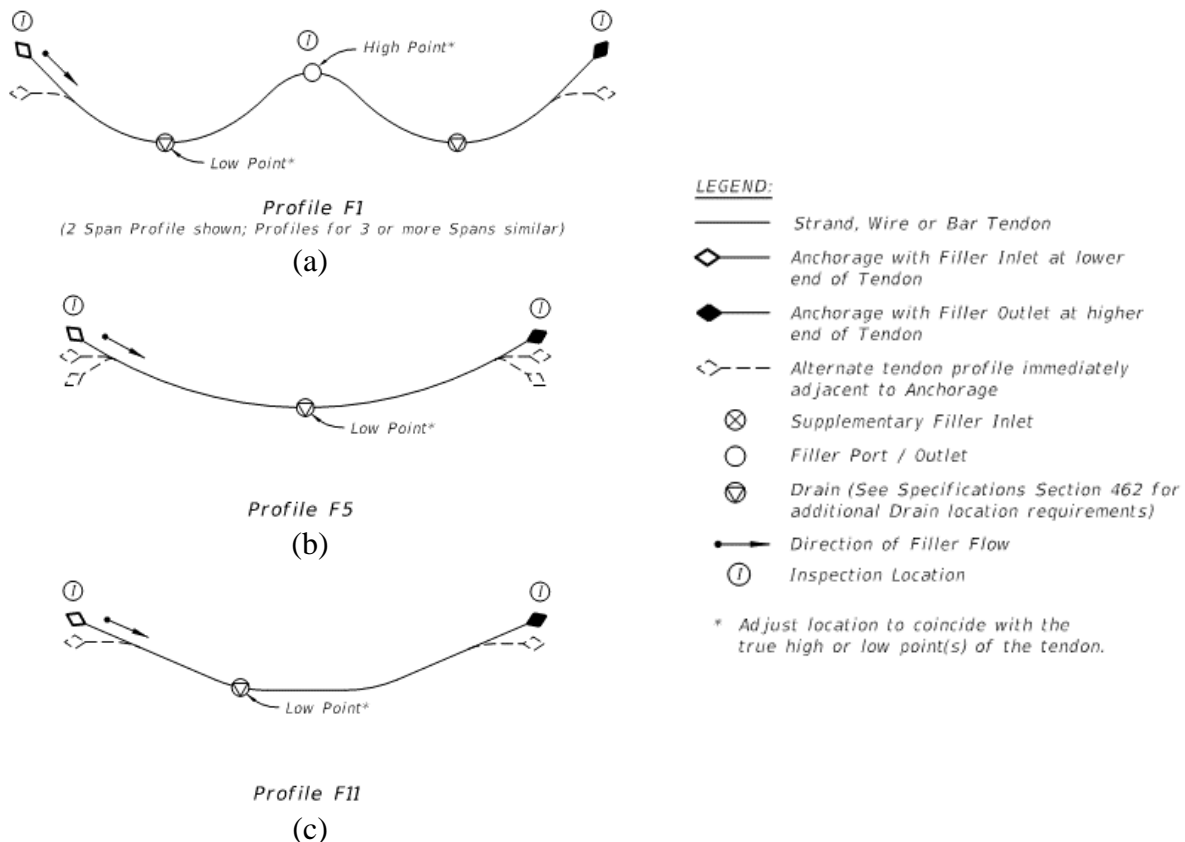
Figure 4.5 Typical FDOT profiles for tendons with flexible ('F') filler (FDOT Index 21801; FDOT 2016) selected for experimental beam specimens: (a) Profile F1, (b) Profile F5, and (c) Profile F11

39

For positive bending (simply-supported) specimens, two different tendon profiles were used. First, PT tendon profile F5 (FDOT Index 21801) was selected for the precast simply-supported specimens (Figure 4.6). Profile F5 is a parabolically draped profile for tendons with flexible fillers. This tendon profile has a low point at midspan, where a concentrated load was applied during experimental testing. In addition, as shown in Figure 4.7, PT tendon profile F11 was selected for the straddle bent cast-in-place specimen. Although the CIP specimen was also subjected to a concentrated load at midspan, a double-harped tendon profile was used conforming to existing CIP straddle bents evaluated for the design of experimental beam specimens.

Figure 4.6 Parabolically draped tendon profile (F5) for precast simply-supported specimens (not to scale)

Figure 4.7 Double-harped tendon profile (F11) for cast-in-place simply-supported specimen (not to scale)

Post-tensioned tendons in negative bending specimens followed the parabolically draped profile F1 depicted in Figure 4.8a. Negative bending specimens were designed to represent the portion corresponding to the negative moment region (enclosed in orange). The inflection points of the PT tendon were located near the ends of the beam (Figure 4.8b) such that the bending moments at the supports were nearly zero.

(a)

(b)
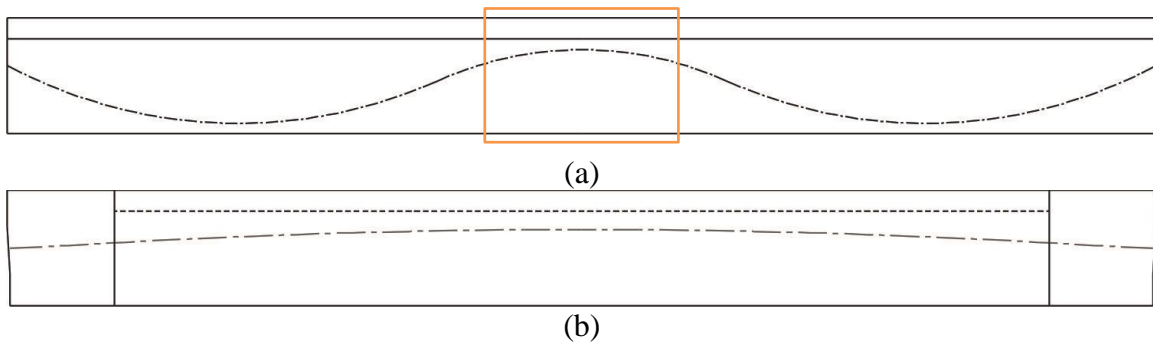
Figure 4.8 Parabolically draped tendon: (a) typical tendon profile F1; (b) profile corresponding to negative bending region (not to scale)

Specified material properties

The specified material properties corresponding to concrete, pretensioned strands, post-tensioned strands and ducts, and mild steel reinforcement are listed in Table 4.1. Experimental test matrix is further discussed in Section 4.3.

The design of precast or prestressed elements that are part of the superstructure generally requires the use of Class IV, V, or VI concrete (SDG, 2021). The minimum 28-day compressive strength required for Class IV, V, and VI are 5.5, 6.5, and 8.5 ksi respectively. However, the compressive strength for cast-in-place components range from 5 to 6.5 ksi. It was determined to use a specified concrete strength of 8.5 ksi for all precast beam specimens and deck while a 6.5 ksi strength was specified for the CIP specimen and most of the end blocks for precast beams. End

blocks for beam specimens NB-2 and NB-3 (see Table 4.2) were specified a strength of 8.5 ksi due to higher stresses from the post-tensioned tendons.

Prestressing steel (bonded and unbonded) consisted of ASTM A416, Grade 270, low-relaxation, seven-wire prestressing strands as specified in the SDG (2021). Ducts used for post-tensioned tendons can be made of either plastic or steel. However, the use of plastic ducts is recommended over steel for durability purposes. Post-tensioned systems injected with grout shall use corrugated polypropylene plastic material, but those injected with flexible fillers shall use smooth wall polyethylene ducts (SDG, 2021). Fabrication of experimental beam specimens will include the use of HDPE DR-17 ducts.

Table 4.1 Material properties

Material/Element	Properties
Precast beams	Concrete strength at transfer, f'_{ci} = 6 ksi
	Concrete strength at 28 days, f'_c = 8.5 ksi
Concrete deck	Concrete strength at 28 days, f'_c = 8.5 ksi
End blocks	• Specimens SS-1, SS-2, SS-3, SS-4, and NB-1: Concrete strength at 28 days, f'_c = 6.5 ksi • Specimens NB-2 and NB-3: Concrete strength at 28 days, f'_c = 8.5 ksi
Cast-in-place specimen	Concrete strength at 28 days, f'_c = 6.5 ksi
Pretensioned strands	• 0.6-in. diameter, seven wire lo-lax strands Area (per strand) = 0.217 in^2 Modulus of elasticity = 28,500 ksi Ultimate strength, f_{pu} = 270 ksi • 0.375-in. diameter, seven wire lo-lax strands Area (per strand) = 0.085 in^2 Modulus of elasticity = 28,500 ksi Ultimate strength, f_{pu} = 270 ksi
Post-tensioned strands	0.6-in. diameter, seven wire lo-lax strands Area (per strand) = 0.217 in^2 Modulus of elasticity = 28,500 ksi Ultimate strength, f_{pu} = 270 ksi
Post-tensioned duct	HDPE 3-in. DR-17
Mild steel reinforcement	Diameter: varies Modulus of elasticity = 29,000 ksi Yield stress, f_y = 60 ksi

4.3 Test matrix

The parameters shown in the test matrix in Table 4.2 were developed to explore varying span-to-depth (L/D) ratios and U/T ratios, which were found to have significant effect on flexural behavior in the analytical study. The ratios of unbonded reinforcement were evaluated in terms of reinforcement area (U_A/T_A) and axial force (U_F/T_F). The ratio U_A/T_A was calculated as the area of post-tensioning reinforcement divided by the total area of longitudinal reinforcement (i.e., pretensioned strands, post-tensioned tendons, and mild steel reinforcement). Conversely, the ratio U_F/T_F was calculated using forces that corresponded to the 'ultimate strength' of each material. An ultimate prestressing stress (f_{pu}) of 270 ksi was used for both pretensioned and post-tensioned strands (without consideration of prestress losses). A stress equal to 60 ksi (f_y), which is the value used in nominal moment calculations, was used to calculate the forces in the mild steel reinforcement. Note that the ratio of unbonded reinforcement only includes reinforcement in the tension side of the beam. The unbonded reinforcement ratios presented in Table 4.2 correspond to U_F/T_F.

The test matrix included simply-supported (SS) and negative bending (NB) specimens. For each SS specimen, the span length refers to the distance between supports. The span length

reported for each NB specimen is the distance between the supports of the ideal spliced continuous girder. Since only the negative region is being considered, the distance between the actual supports of each NB specimen is the distance between the inflection points of the PT tendon. Different span-to-depth ratios were selected to represent typical ratios found in spliced girders and/or straddle bents of actual bridges constructed in Florida. Representative span-to-depth ratios varied from 12 to 35. A CIP straddle bent specimen was included in the test matrix to address elements with lower span-to-depth ratios. As shown in Figure 4.9, the proposed CIP test specimen can be considered to represent both a straddle bent cap at L/D = 15 and a cantilever hammer head pier cap at L/D = 7.5. The ratios of unbonded reinforcement to total reinforcement were selected to replicate the ratios in existing bridge girders and straddle bents given the associated areas of mild steel, pretensioning strands, and post-tensioning tendons.

Table 4.2 Test matrix

Specimen	Cross Section	+/- Bending	Span Length (ft)	Specimen Length (ft)	L/D	U/T	No. PreT Strands	No. PT Strands	PT tendon profile
SS-1	Modified AASHTO Type II	Positive	75	76	25	0.4	10	6	F5
SS-2	Modified AASHTO Type II	Positive	75	76	25	0.6	8	10	F5
SS-3	Modified AASHTO Type II	Positive	45	46	15	0.4	6	4	F5
SS-4	Modified AASHTO Type II	Positive	45	46	15	0.6	4	6	F5
SS-5	CIP 20" x 24"	Positive	30	31	15	0.9	--	12	F11
NB-1	Modified AASHTO Type II	Negative	60	33	20	0.5	12	12	F1
NB-2	Modified AASHTO Type II	Negative	60	33	20	0.6	10	18	F1
NB-3	Modified AASHTO Type II	Negative	60	33	20	0.7	6	22	F1
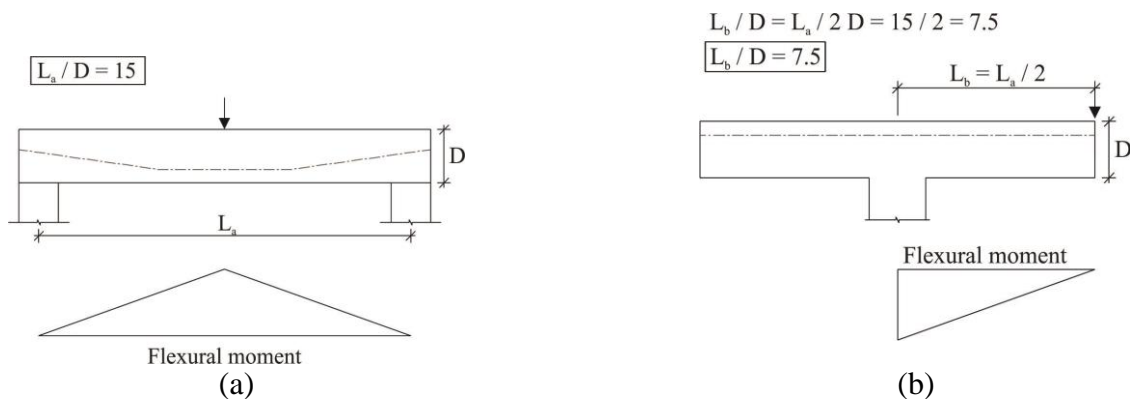
Figure 4.9 Cast-in-place beams showing span-to-depth ratios and moment diagrams:
(a) straddle bent cap and (b) cantilever pier cap

CHAPTER 5
EXPERIMENTAL STUDY ON SIMPLY-SUPPORTED PRECAST BEAMS

5.1 Specimen construction

Two 70-ft long beams and two 40-ft long beams were constructed as simply-supported specimens. These beam specimens consisted of modified AASHTO Type II sections and an 8-in. concrete deck (Figure 4.2a). As discussed in Section 4.2, the side forms of an AASHTO Type II girder were used, but AASHTO Type III bottom liners were installed on the bed. Specimen orientation on the prestressing bed is shown in Figure 5.1. The modified AASHTO shape was cast first and the deck was cast next (before strand detensioning) in the same prestressing bed; Table 5.1 presents the fabrication timeline.
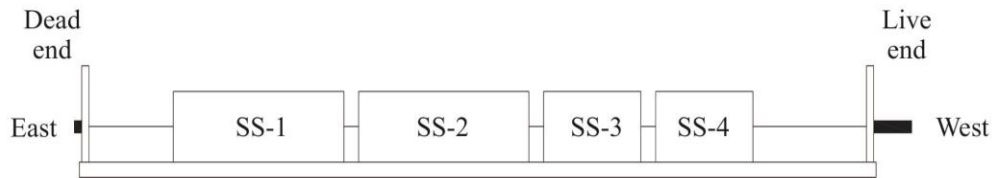
Figure 5.1 Specimen orientation on prestressing bed: SS precast beams (not to scale)

Table 5.1 Specimen fabrication timeline: SS precast beams

Specimen	Strands tensioned	Concrete Placement		Detensioned
		Mod. AASHTO section	Concrete deck	
SS-1	Jan. 21, 2020	Jan. 23, 2020	Jan. 27, 2020	Jan. 30, 2020
SS-2	Jan. 21, 2020	Jan. 23, 2020	Jan. 28, 2020	Jan. 30, 2020
SS-3	Jan. 21, 2020	Jan. 23, 2020	Jan. 27, 2020	Jan. 30, 2020
SS-4	Jan. 21, 2020	Jan. 23, 2020	Jan. 28, 2020	Jan. 30, 2020

As depicted in Figure 5.2, custom plywood bulkheads were used to accommodate the pretensioned strands and post-tensioning ducts while also allowing an increase of the web width to 10 in. The bulkheads also included shear keys for the future construction of end blocks for PT anchorage systems. Strands were individually inserted from the dead end through the bulkheads and the live end. Some of the strands were debonded as specified on fabrication drawings (Appendix A) and shown in Figure 5.3. PVC sheathing was used to debond the prestressing strands, leaving 1 ft of strand to be bonded at midspan. The sheathing was secured at the desired location using duct tape after the prestressing strands were tensioned.

Pre-fabricated concrete pieces (Figure 5.4a) were used in SS specimens to prevent sag of the bottom prestressing strands while providing appropriate separation between strand layers. As shown in Figure 5.4b, these concrete pieces were placed on the liner as well as between strands at one and two thirds of the precast beam length. Note that the concrete type used for the concrete pieces is the same (Class VI) as specified for the beam specimens.

Prestressing strands were tensioned using a monostrand hydraulic jack (Figure 5.5). For SS specimens, the bottom prestressing consisted of 0.6-in. diameter strands tensioned to a target force of 45.25 kip, within a tolerance of ± 2.5%. Additionally, two 3/8-in. diameter strands were placed on the top of the section to tie the transverse mild steel reinforcement and were pretensioned to a target force of 10 kip. Prestressing strands for SS specimens were tensioned following the pattern presented in Figure 5.6.

Figure 5.2 Custom plywood bulkheads for SS precast beams

| (a) | (b) |

Figure 5.3 Strand debonding at (a) the end of the beam and (b) midspan using PVC sheathing (note: 1-ft length remained bonded)

Figure 5.4 Pre-fabricated concrete pieces used to provide separation for prestressing strands

Figure 5.5 Prestressing strands at live end and monostrand hydraulic jack
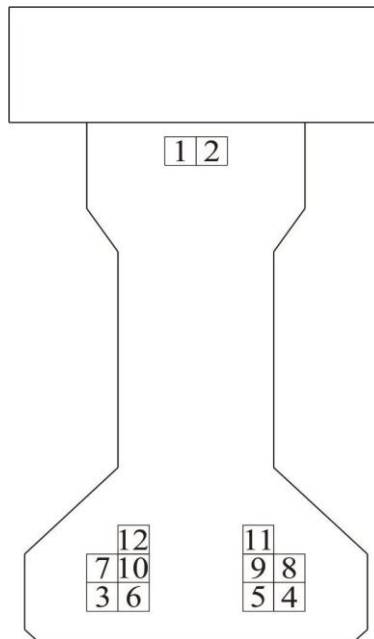
Figure 5.6 Prestressing strand jacking sequence for SS precast beams

Following the tensioning of prestressing strands, 3-in. diameter, DR 17 smooth HDPE ducts were installed for future post-tensioning of the beam specimens. As shown in Figure 5.7a, HDPE ducts were inserted in the bulkhead cutouts at specific elevations corresponding to the PT tendon profile. The ducts were secured in place using tie wires (Figure 5.7b).

Pre-bent mild steel bars were used to assemble rebar cages for the beams as depicted in Figure 5.8 and specified in fabrication drawings (Appendix A). Figure 5.9 shows the rebar cages and HDPE ducts in place for the 70-ft and 40-ft long SS precast specimens. Figure 5.10 depicts lifting loops (consisting of four ½-in. diameter strands) installed at the end of each beam for transportation.

(a)

(b)

Figure 5.7 Duct installation: (a) insertion of ducts in bulkhead cutouts,
(b) adjustment of duct profile

Figure 5.8 Rebar cage for SS specimen

(a)

(b)

Figure 5.9 Rebar cage and HDPE duct installation for (a) 70 ft and (b) 40 ft
(before the ducts were tied for final configuration of tendon profile)

Figure 5.10 Lifting loops for transportation

AASHTO Type II forms were placed on the bed around the rebar cages using a mobile gantry crane. Since the precast beam specimens consisted of modified AASHTO Type II beams, custom cut pieces of Styrofoam were glued to the surface of the side forms to create the desired cross-section (Figure 5.11). The side forms of AASHTO Type II beams were used along with AASHTO Type III liners, which produced a 22-in. bottom flange, 10-in. web, and 16-in. top flange. However, the top flange was specified to have the typical width of an AASHTO Type II girder. The side forms were adjusted to produce a 14-in. top flange.

(a)

(b)
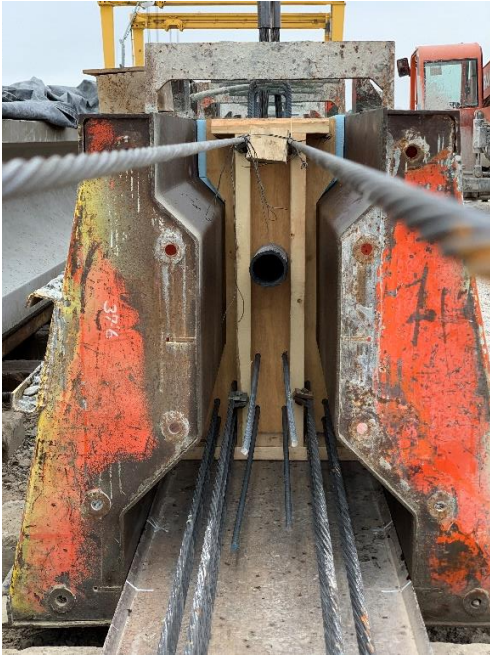
(c)

Figure 5.11 Styrofoam glued to side form for top flange: (a) exterior, (b) interior, and (c) front view of AASHTO Type II side forms

Concrete was placed in separate stages for the modified AASHTO Type II shape and concrete deck. Class VI (8500 psi) concrete mixes were prepared at a batch plant on-site for all beam specimens. Concrete cylinders were taken from each batch to conduct strength tests (performed by plant quality control team) for detensioning and experimental testing.

Once the Styrofoam was installed on the side forms, the modified AASHTO shape was cast as depicted in Figure 5.12a and the top surface was given a trowel finish (Figure 5.12b). After each concrete placement, the girders were covered with a tarp. A day after, the AASHTO Type II forms were removed and reusable plywood formwork was installed on the girders for the placement of the concrete deck. After placing concrete for the modified AASHTO shape, longitudinal and transverse mild steel reinforcement was installed for construction of the concrete deck (Figure 5.13). Figure 5.14 depicts concrete placement of the deck. As shown in Figure 5.14c, the deck was given a smooth finished surface.

(a)	(b)
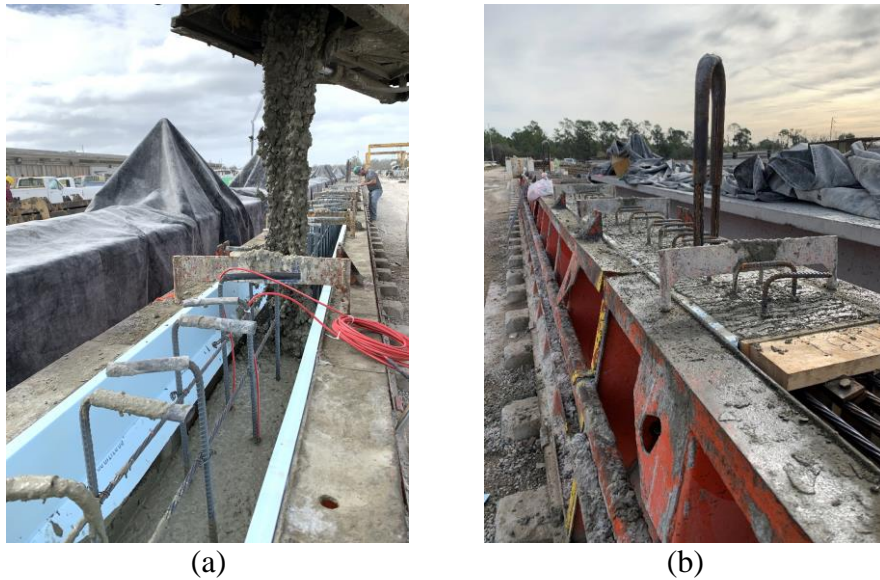
Figure 5.12 (a) Concrete placing and (b) roughened top surface

Figure 5.13 Mild steel reinforcement for concrete deck

(a)

(b)

(c)

Figure 5.14 Concrete deck: (a) concrete placement, (b) vibration, and (c) finished surface

The concrete strength for release was specified as 6000 psi for all beam specimens, including both the modified AASHTO shape and the concrete deck. Field cured concrete cylinders

were tested by the quality control team from the precast plant a day after concrete placement and before detensioning. The concrete strengths from these tests are summarized in Table 5.2.

Table 5.2 Concrete strengths prior detensioning of pretensioned strands: SS precast beams

Concrete Placement	Date cast	Date tested	Concrete strength (psi)
#1: Mod. Type II section (SS)	Jan. 23, 2020	Jan. 24, 2020	4,720
		Jan. 27, 2020	8,650
		Jan. 27, 2020	8,540
#2: Deck (SS-1 & SS-3)	Jan. 27, 2020	Jan. 28, 2020	4,400
		Jan. 29, 2020	6,370
		Jan. 29, 2020	6,440
#3: Deck (SS-2 & SS-4)	Jan. 28, 2020	Jan. 29, 2020	3,830
		Jan. 30, 2020	6,130
		Jan. 30, 2020	6,180

The pretensioned strands were cut following the sequence shown in Figure 5.15 using acetylene torches at the locations depicted in Figure 5.16. Figure 5.17a depicts the strands being cut at one of the ends of the prestressing bed while Figure 5.17b shows the detensioning between specimens.
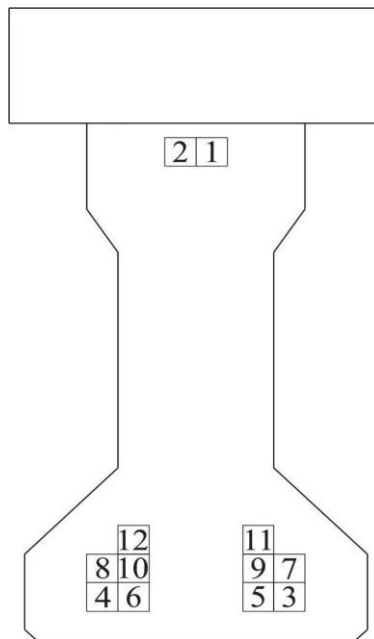
Figure 5.15 Detensioning pattern for SS specimens
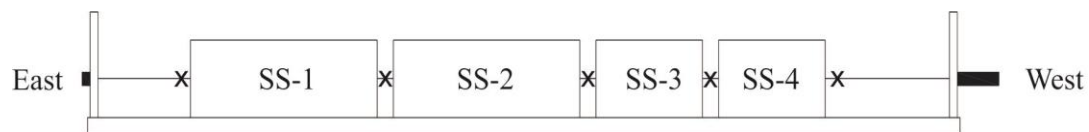
Figure 5.16 Detensioning locations for SS specimens (identified with 'X' marks)

(a)	(b)

Figure 5.17 Detensioning of SS specimens at (a) east end of prestressing bed and
(b) between specimens SS-2 and SS-3

Following detensioning, all beams were inspected before moving them from the prestressing bed and no cracks were found. However, later, when conducting additional visual inspections of the beams in the storage location, cracks were found in specimens SS-1 and SS-2. Vertical cracks were found on specimen SS-2 at a distance of 20 ft (approximately 30% of the beam length) from the west end on both sides of the beam (Figures 5.18 and 5.19). On both sides, the cracks extended from the interface between the deck and the top flange approximately 21 in. down to the beam web as shown in Figure 5.19 (cracks indicated with black marker). Although these cracks were not noted during the initial inspection, they could be attributed to shrinkage of the concrete in the AASHTO section (first concrete pour) and the concrete deck (second pour) preventing the cracks from closing. Crack widths measured on both sides of the beam did not exceed 0.25 mm (0.01 in.).

Figure 5.18 Formation of crack on specimen SS-2 at a distance of 20 ft from west end
(north side)

<center>(a)   (b)</center>
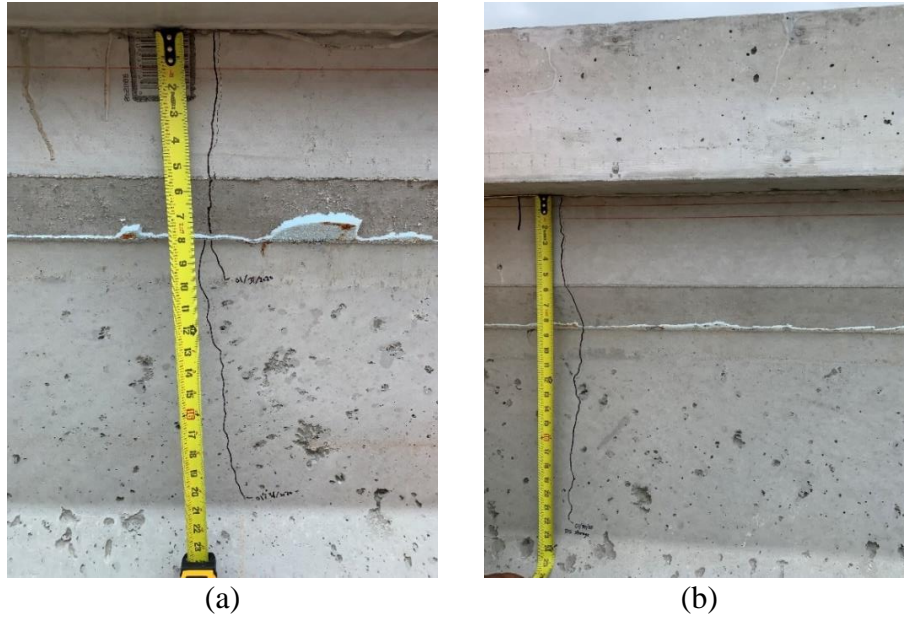
Figure 5.19 Formation of cracks on specimen SS-2 at a distance of 20 ft from west end
(a) south and (b) north sides

The precast beams were transported to the FDOT Structures Research Center, where concrete end blocks were fabricated. Custom plywood formwork (Figure 5.20) was used. Since most of the end blocks had the same dimensions, some formwork was reused. Pre-bent mild steel bars as shown in Figure 5.21a were used to assemble rebar cages conforming to the fabrication drawings included in Appendix A. Figures 5.21b and 5.21c show rebar cages for beam specimens SS-1 and SS-3. As listed in Table 4.1, the specified concrete strength for end blocks for the precast SS specimens was 6500 psi. Figure 5.22 shows end blocks during concrete placement and after formwork was removed. Concrete cylinders were collected from each concrete batch and tested at 28 days. Beams were post-tensioned after the end blocks reached the specified compressive concrete strength. Post-tensioned strands were prestressed to a target of $0.75f_{pu}$ using a multi-strand jack as shown in Figure 5.23.

Figure 5.20 Installation of formwork for fabrication of end blocks for precast SS specimens

<center>53</center>

| (a) | (b) | (c) |
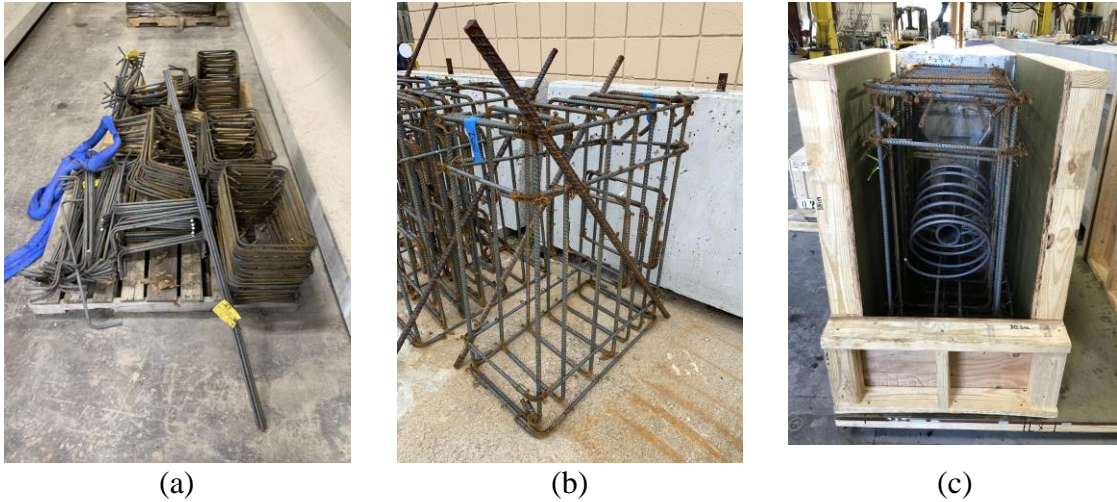
Figure 5.21 Assembly of rebar cage for end blocks: (a) pre-bent mild steel bars; (b) perspective view of rebar cage; (c) rebar cage and formwork for SS-3

| (a) | (b) |

Figure 5.22 Fabrication of end blocks: (a) concrete placement; (b) end blocks (SS-3 and SS-4) after removal of formwork

Figure 5.23 Post-tensioning of precast SS specimen

5.2 Test setup

Simply-supported precast beam specimens were tested in three-point bending as depicted in Figures 5.24 and 5.25. The beams were supported by a pair of steel I-beams (W14x370) and steel-reinforced neoprene bearing pads (24 in. x 10 in. x 2¼ in.). A concentrated load was applied at midspan using an Enerpac RR-40018 actuator (Figure 5.26). For detailed dimensions see Appendix B.
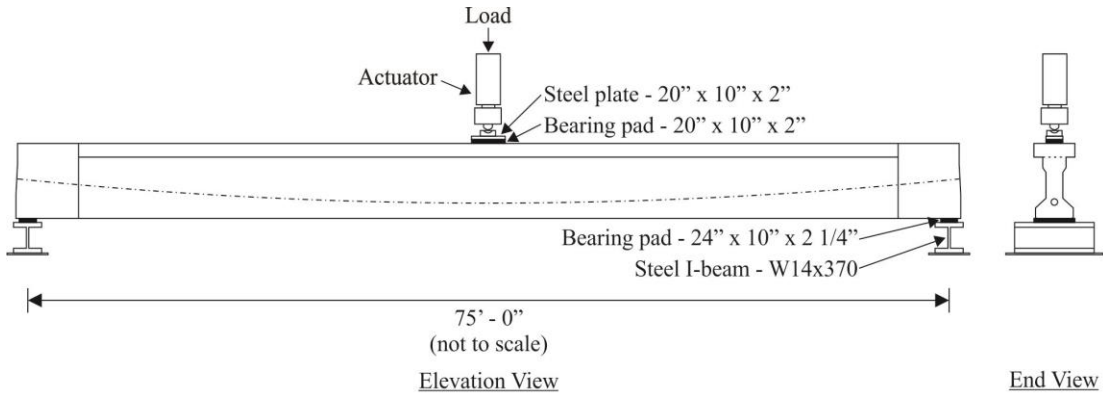
Figure 5.24 Flexural test setup: Beam specimens SS-1 and SS-2
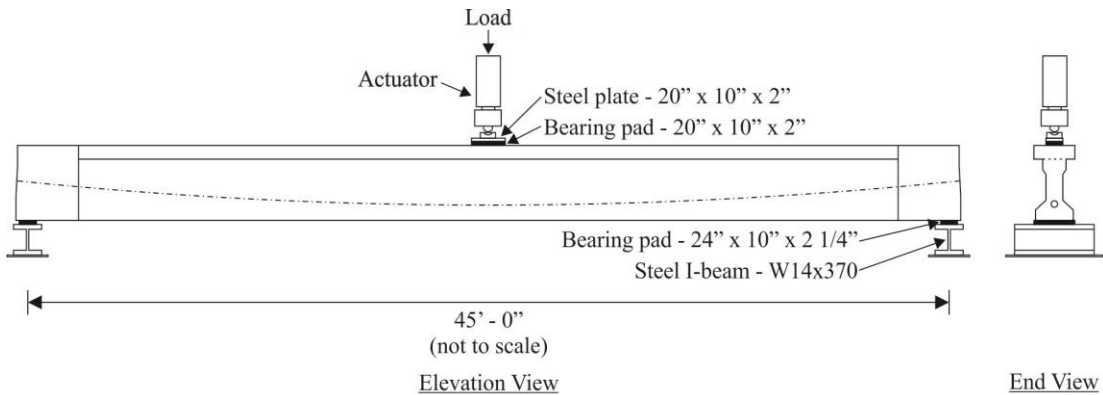
Figure 5.25 Flexural test setup: Beam specimens SS-3 and SS-4

Figure 5.26 Enerpac RR-40018 actuator

5.3 Instrumentation

Instrumentation on simply-supported precast beam specimens included displacement gages, strain gages, and load cells. Data were gathered from the instrumentation during two key phases: stressing of post-tensioned tendons, and load-testing.

Load cells

The axial force in the post-tensioned tendons was directly measured using 850-kip Geokon hollow-core load cells. As shown in Figure 5.27, the load cells were located at the dead end of the beams with the PT tendon(s) passing through them.

Figure 5.27 Geokon hollow-core load cell installed at dead end of beam specimen SS-3

Displacement transducers

Vertical displacements were monitored through the use of laser displacement transducers (LTS-300-200). Parametric studies conducted using numerical simulation indicated that the length of the plastic hinge region in beams subjected to concentrated loads at midspan was limited to less than 30% of the overall length of the beam. Therefore, laser displacement transducers were distributed along the middle 40% of the length of the specimens. Additional laser displacement transducers were also positioned near the span ends. Figure 5.28a shows the general distribution of laser displacement transducers along the length of SS precast beam specimens (see Appendix B for specific locations).
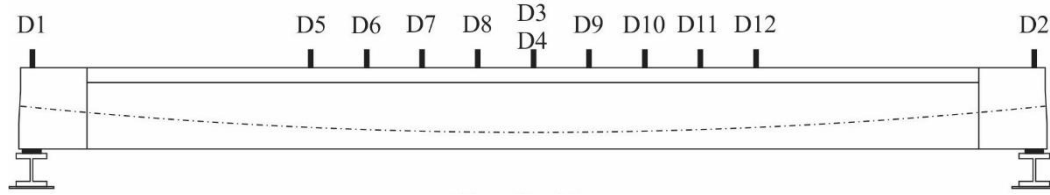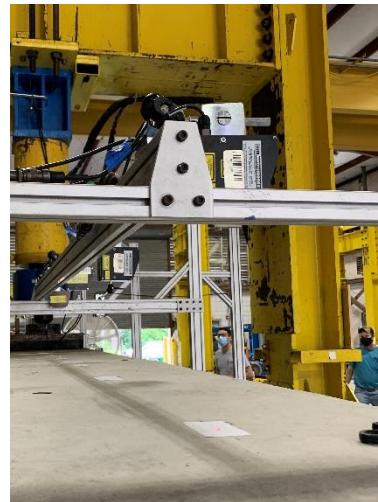
Figure 5.28 Laser displacement transducers – SS precast specimens: (a) location of laser displacement transducers, (b) typical transducers installed on a SS precast beam specimen along the length of the beam and (c) at the load point, and (d) close-up showing a laser displacement transducer and the surface to which the laser was projected

Strain gages

Vibrating wire (VW) strain gages (Geokon Model 4200) were installed during fabrication of specimens at the precast plant. These gages were installed to determine prestress losses and, therefore, effective prestress forces in the pretensioned strands. As shown in Figure 5.29a, VW gages were positioned by attaching them to the prestressing strands using plastic zip ties. Two VW gages were installed at midspan in the bottom layer of prestressing strands (Figure 5.29b).

57

(a)

(b)

Figure 5.29 Vibrating wire gages installed in SS precast specimens: (a) close-up view of gages attached to pretensioned strands and (b) view of gages and cables prior to concrete placement

Concrete strains were measured using two different approaches. The first technique consisted of the use of 60-mm foil-type strain gages (Kyowa Model KC-60-120-A1-11) attached to the concrete surface. As depicted in Figure 5.30, foil-type strain gages were located along the middle 30% of the beam on both top and bottom of the specimen. Additional foil-type strain gages were placed on one side of the web to monitor concrete strain at different elevations near the center of the beam. Detailed location information for foil strain gages is presented in Appendix B.

Figure 5.30 Location of 60-mm foil strain gages: SS precast specimens

Figure 5.31 Typical 60-mm foil strain gages installed on SS precast specimens

In addition to foil strain gages, fiber optic sensors (FOS) were also installed to allow the monitoring of distributed concrete surface strains. Placing FOS at different elevations on the beam specimen allowed for the calculation of beam curvature and deflection at the point in time that the measured data indicated crack formation. For SS specimens, individual FOS were placed on one side (lateral face) of the concrete deck to capture compressive strains while tensile strains were monitored on the bottom of the specimen. Since the formation and propagation of cracks were expected to occur in the bottom center of the beam, two FOS were bonded to the bottom concrete surface to prevent or minimize data loss in case there was breakage of the FOS. Additional FOS were placed on the web to monitor distributed concrete strains at different elevations. Figure 5.32 show the general location of FOS on SS precast beams; see Appendix B for specific locations and dimensions.
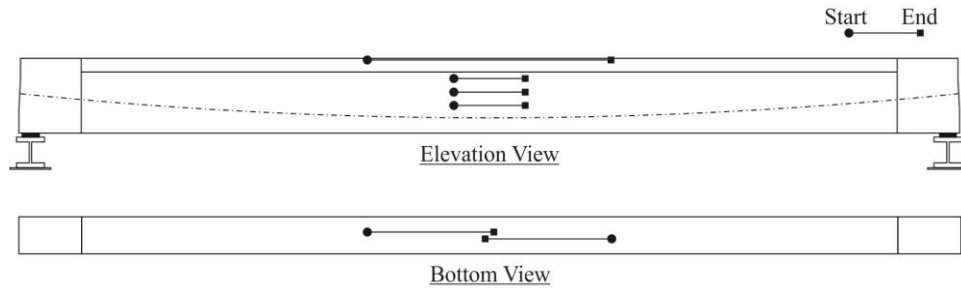
Figure 5.32 Location of fiber optic sensors: SS precast specimens

Figure 5.33 Typical fiber optic sensors installed on SS precast specimens

5.4 Test procedure

Following completion of construction and installation of instrumentation, the beam specimens were moved into the loading frame for testing. Specimens were tested incrementally by applying load at a rate of 0.25 kip/sec at midspan. Loading was paused (held constant) periodically at specified load levels to inspect the beam, mark cracks, and take readings from VW strain gages. Once load exceeded levels that were deemed safe for marking cracks, loading was continued until the test was terminated. Tests were terminated when either compressive failure occurred, compressive concrete strains were larger than 0.003, a maximum predicted load was exceeded, or bonded pretensioned strands rupture.

5.5 Experimental test results

This section presents a summary of the results obtained from experimental tests conducted on precast simply-supported beams with different amounts of unbonded and bonded prestressed reinforcement. Detailed test results, including photographs, sketches of crack patterns, and plots of selected data from instrumentation, are provided in Appendix C.

A summary of the nominal load capacity (P_n, load at which concrete strain $\varepsilon_c = 0.003$) and maximum load (P_{max}) is presented in Table 5.3. Figure 5.34 shows a comparison of load-displacement plots for all four precast simply-supported beam specimens. Beam specimens

with greater span-to-depth ratios exhibited more flexibility than those with lower span-to-depth ratios. Beam specimens with the same total amount of reinforcement (SS-3 and SS-4) demonstrated that higher unbonded ratios (U/T) result in a reduction in capacity. On all beam specimens, cracks were initially observed at midspan on the bottom flange and eventually propagated for approximately 20% to 30% of the beam length. The stress in the PT tendons remained constant until pretensioned strands started yielding. The PT stresses did not exceed $0.8\ f_{pu}$ on any of the experimental specimens. Contrary to the PT tendons, pretensioned strands exhibited a significant increase in stress as load was applied and exceeded $0.9\ f_{pu}$. Beam specimen SS-4 presented rupture of all four bonded pretensioned strands (Figure C.40).

Table 5.3 Flexural capacity of precast simply-supported beams

Beam specimen	U/T	L/D	Applied load (kip) at $\varepsilon_c = 0.003$	Max. load (P_{max}, kip)	Rupture of PreT strand
SS-1	0.4	25	119.6	122.0	No
SS-2	0.6	25	128.6	131.4	No
SS-3	0.4	15	132.7	135.8	No
SS-4	0.6	15	124.0	126.8	Yes
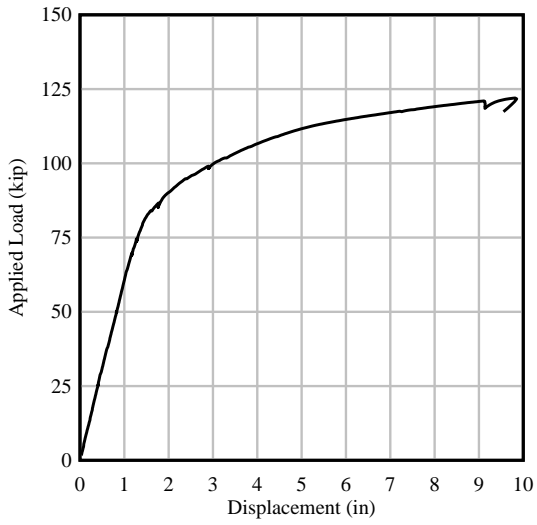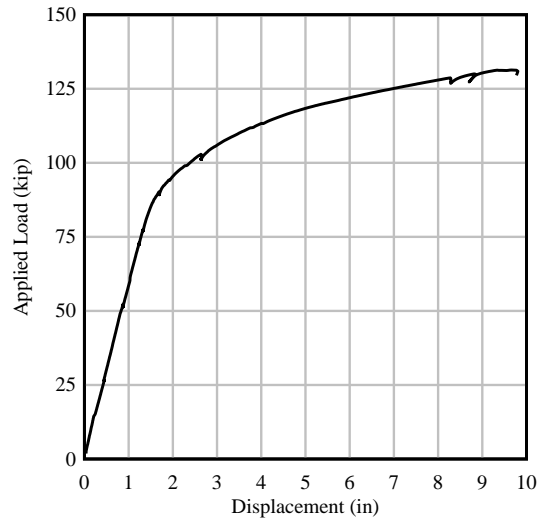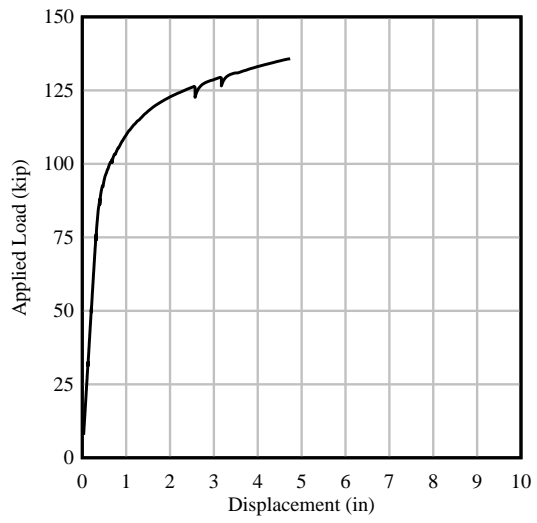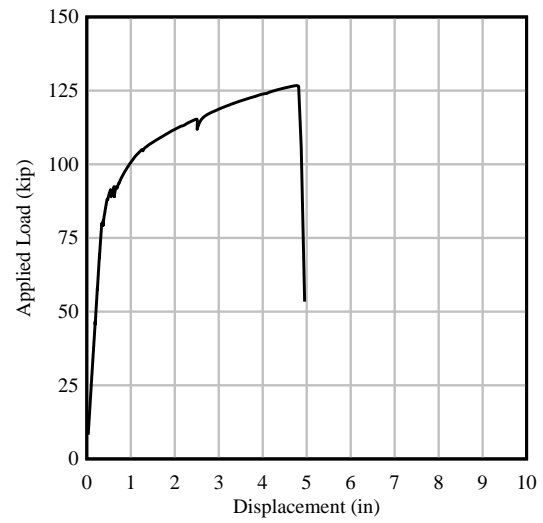
Figure 5.34 Load-displacement plots: (a) SS-1, (b) SS-2, (c) SS-3, and (d) SS-4

CHAPTER 6
EXPERIMENTAL STUDY ON SIMPLY-SUPPORTED CAST-IN-PLACE BEAM

6.1 Specimen construction

A 31-ft long cast-in-place beam was constructed as a simply-supported specimen. CIP beam specimen SS-5 was fabricated at the FDOT Structures Research Center in Tallahassee, FL. This beam specimen consisted of a rectangular concrete section (Figure 4.4). Custom plywood formwork was used for the fabrication of this beam specimen as shown in Figure 6.1. Pre-bent mild steel bars were used to assemble rebar cages for the beams as depicted in Figure 6.2a and specified in fabrication drawings (Appendix A). As shown in Figure 6.2b, 3-in. diameter, DR 17 smooth HDPE duct was installed for future post-tensioning of the beam specimen. The HDPE duct was secured in place at specific elevations corresponding to the PT tendon profile.

Figure 6.1 Plywood formwork used in the fabrication of CIP specimen SS-5

Figure 6.2 Rebar cage and HDPE duct installation for CIP beam specimen SS-5

Contrary to SS precast beam specimens, the CIP beam specimen SS-5 was fabricated in a single concrete pour and did not include a concrete deck. Concrete cylinders were taken from each batch to conduct strength tests for experimental testing. Figure 6.3 depicts concrete placement for specimen SS-5. After 28 days, prestressing strands were inserted into the HDPE duct and CIP specimen SS-5 was post-tensioned using a multi-strand jack.

Figure 6.3 Concrete placement: CIP beam specimen SS-5

6.2 Test setup

CIP beam specimen SS-5 was subjected to a static concentrated load applied at midspan (Figure 6.4). The beam was supported by a pair of steel I-beams (W14x370) and steel-reinforced neoprene bearing pads (24 in. x 10 in. x 2¼ in.). Load was applied using an Enerpac RR-40018 actuator (Figure 5.26). For detailed dimensions see Appendix B.
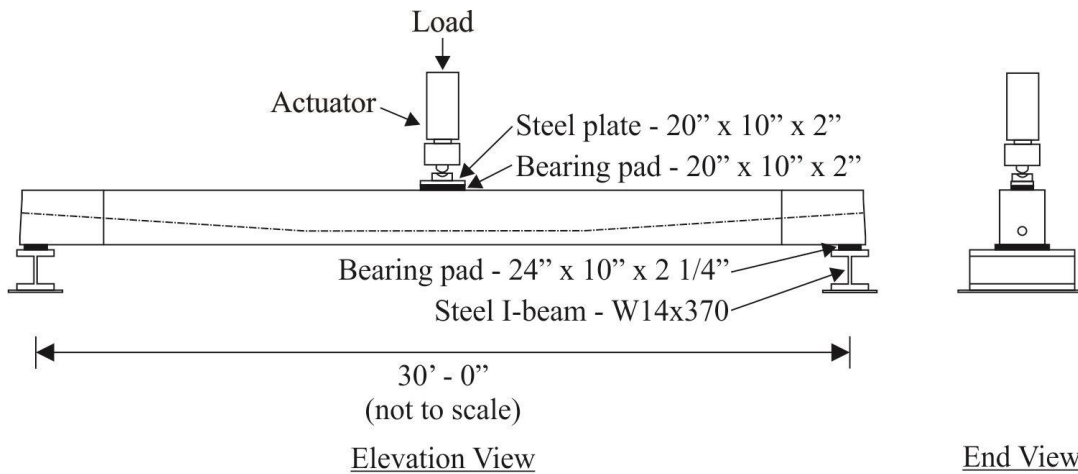
Figure 6.4 Flexural test setup: Beam specimen SS-5

6.3 Instrumentation

Instrumentation on CIP beam specimen SS-5 included displacement gages, strain gages, and load cells. Data were gathered from the instrumentation during two key phases: stressing of post-tensioned tendons, and load-testing.

Load cells

The axial force in post-tensioned tendons was directly measured using an 850-kip Geokon hollow-core load cell. As shown in Figure 6.5, the load cell was located at the dead end of the beams with the PT tendon passing through it.

Figure 6.5 Geokon hollow-core load cell installed at dead end of beam specimen SS-5

Displacement transducers

Vertical displacements were monitored through the use of laser displacement transducers (LTS-300-200) distributed along the middle 40% of the length of the specimen, and which were located near the span ends. Figure 6.6a shows the distribution of laser displacement transducers along the length of CIP beam specimen SS-5 (see Appendix B for specific locations).
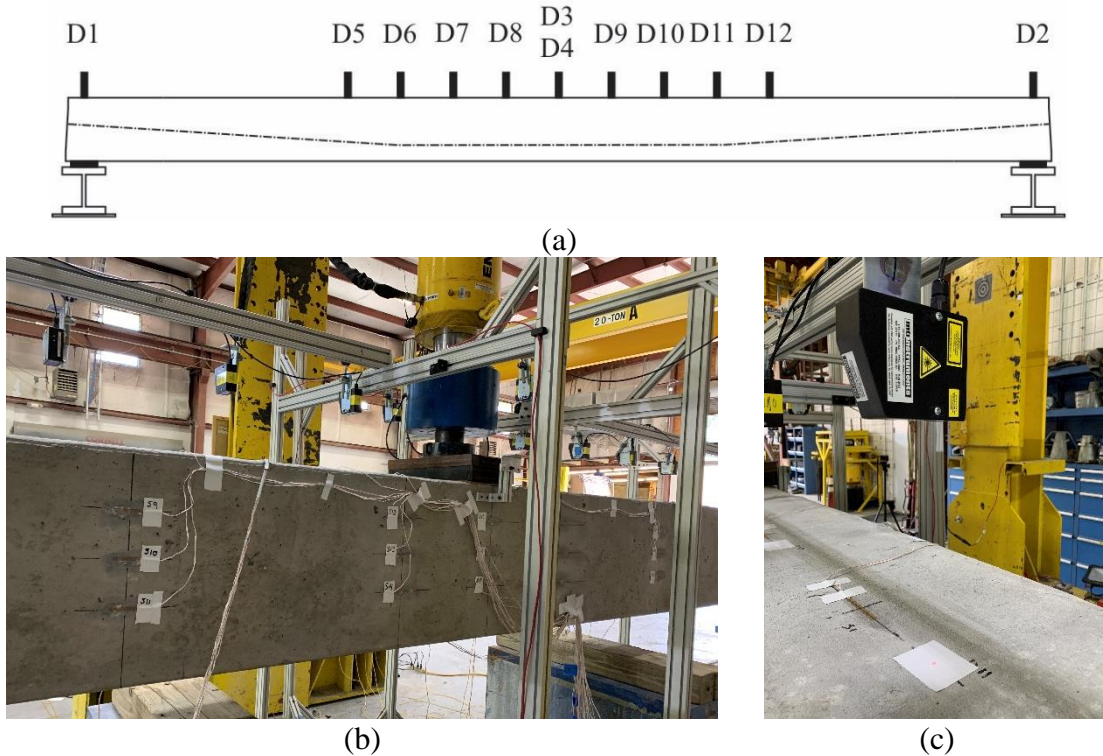
Figure 6.6 Laser displacement transducers – CIP beam specimen SS-5: (a) location of laser displacement transducers, (b) transducers installed along the length of the beam and (c) close-up showing a laser displacement transducer and the surface to which the laser was projected

Strain gages

Concrete strains were measured using 60-mm foil-type strain gages and fiber optic sensors attached to the concrete surface. As depicted in Figure 6.7, 60-mm foil-type strain gages (Kyowa Model KC-60-120-A1-11) were located along the middle 30% of the beam on both top and bottom of the specimen. Additional foil-type strain gages were placed on one side of the web to monitor concrete strain at different elevations near the center of the beam. Specific details about the location of foil strain gages are presented in Appendix B.
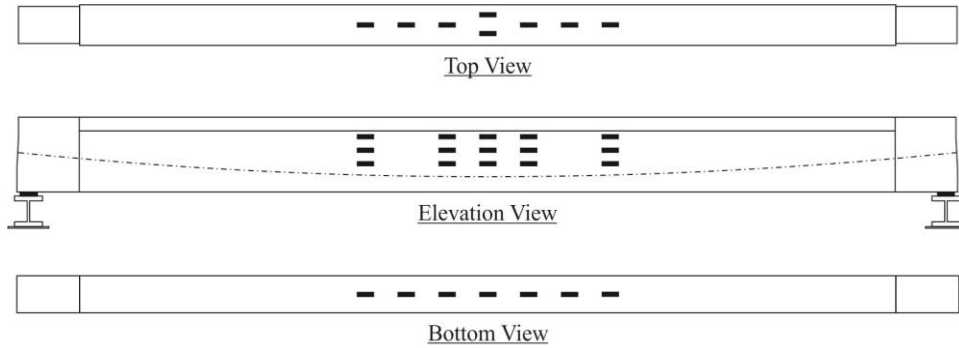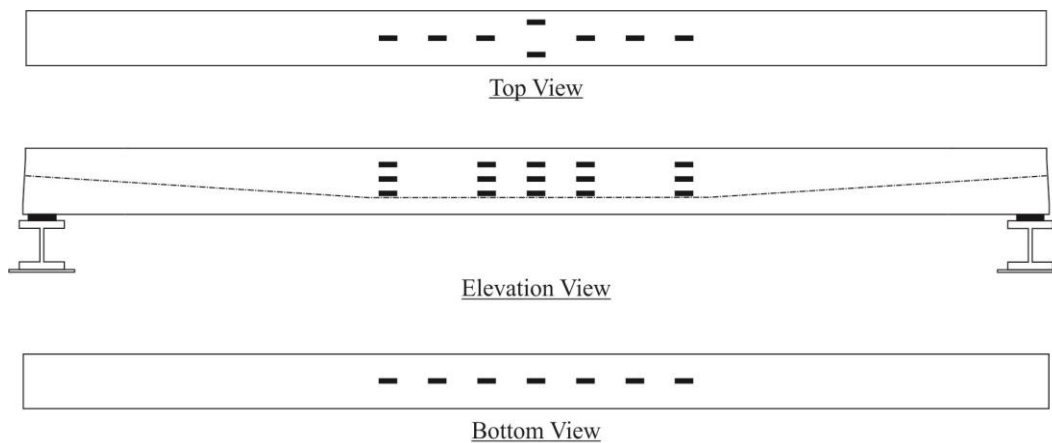

Figure 6.7 Location of 60-mm foil strain gages: CIP beam specimen SS-5

Figure 6.8 60-mm foil strain gages installed on CIP beam specimen SS-5

Along with foil strain gages, fiber optic sensors (FOS) were installed to allow the monitoring of distributed concrete surface strains. FOS were placed on the bottom and on one side of the beam web to monitor tensile and compressive concrete strain. Figure 6.9 shows the location of FOS on specimen SS-5; see Appendix B for specific locations and dimensions.
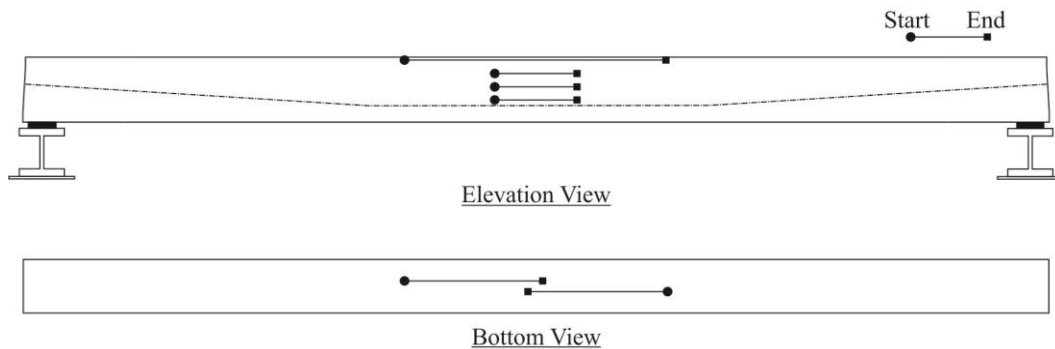
Figure 6.9 Location of fiber optic sensors: CIP beam specimen SS-5

Figure 6.10 Fiber optic sensors installed on CIP beam specimen SS-5

To provide an additional means of estimating the plastic hinge length for the CIP beam, 5-mm foil-type strain gages (Kyowa Model KFGS-5-120-C1-11) were attached to mild steel

longitudinal reinforcing bars. The steel strains were monitored in the bottom longitudinal bars of specimen SS-5 at different locations along the length of the beam as shown in Figures 6.11 and 6.14. Fiber optic sensors were also installed in some of the longitudinal bars on the bottom of the beam as shown in Figure 6.12. The longitudinal rib of the bar was sanded with an 80 grit sanding disc on an angle grinder and cleaned with alcohol thoroughly. Then, the fiber was glued to the bar (Figures 6.13 b and 6.14 b) with M-bond 200 adhesive and catalyst.
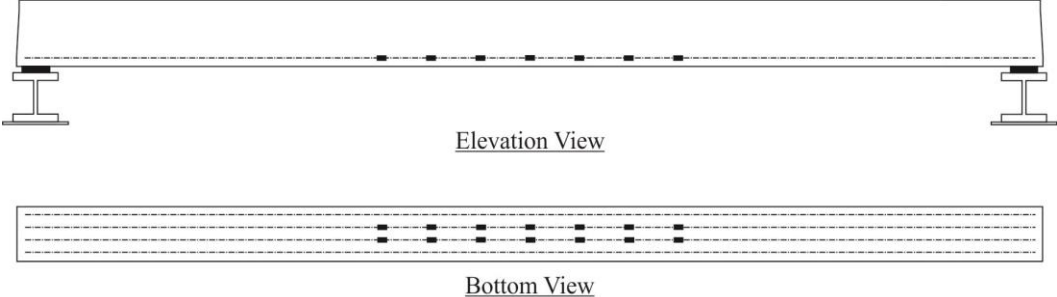
Figure 6.11 Location of 5-mm foil strain gages: CIP beam specimen SS-5
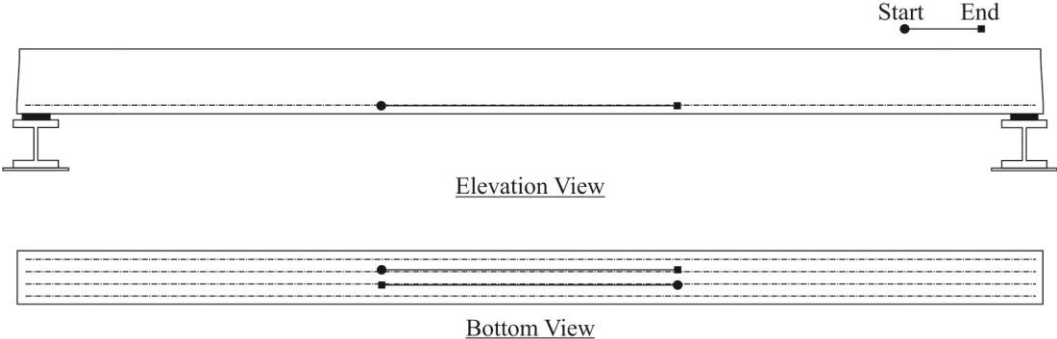
Figure 6.12 Location of fiber optic sensors on longitudinal rebar: CIP beam specimen SS-5

(a)

(b)
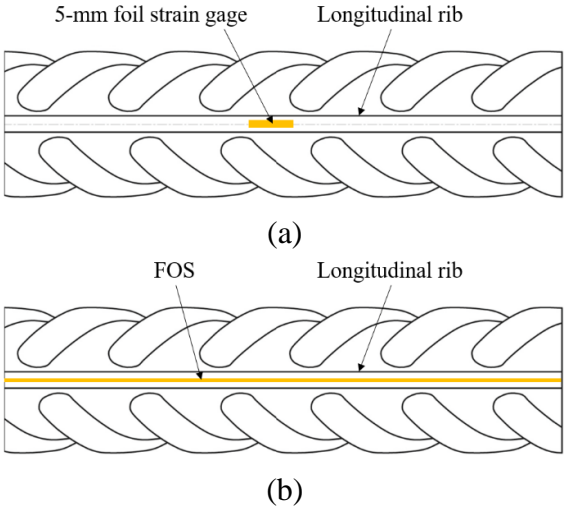
Figure 6.13 Location of instrumentation on the longitudinal rib of rebar: (a) 5-mm foil strain gage and (b) FOS

<div style="text-align:center">(a)   (b)</div>
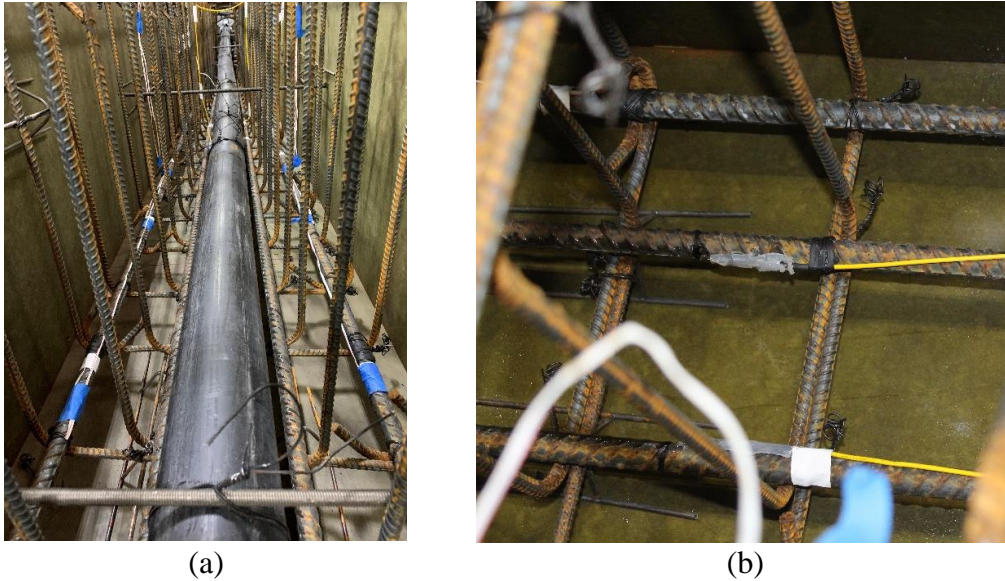
Figure 6.14 Instrumentation on mild steel bars: CIP beam specimen SS-5
(a) 5-mm foil strain gages and (b) FOS

6.4 Test procedure

Following completion of construction and installation of instrumentation, beam specimen SS-5 was moved into the loading frame for testing. The beam was tested incrementally by applying load at a rate of 0.25 kip/sec at midspan. Loading was paused (held constant) periodically at specified load levels to inspect the beam and mark cracks. Once the load exceeded levels that were deemed safe for marking cracks, loading was continued until the test was terminated. The test was terminated after compressive failure occurred.

6.5 Experimental test results

This section presents a summary of results obtained from the experimental test conducted on beam specimen SS-5. Detailed test results, including photographs, sketches of crack patterns, and plots of selected data from instrumentation, are provided in Appendix D.

The CIP beam specimen indicated a nominal load capacity (P_n, load at which concrete strain $\varepsilon_c = 0.003$) of 126.6 kip and maximum load (P_{max}) of 135.0 kip. Figure 6.15 shows the experimental load-displacement curve. Rebar strain data indicated bar yielding at an applied load of approximately 85 kip (Figure D.8), but stresses in the PT tendon remained below 0.8 f_{pu} (Figure D.7) for the entire duration of the test.

Cracks were initially observed at midspan near the bottom of the beam and eventually propagated for approximately 35% of the beam length. Specimen SS-5 exhibited compressive failure with crushing of the concrete on top of the beam at midspan.
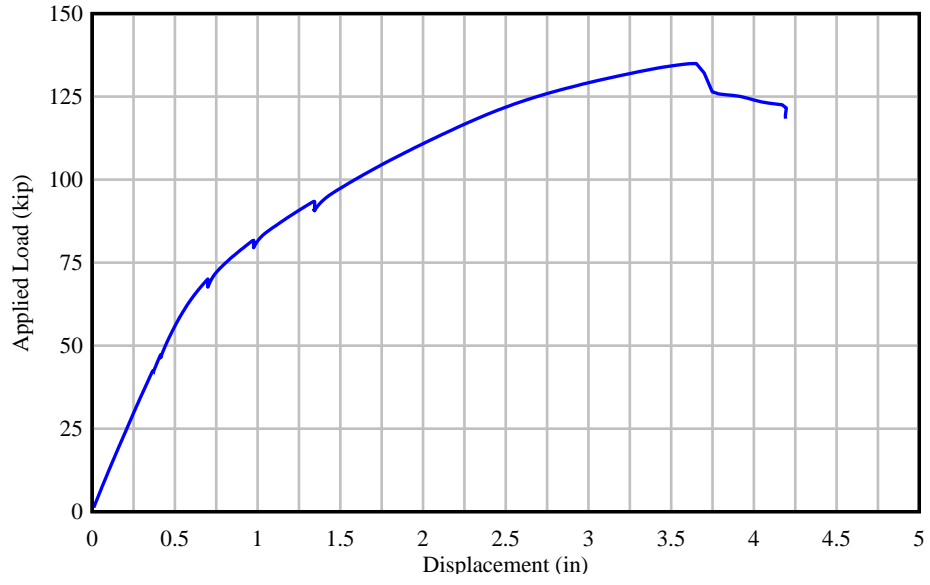
Figure 6.15 Load-displacement plot: SS-5

CHAPTER 7
EXPERIMENTAL STUDY ON NEGATIVE BENDING PRECAST BEAMS

7.1 Specimen construction

Three 27-ft-long beams were constructed as negative bending specimens. These beam specimens consisted of modified AASHTO Type II sections and an 8-in.-thick concrete deck (Figure 4.2a). Similar to SS precast specimens, the side forms of an AASHTO Type II girder and AASHTO Type III bottom liners were used. Specimen orientation on the prestressing bed is shown in Figure 7.1. The modified AASHTO shape was cast first and the deck was cast afterwards in the same prestressing bed; Table 7.1 presents the fabrication timeline.
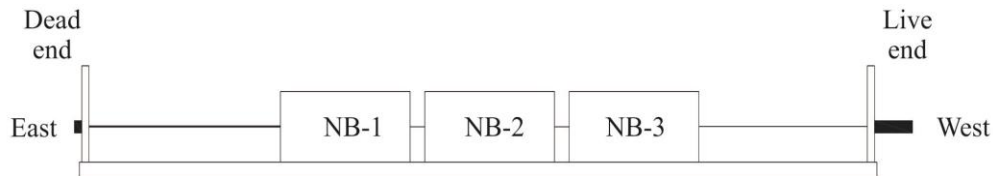
Figure 7.1 Specimen orientation on prestressing bed: NB precast beams (not to scale)

Table 7.1 Specimen fabrication timeline: NB precast beams

Specimen	Strands tensioned	Concrete Placement		Detensioned
		Mod. AASHTO section	Concrete deck	
NB-1	Jan. 31, 2020	Feb. 4, 2020	Feb. 5, 2020	Feb. 6, 2020
NB-2	Jan. 31, 2020	Feb. 4, 2020	Feb. 5, 2020	Feb. 6, 2020
NB-3	Jan. 31, 2020	Feb. 4, 2020	Feb. 5, 2020	Feb. 6, 2020

Custom plywood bulkheads (Figure 7.2) were used to accommodate the pretensioned strands and post-tensioning ducts while also allowing an increase of the web width to 10 in. Strands were individually inserted from the dead end through the bulkheads and the live end. Some of the strands were debonded as specified on fabrication drawings (Appendix A) using PVC sheathing, but 1 ft of strand was left to be bonded at the center of the beams.

Prestressing strands were tensioned using a monostrand hydraulic jack (Figure 5.5). Note that an atypical strand layout was used for NB specimens. Therefore, it was necessary to add deflectors at the ends of the prestressing bed. Custom-made steel sawhorses were placed before the bulkheads for specimen NB-1 (Figure 7.3a) and after the bulkheads of specimen NB-3 (Figure 7.3b). In addition to the steel deflectors, plywood bulkheads (as shown in Figure 7.4) were used to provide the proper separation between prestressing strands. The prestressing strands were sloped from the deflectors to the dead and live ends. All prestressing strands in NB specimens consisted of 0.6-in. diameter strands tensioned to a target force of 43.75 kip within a tolerance of ± 2.5%, following the tensioning pattern shown in Figure 7.5.

Following the tensioning of prestressing strands, 3-in. diameter, DR 17 smooth HDPE ducts were installed for future post-tensioning of the beam specimens. The HDPE ducts were inserted in the bulkhead cutouts at specific elevations corresponding to the PT tendon profile and secured in place using tie wires.

Pre-bent mild steel bars were used to assemble rebar cages for the beams as specified in fabrication drawings (Appendix A). Figure 7.6 shows the rebar cages and HDPE ducts in place for

the NB precast specimens. Lifting loops (consisting of four ½-in. diameter strands) were installed at the end of each beam for transportation.

Figure 7.2 Custom plywood bulkheads for NB precast beams

(a)

(b)

Figure 7.3 Bulkheads and steel deflectors for prestressing strands: NB precast beams

Figure 7.4 Plywood bulkhead for prestressing strands on NB specimens
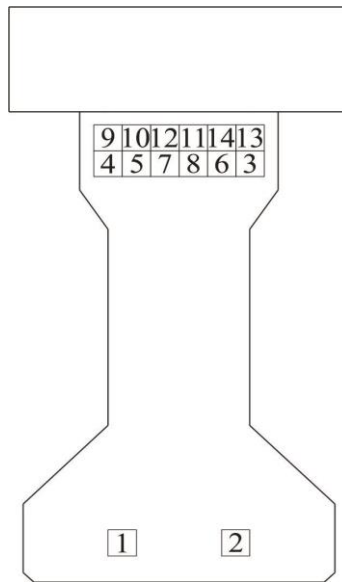
Figure 7.5 Prestressing strand jacking sequence for NB precast beams

Figure 7.6 Rebar cage and HDPE duct installation for NB precast beams
(before the ducts were tied for final configuration of tendon profile)

Along with AASHTO Type III liners, AASHTO Type II forms were placed on the bed around the rebar cages and custom cut pieces of Styrofoam were glued to the surface of the side forms to create the desired cross-section (Figure 5.11).

Concrete was placed in separate stages for the modified AASHTO Type II shape and the concrete deck. Class VI (8500 psi) concrete mixes prepared at an on-site batch plant were used for all NB beam specimens. Concrete cylinders were taken from each batch to conduct strength tests (performed by plant quality control team) for detensioning and experimental testing.

Similar to SS precast beams, the top surface of NB beams was given a trowel finish (Figure 5.12b) for future cast of the concrete deck. Once the AASHTO Type II forms were removed, reusable plywood formwork and longitudinal and transverse mild steel reinforcement were installed for construction of the concrete deck.

The concrete strength for release was specified as 6000 psi for all beam specimens, including both the modified AASHTO shape and the concrete deck. Field cured concrete cylinders were tested by the quality control team from the precast plant a day after concrete placement and before detensioning. The concrete strengths from these tests are summarized in Table 7.2.

Table 7.2 Concrete strengths prior detensioning of pretensioned strands: NB precast beams

Concrete Placement	Date cast	Date tested	Concrete strength (psi)
#1: Mod. Type II section (NB)	Feb. 4, 2020	Feb. 5, 2020	5,440
		Feb. 6, 2020	6,780
		Feb. 6, 2020	7,020
#2: Deck (NB)	Feb. 5, 2020	Feb. 6, 2020	5,430
		Feb. 6, 2020	6,040
		Feb. 6, 2020	6,360

The pretensioned strands were cut following the sequence shown in Figure 7.7 using acetylene torches. Due to the unconventional strand layout, NB specimens were detensioned by cutting the strands in two phases: (1) east and west ends of prestressing bed and (2) between specimens NB-1 and NB-2 and between specimens NB-2 and NB-3 (as depicted in Figure 7.8). Figure 7.9 shows the strands being cut at one of the ends of the prestressing bed and between beam specimens.
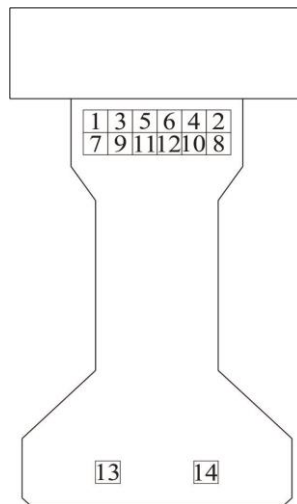
Figure 7.7 Detensioning pattern for NB specimens

74
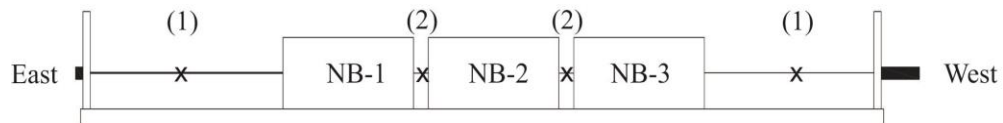
Figure 7.8 Detensioning locations for NB specimens (identified with 'X' marks)

(a)

(b)

(c)

Figure 7.9 Detensioning of NB specimens: (a) strand cut on west end of prestressing bed, (b) cut strands on specimen NB-3, and (c) strand cut between specimens NB-2 and NB-3

A visual inspection was conducted following the detensioning of NB specimens. End-region inclined cracks were found in the top flange at the ends of specimens NB-1 and NB-2 as shown in Figure 7.10. Specimen NB-3 did not present this type of cracks, but concrete spalling occurred on the south side of the beam (Figure 7.11a) starting at approximately 12 ft from the west end and extending for about 5 ft, which was near the midspan region. Note that although some of

the top pretensioned strands were designed as 'debonded', they were still bonded for a distance of 1 ft at midspan. The concrete spalling in this region was attributed to the fact that rapid (dynamic) elastic shortening (from detensioning) of the debonded strands was halted by just 1 ft of bonded length. As discussed in Section 4.2, the width of the web was increased to fit HDPE ducts for internal PT tendons, but the top flange conserved the original dimensions from a typical AASHTO Type II section although pretensioned strands were located in the top flange. The concrete clear cover at the location of the top pretensioned strands was only 1½ in, which contributed to the occurrence of spalling in that area. The concrete was sounded with a hammer to determine areas of delamination and areas producing a 'hollow' sound were marked with a red crayon as shown in Figure 7.11b. Although the cracks extend for the entire height of the top flange, partial demolition on the top flange of the beam later confirmed there were no through cracks. As shown in Figure 7.11c, one spall coincided with the end of debonding of the pretensioned strands. Concrete spalling was attributed to the local impact from strand release. The affected area was repaired at the FDOT Structures Research Center using Fast Patch 2 (APL no. 930-011-003), which is an FDOT approved product for concrete repair on predominately vertical surfaces (Figure 7.12).

The precast beams were transported to the FDOT Structures Research Center, where concrete end blocks were fabricated. Figure 7.13 shows part of the formwork used for fabrication of the end blocks. Rebar cages (Figure 7.14) were assembled using pre-bent mild steel bars conforming to the fabrication drawings included in Appendix A. As listed in Table 4.1, the specified concrete strength for end blocks NB-1 was 6500 psi while the specified concrete strength for end blocks NB-2 and NB-3 was 8500 psi since the latter beams have two post-tensioned tendons and required higher concrete strength per strut-and-tie calculations. Figure 7.15 shows the end blocks during concrete placement and after formwork was removed. Concrete cylinders were collected from each concrete batch and tested at 28 days. Beams were post-tensioned after the end blocks reached the specified compressive concrete strength. Post-tensioned strands were prestressed to a target of $0.75f_{pu}$ using a multi-strand jack as shown in Figure 7.16.

(a)   (b)
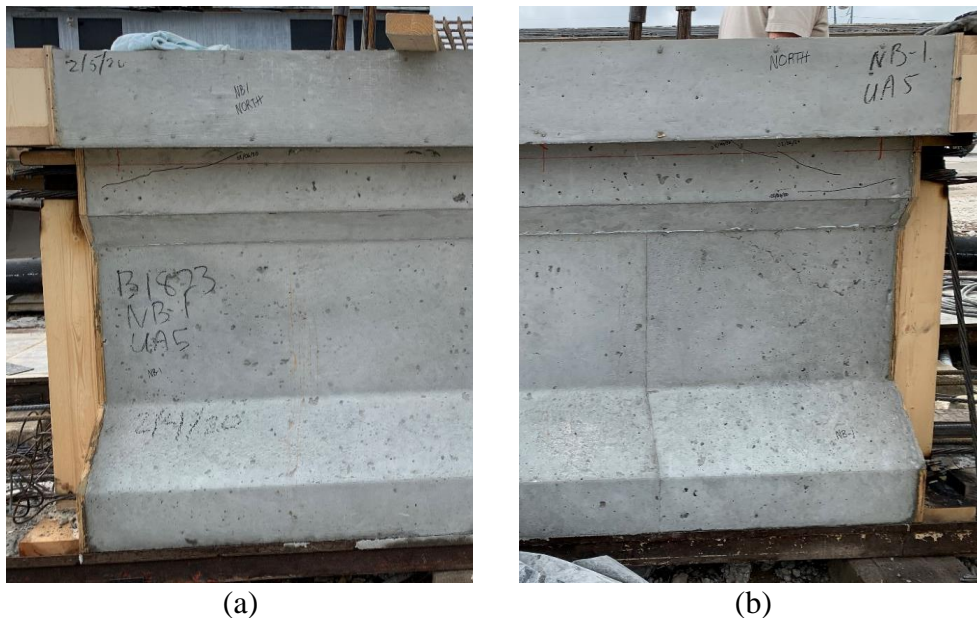
Figure 7.10 Formation of cracks on north side of specimen NB-1: (a) east and (b) west ends

(a)
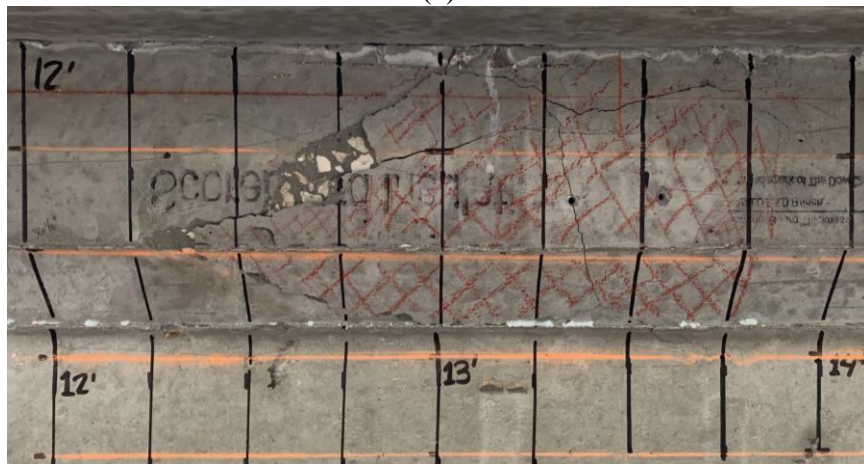
(b)
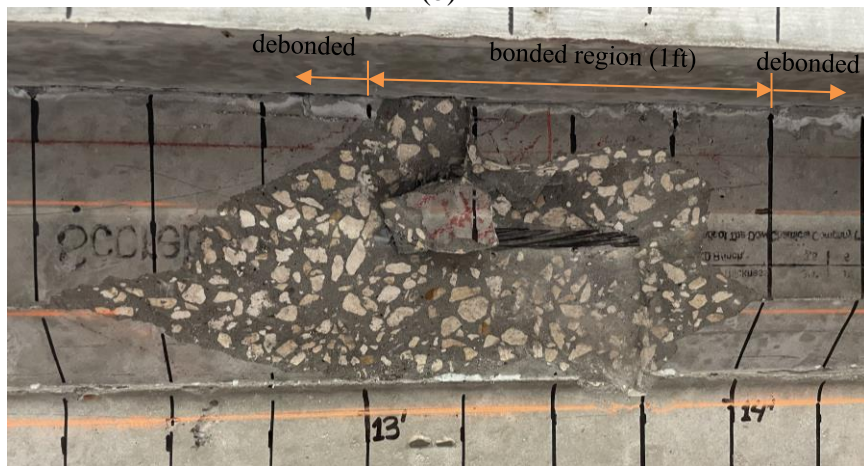
(c)

Figure 7.11 Close-up photos of concrete spalling on south side of specimen NB-3 starting at 12 ft 3 in. from west end: (a) marked cracks after detensioning of pretensioned strands at precast plant; (b) 3-in. x 3-in. grid and red marks showing 'hollow' areas; (c) partial demolition on top flange showing pretensioned strand at the end of debonding

Figure 7.12 Top flange repair on beam specimen NB-3

| (a) | (b) |

Figure 7.13 Installation of formwork for fabrication of end blocks for NB specimens: (a) view of side forms at one end of beam specimen NB-3, (b) completed formwork for end blocks for beam specimens NB-2 and NB-3

<div align="center">(a)   (b)</div>

Figure 7.14 Rebar cage for end blocks – beam specimen NB-3: (a) perspective view of rebar cage; (b) top view showing rebar cage and post-tensioning anchorage system

<div align="center">(a)   (b)</div>

Figure 7.15 Fabrication of end blocks: (a) concrete placement; (b) end blocks (NB-2 and NB-3) after removal of formwork

Figure 7.16 Post-tensioning of NB specimens

7.2 Test setup

Negative bending specimens were subjected to a static concentrated load applied at one end of the beam (Figure 7.17) such that a negative moment was generated over the interior support. The beams were supported by steel load blocks (height = 24 in., plan area = 18 in. x 48 in.). At the other end (opposite from the load point) the beam was tied down to the laboratory strong floor using a frame consisting of W16x100 (R33) and C12x30 (R14) spreader beams and 1.5 in. diameter high strength threaded bars. Load was applied using an Enerpac RR-40018 actuator (Figure 5.26). For detailed dimensions see Appendix B.
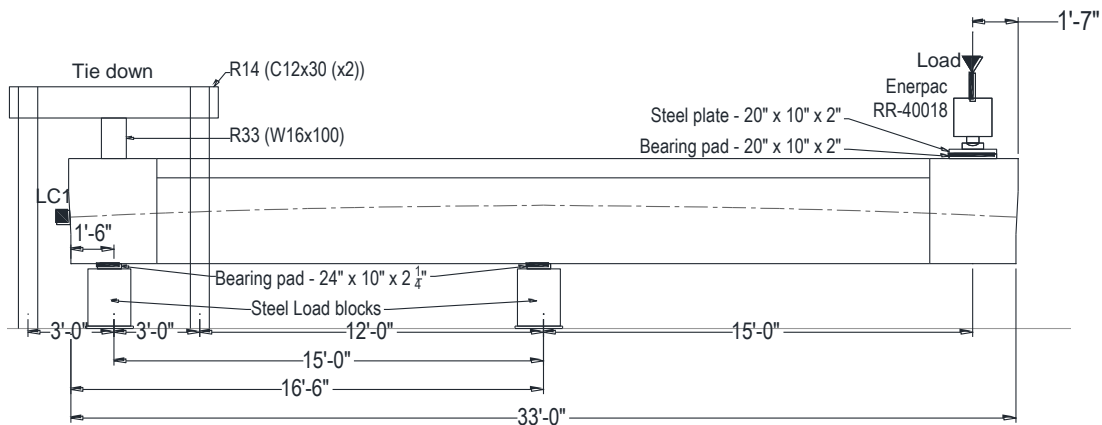
Figure 7.17 General flexural test setup: NB beam specimens

7.3 Instrumentation

Instrumentation on negative bending precast beam specimens included displacement gages, strain gages, and load cells. Data were gathered from the instrumentation during two key phases: during stressing of post-tensioned tendons and during load-testing.

Load cells

The axial force in post-tensioned tendons was directly measured using 850-kip Geokon hollow-core load cells. As shown in Figure 7.18, the load cells were located at the dead end of the beams with the PT tendon(s) passing through them.
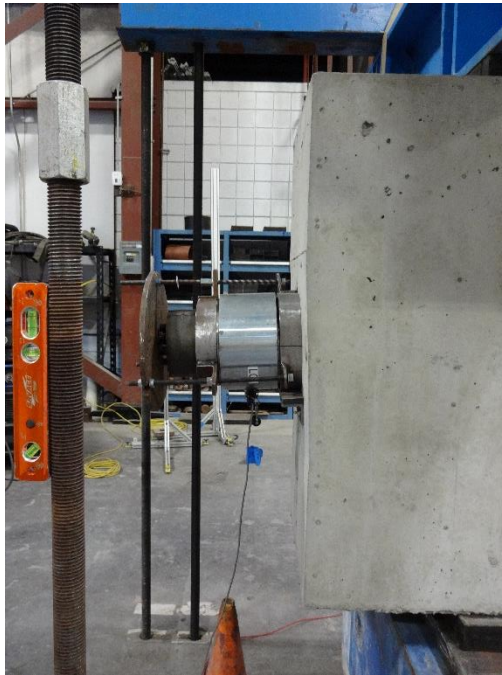
Figure 7.18 Geokon hollow-core load cell installed at dead end of beam specimen NB-1

Displacement transducers

Vertical displacements were monitored through the use of laser displacement transducers distributed along the middle 40% of the length of the specimens. Additional laser displacement transducers were also positioned near the span ends. Figure 7.19a shows the general distribution of laser displacement transducers along the length of NB precast beam specimens (see Appendix B for specific locations).
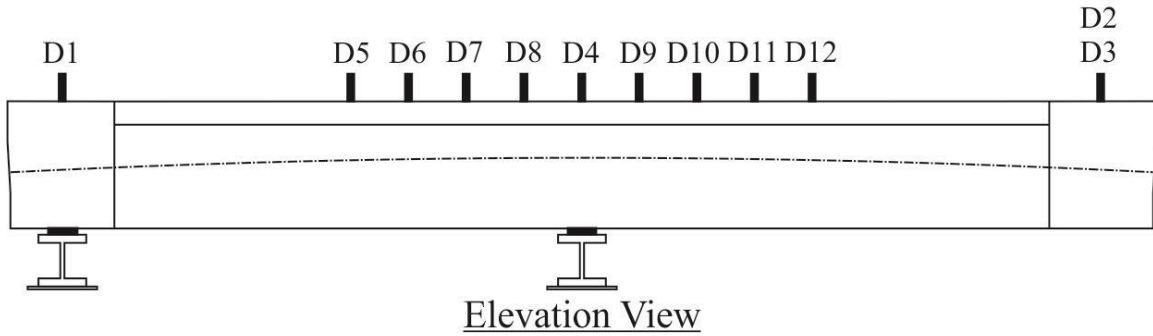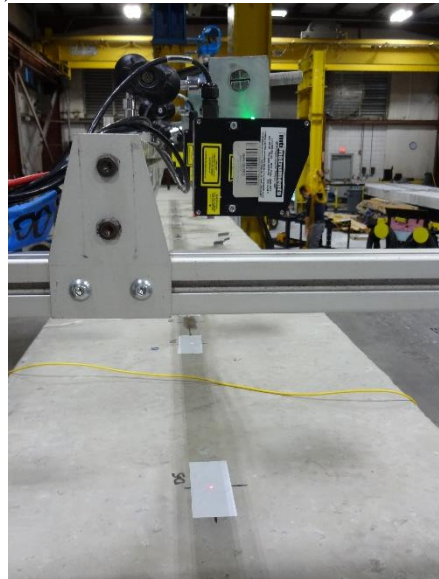
Figure 7.19 Laser displacement transducers – NB precast specimens: (a) location of laser displacement transducers, (b) typical transducers installed on a NB beam specimen along the length of the beam and (c) at the loaded end, and (d) close-up showing a laser displacement transducer and the surface to which the laser was projected

Vibrating wire (VW) strain gages (Geokon Model 4200) were installed during fabrication of specimens at the precast plant. These gages were installed to determine prestress losses and, therefore, effective prestress forces in the pretensioned strands. As shown in Figure 7.20, VW gages were installed at the center of the beams midspan in the bottom and top layers of prestressing strands.

Figure 7.20 Vibrating wire gages installed in NB precast specimens

Concrete strains were measured using 60-mm foil-type strain gages and fiber optic sensors attached to the concrete surface. As depicted in Figure 7.21, 60-mm foil-type strain gages (Kyowa Model KC-60-120-A1-11) were located along the middle 30% of the beam on both top and bottom of the specimen. Additional foil-type strain gages were placed on one side of the web to monitor concrete strain at different elevations near the center of the beam. Detailed location information for the foil strain gages is presented in Appendix B.
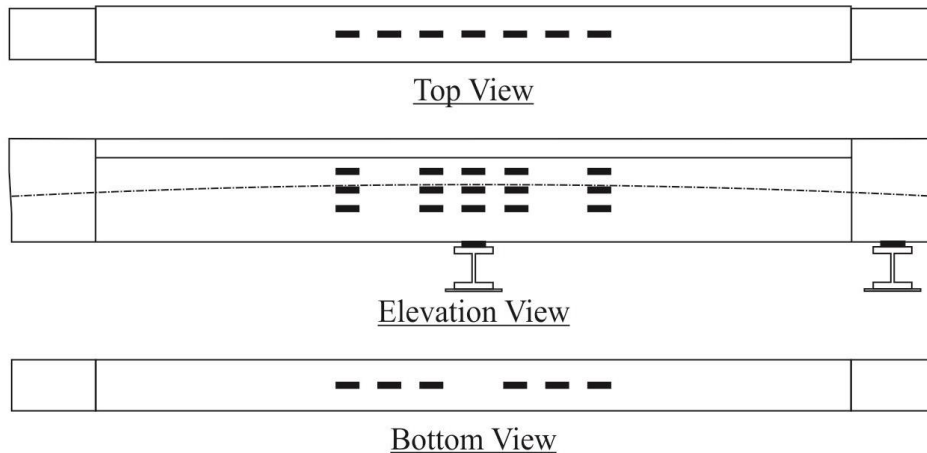
Figure 7.21 Location of 60-mm foil strain gages: NB precast specimens

Figure 7.22 Typical 60-mm foil strain gages installed on NB precast specimens

Along with traditional strain gages, fiber optic sensors (FOS) were installed to allow the monitoring of distributed concrete surface strains. Placing FOS at different elevations on the beam specimen allowed for the calculation of beam curvature and deflection at the point in time that the measured data indicate crack formation. For NB specimens, FOS were placed on the web surface and near the top and bottom of the beam to monitor both tensile and compressive concrete strains. Figure 7.23 show the general location of FOS on NB precast beams; see Appendix B for specific locations and dimensions.
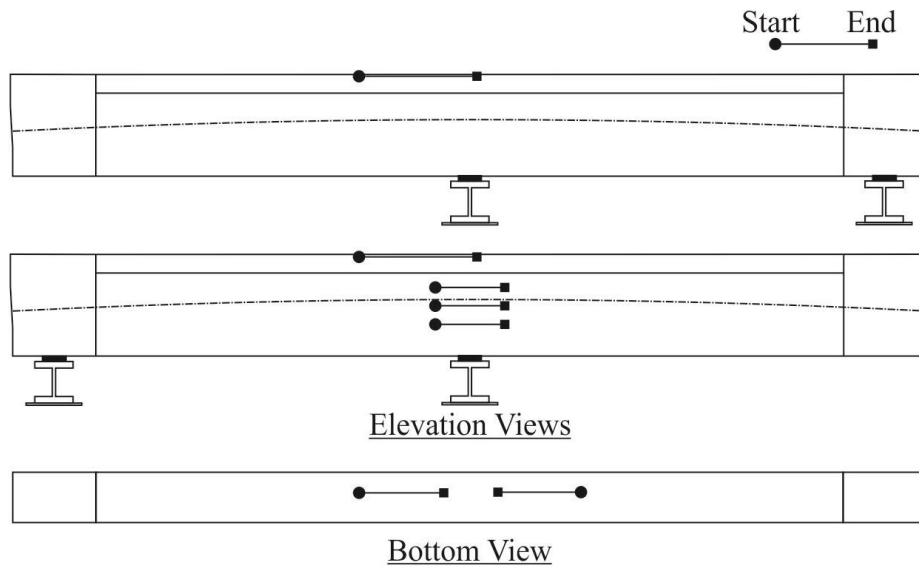
Figure 7.23 Location of fiber optic sensors: NB precast specimens
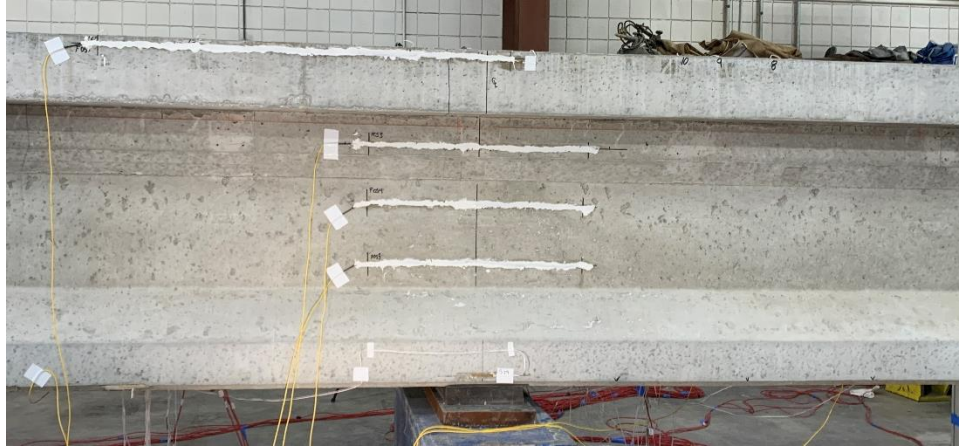
Figure 7.24 Typical fiber optic sensors installed on NB precast specimens

To provide an additional means of estimating the plastic hinge length for the NB specimens, 5-mm foil-type strain gages (Kyowa Model KFGS-5-120-C1-11) were attached to mild steel longitudinal reinforcing bars. Steel strains were monitored in the top bars of the NB specimens at different longitudinal locations as shown in Figures 7.25 and 7.26.

Top View

Elevation View
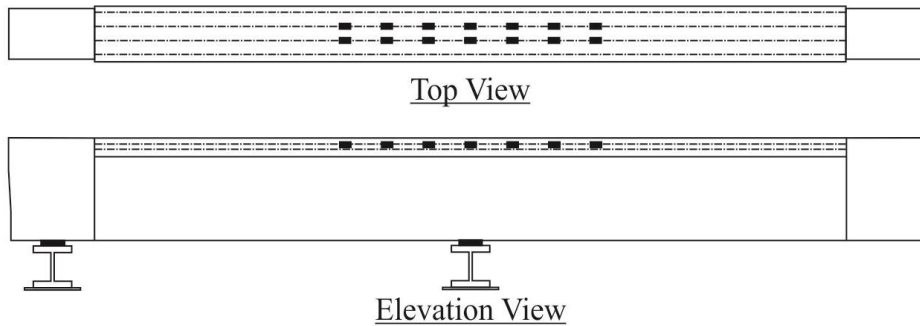
Figure 7.25 Location of 5-mm foil strain gages: NB precast specimens

Figure 7.26 5-mm foil strain gages installed on NB precast specimens

7.4 Test procedure

Following completion of construction and installation of instrumentation, the beam specimens were moved into the loading frame for testing. Specimens were tested incrementally by applying load at a rate of 0.25 kip/sec at one end of the beams. Loading was paused (held constant) periodically at specified load levels to inspect the beam, mark cracks, and take readings from VW strain gages. Once load exceeded levels that were deemed safe for marking cracks, loading was continued until the test was terminated. Tests were terminated when either compressive failure occurred, compressive concrete strains were larger than 0.003, or a maximum predicted load was exceeded.

7.5 Experimental test results

This section presents a summary of the results obtained from experimental tests conducted on negative bending precast beams with different amounts of unbonded and bonded prestressed reinforcement. Detailed test results, including photographs, sketches of crack patterns, and plots of selected data from instrumentation, are provided in Appendix E.

A summary of the nominal load capacity (P_n, load at which concrete strain $\varepsilon_c = 0.003$) and maximum load (P_{max}) is presented in Table 7.3. Figure 7.27 shows a comparison of load-displacement plots for all three negative bending beam specimens. All three NB specimens exhibited similar flexibility. Similar to simply-supported beams, NB beam specimens with the same total amount of reinforcement (NB-2 and NB-3) demonstrated that higher unbonded ratios (U/T) result in a reduction in capacity. On all beam specimens, cracks were initially observed near the middle of the beam on the concrete deck. As load was applied, cracks on specimen NB-1 propagated for approximately 60% of the beam length while cracks on specimens NB-2 and NB-3 propagated for approximately 30% of the beam length. The stress in the PT tendons remained almost constant during most of the loading test. PT stresses remained below 0.75 f_{pu} on all of the NB specimens. Contrary to the PT tendons, pretensioned strands exhibited a significant increase in stress as load was applied. Beam specimen NB-2 exhibited sudden compression failure in the bottom flange (Figure E.19).

Table 7.3 Flexural capacity of precast negative bending beams

Beam specimen	U/T	L/D	Applied load (kip) at $\varepsilon_c = 0.003$	Max. load (P_{max}, kip)	Rupture of PreT strand
NB-1	0.5	20	220.0	223.4	No
NB-2	0.6	20	207.0	222.9	No
NB-3	0.7	20	186.1	191.2	No
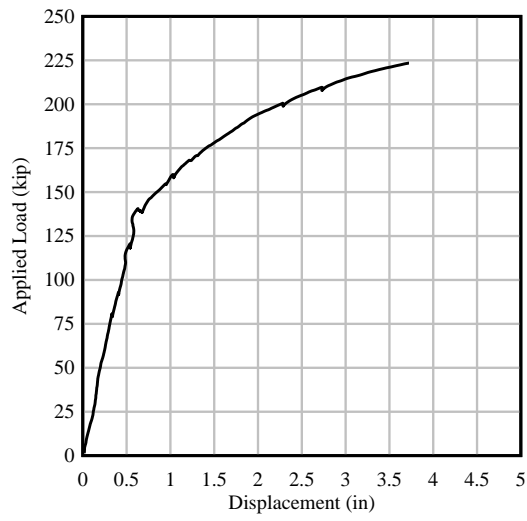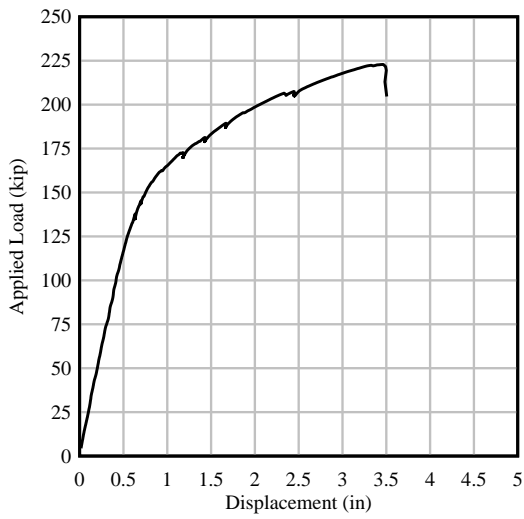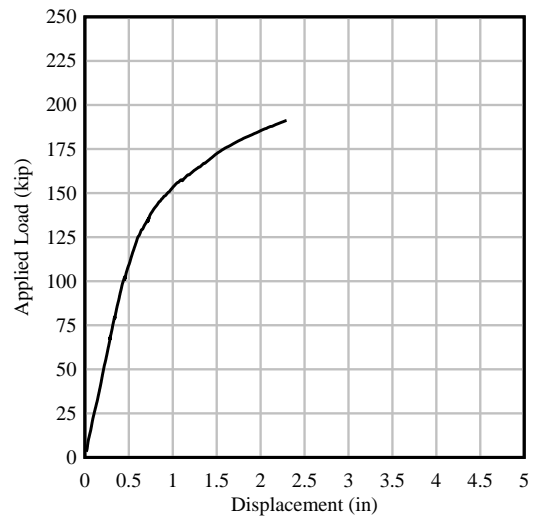
Figure 7.27 Load-displacement plots: (a) NB-1, (b) NB-2, and (c) NB-3

CHAPTER 8
FINITE ELEMENT MODELING

8.1 Introduction

This chapter discusses the techniques used to model full-scale prestressed concrete beams with mixed reinforcement using LS-DYNA (Section 8.2). Finite element analyses simulating the experimental beam specimens described in Chapter 4 were validated using experimental data (Section 8.3). Using validated numerical modeling techniques, a series of numerical parametric studies were conducted for different beam sections varying the boundary conditions, reinforcement ratios, loading types, and friction coefficients. Section 8.4.1 presents a parametric study conducted on simply-supported and continuous (negative bending) beams consisting of FIBs of different cross-sectional dimensions with parabolic PT tendon profiles. Section 8.4.2 presents a parametric study on FIB-72 beams with straight PT tendon profiles while Section 8.4.3 discusses a parametric study on AASHTO Type II beams with straight PT tendon profiles. Finite element models were used to evaluate moment capacity, beam curvature, stresses in pretensioned and post-tensioned strands, strain in the concrete surface as well as in mild steel reinforcement bars and prestressing strands, strand rupture, and concrete damage. Results and trends observed from parametric studies are summarized in Section 8.5. Results from finite element models were used to expand the knowledge regarding the behavior of prestressed concrete beams with mixed reinforcement that was obtained from experimental tests.

8.2 Numerical modeling procedures

Analytical models were developed and analyzed using LS-DYNA (R11.0.0; LSTC, 2018). This finite element software package has all the analysis features required to represent the constituents of the prestressed concrete beams investigated in this study. The main constituents and analytical features that need to be considered when modeling prestressed concrete beams are listed below. These are discussed in more detail in the following subsections.

- Concrete
- Mild steel reinforcing bars
- Pretensioned tendons
- Post-tensioned tendons
- Construction stages
- Loads
- Constraints

Material models (properties and stress-strain curves) that are provided in the following subsections correspond to the target design material strengths for each component (e.g., 8.5 ksi concrete for precast girders, 60 ksi for steel rebar, 270 ksi for steel strand). These material models were used in all parametric simulations that were performed in this study. However, in Section 8.3, validation models will be also presented, where finite element results are compared to results obtained from the physical tests that were described in the previous chapters. Material models used in the validation simulations were of the same general form as those presented in the following subsections; however, the specific strength values (e.g., f_c', F_y, f_{pu}) were adjusted to reflect the laboratory measured values of material strengths for components used in the physical tests.

<u>Concrete</u>

All concrete constituents were modeled using 8-node three-dimensional (3D) solid brick elements (Figure 8.1). Generally, to represent concrete it is necessary to specify a compressive strength and other material properties such as the modulus of elasticity, Poisson's ratio, and mass density. However, it is also important to address the nonlinearities of the material in order to represent tensile cracking or compressive crushing. The LS-DYNA concrete material model `MAT_CSCM` (the 'continuous surface cap model') was selected to model the nonlinearities of the concrete. This material model has been shown to be applicable in static and moderate-speed dynamic (e.g. vehicle or vessel impact) scenarios, and includes modeling of both nonlinear deformation and failure (Murray, 2007). A useful feature of the `MAT_CSCM` model is that damage can be visualized with color contours of 'damage index' (Figure 8.2). The damage index parameter ranges from 0 (undamaged; shown as blue) to 1 (fully damaged; shown as red). As depicted in Figure 8.3, before an element reaches maximum strength, all the residual capacity of the material is still available and no damage has occurred (Han and Consolazio, 2018). Therefore, the damage index is equal to 0. Once an element reaches and exceeds maximum strength, damage starts to accumulate. The damage index reaches a value of 1 when no further residual capacity is available. Another feature of this material model that is useful is that it allows for the deletion of elements (referred to as 'erosion' of elements) once the damage index exceeds 0.99 and the maximum principal strain exceeds a value equal to `ERODE-1`. `ERODE` is a user defined value; all the analyses discussed within this report used a value of `ERODE` equal to 1.05.

Since the terminal ends of each beam model were not areas of interest in the numerical simulations—in terms of damage and flexural strength—these areas were modeled using a simpler elastic material model (`MAT_ELASTIC` in LS-DYNA). Using the elastic modeling approach allowed each beam to be analyzed without undergoing localized damage due to high stress concentrations at the post-tensioning anchorage locations. It is important to note that neither the `MAT_CSCM` concrete material model nor the `MAT_ELASTIC` model represented the steel reinforcement; steel reinforcing bars were instead modeled separately.

Concrete constituents were modeled with target design properties. The following compressive strengths were specified for concrete elements: 8.5 ksi for precast concrete sections, 6.5 ksi for cast-in-place concrete, and 4.5 ksi for deck slabs. Appendix F provides details of the cards used in LS-DYNA to define material models `MAT_CSCM` and `MAT_ELASTIC`.
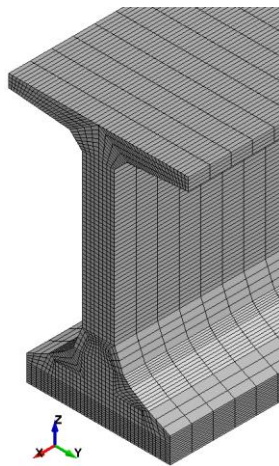

Figure 8.1 Finite element model of FIB 72 girder depicting solid concrete elements
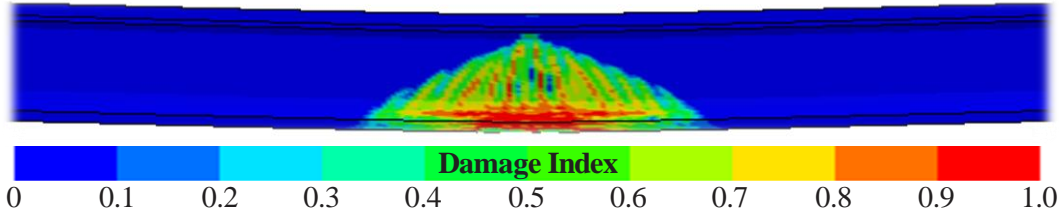
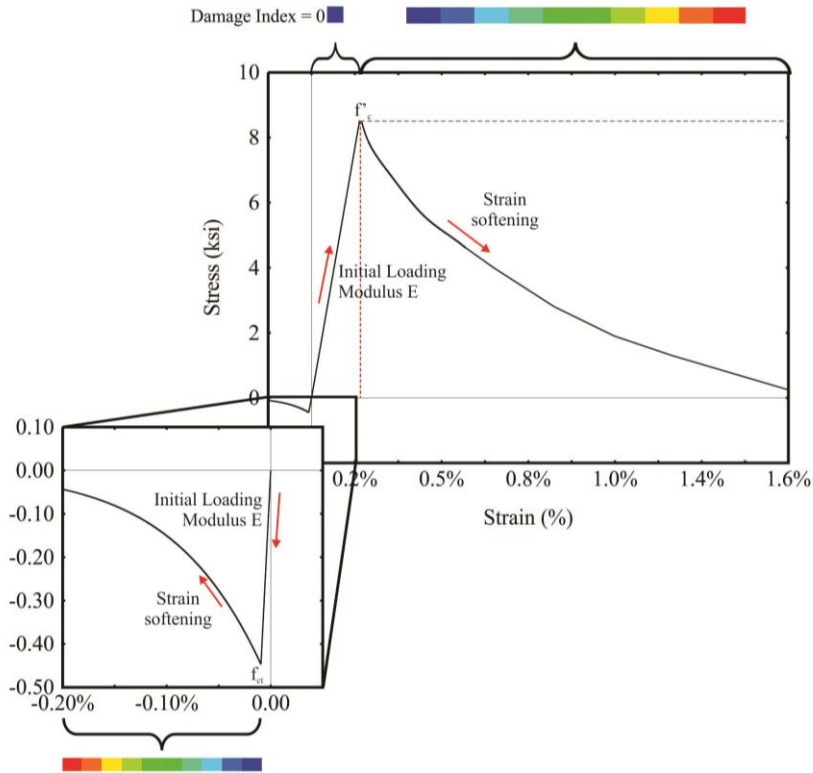Figure 8.2 Damage index on a FIB segment under flexure

Figure 8.3 Damage index as reported by the `MAT_CSCM` material model
(adapted from Murray, 2007)

Mild Steel

Each mild steel reinforcing bar was explicitly meshed using a collection of beam elements that were separate from, but coupled to, the surrounding concrete solid elements (i.e., steel rebar was *not* represented using a 'smeared' approach) as depicted in Figure 8.4. The material behavior of the reinforcing bars was represented using the material model `MAT_PIECEWISE_LINEAR_-PLASTICITY`, which models elastic, plastic, and strain-hardening behaviors. For models that were used in parametric studies, the material properties of mild steel were those corresponding to ASTM A615 Grade 60 reinforcing bars. Figure 8.5a shows an engineering stress (force/original area) versus engineering strain (elongation/original length) curve. Figure 8.5b shows the true stress (force/current area) versus effective plastic true strain (plastic elongation/current length) curve. The data shown in Figure 8.5b, together with parameters such as elastic modulus (E) and Poisson's ratio (ν), constitute the data that are specified in the `MAT_PIECEWISE_LINEAR_PLASTICITY` material model (Appendix F). Note that the effective plastic strain values are equivalent to the

90

residual (i.e., plastic) true strains that would remain after unloading elastically from a given deformation level. To represent the bond between the deformed steel reinforcing bars and the surrounding concrete, degree-of-freedom (e.g. displacement) coupling constraints were automatically-generated using the CONSTRAINED_BEAM_IN_SOLID command (LSTC 2018).
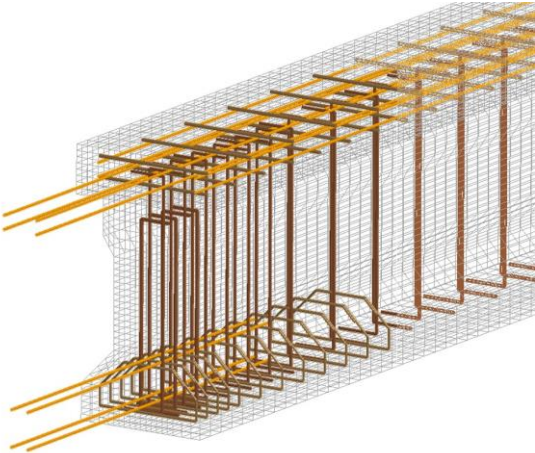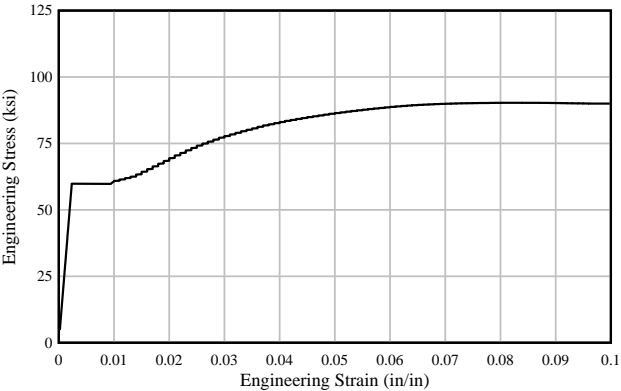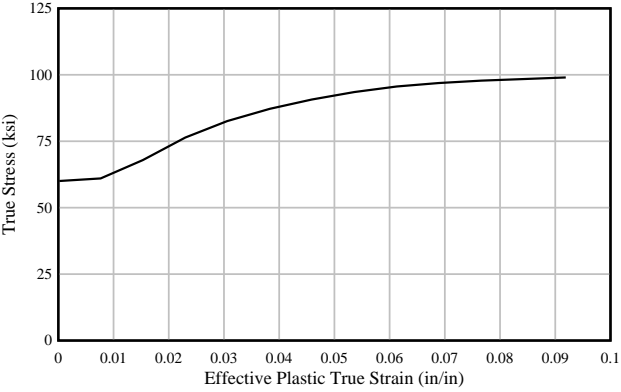

Figure 8.4 Mild steel reinforcing bars modeled in an AASHTO beam section using beam elements coupled to the surrounding concrete elements

(a)

(b)

Figure 8.5 Mild steel reinforcement: (a) engineering stress as a function of engineering strain and (b) true stress as function of effective plastic true strain

Pretensioned tendons (bonded prestressing)

When a concrete member is pretensioned, the tendon is stressed prior to placement of concrete. After the concrete hardens, the individual pretensioned strands are cut, thus allowing transfer of the prestress force to the concrete. A pretensioned tendon is composed of one or more prestressing steel elements (i.e. seven-wire strands). In the finite element models, bonded pretensioning strands were modeled with a specialized type of beam element called a 'discrete beam element'. In this type of element formulation, the shape of the element cross-section is not explicitly identified. Instead, element stiffness is described by a material model and resultant cross-sectional properties (area and moment of inertia). The area of each discrete beam element was defined as the area of individual strands.

In a discrete beam element, material behavior can be nonlinear in form, and element failure criteria (based on ultimate force and/or strain) can be specified. Axial pretensioning of discrete beam elements is achieved by direct specification of the target prestress level (thus avoiding the need to resort to numerical procedures such as the application of artificial 'temperature changes'). The element pretensioning process increases the prestress force linearly over a chosen duration of time (Figure 8.6); automatically tracks total material strain (including the pre-strain); and accounts for elastic shortening of the concrete girder (Figure 8.7). Prestressing forces were applied to all the discrete beam elements representing the pretensioned strands. Since this approach represents the 'perfect bond' condition, transition length effects at each end of each pretensioned strand were modeled by increasing (step increments) the prestress force over the elements that fell within the transition length (Figure 8.8). Since the pretensioned strands were bonded with the surrounding concrete, once external loads were applied to the girder model, element force levels varied within the beam elements.
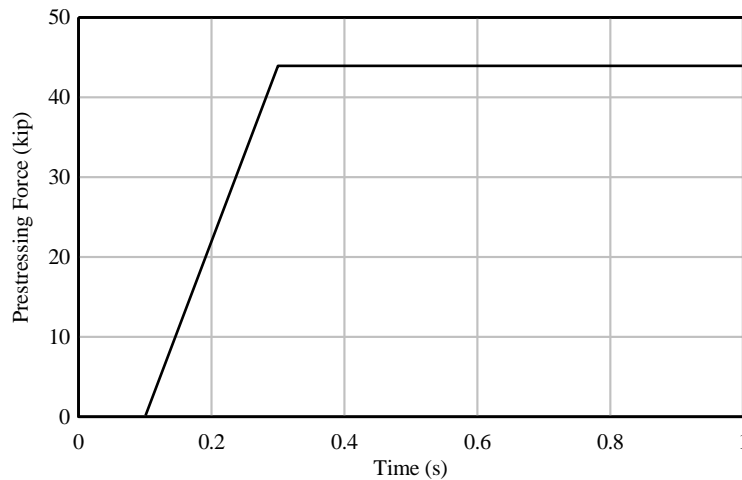

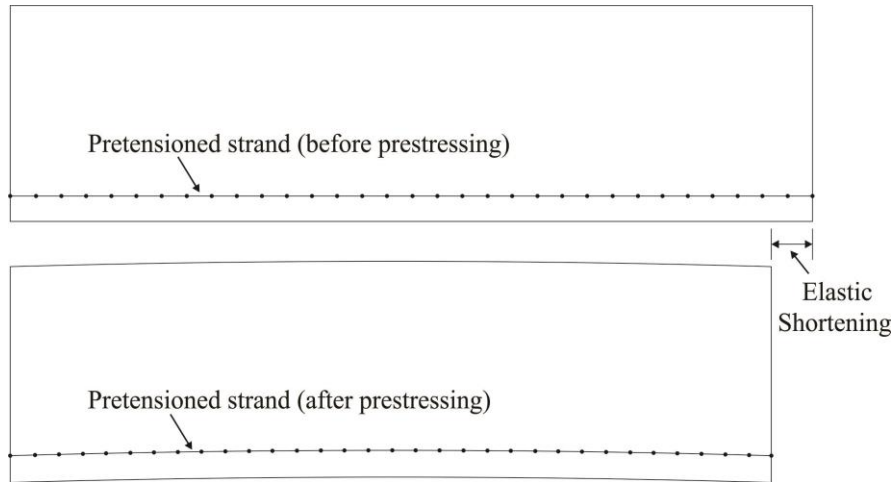Figure 8.6 Prestressing force on individual pretensioned strands

92

Figure 8.7 Elastic shortening on concrete beam due to prestressing of pretensioned strand
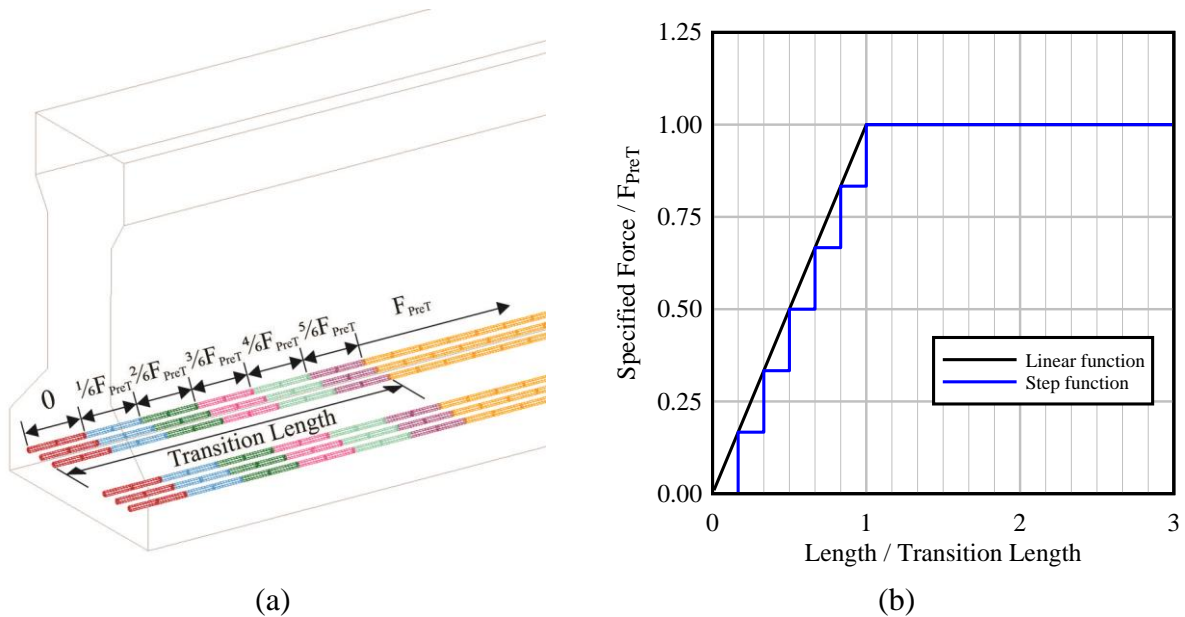

(a)

(b)

Figure 8.8 Specified prestressing force for pretensioned strand elements within transition length: (a) pretensioned strands modeled in an AASHTO beam section using discrete beam elements with different specified target prestressing force (using step function); (b) plot showing linear and step functions for force in pretensioned strands

Material behavior of grade 270 bonded prestressing strands was described in the form of a stress-strain curve (Figure 8.9) and was based on ASTM A416. Appendix F provides details of the cards used in LS-DYNA to define material model MAT_CABLE_DISCRETE_BEAM. To represent bond between the prestressing strands and the surrounding concrete, strain compatibility was imposed by nodal merging between the discrete beam strand elements and the surrounding solid concrete elements (Figure 8.10). However, in cases where the discrete beam nodes and the solid concrete nodes did not coincide, modeling bond between strand and concrete was achieved using degree-of-freedom coupling constraints. These constraints were automatically-generated using the LS-DYNA CONSTRAINED_BEAM_IN_SOLID command.
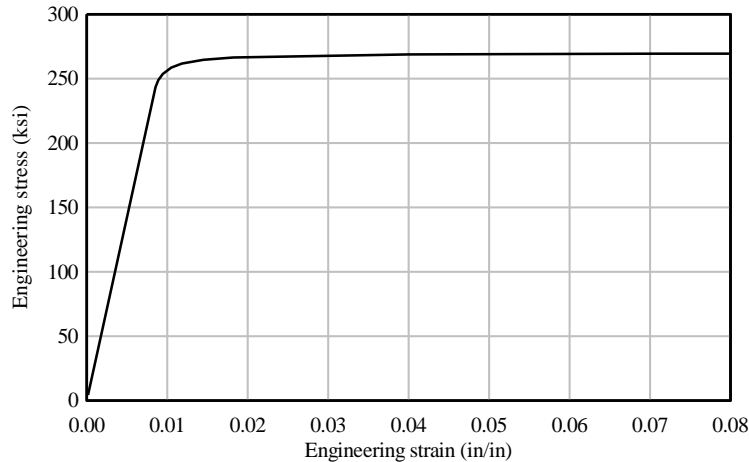
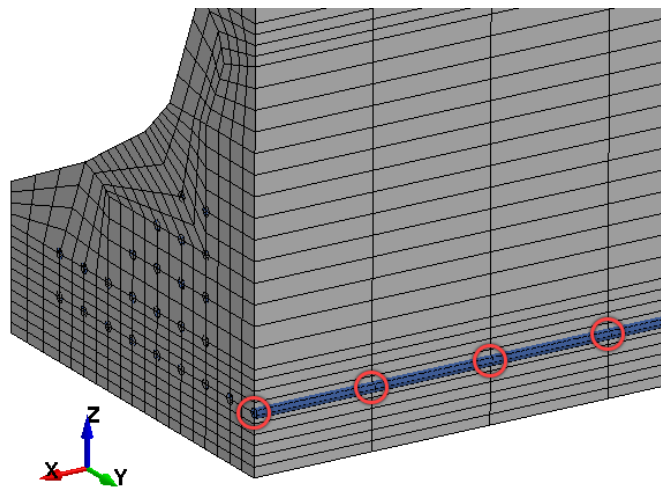Figure 8.9 Material model for prestressing steel

Figure 8.10 Section-cut of beam showing nodal merging between a pretensioned strand and surrounding concrete elements in the beam bottom flange

<u>Post-tensioned tendons (unbonded prestressing)</u>

Post-tensioning tendons consist of one or more prestressing steel elements (i.e. seven-wire strands) placed in ducts within the concrete. PT tendons were modeled using discrete beam elements such that the beam elements had an area equivalent to the total area of the tendon. Axial prestressing forces associated with post-tensioning are applied to the ends of the hardened concrete beam, at either jacking locations or anchorage locations. PT tendons can be classified as either bonded or unbonded. When the PT tendon is located outside the concrete section or injected with flexible fillers, it is considered to be unbonded. All PT tendons in this parametric study were modeled as unbonded prestressing.

For the PT tendons, slip and friction between the tendon and duct were represented using guidance elements (i.e. 'beam pulley' elements in LS-DYNA) as depicted in Figure 8.11. These elements model perpendicular force transfer from unbonded tendons to either PT ducts or deviators, while simultaneously permitting continuous longitudinal sliding. Essentially, the

guidance elements enforce the geometry of the slide-path along which unbonded PT tendons may move. Figure 8.11a depicts a post-tensioning duct passing through a diabolo deviator, which serves as a guidance element for the PT tendon. Friction forces are a function of the curvature of the tendon profile, and friction losses occur when there is a change in angle of the tendon. The frictional model follows the belt friction equation $P - dP \leq Pe^{\mu\alpha}$, where μ is the friction coefficient and α is the wrap angle. The differential friction loss can be expressed as $dP = \mu P d\alpha$. Figure 8.11b presents the idealized mechanism for PT tendons passing through guidance elements. In the finite element models, post-tensioned tendons were prestressed only from one end (the jacking was simulated from one end) of the girder. The tendons were anchored at the other end and were able to slide with unsymmetrical movement. While Figure 8.11c shows a prestressed concrete beam with a PT tendon passing through a diabolo, Figure 8.11d presents a parabolically-draped tendon. To represent the proper geometry of a post-tensioned tendon with a parabolic drape, it was necessary to place guidance elements along the entire length of the beam. Note that, contrary to the bonded pretensioned strands, during beam flexure, the axial force along the unbonded post-tensioned tendons remained approximately constant along the length. For cases in which friction was taken as zero, the axial force remained constant along the entire beam length.
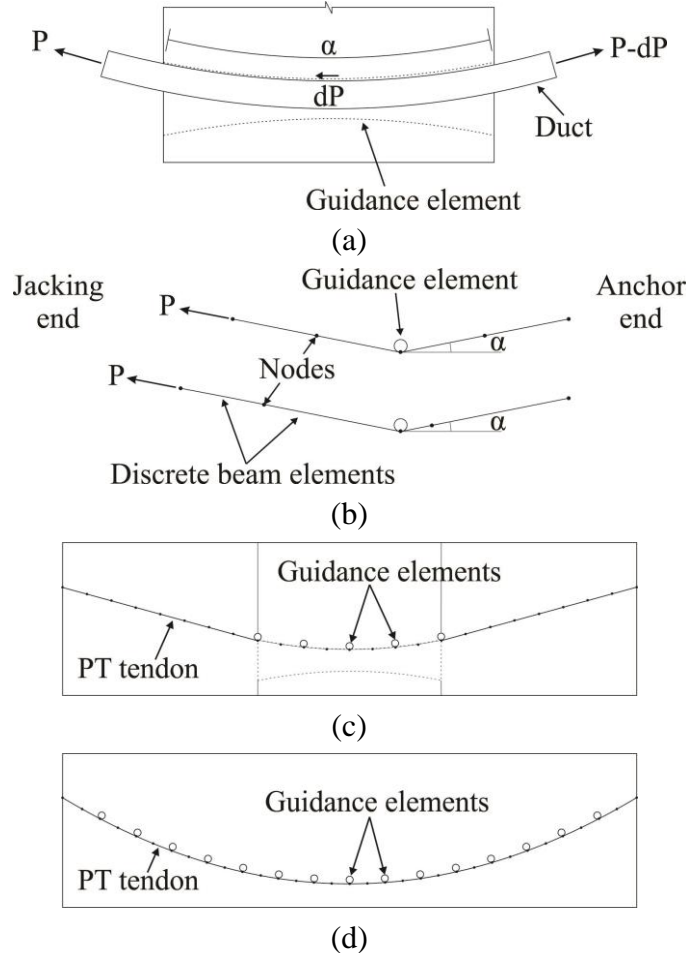

Figure 8.11 (a) PT tendon passing through diabolo deviator; (b) idealized mechanism for PT tendons passing through guidance elements before and after prestressing; (c) post-tensioned concrete member with a diabolo deviator; (d) post-tensioned concrete member with a parabolically draped tendon

<u>Construction Stages</u>

In addition to the physical constituents previously discussed, it was also necessary to represent 'construction stages' in the model. A construction stage in an LS-DYNA finite element model represents a specific structural configuration. Whenever a significant change in structural configuration occurs, e.g., the casting of girder splices or the introduction of the bridge deck, then a new construction stage is initialized. Stress and strain data from each construction stage are carried forward to initialize the pre-existing elements in the next stage. For example, a construction stage representing deck casting carries forward all prior stress and strain data for the pretensioned girder elements (strands, tendons, concrete), but the newly created concrete deck elements are initialized as stress free (until subsequent loading is applied). Sequencing of pretensioning, post-tensioning, gravity, and external load application was also modeled using construction stages. Construction stages represented in the finite element models included:

- Precast concrete segments
  - Application of gravity
  - Prestressing of bonded pretensioned strands
- Addition of splices or deviators (if applicable)
- Addition of end blocks (if applicable)
- Post-tensioning of unbonded tendons
- Addition of concrete deck (if applicable)
- Application of external load

When using the LS-DYNA construction stage feature, a 'set' (collection) of one or more elements can be introduced into the model (e.g., splice elements) at a specified time in the analysis. Conversely, a set of elements can also be removed from the model (e.g., casting bed elements) at a specified time. Both types of construction stage changes (element introductions, element removals) were used in modeling both simply-supported single span beams and continuous beams.

<u>Loads</u>

A primary focus of this study was to investigate the parameters that affect the flexural behavior and capacity of prestressed concrete beams. Since loading type (concentrated or distributed) influences the distribution of bending moment in the beam and influences the extent of the plastic hinge region, multiple loading scenarios were considered. Previous research (Kheyroddin and Naderpour, 2007) has addressed the effect of loading type on reinforced concrete beam flexural behavior. In that study, the plastic hinge rotation (angle) increased as the loading type went from a midspan concentrated load, to a third-point loading. The plastic hinge rotation was a maximum for the case of uniform load. It was also noted that the effect of loading type on the plastic rotation capacity of heavily reinforced beams was not as significant as for lightly reinforced beams.

The finite element parametric study reported in the following sections considered three distinct loading conditions: a single concentrated load at midspan; dual concentrated loads (referred to as a widely spaced 'tandem' load); and uniformly distributed load. For the concentrated loading conditions (midspan load and tandem load), each load was applied using a load block under 'displacement control'. Rectangular blocks were placed adjacent to top of the girder simulating the approximate contact area (but not the stiffness) of a tire. A prescribed vertical displacement was applied to the load block, and contact detection was defined between the block

(Figure 8.12a) and the concrete deck to transmit and quantify the applied load. In contrast, uniformly distributed loading conditions were produced by applying an increasing pressure (i.e., 'load control') to top of the concrete deck (Figure 8.12b).
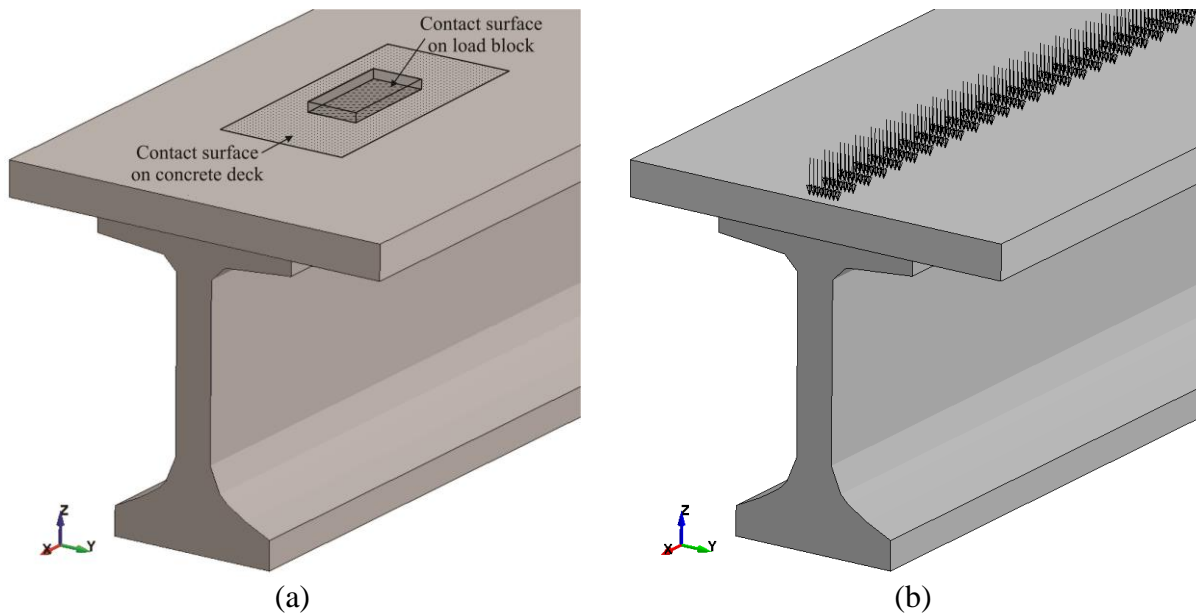

(a)	(b)

Figure 8.12 Modeling of external loads: (a) contact surfaces on concrete deck and load block, concentrated load and (b) pressure load on top of concrete deck

Constraints

When a crack forms physically, local debonding of strand occurs. When modeling a prestressed concrete beam using the material model MAT_CSCM, deletion of concrete elements (referred to as 'erosion') occurs once the damage index exceeds 0.99 as previously discussed. In the FE model, with erosion representing crack formation, the length of strand debonding can be 2, 3, or more element lengths. Therefore, erosion could lead to a much larger length of strand to become unbonded in the FE model than in real life (see Figure 8.13). To address this, rigid links (in the form of CONSTRAINED_NODAL_RIGID_BODY, CNRB) were added, at each longitudinal position along the mesh, to prevent formation of inappropriately long lengths of strand debonding. Rigid links included nodes corresponding to pretensioned strands, rebar, and concrete elements outside the area presenting erosion (Figure 8.14). Rigid links were defined at the center of the beam along one quarter of the beam length as shown in Figure 8.15.

(a)

Excessive debonded length on PreT strands due to
erosion of surrounding concrete elements

(b)

Partial-depth rigid links used to maintain relationship
between section curvature and strain in PreT strands

(c)
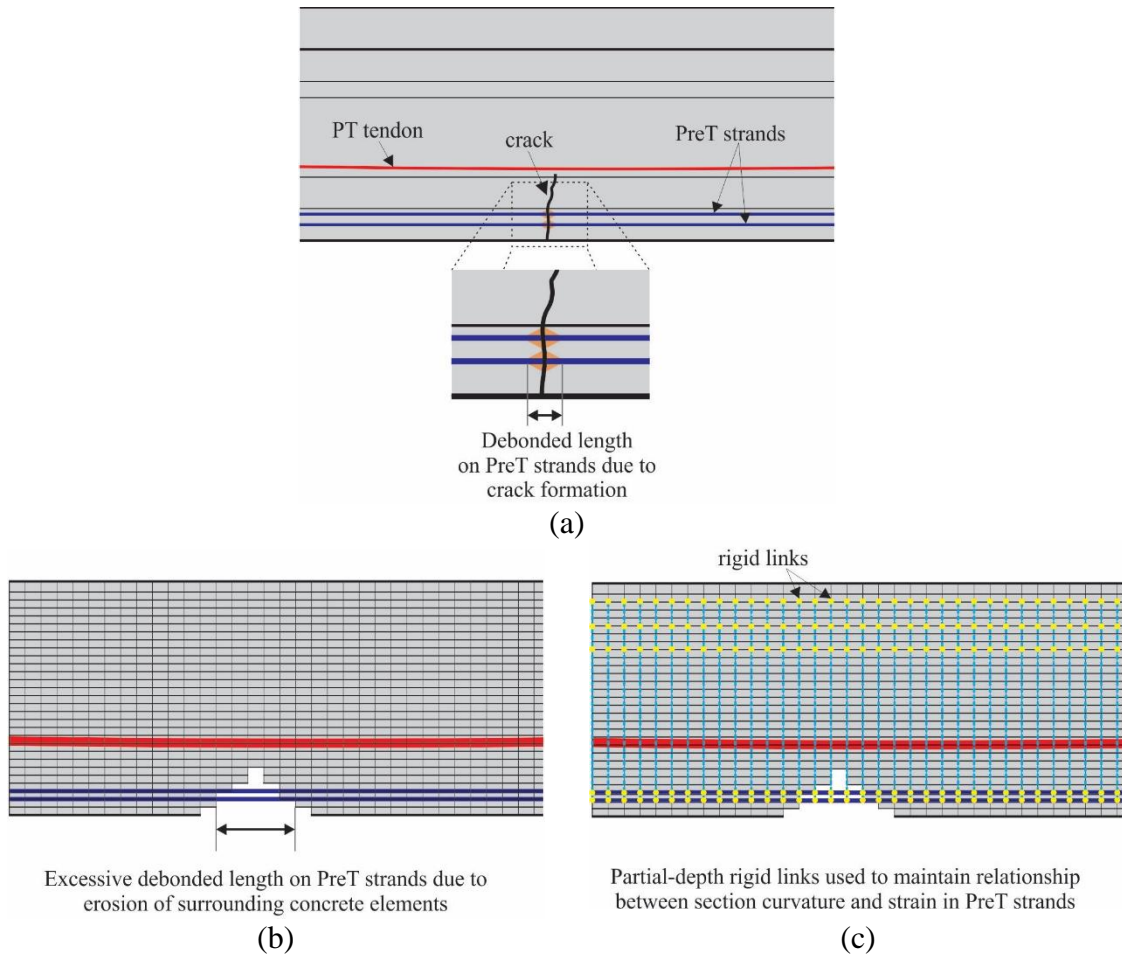
Figure 8.13 Sketches of a portion of a SS beam showing: (a) debonded length on PreT strands
due to crack formation at midspan; (b) longer debonded length on PreT strands due to erosion of
surrounding bonded PreT strands in FE model; (c) use of partial-depth rigid links to maintain
appropriate strains in PreT strands
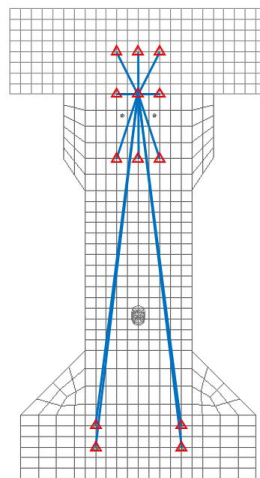
Figure 8.14 Rigid links defined on beam specimen SS-4: Beam cross-section showing location of
constrained nodes (with red triangles)
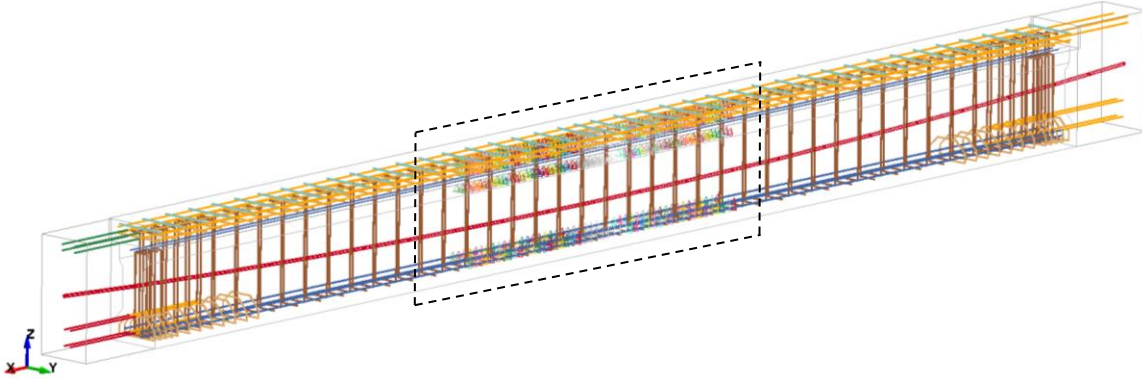
Figure 8.15 Nodes constrained by rigid links on beam specimen SS-4: Isometric view showing CNRBs along the center of the beam

8.3 Validation of numerical model procedures

Upon completion of experimental tests on full-scale prestressed beam specimens, finite element analyses (FEA) were conducted using parameters corresponding to the actual material properties and prestressing forces present on the experimental specimens. These are referred to as validation models. The following experimental results were used to validate the FEA models:

- Load-displacement

- Load-strain in concrete

- Stress in post-tensioned tendon

- Maximum load

- Rupture of bonded prestressing strands (if applicable)

A comparison between FEA results and experimental data for each of the experimental beam specimens is presented in the following subsections.

8.3.1 Simply-supported precast beam specimens

A total of four precast beams were tested in positive bending: two 76-ft long beams (SS-1 and SS-2) and two 46-ft long beams (SS-3 and SS-4). These beam specimens consisted of modified AASHTO Type II sections (70 ft and 40 ft long, respectively) with an 8-in. thick concrete deck and 3-ft long rectangular cast-in-place concrete end blocks. All specimens had different amounts of pretensioned (PreT, bonded) and post-tensioned (PT, unbonded) prestressing reinforcement. Pretensioned tendons located in the bottom of the beam consisted of 0.6-in. diameter strands while pretensioned tendons located on the top of the beam consisted of 0.375-in. diameter strands. All post-tensioned tendons consisted of 0.6-in. diameter strands.

Beam specimen SS-1

Beam specimen SS-1 is a 76-ft long beam with a span length (distance from centerline of bearing to centerline of bearing) of 75 ft and span-to-depth ratio of 25. As shown in Figure 8.16, prestressing reinforcement consisted of 1 post-tensioned tendon (equivalent to 6 post-tensioned

99

strands), 10 pretensioned strands located in the bottom, and 2 pretensioned strands located in the top, which resulted in an unbonded reinforcement ratio (U/T) of 0.4. The U/T ratio was defined as the amount of unbonded reinforcement divided by the total amount of reinforcement in terms of force: $U/T = \frac{A_{psu}f_{pu}}{A_{psu}f_{pu}+A_{psb}f_{pu}+A_s f_y}$, where A_{psu} is the area of unbonded prestressing, A_{psb} is the area of bonded prestressing, and A_s is the area of bonded mild steel bars. Note that the reinforcement ratio only includes reinforcement on the tension side of the beam. All six post-tensioned strands were modeled as a single tendon. The concrete compressive strengths used in the validation model were input in units of ksi and were based in the average concrete compressive strengths at the day of the test (Table 8.1). The specified pretensioned force used in the validation model was based on the vibrating wire gage readings after pretensioning (to be consistent with construction stages included in the model), while the specified post-tensioned force was based on the load cell reading after post-tensioning and prior to loading.

Table 8.1 Beam specimen SS-1: Concrete compressive strengths at day of flexural test

Description	Specified Compressive Strength (psi)	Avg. Compressive Strength (psi)
Precast girder	8,500	13,404
Deck	8,500	13,713
End blocks	8,500	10,035
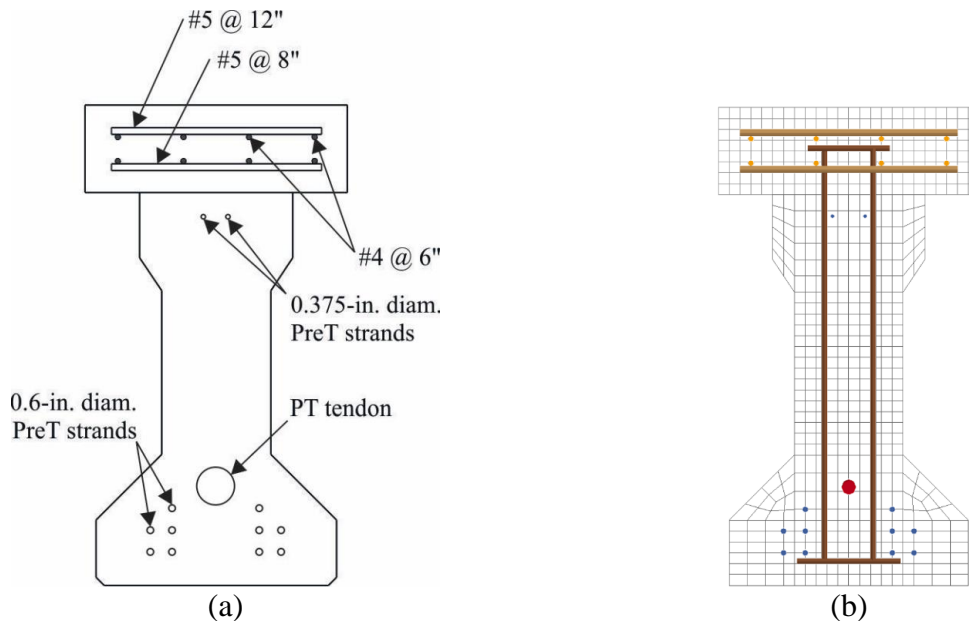
Figure 8.16 Beam specimen SS-1 cross-section:
(a) sketch showing location of longitudinal reinforcement, (b) FE model

During the experimental test, the first visible cracks on specimen SS-1 were identified at a load of 74 kip on the east side of the beam (Figure 8.17). Although the material model (MAT_CSCM) used to model the nonlinearities of concrete in the validation model does not produce visual cracking of the material, damage can be visualized with color contours of 'damage index' as discussed in Section 8.2. Figure 8.18 shows the damage index at different load levels. As seen in

Figure 8.18a, damage started accumulating near midspan on the bottom of the beam. As previously noted, when using MAT_CSCM to model concrete, once an element reaches maximum capacity (no residual strength), element deletion ('erosion') occurs. At the point of initiation of erosion, the use of sectional constraints (rigid links) on the bonded pretensioned strands becomes particularly relevant. As depicted in Figure 8.19, the validation model for SS-1 began exhibiting erosion at a load P = 128 kip.
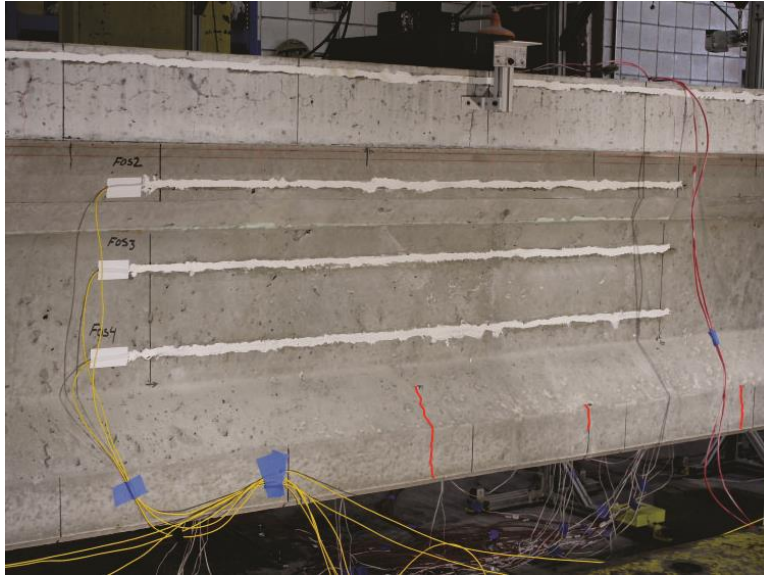
Figure 8.17 Specimen SS-1: First observed cracks (marked in red) at P = 74 kip

(a) P = 83 kip

(b) P = 94 kip

(c) P = 103 kip

(d) P = 113 kip

(e) P = 117 kip

(f) P = 120 kip

(g) P = 122 kip

(h) P = 124 kip (ε_c = 0.003)

(i) P = 130 kip

(j) P_{max} = 135 kip (strand rupture)

Damage Index

| 0 | 0.1 | 0.2 | 0.3 | 0.4 | 0.5 | 0.6 | 0.7 | 0.8 | 0.9 | 1.0 |
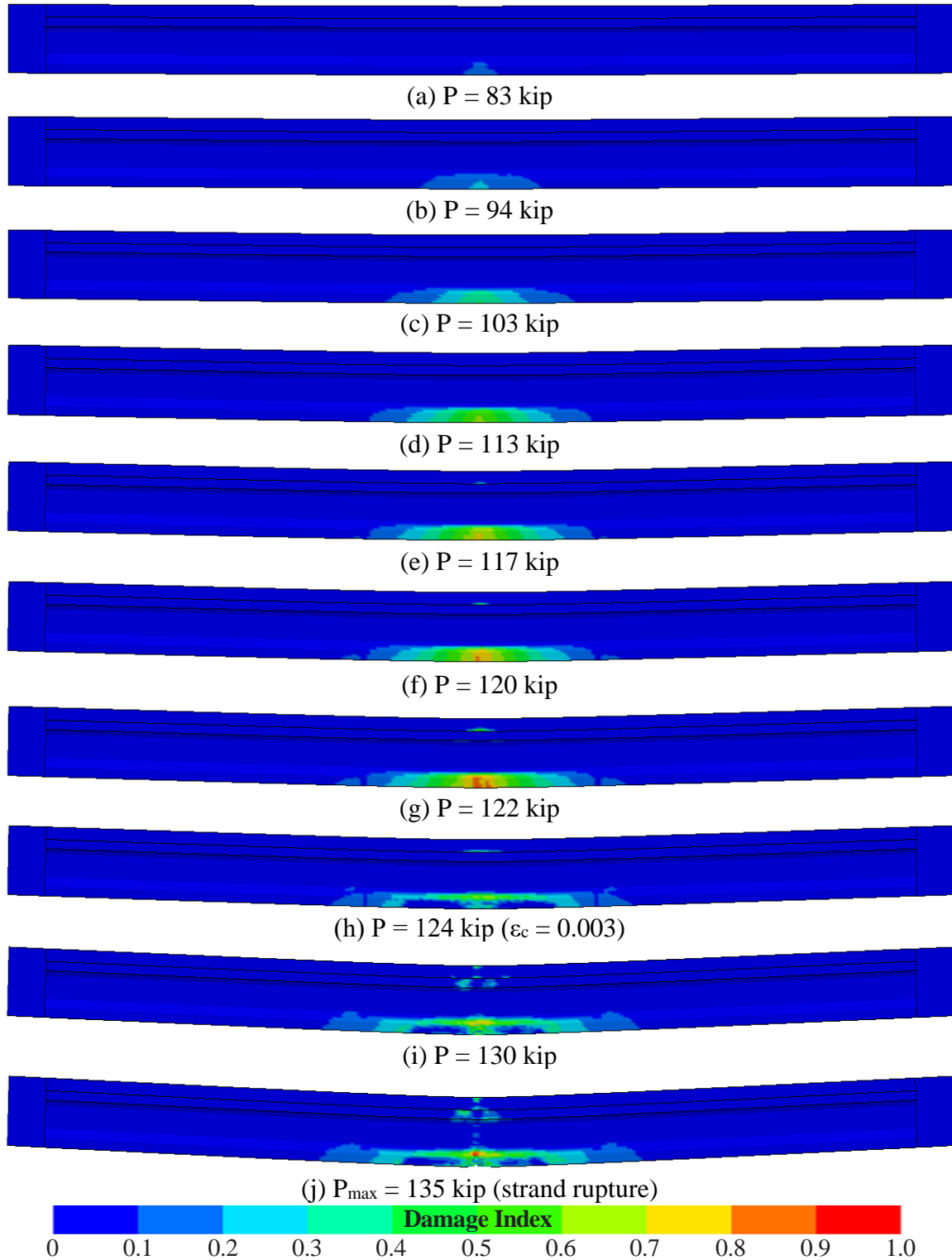
Figure 8.18 Specimen SS-1 [not to scale]: FE model showing damage index at different load levels

(a)

(b)
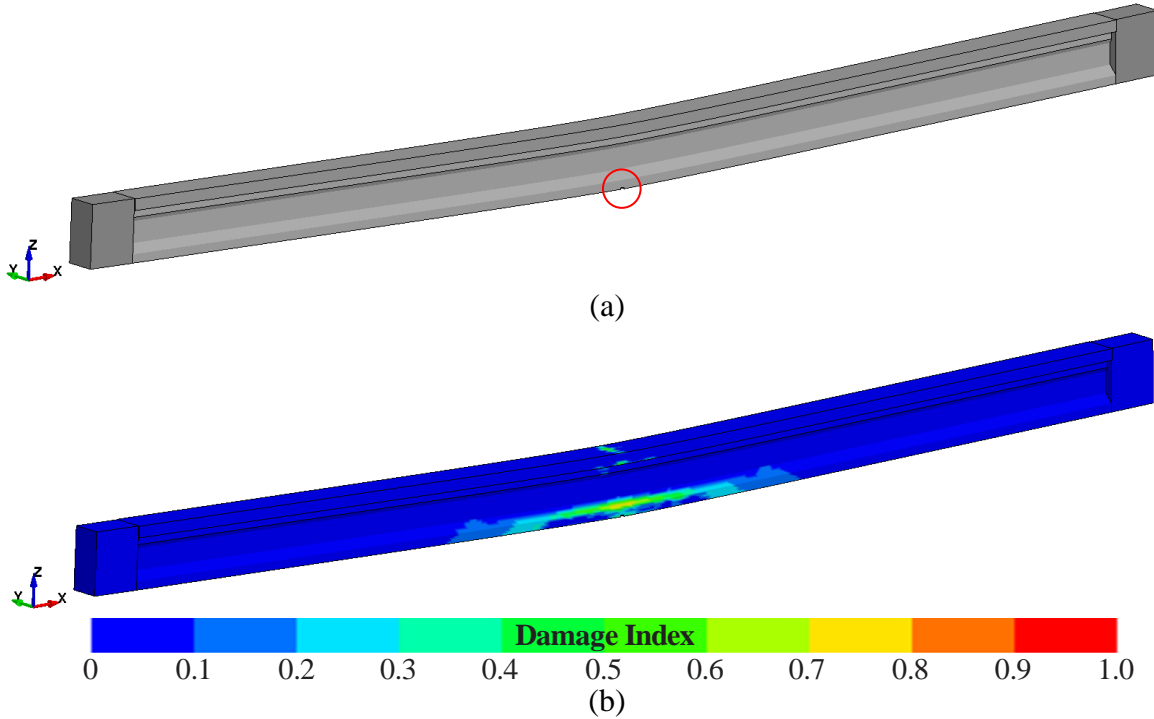
Figure 8.19 Specimen SS-1: FE model showing (a) initiation of 'erosion' (circled in red) near midspan and (b) damage index at P = 128 kip

Table 8.2 presents a comparison of the nominal load (at $\varepsilon_c = 0.003$) and maximum load values obtained from experimental data and FEA. The validation model presented good agreement with the experimental data in terms of both load and displacement up until the concrete reached a compressive strain of 0.003 at an applied load of 124.4 kip (<10% higher than the experimental load). Afterwards, the validation model presented more flexibility than the experimental specimen but the maximum load (P_{max}) was 135.4 kip, which was just 11% higher than the experimental load. As shown in Figure 8.20, the validation model presents good overall agreement with the experimental load-displacement curve. Figure 8.21 shows the strain on top of the concrete deck, obtained from both FEA and experimental data.

Table 8.2 Beam specimen SS-1: Comparison of capacity between experimental results and FEA

	Applied load (kip) at ε_c=0.003	Displacement (in.) at ε_c=0.003	Max. Load (P_{max}, kip)	Displacement (in.) at P_{max}
Experimental data	119.6	8.3	122.0	9.8
FEA	124.4	9.5	135.4	13.9
Difference	4%	15%	11%	41%

Figure 8.22 shows the stress in prestressing tendons as a function of applied load. The axial force in the post-tensioned tendon was monitored during the experimental test though a load cell at the dead end. The stress in the PT tendon indicated by the validation model was in good agreement with the experimental data as depicted in Figure 8.22 (blue and black traces). Additionally, vibrating wire (VW) gages were used to determine the pretensioned strand force (and losses) during: stressing of pretensioned strands (at the precast plant); post-tensioning of the test

specimen (at the lab); and during loading. Figure 8.22 shows the experimental stress in PreT strands with solid circles. Regarding the validation model, axial forces in PreT strands were obtained at different locations along the length of the beam at different load levels. The finite element model indicated that PreT strands located in the bottom layer presented higher axial forces and the maximum force in PreT strands occurred at midspan. Both the experimental data and validation model exhibited a significant increase in the pretensioned stress as load was applied. However, none of the PreT strands presented rupture.
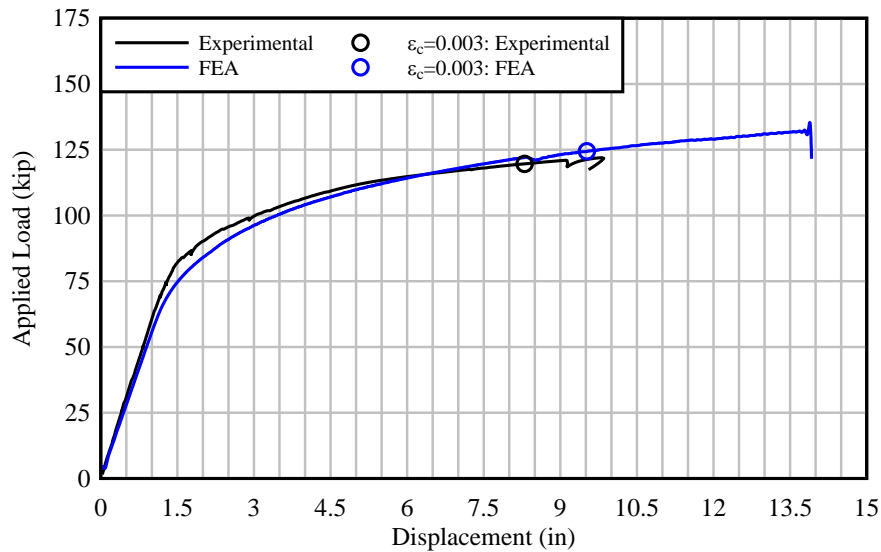
Figure 8.20 Comparison of load-displacement curves obtained from experimental data and FEA: Beam specimen SS-1
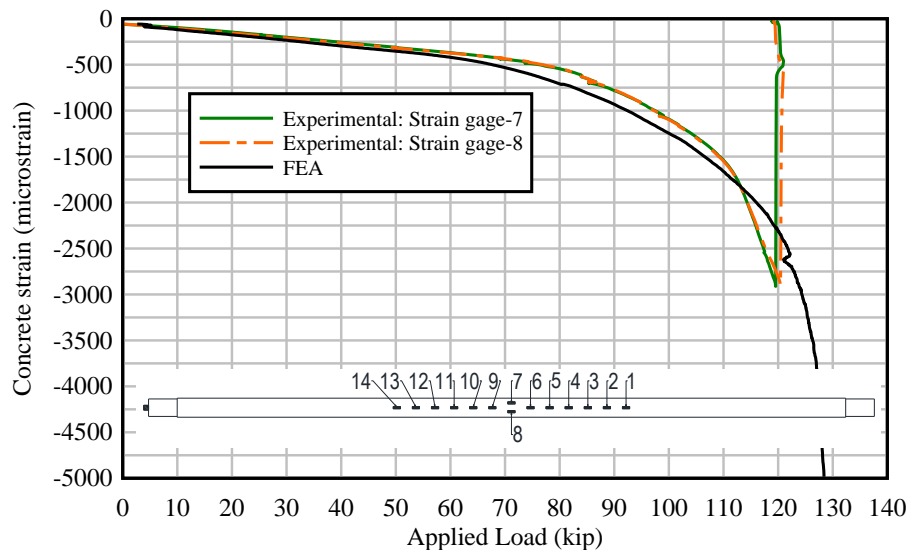
Figure 8.21 Strain on top of concrete deck as a function of applied load – comparison between experimental data and FEA: Beam specimen SS-1
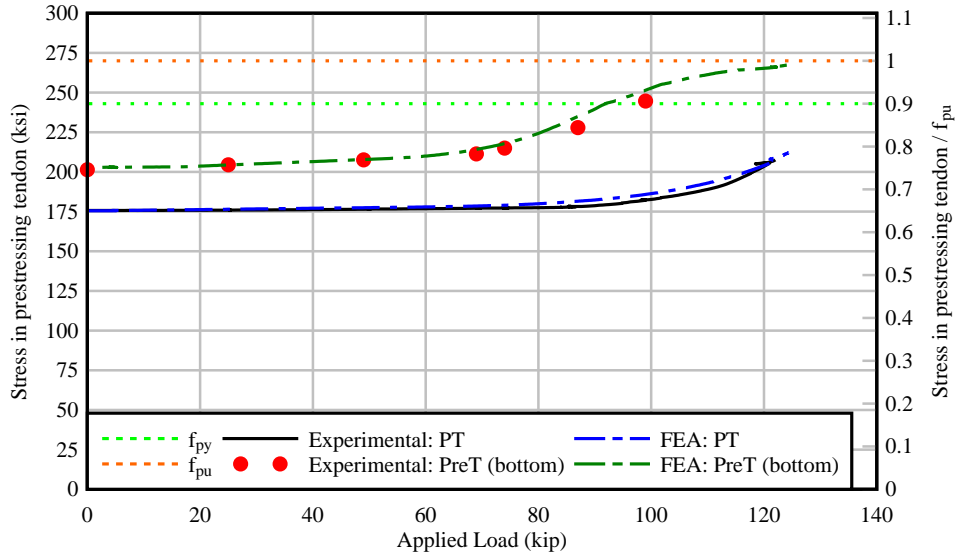
Figure 8.22 Stress in prestressing tendons as a function of applied load – comparison between experimental data and FEA: Beam specimen SS-1

The deflected shape of the beam and curvature computed from the FE model are compared to the corresponding experimental beam data in Figures 8.23 and 8.24. Deflection and curvature data for load levels at which concrete strains were approximately $\varepsilon_c = 0.003$ are indicated with bold lines, and data for higher load levels are indicated with dashed lines. The FE model indicated a higher maximum load, however, both the FEA and experimental data were generally in good agreement.
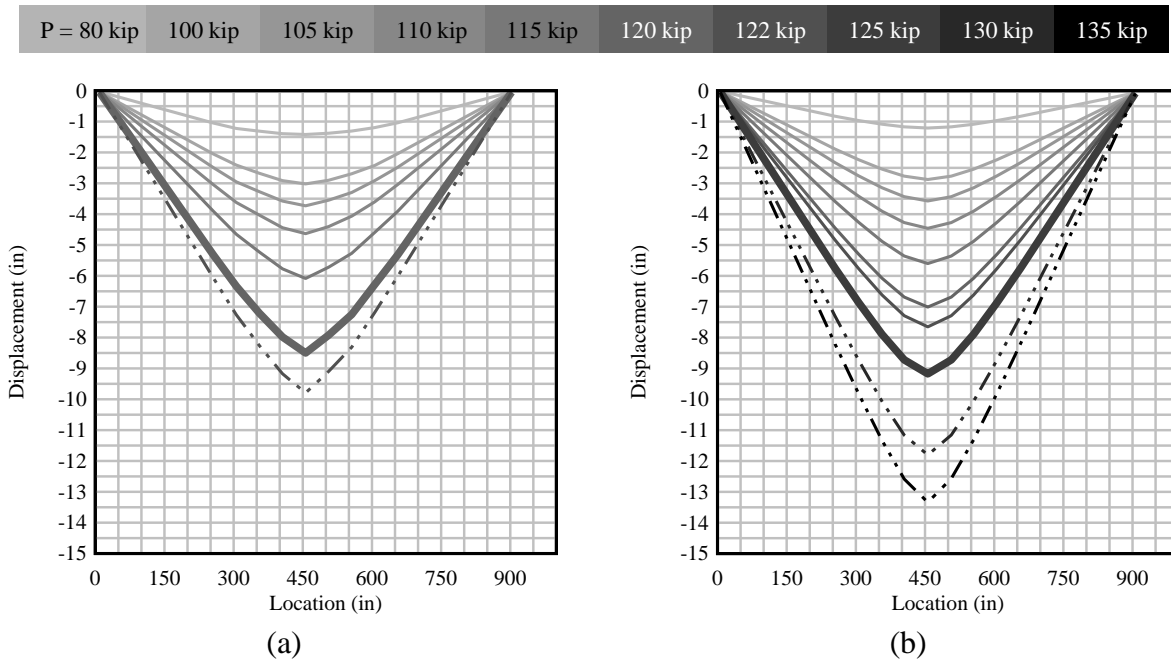
Figure 8.23 Displacement as a function of location along the length of beam specimen SS-1: (a) experimental data and (b) FEA

| P = 80 kip | 100 kip | 105 kip | 110 kip | 115 kip | 120 kip | 122 kip | 125 kip | 130 kip | 135 kip |
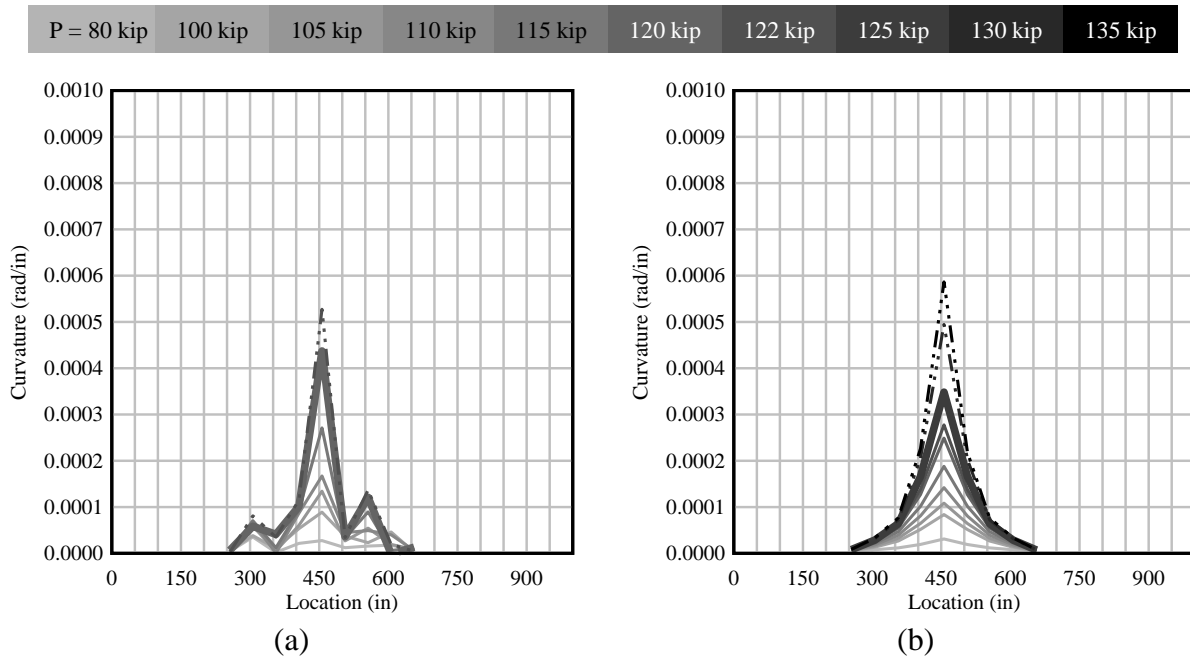
Figure 8.24 Curvature as a function of location along the length of beam specimen SS-1: (a) experimental data and (b) FEA

Beam specimen SS-2

Beam specimen SS-2 is a 76-ft long beam with a span length of 75 ft and span-to-depth ratio of 25. As shown in Figure 8.25, prestressing reinforcement consisted of 1 post-tensioned tendon (equivalent to 10 post-tensioned strands), 8 pretensioned strands located in the bottom, and 2 pretensioned strands located in the top, which resulted in an unbonded reinforcement ratio (U/T) of 0.6. The concrete compressive strengths used in the validation model were input in units of ksi and were based in the average concrete compressive strengths at the day of the test (Table 8.3). However, due to limitations in the MAT_CSCM material model, the maximum compressive strength that was permitted to be specified was 13.8 ksi. Therefore, a compressive strength of 13.8 ksi was used to approximate the concrete deck instead of using the experimental value of 14.4 ksi. The specified pretensioned force used in the validation model was based on the vibrating wire gage readings after pretensioning (to be consistent with construction stages included in the model), while the specified post-tensioned force was based on the load cell reading after post-tensioning and prior to loading.

Table 8.3 Beam specimen SS-2: Concrete compressive strengths at day of flexural test

Description	Specified Compressive Strength (psi)	Avg. Compressive Strength (psi)
Precast girder	8,500	13,190
Deck	8,500	14,362
End blocks	8,500	10,035
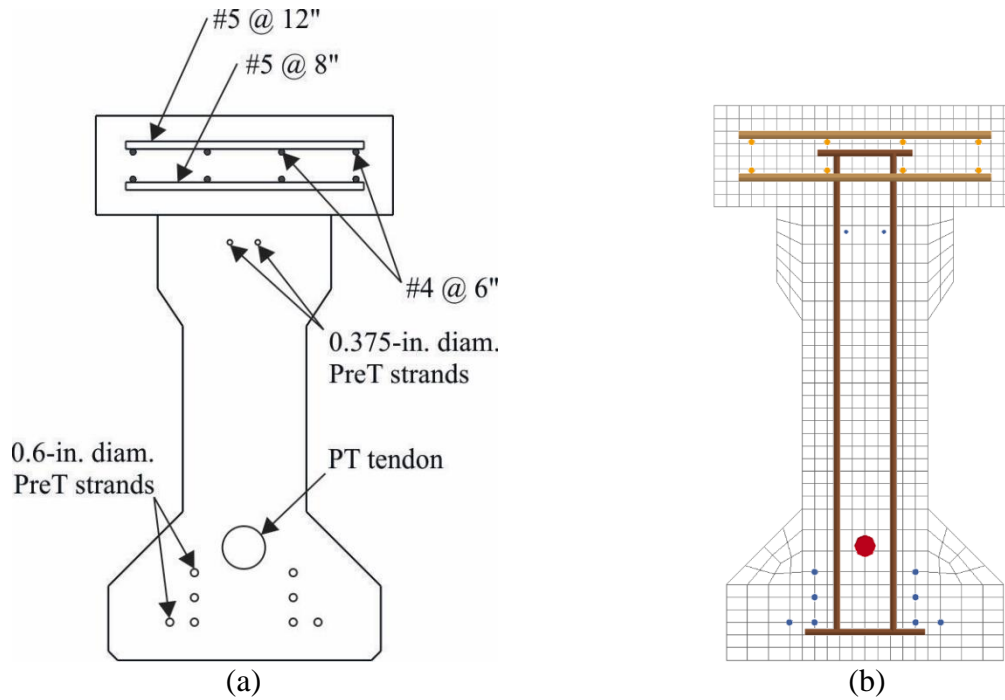
Figure 8.25 Beam specimen SS-2 cross-section:
(a) sketch showing location of longitudinal reinforcement, (b) FE model

During the experimental test, the first visible cracks on specimen SS-2 were identified at a load of 77 kip on the east side of the beam (Figure 8.26). Figure 8.27 shows the damage index at different load levels. As seen in Figure 8.27a, damage started accumulating near midspan on the bottom of the beam. As depicted in Figure 8.28, the validation model for SS-2 began exhibiting erosion at a load $P = 134$ kip.

Figure 8.26 Specimen SS-2: First observed cracks (marked in red) at $P = 77$ kip

107

(a) P = 88 kip

(b) P = 99 kip

(c) P = 109 kip

(d) P = 113 kip

(e) P = 117 kip

(f) P = 121 kip

(g) P = 122 kip

(h) P = 128 kip

(i) P = 131 kip (ε_c = 0.003)

(j) P_{max} = 139 kip

Damage Index

| 0 | 0.1 | 0.2 | 0.3 | 0.4 | 0.5 | 0.6 | 0.7 | 0.8 | 0.9 | 1.0 |
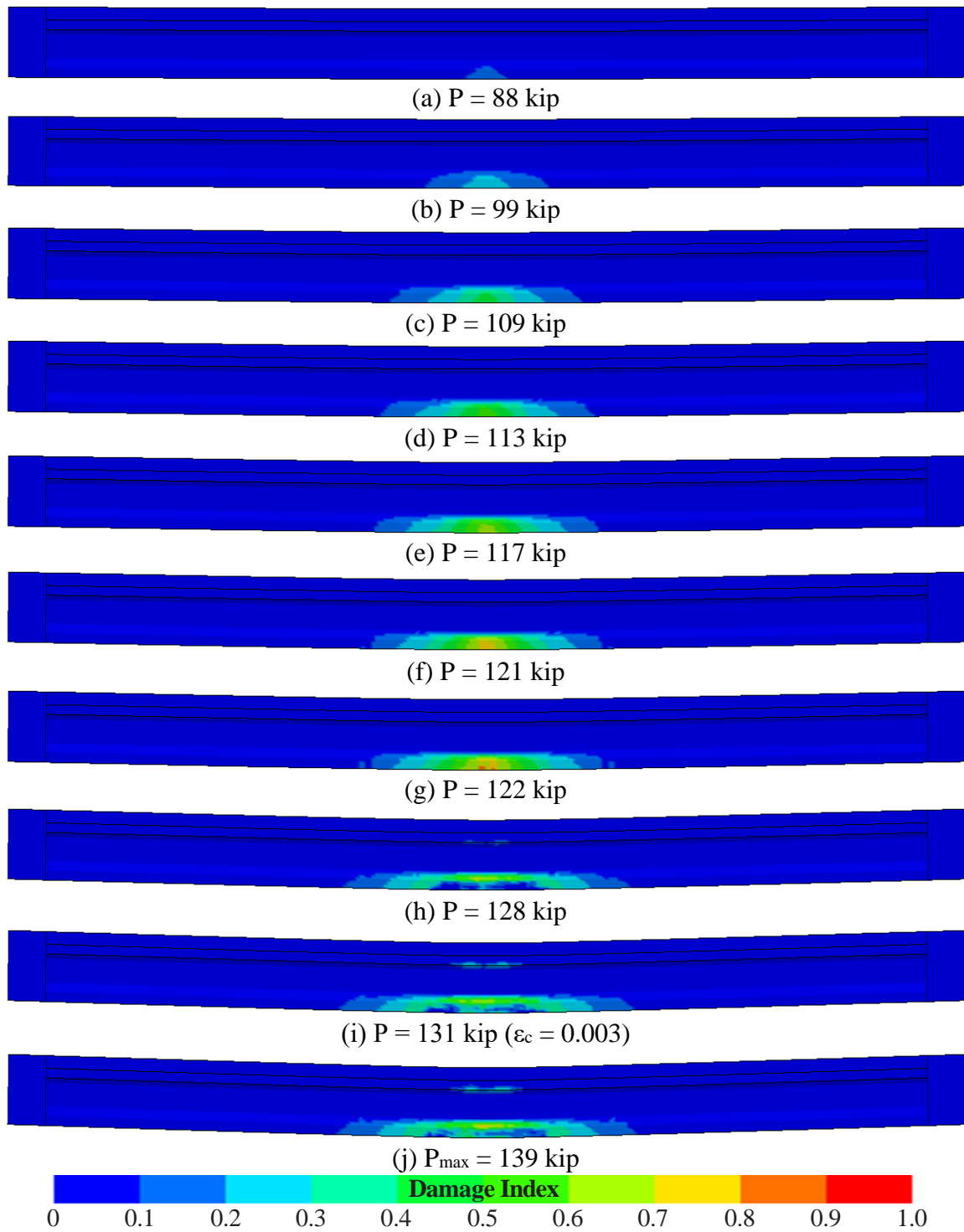
Figure 8.27 Specimen SS-2 [not to scale]: FE model showing damage index at different load levels

(a)

| Damage Index |
| 0   0.1   0.2   0.3   0.4   0.5   0.6   0.7   0.8   0.9   1.0 |

(b)
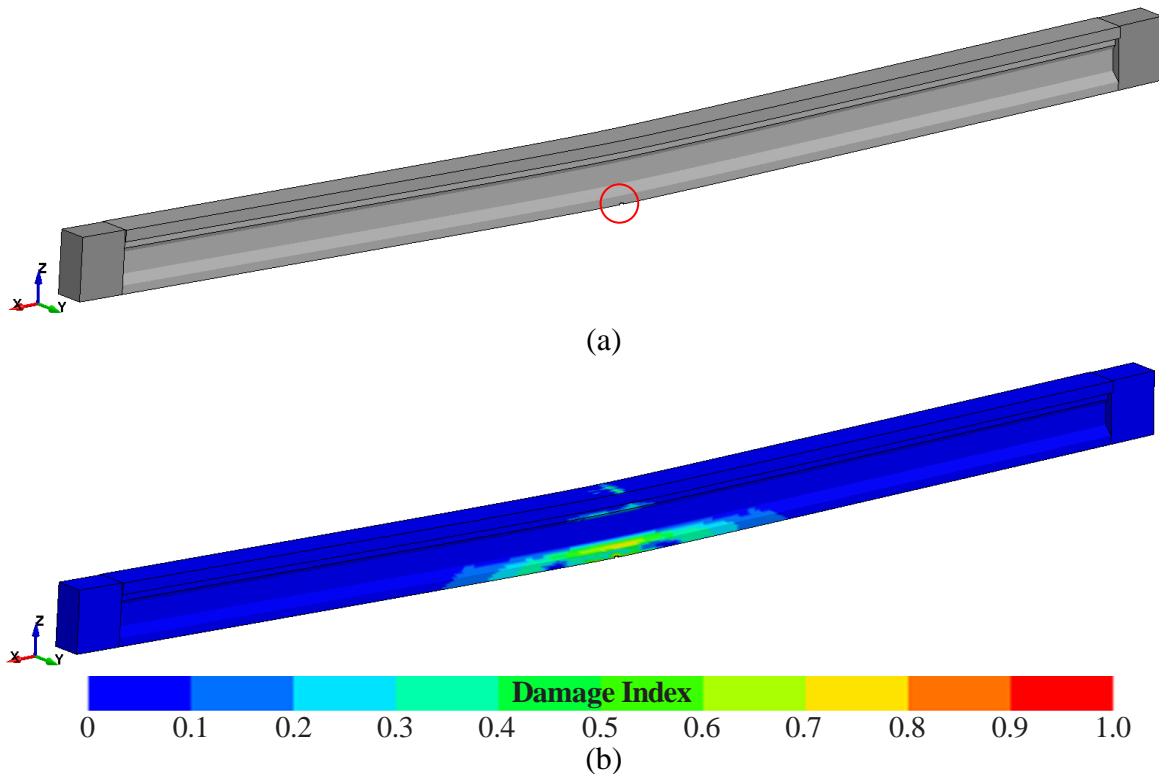
Figure 8.28 Specimen SS-2: FE model showing (a) initiation of 'erosion' (circled in red) near midspan and (b) damage index at P = 134 kip

Table 8.4 presents a comparison of the nominal load (at $\varepsilon_c = 0.003$) and maximum load values obtained from experimental data and FEA. The validation model reached a compressive concrete strain of 0.003 at an applied load of 131.1 kip (<2% higher than the experimental load) and the maximum load (P_{max}) was 138.9 kip (<6% higher than the experimental load). Similar to specimen SS-1, the validation model for beam specimen SS-2 resulted in slightly more flexibility of the beam after the compressive concrete strain exceeded 0.003 compared to the experimental data. As shown in Figure 8.29, the validation model presents good overall agreement with the experimental load-displacement curve. Figure 8.30 shows the strain on top of the concrete deck, obtained from both FEA and experimental data.

Table 8.4 Beam specimen SS-2: Comparison of capacity between experimental results and FEA

	Applied load (kip) at $\varepsilon_c=0.003$	Displacement (in.) at $\varepsilon_c=0.003$	Max. Load (P_{max}, kip)	Displacement (in.) at P_{max}
Experimental data	128.6	8.2	131.4	9.7
FEA	131.1	8.5	138.9	11.9
Difference	2%	3%	6%	23%

Figure 8.31 shows the stress in prestressing tendons as a function of applied load. The stress in the PT tendon indicated by the validation model presented good agreement with the experimental data as depicted in Figure 8.31. Regarding PreT strands, the stresses obtained from both the validation model and experimental data (VW gages) exhibited a significant increase towards the end of loading. No strands ruptured during the experimental test. Although the PreT stress indicated by the FE model exceeds $f_{pu} = 270$ ksi, no strands ruptured at or before P_{max}. Note

that the material model used to simulate the prestressing strands was specified to rupture at $\varepsilon_{PreT} = 0.05$ ($f_{PreT} = 282$ ksi) based on tensile tests performed on a series of prestressing strand samples.
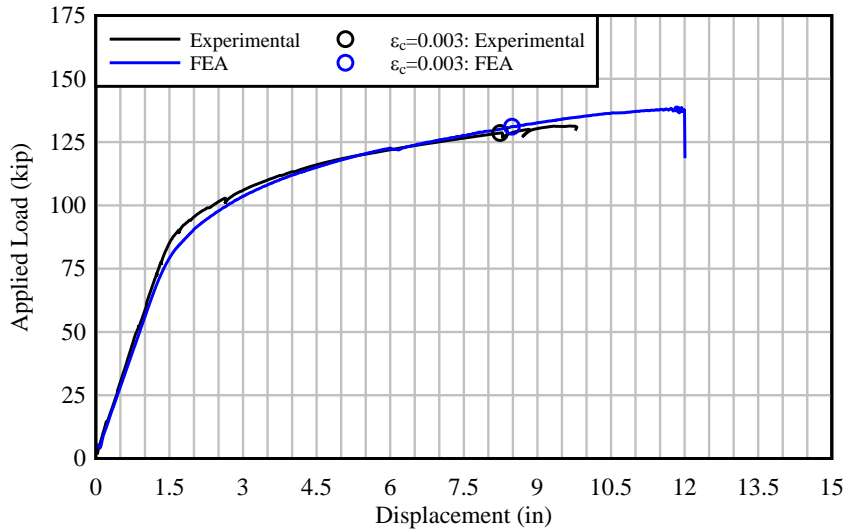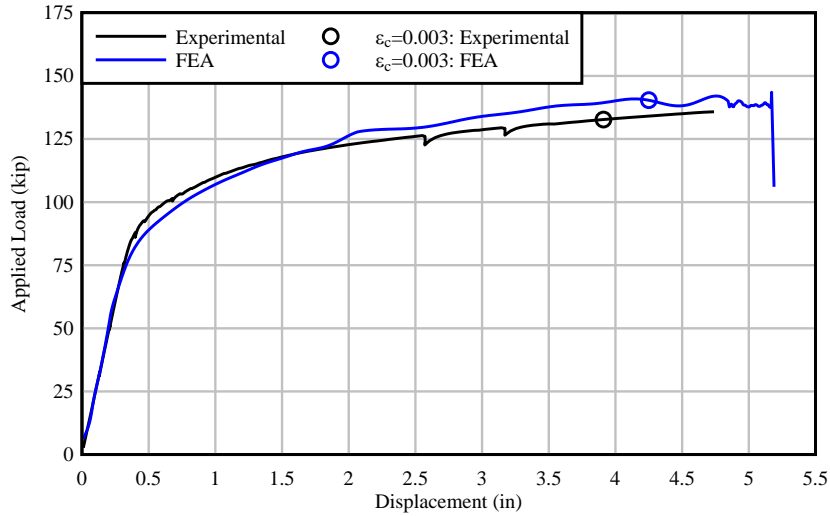

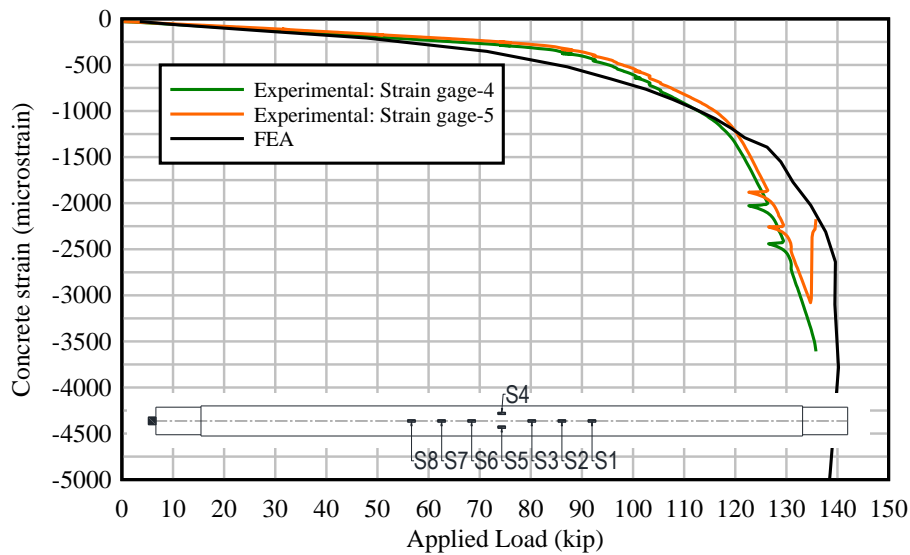Figure 8.29 Comparison of load-displacement curves obtained from experimental data and FEA: Beam specimen SS-2
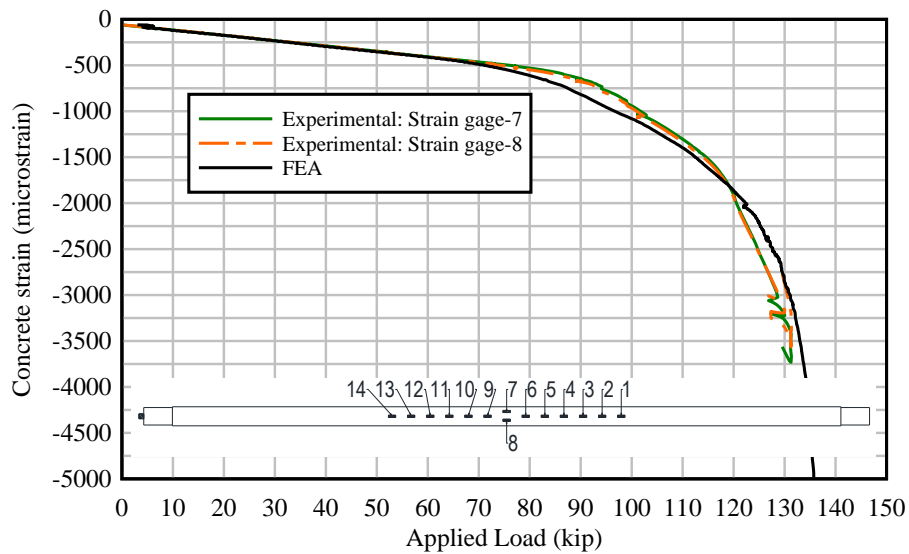
Figure 8.30 Strain on top of concrete deck as a function of applied load – comparison between experimental data and FEA: Beam specimen SS-2
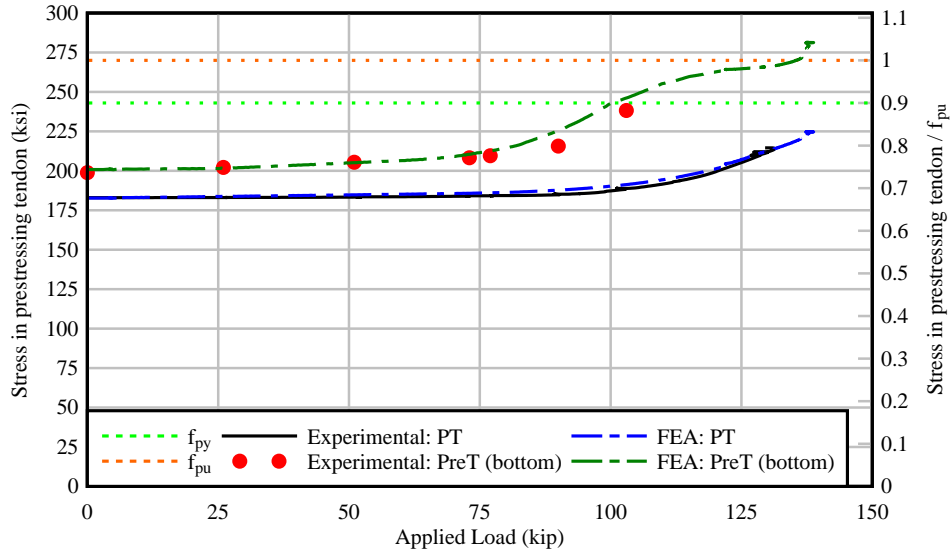
Figure 8.31 Stress in prestressing tendons as a function of applied load – comparison between experimental data and FEA: Beam specimen SS-2

The deflected shape of the beam and curvature computed from the FE model are compared to the corresponding experimental beam data in Figures 8.32 and 8.33. Deflection and curvature data for load levels at which concrete strains were approximately $\varepsilon_c = 0.003$ are indicated with bold lines, and data for higher load levels are indicated with dashed lines. The FE model indicated a higher maximum load and more flexibility. However, both the FEA and experimental data were generally in good agreement up to about $\varepsilon_c = 0.003$.
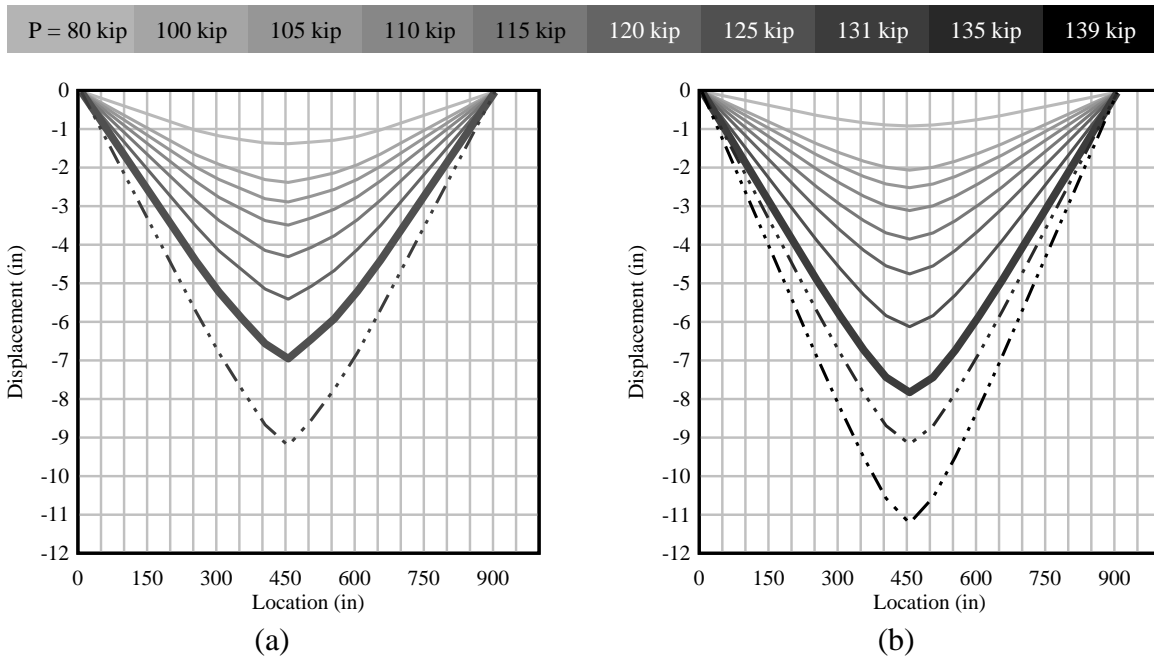
Figure 8.32 Displacement as a function of location along the length of beam specimen SS-2: (a) experimental data and (b) FEA

| P = 80 kip | 100 kip | 105 kip | 110 kip | 115 kip | 120 kip | 125 kip | 131 kip | 135 kip | 139 kip |
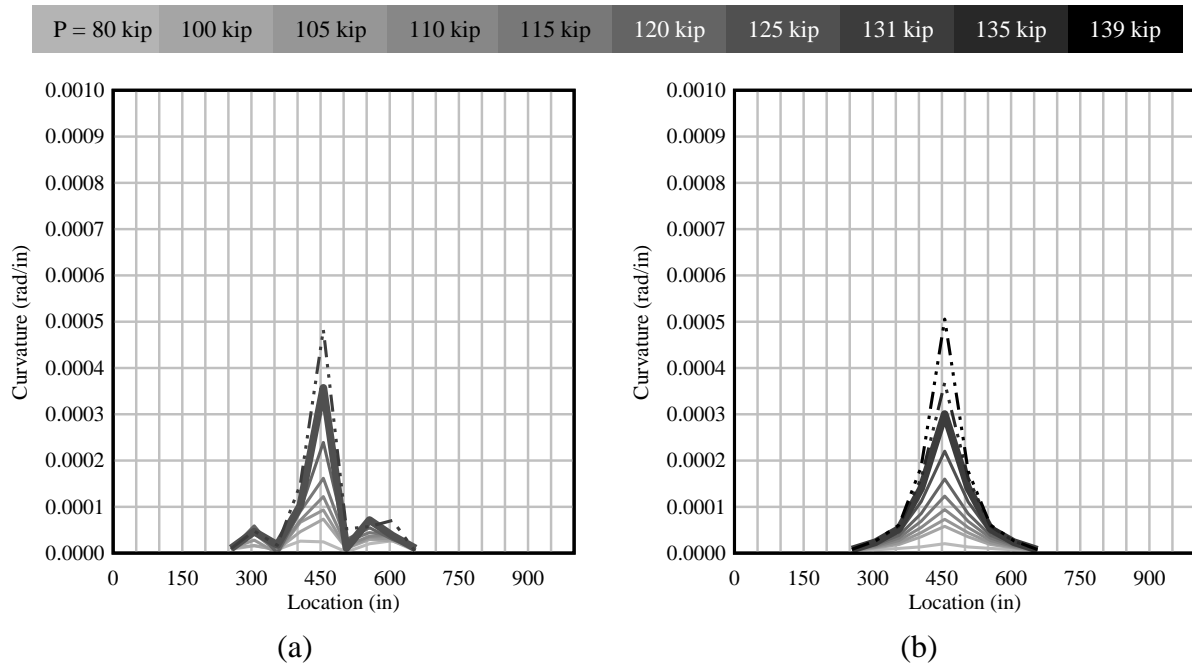
Figure 8.33 Curvature as a function of location along the length of beam specimen SS-2: (a) experimental data and (b) FEA
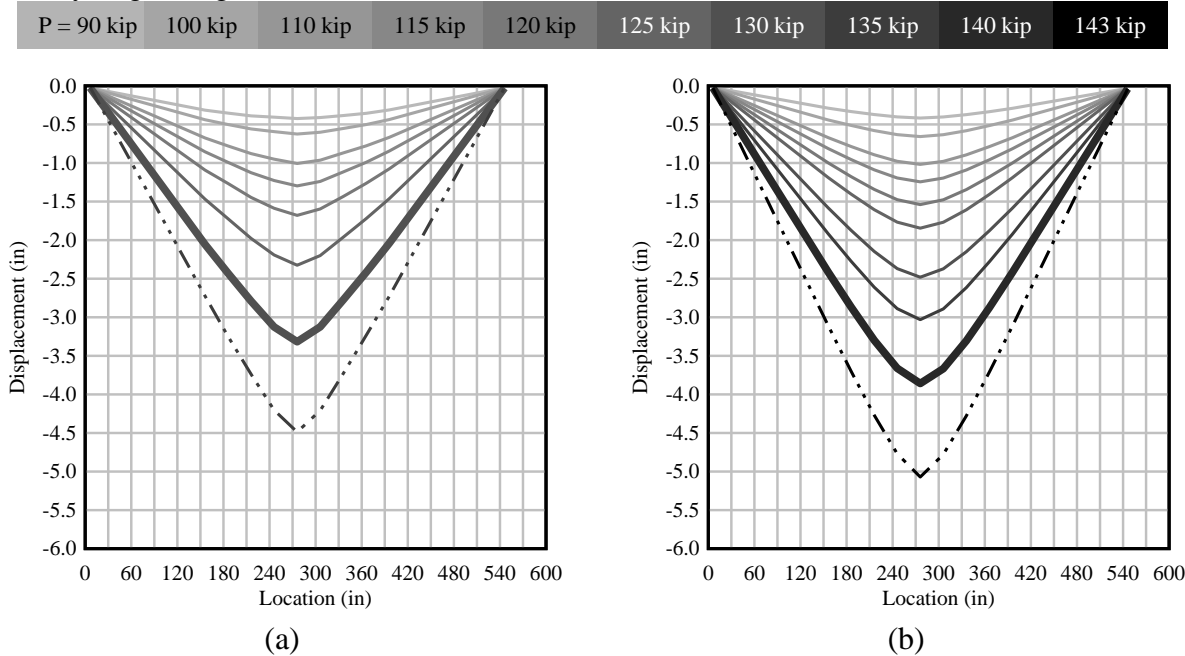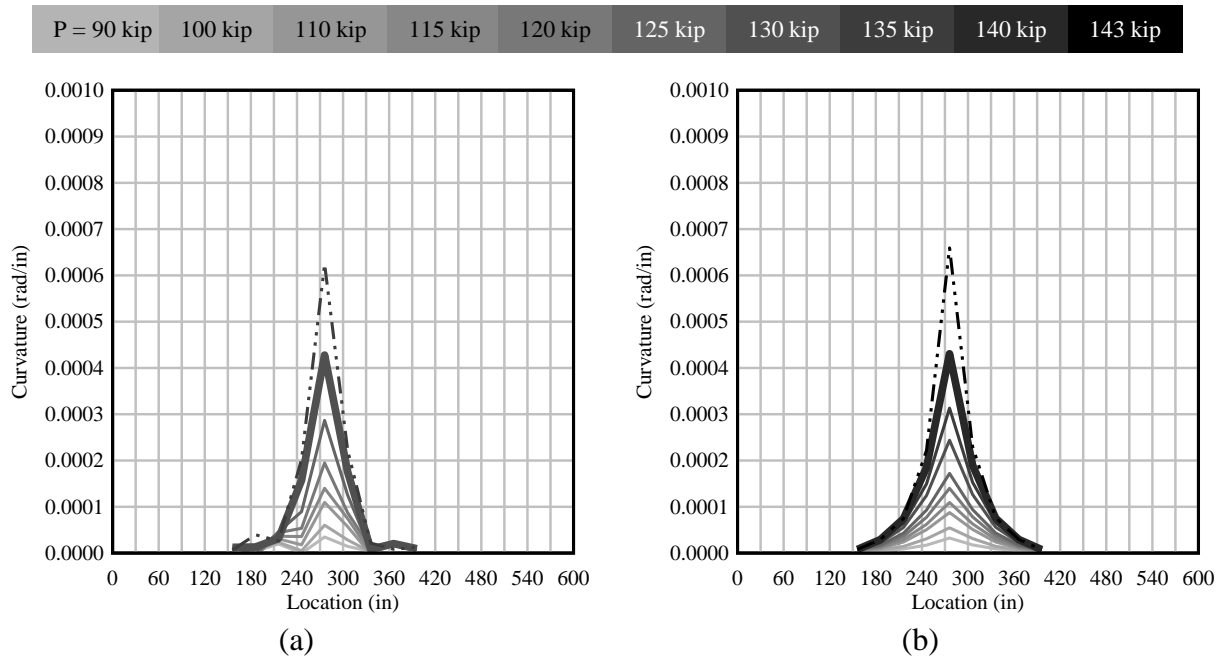
Beam specimen SS-3

Beam specimen SS-3 is a 46-ft long beam with a span length (distance from centerline of bearing to centerline of bearing) of 45 ft and span-to-depth ratio of 15. As shown in Figure 8.34, prestressing reinforcement consisted of 1 post-tensioned tendon (equivalent to 4 post-tensioned strands), 6 pretensioned strands located in the bottom, and 2 pretensioned strands located in the top, which resulted in an unbonded reinforcement ratio (U/T) of 0.4. The concrete compressive strengths used in the validation model were based in the average concrete compressive strengths at the day of the test (Table 8.5). The specified pretensioned force used in the validation model was based on the vibrating wire gage readings after pretensioning (to be consistent with construction stages included in the model), while the specified post-tensioned force was based on the load cell reading after post-tensioning and prior to loading.

Table 8.5 Beam specimen SS-3: Concrete compressive strengths at day of flexural test

Description	Specified Compressive Strength (psi)	Avg. Compressive Strength (psi)
Precast girder	8,500	13,578
Deck	8,500	13,132
End blocks	6,500	10,992

112
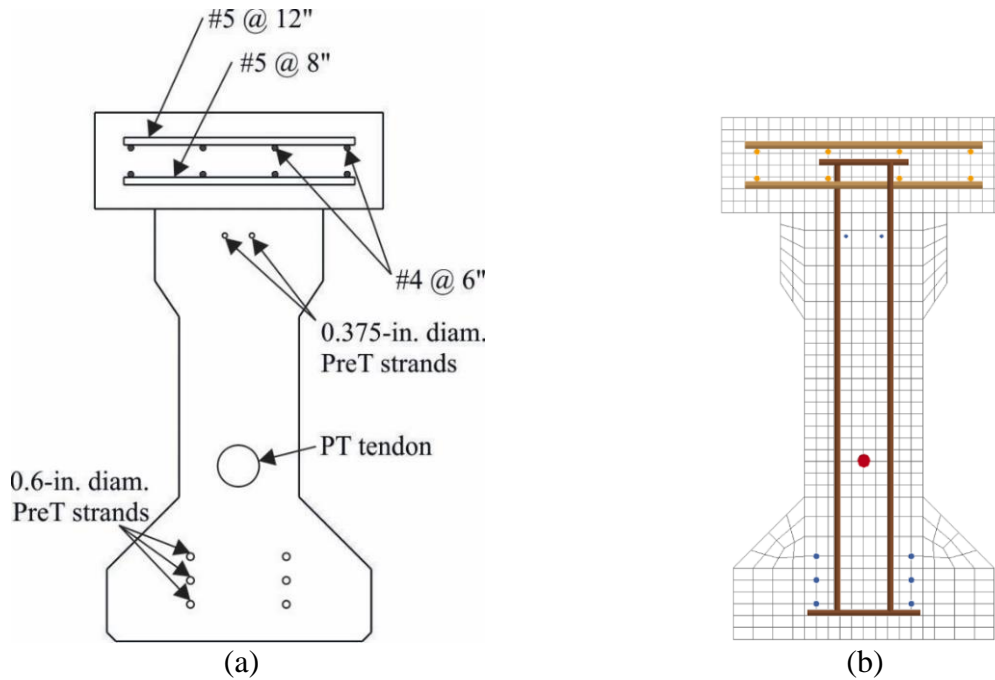
Figure 8.34 Beam specimen SS-3 cross-section:
(a) sketch showing location of longitudinal reinforcement, (b) FE model

The first visible cracks on specimen SS-3 during the experimental test were identified at a load of 75 kip on the west side of the beam (Figure 8.35). Figure 8.36 shows the damage index at different load levels. At an applied load $P = 96$ kip, the validation model presented a damage index of approximately 0.1 near midspan on the bottom of the beam (Figure 8.36a). The validation model for SS-3 began exhibiting erosion at a load $P = 138$ kip as shown in Figure 8.37.
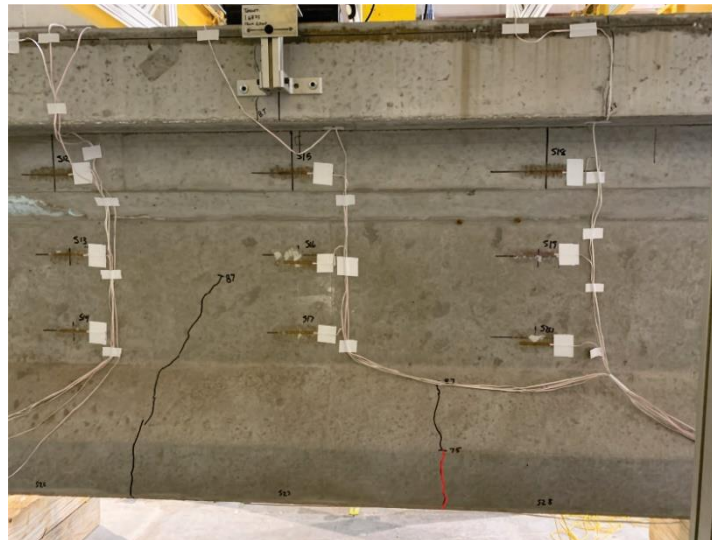
Figure 8.35 Specimen SS-3: First observed cracks (marked in red) at $P = 75$ kip

(a) P = 96 kip

(b) P = 109 kip

(c) P = 120 kip

(d) P = 133 kip

(e) P = 138 kip

(f) P = 140 kip (ε_c = 0.003)

(g) P = 140 kip

(h) P = 138 kip

(i) P = 137 kip

(j) P_{max} = 144 kip (strand rupture)

Damage Index

| 0 | 0.1 | 0.2 | 0.3 | 0.4 | 0.5 | 0.6 | 0.7 | 0.8 | 0.9 | 1.0 |
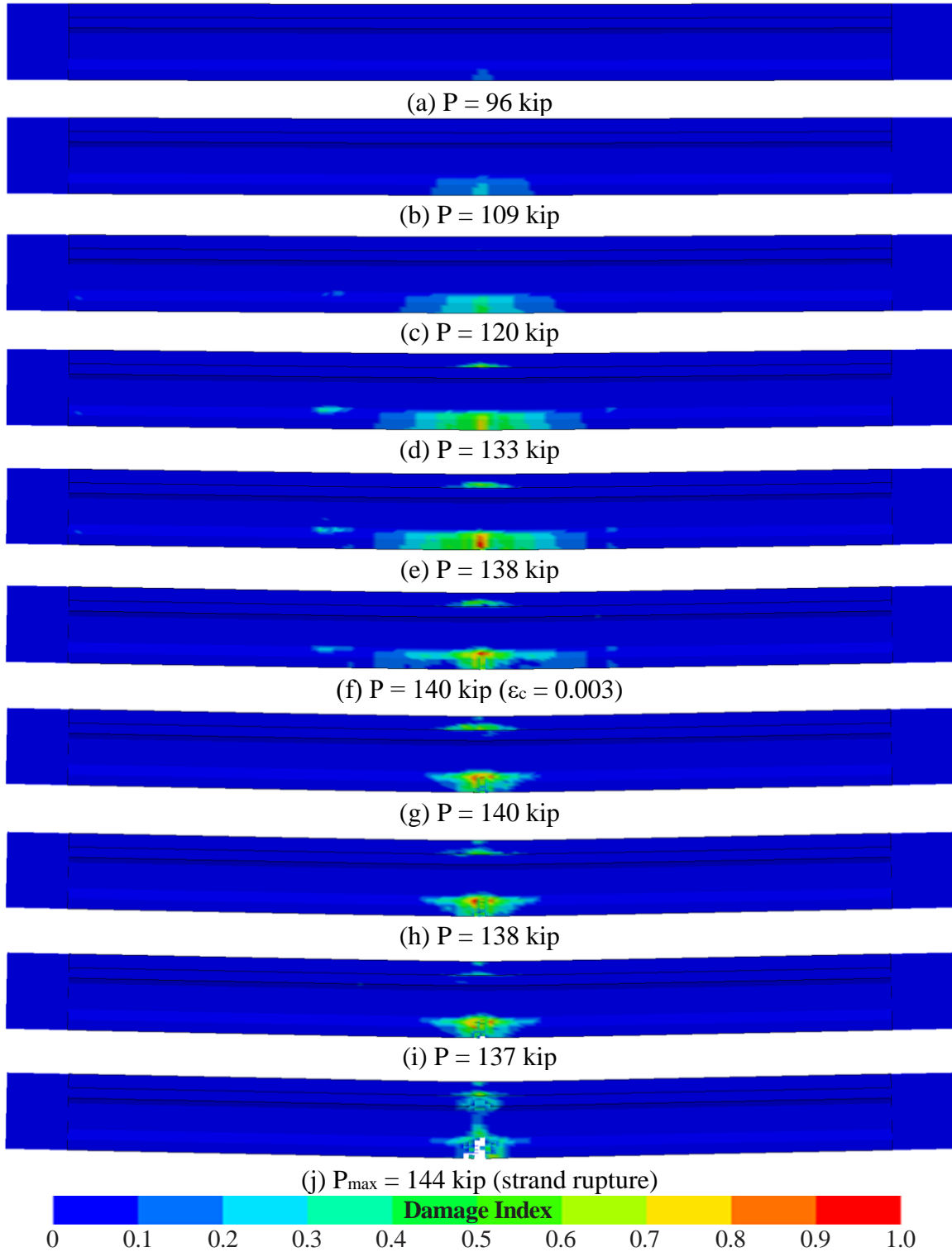
Figure 8.36 Specimen SS-3: FE model showing damage index at different load levels

(a)

(b)
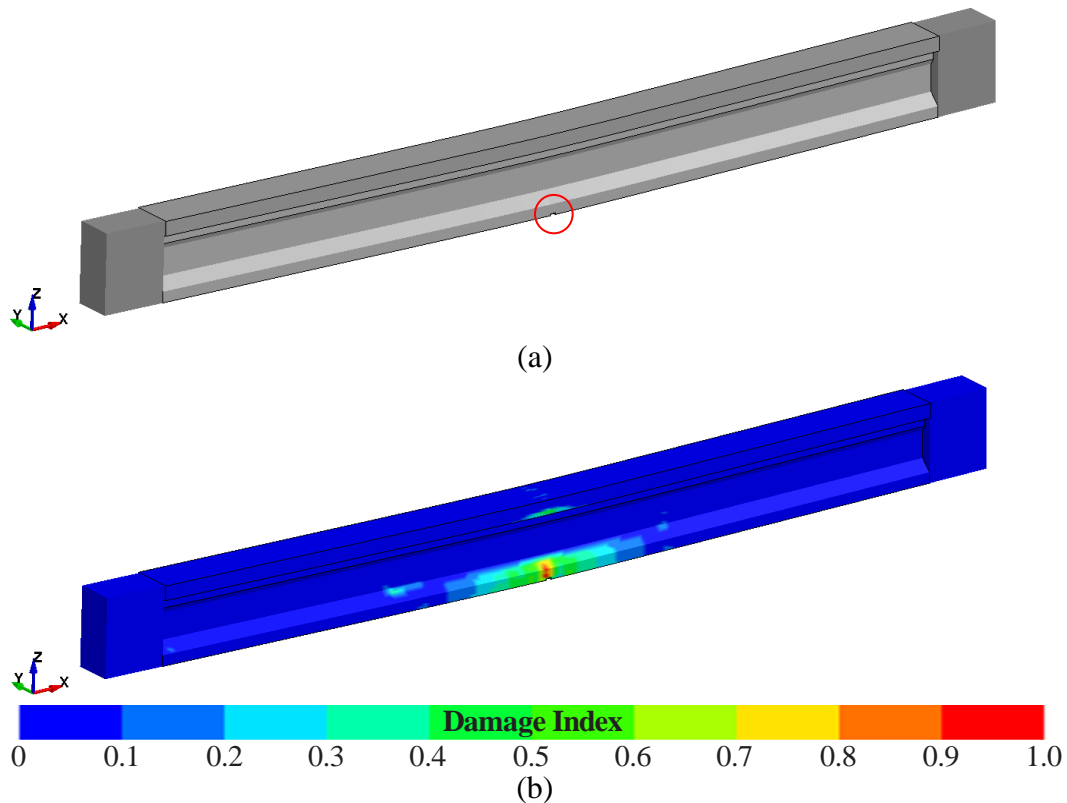
Figure 8.37 Specimen SS-3: FE model showing (a) initiation of 'erosion' (circled in red) near midspan and (b) damage index at P = 138 kip

Table 8.6 presents a comparison of the nominal load (at $\varepsilon_c = 0.003$) and maximum load values obtained from experimental data and FEA. The validation model reached a compressive concrete strain of 0.003 at an applied load (P_n) of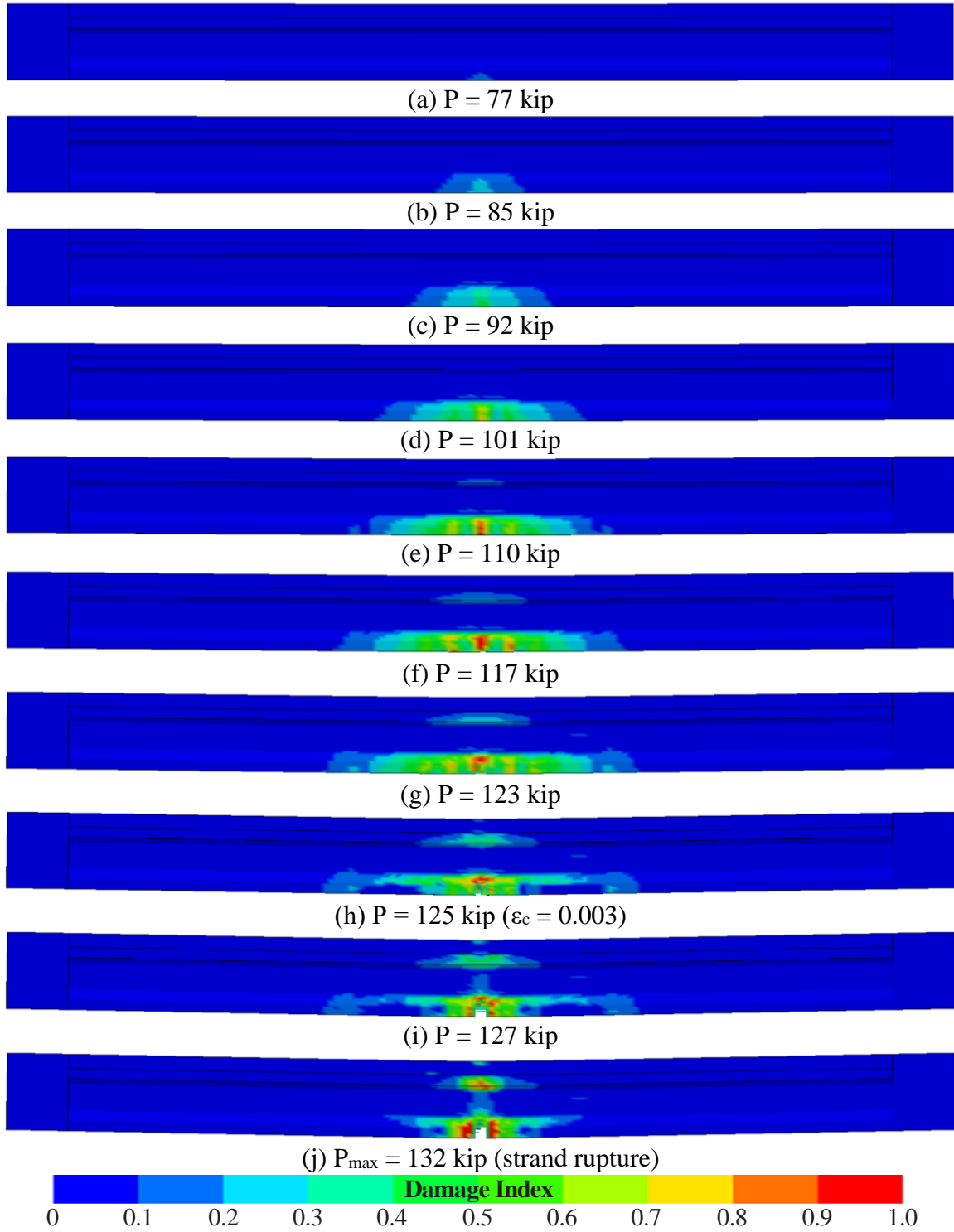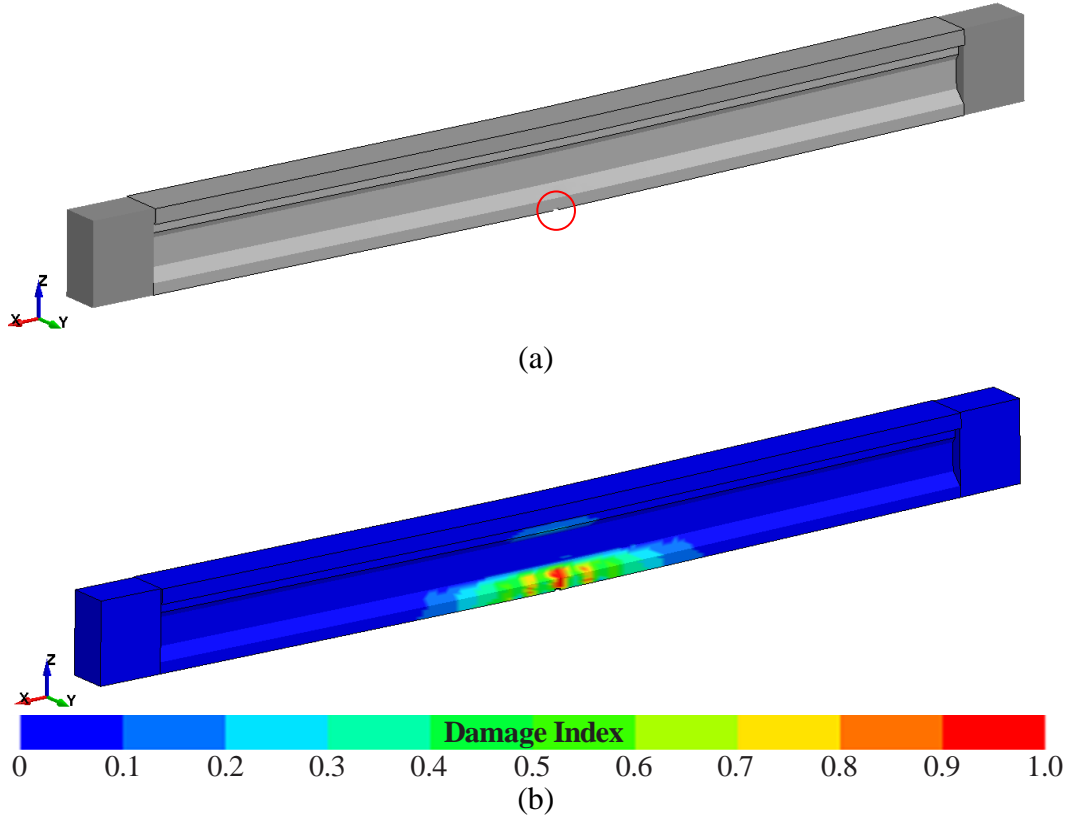 140.4 kip (<6% higher than the experimental load) and indicated a maximum load (P_{max}) of 143.5 kip (<6% higher than the experimental load). It is important to note that, once the compressive concrete strain reached 0.003, the applied load per FEA oscillated around 140 kip until all six pretensioned strands experienced rupture at a load $P = 143.5$ kip. As shown in Figure 8.38, the validation model presents good agreement with the experimental load-displacement curve. Experimental beam specimen SS-3 did not present strand rupture. Loading was halted shortly after the concrete deck reached $\varepsilon_c = 0.003$. Figure 8.39 shows the strain on top of the concrete deck, obtained from both FEA and experimental data. The experimental specimen could have experienced strand rupture at a higher applied load.

Table 8.6 Beam specimen SS-3: Comparison of capacity between experimental results and FEA

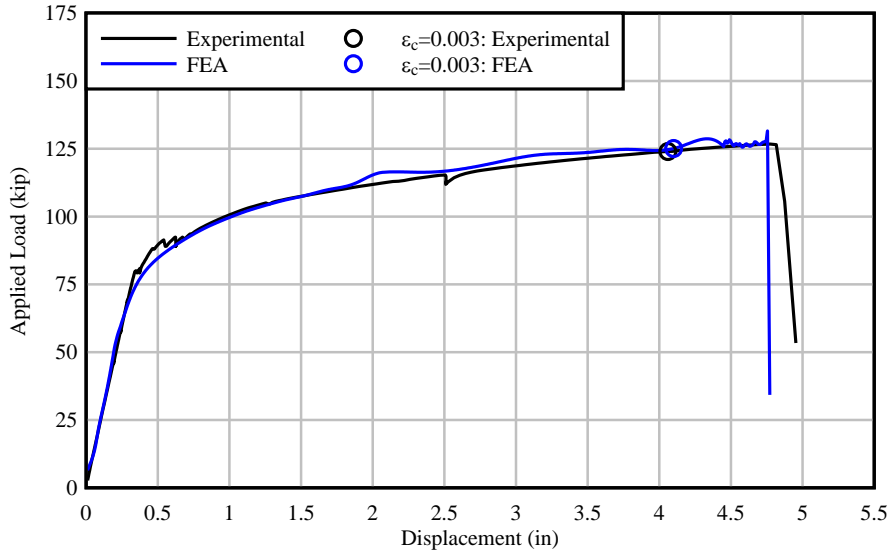|	Applied load (kip) at $\varepsilon_c=0.003$	Displacement (in.) at $\varepsilon_c=0.003$	Max. Load (P_{max}, kip)	Displacement (in.) at P_{max}
Experimental data	132.7	3.9	135.8	4.7
FEA	140.4	4.3	143.5	5.2
Difference	6%	9%	6%	9%

115

Figure 8.38 Comparison of load-displacement curves obtained from experimental data and FEA: Beam specimen SS-3
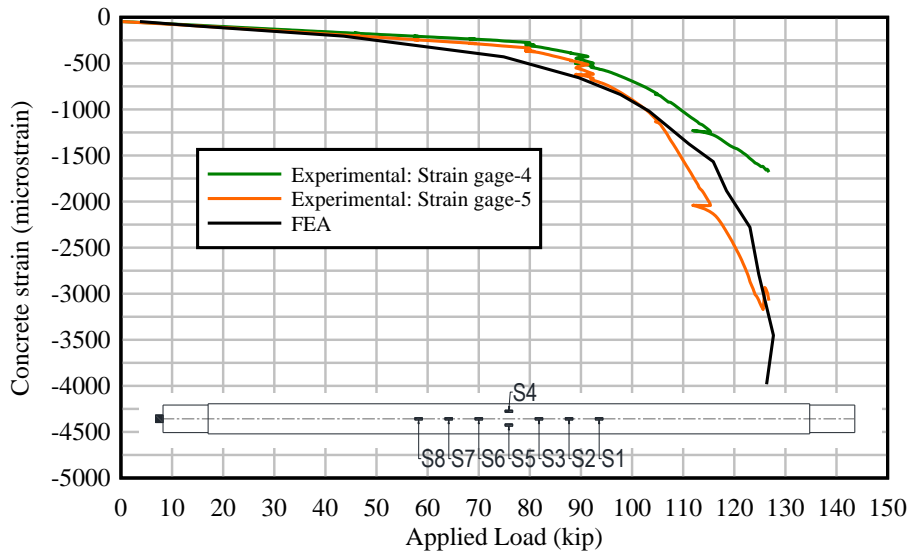

Figure 8.39 Strain on top of concrete deck as a function of applied load – comparison between experimental data and FEA: Beam specimen SS-3

Figure 8.40 shows the stress in prestressing tendons as a function of applied load. Vibrating wire gages were used to determine the pretensioned strand force (and losses) during: stressing of pretensioned strands (at the precast plant); post-tensioning of the test specimen (at the lab); and during loading. However, as shown in Figure 8.40, readings from VW gages remained almost constant during loading. Contrary to the experimental data, the validation model exhibited a significant increase in the pretensioned stress as load was applied. All six PreT strands ruptured in the validation model at a stress higher than 270 ksi because the material model used to simulate the prestressing strands was specified to rupture at $\varepsilon_{PreT} = 0.05$ ($f_{PreT} = 282$ ksi) based on tensile tests performed on a series of prestressing strand samples. The stress in post-tensioned tendons

indicated by the validation model presented good agreement with the experimental data as depicted in Figure 8.40.
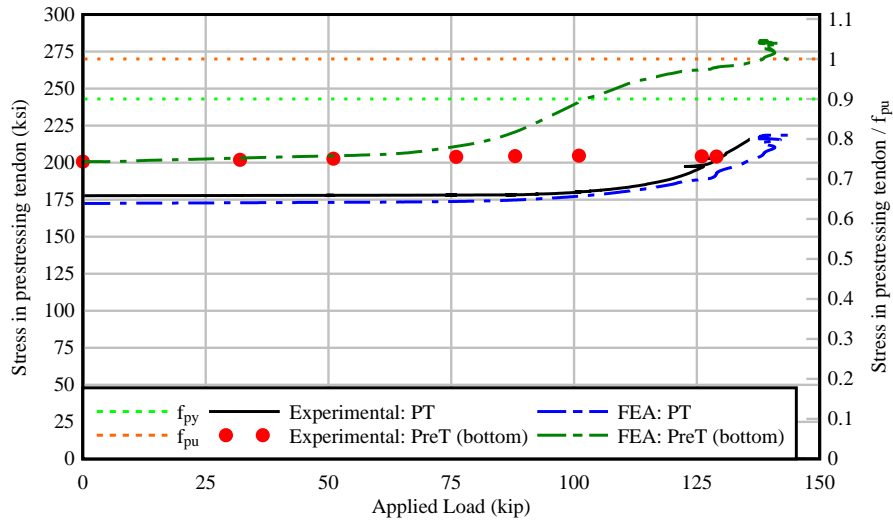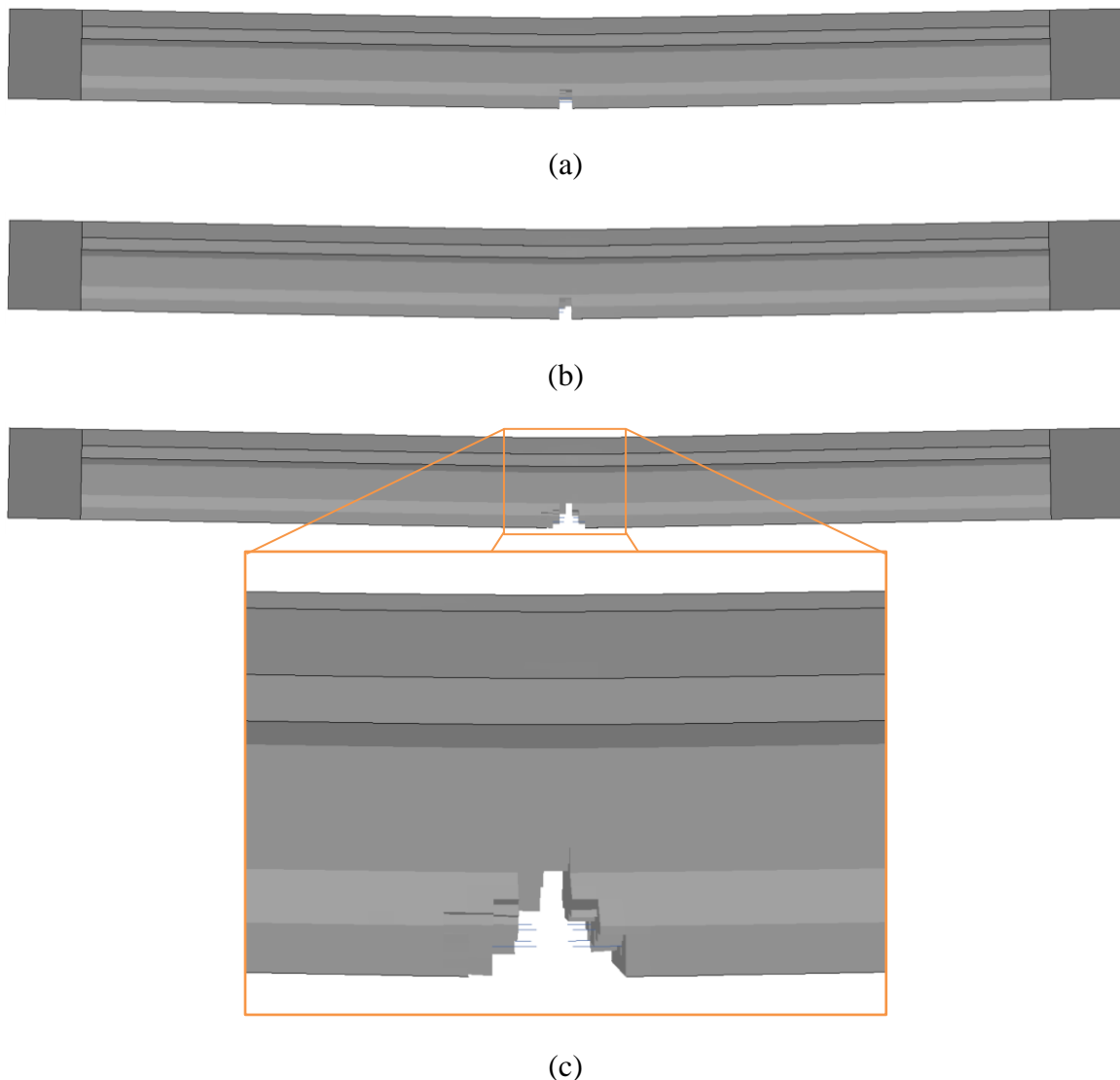

Figure 8.40 Stress in prestressing tendons as a function of applied load – comparison between experimental data and FEA: Beam specimen SS-3

The deflected shape of the beam and curvature computed from the FE model are compared to the experimental beam data in Figures 8.41 and 8.42. Deflection and curvature data for load levels at which concrete strains were approximately $\varepsilon_c = 0.003$ are indicated with bold lines, and data for higher load levels are indicated with dashed lines. Although the FE model indicated a higher maximum load than the experimental specimen, both the FEA and experimental data were generally in good agreement.

Figure 8.41 Displacement as a function of location along the length of beam specimen SS-3: (a) experimental data and (b) FEA

| P = 90 kip | 100 kip | 110 kip | 115 kip | 120 kip | 125 kip | 130 kip | 135 kip | 140 kip | 143 kip |

Figure 8.42 Curvature as a function of location along the length of beam specimen SS-3:
(a) experimental data and (b) FEA

Beam specimen SS-4

Beam specimen SS-4 is a 46-ft long beam with a span length of 45 ft and span-to-depth ratio of 15. As shown in Figure 8.43, prestressing reinforcement consisted of 1 post-tensioned tendon (equivalent to 6 post-tensioned strands), 4 pretensioned strands located in the bottom, and 2 pretensioned strands located in the top, which resulted in an unbonded reinforcement ratio (U/T) of 0.6. The concrete compressive strengths used in the validation model were input in units of ksi and were based in the average concrete compressive strengths at the day of the test (Table 8.7). However, due to limitations in the MAT_CSCM material model, the maximum compressive strength that was permitted to be specified was 13.8 ksi. Therefore, a compressive strength of 13.8 ksi was used to approximate the concrete deck instead of using the experimental value of 14.4 ksi. The specified pretensioned force used in the validation model was based on the vibrating wire gage readings after pretensioning (to be consistent with construction stages included in the model), while the specified post-tensioned force was based on the load cell reading after post-tensioning and prior to loading.

Table 8.7 Beam specimen SS-4: Concrete compressive strengths at day of flexural test

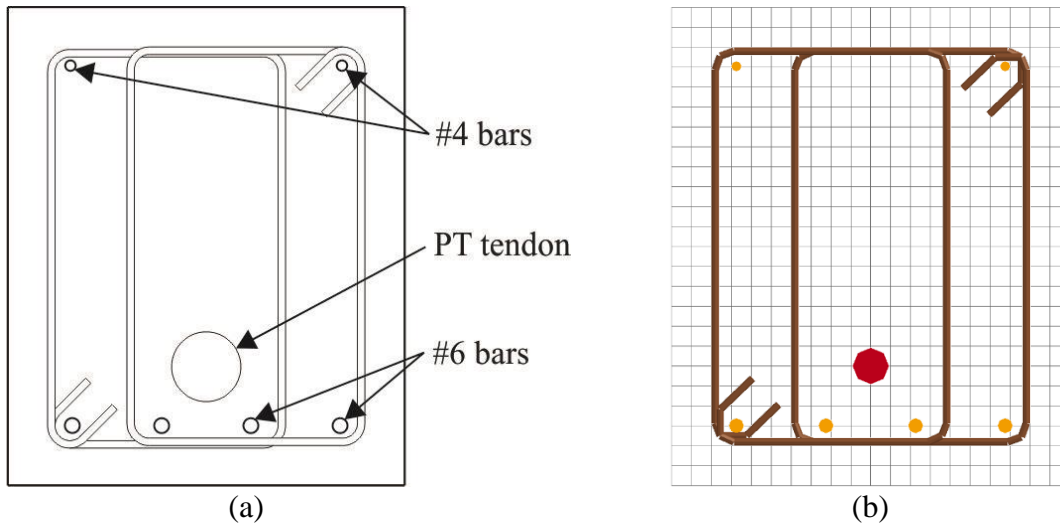| Description	Specified Compressive Strength (psi)	Avg. Compressive Strength (psi)
Precast girder	8,500	12,990
Deck	8,500	14,362
End blocks	6,500	11,167
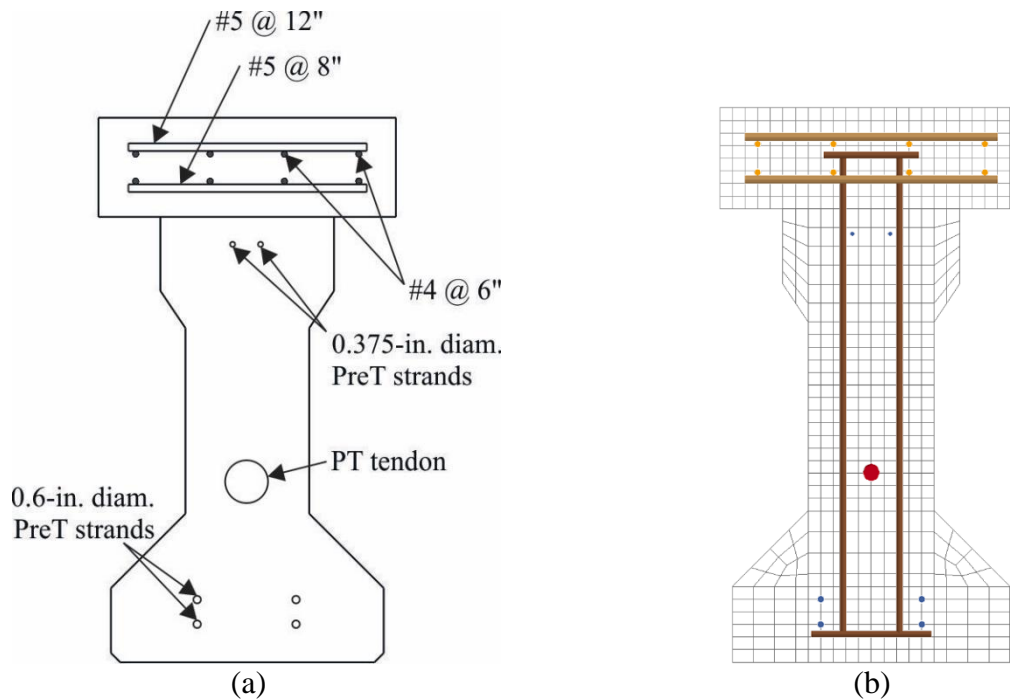
Figure 8.43 Beam specimen SS-4 cross-section:
(a) sketch showing location of longitudinal reinforcement, (b) FE model

During the experimental test, the first visible cracks on specimen SS-4 were identified at a load of 80 kip on the east side of the beam (Figure 8.44). Figure 8.45 shows the damage index at different load levels. As seen in Figure 8.45a, damage started accumulating (damage index = 0.1) near midspan on the bottom of the beam at an applied load $P = 77$ kip. At the point of initiation of erosion, the use of sectional constraints (rigid links) on the bonded pretensioned strands becomes particularly relevant. As depicted in Figure 8.46, the validation model for SS-4 started began exhibiting at a load $P = 116$ kip.
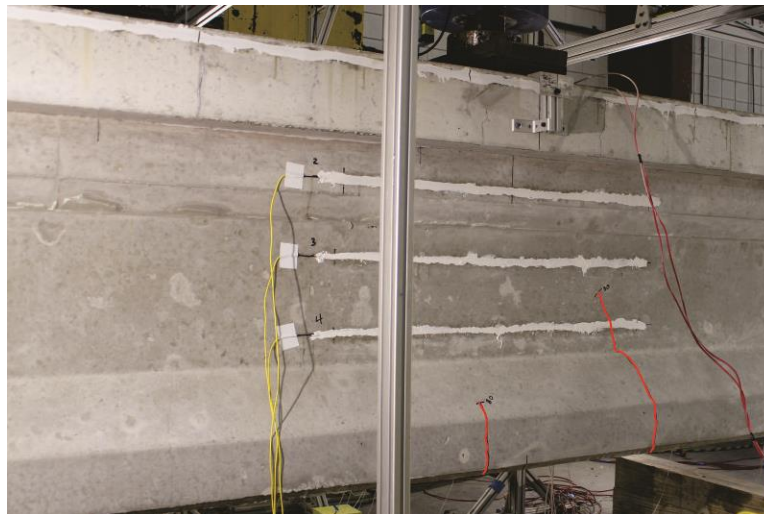
Figure 8.44 Specimen SS-4: First observed cracks (marked in red) at $P = 80$ kip

(a) P = 77 kip

(b) P = 85 kip

(c) P = 92 kip

(d) P = 101 kip

(e) P = 110 kip

(f) P = 117 kip

(g) P = 123 kip

(h) P = 125 kip ($\varepsilon_c = 0.003$)

(i) P = 127 kip

(j) P_{max} = 132 kip (strand rupture)

Damage Index

| 0 | 0.1 | 0.2 | 0.3 | 0.4 | 0.5 | 0.6 | 0.7 | 0.8 | 0.9 | 1.0 |

Figure 8.45 Specimen SS-4: FE model showing damage index at different load levels

(a)

(b)

Figure 8.46 Specimen SS-4: FE model showing (a) initiation of 'erosion' (circled in red) near midspan and (b) damage index at P = 116 kip
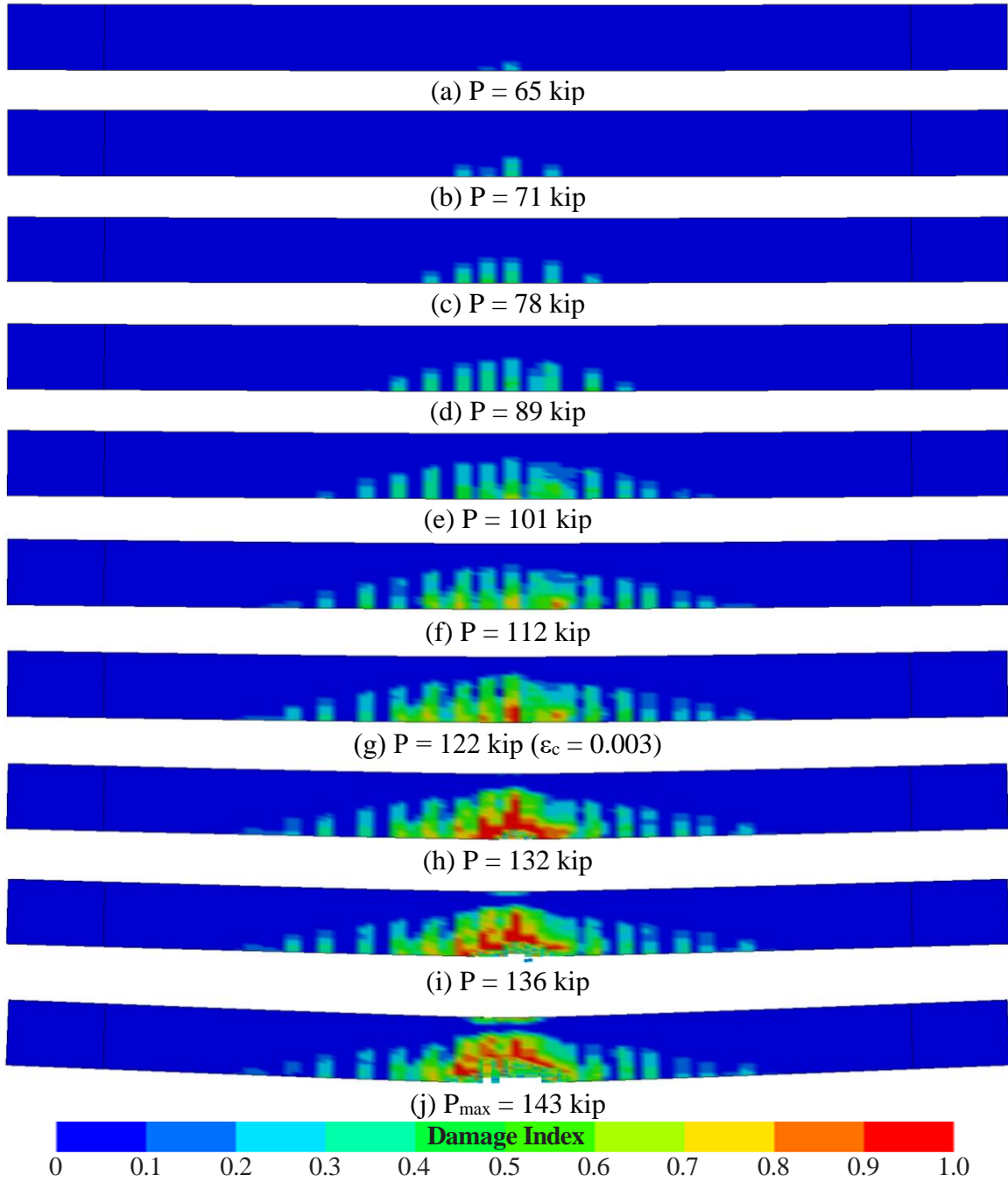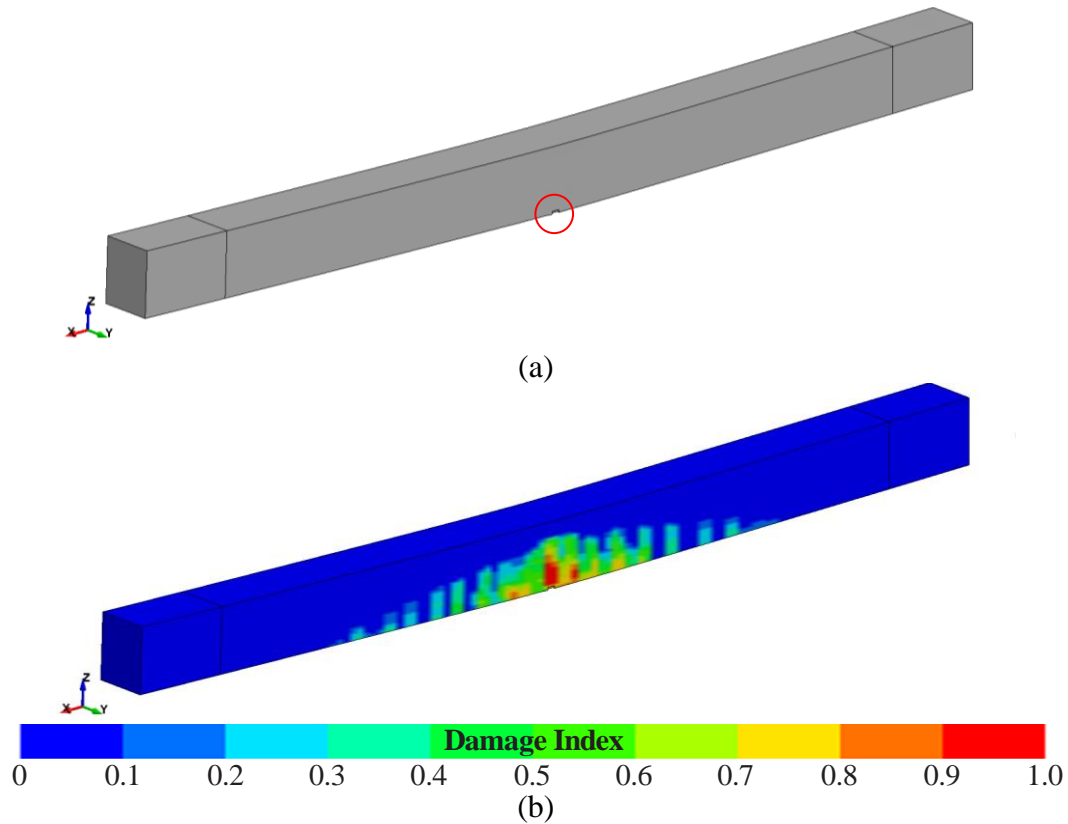
Table 8.8 presents a comparison of the nominal load (at $\varepsilon_c = 0.003$) and maximum load values obtained from experimental data and FEA. The validation model reached a compressive concrete strain of 0.003 at an applied load of 125.1 kip (<1% higher than the experimental load) and indicated a maximum load (P_{max}) of 131.6 kip (<4% higher than the experimental load). As shown in Figure 8.47, the validation model presents good agreement with the experimental load-displacement curve. Figure 8.48 shows the strain on top of the concrete deck, obtained from both FEA and experimental data.

Table 8.8 Beam specimen SS-4: Comparison of capacity between experimental results and FEA

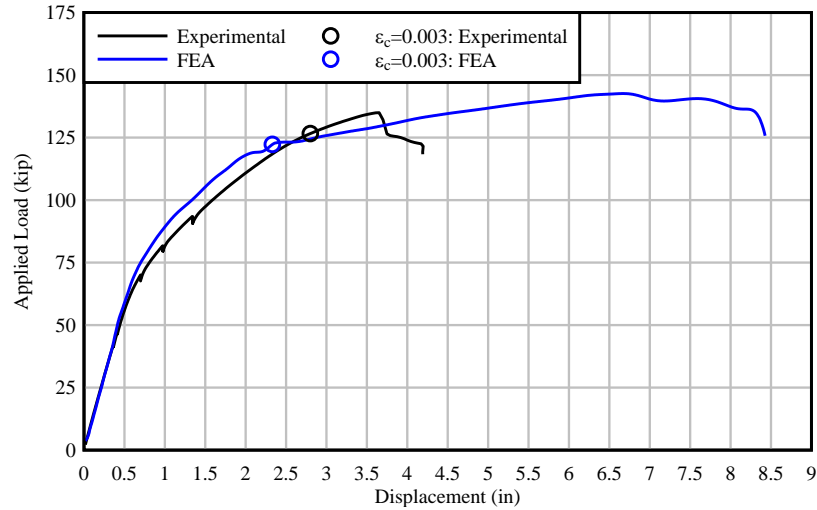|	Applied load (kip) at ε_c=0.003	Displacement (in.) at ε_c=0.003	Max. Load (P_{max}, kip)	Displacement (in.) at P_{max}
Experimental data	124.0	4.1	126.8	4.8
FEA	125.1	4.1	131.6	4.8
Difference	1%	1%	4%	-1%

Figure 8.47 Comparison of load-displacement curves obtained from experimental data and FEA: Beam specimen SS-4

Figure 8.48 Strain on top of concrete deck as a function of applied load – comparison between experimental data and FEA: Beam specimen SS-4

During the experimental test four consecutive noises, presumably from the rupture of pretensioned strands, were heard followed by a drop in the load-displacement curve. Partial demolition conducted on specimen SS-4 following the load test confirmed the rupture of all four bonded pretensioned strands as shown in Figure C.40. Note that there were a total of ten pretensioned strands, but six of them were 'debonded'. Debonded strands (only bonded for a distance of 1 ft at midspan) were included in the precast beam specimen for purposes of fabricating all SS precast beams in the same prestressing bed at the precast plant, and therefore did not contribute to flexural capacity and were not included in the validation model. The validation model exhibited rupture of all four pretensioned strands in the bottom of the beam (Figure 8.49) at

122

P_{max} = 131.6 kip. Vibrating wire gages were used to determine the pretensioned strand force (and losses) during: stressing of pretensioned strands (at the precast plant); post-tensioning of the test specimen (at the lab); and during loading. However, readings from VW gages remained almost constant during loading. Contrary to the experimental data, the validation model exhibited a significant increase in the pretensioned stress as load was applied, which is consistent with the experimental strand rupture. Note that PreT strands in the model ruptured at a stress higher than 270 ksi because the material model used to simulate the prestressing strands was specified to rupture at $\varepsilon_{PreT} = 0.05$ ($f_{PreT} = 282$ ksi) based on tensile tests performed on a series of prestressing strand samples. The stress in post-tensioned tendons indicated by the validation model presented good agreement with the experimental data as depicted in Figure 8.50.

(a)

(b)

(c)

Figure 8.49 Specimen SS-4 – rupture of pretensioned strands on FE model:
(a) model before strand rupture, (b) model immediately after strand rupture,
(c) close-up showing ruptured PreT strands
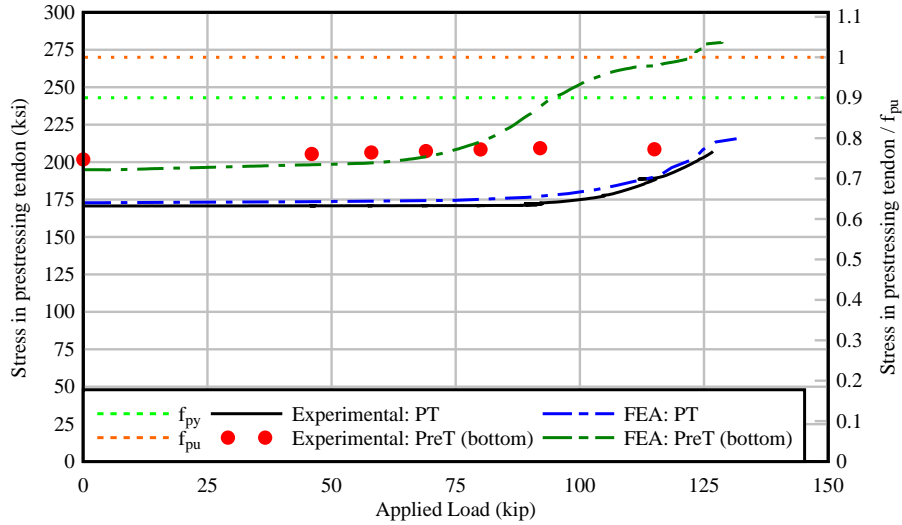
Figure 8.50 Stress in prestressing tendons as a function of applied load – comparison between experimental data and FEA: Beam specimen SS-4

The deflected shape of the beam and curvature computed from the FE model are compared to the experimental beam data in Figures 8.51 and 8.52. Deflection and curvature data for load levels at which concrete strains were approximately $\varepsilon_c = 0.003$ are indicated with bold lines, and data for higher load levels are indicated with dashed lines. Both the FEA and experimental data were generally in good agreement.
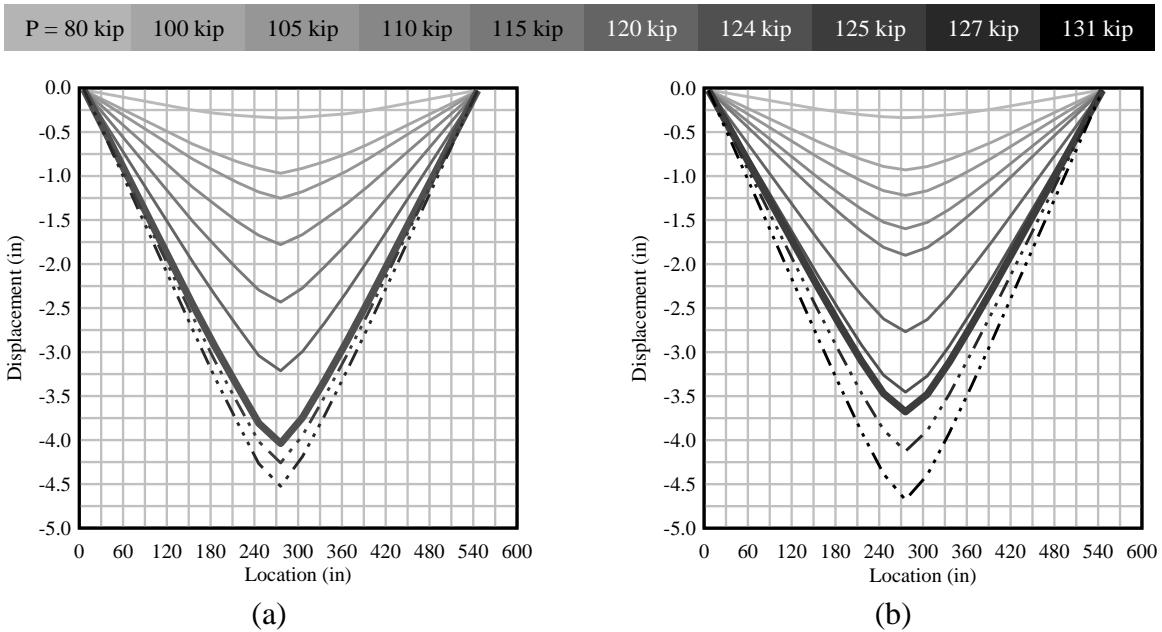
Figure 8.51 Displacement as a function of location along the length of beam specimen SS-4: (a) experimental data and (b) FEA

P = 80 kip	100 kip	105 kip	110 kip	115 kip	120 kip	124 kip	125 kip	127 kip	131 kip
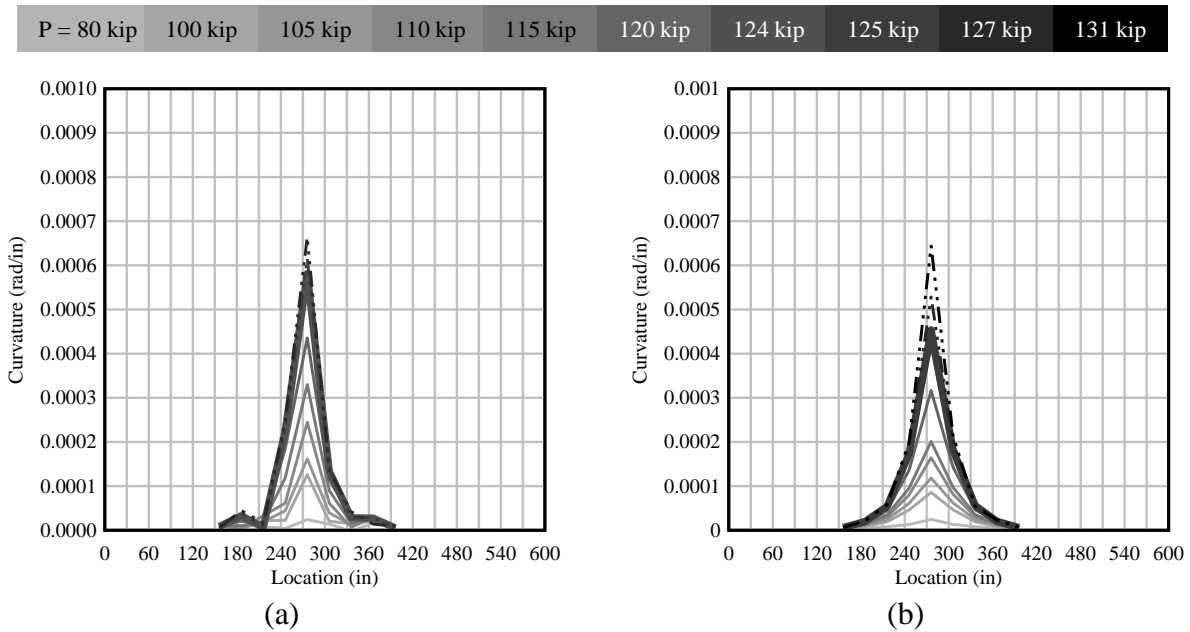
Figure 8.52 Curvature as a function of location along the length of beam specimen SS-4: (a) experimental data and (b) FEA

8.3.1 Simply-supported cast-in-place beam specimens (SS-5)

A 31-ft long cast-in-place simply-supported beam was tested in positive bending. This beam specimen consisted of a rectangular concrete section (20 in. x 24 in.) with a span length (distance from centerline of bearing to centerline of bearing) of 30 ft and span-to-depth ratio of 15. As shown in Figure 8.53, the bonded reinforcement consisted of 4 No. 6 mild steel bars while the unbonded reinforcement consisted of 1 post-tensioned tendon (equivalent to 12 0.6-in. diameter strands), which resulted in an unbonded reinforcement ratio (U/T) of 0.9. The concrete compressive strengths used in the validation model were input in units of ksi and were based in the average concrete compressive strengths at the day of the test (Table 8.9). The specified post-tensioned force was based on the load cell reading after post-tensioning and prior to loading.

It is important to note that all precast beam specimens were fabricated using a class VI concrete, but cast-in-place (CIP) beam specimen SS-5 was fabricated using a class V concrete. Taking into consideration that specimen SS-5 experimentally exhibited compressive failure and significant concrete crushing, while also having a lower concrete compressive strength (than the precast beams) and no bonded pretensioned strands, this beam was modeled using a modified version of the MAT_CSCM material model. When using MAT_CSCM, parameters can be modified in order to input the desired material properties. The shape of the softening portion of the stress-strain curve (Figure 8.3) is sensitive to parameters b (ductile shape softening parameter) and pmod (pressure softening parameter). The modified MAT_CSCM material model used for beam specimen SS-5 uses parameters b = 1000 (instead of the default value of 100) and pmod = 10 (instead of the default value of 0).

(a)   (b)
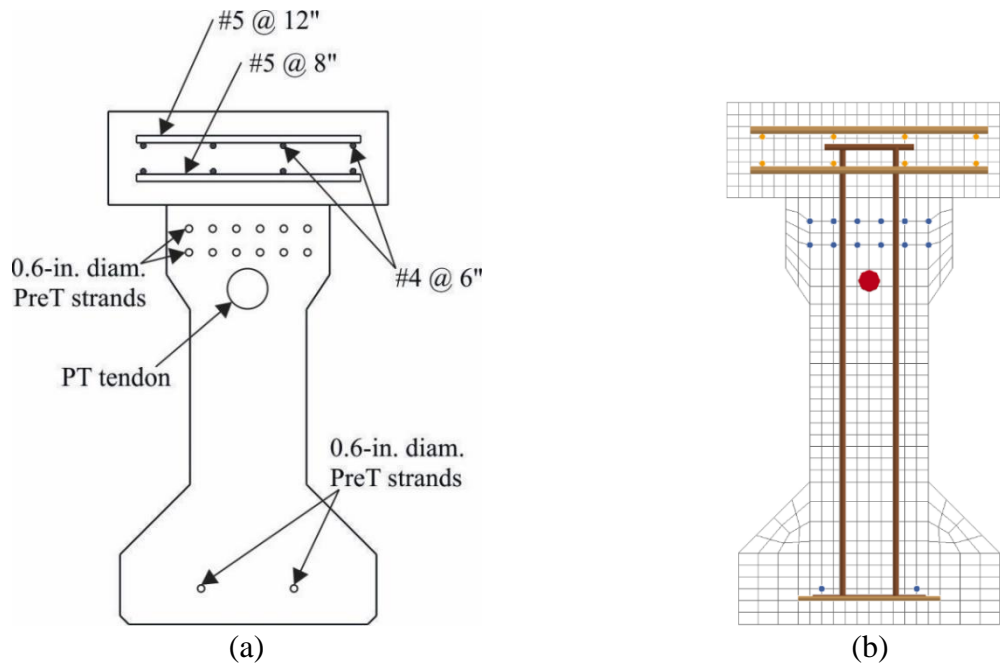
Figure 8.53 Beam specimen SS-5 cross-section:
(a) sketch showing location of longitudinal reinforcement, (b) FE model

Table 8.9 Beam specimen SS-5: Concrete compressive strengths at day of flexural test

Description	Specified Compressive Strength (psi)	Avg. Compressive Strength (psi)
CIP beam	6,500	8,401

During the experimental test, the first visible cracks on specimen SS-5 were identified at a load of 69 kip on the east side of the beam (Figure 8.54). Figure 8.55 shows the damage index at different load levels. At an applied load P = 65 kip, damage started accumulating (damage index = 0.1) in the validation model near midspan on the bottom of the beam (Figure 8.55a). The validation model for SS-5 began exhibiting erosion at a load P = 126 kip as depicted in Figure 8.56.
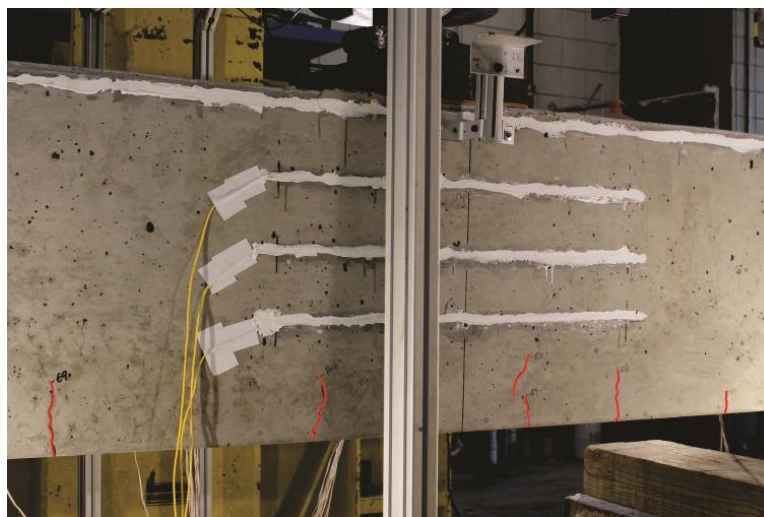
Figure 8.54 Specimen SS-5: First observed cracks (marked in red) at P = 69 kip

(a) P = 65 kip

(b) P = 71 kip

(c) P = 78 kip

(d) P = 89 kip

(e) P = 101 kip

(f) P = 112 kip

(g) P = 122 kip (ε_c = 0.003)

(h) P = 132 kip

(i) P = 136 kip

(j) P_{max} = 143 kip

Damage Index

0   0.1   0.2   0.3   0.4   0.5   0.6   0.7   0.8   0.9   1.0

Figure 8.55 Specimen SS-5: FE model showing damage index at different load levels

(a)

(b)

Figure 8.56 Specimen SS-5: FE model showing (a) initiation of 'erosion' (circled in red) near midspan and (b) damage index at P = 126 kip

Table 8.10 presents a comparison of the nominal load (at $\varepsilon_c = 0.003$) and maximum load values obtained from experimental data and FEA. The validation model presented good agreement with the experimental data in terms of both load and displacement up until the concrete reached a compressive strain of 0.003 at an applied load of 122.3 kip (<4% lower than the experimental load). Beyond this point, the FE model indicated a maximum load (P_{max}) of 142.6 kip (<6% higher than the experimental load). The validation model became more flexible than the experimental specimen after the compressive concrete strain reached 0.003 (Figure 8.57). Figure 8.58 presents the strain on top of the beam, obtained from both FEA and experimental data.

Table 8.10 Beam specimen SS-5: Comparison of capacity between experimental results and FEA

	Applied load (kip) at $\varepsilon_c=0.003$	Displacement (in.) at $\varepsilon_c=0.003$	Max. Load (P_{max}, kip)	Displacement (in.) at P_{max}
Experimental data	126.6	2.8	135.0	3.6
FEA	122.3	2.3	142.6	6.7
Difference	-3%	-17%	6%	83%

Figure 8.57 Comparison of load-displacement curves obtained from experimental data and FEA: Beam specimen SS-5
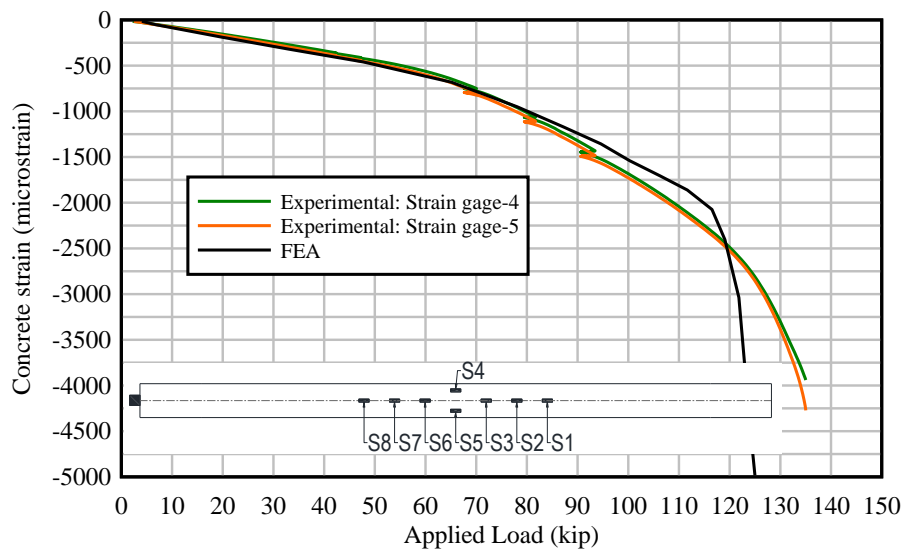
Figure 8.58 Strain on top of beam as a function of applied load – comparison between experimental data and FEA: Beam specimen SS-5

The axial force in the post-tensioned tendon was monitored during the experimental test though a load cell at the dead end. As depicted in Figure 8.22, the stress in the PT tendon resulting from the validation model presented good agreement with the experimental data.

The deflected shape of the beam and curvature computed from the FE model are compared to the experimental beam data in Figures 8.60 and 8.61. Deflection and curvature data for load levels at which concrete strains were approximately $\varepsilon_c = 0.003$ are indicated with bold lines, and data for higher load levels are indicated with dashed lines. In a similar way to the previously discussed precast simply-supported beams, the experimental specimen was slightly more flexible than the validation model.

129
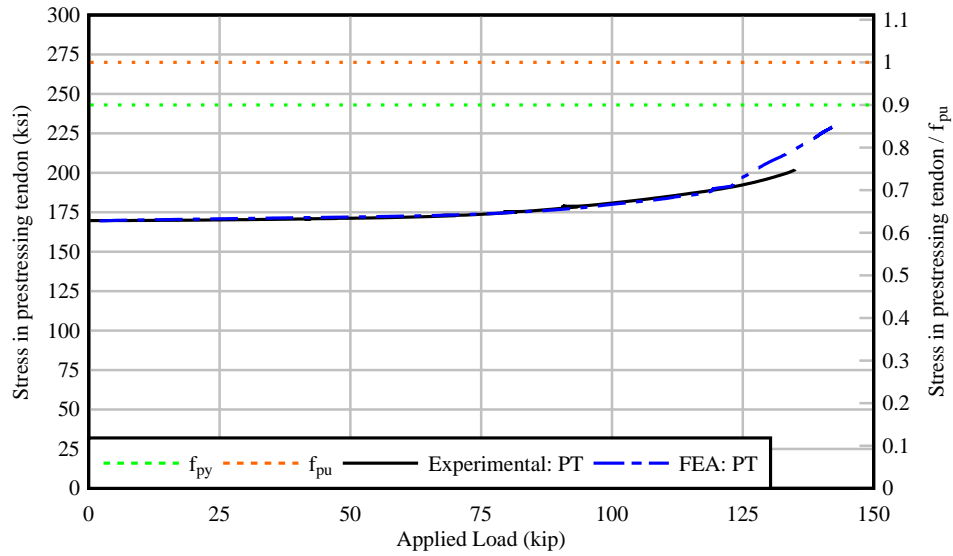
Figure 8.59 Stress in post-tensioned tendon as a function of applied load – comparison between experimental data and FEA: Beam specimen SS-5
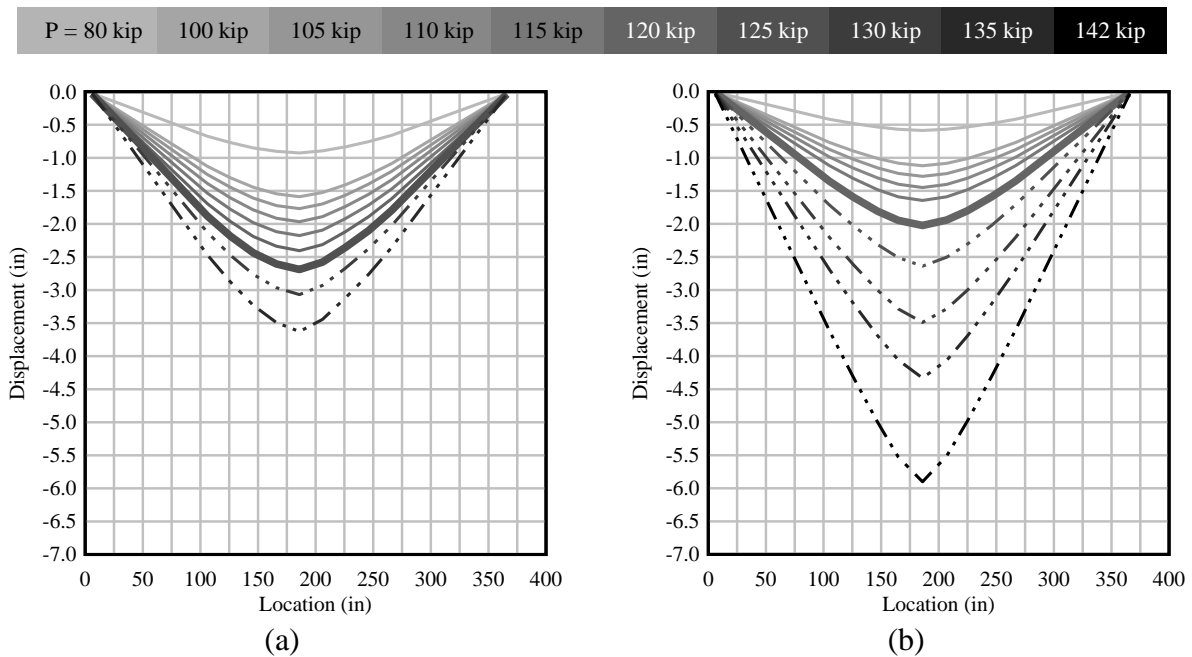
Figure 8.60 Displacement as a function of location along the length of beam specimen SS-5: (a) experimental data and (b) FEA
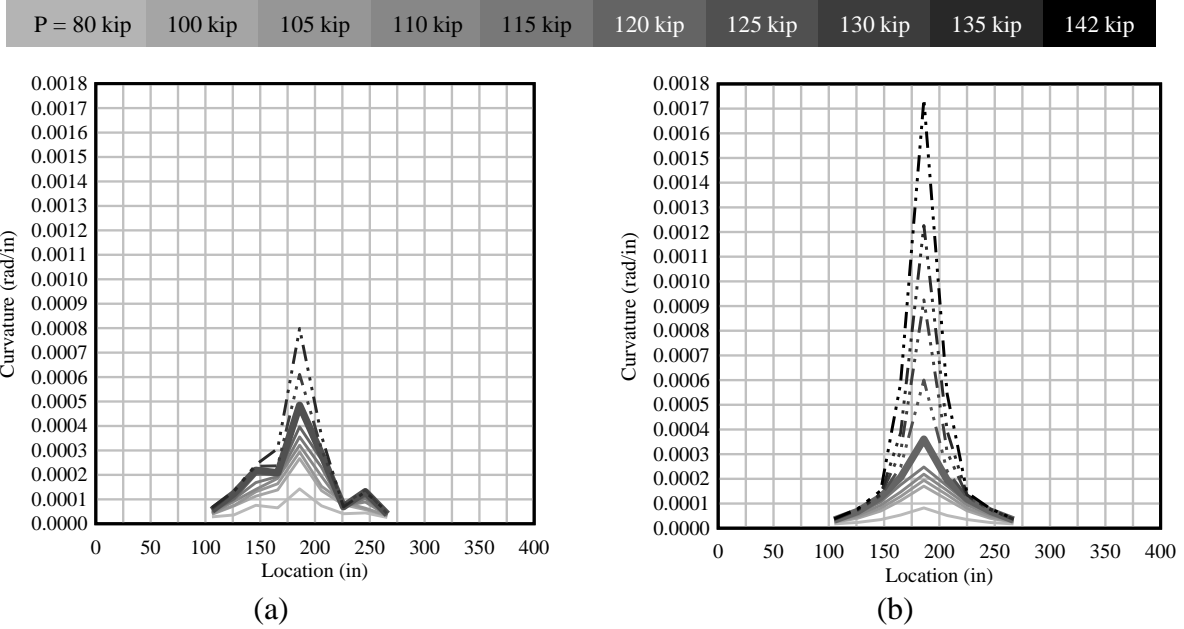
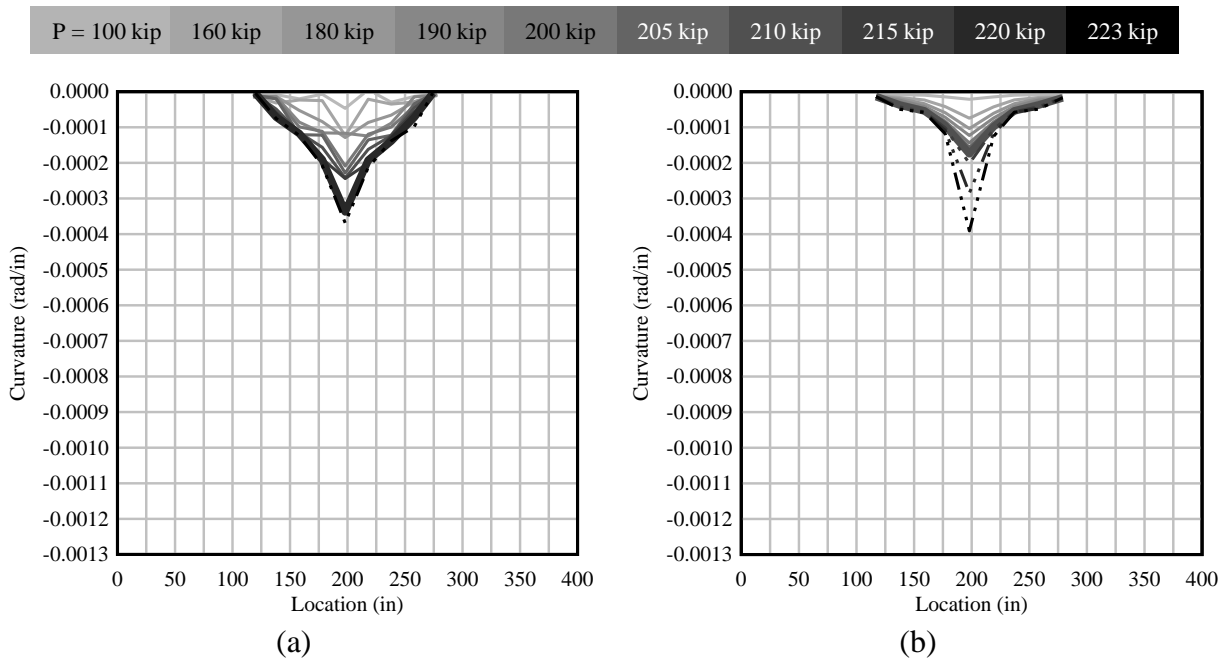Figure 8.61 Curvature as a function of location along the length of beam specimen SS-5:
(a) experimental data and (b) FEA

8.3.1 Negative bending precast beam specimens

A total of three precast beams were tested in negative bending: NB-1, NB-2, and NB-3. These beam specimens consisted of modified AASHTO Type II sections (27 ft long) with an 8-in. thick concrete deck and 3-ft long rectangular cast-in-place concrete end blocks. All specimens had different amounts of pretensioned (PreT, bonded) and post-tensioned (PT, unbonded) prestressing reinforcement. All pretensioned and post-tensioned tendons consisted of 0.6-in. diameter strands.

Beam specimen NB-1

Beam specimen NB-1 is a 33-ft long beam with a span-to-depth ratio of 20. As shown in Figure 8.62, prestressing reinforcement consisted of 1 post-tensioned tendon (equivalent to 12 post-tensioned strands), 12 pretensioned strands located in the top, and 2 pretensioned strands located in the bottom, which resulted in an unbonded reinforcement ratio (U/T) of 0.5. The concrete compressive strengths used in the validation model were based in the average concrete compressive strengths at the day of the test (Table 8.11). The specified pretensioned force used in the validation model was based on the vibrating wire gage readings after pretensioning (to be consistent with construction stages included in the model), while the specified post-tensioned force was based on the load cell reading after post-tensioning and prior to loading.

Table 8.11 Beam specimen NB-1: Concrete compressive strengths at day of flexural test

Description	Specified Compressive Strength (psi)	Avg. Compressive Strength (psi)
Precast girder	8,500	12,537
Deck	8,500	12,537
End blocks	6,500	10,992

(a)   (b)

Figure 8.62 Beam specimen NB-1 cross-section:
(a) sketch showing location of longitudinal reinforcement, (b) FE model

The first visible cracks on specimen NB-1 during the experimental test were identified at a load of 120 kip on the east side of the beam (Figure 8.63). Figure 8.64 shows the damage index at different load levels. At an applied load P = 134 kip, damage started accumulating (damage index = 0.1) at the center of the beam on top of the concrete deck (Figure 8.64a). The validation model for NB-1 began exhibiting erosion at a load P = 228 kip as shown in Figure 8.65.
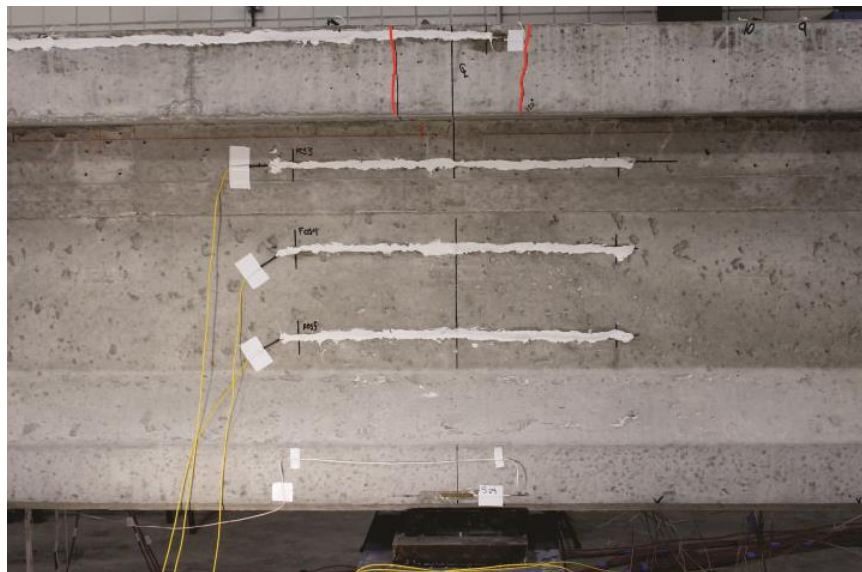
Figure 8.63 Specimen NB-1: First observed cracks (marked in red) at P = 120 kip

132

(a) P = 134 kip

(b) P = 148 kip

(c) P = 160 kip

(d) P = 169 kip

(e) P = 194 kip

(f) P = 210 kip (ε_c = 0.003)

(g) P = 215 kip

(h) P = 222 kip

(i) P = 225 kip

(j) P_{max} = 229 kip

Damage Index

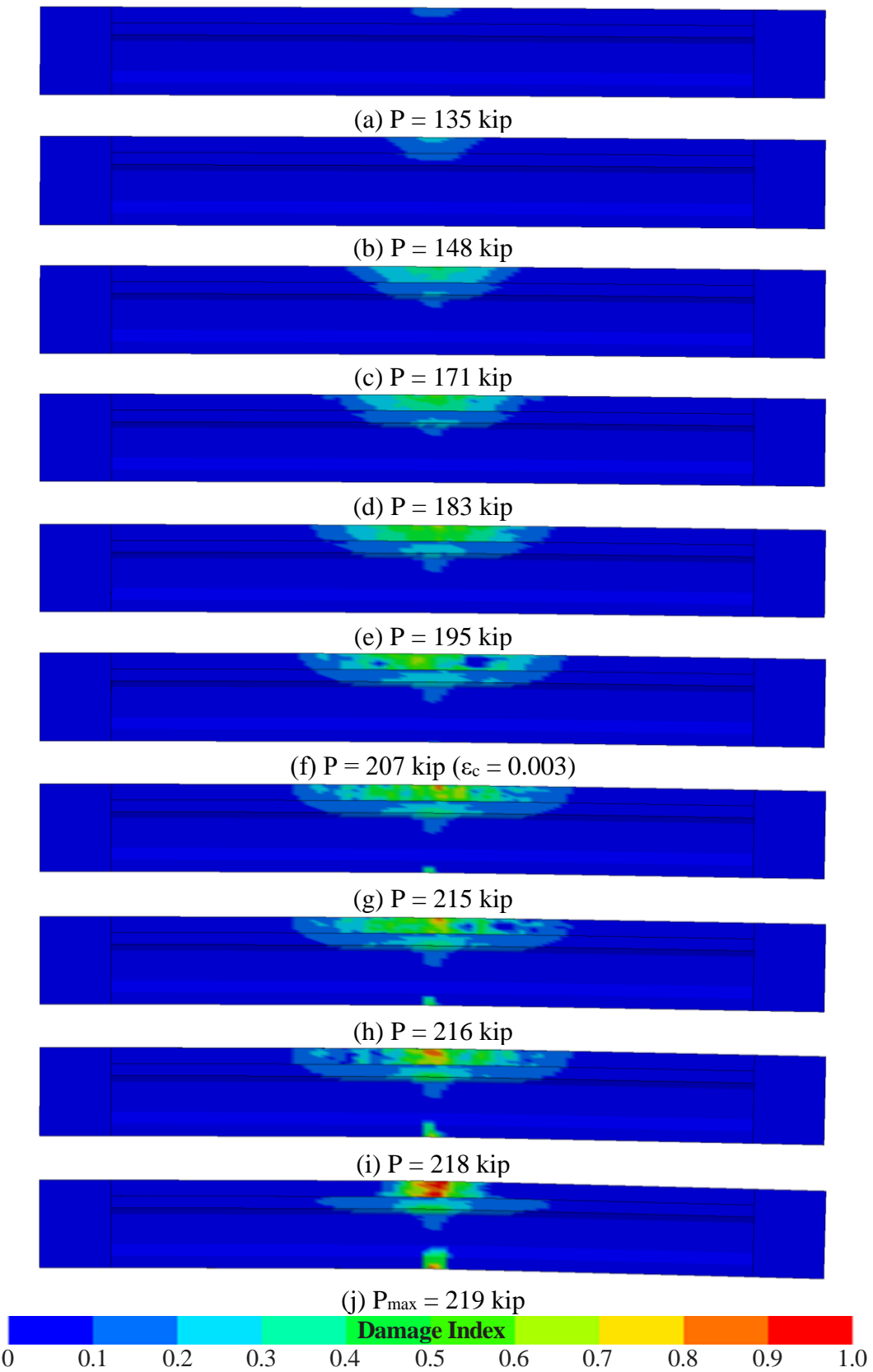0   0.1   0.2   0.3   0.4   0.5   0.6   0.7   0.8   0.9   1.0
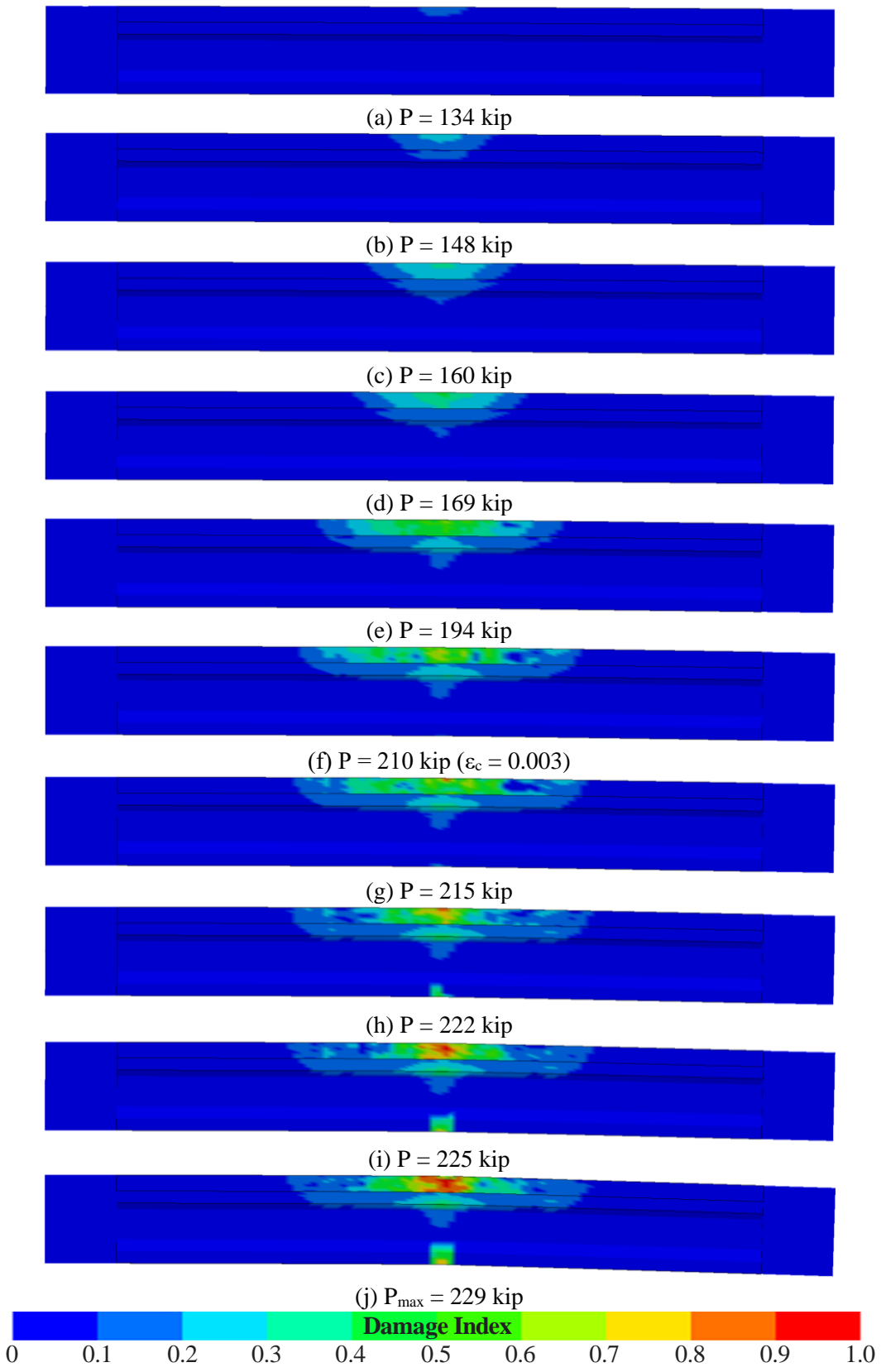
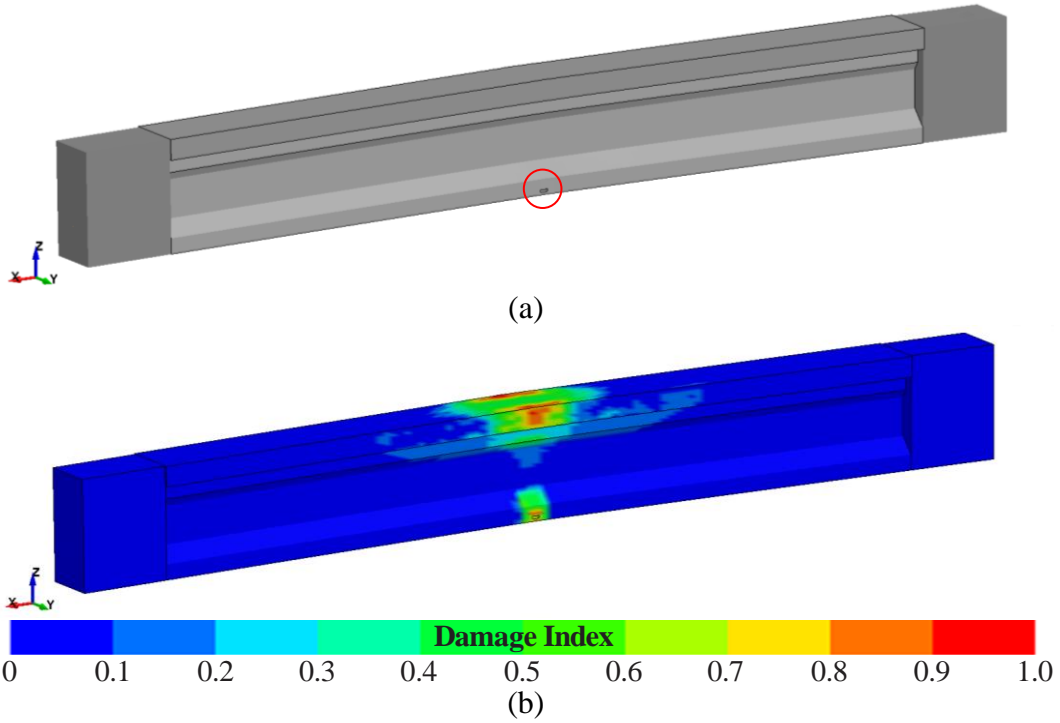Figure 8.64 Specimen NB-1: FE model showing damage index at different load levels
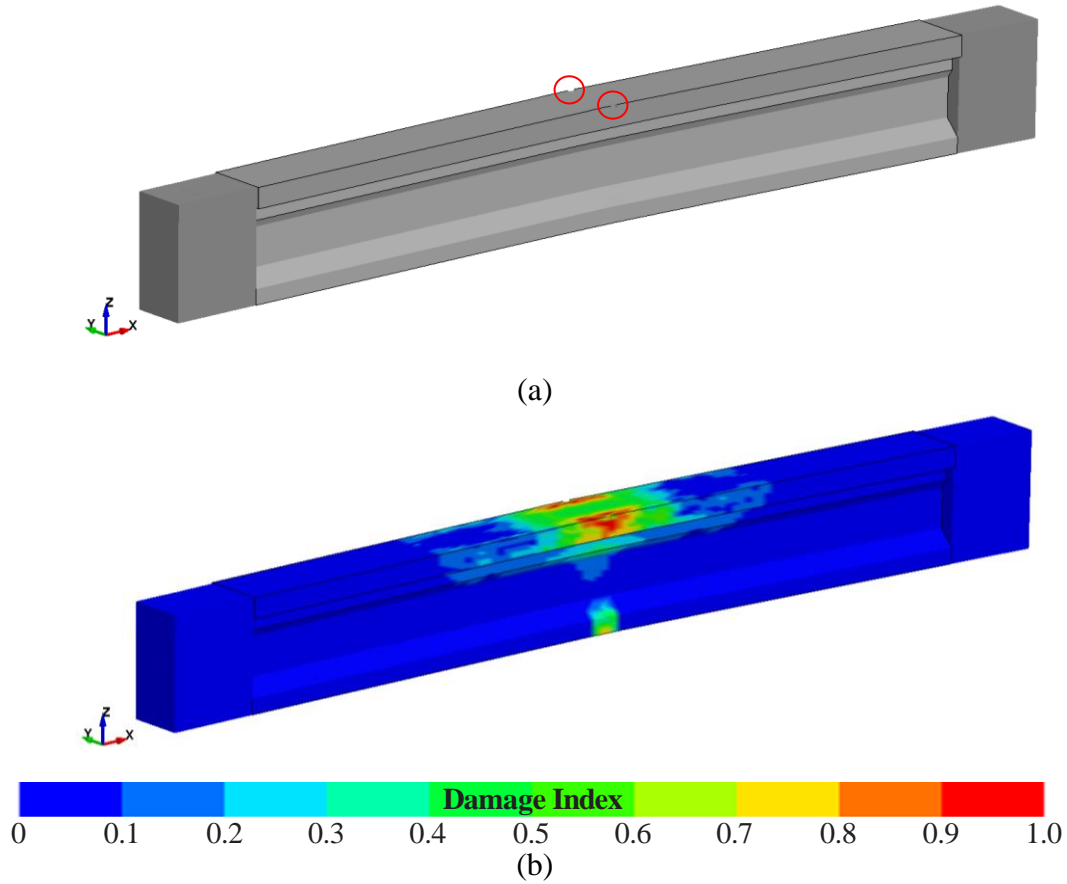
Figure 8.65 Specimen NB-1: FE model showing (a) initiation of 'erosion' (circled in red) and (b) damage index at P = 228 kip

Table 8.12 presents a comparison of the nominal load (at $\varepsilon_c = 0.003$) and maximum load values obtained from experimental data and FEA. As shown in Figure 8.66, the validation model presents good overall agreement with the experimental load-displacement curve. The validation model reached a compressive strain of 0.003 at an applied load of 210.1 kip (approximately 5% lower than the experimental load). Note that foil strain gages were located along the web of the beam and on the sides of the bottom flange at the middle support. However, for specimen NB-1, no strain gages were placed on the bottom of the beam at the middle support. Therefore, the strains at the bottom of the beam were determined by extrapolation (Figure 8.67, dashed line). The extrapolated strains present good agreement with the FEA data up until a strain of 0.0025, when the FEA strains start increasing at a higher rate. The maximum load (P_{max}) was 229.2 kip, which was approximately 3% higher than the experimental maximum load. However, note that the experimental test was terminated shortly after the strains in the bottom flange at the center support exceeded 0.003. Hence, the experimental P_{max} value corresponds to the maximum load recorded before the beam was unloaded.

134

Table 8.12 Beam specimen NB-1: Comparison of capacity between
experimental results and FEA

	Applied load (kip) at ε_c=0.003	Displacement (in.) at ε_c=0.003	Max. Load (P_{max}, kip)	Displacement (in.) at P_{max}
Experimental data	220.0	3.4	223.4	3.7
FEA	210.1	2.1	229.2	4.7
Difference	-5%	-39%	3%	27%
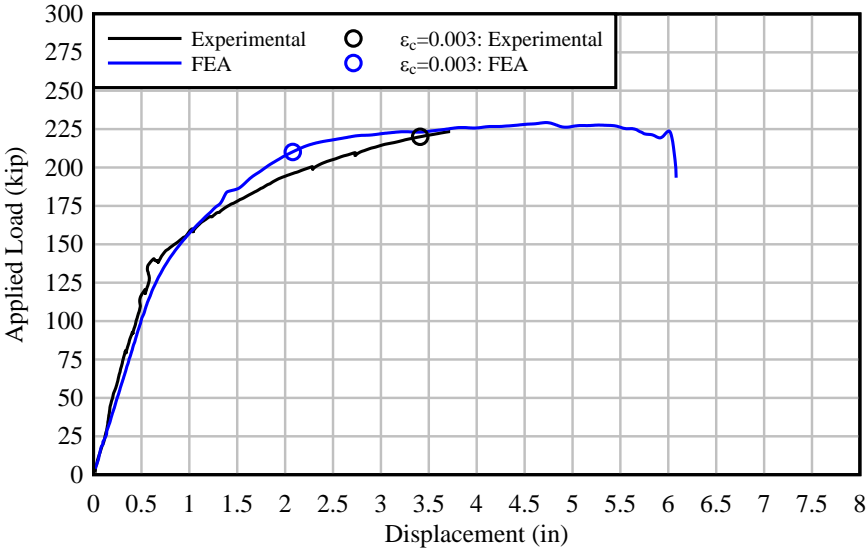
Figure 8.66 Comparison of load-displacement curves obtained from experimental data and FEA:
Beam specimen NB-1
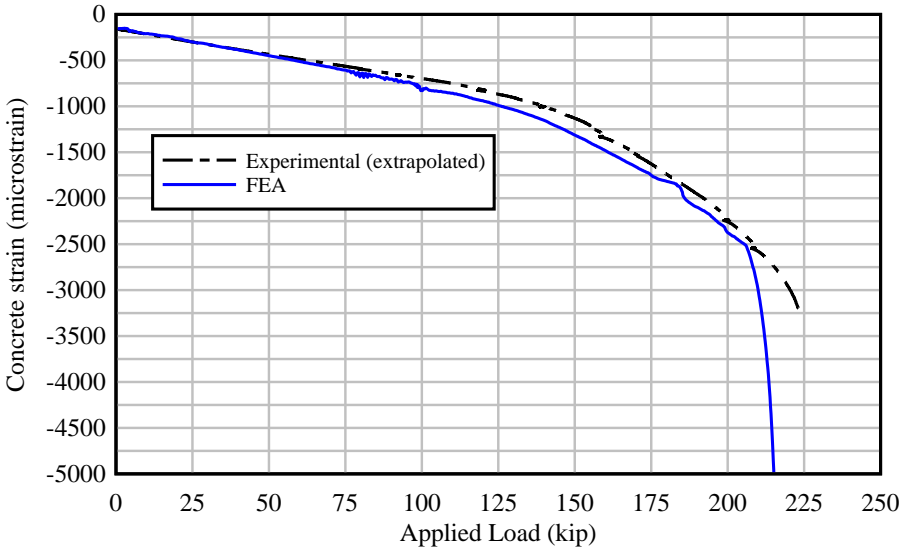
Figure 8.67 Strain at bottom-center of beam as a function of applied load – comparison between
experimental data and FEA: Beam specimen NB-1

135

Figure 8.68 shows the stress in prestressing tendons as a function of applied load. The axial force in the post-tensioned tendon was monitored during the experimental test though a load cell at the dead end. The stress in the PT tendon indicated by the validation model presented good agreement with the experimental data as depicted in Figure 8.68. Additionally, vibrating wire (VW) gages were used to determine the pretensioned strand force (and losses) during stressing of pretensioned strands (at the precast plant), post-tensioning of the test specimen (at the lab), and during loading. Figure 8.68 shows the experimental stress in PreT strands with solid circles. Regarding the validation model, axial forces in PreT strands were obtained at different locations along the length of the beam at different load levels. The finite element model indicated that PreT strands located in the top layer presented higher axial forces, and the maximum force in PreT strands occurred at the midspan of the beam. Both the experimental data and validation model exhibited a significant increase in the pretensioned stress as load was applied. However, none of the PreT strands presented rupture on neither FEA nor experimental test. Although the PreT stress exceeded $f_{pu} = 270$ ksi, no strands ruptured at or before P_{max} in either the validation model or the experimental test. Note that the material model used to simulate the prestressing strands was specified to rupture at $\varepsilon_{PreT} = 0.075$ ($f_{PreT} = 287$ ksi) based on tensile tests performed on a series of prestressing strand samples.
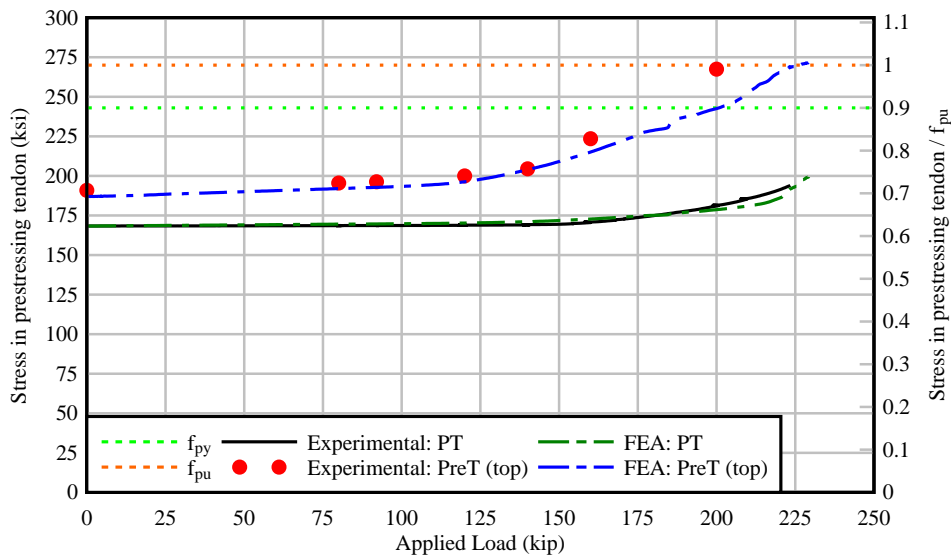
Figure 8.68 Stress in prestressing tendons as a function of applied load – comparison between experimental data and FEA: Beam specimen NB-1

The deflected shape of the beam and curvature computed from the FE model are compared to the experimental beam data in Figures 8.69 and 8.70. Deflection and curvature data for load levels at which concrete strains were approximately $\varepsilon_c = 0.003$ are indicated with bold lines, and data for higher load levels are indicated with dashed lines. It can be observed that the validation model was slightly more flexible than the experimental specimen.

136

| P = 100 kip | 160 kip | 180 kip | 190 kip | 200 kip | 205 kip | 210 kip | 215 kip | 220 kip | 223 kip |

(a)   (b)
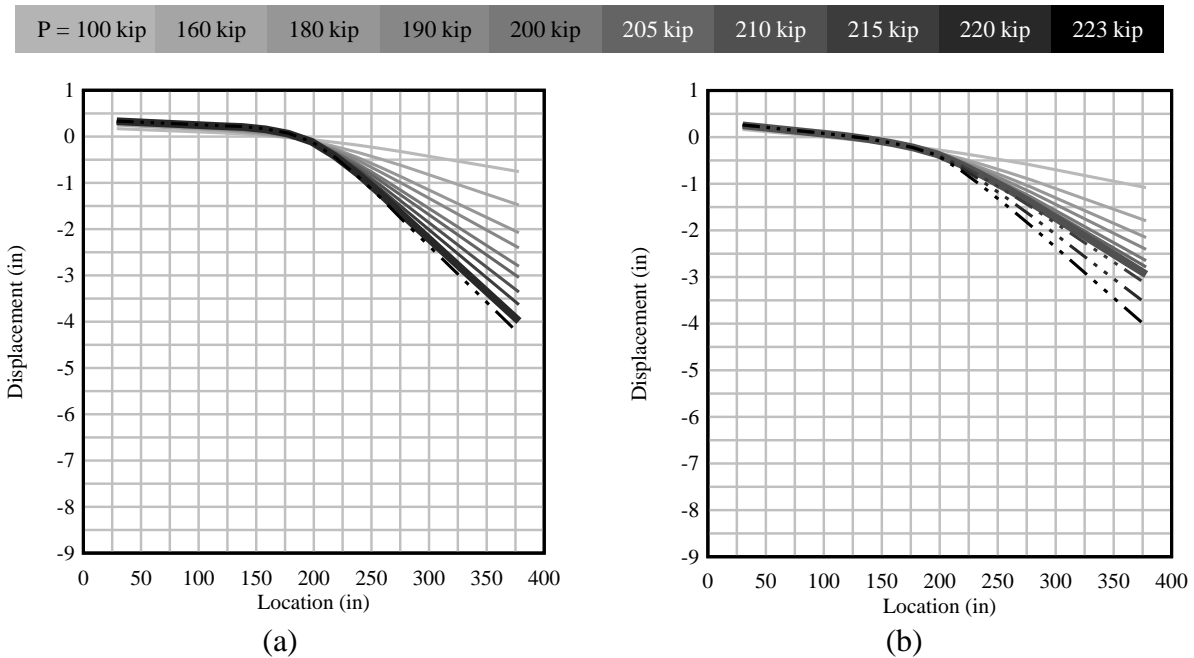
Figure 8.69 Displacement as a function of location along the length of beam specimen NB-1:
(a) experimental data and (b) FEA

| P = 100 kip | 160 kip | 180 kip | 190 kip | 200 kip | 205 kip | 210 kip | 215 kip | 220 kip | 223 kip |

(a)   (b)

Figure 8.70 Curvature as a function of location along the length of beam specimen NB-1:
(a) experimental data and (b) FEA

137

Beam specimen NB-2

Beam specimen NB-2 is a 33-ft long beam with a span-to-depth ratio of 20. As shown in Figure 8.71, prestressing reinforcement consisted of 2 post-tensioned tendons (equivalent to 9 post-tensioned strands each), 10 pretensioned strands located in the top, and 2 pretensioned strands located in the bottom, which resulted in an unbonded reinforcement ratio (U/T) of 0.6. The concrete compressive strengths used in the validation model were based in the average concrete compressive strengths at the day of the test (Table 8.13). The specified pretensioned force used in the validation model was based on the vibrating wire gage readings after pretensioning (to be consistent with construction stages included in the model), while the specified post-tensioned force was based on the load cell reading after post-tensioning and prior to loading.

(a)   (b)
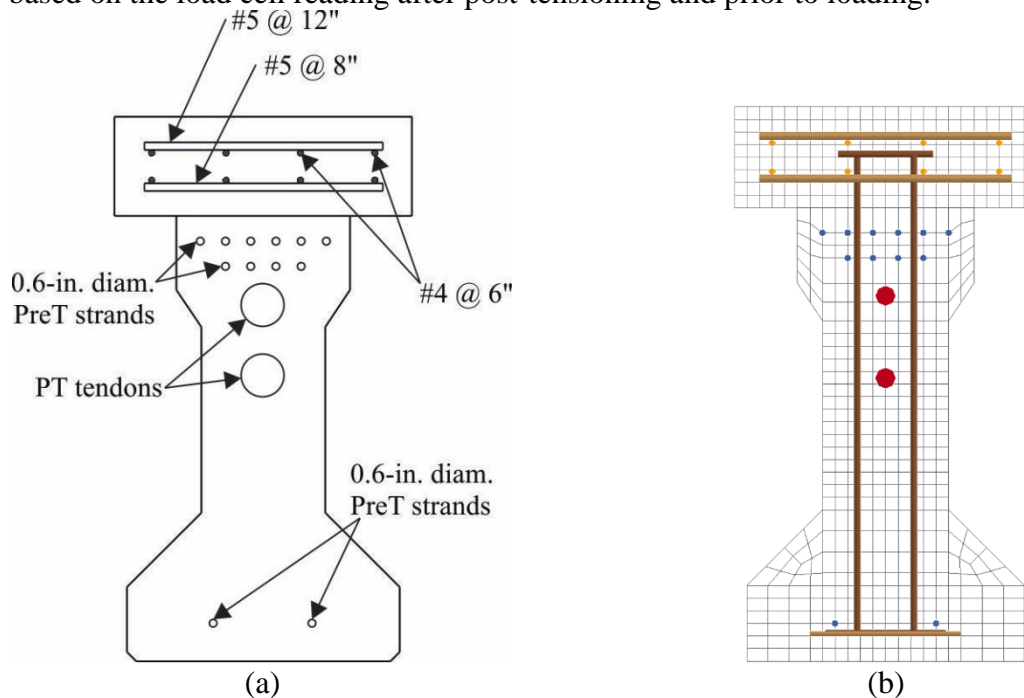
Figure 8.71 Beam specimen NB-2 cross-section:
(a) sketch showing location of longitudinal reinforcement, (b) FE model

Table 8.13 Beam specimen NB-2: Concrete compressive strengths at day of flexural test

Description	Specified Compressive Strength (psi)	Avg. Compressive Strength (psi)
Precast girder	8,500	12,537
Deck	8,500	12,537
End blocks	8,500	11,223

The first visible cracks on specimen NB-2 during the experimental test were identified at a load of 136 kip on the east side of the beam (Figure 8.72). Figure 8.73 shows the damage index at different load levels. At an applied load P = 135 kip, damage started accumulating (damage index = 0.1) at the center of the beam on top of the concrete deck (Figure 8.73a). The validation model for NB-2 began exhibiting erosion at a load P = 219 kip as shown in Figure 8.74.
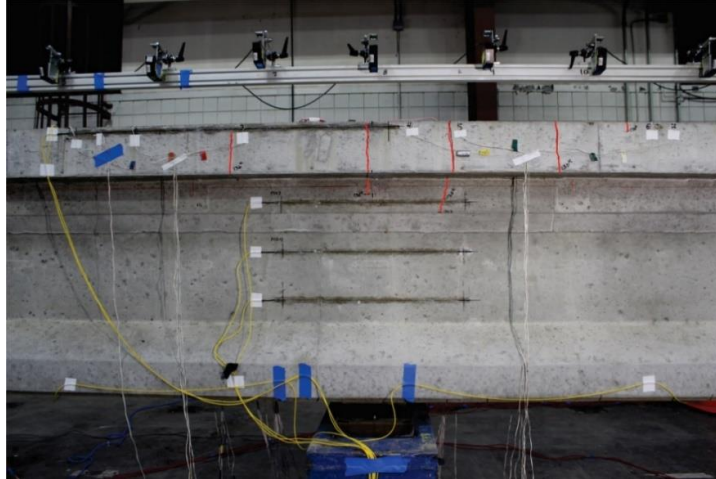
Figure 8.72 Specimen NB-2: First observed cracks (marked in red) at P = 136 kip

Table 8.14 presents a comparison of the nominal load (at $\varepsilon_c = 0.003$) and maximum load values obtained from experimental data and FEA. As shown in Figure 8.75, the validation model presented very good agreement with the experimental data in terms of load. The validation model indicated a maximum load (P_{max}) of 218.9 kip, which was less than 2% lower than the experimental maximum load. However, the displacement at P_{max} was approximately 12% higher than the experimental value. The experimental test on specimen NB-2 terminated with complete compression failure of the bottom flange at a load of 222.9 kip. It was evident that the compressive strains exceeded 0.003, but foil strain gages installed at midspan were damaged prior to P = 150 kip. In order to validate the finite element model, data from strain gages on the bottom of the beam near the middle support, as a function of applied load, were compared to the strains obtained from FEA at their corresponding location (Figure 8.76); the results showed very good agreement. Figure 8.76 also shows the strain in the bottom flange at midspan obtained from FEA. The validation model reached a compressive concrete strain of 0.003 at an applied load of 207.0 kip. Based on the agreement of the experimental strains on the bottom of the beam (near the middle support) with the FEA data, it was estimated that the strain on the bottom surface of the beam (at the middle support) reached 0.003 at a load of 207.0 kip and a deflection of 2.42 in.

Table 8.14 Beam specimen NB-2: Comparison of capacity between
experimental results and FEA

	Applied load (kip) at ε_c=0.003	Displacement (in.) at ε_c=0.003	Max. Load (P_{max}, kip)	Displacement (in.) at P_{max}
Experimental data	207.0*	2.4*	222.9	3.5
FEA	207.0	1.9	218.9	3.9
Difference	--	-20%	-2%	12%

*Estimate based on FE model and strain gages adjacent to middle support

Figure 8.77 shows the stress in prestressing tendons as a function of applied load. The stress in the PT tendons indicated by the validation model was in good agreement with the experimental data as depicted in Figure 8.77. Additionally, the experimental data and validation model exhibited a significant increase in the pretensioned stress as load was applied. However, none of the PreT strands in the FE model presented rupture.

(a) P = 135 kip

(b) P = 148 kip

(c) P = 171 kip

(d) P = 183 kip

(e) P = 195 kip

(f) P = 207 kip (ε_c = 0.003)

(g) P = 215 kip

(h) P = 216 kip

(i) P = 218 kip

(j) P_{max} = 219 kip

Damage Index

0   0.1   0.2   0.3   0.4   0.5   0.6   0.7   0.8   0.9   1.0

Figure 8.73 Specimen NB-2: FE model showing damage index at different load levels

(a)

(b)

Figure 8.74 Specimen NB-2: FE model showing (a) initiation of 'erosion' (circled in red) and (b) damage index at P = 219 kip
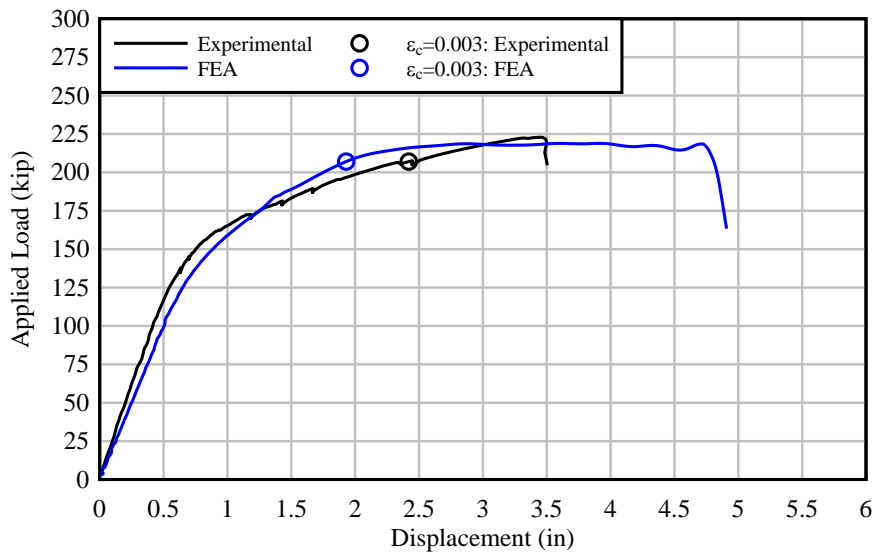
Figure 8.75 Comparison of load-displacement curves obtained from experimental data and FEA: Beam specimen NB-2
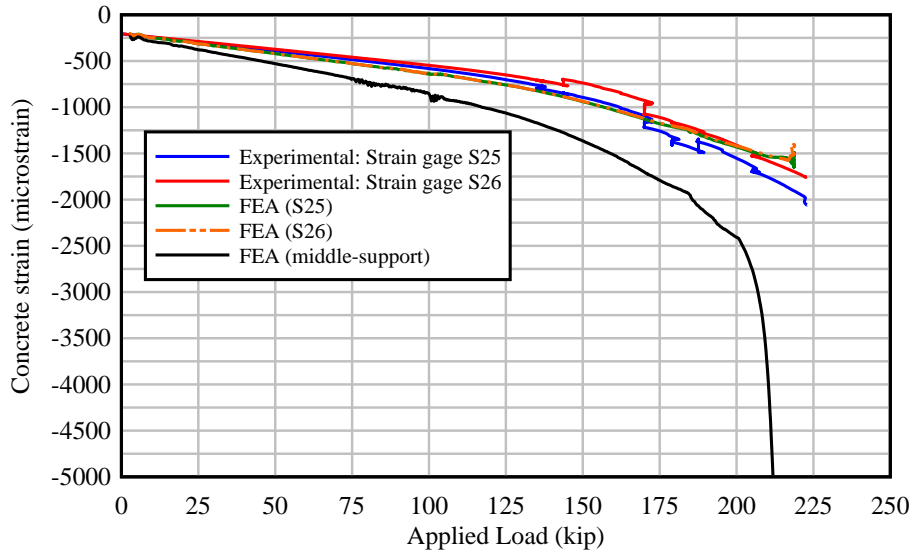
Figure 8.76 Strain at bottom-center of beam as a function of applied load – comparison between experimental data and FEA: Beam specimen NB-2
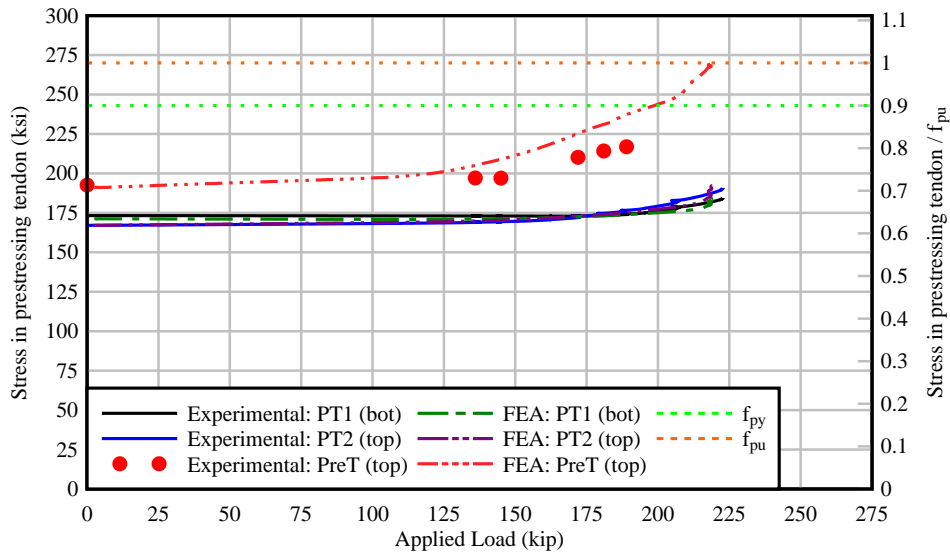
Figure 8.77 Stress in prestressing tendons as a function of applied load – comparison between experimental data and FEA: Beam specimen NB-2

The deflected shape of the beam and curvature computed from the FE model are compared to the experimental beam data in Figures 8.78 and 8.79. Deflection and curvature data for load levels at which concrete strains were approximately $\varepsilon_c = 0.003$ are indicated with bold lines, and data for higher load levels are indicated with dashed lines. The FEA and experimental data presented good overall agreement.

| P = 100 kip | 160 kip | 180 kip | 190 kip | 200 kip | 205 kip | 210 kip | 215 kip | 220 kip | 222 kip |
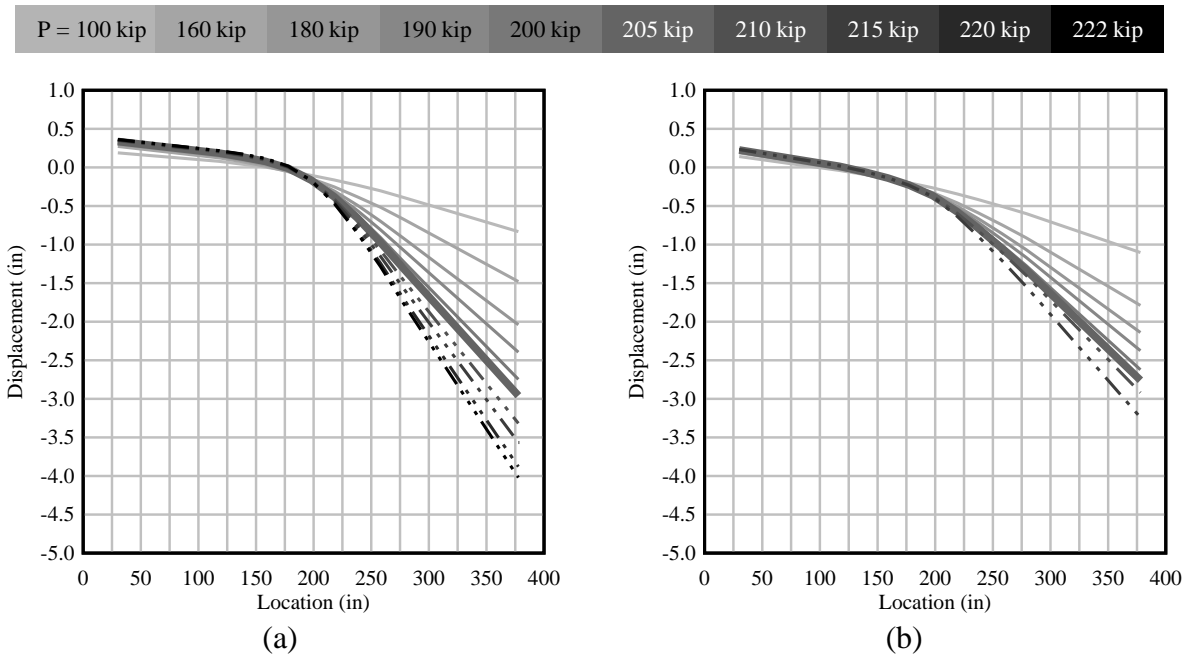
Figure 8.78 Displacement as a function of location along the length of beam specimen NB-2:
(a) experimental data and (b) FEA

| P = 100 kip | 160 kip | 180 kip | 190 kip | 200 kip | 205 kip | 210 kip | 215 kip | 220 kip | 222 kip |
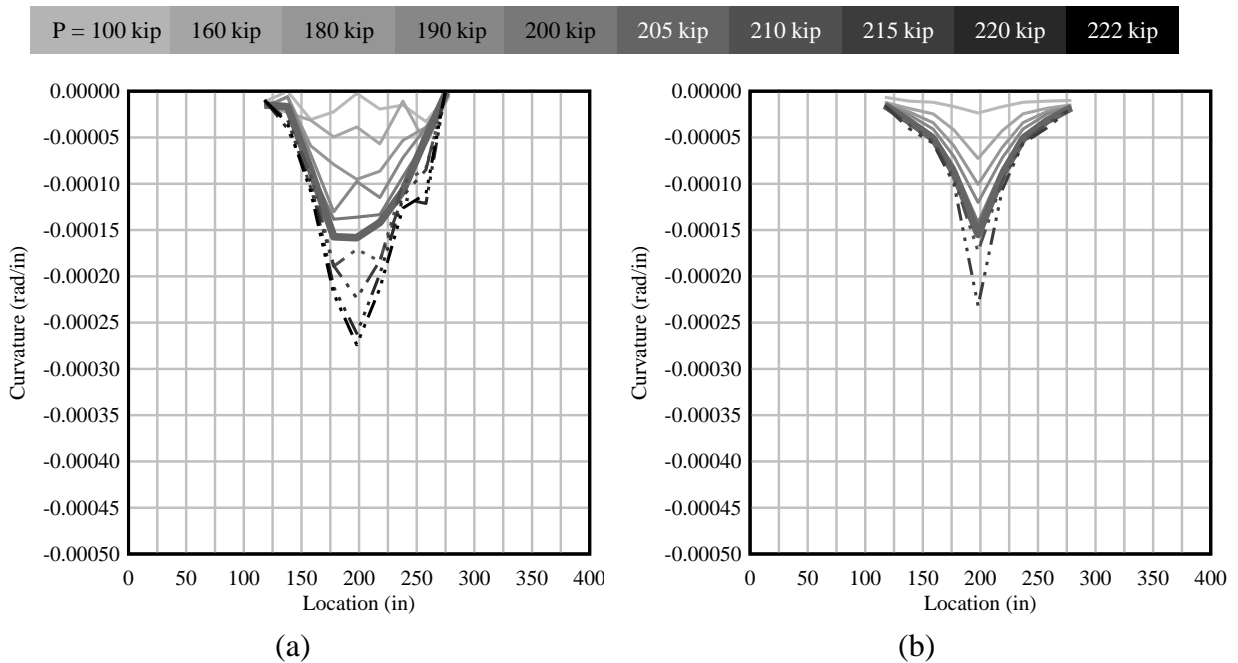
Figure 8.79 Curvature as a function of location along the length of beam specimen NB-2:
(a) experimental data and (b) FEA

Beam specimen NB-3

Beam specimen NB-3 is a 33-ft long beam with a span-to-depth ratio of 20. As shown in Figure 8.80, prestressing reinforcement consisted of 2 post-tensioned tendons (equivalent to 11 strands each), 6 pretensioned strands located in the top, and 2 pretensioned strands located in the bottom, which resulted in an unbonded reinforcement ratio (U/T) of 0.7. The concrete compressive strengths used in the validation model were based in the average concrete compressive strengths at the day of the test (Table 8.15). The specified pretensioned force used in the validation model was based on the vibrating wire gage readings after pretensioning (to be consistent with construction stages included in the model), while the specified post-tensioned force was based on the load cell reading after post-tensioning and prior to loading.
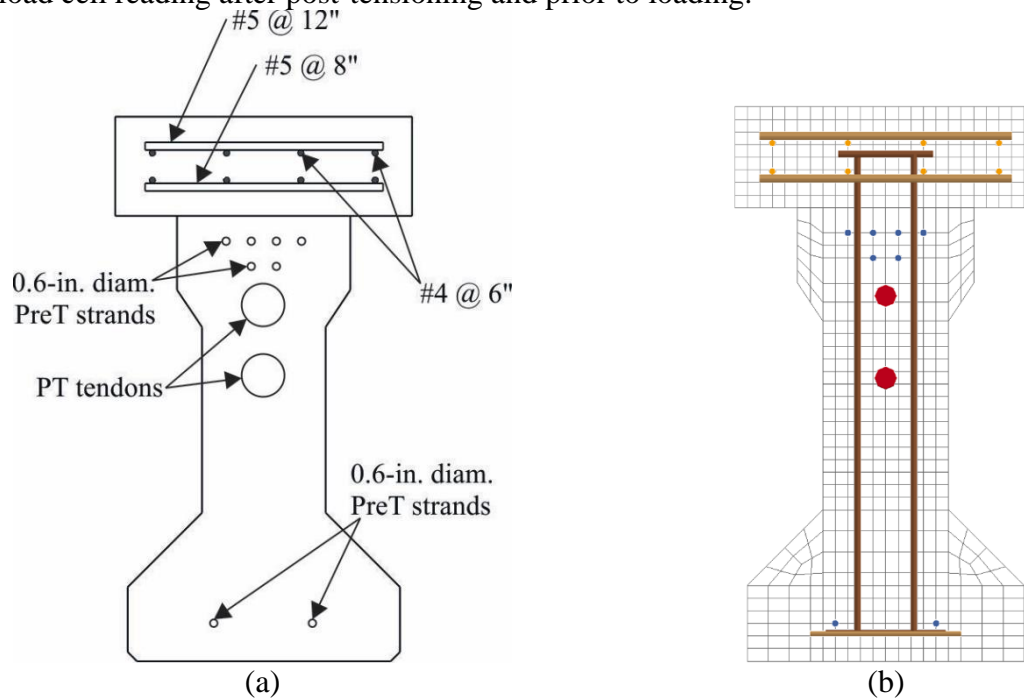
Figure 8.80 Beam specimen NB-3 cross-section:
(a) sketch showing location of longitudinal reinforcement, (b) FE model

Table 8.15 Beam specimen NB-3: Concrete compressive strengths at day of flexural test

Description	Specified Compressive Strength (psi)	Avg. Compressive Strength (psi)
Precast girder	8,500	12,537
Deck	8,500	12,537
End blocks	8,500	11,223

The first visible cracks on specimen NB-3 during the experimental test were identified at a load of 102 kip on the east side of the beam (Figure 8.81). Figure 8.82 shows the damage index at different load levels. At an applied load P = 125 kip, damage started accumulating (damage index = 0.1) at the center of the beam on top of the concrete deck (Figure 8.82a). The validation model for NB-3 began exhibiting erosion at a load P = 206 kip as shown in Figure 8.83.

144
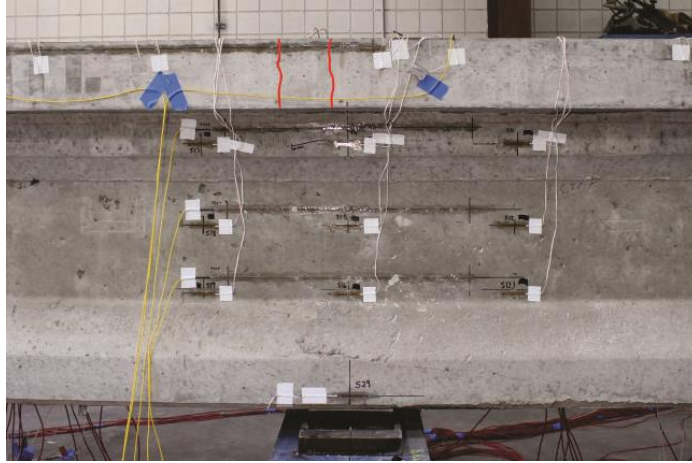
Figure 8.81 Specimen NB-3: First observed cracks (marked in red) at P = 102 kip

Table 8.16 presents a comparison of the nominal load (at $\varepsilon_c = 0.003$) and maximum load values obtained from experimental data and FEA. As shown in Figure 8.84, the validation model presents very good agreement with the experimental load-displacement curve. The validation model reached a compressive strain of 0.003 at an applied load of 195.6 kip (<5% higher than experimental load). Similar to beam specimen NB-1, foil strain gages were installed on the sides of the bottom flange, allowing determination of strains at the bottom surface of the beam through extrapolation (Figure 8.85, dashed line).For safety reasons, the experimental test was terminated shortly after audible indications of strand movement in the unbonded PT tendons because the prestressing tendons in beam specimen NB-3 were composed of mostly unbonded strands. Although the strain gages on sides of the bottom flange did not reach a strain of 0.003, experimental data were in good agreement with the FEA data over the range for which experimental data were available. The experimental strain curve facilitated estimation of a strain of 0.003 on the bottom of the beam at a load of 186.1 kip. The maximum load (P_{max}) was 207.0 kip which was approximately 8% higher than the maximum load recorded before the experimental specimen was unloaded.

Figure 8.86 shows the stress in prestressing tendons as a function of applied load. The stress in the PT tendons indicated by the validation model presented very good agreement with the experimental data as depicted in Figure 8.86. Additionally, vibrating wire (VW) gages were used to determine the pretensioned strand force (and losses) during stressing of pretensioned strands (at the precast plant), post-tensioning of the test specimen (at the lab), and during loading. Although the validation model exhibited a significant increase in the pretensioned stress, none of the PreT strands presented rupture on either the FEA or the experimental test. Note that the material model used to simulate the prestressing strands was specified to rupture at $\varepsilon_{PreT} = 0.075$ ($f_{PreT} = 287$ ksi) based on tensile tests performed on a series of prestressing strand samples.

The deflected shape of the beam and curvature computed from the FE model are compared to the experimental beam data in Figures 8.87 and 8.88. Deflection and curvature data for load levels at which concrete strains were approximately $\varepsilon_c = 0.003$ are indicated with bold lines, and data for higher load levels are indicated with dashed lines. It can be observed that the FE model was slightly more flexible than the experimental specimen. However, both the FEA and experimental data were generally in good agreement up to $\varepsilon_c = 0.003$.

145

(a) P = 125 kip

(b) P = 141 kip

(c) P = 153 kip

(d) P = 175 kip

(e) P = 196 kip (ε_c = 0.003)

(f) P = 201 kip

(g) P = 203 kip

(h) P = 205 kip

(i) P = 206 kip

(j) P_{max} = 207 kip

Damage Index

| 0 | 0.1 | 0.2 | 0.3 | 0.4 | 0.5 | 0.6 | 0.7 | 0.8 | 0.9 | 1.0 |
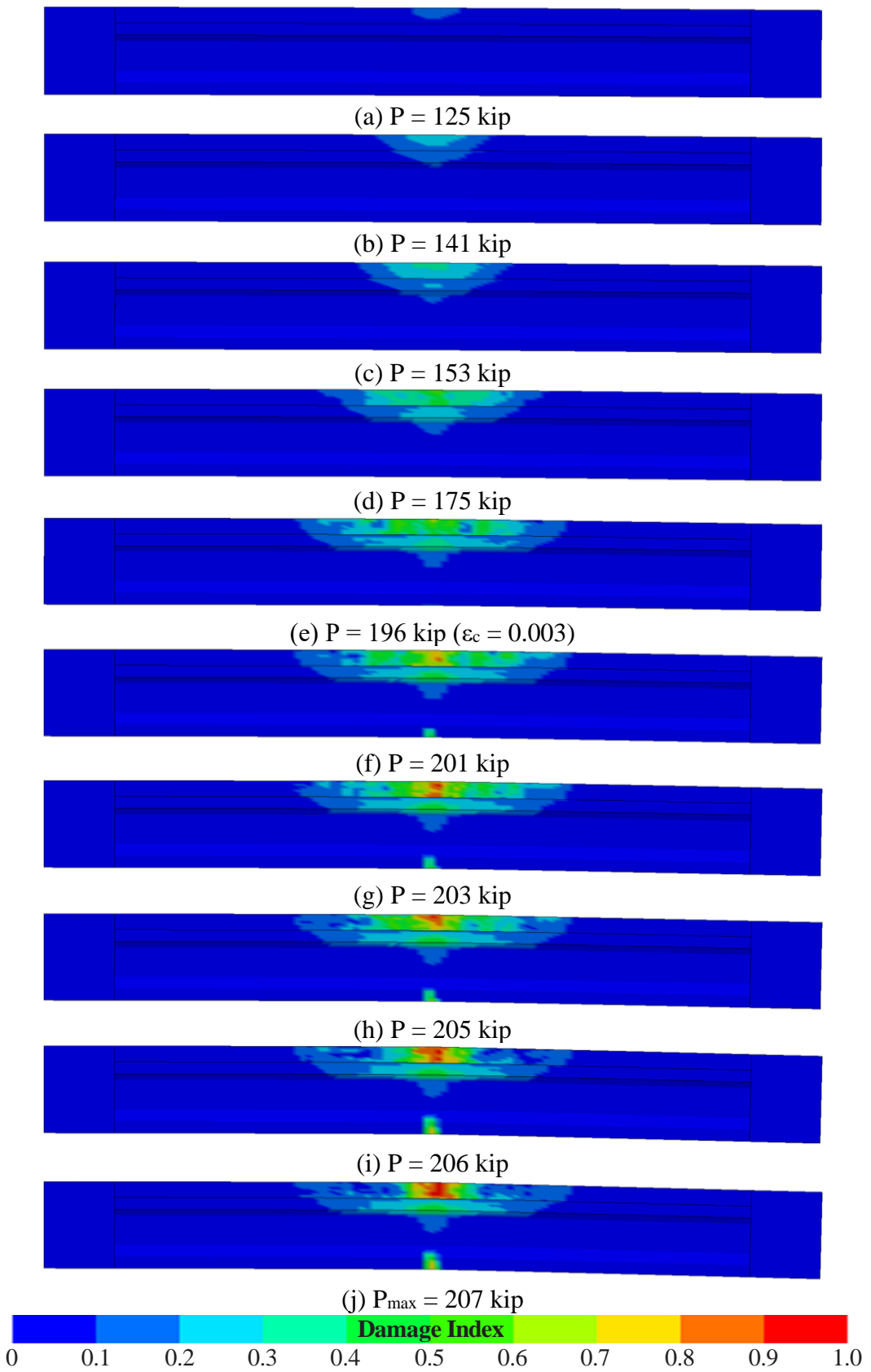
Figure 8.82 Specimen NB-3: FE model showing damage index at different load levels

146

(a)

Damage Index
0   0.1   0.2   0.3   0.4   0.5   0.6   0.7   0.8   0.9   1.0
(b)
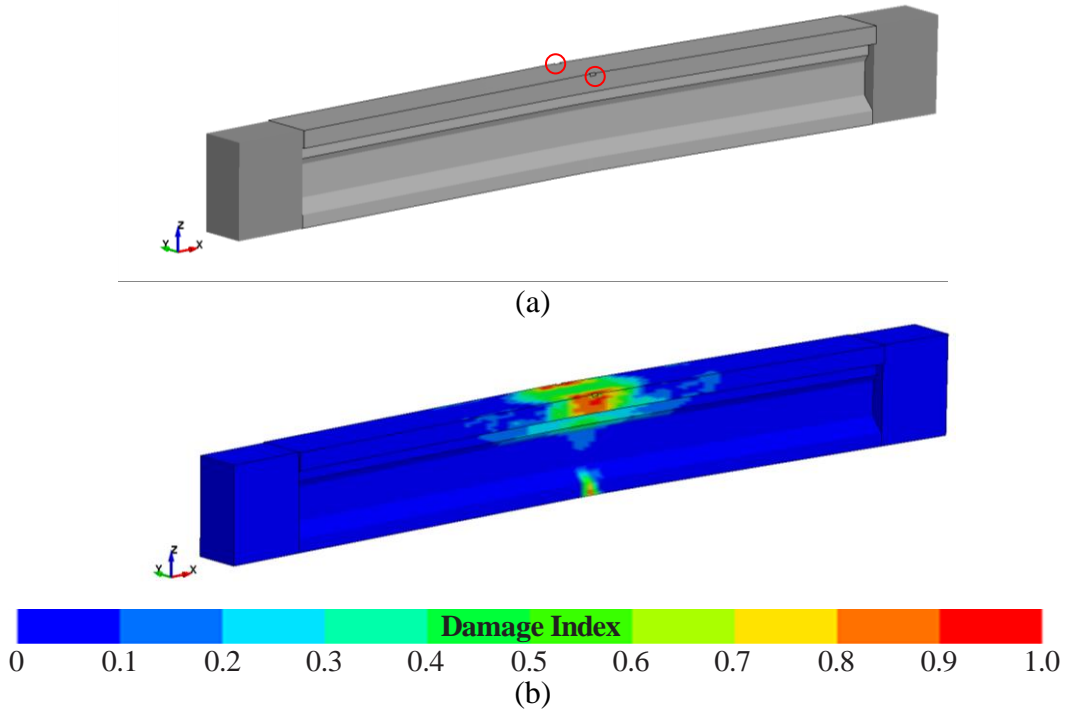
Figure 8.83 Specimen NB-3: FE model showing (a) initiation of 'erosion' (circled in red) and (b) damage index at P = 206 kip

Table 8.16 Beam specimen NB-3: Comparison of capacity between experimental results and FEA

	Applied load (kip) at ε_c=0.003	Displacement (in.) at ε_c=0.003	Max. Load (P_{max}, kip)	Displacement (in.) at P_{max}
Experimental data	186.1	2.0	191.2	2.3
FEA	195.6	2.0	207.0	3.9
Difference	5%	0%	8%	68%
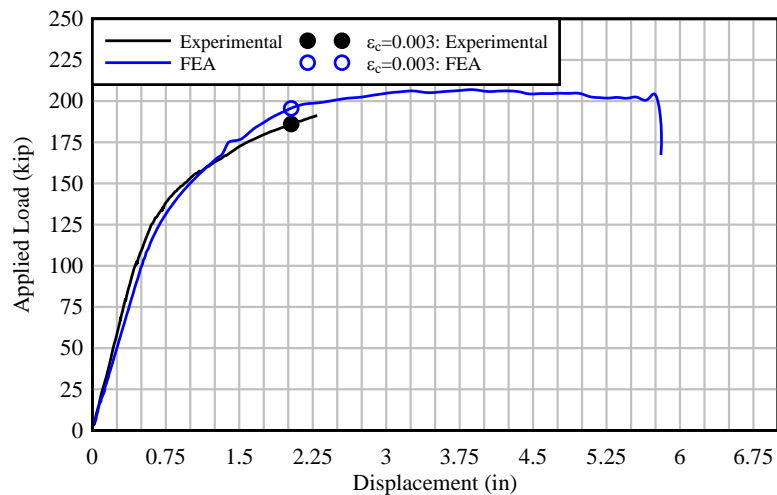
Figure 8.84 Comparison of load-displacement curves obtained from experimental data and FEA: Beam specimen NB-3

147
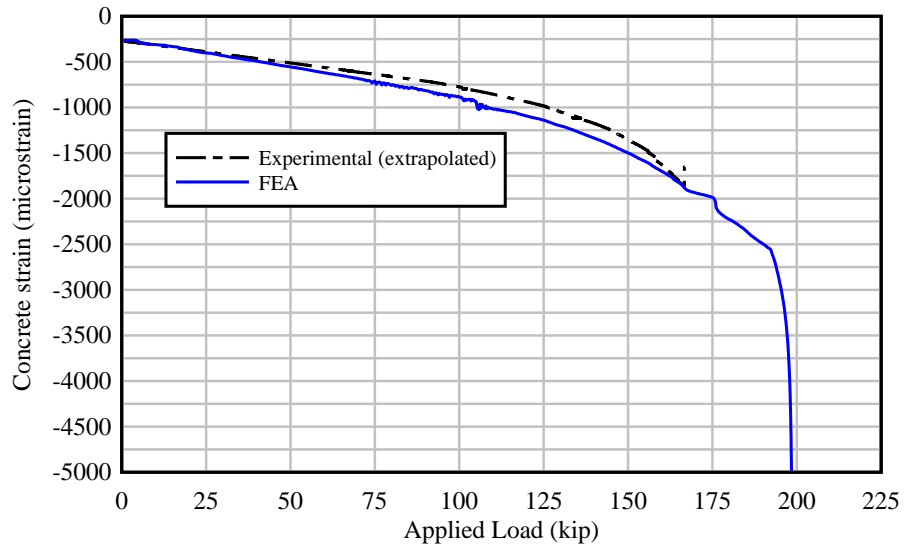
Figure 8.85 Strain at bottom-center of beam as a function of applied load – comparison between experimental data and FEA: Beam specimen NB-3
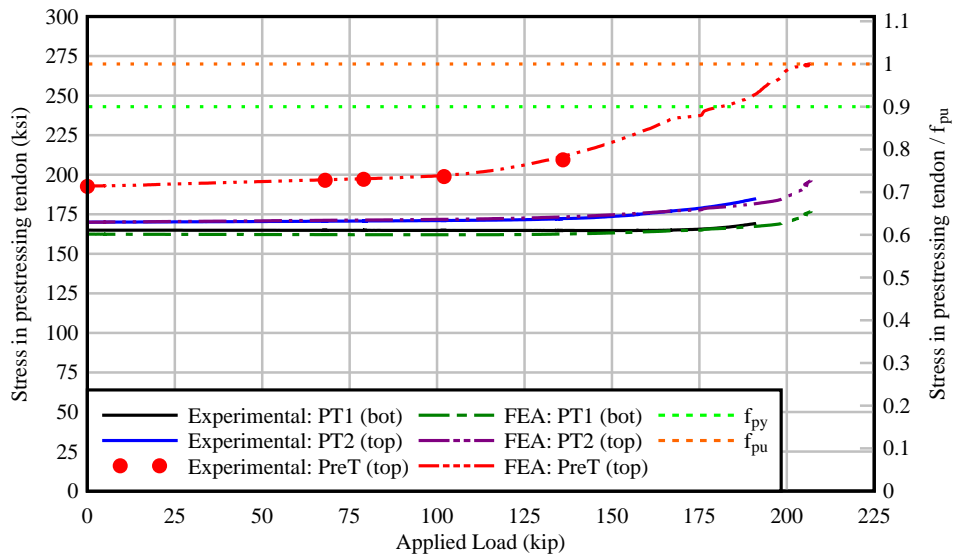
Figure 8.86 Stress in prestressing tendons as a function of applied load – comparison between experimental data and FEA: Beam specimen NB-3

P = 100 kip	120 kip	140 kip	160 kip	170 kip	180 kip	185 kip	190 kip	195 kip	207 kip

(a)   (b)
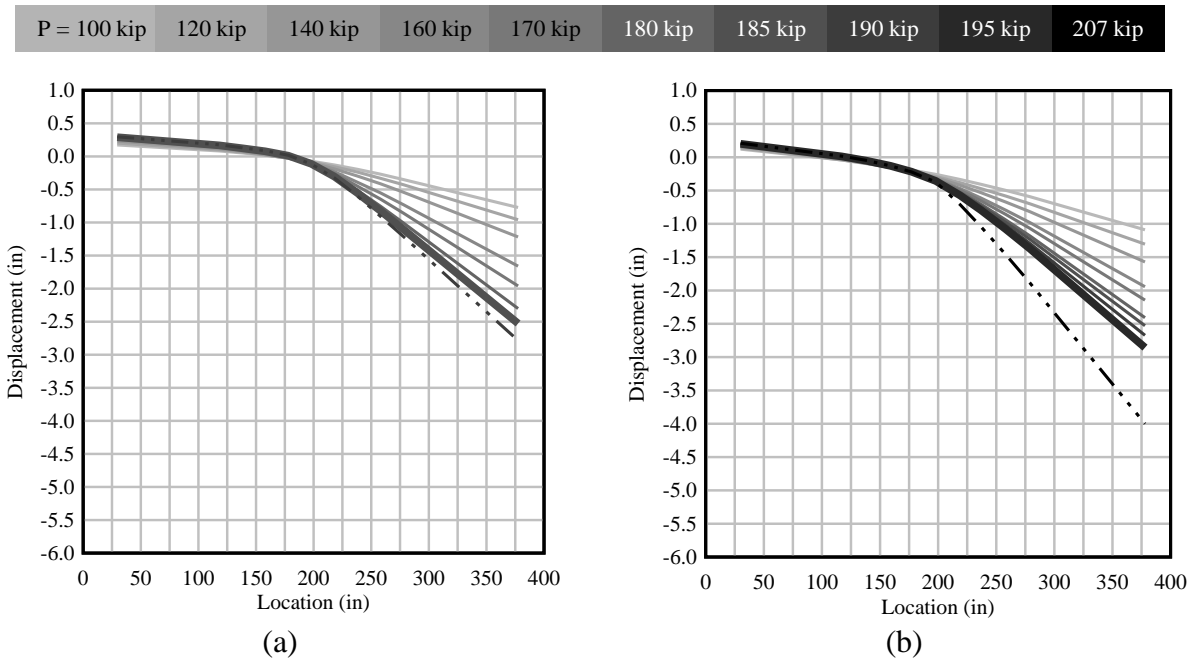
Figure 8.87 Displacement as a function of location along the length of beam specimen NB-3:
(a) experimental data and (b) FEA

P = 100 kip	120 kip	140 kip	160 kip	170 kip	180 kip	185 kip	190 kip	195 kip	207 kip

(a)   (b)
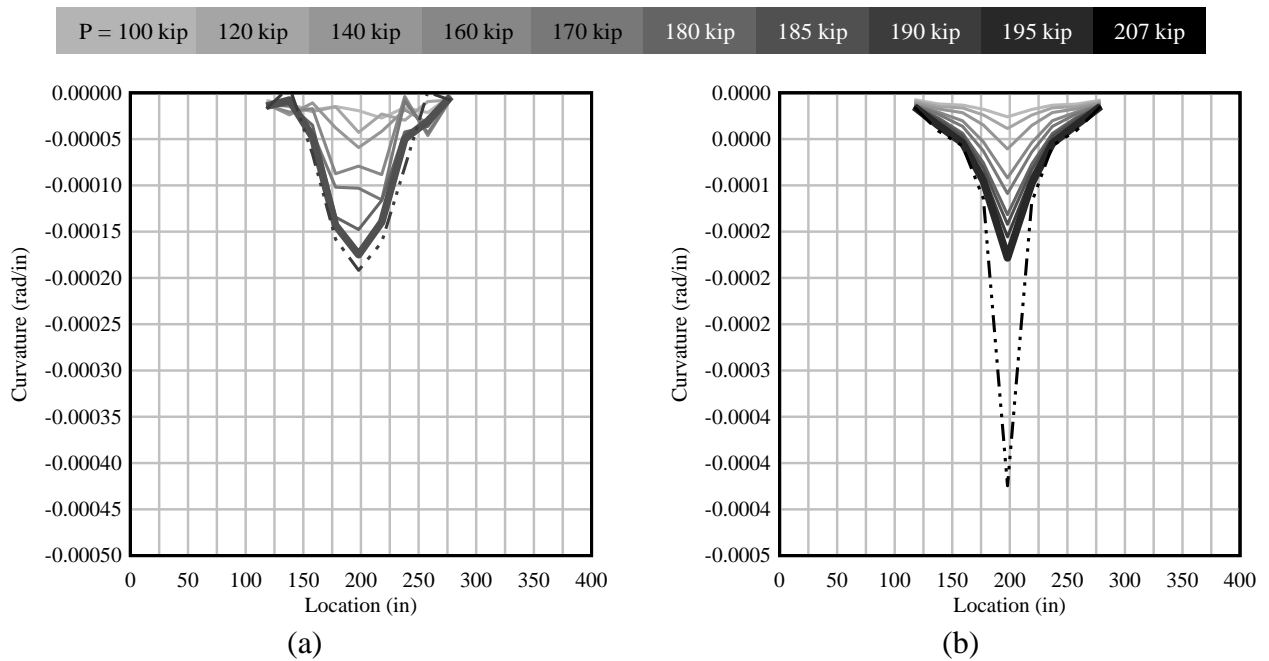
Figure 8.88 Curvature as a function of location along the length of beam specimen NB-3:
(a) experimental data and (b) FEA

8.4 Parametric studies

Using the modeling methods described and validated above, a series of parametric finite element studies were conducted by analyzing AASHTO beams and Florida I-beams (FIBs) varying the boundary conditions, reinforcement ratios, loading types, and friction coefficients.

8.4.1 Florida I-Beams (with parabolic PT tendons)

Scope of parametric study

In the FIB cases investigated, the girder cross-section was based on a FIB-72 girder. The typical FIB section width was increased to produce a 9-in. thick web (to accommodate the internal post-tensioning tendons) and a slab was added to the top of the beam to represent a concrete deck. Figure 8.89 shows the cross-sectional dimensions for a modified FIB-72.

In regard to beam boundary conditions, two cases were considered: simply-supported (SS) beams and continuous beams (negative bending, NB). Simply-supported beams were modeled with parabolic PT tendons (FDOT profile F5, as shown in Figure 4.6). The continuous beam model included parabolic PT tendons (FDOT profile F1, as shown in Figure 4.8a) and was composed of three precast beam segments and two splices.
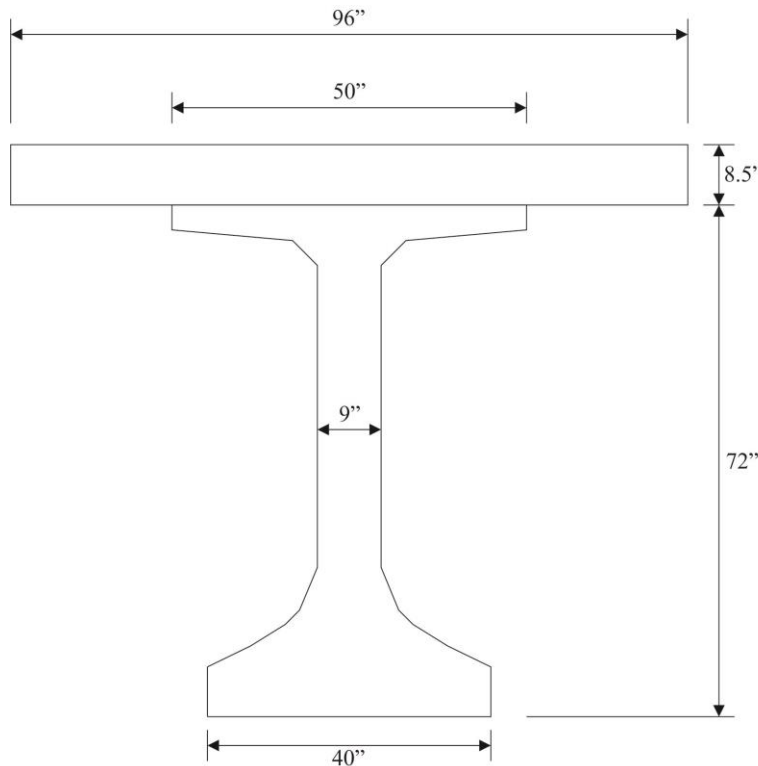
Figure 8.89 Cross-sectional dimensions: Modified FIB-72

Varying ratios of unbonded reinforcement to total reinforcement (U/T) were considered as specified in Appendix G (Tables G.1 and G.2). The ratios of unbonded reinforcement were evaluated in terms of reinforcement area (U_A/T_A) and axial force (U_F/T_F). The ratio U_A/T_A was calculated as the area of post-tensioning reinforcement divided by the total area of longitudinal reinforcement (i.e., pretensioned strands, PT tendons, and mild steel reinforcement in the concrete deck). Conversely, the ratio U_F/T_F was calculated using forces that corresponded to the 'ultimate strength' of each material. An ultimate prestressing stress (f_{pu}) of 270 ksi was used for both pretensioned and post-tensioned strands (without consideration of prestress losses). A stress equal

150

to 60 ksi (f_y), which is the value used in nominal moment calculations, was used to calculate the forces in the mild steel reinforcement. Due to the use of both prestressing and mild steel as longitudinal reinforcement in continuous beams, the unbonded reinforcement ratio (U/T) for continuous beams discussed in this report refers to the ratio in terms of axial force (U_F/T_F).

Some beams were designed to have multiple PT tendons, but the centroid of the PT tendons for all beams was maintained the same. Therefore, all PT tendons were grouped into a single PT tendon centroid (Figure 8.90). The same profile of PT centroid eccentricity was used for all beam cases (i.e., regardless of the ratio of unbonded and bonded prestressing). Although PT tendons are composed of several individual strands, for purposes of this study each tendon was assigned a cross-sectional area and prestressing force that represented all strands contained within the 'aggregated tendon'. The longitudinal reinforcement distribution for positive and negative bending is depicted in Appendix G.
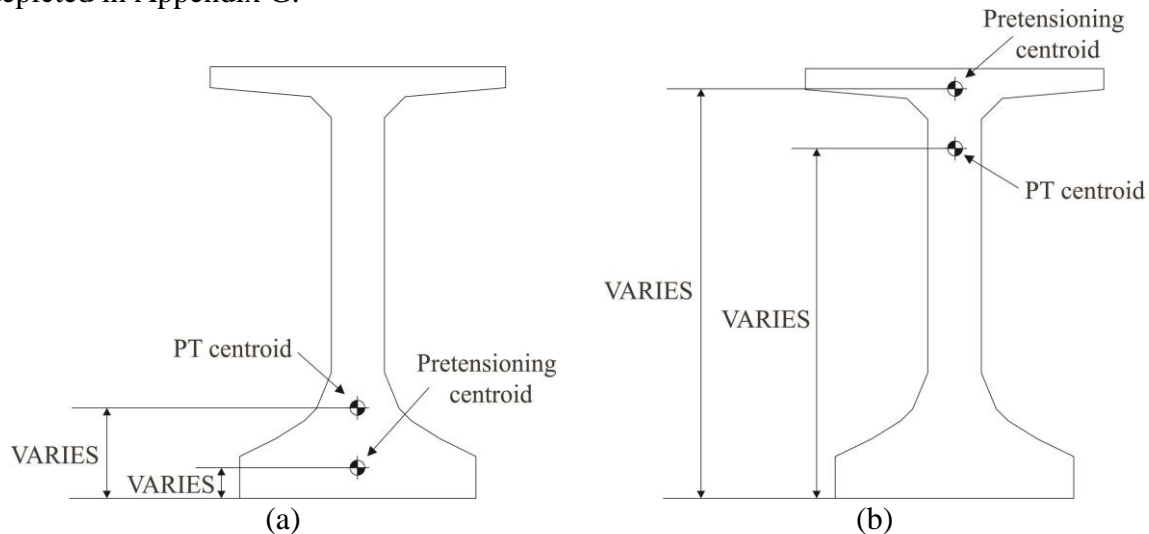
Figure 8.90 Location of pretensioning and post-tensioning centroid in cross-section at (a) midspan for positive and negative bending scenarios, and (b) at interior support of continuous beam (negative bending).

Regarding staging, one PT tendon (Model PT1) was prestressed before the addition of the concrete deck, and a second (Model PT2) was prestressed after the deck became structurally effective. Concrete beam segments (solid elements) were placed on top of a steel bed (thin layer of solid elements) intended to simulate a prestressing bed and gravity was applied. Boundary conditions were applied to the bottom surface of the steel bed to prevent movement. Solid elements in the concrete girder interacted with solid elements in the steel bed through contact surface definitions (Figure 8.91a). After gravity was applied, the pretensioning strands were prestressed thus causing the beam to camber upward. Next, one-half of the total unbonded post-tensioned tendons were prestressed (Model PT1). The steel bed was then replaced by a pair of much smaller steel plates (loosely referred to as 'bearing plates') which were located at the ends of the beam (Figure 8.91b). The concrete deck was then introduced at the top surface of the girder top flange. The bearing plates were fixed in space to prevent movement and contact surfaces were defined between the girder and the pads. Subsequently, the second-half of the post-tensioned tendons (Model PT2) were prestressed. Finally, external loads were applied. Figure 8.92 illustrates the construction stages that were used in defining simply-supported single span beam models.

151

(a)

(b)
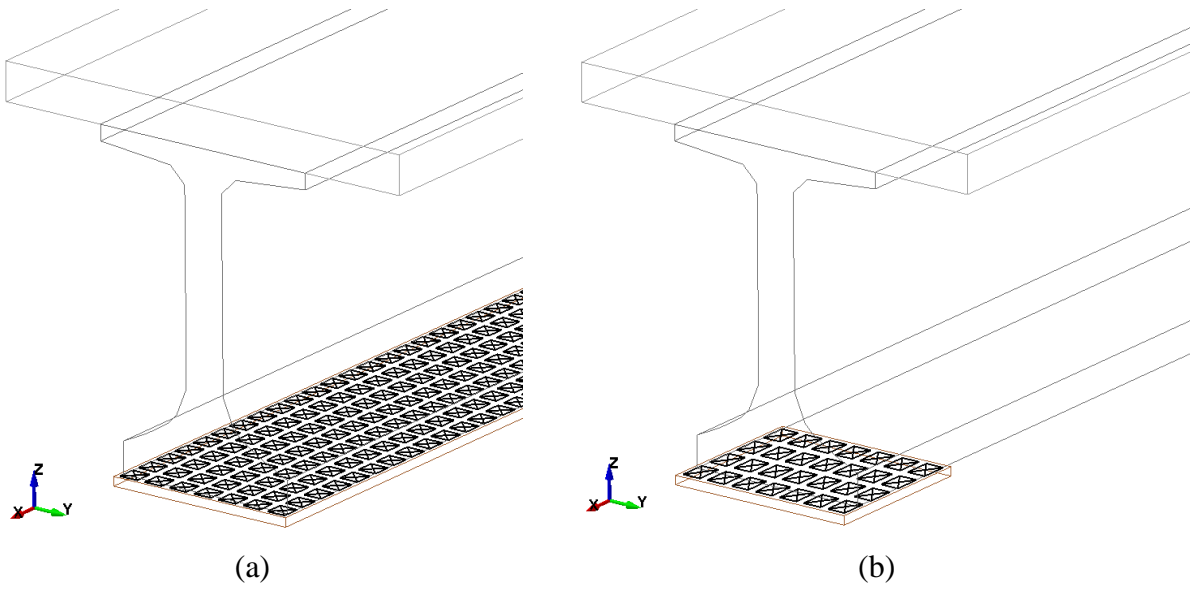
Figure 8.91 Contact surface definition between girder and (a) steel bed and (b) bearing plates

(a)

(b)

(c)

(d)

(e)
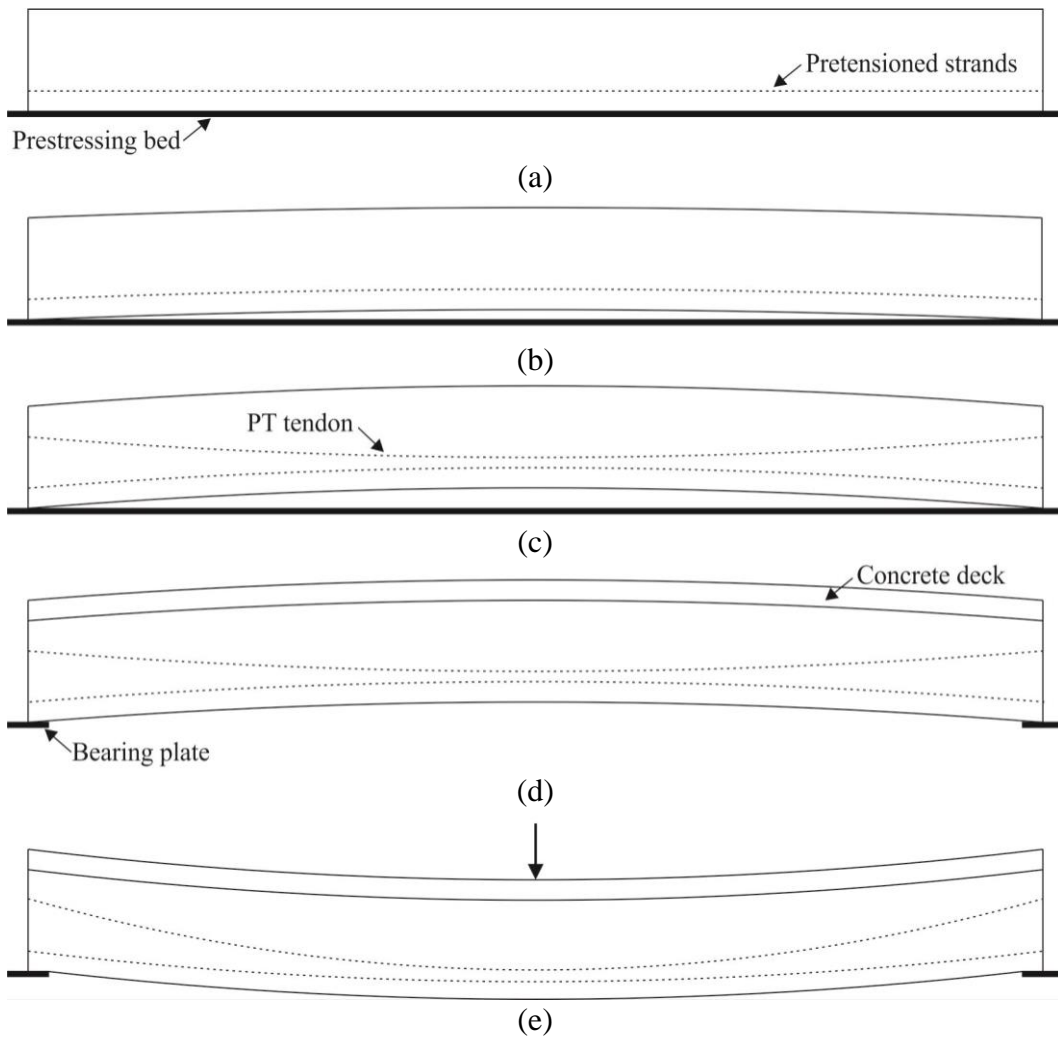
Figure 8.92 Constructions stages for simply-supported beams: (a) application of gravity to girder placed over prestressing bed, (b) pretensioning, (c) post-tensioning, (d) girder on bearing plates, addition of concrete deck and post-tensioning, (e) external loads

Multiple span continuous beam models (Figure 8.93) were composed of three (3) individual beam segments that were joined together (using construction staging) by two (2) splices. Bearing plates were introduced into the model immediately following pretensioning of the individual beam segments. To follow a realistic construction sequence, splices with confinement stirrup reinforcement were then introduced in the model. During this stage, splices were supported on steel plates, and the first-half of the total unbonded post-tensioning force was applied. Next, the concrete deck was added on top of the girder. The second-half of post-tensioning reinforcement was then introduced into the model and prestressed. Finally, external loads were applied.
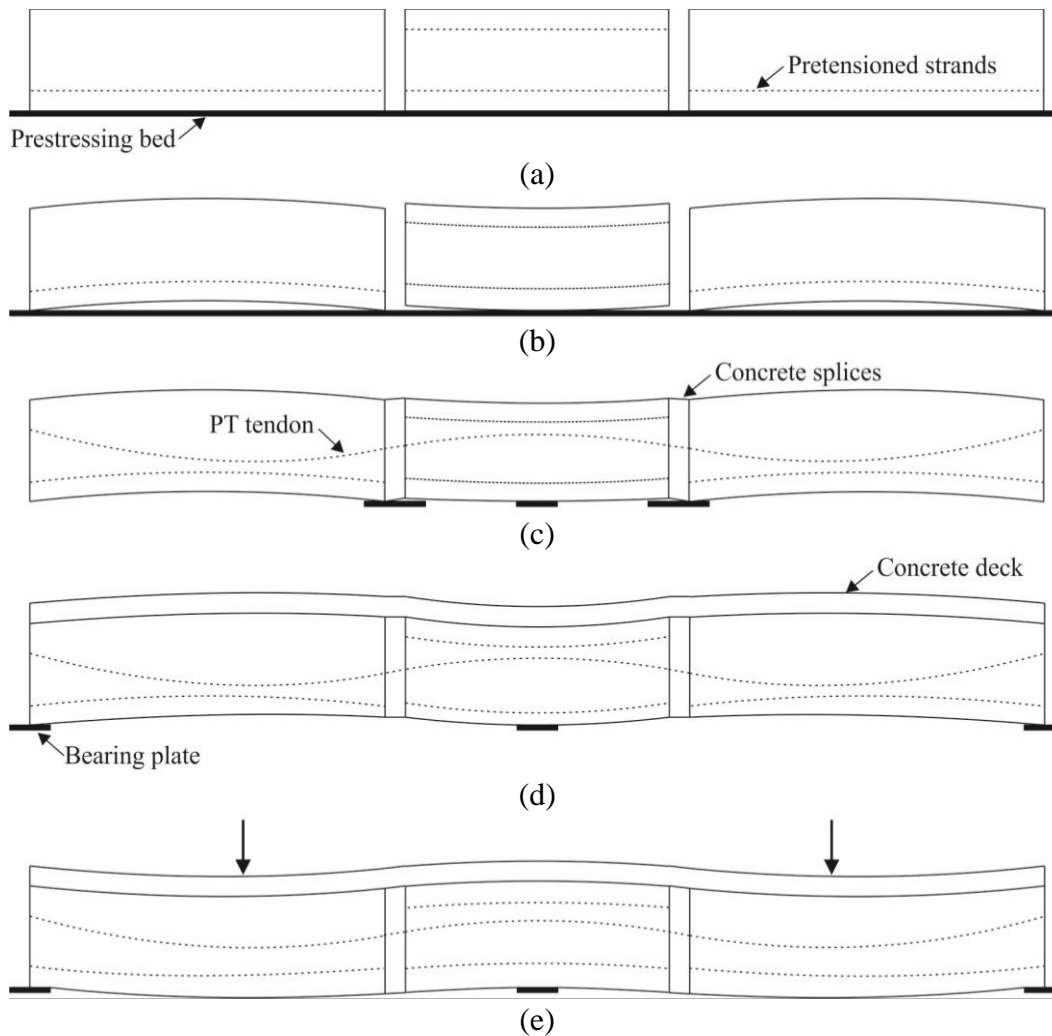
Figure 8.93 Constructions stages for negative bending beams: (a) application of gravity to beam segments placed over prestressing bed, (b) pretensioning, (c) addition of splices and post-tensioning, (d) addition of concrete deck and post-tensioning, (e) external loads

Three loading cases were considered to evaluate the influence of load configuration on the generation and location of plastic hinges: a concentrated load at midspan, a wide 'tandem' of two concentrated loads, and a uniformly distributed load (Figures 8.94 and 8.95). The friction coefficient (μ) between the PT tendons and the 'virtual' PT duct (modeled using LS-DYNA 'beam pulley' elements) was set to $\mu=0.0$ for most models. However, to evaluate the influence of friction on the flexural strength of prestressed concrete beams with mixed reinforcement conditions, additional cases were analyzed. Friction between a post-tensioned tendon and the surrounding duct produces losses during the stressing operation (ACI, 2016). Practice has shown that friction losses

153

can vary from case to case. Although certain values are recommended for design (e.g. PTI 2016), investigation of extreme values can provide bounds on the maximum expected influence of friction. For greased and wrapped tendons, the recommended range for design extends from approximately 0.05 to 0.15, but a friction coefficient equal to 0.07 is suggested (PTI, 2016). FDOT specifies a friction coefficient of 0.14 for wire or strand tendons (FDOT, 2018). In the parametric study, selected cases of simply-supported and negative bending beams were analyzed with friction coefficients of 0.14 (i.e., the FDOT specified value), and extreme values either 0.3 (SS) or 0.5 (NB). Tables 8.17 and 8.18 presents the complete matrix of FIBs with parabolic PT tendons that were included in the parametric study.
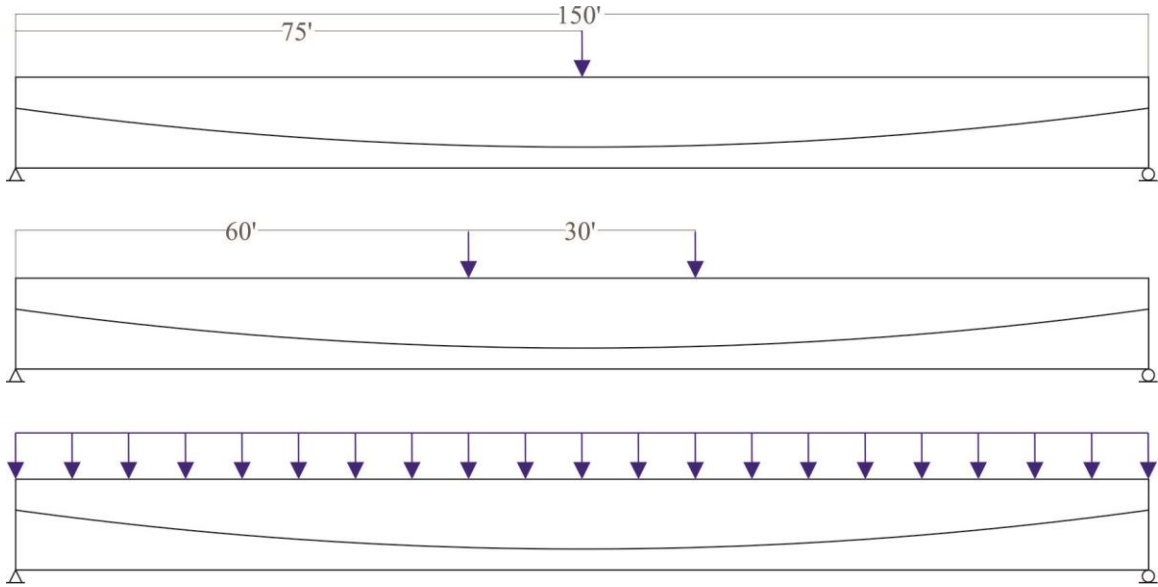
Figure 8.94 Loading cases on simply-supported (FIB-72) beam (not to scale)
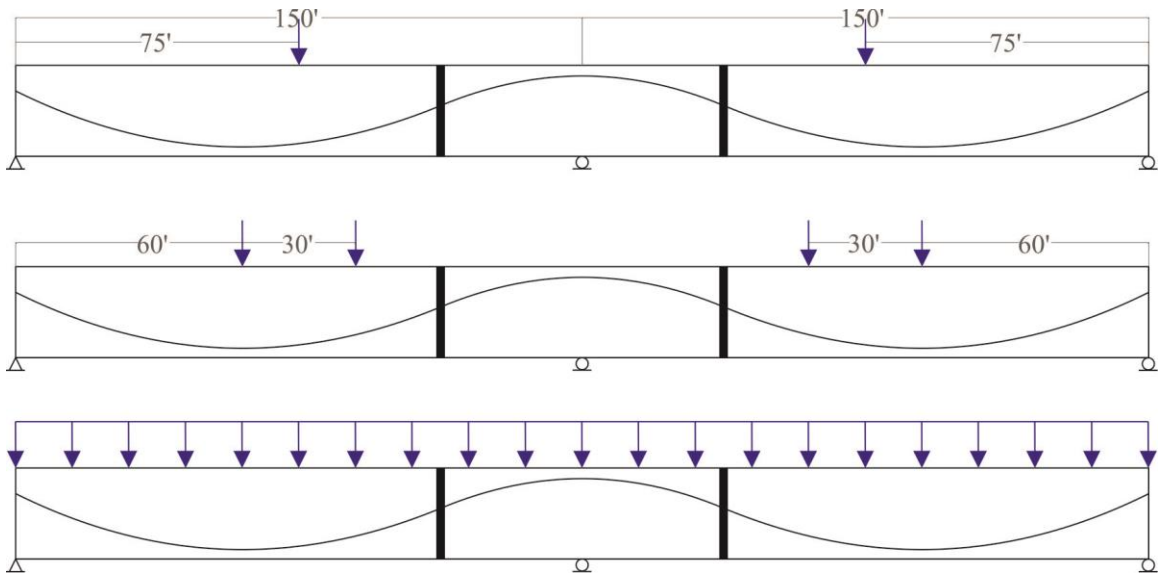
Figure 8.95 Loading cases on negative bending (FIB-72) beam (not to scale)

154

Table 8.17 Parametric study matrix – SS Florida I-Beams (parabolic PT tendon)

Model	Length (ft)	Span-to-Depth Ratio	f'c (psi) Beam section	Deck	Reinforcement Ratio (U/T) +M	Friction Coeff.	Loading
FIB72-SS-01	150	25	8,500	4,500	0.2	0.00	PL
FIB72-SS-02	150	25	8,500	4,500	0.5	0.00	PL
FIB72-SS-03	150	25	8,500	4,500	0.8	0.00	PL
FIB72-SS-04	150	25	8,500	4,500	0.2	0.00	TL
FIB72-SS-05	150	25	8,500	4,500	0.5	0.00	TL
FIB72-SS-06	150	25	8,500	4,500	0.8	0.00	TL
FIB72-SS-07	150	25	8,500	4,500	0.2	0.00	UL
FIB72-SS-08	150	25	8,500	4,500	0.5	0.00	UL
FIB72-SS-09	150	25	8,500	4,500	0.8	0.00	UL
FIB72-SS-10	150	25	8,500	4,500	0.5	0.14	UL
FIB72-SS-11	150	25	8,500	4,500	0.5	0.30	UL

U/T = U_F/T_F = ratio of unbonded force to total force
PL = Point load, TL = Tandem load, UL = Uniform load

Table 8.18 Parametric study matrix – NB Florida I-Beams (parabolic PT tendon)

Model	Length (ft)	Span-to-Depth Ratio	f'c (psi) Beam section	Deck	Reinforcement Ratio (U/T) +M	-M	Friction Coeff.	Loading
FIB72-NB-01	300	25	8,500	4,500	0.2	0.3	0.00	PL
FIB72-NB-02	300	25	8,500	4,500	0.5	0.6	0.00	PL
FIB72-NB-03	300	25	8,500	4,500	0.8	0.8	0.00	PL
FIB72-NB-04	300	25	8,500	4,500	0.2	0.3	0.00	TL
FIB72-NB-05	300	25	8,500	4,500	0.5	0.6	0.00	TL
FIB72-NB-06	300	25	8,500	4,500	0.8	0.8	0.00	TL
FIB72-NB-07	300	25	8,500	4,500	0.2	0.3	0.00	UL
FIB72-NB-08	300	25	8,500	4,500	0.5	0.6	0.00	UL
FIB72-NB-09	300	25	8,500	4,500	0.8	0.8	0.00	UL
FIB72-NB-10	300	25	8,500	4,500	0.5	0.6	0.14	UL
FIB72-NB-11	300	25	8,500	4,500	0.5	0.6	0.30	UL
FIB72-NB-12	300	25	8,500	4,500	0.5	0.6	0.50	UL

U/T = U_F/T_F = ratio of unbonded force to total force
PL = Point load, TL = Tandem load, UL = Uniform load

Results: Simply-supported beams

Two representative simply-supported beam cases were selected for detailed discussion in this section: a simply-supported beam subjected to concentrated load at midspan (FIB72-SS-01, Table 8.17) and a simply-supported beam subjected to a uniformly distributed load (FIB72-SS-07, Table 8.17). However, results for *all* cases investigated are presented, in graphical form, in Appendix G. Summarized numerical results (e.g., computed nominal flexural capacities, damage lengths, etc.) for all cases, along with observations and discussions of data trends, are included at the end of this section.

Models FIB72-SS-01 and FIB72-SS-03 consisted of 150-ft long simply-supported beams with an unbonded reinforcement ratio (U/T) of 0.2. These beams contained 49 individual bonded

pretensioned strands and two unbonded post-tensioned tendons (where each tendon contained six 0.6-in. diameter strands). All pretensioned strands were prestressed to a target force equal to 43.9 kips (202.5 ksi) while the target force during post-tensioning was defined as 263.7 kips (202.5 ksi).

Prestressing forces on both the pretensioned strands and PT tendons were evaluated for each analysis. The yield stress of the prestressing strands is specified as 243 ksi (ASTM A416), therefore the yield force for each strand (0.6 in. diameter, 0.217 in^2 cross-sectional area) was set equal to 52.7 kips. Initially, the formation of plastic hinges was defined as the condition where the axial force in the pretensioned strands exceeded the specified yield force. Hence, plastic hinge length was estimated as the length over which the axial force in the pretensioned strands was higher than the yield force. However, it was observed that concrete damage extended beyond the yield force threshold. Concrete damage is consistent with the abrupt change in slope in axial force in pretensioned strands. Therefore, a parameter denoted 'damage length' was defined as the length over which the axial force in the pretensioned strands presented nonlinear behavior. In other words, damage length was measured between the points where the axial force vs. location curve presented a change in slope as depicted in Figure 8.96.
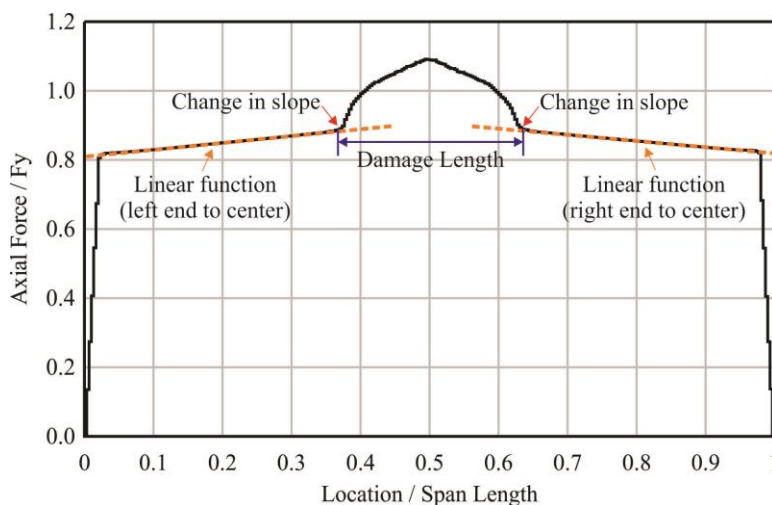
Figure 8.96 Definition of 'damage length'

Figure 8.97 depicts axial forces in pretensioned strands as a function of location along the length of simply-supported beams. The axial forces are presented for different load levels during the analysis. Note that the load levels were selected to provide a qualitative graphical representation of the concrete damage region; these levels do not, however, necessarily represent equal increments of load. Data at the start of the analysis (i.e., pretensioning) are shown in light gray transitioning to black towards the end of the analysis. The last (i.e., black) trace plotted in each figure corresponds to the load level at which at the flexural moment capacity was reached. During both concentrated (Figure 8.97a) and uniform (Figure 8.97b) load application, the maximum pretensioned axial force was achieved with a value of 57.9 kips (266.8 ksi). The bonded reinforcement exhibited a significant increase in axial force near midspan for both models. However, the two models exhibited different damage lengths. For the concentrated load condition, the nonlinear portion of the axial force curve extended for 450 in.; which was defined as the damage length. It can be observed that the damage length corresponding to uniform loading is longer; it was determined to be approximately 780 in.

For all models, the axial forces in both of the PT tendons remained almost constant with respect to longitudinal location, remaining well below the corresponding total yield force. Since the PT tendons were modeled as unbonded and the friction coefficient was zero for most cases, as

expected, the axial forces were equally distributed along the whole length of the tendons, despite formation of a plastic hinge zone.
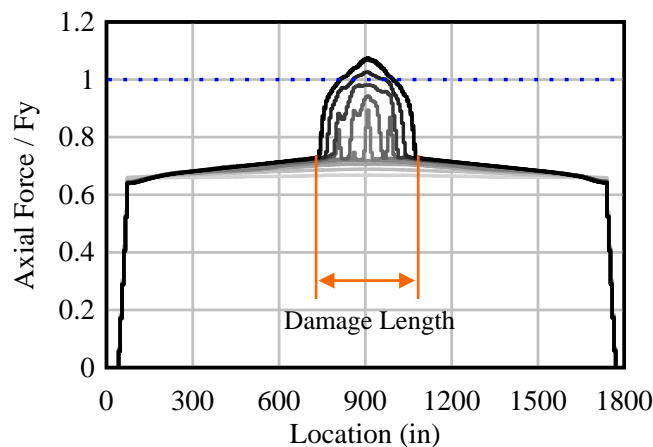

(a)

(b)
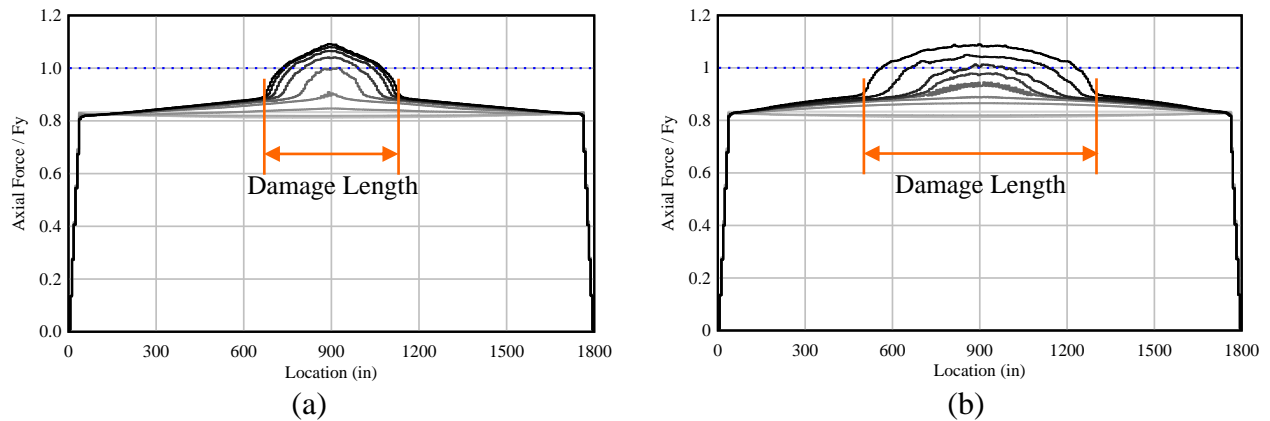
Figure 8.97 Axial force as a function of location, pretensioned strands:
(a) simply-supported beam subjected to concentrated load (U/L = 0.2),
(b) simply-supported beam subjected to uniformly distributed load (U/L = 0.2)

To assess the flexural capacity of the beams, not only was the applied force checked, but also bending moments were evaluated at midspan. As depicted in Figure 8.98a, the maximum moments (shown with a blue × marker) were compared to the nominal moments (moments corresponding to $\varepsilon = 0.003$ in/in; shown with an orange * marker). The maximum moments were in good agreement with the nominal moment, which is the value used in design equations. Beam curvatures (Figure 8.98b) were computed for each load level and longitudinal positions spaced every 6 in. along the beams. For purposes of plotting moment-curvature relationships, curvature was taken as the average curvature within the damage length. As depicted in Figure 8.98b, there was a sharp increase in curvature values near midspan towards the end of the analysis. The extent of this increase was determined to be approximately the same as the damage length previously identified through axial force in the pretensioned strands along the length of the beam. Fluctuations in curvature values were consistent with damage bands observed on the beam (Figure 8.99).
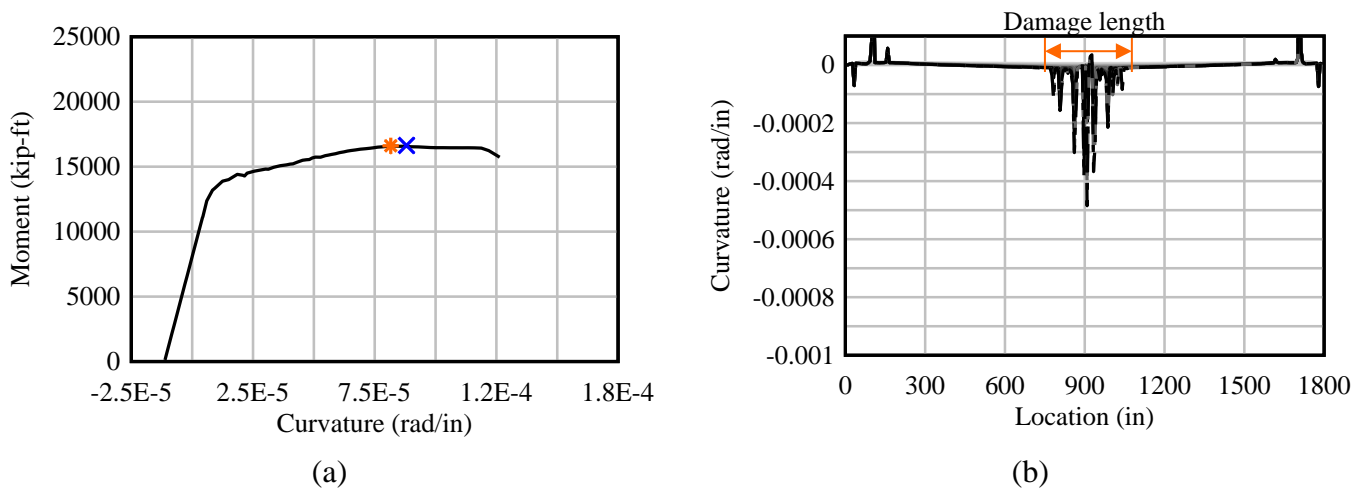

(a)

(b)
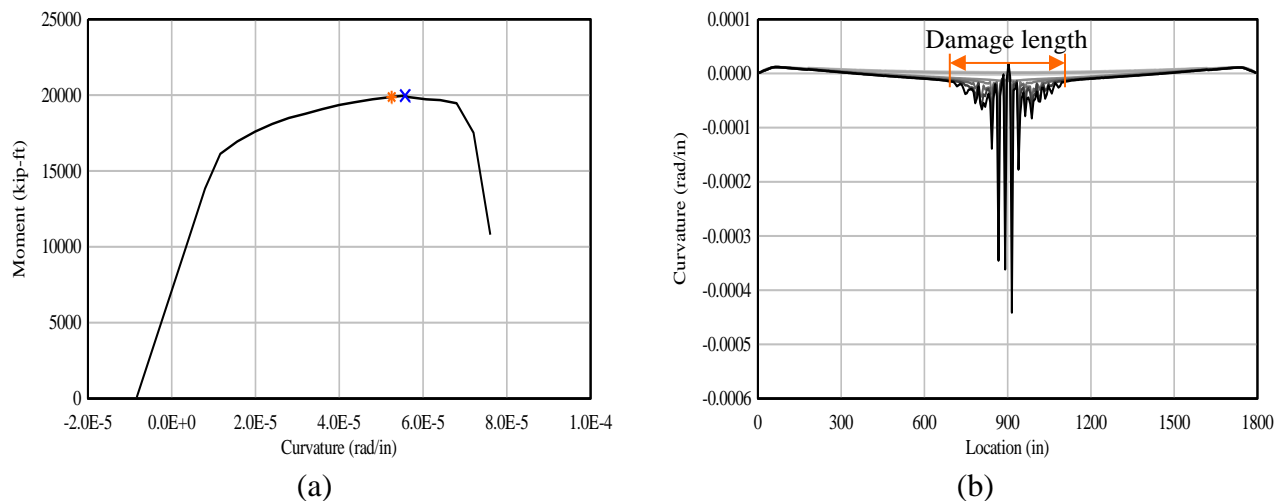
Figure 8.98 Simply-supported beam subjected to concentrated load at midspan with U/T = 0.2 (FIB72-SS-01): (a) moment as a function of curvature, (b) curvature as a function of location

The flexural behavior of each prestressed concrete beams is presented through renderings showing the concrete damage index (recall Figure 8.3). Figure 8.99 depicts renderings of damage in the middle section of the beam. These figures are not to scale—to aid in visual interpretation of results along the entire length of the beam, the vertical scale has been exaggerated. The damage contours represent the ratio of damage experienced by the beam. As the damage index approaches a value of 1, the specimen is reaching 'failure'. These renderings illustrate the progression of damage as the beams are loaded until failure. Damage can be observed in the bottom of the beams, near midspan. It is noted that damage is distributed along a longer area for the uniform load case.
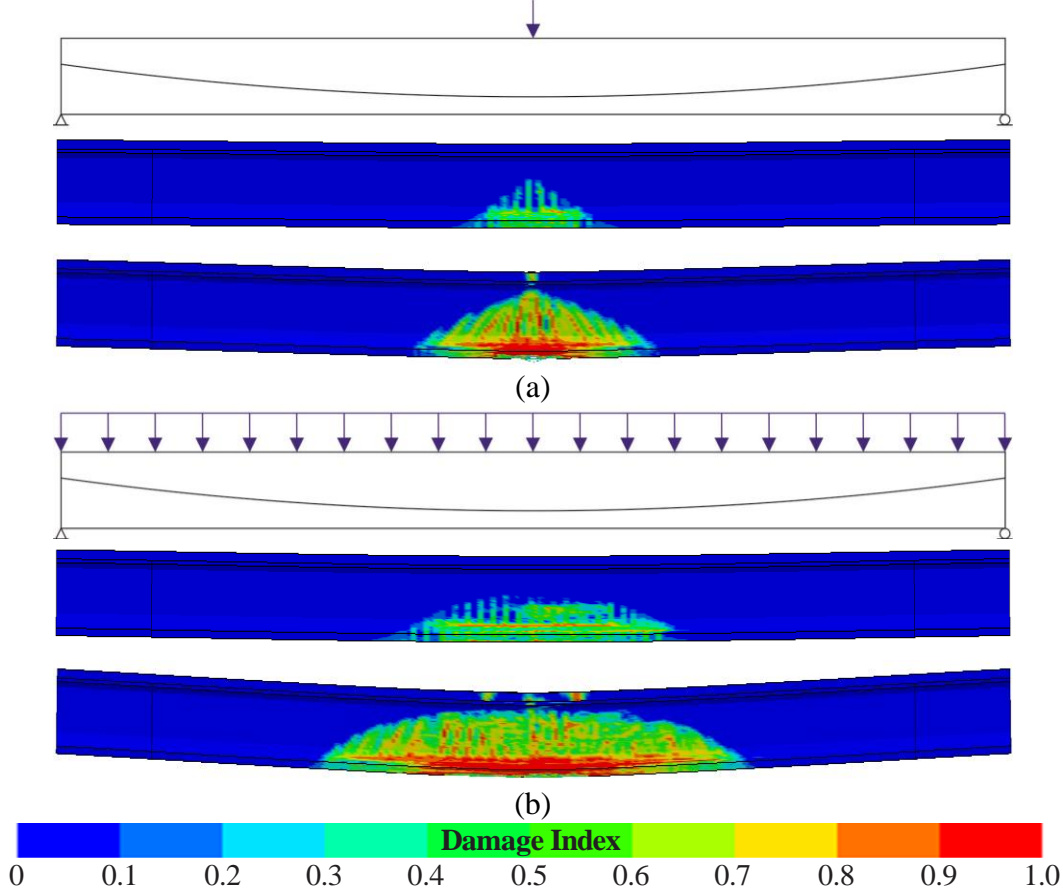
Figure 8.99 Elevation view of damage progression at midspan section:
(a) simply-supported beam subjected to concentrated load (U/L = 0.2),
(b) simply-supported beam subjected to uniformly distributed load (U/L = 0.2)

Results: Negative bending beams

Two negative bending beams were selected as representative cases for detailed discussion: a negative bending beam subjected to a concentrated loading at midspan (FIB72-NB-03, Table 8.18) and a beam subjected to a uniformly distributed load (FIB72-NB-09, Table 8.18). This section will focus on the flexural behavior of the center segment over the interior support and results for *all* cases investigated are presented, in graphical form, in Appendix G.

Finite element models FIB72-NB-03 and FIB72-NB-09 consisted of three precast beam segments that were joined together with concrete splices (for a total length of 300 ft) and subsequently post-tensioned. These beams had an unbonded reinforcement ratio (U/T) of 0.8 in the middle segment. Bonded reinforcement consisted of mild steel in the concrete deck and 4 pretensioned strands in the top of the beam. Unbonded reinforcement consisted of two PT tendons, each consisting of 24 0.6-in. diameter unbonded strands.

Figure 8.100 depicts axial forces in the top pretensioned strands as a function of location along the length of the middle segment (which spanned over the interior support) of negative bending beams. During concentrated loading (Figure 8.100a), the maximum pretensioned axial force was achieved with a value of 57.9 kips (266.8 ksi). Meanwhile, during uniform load application (Figure 8.100b), the top pretensioned strands reached a maximum axial force of 58.0 kips (267.3 ksi). A significant increase in axial force was observed in the bonded strands near the interior support. The damage length for negative moment at the interior support corresponding to the concentrated load case was determined to be 336 in. while the damage length for the uniform load case was determined to be 276 in. (18% shorter than concentrated load case). After formation of the interior support plastic hinge, additional positive moment hinges formed in the end beam segments under the concentrated load application points. These secondary positive moment hinges presented shorter damage lengths.
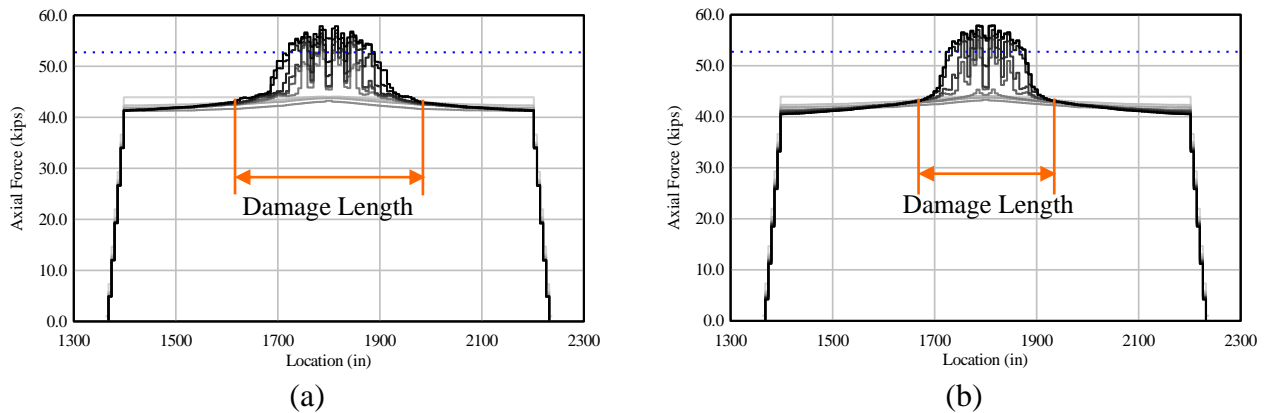
Figure 8.100 Axial force as a function of location, pretensioned strands:
(a) negative bending beam subjected to concentrated load (U/L = 0.8),
(b) negative bending beam subjected to uniformly distributed load (U/L = 0.8)

Figure 8.101 depicts renderings of concrete damage in the beams. Note that these figures are not to scale–to aid in visualization, the vertical scale is exaggerated. Selected load levels are presented to illustrate the progression of damage as the beam is loaded to failure. As previously noted, the primary negative moment plastic hinge developed at the interior support, and secondary positive moment hinges formed under the concentrated loads at midspan. The damage renderings at the point of nominal negative moment were visually consistent with the damage length that was computed from the axial force data corresponding to the pretensioned strands in the top flange of the beam.

159
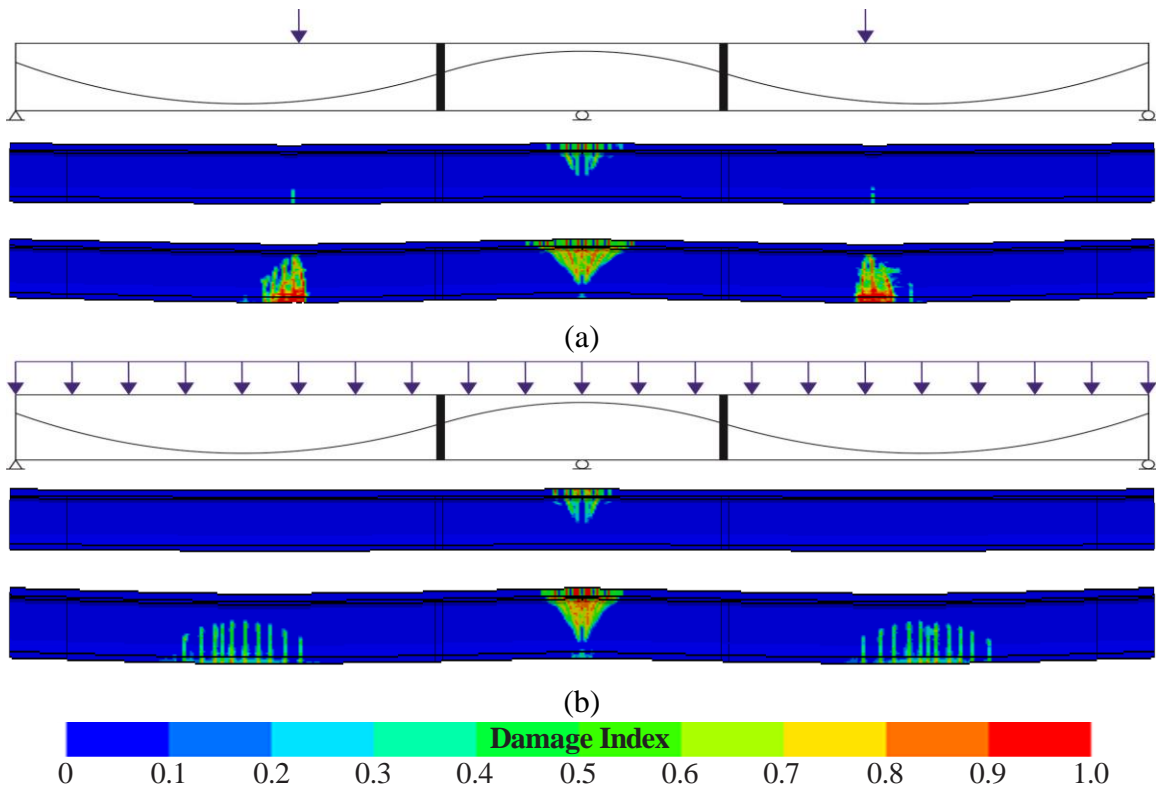
Figure 8.101 Elevation view of damage progression at midspan section:
(a) negative bending beam subjected to concentrated load (U/L = 0.8),
(b) negative bending beam subjected to uniformly distributed load (U/L = 0.8)

Observed trends

Discussions of trends observed in the results obtained for all analysis cases listed in Tables 8.17 and 8.18 are presented below.

Simply-supported beams

The simply-supported beams were analyzed for a total of 11 different cases (see Table 8.17). The main parameters that were varied were the ratio of unbonded reinforcement (U/T) and the load type. However, cases with varying friction coefficients were also considered. The main interest of these analyses was the flexural behavior of the beams, specifically the nominal moment capacity under different scenarios. Moments for cases with varying U/T ratios and varying load types are plotted in Figure 8.102a. It was found that the moment capacity did not vary significantly due to the load type. In spite of the different load types, the differences between the moments in beams with the same unbonded reinforcement ratio (U/T), but different loading types, were less than 5%. In contrast, the moment capacity was affected by the ratio of unbonded reinforcement. As shown in Figure 8.102a for all three load cases, the moment capacities decreased as the unbonded reinforcement ratio increased. Within the same load type, the moment capacity decreased approximately linearly with respect to the ratio of unbonded reinforcement.

Beyond variations in reinforcement ratio and load type, the friction coefficients employed for the post-tensioning were also varied for two additional models. Frictional variations were introduced to produce models with $\mu=0.14$ and $\mu=0.30$ so that the influence of friction (on flexural capacity) could be investigated. The maximum and 'nominal' moments were essentially the same for all three levels of friction. The nominal moments for different friction coefficients are presented in Figure 8.102b.

160
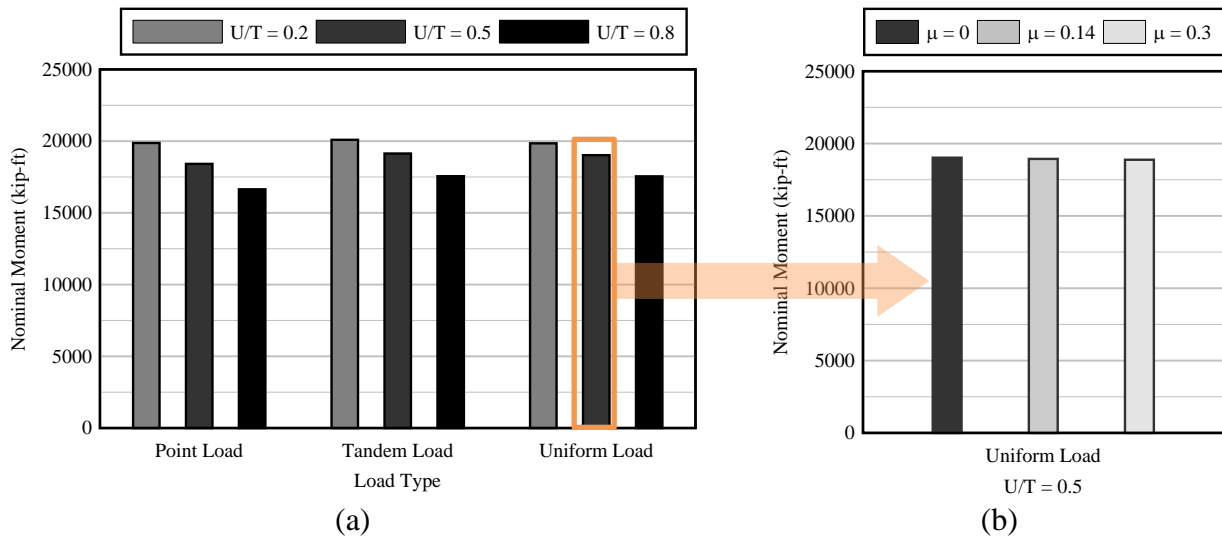
Figure 8.102 Nominal bending moments at midspan by load type and unbonded reinforcement ratio: (a) simply-supported beams with μ = 0,
(b) simply-supported beams with varying friction (μ) coefficients (UL, U/T = 0.5)

The damage length was also evaluated for the different types of loading and ratios of unbonded reinforcement as well as for varying friction coefficients. The lengths reported herein were determined from axial force data from the pretensioned strands. These lengths were analogous to the distance over which the curvature increased significantly as well as to the beam length that experienced a concrete damage index greater than 50%. As depicted in Figure 8.103, contrary to the moment capacity, the hinge length was influenced by both the load type and the unbonded reinforcement ratio. It was observed that the beams with the highest levels of unbonded reinforcement (U/T=0.8) consistently exhibited the lowest damage lengths, regardless of load type. Beams with U/T=0.2 and U/T=0.5 had similar damage lengths to each other. For example, under a concentrated load at midspan, the damage length of a beam with U/T=0.2 was only 10% longer than for a beam with U/T=0.5. Likewise, under tandem and uniform loads, the beams with U/T=0.2 resulted in longer damage lengths than the beams with U/T=0.5. Regarding the type of loading, the damage length increased as the loading went from a concentrated load at midspan (point load) to a tandem load, and eventually to a uniformly distributed load. The tandem loading resulted in lengths significantly longer than the point load. Differences between the values obtained for the distributed and tandem loads, however, were less than approximately 20%. Note that damage lengths in beams subjected to uniform loading were at least 80% longer than damage lengths determined from beams under a concentrated load at midspan.
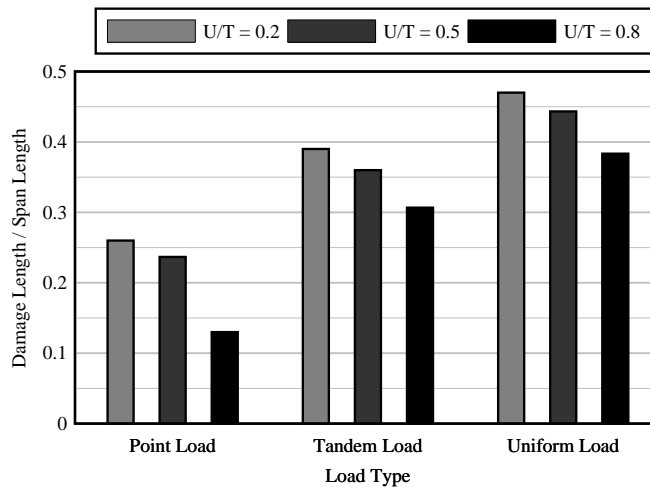
Figure 8.103 Damage lengths by load type and unbonded reinforcement ratio:
Simply-supported beams with μ = 0

Negative bending beams

Negative bending beams were analyzed for a total of 12 different cases (see Table 8.18), including variations in loading type, ratio of unbonded reinforcement, and friction between the post-tensioning and the PT ducts. As the coefficient of friction was not found to have a strong influence on ultimate flexural strength, most of the beams were modeled with a zero friction condition. However, a typical friction level (μ=0.14) and two elevated friction levels (μ=0.3 and μ=0.5) were also considered in the modeling of negative bending beams. The main interest of these analyses was the flexural behavior of the beams, specifically the nominal negative moment at the interior support under different scenarios. Figure 8.104a shows that the moment capacity did not vary significantly due to the load type. For example, differences between the moment capacities of beams with the same unbonded reinforcement ratio were less than 5%. Moment capacity was affected by the ratio of unbonded reinforcement. For all three load cases, the moment capacity increased as the unbonded reinforcement ratio increased. Within the same load type, the moment capacity increased approximately linearly with a growing ratio of unbonded reinforcement. Figure 8.104b depict the moment capacities computed for negative bending beams with an unbonded ratio of 0.6, but with different coefficients of friction. Using Model FIB72-NB-08 as a baseline, modified models were used to study the influence that friction had on flexural behavior. Maximum and 'nominal' moments were approximately the same for all four friction levels, indicating that moment capacity was not sensitive to friction coefficient.

162
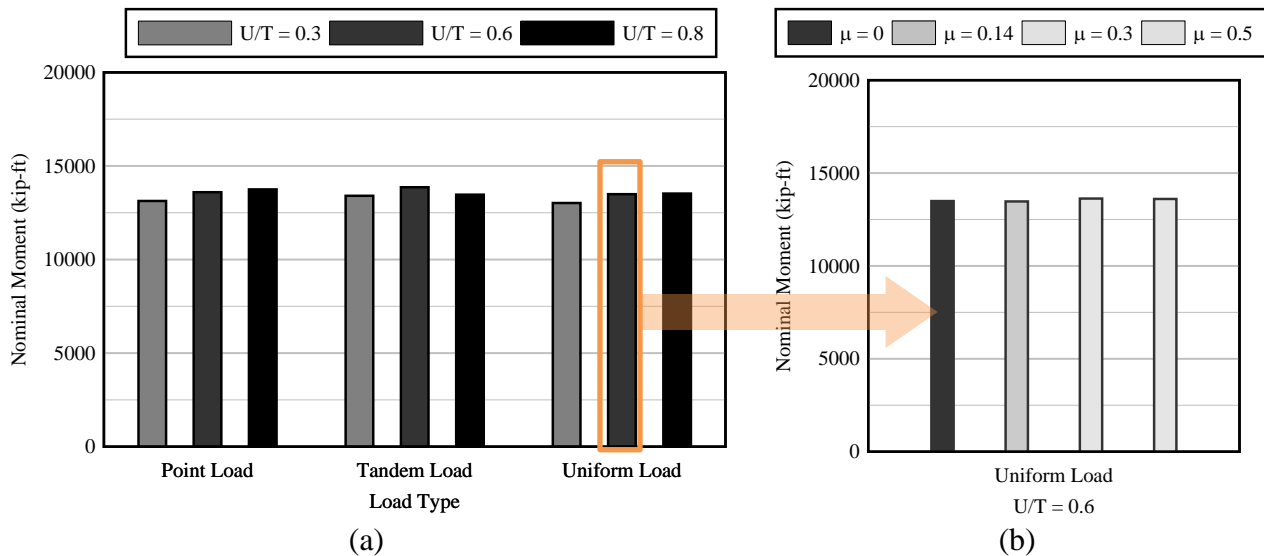
Figure 8.104 Nominal bending moments at midspan by load type and unbonded reinforcement ratio: (a) negative bending beams with μ = 0, (b) negative bending beams with varying friction (μ) coefficients (UL, U/T = 0.6)

Damage lengths were also evaluated for the different types of loading, different ratios of unbonded reinforcement, and varying friction coefficients. The lengths reported herein were determined from pretensioned strand axial forces at the top of the beam over the interior support. These lengths were analogous to the distance over which the curvature increased significantly, as well as to the beam length that experienced a concrete damage index greater than 50%. As depicted in Figure 8.105, damage lengths exhibited a general downward trend with respect to increasing ratios of unbonded reinforcement.
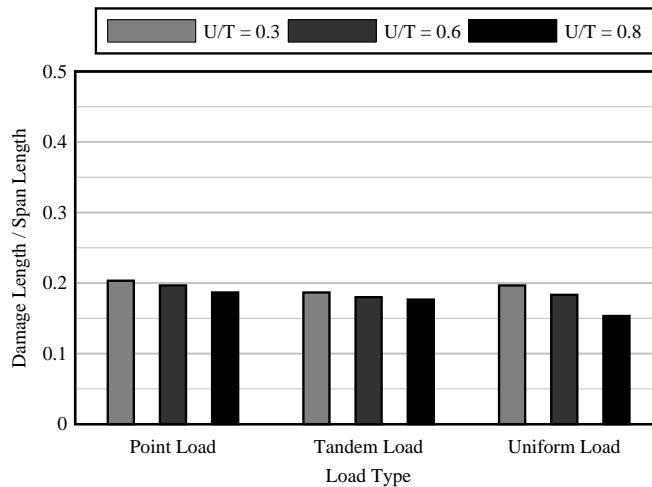
Figure 8.105 Damage lengths by load type and unbonded reinforcement ratio: Negative bending beams with μ = 0

Contrary to the trends observed for simply-supported beams, nominal moment capacities for the negative bending beams increased with an increasing U/T ratios. However, higher ratios of unbonded reinforcement resulted in less system ductility—again, in contrast to trends observed for simply-supported beams. The general trends of increasing capacity and decreasing ductility, as U/T increased, were generally observed among all the negative bending beam models regardless of loading type.

8.4.2 Florida I-Beams (with straight PT tendons)

Scope of parametric study

Finite element models of modified FIBs were analyzed with straight PT tendon profiles to allow isolation of the effects of U/T ratios and load types on the flexural behavior of beams with mixed reinforcement. All models in this section consisted of simply-supported modified FIB-72 girders (Figure 8.89) with a span length of 150 ft (span-to-depth ratio = 25). The compressive concrete strength of the FIB section was defined as 8500 psi while the compressive strength of the concrete deck was defined as 4500 psi. Table 8.19 presents the matrix of FIBs with straight PT tendons that were included in the parametric study.

Table 8.19 Parametric study matrix – SS Florida I-Beams (straight PT tendon)

Model	Reinforcement Ratio (U/T)	Loading
FIB72-SS-12	0.95	PL
FIB72-SS-13	0.90	PL
FIB72-SS-14	0.90	TL
FIB72-SS-15	0.90	UL
FIB72-SS-16	0.80	PL
FIB72-SS-17	0.80	TL
FIB72-SS-18	0.80	UL
FIB72-SS-19	0.70	PL
FIB72-SS-20	0.70	TL
FIB72-SS-21	0.70	UL
FIB72-SS-22	0.50	PL
FIB72-SS-23	0.35	PL
FIB72-SS-24	0.25	PL
FIB72-SS-25	0.10	PL
FIB72-SS-26	0 (bonded)	PL

PL = Point load, TL = Tandem load, UL = Uniform load

Varying ratios of unbonded reinforcement to total reinforcement (U/T) were considered as listed in Table 8.19; strand layouts are presented in Appendix H. The total amount of PT strands was divided into two PT tendons; each tendon was assigned a cross-sectional area and prestressing force that represented all strands contained within the 'aggregated tendon'.

Figure 8.106 illustrates the construction stages that were used in defining the single span beam models with straight tendons. Concrete beam segments (solid elements) corresponding to the FIB section and concrete deck were placed on top of a steel bed (thin layer of solid elements) and gravity was applied. Boundary conditions were applied to the bottom surface of the steel bed to prevent movement. Solid elements in the concrete girder interacted with solid elements in the steel bed through contact surface definitions (Figure 8.91a). After gravity was applied, the pretensioning strands were prestressed thus causing the beam to camber upward. Next, concrete end blocks were added to both ends of the beam and both PT tendons were prestressed simultaneously. The steel bed was then replaced by displacement constraints along a set of nodes at a distance of 6 in. from the ends of the beam. Subsequently, external loads were applied.
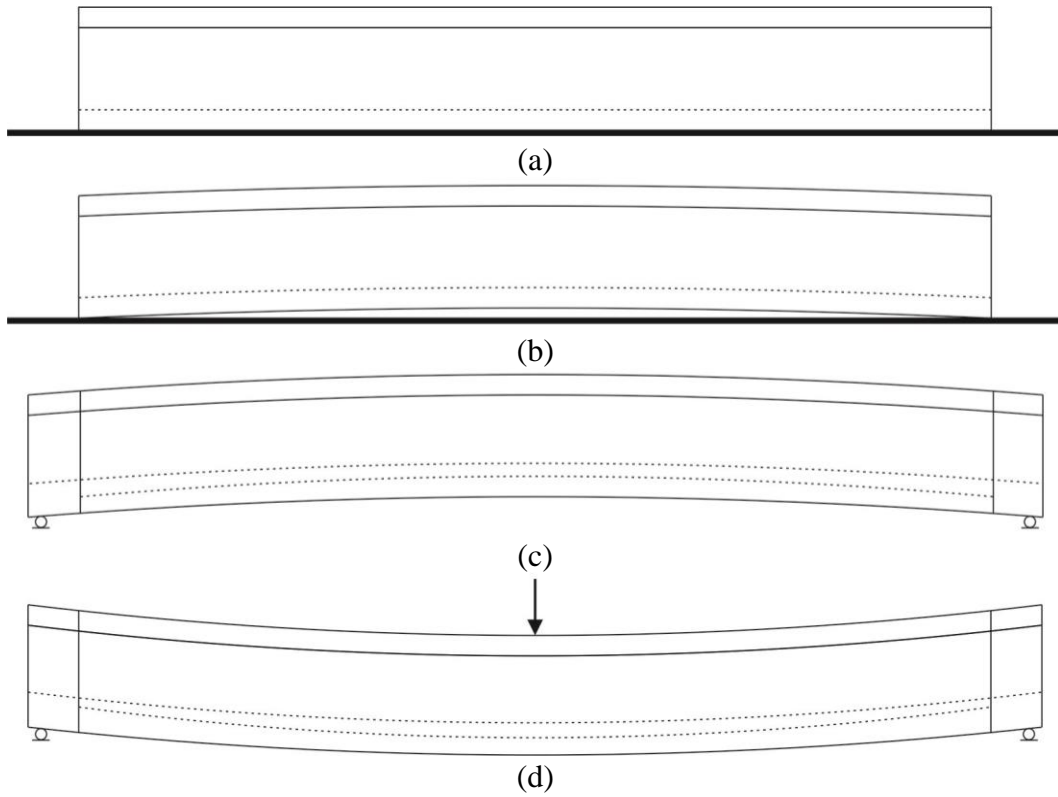
Figure 8.106 Constructions stages for simply-supported beams: (a) application of gravity to girder placed over prestressing bed, (b) pretensioning, (c) addition of end blocks and post-tensioning, (d) external loads

Loading cases considered: a concentrated load at midspan (PL), a wide 'tandem' of two concentrated loads (third-point loading, TL), and a uniformly distributed load (UL) (Figure 8.107). The friction coefficient (μ) between the PT tendons and the 'virtual' PT duct was set to μ=0.0 for all models.
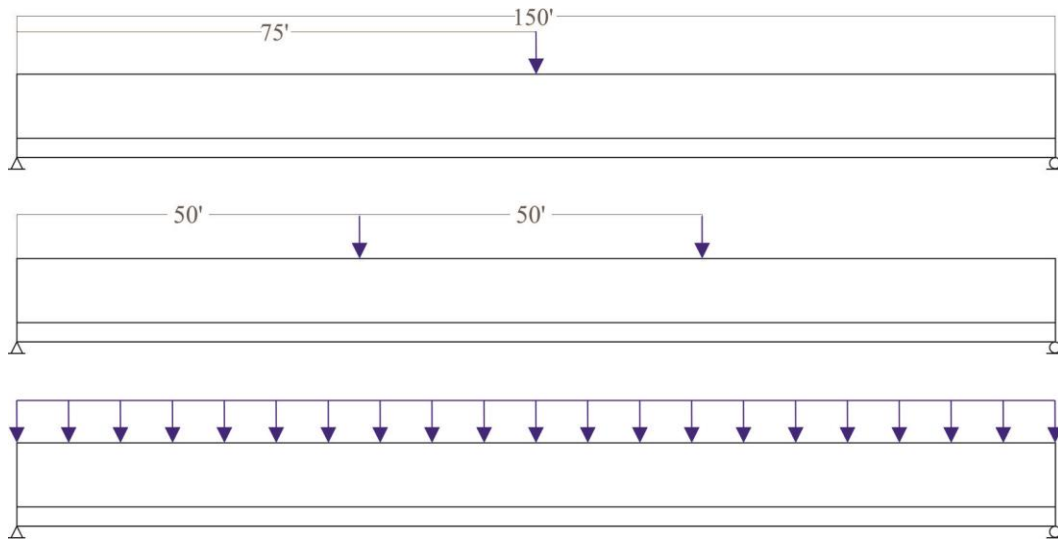
Figure 8.107 Loading cases on simply-supported (FIB-72, straight PT tendon) beam (not to scale)

A representative beam case was selected for detailed discussion in this section: a beam subjected to concentrated load at midspan with a U/T ratio of 0.70 (FIB72-SS-19, Table 8.19). Results for *all* cases listed in Table 8.19 are presented, in graphical form, in Appendix H. Summarized numerical results (e.g., computed nominal flexural capacities, damage lengths, etc.) for all cases, along with observations and discussions of data trends, are included at the end of this section.

Model FIB72-SS-19 contained 18 individual bonded pretensioned strands and two unbonded post-tensioned tendons (where each tendon contained 21 0.6-in. diameter strands). All pretensioned strands were prestressed to a target force equal to 37.43 kips (172.5 ksi) while the target force during post-tensioning was defined as 786.1 kips (172.5 ksi), assuming a lump prestress loss of 30 ksi for both pretensioned and post-tensioned tendons.

Prestressing forces on both the pretensioned strands and PT tendons were evaluated for each analysis. Figure 8.108 depicts axial forces on pretensioned strands as a function of location along the length of simply-supported beams. The axial forces are presented for different load levels during the analysis. Data at the start of the analysis (i.e., pretensioning) are shown in light gray transitioning to black towards the end of the analysis. The bonded reinforcement exhibited a significant increase in axial force near midspan. The reported damage length was based on the axial force data from pretensioned strands in the bottom layer. The axial forces in both of the PT tendons remained almost constant with respect to longitudinal location, remaining well below the corresponding total yield force. The axial forces were equally distributed along the whole length of the tendons, despite formation of a plastic hinge zone.

Figure 8.108 Axial force as a function of location, pretensioned strands:
Simply-supported FIB-72 subjected to concentrated load (U/L = 0.70)

Bending moments were evaluated at midspan in a similar way as discussed in Section 8.4.1. Figure 8.109a depicts a moment-curvature plot where maximum and nominal moments have been identified in blue and orange. Beam curvatures were computed for each load level and Figure 8.109b presents a sharp increase in curvature near midspan towards the end of the analysis. Renderings of concrete damage index are shown in Figure 8.110. In despite of different PT tendon profiles, results from FIB girders with straight PT tendons were consistent to those from FIB girders with parabolic PT tendons.

(a)   (b)

Figure 8.109 Simply-supported FIB-72 subjected to concentrated load with U/L = 0.70
(FIB72-SS-19): (a) moment as a function of curvature, (b) curvature as a function of location
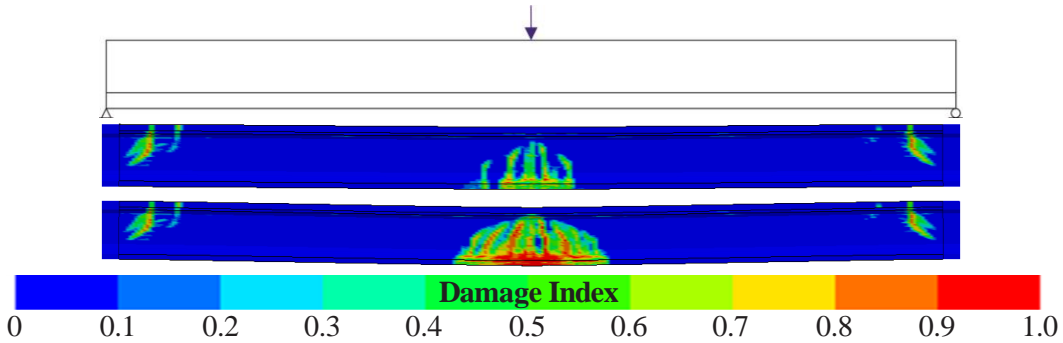
Figure 8.110 Elevation view (not-to-scale) of damage progression at midspan section:
Simply-supported FIB-72 subjected to concentrated load (U/L = 0.70)

Observed trends

The main parameters that were varied for the beam cases listed in Table 8.19 were the ratio of unbonded reinforcement (U/T) and the load type. Moments for beam cases with varying U/T ratios and varying load types are plotted in Figure 8.111. In contrast to FIB girders with parabolic PT tendons, FIBs with straight PT tendons and load type PL resulted in lower moment capacities than beams subjected to load types TL and UL. On the other hand, results from models subjected to load types TL and UL did not show significant variations in moment capacity due to load type.

As shown in Figure 8.112, the moment capacity was affected by the ratio of unbonded reinforcement. Moment capacities decreased as the unbonded reinforcement ratio increased. Within the same load type, the moment capacity decreased approximately linearly with respect to the ratio of unbonded reinforcement.

The damage length was evaluated for the different types of loading and ratios of unbonded reinforcement. As in previous sections, damage lengths were determined from axial force data corresponding to the pretensioned strands. As shown in Figure 8.113, the damage length was significantly influenced by both the load type and the unbonded reinforcement ratio. The longest damage lengths were found on beams subjected to tandem loads (TL), followed by beams under a uniformly distributed load. Beams subjected to a single concentrated load at midspan resulted in shorter damage lengths. As depicted in Figure 8.114, damage lengths presented a general downward trend with respect to increasing ratios of unbonded reinforcement.

167
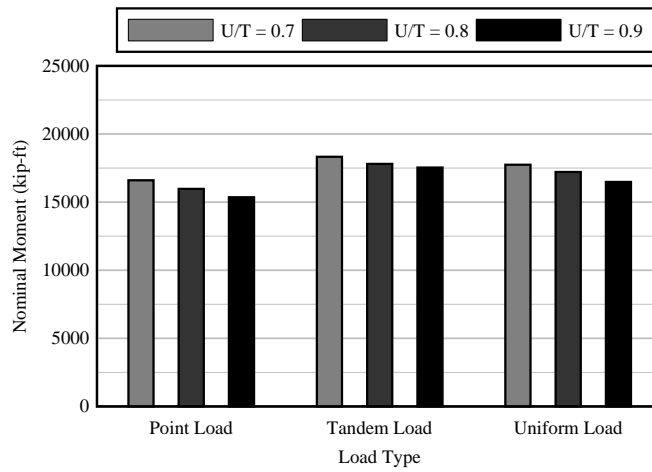
Figure 8.111 Nominal bending moments at midspan by load type and unbonded
reinforcement ratio: Mod. FIB-72 with straight tendons
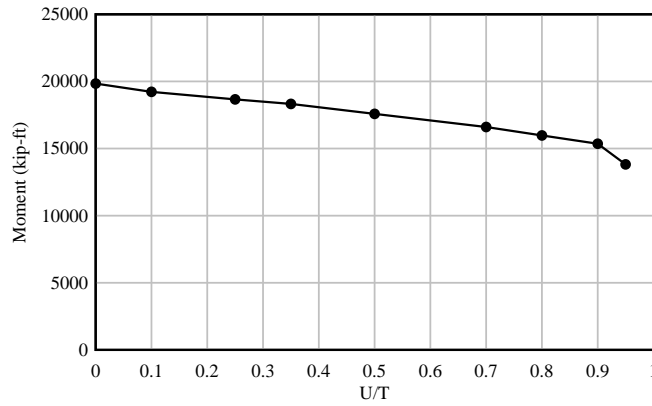
Figure 8.112 Nominal bending moments at midspan by unbonded reinforcement ratio:
Mod. FIB-72 with straight tendons subjected to concentrated load at midspan (PL)
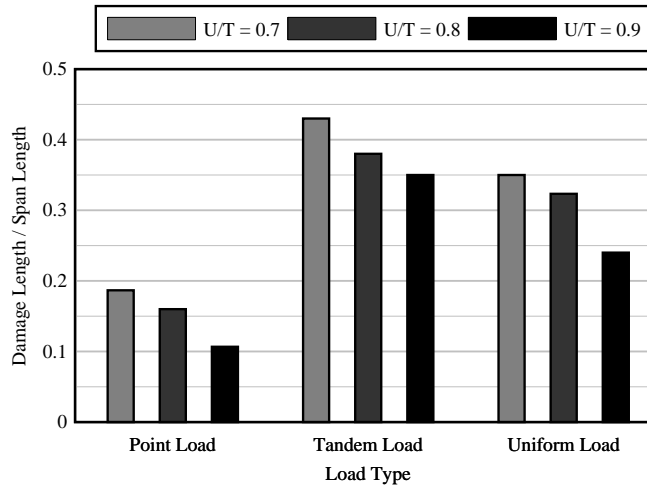
Figure 8.113 Damage lengths by load type and unbonded reinforcement ratio:
Mod. FIB-72 with straight tendons

168
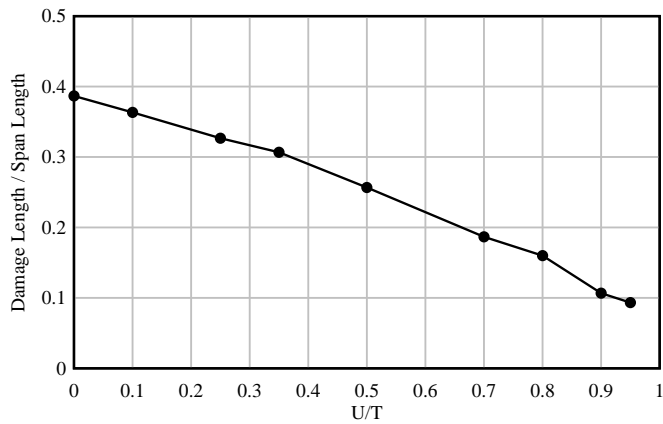
Figure 8.114 Damage lengths by unbonded reinforcement ratio:
Mod. FIB-72 with straight tendons subjected to concentrated load at midspan (PL)

8.4.3 AASHTO Type II beams (with straight PT tendons)

Scope of parametric study

All models in this section consisted of simply-supported modified AASHTO Type II girders (Figure 4.2) with a span length of 75 ft (span-to-depth ratio = 25) and unbonded reinforcement consisting of straight PT tendons. The compressive concrete strength of the AASHTO beam section was defined as 8500 psi while the compressive strength of the concrete deck was defined as 4500 psi. Table 8.20 presents the complete matrix of AASHTO beams with straight PT tendons that were included in the parametric study.

Varying ratios of unbonded reinforcement to total reinforcement (U/T) were considered as listed in Table 8.20; strand layouts are presented in Appendix I. The total amount of PT strands was divided into two PT tendons; each tendon was assigned a cross-sectional area and prestressing force that represented all strands contained within the 'aggregated tendon'.

Construction stages for AASHTO beams with straight PT tendons were defined in a similar way as discussed in Section 8.4.2 for FIB girders with straight PT tendons. Concrete beam segments (solid elements) corresponding to the AASHTO beam section and concrete deck were placed on top of a steel bed and gravity was applied. Boundary conditions were applied to the bottom surface of the steel bed to prevent movement. Solid elements in the concrete girder interacted with solid elements in the steel bed through contact surface definitions. After gravity was applied, the pretensioning strands were prestressed thus causing the beam to camber upward. Next, concrete end blocks were added to both ends of the beam and both PT tendons were prestressed simultaneously. The steel bed was then replaced by displacement constraints along a set of nodes at a distance of 6 in. from the ends of the beam. Subsequently, external loads were applied. Figure 8.106 illustrates the construction stages that were used in defining the single span beam models with straight tendons.

Loading cases included: a concentrated load at midspan (PL), a wide 'tandem' of two concentrated loads (third-point loading, TL), and a uniformly distributed load (UL) (Figure 8.115). The friction coefficient (μ) between the PT tendons and the 'virtual' PT duct was set to μ=0.0 for all models.

169
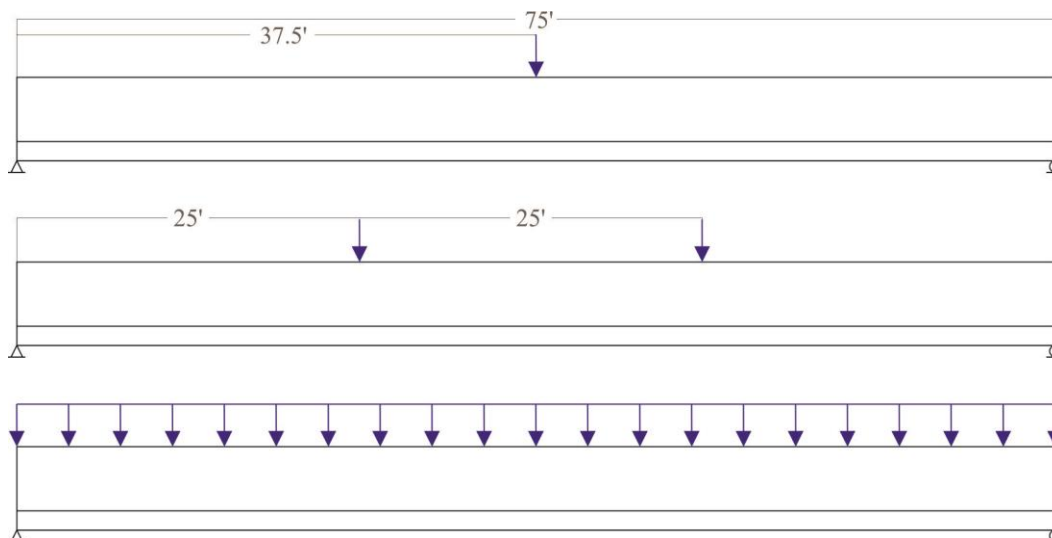
Figure 8.115 Loading cases on simply-supported (AASHTO Type II, straight PT tendon) beam (not to scale)

Table 8.20 Parametric study matrix – SS AASHTO Type II Beams (straight PT tendon)

Model	Reinforcement Ratio (U/T)	Loading
AASHTO-II-SS-1	0.90	PL
AASHTO-II-SS-2	0.90	TL
AASHTO-II-SS-3	0.90	UL
AASHTO-II-SS-4	0.80	PL
AASHTO-II-SS-5	0.80	TL
AASHTO-II-SS-6	0.80	UL
AASHTO-II-SS-7	0.70	PL
AASHTO-II-SS-8	0.70	TL
AASHTO-II-SS-9	0.70	UL
AASHTO-II-SS-10	0.50	PL
AASHTO-II-SS-11	0.35	PL
AASHTO-II-SS-12	0.25	PL
AASHTO-II-SS-13	0.10	PL

PL = Point load, TL = Tandem load, UL = Uniform load

Results

A representative beam case was selected for detailed discussion in this section: a beam subjected to concentrated load at midspan with a U/T ratio of 0.70 (AASHTO-II-SS-7, Table 8.20). Results for *all* cases listed in Table 8.20 are presented, in graphical form, in Appendix I. Summarized numerical results (e.g., computed nominal flexural capacities, damage lengths, etc.) for all cases, along with observations and discussions of data trends, are included at the end of this section.

Model AASHTO-II-SS-7 contained 6 individual bonded pretensioned strands and two unbonded post-tensioned tendons (where each tendon contained 7 0.6-in. diameter strands). All pretensioned strands were prestressed to a target force equal to 37.43 kips (172.5 ksi) while the target force during post-tensioning was defined as 262.0 kips (172.5 ksi), assuming a lump prestress loss of 30 ksi for both pretensioned and post-tensioned tendons.

170

Prestressing forces on pretensioned strands and PT tendons were evaluated for each analysis. Figure 8.116 depicts axial forces on pretensioned strands as a function of location along the length of simply-supported beams.
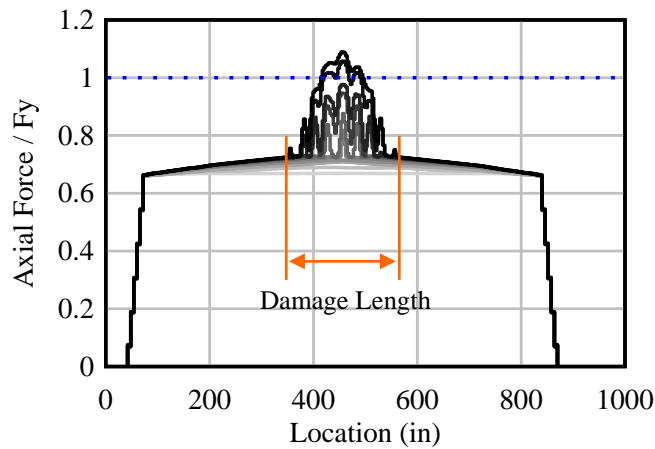
Figure 8.116 Axial force as a function of location, pretensioned strands:
Simply-supported AASHTO Type II subjected to concentrated load (U/L = 0.70)

Bending moments and curvature were evaluated at midspan as discussed in Section 8.4.1. A moment-curvature plot is depicted in Figure 8.117a while Figure 8.117b shows curvature along the length of the beam. Figure 8.118 depicts renderings of concrete damage index in the middle section of the beam.

(a)

(b)
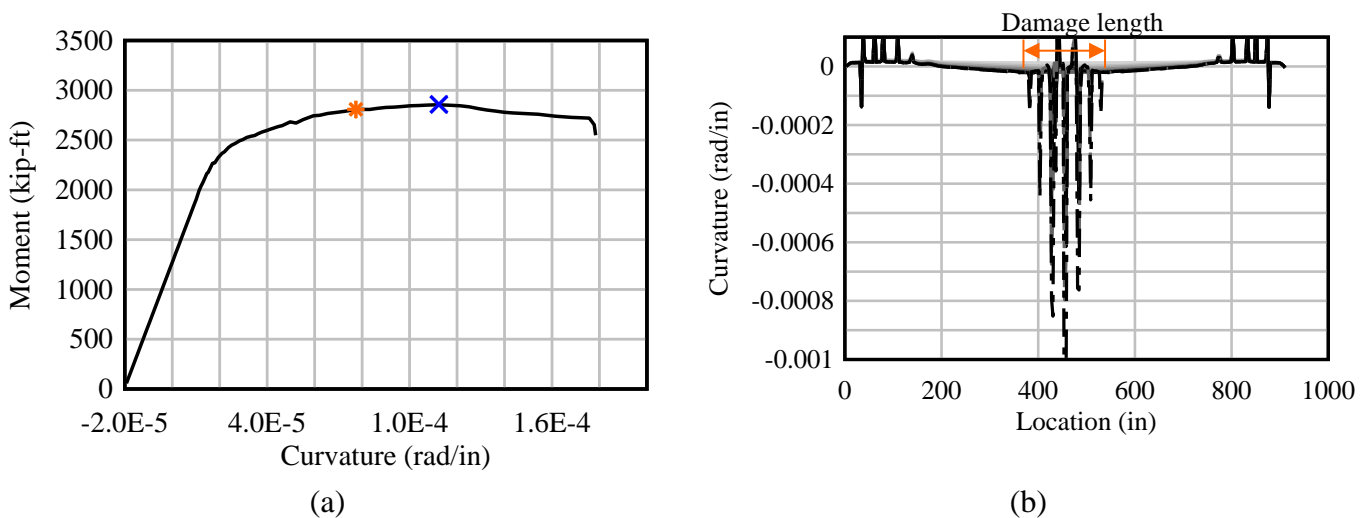
Figure 8.117 Simply-supported FIB-72 subjected to concentrated load with U/L = 0.70
(AASHTO-II-SS-7): (a) moment as a function of curvature, (b) curvature as a function of location
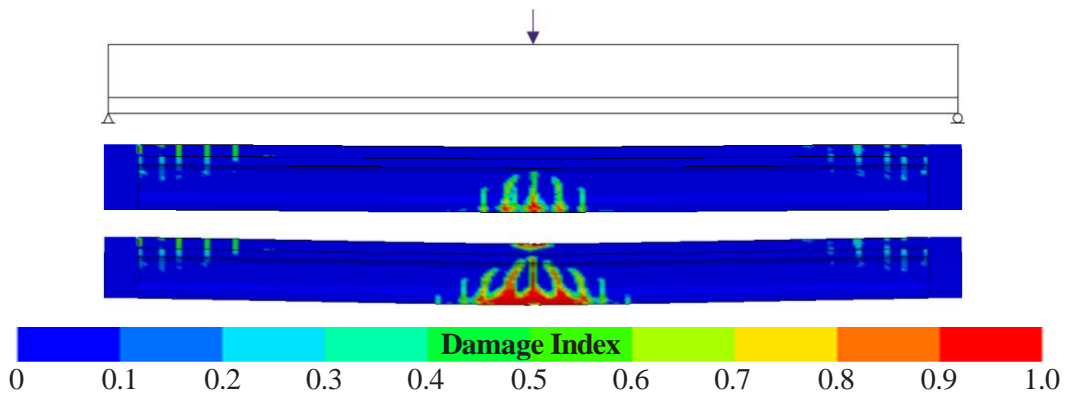
Figure 8.118 Elevation view (not-to-scale) of damage progression at midspan section:
Simply-supported AASHTO Type II subjected to concentrated load (U/L = 0.70)

Observed trends

The main parameters that were varied for the beam cases listed in Table 8.20 were the ratio of unbonded reinforcement (U/T) and the load type. Moments for AASHTO beam cases with varying U/T ratios and varying load types are plotted in Figure 8.119.

Similar to FIB girders, AASHTO beams with straight PT tendons did not present significant variations in moment capacities due to load type. Moment capacities of AASHTO beams with straight tendons were significantly lower than those of FIB girders presented in Sections 8.4.1 and 8.4.2 due to differences in cross-section dimensions, amounts of reinforcement, and span lengths. However, the overall trends were the same.

As shown in Figure 8.120, the moment capacity was affected by the ratio of unbonded reinforcement. Moment capacities decreased as the unbonded reinforcement ratio increased. Within the same load type, the moment capacity decreased approximately linearly with respect to the ratio of unbonded reinforcement.

The damage length was evaluated for the different types of loading and ratios of unbonded reinforcement and also presented similar trends to those observed on FIB girders. As shown in Figure 8.121, the damage length was significantly influenced by both the load type and the unbonded reinforcement ratio. The longest damage lengths were found on beams subjected to tandem loads (TL), followed by beams under a uniformly distributed load. Beams subjected to a single concentrated load at midspan resulted in shorter damage lengths. As depicted in Figure 8.122, damage lengths presented a general downward trend with respect to increasing ratios of unbonded reinforcement.

172
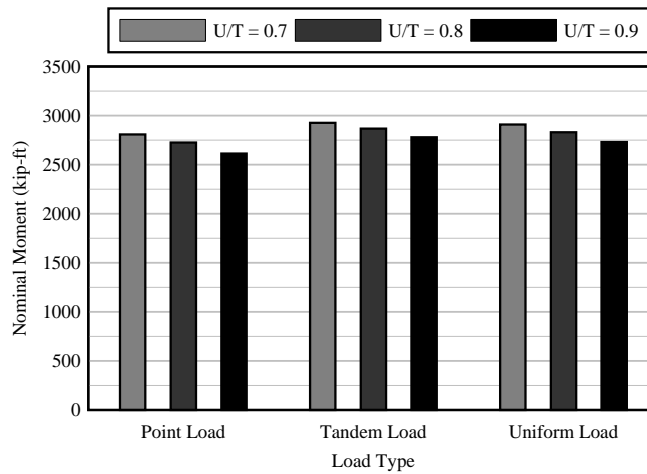
Figure 8.119 Nominal bending moments at midspan by load type and unbonded
reinforcement ratio: Mod. AASHTO Type II with straight tendons
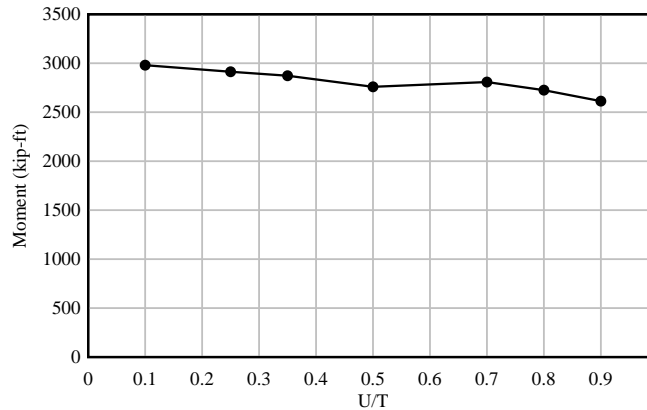
Figure 8.120 Nominal bending moments at midspan by unbonded reinforcement ratio:
Mod. AASHTO Type II with straight tendons subjected to concentrated load at midspan (PL)
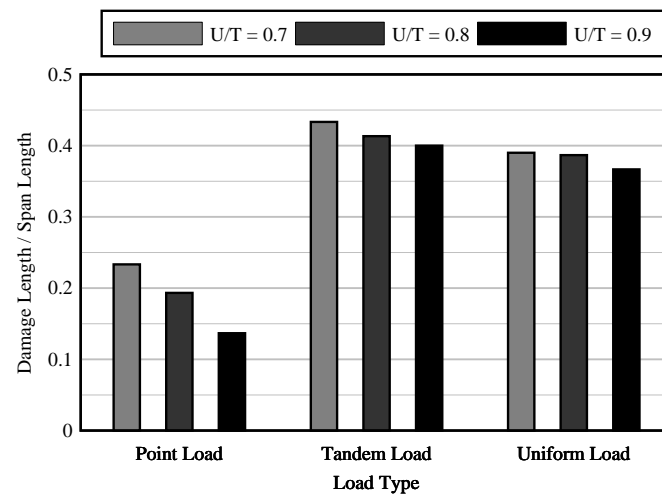
Figure 8.121 Damage lengths by load type and unbonded reinforcement ratio:
Mod. AASHTO Type II with straight tendons

173
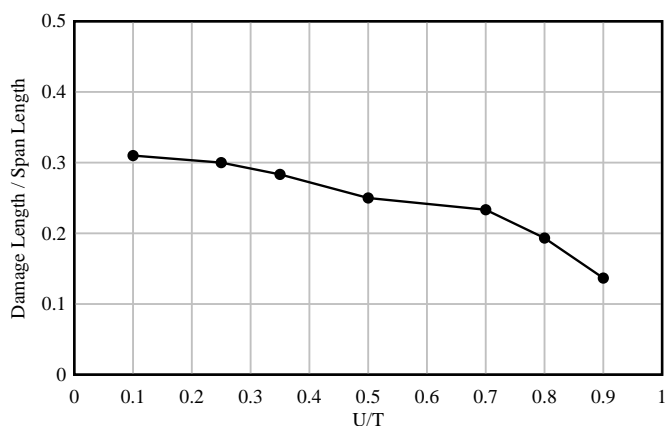
Figure 8.122 Damage lengths by unbonded reinforcement ratio:
Mod. AASHTO Type II with straight tendons subjected to concentrated load at midspan (PL)

8.5 Summary of observations from parametric study

The scope of the parametric study discussed in Section 8.4 was limited to evaluate the flexural behavior and capacity of a series of beams to identify factors that might significantly affect the flexural capacities of prestressed concrete beams with mixed unbonded and bonded reinforcement. To achieve this goal, various ratios (0.0 < U/T < 1.0) of unbonded (U) to total (T = unbonded + bonded) reinforcement were investigated.

The parametric study included an investigation into the sensitivity of flexural capacity to various system parameters, including: the ratio (U/T) of unbonded reinforcement to total reinforcement; friction between unbonded reinforcement and post-tensioning (PT) duct; loading type (concentrated loading vs. uniform loading); and beam configuration (supply-supported with positive moment vs. continuous span with negative moment). It is important to note that both the pretensioned strands and the mild steel reinforcement in the concrete deck were considered as bonded reinforcement for purposes of calculating the ratio (U/T) of unbonded to total reinforcement. Damage lengths were computed, both in positive and negative moment regions, using multiple approaches (force data from prestressing strands; elevated section curvature; concrete damage index) that produced generally consistent results.

The following observations were made:
- The flexural behavior and capacity of prestressed concrete beams with mixed bonded reinforcement (prestress and/or mild) and unbonded reinforcement is affected by the amount of unbonded reinforcement that is present in the system.
- Moment capacities of prestressed concrete beams were generally not sensitive to friction coefficients for the range of values that would be reasonably expected in design.
- Moment capacities were found to be sensitive to the U/T ratio. In general, finite element analysis demonstrated that increasing the unbonded reinforcement ratios in concrete elements with mixed reinforcement conditions resulted in lower ultimate flexural strength.
- For simply-supported beams subjected to positive moment, the flexural capacity consistently decreased as the ratio of unbonded reinforcement (U/T) increased. However, for continuous FIB girders subjected to negative moment the relationship between flexural capacity and U/T was more varied. It is important to note that NB beams evaluated in the parametric study consisted of FIB-72 girders with a concrete deck considerably wider (8 ft) than the experimental specimens. Hence, it is

174

believed that mild steel reinforcement in the deck provided some crack control and enhanced the flexural behavior of the FIB girders considered in the parametric study.

- For both simply-supported beams in positive flexure and continuous beams in negative flexure, damage lengths decreased with increasing unbonded reinforcement (U/T).
- It is considered that the mild steel reinforcement in the deck of NB beams provided crack control and enhanced the flexural behavior of NB FIB girders.

CHAPTER 9
PROPOSED DESIGN APPROACH FOR CONCRETE ELEMENTS WITH MIXED REINFORCEMENT

9.1 Introduction

Using results from the experimental and analytical investigations presented in previous chapters, an approach to design concrete elements in flexure with a combination of unbonded and bonded reinforcement is proposed. This study considered different types of beams with varying amounts (and ratios) of unbonded and bonded reinforcement, tendon profiles, span-to-depth ratios, concrete strengths, and loading conditions. Therefore, the equations proposed in this report are developed to be applicable to flexural elements with variations found in a wide range of projects.

9.2 Flexural capacity

The nominal moment capacity of prestressed concrete beams is affected by the degree of unbonded reinforcement present in the system. Past studies published in the literature have demonstrated that the use of mixed reinforcement conditions results in lower ultimate flexural strength when compared to fully-bonded members with the same total amount of steel reinforcement. In the present study, it was not feasible to construct and test fully-bonded 'control' specimens for the purpose of comparing to the mixed-reinforcement beams that were the primary focus of the investigation. Constructing fully-bonded and mixed-reinforcement beams would have required twice as many experimental specimens which was not practical. Instead, the mixed-reinforcement finite element models that were validated against the collected experimental data were converted into fully-bonded models. The fully-bonded models then served as computational surrogates for fully-bonded test beams. Data obtained from the fully-bonded surrogate finite element models were utilized as the best available prediction for $M_{n,bonded}$ (U/T=0). Figure 9.1 shows the ratio of experimental moment capacity for beams with mixed bonded and unbonded reinforcement ($M_{n,exp}$) over the moment capacity for the corresponding beam assuming all tendons were fully-bonded ($M_{n,bonded}$, U/T=0). Figure 9.1 agrees with the literature in that a reduction in nominal moment capacity is associated with increasing U/T ratios.
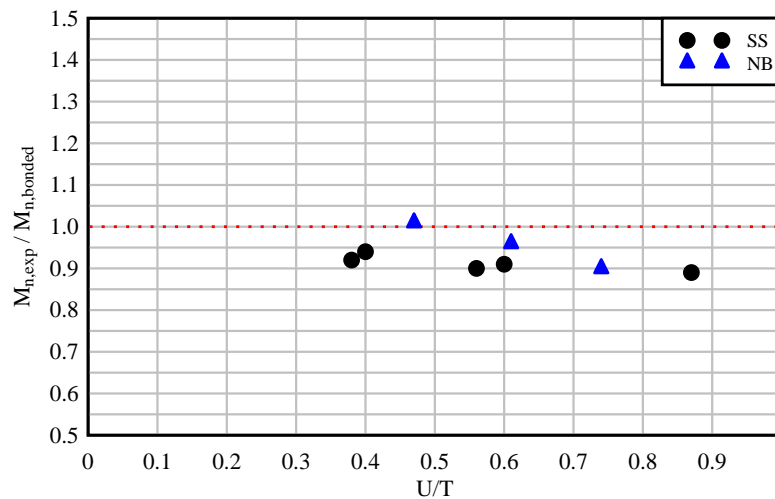
Figure 9.1 Ratio of experimental moment capacity ($M_{n,exp}$) over moment capacity of fully-bonded system ($M_{n,bonded}$, obtained from validated FE models with fully-bonded tendons) as a function of U/T ratio

When calculating the nominal moment capacity of components with both bonded and unbonded tendons, the simplified analysis approach presented in AASHTO-LRFD (AASHTO, 2020) Sections 5.6.3.1.3b and 5.6.3.2, specifies that the stress in unbonded tendons may be conservatively taken as the effective stress in the prestressing steel after losses, f_{pe}. This approach is conservative in the sense that the increase in unbonded tendon stress that occurs during flexural deformation (which would increase section capacity) is ignored. For mixed conditions, AASHTO further indicates that the stress in the bonded tendons shall be computed by replacing the term $A_{ps}f_{pu}$ with $A_{psb}f_{pu}+A_{psu}f_{pe}$ in AASHTO Equations 5.6.3.1.1-3 and 5.6.3.1.1-4. This simplified approach was found to be conservative but inaccurate for predicting the flexural resistance of concrete members with both bonded and unbonded tendons as depicted in Figure 9.2.
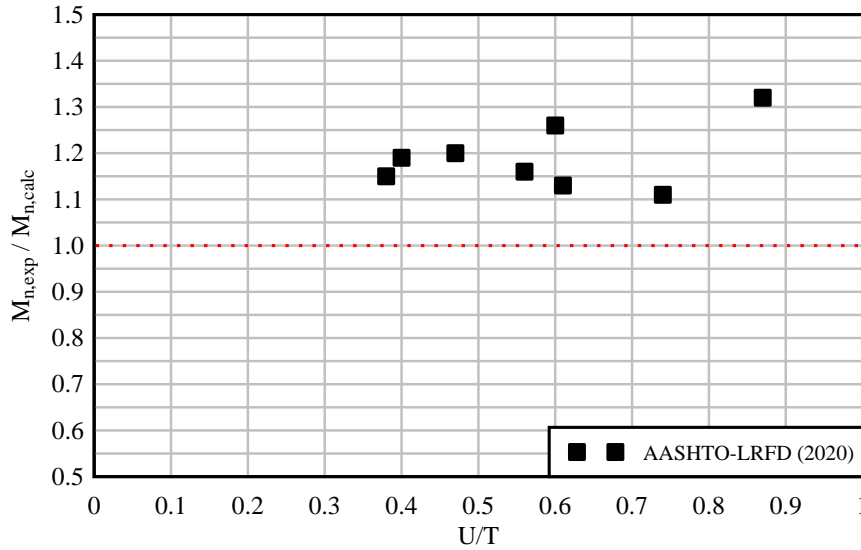
Figure 9.2 Ratio of experimental moment capacity ($M_{n,exp}$) over calculated moment capacity ($M_{n,calc}$) using current AASHTO-LRFD equations

Modifications to the simplified AASHTO-LRFD (AASHTO, 2020) approach are therefore proposed here to better predict the flexural capacity of concrete members with mixed reinforcement conditions. The allowable omission of the increase in stress in unbonded tendons, Δf_{psu}, results in an overly conservative approximation of the flexural capacity. Instead, it is recommended to incorporate the increase in stress in unbonded tendons into AASHTO Equations 5.6.3.1.2-3 and 5.6.3.1.2-4 from the AASHTO (2020). This modification is shown in Equation 9-1 for T-section behavior and Equation 9-2 for rectangular section behavior.

$$c = \frac{A_{psb}f_{pu} + A_{psu}f_{ps,u} + A_sf_s - A_s'f_s' - 0.85f_c'(b - b_w)h_f}{\alpha_1 f_c'\beta_1 b_w + k\left(A_{psb}\dfrac{f_{pu}}{d_{pb}}\right)} \tag{9-1}$$

$$c = \frac{A_{psb}f_{pu} + A_{psu}f_{ps,u} + A_sf_s - A_s'f_s'}{\alpha_1 f_c'\beta_1 b + k\left(A_{psb}\dfrac{f_{pu}}{d_{pb}}\right)} \tag{9-2}$$

$$f_{ps,u} = f_{pe} + \Delta f_{psu} = f_{pe} + 900\left(\frac{d_{pu} - c}{l_e}\right) \leq f_{py} \tag{9-3}$$

177

Where:

A_{psb} =   area of bonded prestressing reinforcement (in.^{2})

A_{psu} =   area of unbonded prestressing reinforcement (in.^{2})

A_s =   area of bonded non-prestressed reinforcement in tension (in.^{2})

A_s' =   area of bonded non-prestressed reinforcement in compression (in.^{2})

f_{pu} =   specified tensile strength of prestressing reinforcement (ksi)

$f_{ps,b}$ =   average stress in bonded prestressing steel (ksi) (Equation 5.6.3.1.1-1, AASHTO, 2020)

$f_{ps,u}$ =   average stress in unbonded prestressing steel (ksi) (Equation 5.6.3.1.2-1, AASHTO, 2020)

f_{pe} =   effective stress in prestressing steel after losses (ksi)

f_{py} =   yield strength of prestressing steel (ksi)

f_s =   stress in non-prestressed reinforcement in tension (ksi)

f_s' =   stress in non-prestressed reinforcement in compression (ksi)

f_c' =   specified compressive strength of concrete (ksi)

d_{pb} =   distance from extreme compression fiber to the centroid of the bonded prestressing force (in.)

d_{pu} =   distance from extreme compression fiber to the centroid of the unbonded prestressing force (in.)

α_1 =   stress block factor specified in Article 5.6.2.2 (AASHTO, 2020)

β_1 =   stress block factor specified in Article 5.6.2.2 (AASHTO, 2020)

b =   width of the compression face of the member (in.)

b_w =   web width (in.)

h_f =   compression flange depth (in.)

k =   reduction factor for calculation of $f_{ps,b}$ (Equation 5.6.3.1.1-2, AASHTO, 2020)

l_e =   effective tendon length (in.) (Equation 5.6.3.1.2-2, AASHTO, 2020)

Since there are two equations with two unknowns (c and Δf_{psu}) for each type of section behavior, Equations 9-1 or 9-2 (depending on the type of section behavior) need to be simultaneously solved with Equation 9-3 to achieve a closed-form solution. Alternatively, multiple iterations may be performed to satisfy the equations.

Once solved, the nominal flexural resistance may be calculated using Equation 9-4 for T-section behavior or Equation 9-5 for rectangular section behavior.

$$M_n = A_{ps,b}f_{ps,b}\left(d_{p,b} - \frac{a}{2}\right) + A_{ps,u}f_{ps,u}\left(d_{p,u} - \frac{a}{2}\right) + A_s f_y \left(d_s - \frac{a}{2}\right)$$
$$- A_s' f'_s \left(d_s' - \frac{a}{2}\right) + \alpha_1 f_c'(b - b_w)h_f\left(\frac{a}{2} - \frac{h_f}{2}\right)$$

(9-4)

$$M_n = A_{ps,b} f_{ps,b} \left(d_{p,b} - \frac{a}{2} \right) + A_{ps,u} f_{ps,u} \left(d_{p,u} - \frac{a}{2} \right) + A_s f_y \left(d_s - \frac{a}{2} \right)$$
$$- A'_s f'_s \left(d'_s - \frac{a}{2} \right) \tag{9-5}$$

The proposed modified equations result in more efficient (economical) designs while still maintaining conservatism. In Figure 9.3, a comparison is provided between section capacities computed using the simplified AASHTO approach of ignoring PT force increase, and the proposed approach of including PT force increase.
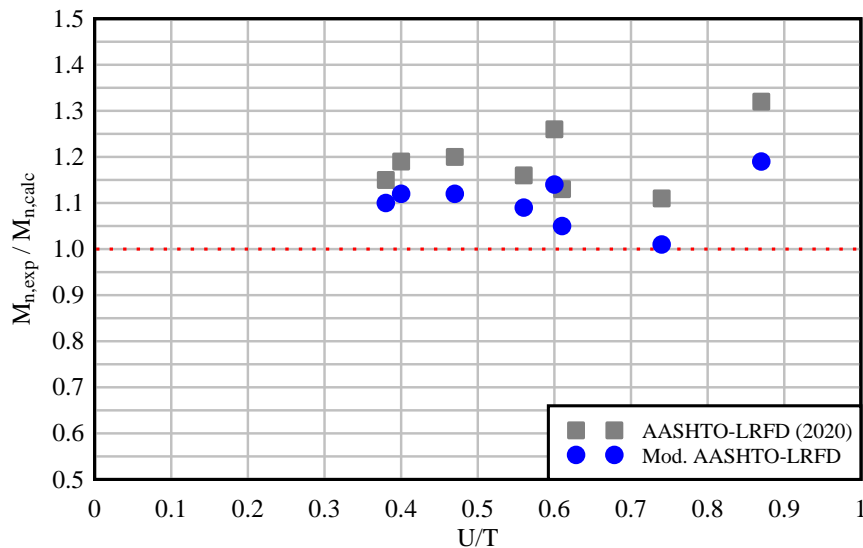
Figure 9.3 Ratio of experimental moment capacity ($M_{n,exp}$) over calculated moment capacity ($M_{n,calc}$) using current AASHTO-LRFD equations and proposed modifications as a function of U/T ratio

9.3 Resistance factor

AASHTO (2020) specifies the resistance factor for tension-controlled prestressed concrete sections as: $\phi = 1.00$ for bonded systems and $\phi = 0.90$ for fully unbonded systems. For mixed unbonded and bonded conditions, AASHTO states that selection of ϕ shall be based on the bonding condition of the tendons providing the majority of the prestressing force at the section. As noted by Mast (1992), one of the primary purposes of using a resistance factor (ϕ) in structural design is to allow for inaccuracies in capacity calculations.

As U/T varies from 0=fully-bonded to 1=fully-unbonded, beam flexural behavior transitions from section-level behavior to member-level behavior. Flexural capacities associated with member-level behavior (at larger U/T) are affected by a larger number of structural parameters (and variabilities) than are capacities associated with section-level behavior. As such, capacities associated with larger U/T possess greater prediction error than those associated with sectional analysis at smaller U/T. As previously discussed, for beams containing unbonded tendons, consideration must be given to the tendon lengths, hinge lengths, and member geometry since unbonded tendons transfer stress only at anchorages and deviation points. The use of simplified code equations fails to capture all of these considerations accurately.

To assess the level of variability that exists in capacity prediction, the proposed capacity equations (discussed in the previous section) are compared to experimental data and to results from parametric finite element analyses. The goal is to assess the level of variability that occurs over a

179

range of different conditions (e.g. beam shapes, span-to-depth ratios, concrete strengths, and U/T ratios).

Figure 9.4 shows the ratio of nominal moment capacity (from experimental data and parametric FE simulations) to the moment capacity computed using the proposed modified equations ($M_{n,calc}$). In addition, for each data set (experimental beam specimens, FE parametric study of modified AASHTO beams, and FE parametric study of modified Florida I-beams), the mean value is also presented. Within each of the three data sets, the computed capacities are all conservative, but indicate no clear correlation to U/T. As U/T increases, the benchmark section capacities (either experimental data or FE simulation) are variously under or over predicted with an error level that increases.
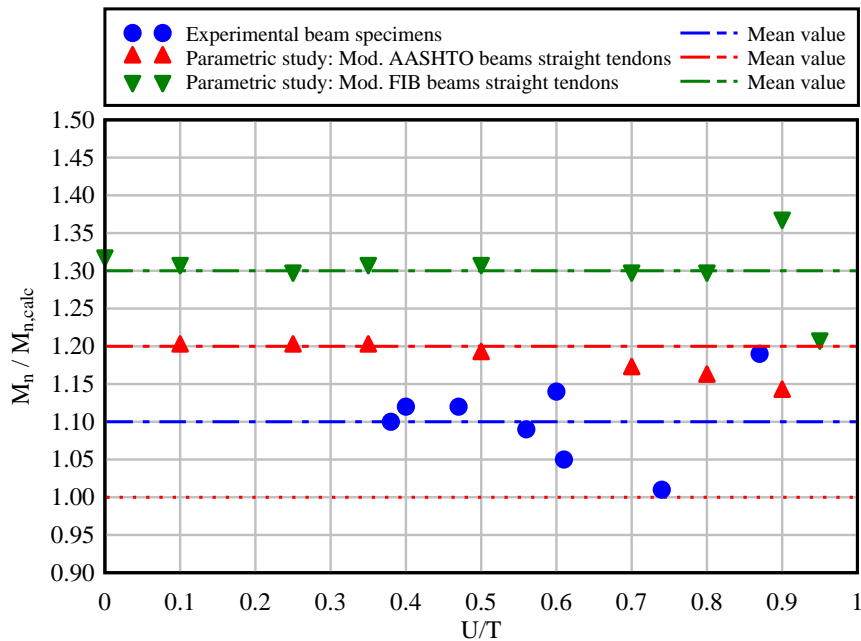
Figure 9.4 Ratio of nominal moment capacity (from experimental data or FEA) over predicted nominal capacity as a function of U/T ratio

To allow the relative variabilities in capacity prediction error for all three data sets to be visualized more consistently, the ratios from Figure 9.4 are normalized relative to the respective mean values and are replotted in Figure 9.5. Evident from Figure 9.5 is the fact that for sections with predominantly bonded reinforcement (U/T<0.5), there is low variability in capacity prediction error. However, for beams with predominantly unbonded reinforcement (U/T>0.5), the variability in capacity prediction error increases approximately linearly from U/T=0.5 to U/T=1.0 (fully-unbonded). Based on these results, it is proposed to maintain the AASHTO value of ϕ=1.00 for 0<U/T≤0.5, then to linearly transition ϕ from ϕ = 1.00 at U/T=0.5 to ϕ = 0.9 at U/T=1.0 (see Figure 9.6). This approach incorporates the experimental and analytical findings from the present study, while also maintaining the established AASHTO ϕ factors at the fully-bonded (U/T=0) and fully-unbonded (U/T=1) boundaries. In the range 0.5<U/T<1, implementation of the proposed variation of ϕ would provide improved design efficiency relative to the current AASHTO provisions.
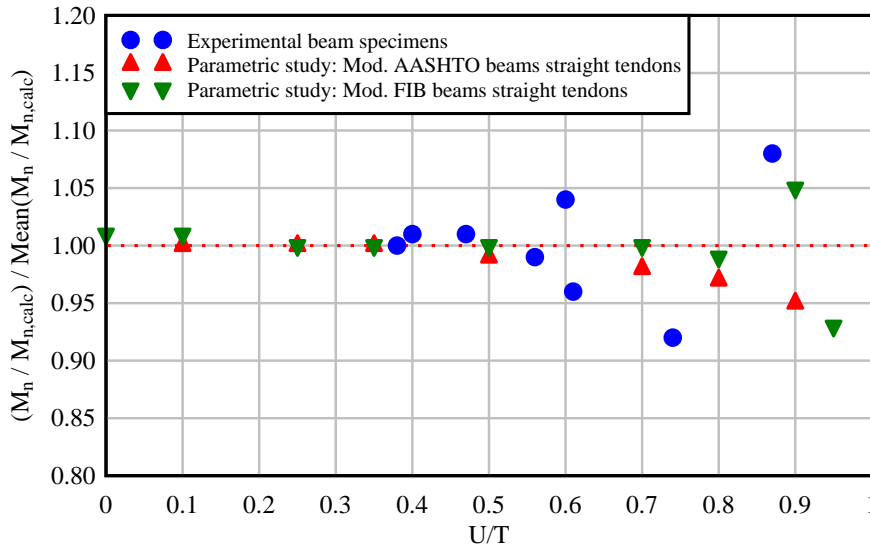
Figure 9.5 Ratio $M_n/M_{n,calc}$ over the mean value of $M_n/M_{n,calc}$ for each set of beams as a function of U/T ratio
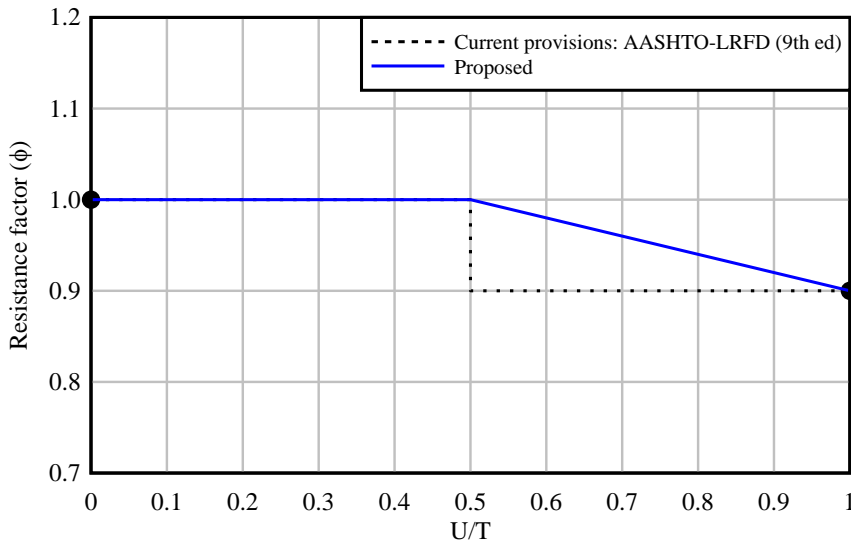
Figure 9.6 Resistance factor as a function of U/T ratio

9.4 Minimum bonded prestressing reinforcement

In general, the experimental and analytical results obtained in this study, for beams with prestressed reinforcement consisting of mixed bonded and unbonded tendons, indicated a greater increase in bonded strand stress than that which would occur in beams with the same amount of prestressing but in a fully-bonded condition (U/T = 0). As a consequence of this relative increase in stress, some of the beams tested in the experimental study resulted in undesirable rupture of bonded strands. In order to avoid (i.e. prevent) strand rupture, it is proposed that a minimum amount of bonded prestressing reinforcement be required in design. Different materials used for prestressing reinforcement (e.g. carbon steel, high strength stainless steel, and CFRP) were

considered in the development of a minimum bonded prestressing reinforcement ratio (ρ_{pb}) for prestressed concrete beams.

Initially, a bonded prestressing reinforcement ratio for fully-bonded beams (U/T = 0) was determined directly from mechanics using the relationship between strains and the sum of forces in a beam section, as shown in Figure 9.7. Equation 9-6 was used to calculate the depth to the neutral axis (c), where ε_{cu} is the ultimate compressive strain in concrete (0.003), ε_{ps} is the specified minimum elongation of the material at rupture, and d_{pb} is the depth to the centroid of the bonded prestressing reinforcement. Substituting Equation 9-6 into Equation 9-7 and solving for $A_{ps}/(bd_{pb})$, ρ_{pb} is obtained from Equation 9-8 for fully-bonded tendons. Note that b is the width of the compression face of the member. The bonded reinforcement ratio at which strand rupture occurs in beams with fully-bonded tendons can be defined using the simplified Equation 9-9. It is important to note that the compressive strength of concrete used in the calculation of $\rho_{pb,rupture}$ is the strength corresponding to the concrete in the compression zone. If the compression zone extends into a concrete section with a different compressive strength (e.g. from deck concrete into precast girder concrete), it is recommended to use the higher compressive strength of concrete for a conservative computation of $\rho_{pb,rupture}$.
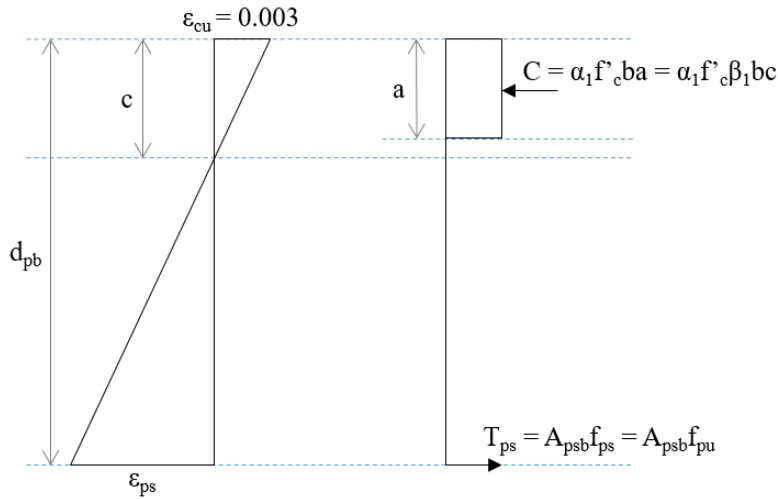
Figure 9.7 Resultant section forces used in derivation of $\rho_{b,min}$ for beams with bonded reinforcement consisting of prestressing strands

$$c = \frac{\varepsilon_{cu}}{\varepsilon_{cu} + \varepsilon_{ps}} d_{pb} \tag{9-6}$$

$$\alpha_1 f'_c \beta_1 bc = A_{psb} f_{pu} \tag{9-7}$$

$$\rho_{b,rupture\ (fully-bonded)} = \frac{A_{psb}}{bd_{pb}} = \frac{\alpha_1 f'_c \beta_1}{f_{pu}} \left(\frac{\varepsilon_{cu}}{\varepsilon_{cu} + \varepsilon_{ps}} \right) \tag{9-8}$$

$$\rho_{b,rupture\ (fully-bonded)} = \gamma \alpha_1 \beta_1 \frac{f'_c}{f_{pu}} \tag{9-9}$$

$$\gamma = \left(\frac{\varepsilon_{cu}}{\varepsilon_{cu} + \varepsilon_{ps}} \right) \tag{9-10}$$

Where:

f'_c =   specified compressive strength of concrete in the compression zone (ksi)

f_{pu} =   specified tensile strength of prestressing reinforcement (ksi)

ε_{cu} =   failure strain of concrete in compression (in./in.) = 0.003

ε_{ps} =   strain in prestressing reinforcement; specified minimum elongation of the material at rupture (ε_{pu}, in./in.)

α_1 =   stress block factor specified in Article 5.6.2.2 (AASHTO, 2020)

β_1 =   stress block factor specified in Article 5.6.2.2 (AASHTO, 2020)

Similarly, a formulation for the amount of bonded prestressing reinforcement required to avoid bonded strand rupture in beams with mixed reinforcement conditions was derived from mechanics as presented in Equations 9-11 through 9-25. The ratio of bonded prestressing reinforcement is defined by Equation 9-11, where A_{psb} is the area of bonded prestressing, b is the width of the compression face of the member, and d_{pb} is the depth to the centroid of the bonded prestressing reinforcement. From similar triangles (Figure 9.8a), d_{pb} is directly proportional to c (Equation 9-13). Therefore, ρ_{pb} at rupture can be expressed as a function of c as presented in Equation 9-14.

$$\rho_{pb} = \frac{A_{psb}}{b d_{pb}} \tag{9-11}$$

$$\gamma = \left(\frac{\varepsilon_{cu}}{\varepsilon_{cu} + \varepsilon_{ps}} \right) \tag{9-12}$$

$$c = \left(\frac{\varepsilon_{cu}}{\varepsilon_{cu} + \varepsilon_{ps}} \right) d_{pb} = \gamma d_{pb} \Rightarrow d_{pb} = \frac{c}{\gamma} \tag{9-13}$$

$$\rho_{pb,rupture} = \frac{\gamma A_{psb}}{bc} \tag{9-14}$$
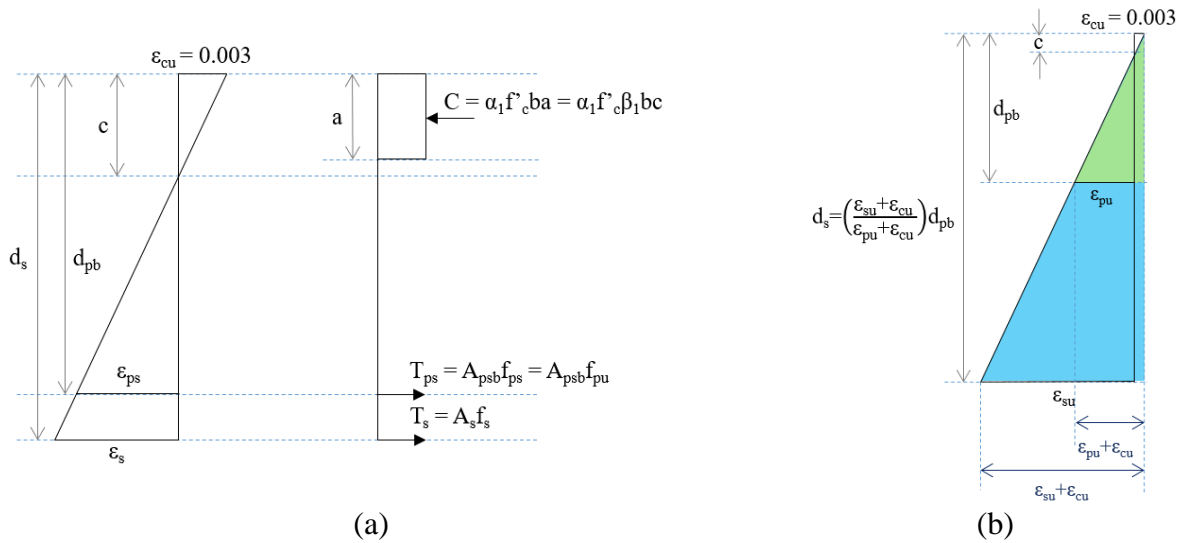
Figure 9.8 Resultant section forces used in derivation of $\rho_{b,min}$ for beams with bonded reinforcement consisting of prestressing strands and mild steel bars: (a) assuming no rupture of mild steel bars, (b) assuming rupture of both prestressing strands and mild steel bars

Substituting Equation 9-15 into Equation 9-14, Equation 9-17 is obtained for ρ_{pb} at rupture. Note that the average stress in the unbonded tendon can be estimated using Equation 9-16.

$$c = \frac{A_{psb}f_{pu} + A_{psu}f_{ps,u} + A_s f_y}{\alpha_1 f_c' \beta_1 b} \tag{9-15}$$

$$f_{ps,u} = f_{pe} + \Delta f_{psu} = f_{pe} + 900 \left(\frac{d_{pu} - c}{l_e} \right) \le f_{py} \tag{9-16}$$

$$\rho_{pb,rupture} = \frac{\gamma A_{psb}}{b} \frac{\alpha_1 f_c' \beta_1 b}{A_{psb}f_{pu} + A_{psu}f_{ps,u} + A_s f_y} \tag{9-17}$$

The ratio of unbonded reinforcement is calculated in terms of force (e.g. $F_{pu} = A_{psu}f_{pu}$) as shown in Equation 9-18. Therefore, the area of unbonded reinforcement can be expressed as a function of the area of bonded reinforcement and U/T ratio (Equation 9-19).

$$\frac{U}{T} = \frac{A_{psu}f_{pu}}{A_{psu}f_{pu} + A_{psb}f_{pu} + A_s f_y} = 1 - \frac{A_{psb}f_{pu} + A_s f_y}{A_{psu}f_{pu} + A_{psb}f_{pu} + A_s f_y} \tag{9-18}$$

$$A_{psu} = \left(A_{psb} + A_s \frac{f_y}{f_{pu}} \right) \left(\frac{\frac{U}{T}}{1 - \frac{U}{T}} \right) \tag{9-19}$$

Replacing A_{psu} by Equation 9-19 in Equation 9-17:

$$\rho_{pb,rupture} = \gamma \alpha_1 \beta_1 f_c' \frac{A_{psb}}{A_{psb}f_{pu} + \left(A_{psb} + A_s \frac{f_y}{f_{pu}} \right) \left(\frac{\frac{U}{T}}{1 - \frac{U}{T}} \right) f_{ps,u} + A_s f_y} \tag{9-20}$$

184

$$\rho_{pb,rupture} = \gamma\alpha_1\beta_1 f_c' \frac{A_{psb}\left(1 - \frac{U}{T}\right)}{A_{psb}f_{pu}\left(1 - \frac{U}{T}\right) + \left(A_{psb} + A_s\frac{f_y}{f_{pu}}\right)\left(\frac{U}{T}\right)f_{ps,u} + A_sf_y\left(1 - \frac{U}{T}\right)} \quad (9\text{-}21)$$

$$\rho_{pb,rupture} = \gamma\alpha_1\beta_1 \frac{f_c'}{f_{pu}} \frac{A_{psb}\left(1 - \frac{U}{T}\right)}{A_{psb}\left(1 - \frac{U}{T}\right) + \left(A_{psb} + A_s\frac{f_y}{f_{pu}}\right)\left(\frac{U}{T}\right)\frac{f_{ps,u}}{f_{pu}} + A_s\frac{f_y}{f_{pu}}\left(1 - \frac{U}{T}\right)} \quad (9\text{-}22)$$

$$\rho_{pb,rupture} = \gamma\alpha_1\beta_1 \frac{f_c'}{f_{pu}} \frac{A_{psb}\left(1 - \frac{U}{T}\right)}{A_{psb} - A_{psb}\frac{U}{T} + A_{psb}\frac{f_{ps,u}}{f_{pu}}\left(\frac{U}{T}\right) + A_s\frac{f_y}{f_{pu}}\frac{f_{ps,u}}{f_{pu}}\left(\frac{U}{T}\right) + A_s\frac{f_y}{f_{pu}} - A_s\frac{f_y}{f_{pu}}\left(\frac{U}{T}\right)} \quad (9\text{-}23)$$

$$\rho_{pb,rupture} = \gamma\alpha_1\beta_1 \frac{f_c'}{f_{pu}} \frac{A_{psb}\left(1 - \frac{U}{T}\right)}{A_{psb}\left(1 - \frac{U}{T} + \frac{f_{ps,u}}{f_{pu}}\left(\frac{U}{T}\right)\right) + A_s\frac{f_y}{f_{pu}}\left(1 - \frac{U}{T} + \frac{f_{ps,u}}{f_{pu}}\left(\frac{U}{T}\right)\right)} \quad (9\text{-}24)$$

Finally, the ratio of bonded prestressing reinforcement at rupture for beams with mixed bonded and unbonded reinforcement, where the bonded reinforcement consists of prestressing strands and mild steel bars is calculated using Equation 9-25.

$$\rho_{pb,rupture} = \gamma\alpha_1\beta_1 \frac{f_c'}{f_{pu}} \frac{A_{psb}}{A_{psb} + A_s\frac{f_y}{f_{pu}}}\left[\frac{1 - \frac{U}{T}}{1 - \frac{U}{T}\left(1 - \frac{f_{ps,u}}{f_{pu}}\right)}\right] \quad (9\text{-}25)$$

Where:

A_{psb} = area of bonded prestressing reinforcement (in.^{2})

A_s = area of bonded non-prestressed reinforcement in tension (in.^{2})

f_{pu} = specified tensile strength of prestressing reinforcement (ksi)

$f_{ps,u}$ = average stress in unbonded prestressing steel (ksi) (Equation 5.6.3.1.2-1, AASHTO, 2020)

f_y = yield strength of non-prestressed reinforcement (ksi)

f_c' = specified compressive strength of concrete (ksi)

α_1 = stress block factor specified in Article 5.6.2.2 (AASHTO, 2020)

β_1 = stress block factor specified in Article 5.6.2.2 (AASHTO, 2020)

It is intended to avoid rupture in bonded prestressing strands and mild steel bars, but for both to occur, the distance from the extreme concrete compression fiber to the rebar has to be significantly larger than the distance to the bonded prestressing strands. When the elongation at rupture for Grade 270 prestressing strands is taken as $\varepsilon_{pu} = 0.035$ and the elongation at rupture for mild steel bars is taken as $\varepsilon_{su} = 0.09$, it was determined by solving similar triangles that the distance d_s is equal to 2.45 times the distance d_{pb}. Rupture of mild steel bars is unlikely to occur since they have a much higher ultimate elongation than prestressing strands. Therefore, no requirement for minimum bonded non-prestressed reinforcement (e.g. mild steel bars) is proposed. However, as

depicted in Figure 9.8(b), when non-prestressed reinforcement bars are present in a section, it is recommended to satisfy $d_s < \left(\frac{\varepsilon_{su}+\varepsilon_{cu}}{\varepsilon_{pu}+\varepsilon_{cu}}\right)d_{pb}$, where d_s is the distance from extreme compression fiber to the centroid of the non-prestressed reinforcement, d_{pb} is the distance to the bonded prestressing strands, ε_{su} is the specified minimum elongation of the non-prestressed reinforcement at rupture, and ε_{pu} is the specified minimum elongation of the prestressed reinforcement at rupture.

For prestressed concrete beams with mixed bonded and unbonded reinforcement, where the bonded reinforcement consists of prestressing strands only, the ratio of bonded prestressing reinforcement at rupture is calculated with the simplified Equation 9-26. Figure 9.9 shows the ratio of bonded prestressing reinforcement at rupture as a function of U/T ratio for varying compressive concrete strengths.

$$\rho_{pb,rupture} = \gamma \alpha_1 \beta_1 \frac{f'_c}{f_{pu}} \left[\frac{1-\frac{U}{T}}{1-\frac{U}{T}\left(1-\frac{f_{ps,u}}{f_{pu}}\right)} \right] \tag{9-26}$$
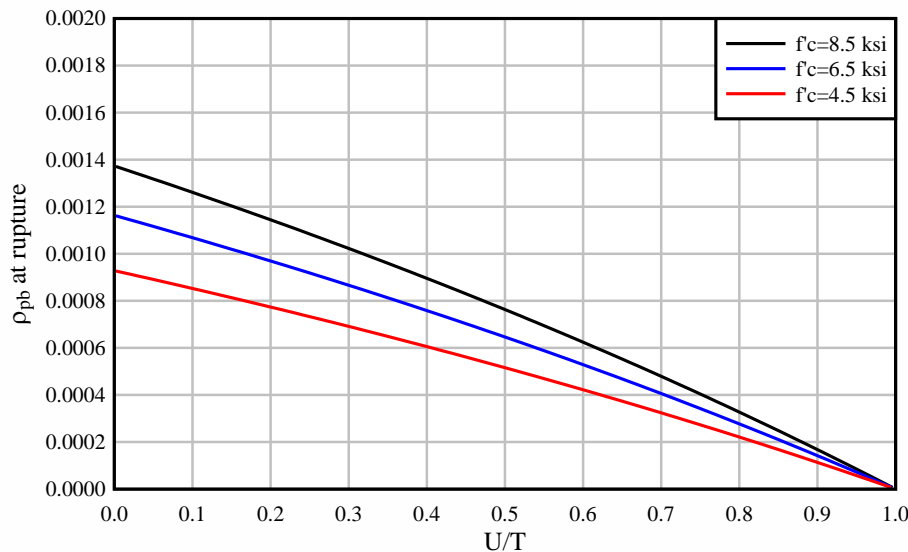
Figure 9.9 Ratio of bonded prestressing reinforcement at strand rupture as a function of U/T ratio for varying concrete strengths (assuming $f_{ps,u} = 0.80 f_{pu}$)

The purpose of requiring a minimum ratio of bonded reinforcement is to guarantee the failure mechanism is concrete crushing instead of bonded strand rupture. In order to prevent strand rupture, an amount of bonded reinforcement exceeding the threshold established in Figure 9.9 needs to be provided. As discussed in the derivation of Equation 9-25, the amount of bonded reinforcement required to prevent bonded strand rupture is dependent on the material properties of concrete and prestressed reinforcement. Therefore, it is important to take into account the variabilities associated with the properties of the materials used (e.g. uncertainties in strength, failure strain of concrete in compression, and failure strain [elongation] of prestressed strands). To account for these material variabilities, it is proposed to incorporate the use of the resistance factor into the calculation of $\rho_{pb,min}$ as presented in Equation 9-27 (for beams including non-prestressed bonded reinforcement) and Equation 9-28 (for beams with bonded reinforcement consisting of prestressing reinforcement only). Over the full range 0<U/T<1, the resistance factor is conservatively taken as ϕ=0.9 (which corresponds to U/T=1.0). Figure 9.10 shows the proposed

minimum ratio of bonded prestressing reinforcement as a function of U/T ratio for varying compressive concrete strengths.

$$\rho_{b,min} = \frac{1}{\phi} \gamma \alpha_1 \beta_1 \frac{f_c'}{f_{pu}} \frac{A_{psb}}{A_{psb} + A_s \frac{f_y}{f_{pu}}} \left[\frac{1 - \frac{U}{T}}{1 - \frac{U}{T}\left(1 - \frac{f_{ps,u}}{f_{pu}}\right)} \right] \tag{9-27}$$

$$\rho_{b,min} = \frac{1}{\phi} \gamma \alpha_1 \beta_1 \frac{f_c'}{f_{pu}} \left[\frac{1 - \frac{U}{T}}{1 - \frac{U}{T}\left(1 - \frac{f_{ps,u}}{f_{pu}}\right)} \right] \tag{9-28}$$
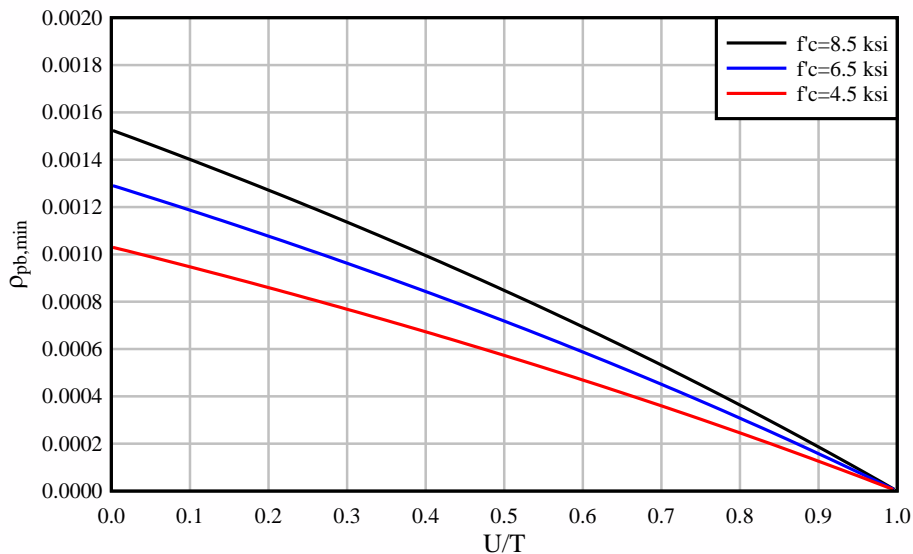
Figure 9.10 Minimum ratio of bonded prestressing reinforcement as a function of U/T ratio for varying concrete strengths (assuming $f_{ps,u} = 0.80 f_{pu}$)

Figure 9.11 shows the strain in pretensioned strands from experimental beam specimens normalized by the specified maximum strand elongation ($\varepsilon_{PreT}/0.035 > 1$ indicates bonded strand rupture) as a function of the ratio of provided bonded prestressing reinforcement (ρ_{pb}) to minimum bonded prestressing reinforcement ($\rho_{pb,min}$). As shown in Figure 9.11, beam specimens SS-3 and SS-4 did not satisfy the proposed ratio of minimum bonded reinforcement and calculations indicated strand rupture, which is in agreement with experimental and analytical results. Bonded strand rupture occurred during experimental testing of beam specimen SS-4. Bonded strand rupture was also exhibited by the validation finite element model of beam SS-4. Strand rupture did not occur during testing of experimental specimen SS-3 because, due to safety concerns, loading was halted shortly after the concrete deck reached $\varepsilon_c = 0.003$. However, the corresponding validation finite element model of SS-3 did exhibit rupture of all bonded strands. Note that tensile tests performed on samples of the experimental prestressing strand indicated an average maximum elongation of 0.05. However, for design purposes, the maximum elongation in pretensioned strands was taken as the design value of 0.035 in the calculation of minimum bonded reinforcement and normalized strain in PreT strands. As depicted in Figure 9.11, 'modified' beams SS-3 and SS-4 that included additional bonded strands (satisfying $\rho_{pb,min}$) would not have exhibited bonded strand rupture.
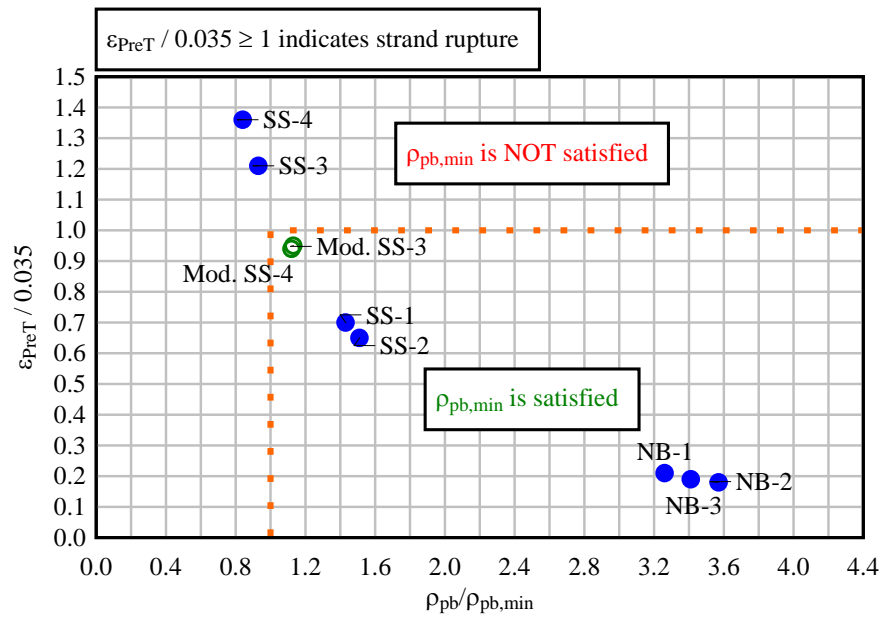
Figure 9.11 Normalized strain in pretensioned strands from experimental beam specimens as a function of $\rho_{pb}/\rho_{pb,min}$

CHAPTER 10
SUMMARY AND CONCLUSIONS

In the present study, full-scale prestressed concrete beams were evaluated using experimental and analytical techniques. This study focused on evaluating the flexural behavior of prestressed concrete elements with a combination of unbonded tendons with bonded prestress and/or mild steel reinforcement, with a particular emphasis on determining how mixed conditions influence post-tensioned system behavior. The goal of this study was to develop guidelines for design and analysis of concrete members with mixed reinforcement conditions.

Experimental tests were conducted on a series of simply-supported and negative bending beam specimens with different combinations of both bonded and unbonded reinforcement. The main parameter varied in the study was the ratio of unbonded reinforcement to total amount of reinforcement (U/T). However, other parameters such as concrete strength, span-to-depth ratio, and boundary conditions were considered during experimental testing. The experimental evaluation consisted of a total of eight beam specimens: four simply-supported precast modified AASHTO Type II beams, one simply-supported cast-in-place (20 in. x 24 in.) beam, and three negative bending precast modified AASHTO Type II beams. Simply-supported beams were tested in three-point bending while negative bending specimens were subjected to a concentrated load applied at one end of the beam such that a negative moment was generated at the interior support.

Following the experimental testing, validation models corresponding to each of the experimental beam specimens were analyzed using finite element simulation and LS-DYNA. The validation models utilized parameter values that corresponded to the actual material properties and prestressing forces present on the experimental specimens. Comparisons between FEA results and experimental data included load-displacement data, concrete strains, nominal load, maximum load, stresses in bonded pretensioned strands and unbonded post-tensioned tendons, and rupture of prestressing strands. All validation models were capable of representing nonlinear behavior and produced results that were in good agreement with the experimental data. The models were capable of exhibiting strand rupture where such rupture occurred experimentally, and indicated nominal capacities that were within a 10% margin of error for all experimental specimens tested.

To evaluate a wider range of the parameters than was possible in the experimental study, parametric finite element studies were conducted. Parametric studies considered AASHTO beams and Florida I-beams with varying boundary conditions, reinforcement ratios, PT tendon profile, loading types, and friction coefficients. Based on the collected experimental data and results from finite element parametric studies, flexural design provisions for prestressed concrete elements with a combination of bonded and bonded reinforcement were developed.

The following conclusions and recommendation are made:

- It was confirmed through experimental testing and finite element analysis that increasing the unbonded reinforcement ratios in concrete beams with mixed reinforcement conditions results in lower ultimate flexural strength. This result is summarized in Table 10.1 where nominal flexural capacities for experimental beams with mixed conditions are normalized by nominal moment capacities of corresponding beams where all tendons are assumed to be fully-bonded.

Table 10.1 Flexural strength of experimental beam specimens

Test Specimen	U/T	$M_{n,experimental}$ / $M_{n,bonded}$
SS-1	0.4	0.92
SS-2	0.6	0.90
SS-3	0.4	0.94
SS-4	0.6	0.91
SS-5	0.9	0.89
NB-1	0.5	1.01
NB-2	0.6	0.96
NB-2	0.7	0.90

- A method for computing the flexural strength of beams with mixed reinforcement has been proposed. The new proposed approach involves modifications to current provisions from AASHTO-LRFD (AASHTO, 2020) and yield flexural capacities that are more accurate, yet remain conservative relative to benchmark data (experimental tests, and nonlinear finite element analyses).

- Variability in the accuracy of design-equation flexural capacities was found to be minimal when U/T < 0.5 but increased significantly when U/T > 0.5. Consequently, for prestressed beams with mixed reinforcement conditions in the range 0.5<U/T<1, implementation of a linear transition of resistance factor (ϕ) from ϕ=1.0 at U/T=0.5 to ϕ=0.9 at U/T=1.0 is proposed.

- Experimental tests and finite element analyses indicated the potential for undesirable bonded strand rupture in beams with inadequate bonded prestressed reinforcement. To prevent strand rupture, a new design provision requiring a minimum amount of bonded prestressing strand has been developed and is proposed for implementation.

CHAPTER 11
IMPLEMENTATION OF PROPOSED DESIGN PROVISIONS

Bridge construction projects in Florida are now incorporating the use of flexible fillers to improve durability and facilitate replacement of damaged or corroded tendons. Although AASHTO-LRFD design specifications (AASHTO, 2020) include separate provisions for flexural design of bonded and unbonded systems, they do not provide a specific approach for prestressed concrete members that contain both bonded and unbonded tendons (mixed reinforcement). This study, which combined full-scale experimental work with extensive analytical modeling, focused on evaluation of the current AASHTO approach and possible development of guidelines for design and analysis of prestressed members containing mixed reinforcement.

Using AASHTO (2020) design provisions to compute flexural capacity of members with mixed reinforcement provided conservative results when compared to both experimental and analytical flexural strengths determined as part of this study; in some cases, however, the AASHTO results could be viewed as overly conservative.

11.1 Factored flexural resistance

The factored flexural resistance (M_r) is computed as the product of the nominal moment resistance (M_n) and the specified resistance factor (ϕ). To calculate M_n, the change in the unbonded tendon stress must either be determined by detailed analysis (AASHTO-LRFD 5.6.3.1.3a) or estimated using the approximate analysis provisions of AASHTO-LRFD 5.6.3.1.3b where the increase in stress of the unbonded tendon at the nominal moment resistance is ignored. The present study found that detailed analysis is a valid option and would typically require advanced analysis techniques to ensure that such a model accurately represents the design conditions.

The present study also found that modifications to the approximate method can be made by incorporating the increase in stress in unbonded tendons into AASHTO-LRFD Equations 5.6.3.1.2-3 and 5.6.3.1.2-4 using Equation 9-1 for T-section behavior and Equation 9-2 for rectangular section behavior. Equation 9-1 and Equation 9-2 are used to determine the depth of the neutral axis (c), which enables computation of M_n.

AASHTO (2020) 5.5.4.2 specifies resistance factors for fully-bonded systems (ϕ=1.0) and fully-unbonded systems (ϕ=0.9) and indicates that for mixed unbonded and bonded conditions ϕ is to be based on the bonding condition of the tendons providing the majority of the prestressing force.

Although no reliability analysis was performed, numerical simulations that were conducted in this study indicated that the variability in capacity prediction error increased approximately linearly for beams with predominantly unbonded reinforcement (U/T>0.5). One proposed approach (shown graphically in Figure 11.1) is to maintain the established AASHTO ϕ factors at the fully-bonded (U/T=0, ϕ=1.0) and fully-unbonded (U/T=1, ϕ=0.9) boundaries and use a step function to adjust ϕ at U/T = 0.5. Given the increase in variability when U/T is greater than 0.5, an alternate approach is to vary the resistance factor linearly when U/T is between 0.5 and 1.0. Since the transition point of U/T = 0.5 was chosen without the benefit of a reliability analysis, some engineering judgment will be required if the current provisions are adjusted.
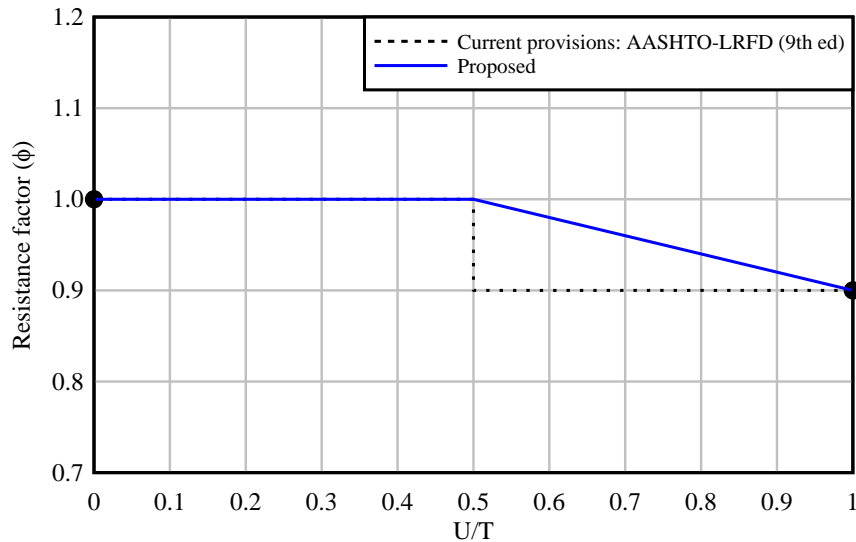
Figure 11.1 Resistance factor as a function of U/T ratio

11.2 Minimum bonded prestressed reinforcement

In addition to modifications to the current AASHTO-LRFD specifications for flexural resistance, it is proposed that a minimum amount of bonded prestressing reinforcement be required in design to prevent bonded strand rupture. AASHTO-LRFD 5.6.3.3 (AASHTO, 2020) specifies that, for noncompression-controlled flexural components, the amount of prestressed and nonprestressed tensile reinforcement must be adequate to develop M_n greater than (or equal to) the lesser of the cracking moment (M_{cr}) and 1.33 times the factored moment required by the applicable load combination. The current minimum reinforcement provisions, which include both bonded and unbonded reinforcement, are intended to reduce the probability of brittle failure by providing flexural capacity greater than the cracking moment, but does not take into consideration the strain and potential rupture of bonded prestressing strands. Therefore, it is proposed that the minimum ratio of bonded prestressing reinforcement ($\rho_{pb,min}$) for beams with mixed bonded and unbonded reinforcement, where the bonded reinforcement may consist of prestressing strands and mild steel bars, is calculated using Equation 9-27. A simplified formulation (Equation 9-28) could be used for beams where the bonded reinforcement consists of prestressing strands only (i.e. no mild steel longitudinal bars). Note that no requirement for bonded non-prestressed reinforcement (i.e. mild steel bars) is proposed since rupture of non-prestressed reinforcement is unlikely to occur due to much higher ultimate elongations than prestressing strands. Additionally, at U/T=1, which refers to fully-unbonded members (beams with no bonded reinforcement), there is no bonded reinforcement requirement.

11.3 Example – FIB-96

Application of the revised provisions is illustrated using the FIB-96 girders shown in Figure 11.2. The provided amounts of bonded and unbonded reinforcement were varied in this section to demonstrate the change in moment strength and minimum bonded prestressing reinforcement with varying U/T ratios. All cases consisted of the same cross-section (FIB-96 with deck), a span length of 175 ft, $d_{pb} = d_{pu}$, and a compressive concrete strength of 8.5 ksi. Prestressing reinforcement consisted of Grade 270 strands.

192
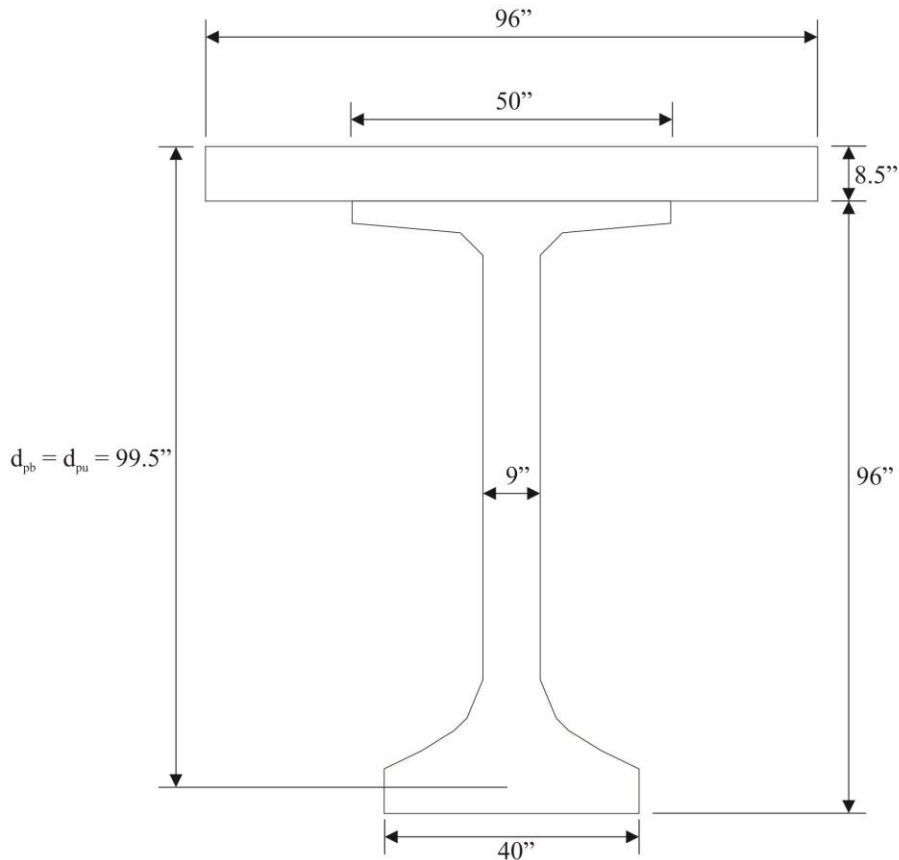
Figure 11.2 Cross-sectional dimensions: Modified FIB-96

Figure 11.3 (a) shows the required minimum ratio of bonded prestressing reinforcement for varying U/T ratios. The purpose of this minimum reinforcement is to minimize the possibility of a bonded strand rupture before moment capacity is reached; consequently, it is envisioned that this provision would apply to bonded prestressing reinforcement only and not deformed mild reinforcement. As indicated in Figure 11.3 (a), no bonded prestressing reinforcement is required in fully-unbonded beams (U/T=1). Conversely, a fully-bonded FIB-96 (U/T=0) would require an area of 14.6 in^2 of bonded prestressing reinforcement to minimize the possibility of strand rupture, which is equivalent to approximately 68 prestressing strands (0.6-in. diameter). The minimum bonded reinforcement required to prevent bonded strand rupture is significantly higher than the amount of reinforcement required to satisfy $M_r \geq M_{cr}$ (AASHTO-LRFD 5.6.3.3); in the case of a fully-bonded condition, the proposed requirement is nearly four times that of the current LRFD requirement. Hence, it is recommended that design implications be evaluated prior to implementation of the $\rho_{pb,min}$ minimum reinforcement requirement.

Figure 11.3 (b) presents the nominal moment capacity (normalized by the nominal moment capacity of a corresponding fully-bonded beam) for varying U/T ratios, while maintaining the same total amount of strands (bonded + unbonded) in all cases. For illustrative purposes, the total amount of prestressing strands was selected to be 68 (minimum amount required for a fully-bonded beam). Figure 11.3 (b) shows that increasing U/T ratios result in a reduction in nominal moment capacity when compared to fully-bonded members with the same total amount of steel reinforcement as previously discussed. Furthermore, it is important to consider that a greater amount of total reinforcement would be required as the U/T ratio increases in order to both maintain the same nominal moment capacity (relative to a fully-bonded beam) and prevent bonded strand rupture.
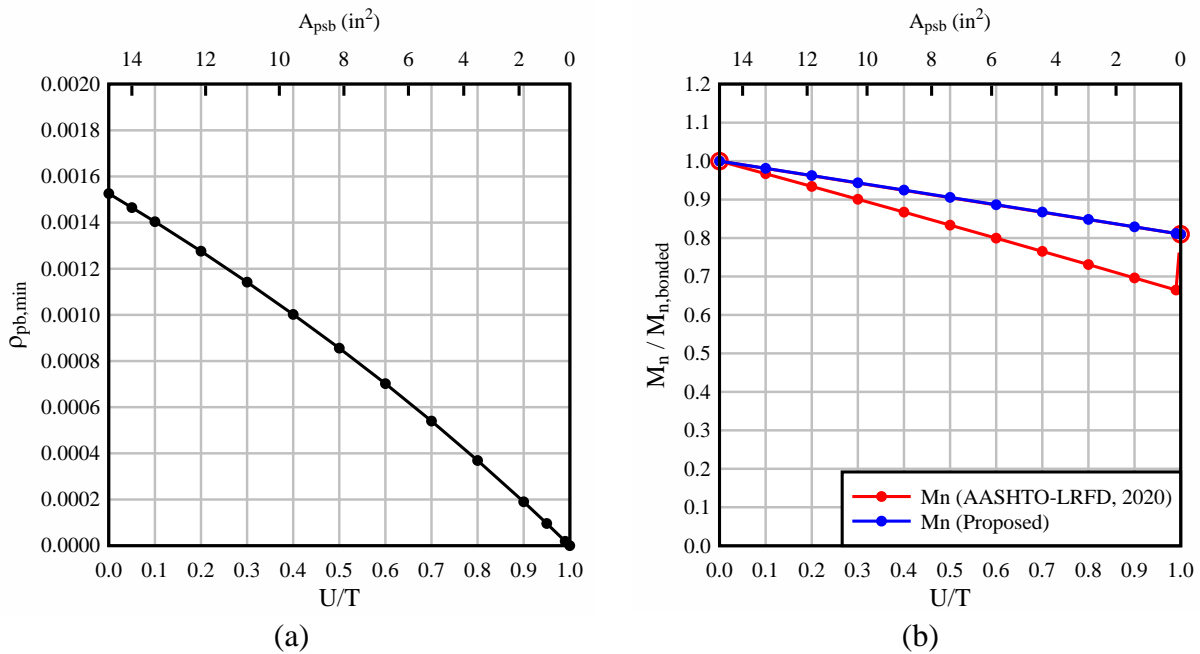
Figure 11.3 Design cases for FIB-96 (with deck) with f'c = 8.5 ksi: (a) required minimum ratio of bonded prestressing reinforcement to prevent bonded strand rupture as a function of U/T ratio and area of bonded prestressing reinforcement for beams; (b) normalized nominal moment capacity as a function of U/T ratio and area of bonded prestressing reinforcement for beams with a total (bonded + unbonded) of 68 prestressing strands

11.4 Concluding remarks

Based on the collected data from experimental work and finite element modeling, flexural design provisions for prestressed concrete elements containing mixed reinforcement were developed. Implementation of these provisions should consider the following:

- Using AASHTO (2020) design provisions to compute flexural capacity of members with mixed reinforcement provided conservative results when compared to both experimental and finite element flexural strengths determined as part of this study; in some cases, however, the AASHTO results could be viewed as overly conservative and empirical design provisions were developed based on the results of this research.

- The proposed design provisions include the use of the current LRFD ϕ factors for fully-bonded (U/T=0, ϕ=1.0) and fully-unbonded (U/T=1, ϕ=0.9) boundaries and use a step function to adjust ϕ at U/T = 0.5. The transition point of U/T = 0.5 was chosen without the benefit of a reliability analysis. Consequently, some engineering judgment will be required if the proposed provisions are implemented.

- For low U/T, the minimum bonded prestressing reinforcement ($\rho_{pb,min}$) required to prevent bonded strand rupture is significantly higher than the amount of reinforcement required to satisfy $M_r \geq M_{cr}$ (AASHTO-LRFD 5.6.3.3). The derivation of $\rho_{pb,min}$ theoretically applies over the full range of U/T. The present study, however, focused primarily on the evaluation of beam cases with an intermediate range of U/T ratios (e.g. U/T = 0.4 to 0.7), which is where strand rupture was observed in laboratory testing. An extended parametric study of design scenarios is recommended to further evaluate the implications of a minimum bonded prestressing reinforcement requirement, and to ensure that the $\rho_{pb,min}$ requirement may be suitably applied.

- The $\rho_{pb,min}$ requirement developed in this research is intended to apply to nominal moment strength under full service-load conditions. Bonded prestressing strands provided for other reasons such as fabrication or transportation purposes can be ignored when computing the minimum bonded prestressing reinforcement requirement.

- If present, mild steel reinforcement will reduce $\rho_{pb,min}$ and reduce the area of bonded prestressed reinforcement required to prevent strand rupture. No minimum amount of mild steel reinforcement, however, is required.

REFERENCES

AASHTO (American Association of State Highway and Transportation Officials). (1994). *AASHTO-LRFD Bridge Design Specifications (1st edition).* American Association of State Highway and Transportation Officials, Washington, D.C.

AASHTO. (2014a). *AASHTO-LRFD Bridge Construction Specifications (3rd edition with 2014 interim revisions).* American Association of State Highway and Transportation Officials, Washington, D.C.

AASHTO. (2014b). *AASHTO-LRFD Bridge Design Specifications (6th edition with 2014 interim revisions).* American Association of State Highway and Transportation Officials, Washington, D.C.

AASHTO. (2016). *AASHTO-LRFD Bridge Design Specifications (6th edition with 2016 interim revisions).* American Association of State Highway and Transportation Officials, Washington, D.C.

AASHTO. (2020). *AASHTO-LRFD Bridge Design Specifications (9th edition).* American Association of State Highway and Transportation Officials, Washington, D.C.

Abdullah, A. B. M., Rice, J. A., Hamilton, H. R., Consolazio, G. R. (2016). "An investigation on stressing and breakage response of a prestressing strand using an efficient finite element model". *Engineering Structures*, 123, 213-224.

ACI (American Concrete Institute). (2016) *Guide to estimating prestress losses (ACI PRC-423.10-16).* American Concrete Institute, Farmington Hills, MI.

ACI. (2019). *Building Code Requirements for Structural Concrete and Commentary (ACI 318R-19).* American Concrete Institute, Farmington Hills, MI.

Alkhairi, F. M. and Naaman, A. E., (1993). "Analysis of beams prestressed with unbonded internal or external tendons". *Journal of Structural Engineering*, 119(9), 2680-2700.

Alqam, M., Alkhairi, F., and Naaman, A. (2020). "An improved methodology for the prediction of the stress at ultimate in unbonded internal and external steel tendons". *Arabian Journal for Science and Engineering*, 45(10), 7915-7954.

Arab, A., Badie, S., and Manzari, M. (2011). "A methodological approach for finite element modeling of pretensioned concrete members at the release of pretensioning". *Engineering Structures*, 33(6), 1918-1929.

AS 5100.5-2004 (2004). *Australian Standard, Bridge Design Part 5: Concrete*. Standards International Ltd., Sydney, Australia.

Ayoub, A. and Filippou, F. (2010). "Finite-element model for pretensioned prestressed concrete girders". *Journal of Structural Engineering*, 136(4), 401-409.

Brenkus, N. R. (2016). "Ultimate strength of post-tensioned girders with mixed bonded and unbonded prestressing" (dissertation). University of Florida, Gainesville, FL.

Brenkus, N. R., Abdullah, A. B. M., Bhatia, R., Skelton, D., Rice, J. A., Hamilton, H. R. (2017a) "Replaceable Unbonded Tendons for Post-Tensioned Bridges". FDOT Research Report No. BDV31-977-15, University of Florida, Gainesville, FL.

Brenkus, N. R., Hamilton, H. R., and Potter, W. A. (2017b) "Flexural strength and hinge behavior of internally post-tensioned members with mixed bonded and unbonded tendons". *PTI Journal*, 13(2), 5-18.

Brenkus, N. R., Bhatia, R., Potter, W. A., and Hamilton, H. R. (2018). "Flexible filler mock-up injections of bridge post-tensioning tendons". *PCI Journal*, 63(3), 65-76.

Burns, N. H. and Hemakom, R. (1985). "Test of Post-Tensioned Flat Plate with Banded Tendons." *Journal of Structural Engineering*, ASCE, 111(9), 1899-1915.

CSA-S6 (2014). *Canadian Highway Bridge Design Code S6-14*. Mississauga, Ontario, Canada.

Cox, W. R. (2017). "Implementation of Flexible Filler for Post-Tensioning Corrosion Protection in Florida". *Aspire – The Concrete Bridge Magazine*, (Winter 2017), 36.

DSI. (DYWIDAG-Systems International) (2000). *Vacuum Grouting successfully introduced as a new standard in the USA*.

El-Mezaini, N., Balkaya, C., and Çitipitioğlu, E. (1991). "Analysis of Frames with Nonprismatic Members". *Journal of Structural Engineering*, ASCE, 117(6), 1573-1592.

EN 1992-1-1:2004 (2004). *Eurocode 2: Design of concrete structures – Part 1-1: General rules and rules for buildings*. European Committee for Standardization, Brussels, Belgium.

EN 1992-2:2005 (2005). *Eurocode 2: Design of concrete structures – Part 2: Concrete bridges – Design and detailing rules*. European Committee for Standardization, Brussels, Belgium.

FDOT. (Florida Department of Transportation) (2002). "New Direction for Florida Post-Tensioned Bridges". *Florida Post-Tensioned Segmental Bridges*, FDOT, (3), Tallahassee, FL.

FDOT. (2016) *Post-tensioning tendon profiles*. Index 21801, Tallahassee, FL.

FDOT. (2017) *Structures Design Bulletin 17-08*. Tallahassee, FL.

Finley Engineering Group. (2008). *SR 79 West Bay Bridge.* Bay County, FL.

Finley Engineering Group. (2015). *Palmetto Section 5 SR-826/SR-836 Interchange.* Miami, FL.

Foutch, D. A., Gamble, W. L., and Sunidja, H. (1990) "Tests of Post-Tensioned Concrete Slab-Edge Column Connections". *ACI Structural Journal*, 87(2), 167-179.

Gauvreau, D. P. (1993) "Ultimate Limit State of Concrete Girders Prestressed with Unbonded Tendons," Institute of Structural Engineering (IBK) - ETH Zürich, Birkhäuser, Basel.

Gerber, L. L., and Burns, N. H. (1971). "Ultimate Strength Tests of Post-Tensioned Flat Plates." *PCI Journal*, 16(6), 40-58.

Han, Z. and Consolazio, G.R. (2018). "Analysis of Concrete Floodwall Failure due to Impacts from Runaway Barges". University of Florida, Gainesville, FL.

Harajli, M. H., Mabsout, M. E. and Al-Hajj, J. A. (2002) "Response of externally post-tensioned continuous members". *ACI Structural Journal*, 99(5), 671-680.

Harajli, M. H. (2006). "On the Stress in Unbonded Tendons at Ultimate: Critical Assessment and Proposed Changes," *ACI Structural Journal*, 103(6), 803- 812.

Harajli, M. H. (2012). "Tendon stress at ultimate in continuous unbonded post-tensioned members: Proposed modification of ACI 318, eq. (18-4) and (18-5)". *ACI Structural Journal*, 109(2), 183-192.

Huang, Y. (2012) "Finite element method for post-tensioned prestressed concrete structures". University of Oklahoma, Norman, OK.

Johnson, K. L. (1987). *Contact mechanics*. Cambridge University Press, Cambridge, UK.

JSCE. (Japan Society of Civil Engineers) (2007). *Standard Specifications for Concrete Structures – 2007 "Design"*. JSCE Guidelines for Concrete, Tokyo.

Kang, Y.-J., and Scordelis, A. C. (1980). "Nonlinear Analysis of Prestressed Concrete Frames". *Journal of Structural Engineering*, 106(2), 445-462.

Kheyroddin, A., and Naderpour, H. (2007). "Plastic Hinge Rotation Capacity of Reinforced Concrete Beams". *International Journal of Civil Engineering*, 5(1), 30-47.

LSTC (Livermore Software Technology Corporation). (2018). *LS-DYNA Keyword User's Manual (LS-DYNA R11)*. Livermore Software Technology Corporation. Livermore, CA.

MacGregor, R. J. G., Kreger, M. E., and Breen, J. E. (1989). "Strength and Ductility of a Three-span Externally Post-Tensioned Segmental Box Girder Bridge Model". Center for Transportation Research Report No. 365-3F, The University of Texas at Austin, 323.

Mast, R. F. (1992). "Unified design provisions for reinforced and prestressed concrete flexural and compression members". *ACI Journal*, 89(2), 185-199.

Mattock, A. H., Yamazaki, J., and Kattula, B. T. (1971). "Comparative Study of Prestressed Concrete Beams, With and Without Bond". *ACI Journal*, 68(2), 116-125.

Megally, S. H., Garg, M., Seibel, F., Dowell, R. K. (2001). "Seismic Performance of Precast Segmental Bridge Superstructures". Structural Systems Research Project, Research Report No. SSRP–2001/24, University of California, San Diego.

Mojtahedi S. and Gamble W.L. (1978). "Ultimate Steel Stresses in Unbonded Prestressed Concrete". *Journal of the Structural Division, ASCE*, 104(7), 1159-1165.

Murray, Y.D. (2007). *User's Manual for LS-DYNA Concrete Material Model 159*. FHWA-HRT-05-062, Federal Highway Administration, McLean, VA.

Naaman, A. E. (2012). *Prestressed Concrete Analysis and Design: Fundamentals*. 3rd Edition, Techno Press 3000, Ann Arbor, MI.

Naaman, A. E., and Alkhairi, F. M. (1991a). "Stress at Ultimate in Unbonded Prestressing Tendons—Part I: Evaluation of the State-of-the-Art". *ACI Structural Journal*, 89(5), 641-651.

Naaman, A. E., and Alkhairi, F. M. (1991b). "Stress at Ultimate in Unbonded Prestressing Tendons—Part II: Proposed Methodology". *ACI Structural Journal*, 89(6), 683-692.

Naaman, A. E., Burns, N., French, C., Gamble, W. L., and Mattock, A. H. (2002). "Stresses in Unbonded Prestressing Tendons at Ultimate: Recommendation". *ACI Structural Journal*, 99(4), 518-529.

Nikolic, Z., and Mihanovic, A. (1997). "Non-Linear Finite Element Analysis of Post-Tensioned Concrete Structures". *Engineering Computations*, 14(5), 509-528.

Nowak, A. S., and Iatsko, O. (2017) "Revised load and resistance factors for the AASHTO LRFD Bridge Design Specifications". *PCI Journal*, 62(3), 46-58.

Okumus, P., Oliva, M., and Becker, S. (2012). "Nonlinear finite element modeling of cracking at ends of pretensioned bridge girders". *Engineering Structures*, 40, 267-275.

Ozkul, O., Nassif, H., Tanchan, P., and Harajli, M. (2008) "Rational Approach for Predicting Stress in Beams with Unbonded Tendons". *ACI Structural Journal*, 105(3), 338-347.

Parsons Brinckerhoff, Inc. (2015). *Review of AASHTO LRFD Bridge Design Specifications and ACI-318 unbonded PT provisions for FDOT implementation*. FDOT, Tampa, FL.

PTI. (Post-tensioning Institute) (2015). "Selection of Filler Material for Multistrand PT Tendons". *PTI Technical Notes*, (19), 1-5.

PTI. (2016). *Post-tensioning Manual*. 6th Edition, Post-tensioning Institute, Farmington Hills, MI.

Roberts-Wollmann, C. L., Kreger, M. E., Rogowsky, D. M., and Breen, J. E. (2005). "Stresses in External Tendons at Ultimate". *ACI Structural Journal*, 102(2), 206-213.

SDG. (Structures Design Guidelines) (2021). *Structures Manual, Volume 1*. Florida Department of Transportation, Tallahassee, FL.

Tam, A., and Pannell, F.N. (1976). "Ultimate Moment Resistance of Unbonded Partially Prestressed Reinforced Concrete Beams". *Magazine of Concrete Research*, 28(97), 203-208.

Van Greunen, J., and Scordelis, A. C. (1983). "Nonlinear Analysis of Prestressed Concrete Slabs". *Journal of Structural Engineering*, 109(7), 1742-1760.

Vecchio, F. J., Gauvreau, P., and Liu, K. (2006). "Modeling of Unbonded Post-Tensioned Concrete Beams Critical in Shear". *ACI Structural Journal*, 103(1), 57-64.

Vector Corrosion Technologies (2014). *Post-Tech PTI Impregnation System*. Winnipeg.

Virlogeux, M. (1983). "La Precontra inte Exterieure". *Annales de l'Institut Technique du Bâtiment et des Travaux Publics*.

VSL International Ltd. (2009). *Bridge Construction Partner*. Labège.

Yapar, O., Basu, P. K., and Nordendale, N. (2015). "Accurate finite element modeling of pretensioned prestressed concrete beams". *Engineering Structures*, 101, 163-178.

APPENDIX A
Fabrication drawings

Fabrication drawings for the experimental beam specimens (precast beams, end blocks, and cast-in-place beam) are provided in the following pages.

General Notes:

FDOT Research
Flexural capacity of concrete elements with unbonded and bonded prestressing
BDV31-977-93

University of Florida
Dept. of Civil and Coastal Engineering
787.201.6874

Design Drawings
General Notes and Specifications
Sheet 1 of 42

1

Materials

Precast section (SS-1, SS-2, SS-3, SS-4, NB-1, NB-2, NB-3):
Concrete shall be FDOT class VI
$f'c$ (28 day) = 8500 psi
fci (release) = 6000 ksi

End blocks for beam specimens SS-1, SS-2, SS-3, SS-4, NB-1:
Concrete shall be FDOT class V
$f'c$ (28 day) = 6500 psi

End blocks for beam specimens NB-2 and NB-3:
Concrete shall be FDOT class VI
$f'c$ (28 day) = 8500 psi

Beam specimen SS-5 (CIP):
Concrete shall be FDOT class V
$f'c$ (28 day) = 6500 psi

Mild reinforcement shall be ASTM A615 grade 60 (fy 60 ksi)
Prestressing strand shall be ASTM A416 270 ksi Lo-Lax

Fabricator shall provide data sheets from concrete, strand, and rebar suppliers.

Fabricator shall provide report of strand stressing.

Fabricator shall provide material samples to UF/FDOT as follows:

(8) 4" dia x 8" cylinders from each concrete batch:
(4) cylinders cure with girder, (4) lab cure
(3) 36" pieces of prestressing strands free from sand, dust, etc.
Samples taken directly off of reel.
(3) 36" pieces of each size/batch of rebar.

Beam Specimen	Pretensioned strands [Force/strand (kip)]		Post-tensioned tendons		
	Bottom	Top	No. tendons	No. strands	Jacking force (kip)
SS-1	10 [45.25]	2 [10]	1	6	264.0
SS-2	8 [45.25]	2 [10]	1	10	439.0
SS-3	6 [45.25]	2 [10]	1	4	176.0
SS-4	4 [45.25]	2 [10]	1	6	264.0
SS-5	--	--	1	12	527.0
NB-1	2 [43.75]	12 [43.75]	1	12	527.0
NB-2	2 [43.75]	10 [43.75]	2	18 (9/tendon)	395.0
NB-3	2 [43.75]	6 [43.75]	2	22 (11/tendon)	483.0

Research Instrumentation

UF/FDOT will provide and install research instrumentation in each of the concrete girders in coordination with the fabricator. Internal instrumentation will mounted to prestressing strands and rebar prior to casting concrete.

Rebar receiving instrumentation are noted with an "i" on the plans. These pieces shall be provided to UF for installation of instrumentation prior to placement of the pieces in the girder.

UF/FDOT will record data before and after release of prestressing. Data will also be recorded during lifting, storing, and shipping of girders.

Other

Specimens SS-1, SS-2, SS-3, SS-4, NB-1, NB-2, NB-3 with concrete decks were fabricated at a precast plant. Specimen SS-5 and all end blocks will be fabricated at the FDOT Structures Research Center in Tallahassee, FL.

Fabricator will transport girders from the fabrication facility to:
FDOT Structures Research Center
2007 East Paul Dirac Drive
Tallahassee, FL 32310

Delivery time to be coordinated with FDOT.

Unless otherwise noted, fabrication of girders shall follow typical procedures and practices for FDOT bridge girders.

HDPE ducts shall be sealed after installation.

Cover beams with heavy tarp during curing.

Roughen top of beams prior cast of deck.

Inspections will be provided by on-site FDOT personal and by UF.

No patch-work or finishing is required.

E E

D A C B

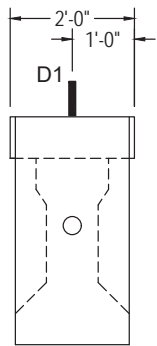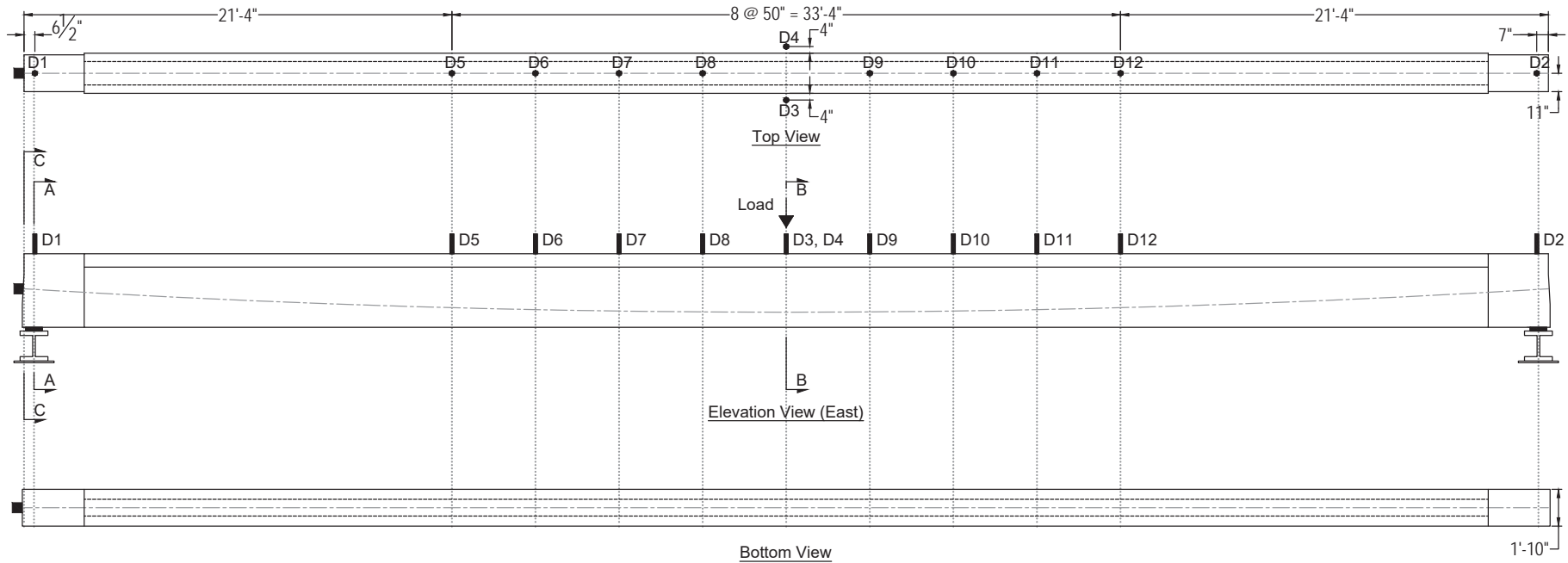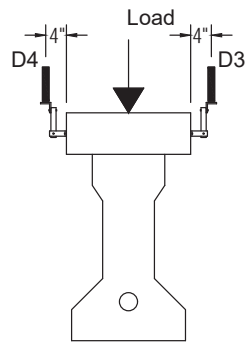Spacing Bars '4K' 2$\frac{3}{4}$"

'4K' (12 sp) @ 3" = 3'-0"

'4K' (63 sp) @ 6" = 31'-6"

6$\frac{1}{2}$"

'4K' (63 sp) @ 6" = 31'-6"

'4K' (12 sp) @ 3" = 3'-0"

2$\frac{3}{4}$"

Spacing '5Z' 3$\frac{3}{8}$"

'5Z' (3 sp) @ 3" = 9"

'4B'

CIP end block

CIP end block

'4A'

'4L'

Construction Joint

V1, V2

CL Duct
R = 613' - 0"
HDPE duct shall be sealed after installation

'3D' (7 sp) @ 6" = 3'-6"

'3D' (4 sp) @ 3" = 1'-0"

Spacing Bars '3D' 2$\frac{1}{8}$"

'3D' (7 sp) @ 6" = 3'-6"

'3D' (4 sp) @ 3" = 1'-0"

2$\frac{1}{8}$"

D A C B

70'-0" overall length
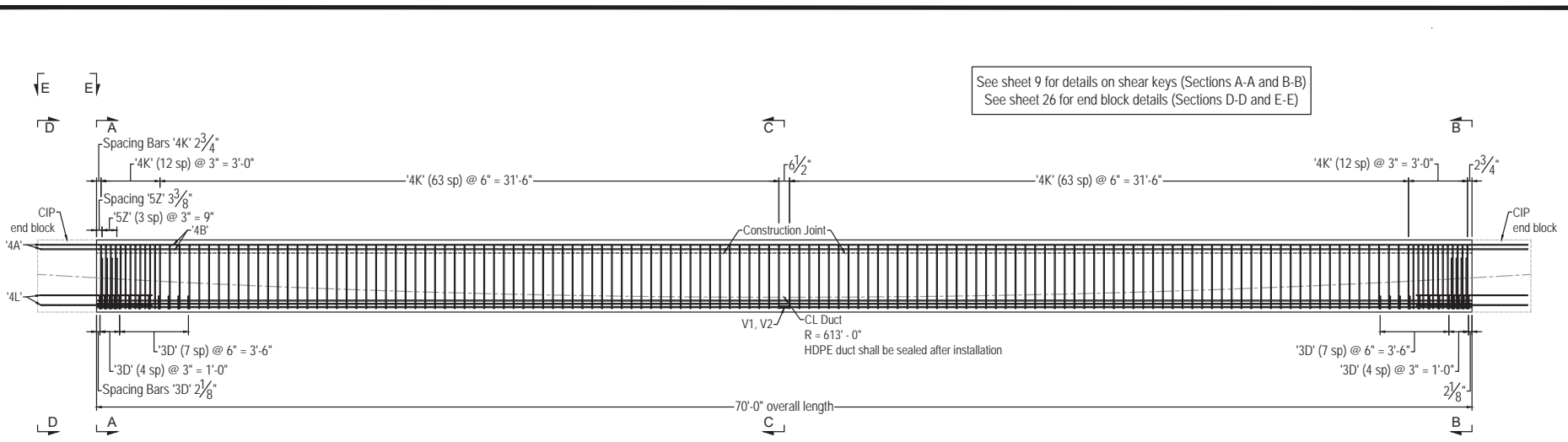
Elevation: SS-1
Flanges not shown for clarity
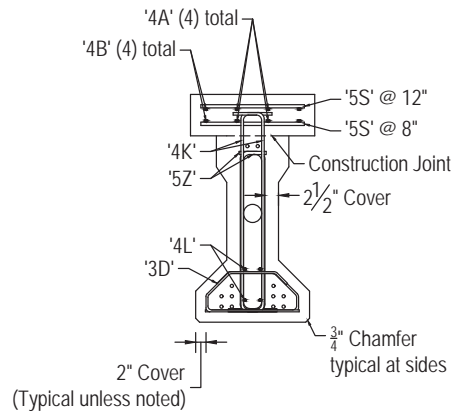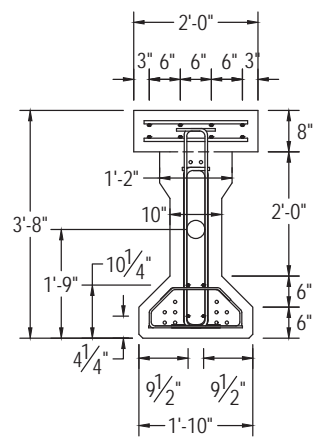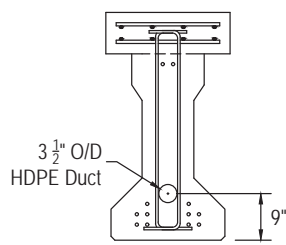
'4A' (4) total

'4B' (4) total

'5S' @ 12"

'5S' @ 8"

'4K'

'5Z'

Construction Joint

2$\frac{1}{2}$" Cover

'4L'

'3D'

$\frac{3}{4}$" Chamfer typical at sides

2" Cover
(Typical unless noted)

Cross Section A - A

2'-0"

3" 6" 6" 6" 3"

8"

1'-2"

2'-0"

3'-8"

10"

6"

1'-9"

10$\frac{1}{4}$"

6"

4$\frac{1}{4}$"

9$\frac{1}{2}$" 9$\frac{1}{2}$"

1'-10"

Cross Section B - B

3 $\frac{1}{2}$" O/D
HDPE Duct

9"

Cross Section C - C

All reinforcement sizes and locations
and quantities are typical each end
unless noted otherwise

See sheet 12 for information on
prestressing and detensioning

See sheet 19 for information on rebar
schedule for precast components

See sheet 33 for information on rebar
schedule for end blocks

SS-1 cross-section = Modified
AASHTO Type II

See sheet 9 for details on shear keys (Sections A-A and B-B)
See sheet 27 for end block details (Sections D-D and E-E)

Spacing Bars '4K' 2¾"
'4K' (12 sp) @ 3" = 3'-0"
'4K' (63 sp) @ 6" = 31'-6"
6½"
'4K' (63 sp) @ 6" = 31'-6"
'4K' (12 sp) @ 3" = 3'-0"
2¾"

Spacing '5Z' 3⅜"
'5Z' (3 sp) @ 3" = 9"
'4B'

CIP end block
'4A'

Construction Joint

CIP end block

'4L'

V1, V2
CL Duct
R = 613' - 0"
HDPE duct shall be sealed after installation

'3D' (7 sp) @ 6" = 3'-6"
'3D' (4 sp) @ 3" = 1'-0"
Spacing Bars '3D' 2⅛"

'3D' (7 sp) @ 6" = 3'-6"
'3D' (4 sp) @ 3" = 1'-0"
2⅛"

70'-0" overall length
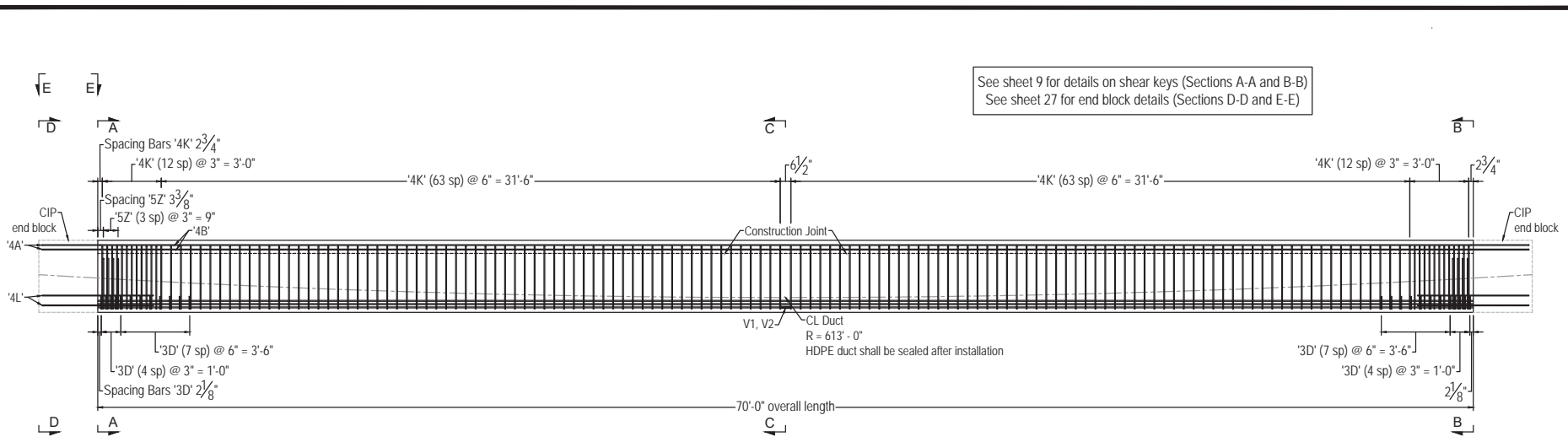
Elevation: SS-2
Flanges not shown for clarity
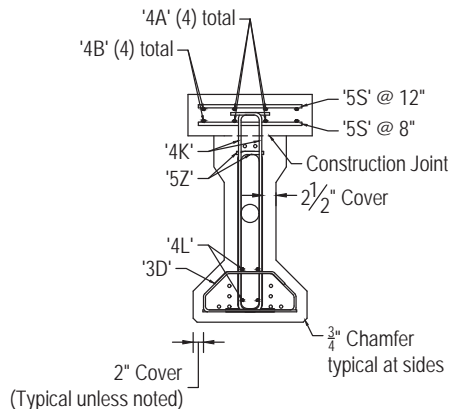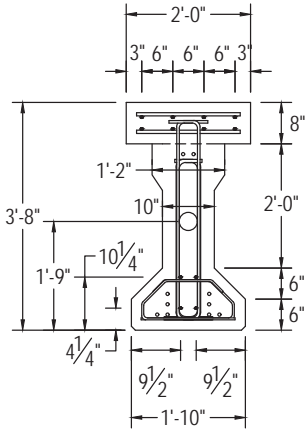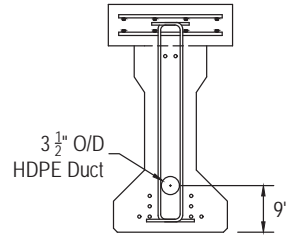
'4A' (4) total
'4B' (4) total

'5S' @ 12"
'5S' @ 8"
'4K'
'5Z'
Construction Joint
2½" Cover

'4L'
'3D'
¾" Chamfer typical at sides

2" Cover
(Typical unless noted)

Cross Section A - A

2'-0"
3" 6" 6" 6" 3"

8"
1'-2"
2'-0"
10"
3'-8"
10¼"
1'-9"
6"
6"
4¼"
9½" 9½"
1'-10"

Cross Section B - B

3 ½" O/D
HDPE Duct
9"

Cross Section C - C

All reinforcement sizes and locations
and quantities are typical each end
unless noted otherwise

See sheet 13 for information on
prestressing and detensioning

See sheet 20 for information on rebar
schedule for precast components

See sheet 34 for information on rebar
schedule for end blocks

SS-2 cross-section = Modified
AASHTO Type II

3
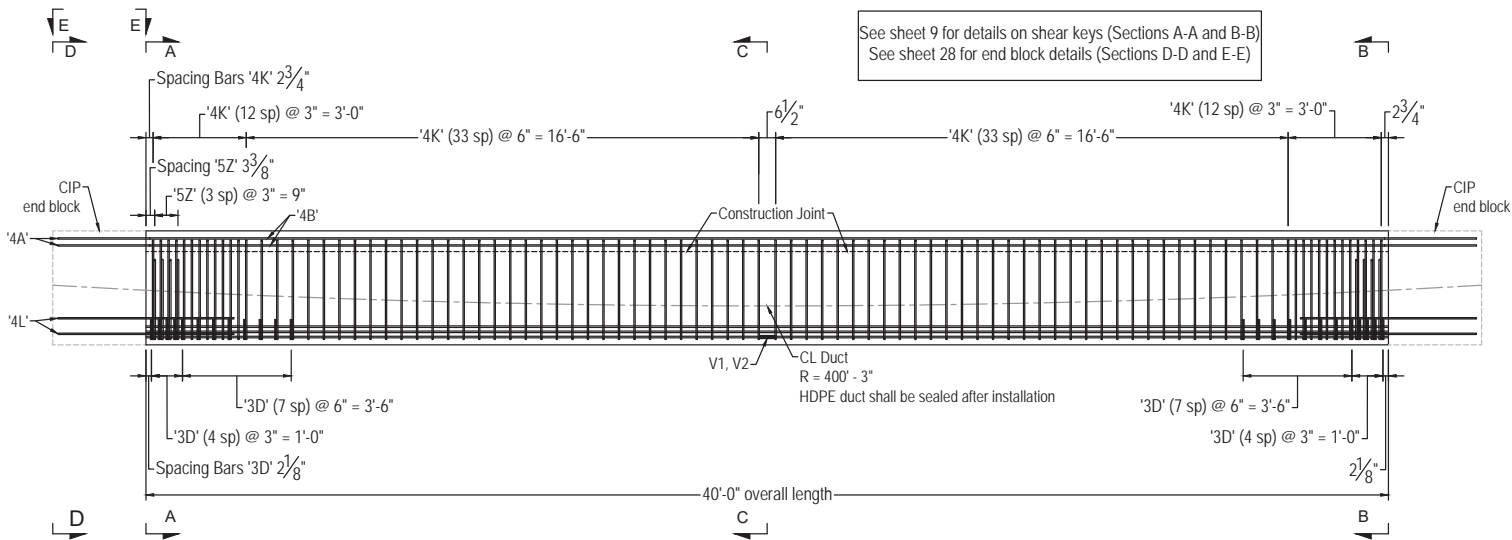
See sheet 9 for details on shear keys (Sections A-A and B-B)
See sheet 28 for end block details (Sections D-D and E-E)

Spacing Bars '4K' 2¾"

'4K' (12 sp) @ 3" = 3'-0"

'4K' (33 sp) @ 6" = 16'-6"

6½"

'4K' (33 sp) @ 6" = 16'-6"

'4K' (12 sp) @ 3" = 3'-0"

2¾"

Spacing '5Z' 3⅜"

'5Z' (3 sp) @ 3" = 9"

'4B'

CIP end block

CIP end block

'4A'

'4L'

V1, V2

Construction Joint

CL Duct
R = 400' - 3"
HDPE duct shall be sealed after installation

'3D' (7 sp) @ 6" = 3'-6"

'3D' (4 sp) @ 3" = 1'-0"

Spacing Bars '3D' 2⅛"

'3D' (7 sp) @ 6" = 3'-6"

'3D' (4 sp) @ 3" = 1'-0"

2⅛"

40'-0" overall length

Elevation: SS-3
Flanges not shown for clarity

'4A' (4) total

'4B' (4) total

'5S' @ 12"

'5S' @ 8"

'4K'

'5Z'

Construction Joint

2½" Cover

'4L'

'3D'

¾" Chamfer
typical at sides

2" Cover
(Typical unless noted)

Cross Section A - A

2'-0"

3" 6" 6" 6" 3"

8"

1'-2"

2'-0"

3'-8"

10"

1'-9"

6"

10¼"

6"

4¼"

9½" 9½"

1'-10"

Cross Section B - B

3½" O/D
HDPE Duct

1'-3"

Cross Section C - C

All reinforcement sizes and locations
and quantities are typical each end
unless noted otherwise

See sheet 14 for information on
prestressing and detensioning

See sheet 21 for information on rebar
schedule for precast components

See sheet 35 for information on rebar
schedule for end blocks

SS-3 cross-section = Modified
AASHTO Type II

Spacing Bars '4K' 2¾"

'4K' (12 sp) @ 3" = 3'-0"

'4K' (33 sp) @ 6" = 16'-6"

6½"

'4K' (33 sp) @ 6" = 16'-6"

'4K' (12 sp) @ 3" = 3'-0"

2¾"

Spacing '5Z' 3⅜"

CIP end block

'5Z' (3 sp) @ 3" = 9"

'4B'

Construction Joint

CIP end block

'4A'

'4L'

V1, V2

CL Duct
R = 400' - 3"
HDPE duct shall be sealed after installation

'3D' (7 sp) @ 6" = 3'-6"

'3D' (4 sp) @ 3" = 1'-0"

Spacing Bars '3D' 2⅛"

'3D' (7 sp) @ 6" = 3'-6"

'3D' (4 sp) @ 3" = 1'-0"

2⅛"

40'-0" overall length
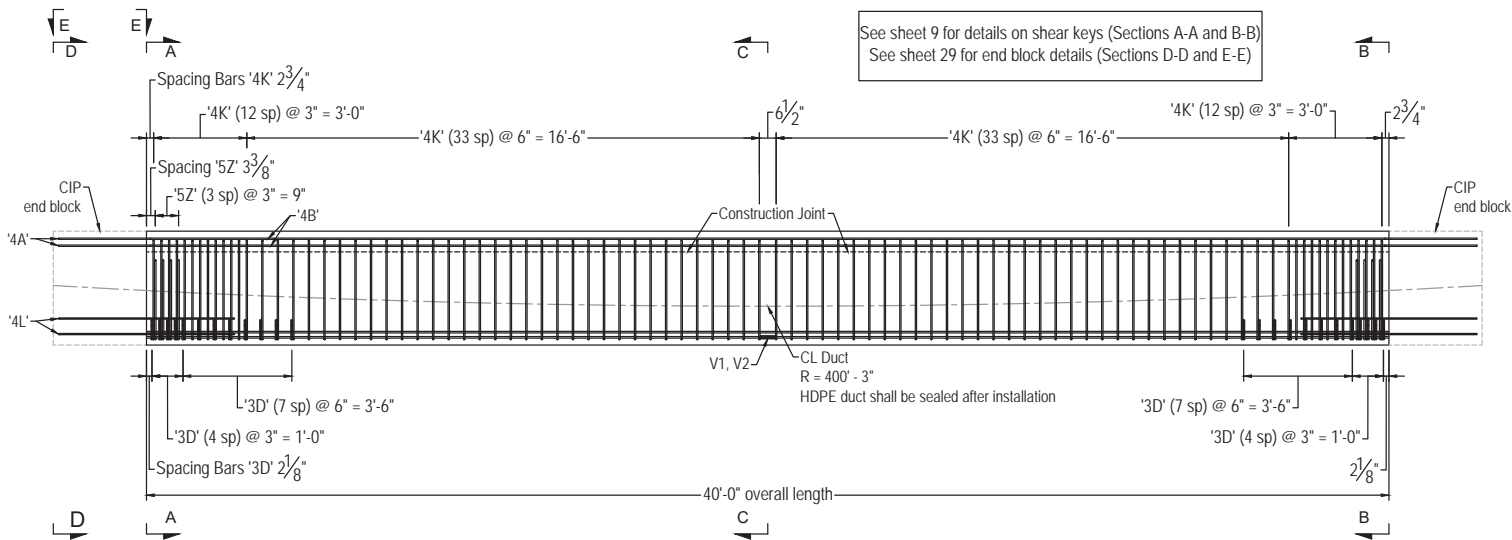
Elevation: SS-4
Flanges not shown for clarity

'4A' (4) total

'4B' (4) total

'5S' @ 12"

'5S' @ 8"

'4K'

'5Z'

Construction Joint

2½" Cover

'4L'

'3D'

¾" Chamfer typical at sides

2" Cover
(Typical unless noted)

Cross Section A - A

2'-0"

3" 6" 6" 6" 3"

8"

1'-2"

2'-0"

10"

3'-8"

6"

1'-9"

10¼"

6"

4¼"

9½"   9½"

1'-10"

Cross Section B - B

3½" O/D
HDPE Duct

1'-3"

Cross Section C - C

All reinforcement sizes and locations
and quantities are typical each end
unless noted otherwise

See sheet 15 for information on
prestressing and detensioning

See sheet 22 for information on rebar
schedule for precast components

See sheet 36 for information on rebar
schedule for end blocks

SS-4 cross-section = Modified
AASHTO Type II

5

206

Elevation: NB-1
Flanges not shown for clarity
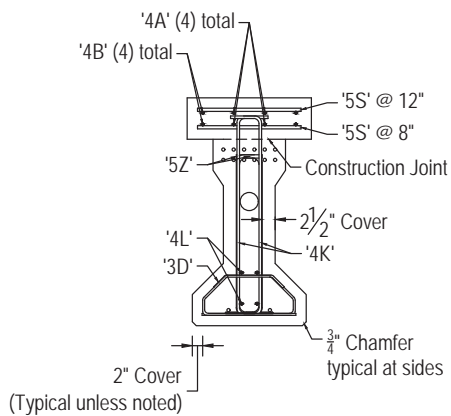
Cross Section A - A
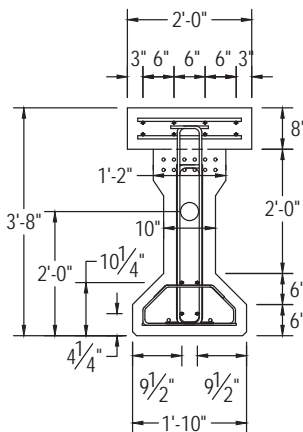
Cross Section B - B

Cross Section C - C

See sheet 10 for details on shear keys (Sections A-A and B-B)
See sheet 30 for end block details (Sections D-D and E-E)

Spacing Bars '4K' $2\frac{3}{4}$"
'4K' (12 sp) @ 3" = 3'-0"
'4K' (20 sp) @ 6" = 10'-0"
$6\frac{1}{2}$"
'4K' (20 sp) @ 6" = 10'-0"
'4K' (12 sp) @ 3" = 3'-0"
$2\frac{3}{4}$"

Spacing '5Z' $3\frac{3}{8}$"
'5Z' (3 sp) @ 3" = 9"
'4B'

CIP end block
CIP end block

'4A'
'4L'

RS1, RS8
RS2, RS9
RS3, RS10
RS4, RS11
RS5, RS12
RS6, RS13
RS7, RS14
Construction Joint

V1
V2

'3D' (7 sp) @ 6" = 3'-6"
'3D' (4 sp) @ 3" = 1'-0"
Spacing Bars '3D' $2\frac{1}{8}$"

CL Duct
R = 218' - 10 $\frac{7}{8}$"
HDPE duct shall be sealed after installation

'3D' (7 sp) @ 6" = 3'-6"
'3D' (4 sp) @ 3" = 1'-0"
$2\frac{1}{8}$"

27'-0" overall length

'4A' (4) total
'4B' (4) total
'5S' @ 12"
'5S' @ 8"
'5Z'
Construction Joint
'4L'
'3D'
'4K'
$2\frac{1}{2}$" Cover
$\frac{3}{4}$" Chamfer typical at sides
2" Cover (Typical unless noted)

2'-0"
3" 6" 6" 6" 3"
8"
1'-2"
2'-0"
3'-8"
10"
2'-0"
$10\frac{1}{4}$"
6"
6"
$4\frac{1}{4}$"
$9\frac{1}{2}$"
$9\frac{1}{2}$"
1'-10"

$3\frac{1}{2}$" O/D HDPE Duct
2'-5"

All reinforcement sizes and locations and quantities are typical each end unless noted otherwise

See sheet 16 for information on prestressing and detensioning

See sheet 23 for information on rebar schedule for precast components

See sheet 37 for information on rebar schedule for end blocks

NB-1 cross-section = Modified AASHTO Type II

See sheet 11 for details on shear keys (Sections A-A and B-B)
See sheet 31 for end block details (Sections D-D and E-E)

Spacing Bars '4K' 2¾"
'4K' (12 sp) @ 3" = 3'-0"
'4K' (20 sp) @ 6" = 10'-0"
6½"
'4K' (20 sp) @ 6" = 10'-0"
'4K' (12 sp) @ 3" = 3'-0"
2¾"

Spacing '5Z' 3⅜"
'5Z' (3 sp) @ 3" = 9"
'4B'

CIP end block
CIP end block

RS1, RS8   RS2, RS9   RS3, RS10   RS4, RS11   RS5, RS12   RS6, RS13   RS7, RS14
Construction Joint

'4A'
'4L'

V1   V2

'3D' (7 sp) @ 6" = 3'-6"
'3D' (4 sp) @ 3" = 1'-0"
Spacing Bars '3D' 2⅛"

CL Duct 1
CL Duct 2
R = 182' - 6"
HDPE ducts shall be sealed after installation

'3D' (7 sp) @ 6" = 3'-6"
'3D' (4 sp) @ 3" = 1'-0"
2⅛"

27'-0" overall length

Elevation: NB-2
Flanges not shown for clarity
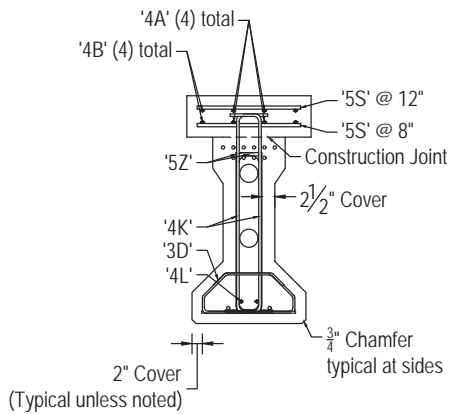
'4A' (4) total
'4B' (4) total
'5S' @ 12"
'5S' @ 8"
'5Z'
Construction Joint
'4K'
2½" Cover
'3D'
'4L'
¾" Chamfer typical at sides
2" Cover
(Typical unless noted)

Cross Section A - A

2'-0"
3" 6" 6" 6" 3"
8"
1'-2"
2'-0"
10"
3'-8"
2'-5"
1'-4½"
4¼"
9½" 9½"
1'-10"

Cross Section B - B

3 ½" O/D
HDPE Duct 1
3 ½" O/D
HDPE Duct 2
1'-10½"
2'-5"

Cross Section C - C

All reinforcement sizes and locations
and quantities are typical each end
unless noted otherwise

See sheet 17 for information on
prestressing and detensioning

See sheet 24 for information on rebar
schedule for precast components

See sheet 38 for information on rebar
schedule for end blocks

NB-2 cross-section = Modified
AASHTO Type II

FDOT Research
Flexural capacity of concrete elements
with unbonded and bonded prestressing
BDV31-977-93

University of Florida
Dept. of Civil and Coastal Engineering
787.201.6874

Design Drawings
Specimen NB-2
Sheet 7 of 42

7

208

Spacing Bars '4K' 2¾"

'4K' (12 sp) @ 3" = 3'-0"

'4K' (20 sp) @ 6" = 10'-0"

6½"

'4K' (12 sp) @ 3" = 3'-0"

2¾"

Spacing '5Z' 3⅜"

CIP end block

'5Z' (3 sp) @ 3" = 9"

'4B'

RS1, RS8 RS2, RS9 RS3, RS10 RS4, RS11 RS5, RS12 RS6, RS13 RS7, RS14

Construction Joint

CIP end block

'4A'

'4L'

V1 V2

'3D' (7 sp) @ 6" = 3'-6"

'3D' (4 sp) @ 3" = 1'-0"

Spacing Bars '3D' 2⅛"

CL Duct 1

CL Duct 2
R = 182' - 6"
HDPE ducts shall be sealed after installation

'3D' (7 sp) @ 6" = 3'-6"

'3D' (4 sp) @ 3" = 1'-0"

2⅛"

27'-0" overall length

Elevation: NB-3
Flanges not shown for clarity
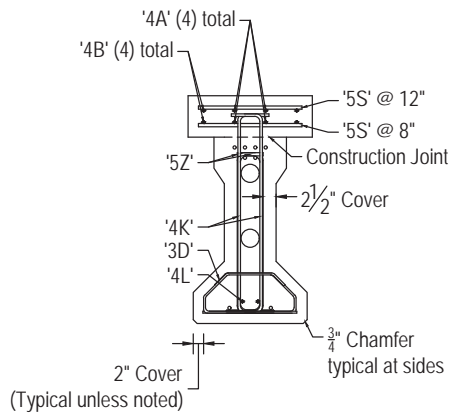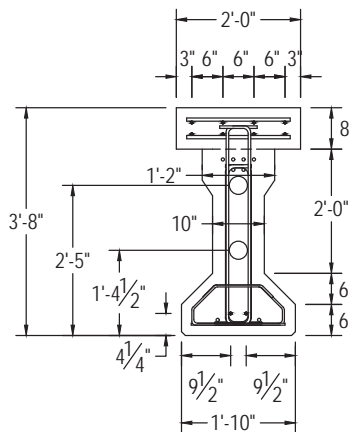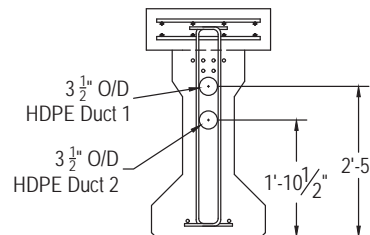
'4A' (4) total
'4B' (4) total

'5S' @ 12"
'5S' @ 8"
'5Z'
Construction Joint
2½" Cover
'4K'
'3D'
'4L'
¾" Chamfer typical at sides
2" Cover
(Typical unless noted)

Cross Section A - A

2'-0"
3" 6" 6" 6" 3"
8"
1'-2"
2'-0"
10"
3'-8"
2'-5"
1'-4½"
6"
6"
4¼"
9½" 9½"
1'-10"

Cross Section B - B

3½" O/D
HDPE Duct 1
3½" O/D
HDPE Duct 2
1'-10½"
2'-5"

Cross Section C - C

All reinforcement sizes and locations
and quantities are typical each end
unless noted otherwise

See sheet 18 for information on
prestressing and detensioning

See sheet 25 for information on rebar
schedule for precast components

See sheet 39 for information on rebar
schedule for end blocks

NB-3 cross-section = Modified
AASHTO Type II

8
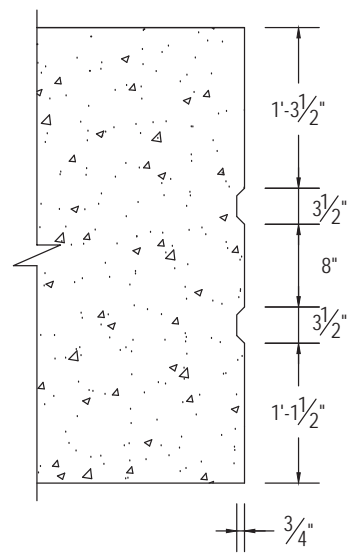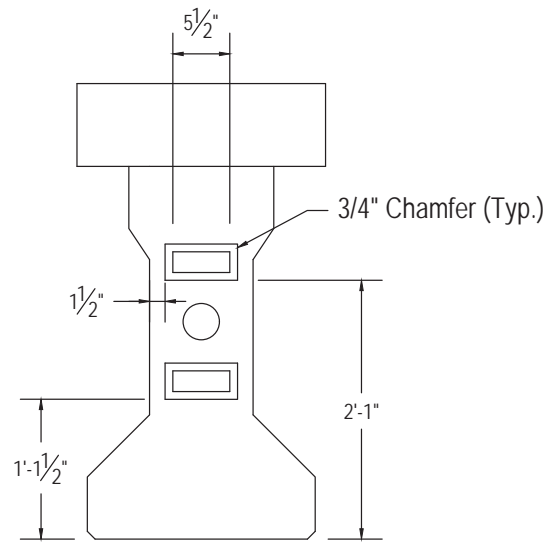
Shear Keys

Cross Sections A-A and B-B
(Refer to sheets 2, 3, 4, and 5)
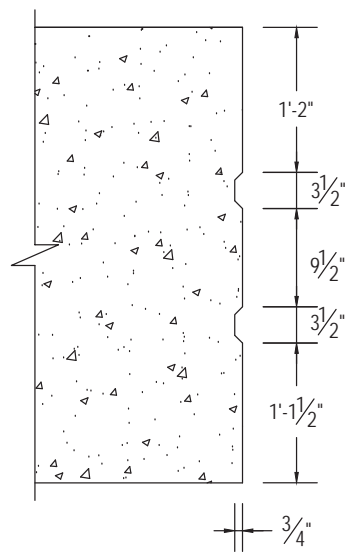
3/4" Chamfer (Typ.)

1'-3½"

3½"

8"

3½"

1'-1½"

3/4"

5½"

1½"

2'-1"

1'-1½"

Shear Keys

Cross Sections A-A and B-B
(Refer to sheet 6)

1'-2"

3½"

9½"

3½"

1'-1½"

¾"

5½"

3/4" Chamfer (Typ.)

1½"

2'-2½"

1'-1½"

1'-7$\frac{9}{16}$"

3$\frac{1}{2}$"

1'-0"

3$\frac{1}{2}$"

5$\frac{1}{2}$"

$\frac{3}{4}$"

Shear Keys

5$\frac{1}{2}$"

1$\frac{1}{2}$"

3/4" Chamfer (Typ.)

1'-9"

5$\frac{1}{2}$"
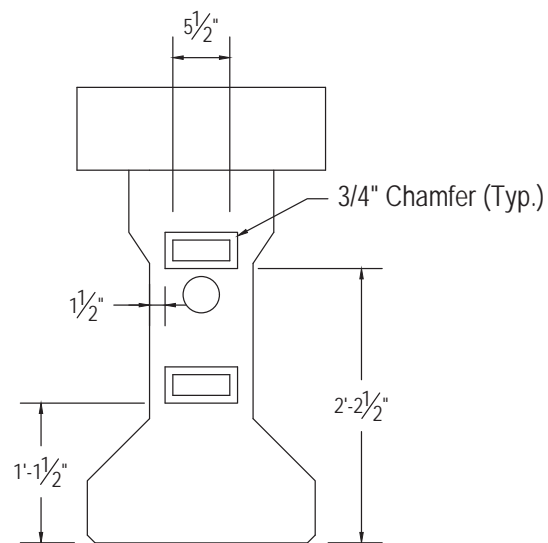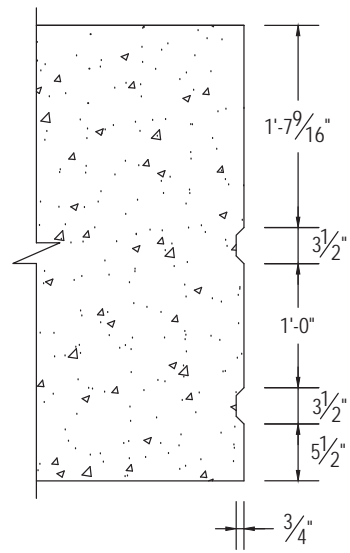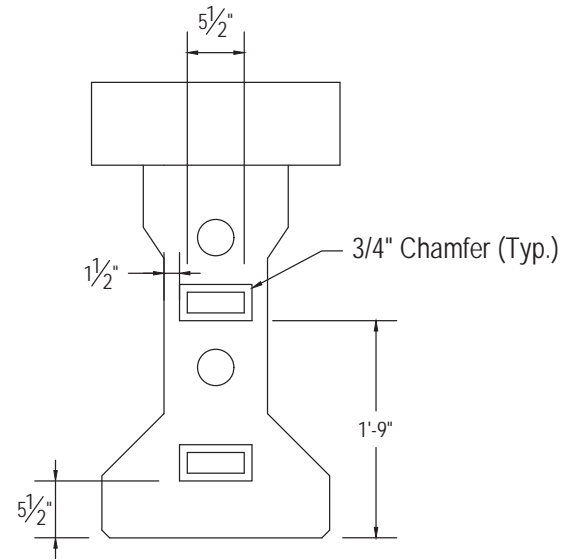
Cross Sections A-A and B-B
(Refer to sheets 7 and 8)

Strand Pattern & Pretensioning
Girder SS-1

2"
5" 5 @ 2" = 10" 2"
5"

8"

2"

10"

(2) 0.375" diam.
270 ksi 'LO LAX'
Pull each strand to 10,000 lbs

(10) 0.6" diam.
270 ksi 'LO LAX'
Pull each strand to 43,000 lbs

2 @ 2" = 4"

3"

5" 8" 5"
2" 2"

Detensioning Sequence
Girder SS-1

| 1 | 1 |

6			6	
4	5		5	4
2	3		3	2

Shielding Legend

○ None required

◈ Debonded 34'-6" from ends of beam

70'-0" (Bonded)

Elevation view
(not to scale)

Strand Pattern & Pretensioning
Girder SS-2

2"
5"
5 @ 2" = 10"
2"
5"

8"

2"

10"

(2) 0.375" diam.
270 ksi 'LO LAX'
Pull each strand to 10,000 lbs

(8) 0.6" diam.
270 ksi 'LO LAX'
Pull each strand to 43,000 lbs

(2) 0.6" diam.
270 ksi 'LO LAX'
debonded 34'-6" from ends of beam

2 @ 2" = 4"

3"

5"   8"   5"
2"   2"

Detensioning Sequence
Girder SS-2

1 1

6
4 5
2 3

6
5 4
3 2

Shielding Legend

○ None required

◈ Debonded 34'-6" from ends of beam

70'-0"

Debonded strands shielded for 34'-6"

Debonded strands shielded for 34'-6"

Bonded for 1'-0
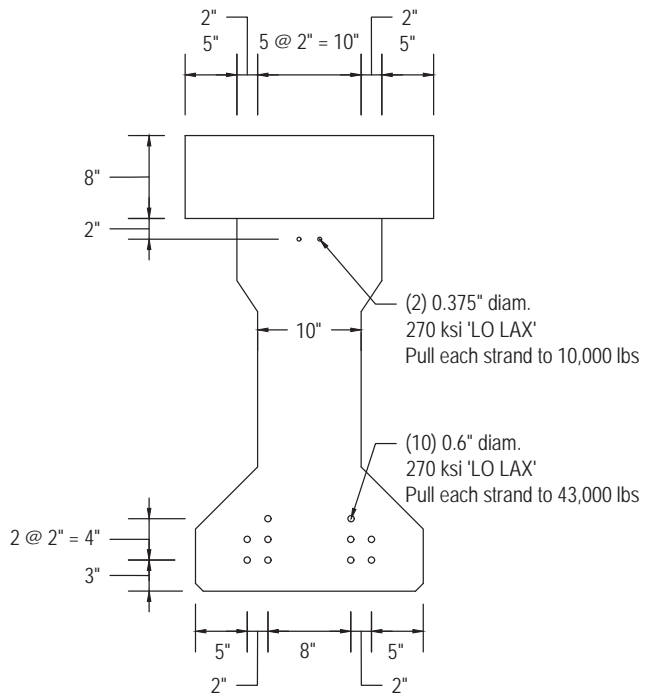
Elevation view
(not to scale)

Strand Pattern & Pretensioning
Girder SS-3

2"
5"   5 @ 2" = 10"   2"
5"

8"

2"

10"

(2) 0.375" diam.
270 ksi 'LO LAX'
Pull each strand to 10,000 lbs

(6) 0.6" diam.
270 ksi 'LO LAX'
Pull each strand to 43,000 lbs

(4) 0.6" diam.
270 ksi 'LO LAX'
debonded 19'-6" from ends of beam

2 @ 2" = 4"

3"

5"   8"   5"

2"   2"

Detensioning Sequence
Girder SS-3

1 1

6
4 5
2 3

6
5 4
3 2
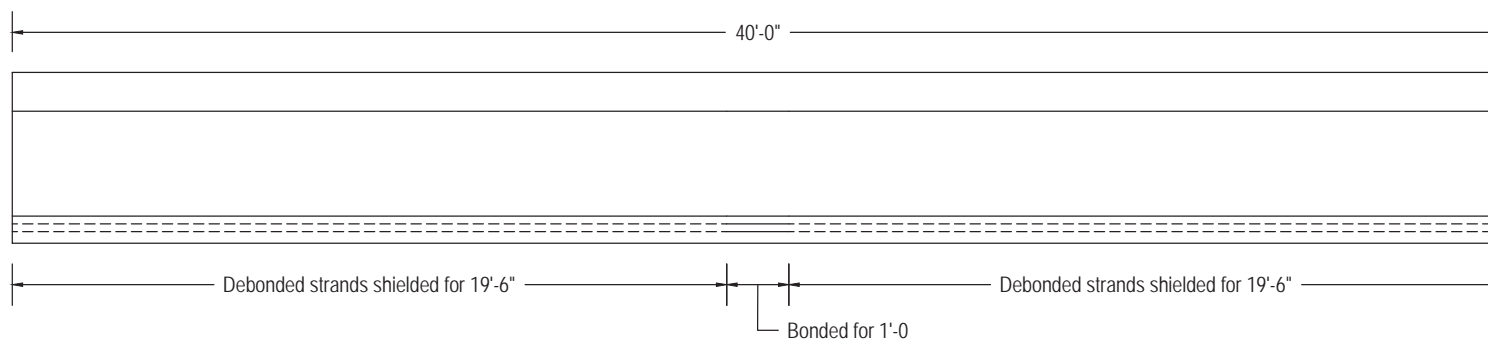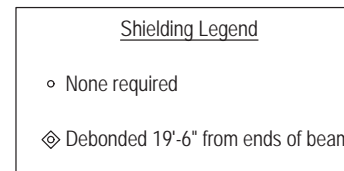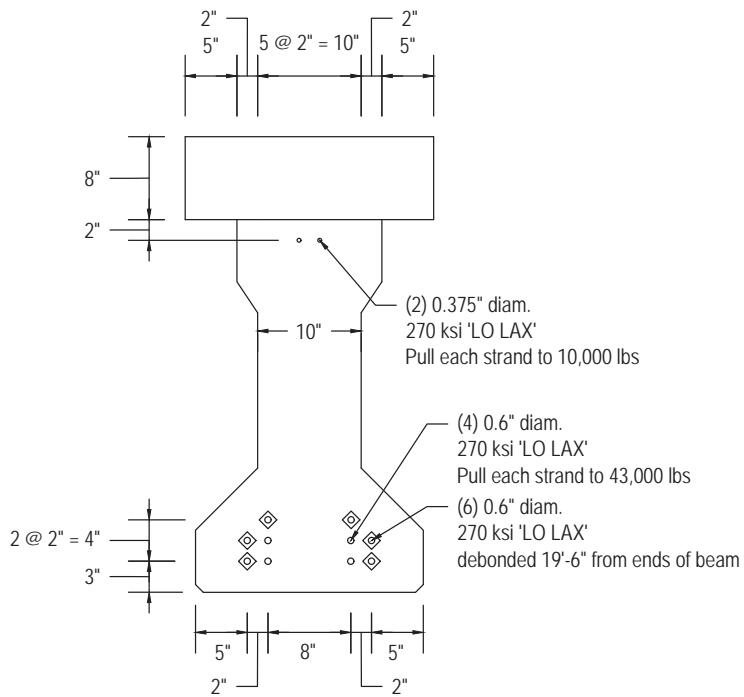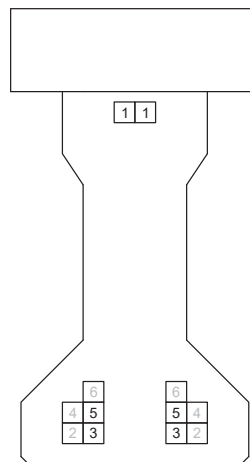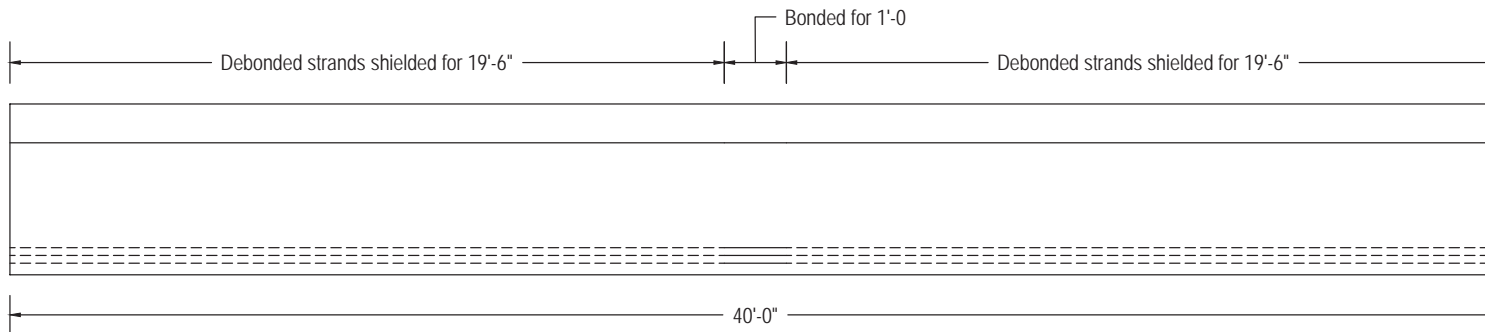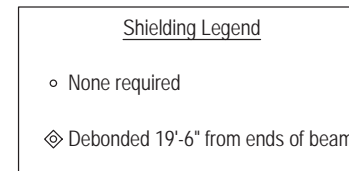
Shielding Legend

○ None required

◈ Debonded 19'-6" from ends of beam

Elevation view
(not to scale)

40'-0"

Debonded strands shielded for 19'-6"   Debonded strands shielded for 19'-6"

Bonded for 1'-0

Strand Pattern & Pretensioning
Girder SS-4

2"
5"
5 @ 2" = 10"
2"
5"

8"

2"

10"

(2) 0.375" diam.
270 ksi 'LO LAX'
Pull each strand to 10,000 lbs

(4) 0.6" diam.
270 ksi 'LO LAX'
Pull each strand to 43,000 lbs

(6) 0.6" diam.
270 ksi 'LO LAX'
debonded 19'-6" from ends of beam

2 @ 2" = 4"

3"

5"
8"
5"
2"
2"

Detensioning Sequence
Girder SS-4

| 1 | 1 |

6		6	
4	5	5	4
2	3	3	2

Shielding Legend

○ None required

◈ Debonded 19'-6" from ends of beam

Bonded for 1'-0

Debonded strands shielded for 19'-6" ⟷ ⟷ Debonded strands shielded for 19'-6"

40'-0"

Elevation view
(not to scale)

15

Strand Pattern & Pretensioning
Girder NB-1

2"
5"
5 @ 2" = 10"
2"
5"

8"

2 @ 2" = 4"

10"

(12) 0.6" diam.
270 ksi 'LO LAX'
Pull each strand to 43,000 lbs

2 @ 2" = 4"

3"

(2) 0.6" diam.
270 ksi 'LO LAX'
Pull each strand to 43,000 lbs

5"
8"
5"
2"
2"

Detensioning Sequence
Girder NB-1

| 1 | 2 | 3 | 3 | 2 | 1 |
| 4 | 5 | 6 | 6 | 5 | 4 |

7   7

Shielding Legend

○ None required

◈ Debonded 13'-0" from ends of beam

27'-0" (Bonded)

Elevation view
(not to scale)

Strand Pattern & Pretensioning
Girder NB-2

2"
5"   5 @ 2" = 10"   2"
5"

8"

2 @ 2" = 4"

(10) 0.6" diam.
270 ksi 'LO LAX'
Pull each strand to 43,000 lbs

10"

(2) 0.6" diam.
270 ksi 'LO LAX'
debonded 13'-0" from ends of beam

2 @ 2" = 4"

3"

(2) 0.6" diam.
270 ksi 'LO LAX'
Pull each strand to 43,000 lbs

5"   8"   5"
2"   2"

Detensioning Sequence
Girder NB-2

1	2	3	3	2	1
4	5	6	6	5	4

| 7 | | 7 |

Shielding Legend

∘ None required

◈ Debonded 13'-0" from ends of beam

Bonded for 1'-0

Debonded strands shielded for 13'-0" ———— Debonded strands shielded for 13'-0"

27'-0"

Elevation view
(not to scale)

17

2" **2"**
5" **5 @ 2" = 10"** **5"**

8"

2 @ 2" = 4"

(6) 0.6" diam.
270 ksi 'LO LAX'
Pull each strand to 43,000 lbs

10"

(6) 0.6" diam.
270 ksi 'LO LAX'
debonded 13'-0" from ends of beam

2 @ 2" = 4"

3"

(2) 0.6" diam.
270 ksi 'LO LAX'
Pull each strand to 43,000 lbs

5" **8"** **5"**
2" **2"**

Strand Pattern & Pretensioning
Girder NB-3

1	2	3	3	2	1
4	5	6	6	5	4

7		7

Detensioning Sequence
Girder NB-3

Shielding Legend

○ None required

◈ Debonded 13'-0" from ends of beam

Bonded for 1'-0

Debonded strands shielded for 13'-0" ——— Debonded strands shielded for 13'-0"

27'-0"

Elevation view
(not to scale)

18

FDOT Research
Flexural capacity of concrete elements with unbonded and bonded prestressing
BDV31-977-93

University of Florida
Dept. of Civil and Coastal Engineering
787.201.6874

Design Drawings
Specimen SS-1: Rebar Schedule (precast components)
Sheet 19 of 42

19

4A 75'-8"
4B 69'-9"
4L 5'-8"
5S 1'-8"

4A, 4B, 4L, 5S

4½" 9" 2¼"
4½" 2¼"
3¼"
1'-6"

2¼" 9" 4½"
2¼" 4½"
3¼"
1'-6"

3D Pair

6"
3'-2½"
7"

4K

5"
2'-7"
7"

5Z

Bill of material: SS-1				
Piece	Size	Qty.	Length	Notes
4A	#4	4	75'-8"	
4B	#4	4	69'-9"	
4L	#4	8	5'-8"	
5S	#5	173	1'-8"	
3D	#3	48	3'-3 7/8"	
4K	#4	152	3'-8"	
5Z	#5	8	4'-3 1/2"	

CL
mark
90.0°
End 1
End 2
90.0°

Plan View

End 1
End 2
mark
90.0°

Elevation

(4) ½" diam. 270 ksi strands x12'-0"
w/ 2 ¼" x 2'-6" steel pipe @ top
(typ each end)

2'-0"
typ.
Dunnage for storage
and shipping

Handling & Dunnage

Bar Bending

#3 Bars: bend around 1 ½" diam. pin

#4 Bars: bend around 2" diam. pin

#5 Bars: bend around 2 ½" diam. pin

All dims are out-to-out

4A, 4B, 4L, 5S

4A — 75'-8"
4B — 69'-9"
4L — 5'-8"
5S — 1'-8"

3D Pair

4½" 9" 2¼"
4½" 2¼"
3¼" 1'-6"

2¼" 9" 4½"
2¼" 4½"
1'-6" 3¼"

4K

6"
3'-2½"
7"

5Z

5"
2'-7"
7"

Bill of material: SS-2

Piece	Size	Qty.	Length	Notes
4A	#4	4	75'-8"	
4B	#4	4	69'-9"	
4L	#4	8	5'-8"	
5S	#5	173	1'-8"	
3D	#3	48	3'-3 7/8"	
4K	#4	152	3'-8"	
5Z	#5	8	4'-3 1/2"	

Plan View

CL — mark — End 1 — End 2 — 90.0°
90.0°

Elevation

End 1 — End 2 — mark
90.0°

Handling & Dunnage

(4) ½" diam. 270 ksi strands x12'-0"
w/ 2 ¼" x 2'-6" steel pipe @ top
(typ each end)

2'-0"
typ.

Dunnage for storage
and shipping

Bar Bending

#3 Bars: bend around 1 ½" diam. pin

#4 Bars: bend around 2" diam. pin

#5 Bars: bend around 2 ½" diam. pin

All dims are out-to-out

20

221

4A, 4B, 4L, 5S

3D Pair

4K

5Z

Bill of material: SS-3				
Piece	Size	Qty.	Length	Notes
4A	#4	4	45'-8"	
4B	#4	4	39'-9"	
4L	#4	8	5'-8"	
5S	#5	98	1'-8"	
3D	#3	48	3'-3 7/8"	
4K	#4	92	3'-8"	
5Z	#5	8	4'-3 1/2"	

Plan View

Elevation

(4) $\frac{1}{2}$" diam. 270 ksi strands x12'-0"
w/ 2 $\frac{1}{4}$" x 2'-6" steel pipe @ top
(typ each end)

Handling & Dunnage

Dunnage for storage
and shipping

Bar Bending

#3 Bars: bend around 1 $\frac{1}{2}$" diam. pin

#4 Bars: bend around 2" diam. pin

#5 Bars: bend around 2 $\frac{1}{2}$" diam. pin

All dims are out-to-out

4A, 4B, 4L, 5S

4A	45'-8"
4B	39'-9"
4L	5'-8"
5S	1'-8"

3D Pair

4K

5Z

Bill of material: SS-4

Piece	Size	Qty.	Length	Notes
4A	#4	4	45'-8"	
4B	#4	4	39'-9"	
4L	#4	8	5'-8"	
5S	#5	98	1'-8"	
3D	#3	48	3'-3 7/8"	
4K	#4	92	3'-8"	
5Z	#5	8	4'-3 1/2"	

Plan View

End 1   End 2   90.0°

CL — mark

90.0°

Elevation

End 1   End 2

mark

90.0°

Handling & Dunnage

(4) $\frac{1}{2}$" diam. 270 ksi strands x12'-0"
w/ 2 $\frac{1}{4}$" x 2'-6" steel pipe @ top
(typ each end)

2'-0"
typ.

Dunnage for storage
and shipping

Bar Bending

#3 Bars: bend around 1 $\frac{1}{2}$" diam. pin

#4 Bars: bend around 2" diam. pin

#5 Bars: bend around 2 $\frac{1}{2}$" diam. pin

All dims are out-to-out

4A, 4B, 4L, 5S

4A	32'-8"
4B	26'-9"
4L	5'-8"
5S	1'-8"

4A, 4B, 4L, 5S

3D Pair

9" 4½" 2¼" 2¼" 4½" 1'-6" 3¼"

4K

6" 3'-2½" 7"

5Z

5" 2'-7" 7"

Bill of material: NB-1

Piece	Size	Qty.	Length	Notes
4A	#4	4	45'-8"	
4B	#4	4	39'-9"	
4L	#4	8	5'-8"	
5S	#5	67	1'-8"	
3D	#3	48	3'-3 7/8"	
4K	#4	66	3'-8"	
5Z	#5	8	4'-3 1/2"	

Plan View

CL — mark — End 1 — End 2 — 90.0°
90.0°

Elevation

End 1 — mark — End 2
90.0°

Handling & Dunnage

(4) ½" diam. 270 ksi strands x12'-0"
w/ 2 ¼" x 2'-6" steel pipe @ top
(typ each end)

2'-0" typ. — Dunnage for storage and shipping

Bar Bending

#3 Bars: bend around 1 ½" diam. pin

#4 Bars: bend around 2" diam. pin

#5 Bars: bend around 2 ½" diam. pin

All dims are out-to-out

23

FDOT Research
Flexural capacity of concrete elements
with unbonded and bonded prestressing
BDV31-977-93

University of Florida
Dept. of Civil and Coastal Engineering
787.201.6874

Design Drawings
Specimen NB-2: Rebar Schedule (precast components)
Sheet 24 of 42

24

4A — 32'-8"
4B — 26'-9"
4L — 5'-8"
5S — 1'-8"

4A, 4B, 4L, 5S

3D Pair

4K

5Z

Bill of material: NB-2				
Piece	Size	Qty.	Length	Notes
4A	#4	4	45'-8"	
4B	#4	4	39'-9"	
4L	#4	4	5'-8"	
5S	#5	67	1'-8"	
3D	#3	48	3'-3 7/8"	
4K	#4	66	3'-8"	
5Z	#5	8	4'-3 1/2"	

CL
mark
End 1   End 2
90.0°
90.0°

Plan View

End 1   End 2
mark
90.0°

Elevation

(4) $\frac{1}{2}$" diam. 270 ksi strands x12'-0"
w/ 2 $\frac{1}{4}$" x 2'-6" steel pipe @ top
(typ each end)

2'-0"
typ.
Dunnage for storage
and shipping

Handling & Dunnage

Bar Bending

#3 Bars: bend around 1 $\frac{1}{2}$" diam. pin

#4 Bars: bend around 2" diam. pin

#5 Bars: bend around 2 $\frac{1}{2}$" diam. pin

All dims are out-to-out

FDOT Research
Flexural capacity of concrete elements
with unbonded and bonded prestressing
BDV31-977-93

University of Florida
Dept. of Civil and Coastal Engineering
787.201.6874

Design Drawings
Specimen NB-3: Rebar Schedule (precast components)
Sheet 25 of 42

25

4A, 4B, 4L, 5S

Mark	Length
4A	32'-8"
4B	26'-9"
4L	5'-8"
5S	1'-8"

3D Pair

(dimensions: 4½", 9", 2¼", 1'-6", 3¼")

4K

6", 3'-2½", 7"

5Z

5", 2'-7", 7"

Bill of material: NB-3

Piece	Size	Qty.	Length	Notes
4A	#4	4	45'-8"	
4B	#4	4	39'-9"	
4L	#4	4	5'-8"	
5S	#5	67	1'-8"	
3D	#3	48	3'-3 7/8"	
4K	#4	66	3'-8"	
5Z	#5	8	4'-3 1/2"	

Plan View

CL — mark — End 1 — End 2 — 90.0°
90.0°

Elevation

End 1 — mark — End 2
90.0°

Handling & Dunnage

(4) $\frac{1}{2}$" diam. 270 ksi strands x12'-0"
w/ 2 $\frac{1}{4}$" x 2'-6" steel pipe @ top
(typ each end)

2'-0" typ.

Dunnage for storage and shipping

Bar Bending

#3 Bars: bend around 1 $\frac{1}{2}$" diam. pin

#4 Bars: bend around 2" diam. pin

#5 Bars: bend around 2 $\frac{1}{2}$" diam. pin

All dims are out-to-out

ECI 6-12
'5H'
'5F'
'4M'
'4N'
3'-8"
1'-11"
1'-10"
F

Section D - D
(Refer to sheet 2)

(2 sp) @ 6" = 1'-0"
(3 sp) @ 4" = 1'-0"
Spacing Bars '5H'
6"
Precast section
'4A'
'4B'
'4N'
'5H'
'5F'
'4M'
2" Cover
2" Cover

Section E - E
(Refer to sheet 2)

3'-0"
2" Cover
2" Cover
'4M'
'4N'
'5F'
Precast section
'4A'
6"
6¾"
1'-2"
'5H'
'4L'
6¼"
6"
2" Cover
3'-1"

Section F - F

Post-tensioned tendons:

1 PT tendon - (6) 0.6" diam. strands

Jacking force = $0.8 f_{pu}$ = 281.2 kip

Strand pattern and wedge plate orientation

3'-0"
1'-0¼"
1'-6 1/16"
3'-8"
1'-1¾"
3'-1"

Endblock Dimensions

26

227

Section D - D
(Refer to sheet 3)

ECI 6-12

'5H'
'5G'
'5F'
'4M'
'4N'

3'-8"

1'-11"

1'-10"

F

F

Section E - E
(Refer to sheet 3)

(2 sp) @ 6" = 1'-0"

(3 sp) @ 4" = 1'-0"

6"

Spacing Bars '5H'

Precast section

'4A'

'4B'

2" Cover

2" Cover

'4N'

'5G'

'5H'

'5F'

'4M'

Section F - F

3'-0"

2" Cover

2" Cover

'4M'

'4N'

'5F'

Precast section

'4A'

6"

$6\frac{3}{4}$"

1'-2"

$6\frac{1}{4}$"

6"

'4L'

2" Cover

'5G'

'5H'

3'-1"

Post-tensioned tendons:

1 PT tendon - (10) 0.6" diam. strands

Jacking force = 0.8 f_{pu} = 468.7 kip

Strand pattern and wedge plate orientation

8 9 10
6 7
3 4 5
1 2

Endblock Dimensions

3'-0"

$1'-0\frac{1}{4}$"

$1'-6\frac{1}{16}$"

$1'-1\frac{3}{4}$"

3'-1"

3'-8"

Section D - D
(Refer to sheet 4)

ECI 6-12

'5H'
'5F'
'4M'
'4N'

3'-8"
1'-11"
1'-10"

F
F

Section E - E
(Refer to sheet 4)

(2 sp) @ 6" = 1'-0"
(3 sp) @ 4" = 1'-0"
6"
Spacing Bars '5H'
Precast section

'4A'
'4B'

2" Cover
2" Cover
'4N'
'5H'
'5F'
'4M'

Section F - F

3'-0"
2" Cover
2" Cover
'4M'
'4N'
'5F'
Precast section
'4A'
6"
$6\frac{3}{4}$"
1'-2"
'5H'
'4L'
$6\frac{1}{4}$"
6"
2" Cover
3'-1"

Post-tensioned tendons:

1 PT tendon - (4) 0.6" diam. strands

Jacking force = $0.8\ f_{pu}$ = 187.5 kip

Strand pattern and wedge plate orientation

3
4
1
2

Endblock Dimensions

$1'-0\frac{1}{4}$"
3'-0"
$1'-6\frac{1}{16}$"
3'-8"
$1'-1\frac{3}{4}$"
3'-1"

Section D - D
(Refer to sheet 5)

ECI 6-12

'5H'
'5F'
'4M'
'4N'

3'-8"
1'-11"
1'-10"

Section E - E
(Refer to sheet 5)

(2 sp) @ 6" = 1'-0"
(3 sp) @ 4" = 1'-0"
6"
Spacing Bars '5H'
Precast section
'4A'
'4B'
'4N'
'5H'
'5F'
'4M'
2" Cover
2" Cover

Section F - F

3'-0"
2" Cover
2" Cover
'4M'
'4N'
'5F'
Precast section
'4A'
6"
$6\frac{3}{4}$"
1'-2"
'5H'
'4L'
$6\frac{1}{4}$"
6"
2" Cover
3'-1"

Post-tensioned tendons:

1 PT tendon - (6) 0.6" diam. strands

Jacking force = 0.8 f_{pu} = 281.2 kip

Strand pattern and wedge plate orientation

Endblock Dimensions

$1'-0\frac{1}{4}$"
3'-0"
$1'-6\frac{1}{16}$"
3'-8"
$1'-1\frac{3}{4}$"
3'-1"

Section D - D
(Refer to sheet 6)

'5H'
'5G'
ECI 6-12
'5F'
'4M'
'4N'

3'-8"
1'-10"
1'-10"
F
F

Section E - E
(Refer to sheet 6)

(2 sp) @ 6" = 1'-0"
(3 sp) @ 4" = 1'-0"
Spacing Bars '5H'
6"
Precast section
'4A'
'4B'
'4N'
'5F'
'4M'
2" Cover
'5G'
'5H'
2" Cover

Section F - F

3'-1"
2" Cover
'4M'
'4N'
'5F'
Precast section
'4A'
6"
$5\frac{1}{4}$"
1'-2"
$7\frac{3}{4}$"
'4L'
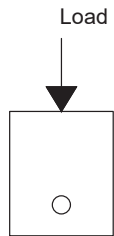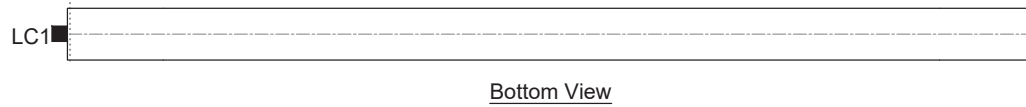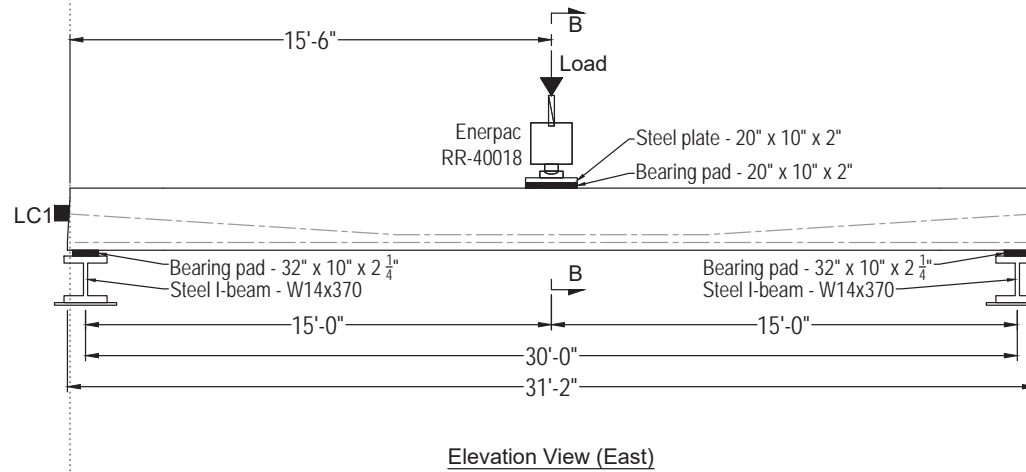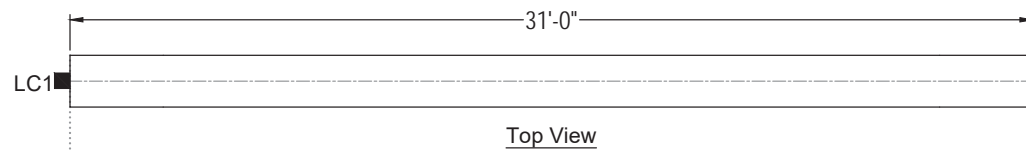6"
2" Cover
'5G'
'5H'
2" Cover
3'-0"

Post-tensioned tendons:

1 PT tendon - (12) 0.6" diam. strands

Jacking force = 0.8 f_{pu} = 562.5 kip

Strand pattern and wedge plate orientation

10 11 12
6 7 8 9
3 9 5
1 2

Endblock Dimensions

3'-1"
$1'-1\frac{3}{4}$"
$1'-6\frac{1}{16}$"
3'-8"
$1'-0\frac{1}{4}$"
3'-0"

Section D - D
(Refer to sheet 7)

'5H'
'5G'
ECI 6-12
'5F'
'4M'
'4N'
3'-8"
2'-5"
1'-1½"
1'-10"
F

Section E - E
(Refer to sheet 7)

(2 sp) @ 6" = 1'-0"
(3 sp) @ 4" = 1'-0"
6"
Spacing Bars '5H'
Precast section
'4A'
'4B'
2" Cover
'4N'
'5F'
'4M'
2" Cover
'5G'
'5H'

Section F - F

3'-1⅜"
2" Cover
'4M' '4N' '5F'
Precast section
'4A'
4½"
1'-2"
½"
1'-2"
'4L'
6"
2" Cover
'5G' '5H'
2" Cover
3'-0"
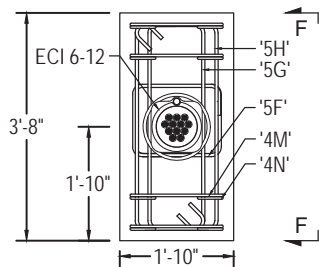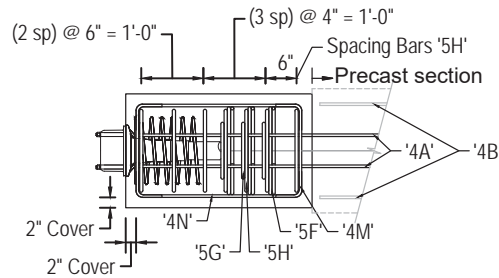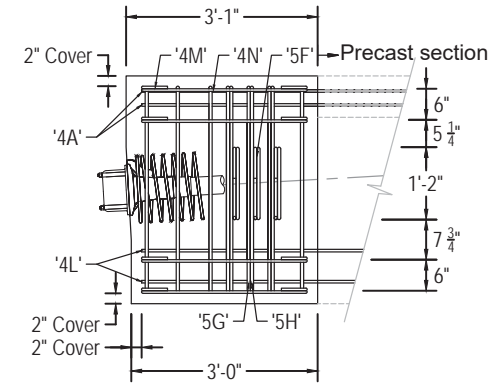
Post-tensioned tendons:

2 PT tendons - (18) 0.6" diam. strands

(9) strands / tendon

Jacking force = $0.8\, f_{pu}$ = 421.8 kip

Strand pattern and wedge plate orientation

7 8 9
5 O O 6
3 O 4
1 2

Endblock Dimensions

3'-1⅜"
1'-11¼"
3'-8"
1'-4⅜"
4½"
3'-0"

Section D - D
(Refer to sheet 8)

ECI 6-12

'5H'
'5G'
'5F'
'4M'
'4N'

3'-8"
2'-5"
1'-1½"
1'-10"

F
F

Section E - E
(Refer to sheet 8)

(2 sp) @ 6" = 1'-0"
(3 sp) @ 4" = 1'-0"
6"
Spacing Bars '5H'
Precast section

'4A'
'4B'
'4N'
'5F'
'4M'
'5G'
'5H'
2" Cover
2" Cover

Section F - F

3'-1⅜"
2" Cover
'4M' '4N' '5F'
Precast section
'4A'
4½"
1'-2"
½"
1'-2"
'4L'
6"
2" Cover
2" Cover
'5G' '5H'
3'-0"

Post-tensioned tendons:

2 PT tendons - (24) 0.6" diam. strands

(12) strands / tendon

Jacking force = 0.8 f_{pu} = 562.5 kip

Strand pattern and wedge plate orientation

10 11 12
6 7 8 9
3 4 5
1 2

Endblock Dimensions

3'-1⅜"
1'-11¼"
1'-4⅜"
3'-8"
4½"
3'-0"

4M

4N

5F Pair

5H

Bill of material: SS-1				
Piece	Size	Qty.	Length	Notes
4M	#4	16	2'-4"	
4N	#4	16	3'-6"	
5F	#5	12	3'-7"	
5H	#5	14	9'-11"	

Bar Bending

#3 Bars: bend around $1\frac{1}{2}$" diam. pin

#4 Bars: bend around 2" diam. pin

#5 Bars: bend around $2\frac{1}{2}$" diam. pin

All dims are out-to-out

4M

4N

5F Pair

5G

5H

Bill of material: SS-2				
Piece	Size	Qty.	Length	Notes
4M	#4	16	2'-4"	
4N	#4	16	3'-6"	
5F	#5	12	3'-7"	
5G	#5	6	9'-1"	
5H	#5	14	9'-11"	

Bar Bending

#3 Bars: bend around $1\frac{1}{2}$" diam. pin

#4 Bars: bend around 2" diam. pin

#5 Bars: bend around $2\frac{1}{2}$" diam. pin

All dims are out-to-out

4M

4N

5F Pair

5H

Bill of material: SS-3				
Piece	Size	Qty.	Length	Notes
4M	#4	16	2'-4"	
4N	#4	16	3'-6"	
5F	#5	12	3'-7"	
5H	#5	14	9'-11"	

Bar Bending

#3 Bars: bend around $1\frac{1}{2}$" diam. pin

#4 Bars: bend around 2" diam. pin

#5 Bars: bend around $2\frac{1}{2}$" diam. pin

All dims are out-to-out

4M

4N

5F Pair

5H

FDOT Research
Flexural capacity of concrete elements
with unbonded and bonded prestressing
BDV31-977-93

University of Florida
Dept. of Civil and Coastal Engineering
787.201.6874

Design Drawings
Specimen SS-4: Rebar Schedule (end blocks)
Sheet 36 of 42

36

Bill of material: SS-4				
Piece	Size	Qty.	Length	Notes
4M	#4	16	2'-4"	
4N	#4	16	3'-6"	
5F	#5	12	3'-7"	
5H	#5	14	9'-11"	

Bar Bending

#3 Bars: bend around $1\frac{1}{2}$" diam. pin

#4 Bars: bend around 2" diam. pin

#5 Bars: bend around $2\frac{1}{2}$" diam. pin

All dims are out-to-out

4M

4N

5F Pair

5G

5H

Bill of material: NB-1				
Piece	Size	Qty.	Length	Notes
4M	#4	16	2'-4"	
4N	#4	16	3'-6"	
5F	#5	12	3'-7"	
5G	#5	6	9'-1"	
5H	#5	14	9'-11"	

Bar Bending

#3 Bars: bend around $1\frac{1}{2}$" diam. pin

#4 Bars: bend around 2" diam. pin

#5 Bars: bend around $2\frac{1}{2}$" diam. pin

All dims are out-to-out

238

4M

4N

5F Pair

5G

5H

Bill of material: NB-2				
Piece	Size	Qty.	Length	Notes
4M	#4	12	2'-4"	
4N	#4	12	3'-6"	
5F	#5	32	3'-7"	
5G	#5	6	9'-1"	
5H	#5	14	9'-11"	

Bar Bending

#3 Bars: bend around $1\frac{1}{2}$" diam. pin

#4 Bars: bend around 2" diam. pin

#5 Bars: bend around $2\frac{1}{2}$" diam. pin

All dims are out-to-out

FDOT Research
Flexural capacity of concrete elements
with unbonded and bonded prestressing
BDV31-977-93

4M

4N

5F Pair

5G

5H

Bill of material: NB-3				
Piece	Size	Qty.	Length	Notes
4M	#4	12	2'-4"	
4N	#4	12	3'-6"	
5F	#5	32	3'-7"	
5G	#5	6	9'-1"	
5H	#5	14	9'-11"	

Bar Bending

#3 Bars: bend around $1\frac{1}{2}$" diam. pin

#4 Bars: bend around 2" diam. pin

#5 Bars: bend around $2\frac{1}{2}$" diam. pin

All dims are out-to-out

Design Drawings
Specimen NB-3: Rebar Schedule (end blocks)
Sheet 39 of 42

39

See sheet 41 for end block details (Sections D-D and E-E)

E E
D A   C   B
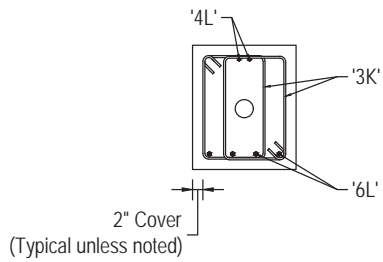
31'-0"

3'-0"
Spacing Bars '3K' 3"   '3K' (7 sp) @ 3" = 1'-9"   7" 5"   '3K' (7 sp) @ 3" = 1'-9"   3'-0"
End block (see details on Sheet 41)   '3K' (20 sp) @ 6" = 10'-0"   '3K' (20 sp) @ 6" = 10'-0"   3"
'4L'   End block (see details on Sheet 41)
'6L'

RS1, RS2, RS3, RS4,   RS5, RS6, RS7,   CL Duct
RS8   RS9   RS10 RS11   RS12 RS13 RS14   HDPE duct shall be sealed after installation

3'-1"   25'-0"   3'-1"
10'-7"   10'-0"   10'-7"
31'-2"

D A   C   B

Elevation: SS-5

Cross Section A - A
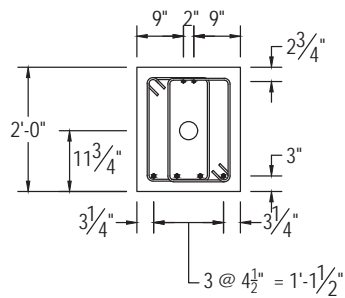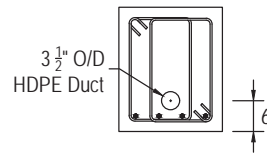
'4L'
'3K'
'6L'
2" Cover
(Typical unless noted)

Cross Section B - B

9" 2" 9"
2 3/4"
2'-0"
11 3/4"   3"
3 1/4"   3 1/4"
3 @ 4 1/2" = 1'-1 1/2"

Cross Section C - C

3 1/2" O/D
HDPE Duct
6"

All reinforcement sizes and locations
and quantities are typical each end
unless noted otherwise

See sheet 42 for information on rebar
schedule

SS-5 cross-section = 20" x 24"

241

ECI 6-12

'5Q'
'5J'
'4N'
'4P'

2'-0"
1'-2"
1'-8"

F
F

Section D - D
(Refer to sheet 40)

(2 sp) @ 6" = 1'-0"
(3 sp) @ 4" = 1'-0"
6"
Spacing Bars '5Q'

'4L'
'6L'

2" Cover
2" Cover

'4N' '5Q' '5J' '4P'

Section E - E
(Refer to sheet 40)

3'-0"
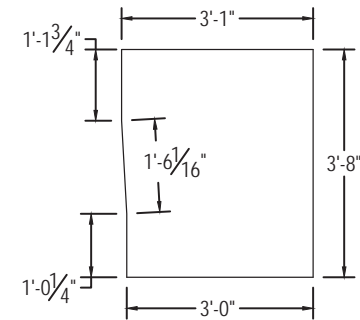2" Cover
2" Cover
'5Q' '5J' '4L'
1"
1'-2"
1"
3"
2" Cover
'4P' '4N' '6L'
3'-1"

Section F - F

Post-tensioned tendons:

1 PT tendon - (12) 0.6" diam. strands

Jacking force = $0.8 f_{pu}$ = 562.5 kip

10 11 12
6 7 8 9
3 4 5
1 2

Strand pattern and wedge plate orientation

3'-0"
$3\frac{3}{4}$"
$1\text{-}4\frac{11}{16}$"
2'-0"
$3\frac{5}{8}$"
3'-1"

Endblock Dimensions

6L — 30'-8"
4L — 5'-8"
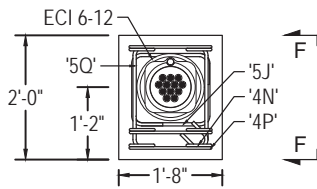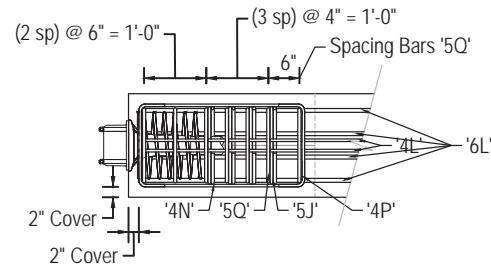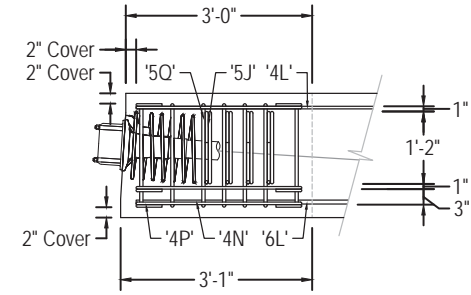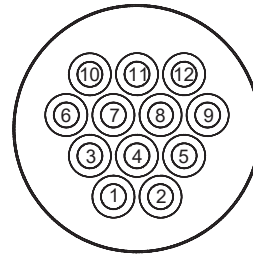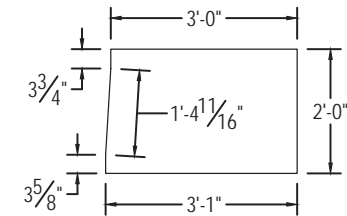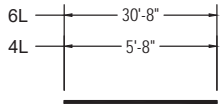
4L, 6L
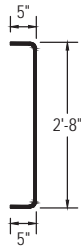
4N

4P
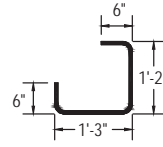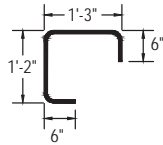
5J Pair

Bill of material: SS-5				
Piece	Size	Qty.	Length	Notes
4L	#4	4	5'-8"	
6L	#6	4	30'-8"	
4N	#4	12	3'-6"	
4P	#4	12	2'-2"	
3K	#3	114	5'-4"	
5Q	#5	14	5'-9"	
5J	#5	16	3'-5"	
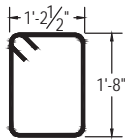
5Q
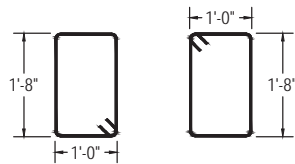
3K Pair

Bar Bending

#3 Bars: bend around $1\frac{1}{2}$" diam. pin

#4 Bars: bend around 2" diam. pin

#5 Bars: bend around $2\frac{1}{2}$" diam. pin

All dims are out-to-out

APPENDIX B
Instrumentation drawings

Instrumentation drawings for the experimental beam specimens are provided on the following pages.

General Notes:

Materials

Precast section (SS-1, SS-2, SS-3, SS-4, NB-1, NB-2, NB-3):
> Concrete shall be FDOT class VI
> f'c (28 day) = 8500 psi
> fci (release) = 6000 ksi

End blocks for beam specimens SS-3, SS-4, NB-1:
> Concrete shall be FDOT class V
> f'c (28 day) = 6500 psi

End blocks for beam specimens SS-1, SS-2, NB-2, NB-3:
> Concrete shall be FDOT class VI
> f'c (28 day) = 8500 psi

Beam specimen SS-5 (CIP):
> Concrete shall be FDOT class V
> f'c (28 day) = 6500 psi

Mild reinforcement shall be ASTM A615 grade 60 (fy 60 ksi)
Prestressing strand shall be ASTM A416 270 ksi Lo-Lax

Fabricator shall provide data sheets from concrete, strand, and rebar suppliers.
Fabricator shall provide report of strand stressing.

Fabricator shall provide material samples to UF/FDOT as follows:
(4) 4" dia x 8" cylinders from each concrete batch
(3) 36" pieces of prestressing strands free from sand, dust, etc. Samples taken directly off of reel.
(3) 36" pieces of each size/batch of rebar.

Schedule

Precast specimens were fabricated by end of Feb. 2020.

Research Instrumentation

UF/FDOT will provide and install research instrumentation in each of the concrete girders in coordination with the fabricator. Internal instrumentation will mounted to prestressing strands and rebar prior to casting concrete.

UF/FDOT will record data before and after release of prestressing. Data will also be recorded during lifting, storing, and shipping of girders.

Other

Fabricator will transport girders from the fabrication facility to:
FDOT Structures Research Center
2007 East Paul Dirac Drive
Tallahassee, FL 32310

Delivery time to be coordinated with FDOT.

Unless otherwise noted, fabrication of girders shall follow typical procedures and practices for FDOT bridge girders.

Cover beams with heavy tarp during curing.

Roughen top of beams after casting to ensure adequate bond with deck.

Inspections will be provided by on-site FDOT personal and by UF.

No patch-work or finishing is required.

These plans assume that all girders will be fabricated at the same time on the same stressing bed. Strand and sheilding patterns may change if girders are constructed at different times and/or on different beds. Fabricator shall coordinate these details with UF prior to fabrication.

FDOT Research
Flexural capacity of concrete elements with unbonded and bonded prestressing
BDV31-977-93

University of Florida
Dept. of Civil and Coastal Engineering
787.201.6874

Task 3: Experimental Test Plan
General Notes and Specifications
Sheet 1 of 62

1

21'-4" | 8 @ 50" = 33'-4" | 21'-4"

6 1/2"

D4 4"

D1 D5 D6 D7 D8 D9 D10 D11 D12 D2

D3 4"

7"

11"

Top View

C

A

B

Load

D1 D5 D6 D7 D8 D3, D4 D9 D10 D11 D12 D2

B

A

C

Elevation View (East)

Bottom View

1'-10"

2'-0"
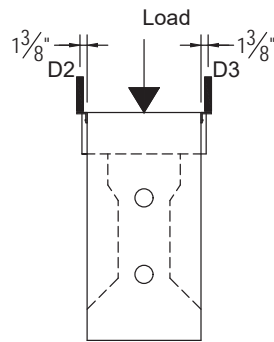
1'-0"

D1

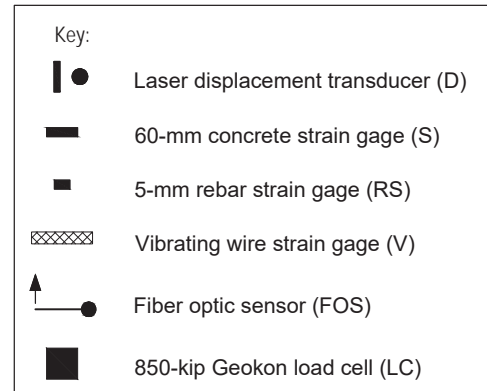Cross Section A - A

Load

4" 4"

D4 D3

Cross Section B - B

Key:

Laser displacement transducer (D)

60-mm concrete strain gage (S)

5-mm rebar strain gage (RS)

Vibrating wire strain gage (V)

Fiber optic sensor (FOS)

850-kip Geokon load cell (LC)

26'-0" · 12 @ 2' = 24'-0" · 26'-0"

S8 6"
6"

S1 S2 S3 S4 S5 S6 S7 S9 S10 S11 S12 S13 S14

Top View

B
Load

S15 S18 S21 S24 S27
S16 S19 S22 S25 S28 8"
S17 S20 S23 S26 S29

11"

1'-10"

8'-0" 4'-0" 4'-0" 8'-0" 26'-1"

B

Elevation View (West)

S30 S31 S32 S33 S34 S35 S36 S37 S38 S39 S40 S41 S42

26'-1" · 12 @ 2' = 22'-0" · 26'-2"
1'-11"

Bottom View

Load

6" 6"

S7 S8

S21
4"
S22 2 @ 8" = 1'-4"
S23
4"

S36 11"

Cross Section B - B

Key:

I ● Laser displacement transducer (D)

— 60-mm concrete strain gage (S)

▬ 5-mm rebar strain gage (RS)

▨ Vibrating wire strain gage (V)

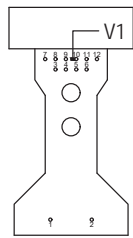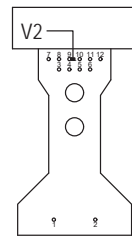▲ ● Fiber optic sensor (FOS)

■ 850-kip Geokon load cell (LC)

FDOT Research
Flexural capacity of concrete elements
with unbonded and bonded prestressing
BDV31-977-93

University of Florida
Dept. of Civil and Coastal Engineering
787.201.6874

Task 3: Experimental Test Plan
Specimen SS-1: Foil-type strain gages on concrete surface
Sheet 3 of 62
Scale: 3/16" = 1'

3

247

Top View

Load

DAQ - FOS1

DAQ - FOS2
DAQ - FOS3
DAQ - FOS4

28'-0"   35'-0"   6'-0"   35'-0"   28'-0"

B

20'-0"

Elevation View (East)

30'-1"   8'-2"

DAQ - FOS5

DAQ - FOS7   DAQ - FOS6

28'-1"   2'-3"   10'-3"   28'-1"

Bottom View

Load

1"

FOS1

FOS2

4"

FOS3

2 @ 8" = 1'-4"   FOS4

4"

FOS6   FOS5

9"   9"

Cross Section B - B

Key:

Laser displacement transducer (D)

60-mm concrete strain gage (S)

5-mm rebar strain gage (RS)

Vibrating wire strain gage (V)

Fiber optic sensor (FOS)

850-kip Geokon load cell (LC)

FDOT Research
Flexural capacity of concrete elements
with unbonded and bonded prestressing
BDV31-977-93

University of Florida
Dept. of Civil and Coastal Engineering
787.201.6874

Task 3: Experimental Test Plan
Specimen SS-1: Fiber-optic sensors
Sheet 4 of 62
Scale: 3/16" = 1'

4

248

Top View

B

Load

Elevation View (East)

V1, V2 ⌐ 3"
B

7" ⌐ V1

V2 ⌐ 7"

38'-1"   38'-1"

Bottom View

Load

Cross Section B - B

V2 ⌐ V1

Key:
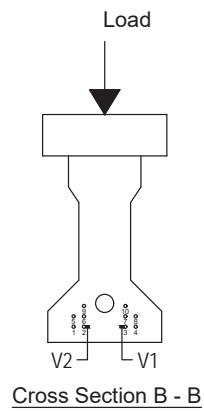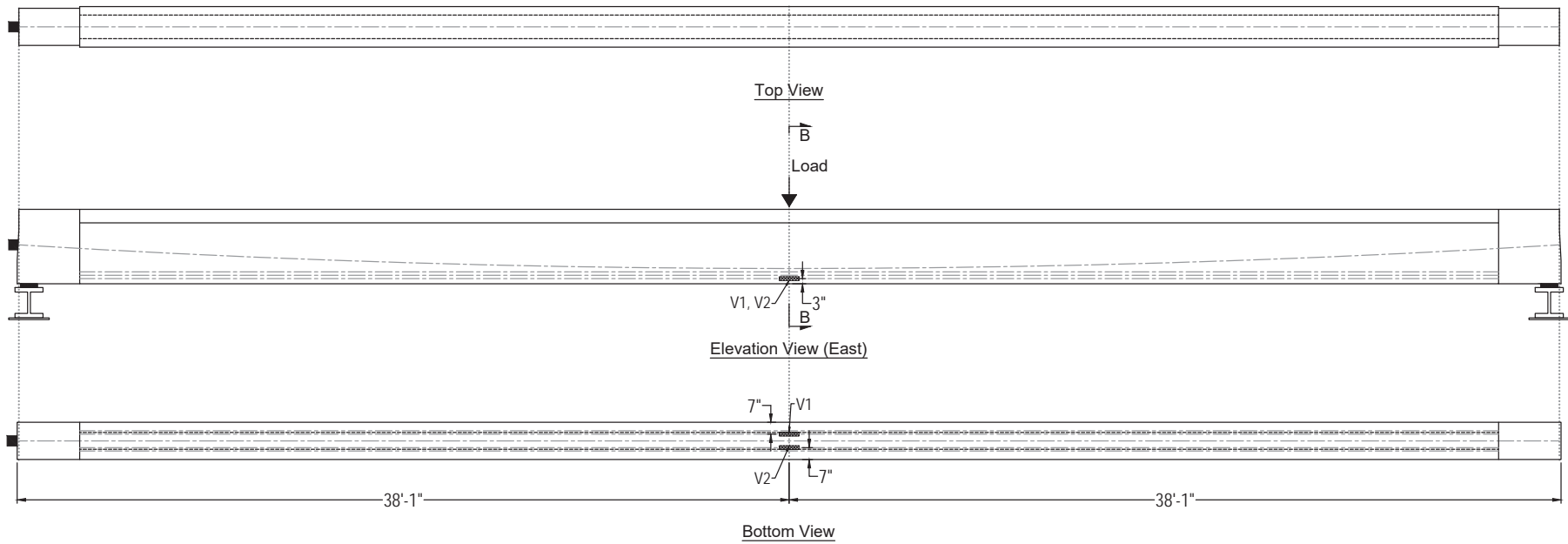
Laser displacement transducer (D)

60-mm concrete strain gage (S)

5-mm rebar strain gage (RS)

Vibrating wire strain gage (V)

Fiber optic sensor (FOS)

850-kip Geokon load cell (LC)

Section C - C
(Refer to sheet 2)
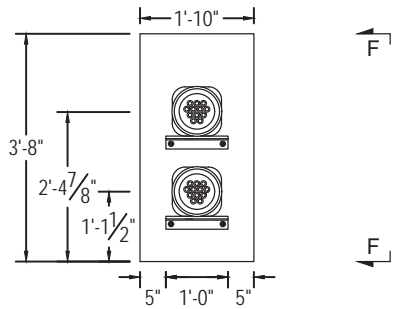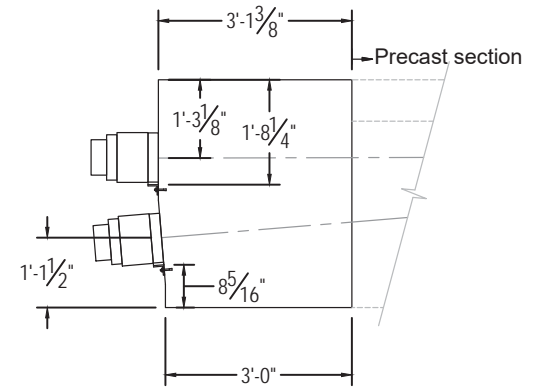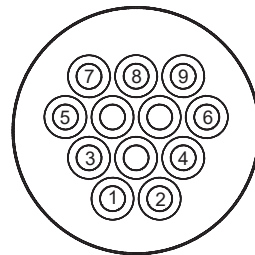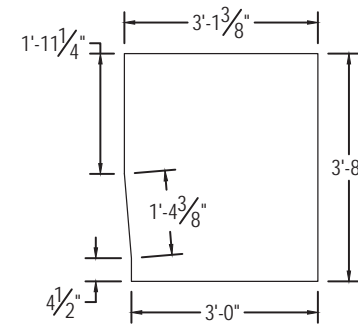
Section D - D

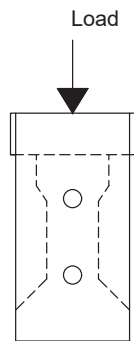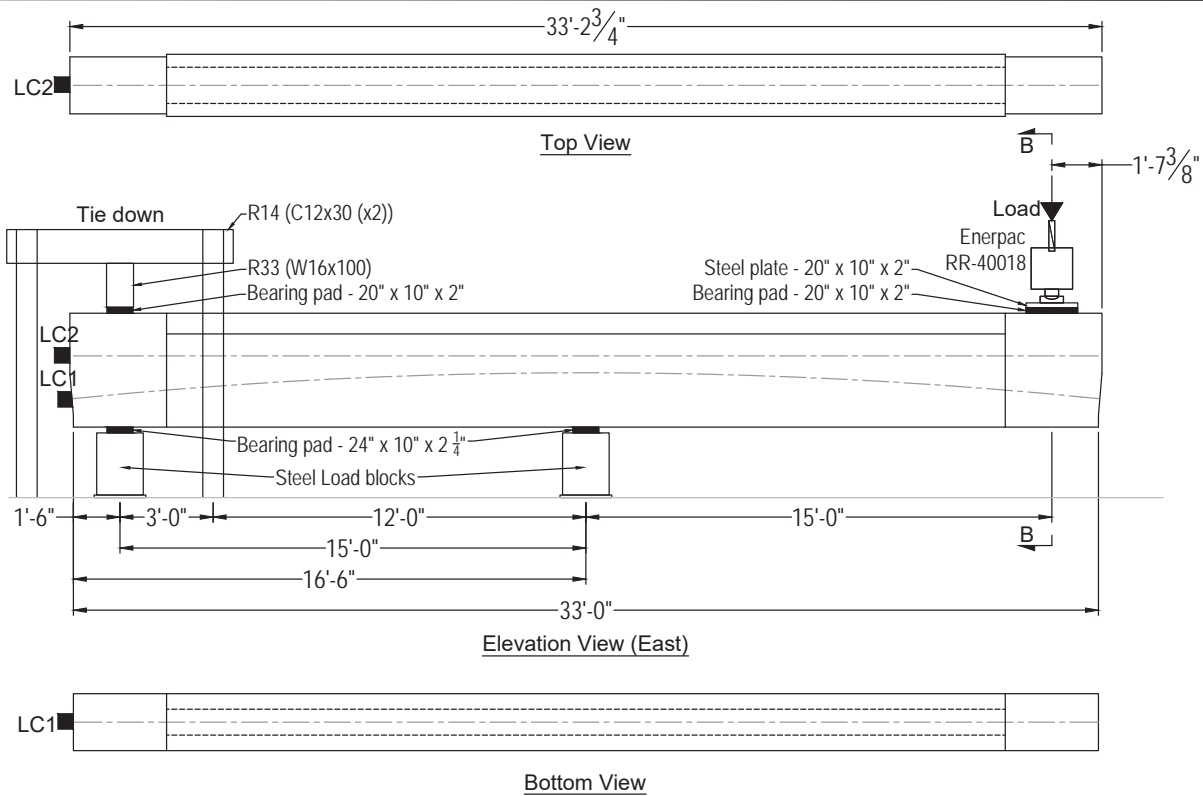Precast section

Post-tensioned tendons:

1 PT tendon - (6) 0.6" diam. strands

Jacking force = 0.8 f_{pu} = 281.2 kip

Strand pattern and wedge plate orientation

Endblock Dimensions
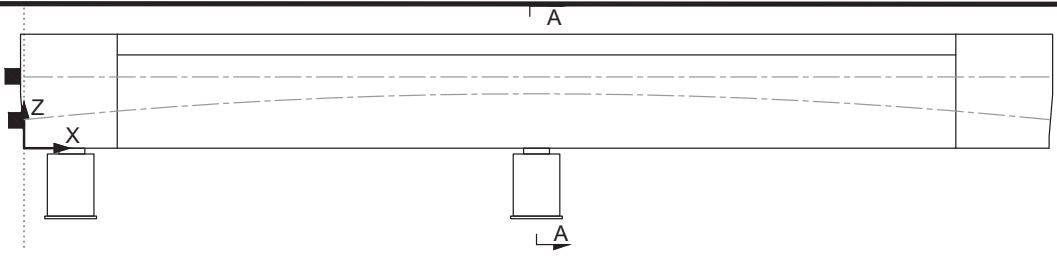
250

76'-0"

LC1

Top View

38'-0"

B
Load

Enerpac
RR-40018

Steel plate - 20" x 10" x 2"
Bearing pad - 20" x 10" x 2"

LC1

Bearing pad - 24" x 10" x 2$\frac{1}{4}$"
Steel I-beam - W14x370

Bearing pad - 24" x 10" x 2$\frac{1}{4}$"
Steel I-beam - W14x370

B

37'-6"
37'-6"
75'-0"
76'-2"

Elevation View (East)

LC1

Bottom View

Load

Cross Section B - B

Key:

Laser displacement transducer (D)

60-mm concrete strain gage (S)

5-mm rebar strain gage (RS)

Vibrating wire strain gage (V)

Fiber optic sensor (FOS)

850-kip Geokon load cell (LC)

Elevation View (East)
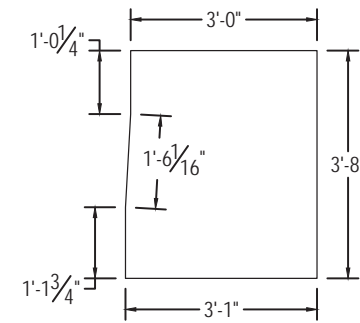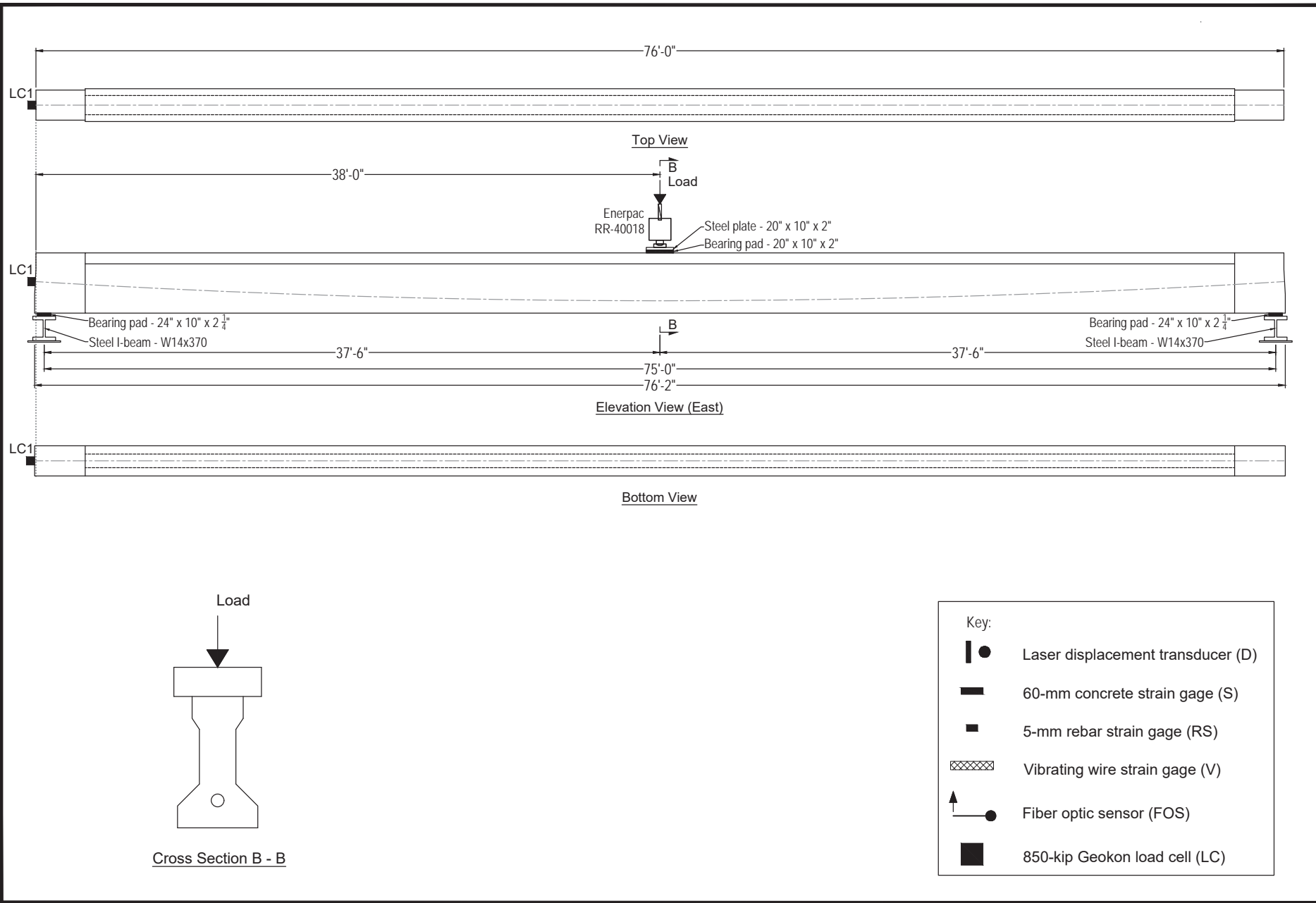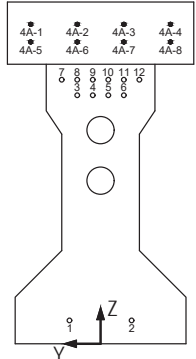
Instrument	X (in.)	Y (in.)	Z (in.)	Orientation
D1	6.5	0	44	Z
D2	905	0	44	Z
D3	456	-16	44	Z
D4	456	16	44	Z
D5	256	0	44	Z
D6	306	0	44	Z
D7	356	0	44	Z
D8	406	0	44	Z
D9	506	0	44	Z
D10	556	0	44	Z
D11	606	0	44	Z
D12	656	0	44	Z
S1	600	0	44	X
S2	576	0	44	X
S3	552	0	44	X
S4	528	0	44	X
S5	504	0	44	X
S6	480	0	44	X
S7	456	6	44	X
S8	456	-6	44	X
S9	432	0	44	X
S10	408	0	44	X
S11	384	0	44	X
S12	360	0	44	X
S13	336	0	44	X
S14	312	0	44	X
S15	600	7	32	X
S16	600	5	23	X
S17	600	5	16	X
S18	504	7	32	X
S19	504	5	24	X
S20	504	5	16	X
S21	456	7	32	X
S22	456	5	24	X
S23	456	5	16	X
S24	408	7	32	X
S25	408	5	24	X

Instrument	X (in.)	Y (in.)	Z (in.)	Orientation
S26	408	5	16	X
S27	312	7	32	X
S28	312	5	24	X
S29	312	5	16	X
S30	600	0	0	X
S31	576	0	0	X
S32	552	0	0	X
S33	528	0	0	X
S34	504	0	0	X
S35	480	0	0	X
S36	456	0	0	X
S37	432	0	0	X
S38	408	0	0	X
S39	384	0	0	X
S40	360	0	0	X
S41	336	0	0	X
S42	313	0	0	X
LC1	0	0	23.5	X

Instrument	Start			End		
	X (in.)	Y (in.)	Z (in.)	X (in.)	Y (in.)	Z (in.)
FOS1	336	-12	43	576	-12	43
FOS2	420	-7	32	492	-7	32
FOS3	420	-5	24	492	-5	24
FOS4	420	-5	16	492	-5	16
FOS5	360	-2	0	458	-2	0
FOS6	576	2	0	453	2	0
FOS7	336	2	0	363	2	0

Instrument	X (in.)	Y (in.)	Z (in.)	Orientation	Strand
V1	456	-4	3	X	3
V2	456	4	3	X	2

Cross Section B - B

Key:

D — Laser displacement transducer

S — 60-mm concrete strain gage

RS — 5-mm rebar strain gage

V — Vibrating wire strain gage

FOS — Fiber optic sensor

LC — 850-kip Geokon load cell

21'-4"

8 @ 50" = 33'-4"

21'-4"

6¼"

4½"

D4

6¼"

D1

D5   D6   D7   D8   D9   D10   D11   D12

D2

4½"

D3

11"

Top View

C

A

Load   B

D1   D5   D6   D7   D8   D3, D4   D9   D10   D11   D12   D2

A

B

C

Elevation View (East)

B

Bottom View

1'-10"

2'-0"
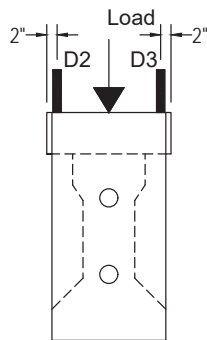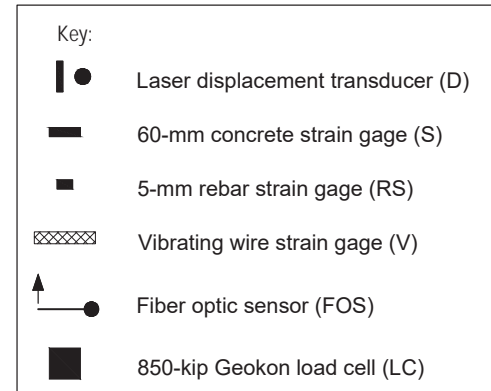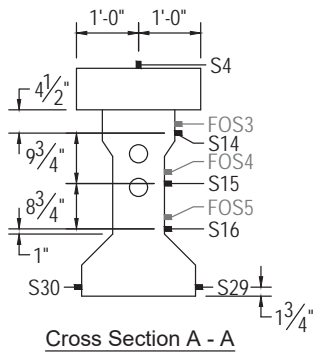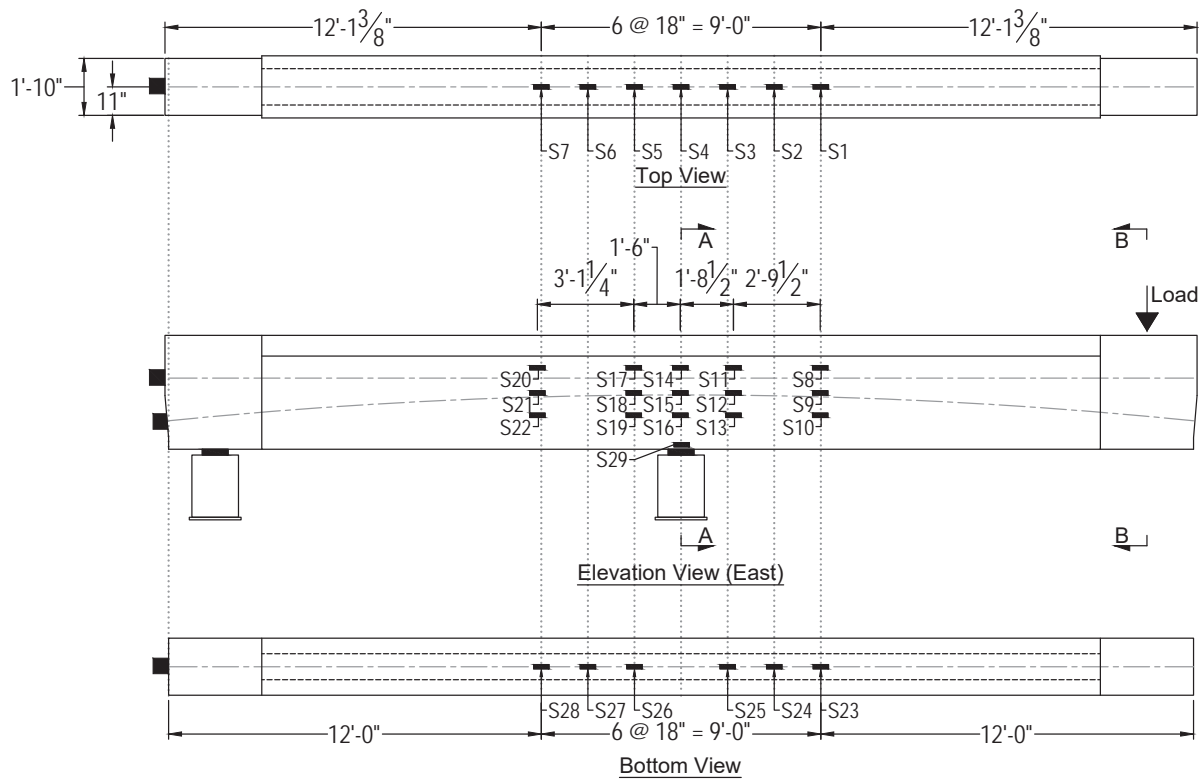
1'-0"

D1

Load

4½"

4½"

D4

D3

Cross Section A - A

Cross Section B - B

Key:

Laser displacement transducer (D)

60-mm concrete strain gage (S)

5-mm rebar strain gage (RS)

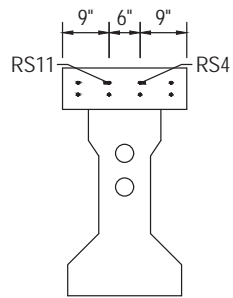Vibrating wire strain gage (V)

Fiber optic sensor (FOS)

850-kip Geokon load cell (LC)

253

Top View

B

Load

28'-0"   35'-0"   6'-0"   35'-0"   28'-0"

DAQ - FOS1

DAQ - FOS2
DAQ - FOS3
DAQ - FOS4

B

20'-0"

Elevation View (East)

28'-1"   10'-3"

DAQ - FOS5

DAQ - FOS6

10'-3"   28'-1"

Bottom View

Cross Section B - B

Load

1"

FOS1

FOS2

4"

2 @ 8" = 1'-4"   FOS3

FOS4

4"

FOS6   FOS5

9"   9"

Key:

Laser displacement transducer (D)

60-mm concrete strain gage (S)

5-mm rebar strain gage (RS)

Vibrating wire strain gage (V)

Fiber optic sensor (FOS)

850-kip Geokon load cell (LC)

FDOT Research
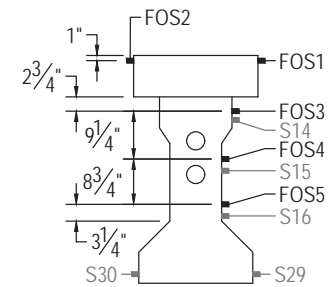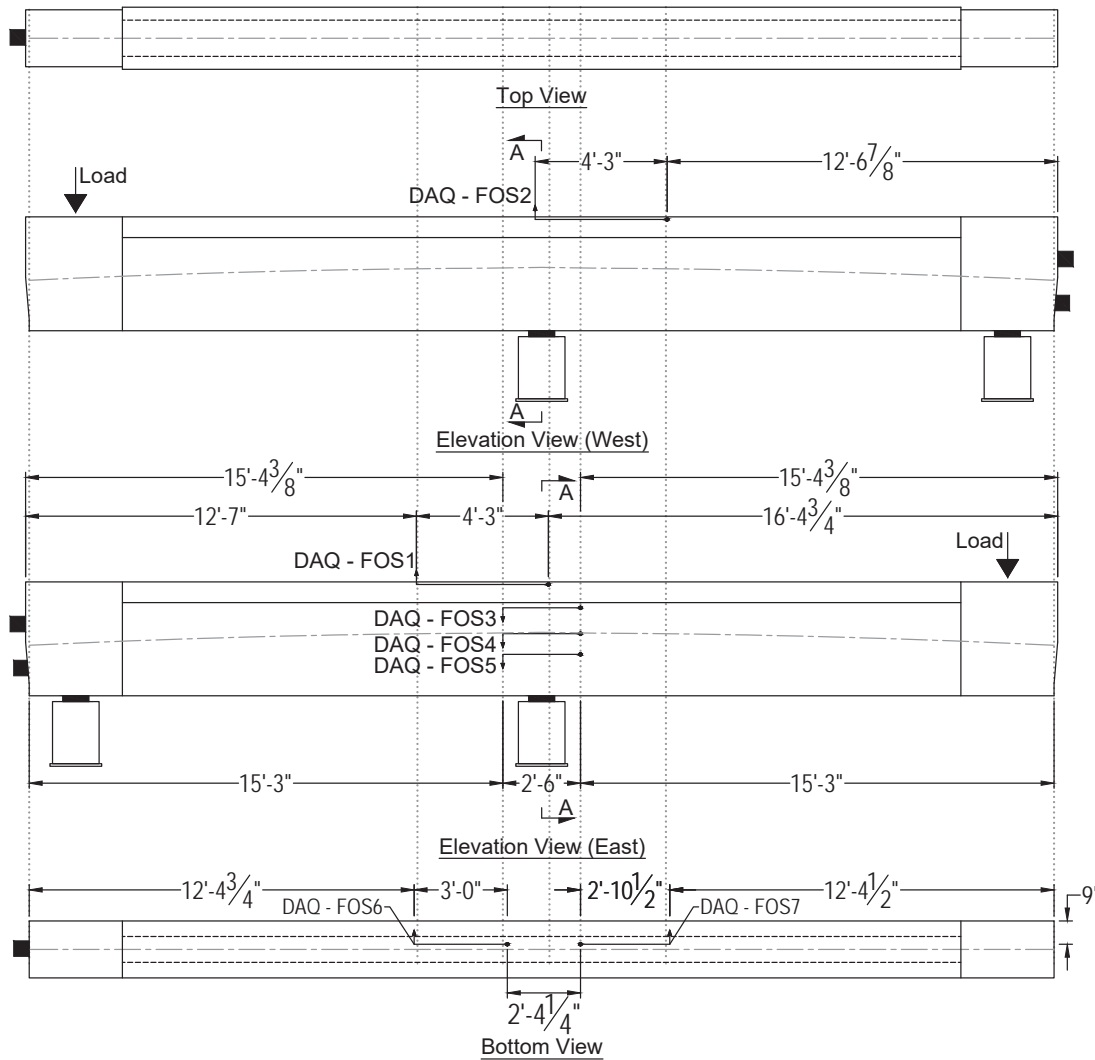Flexural capacity of concrete elements
with unbonded and bonded prestressing
BDV31-977-93

University of Florida
Dept. of Civil and Coastal Engineering
787.201.6874

Task 3: Experimental Test Plan
Specimen SS-2: Fiber-optic sensors
Sheet 11 of 62
Scale: 3/16" = 1'

11
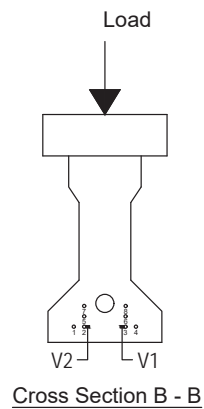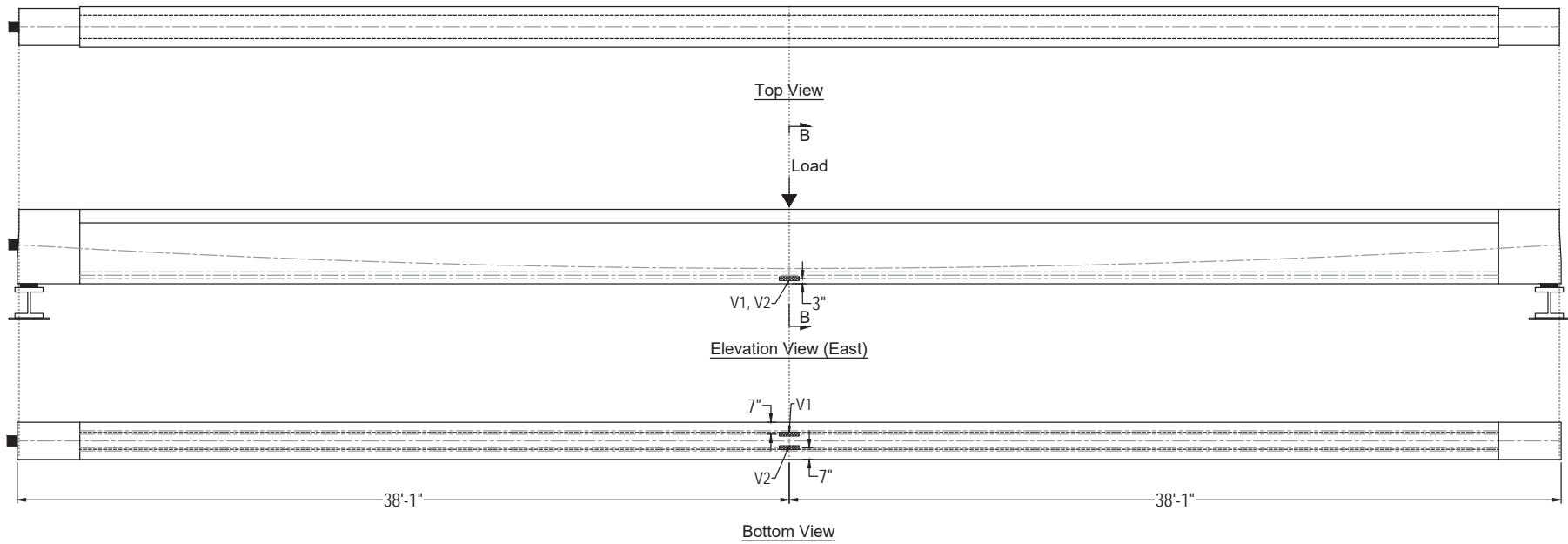
255

Top View

B
Load

Elevation View (East)

V1, V2   3"
B

7"   V1

V2   7"

38'-1"   38'-1"

Bottom View

Load

Cross Section B - B

V2   V1

Key:

Laser displacement transducer (D)

60-mm concrete strain gage (S)

5-mm rebar strain gage (RS)

Vibrating wire strain gage (V)

Fiber optic sensor (FOS)

850-kip Geokon load cell (LC)
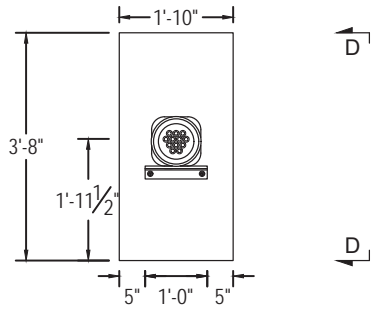
Section C - C
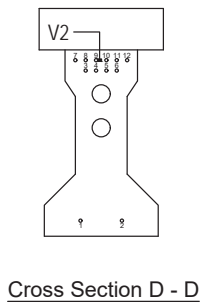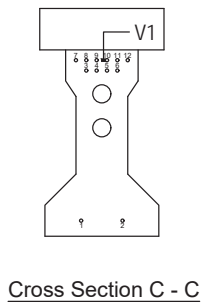(Refer to sheet 9)

Section D - D

Precast section

Post-tensioned tendons:

1 PT tendon - (10) 0.6" diam. strands

Jacking force = 0.8 f_{pu} = 468.7 kip

Strand pattern and wedge plate orientation

Endblock Dimensions

76'-0"

LC1

Top View

38'-0"

B
Load

Enerpac
RR-40018

Steel plate - 20" x 10" x 2"
Bearing pad - 20" x 10" x 2"

LC1

Bearing pad - 24" x 10" x 2 1/4"
Steel I-beam - W14x370

B

Bearing pad - 24" x 10" x 2 1/4"
Steel I-beam - W14x370

37'-6"
75'-0"
76'-2"
37'-6"

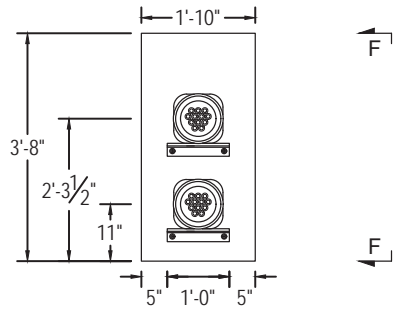Elevation View (East)

LC1

Bottom View

Load

Cross Section B - B

Key:

Laser displacement transducer (D)

60-mm concrete strain gage (S)

5-mm rebar strain gage (RS)

Vibrating wire strain gage (V)

Fiber optic sensor (FOS)

850-kip Geokon load cell (LC)

258
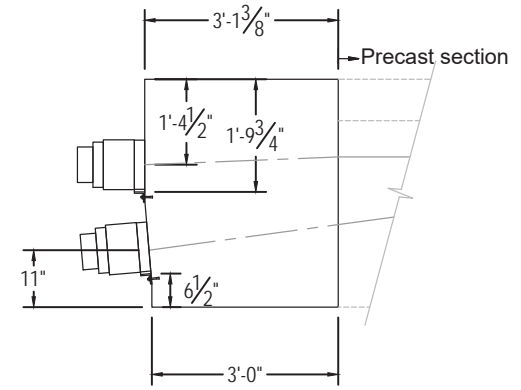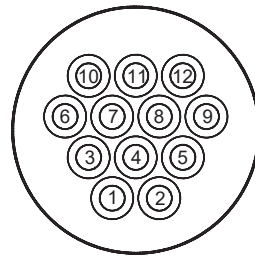
Elevation View (East)
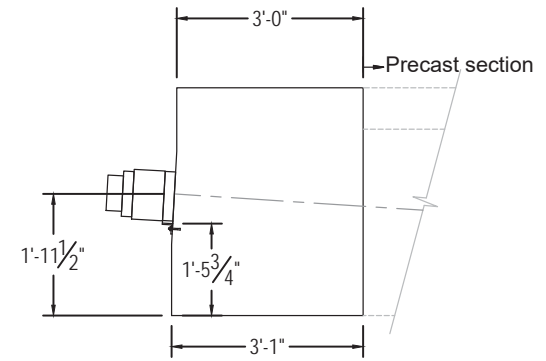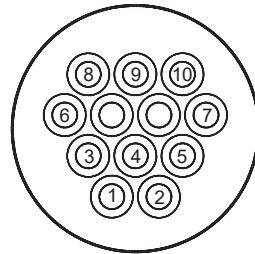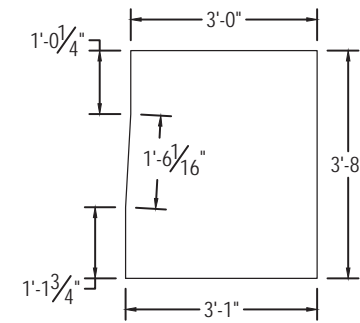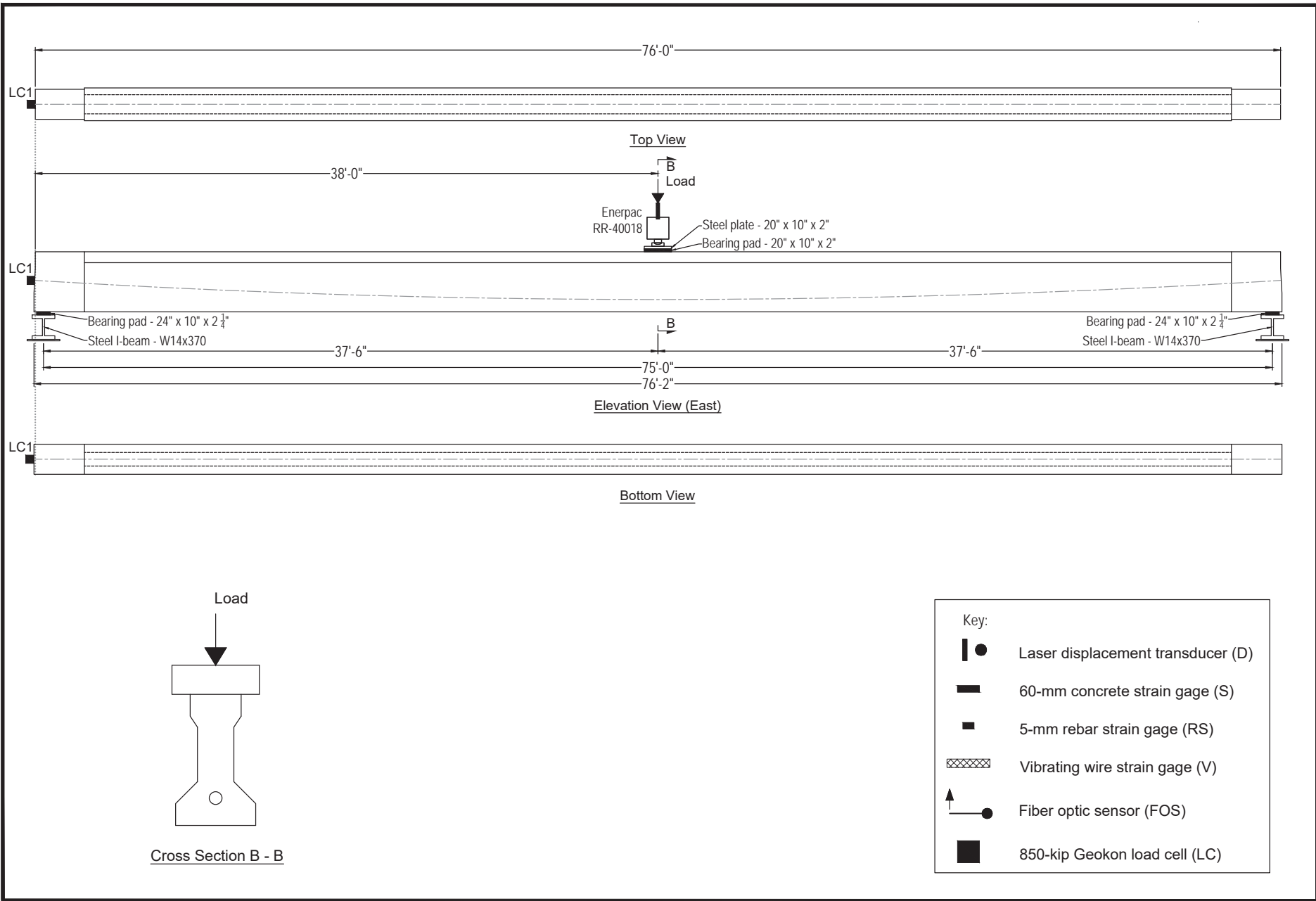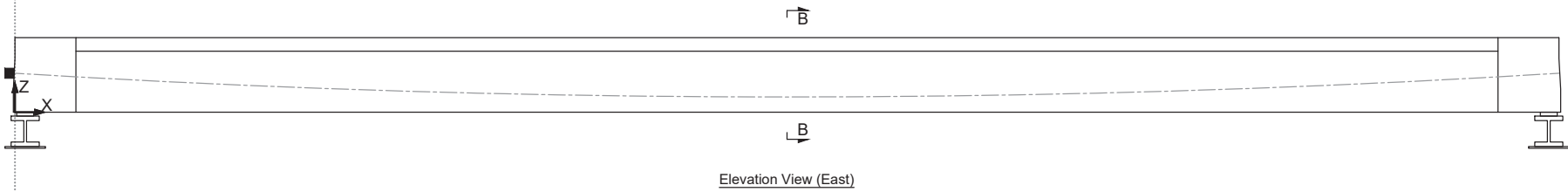
Instrument	X (in.)	Y (in.)	Z (in.)	Orientation
D1	6.25	0	44	Z
D2	905.75	0	44	Z
D3	456	-16.5	44	Z
D4	456	16.5	44	Z
D5	256	0	44	Z
D6	306	0	44	Z
D7	356	0	44	Z
D8	406	0	44	Z
D9	506	0	44	Z
D10	556	0	44	Z
D11	606	0	44	Z
D12	656	0	44	Z
S1	600	0	44	X
S2	576	0	44	X
S3	552	0	44	X
S4	528	0	44	X
S5	504	0	44	X
S6	480	0	44	X
S7	456	6	44	X
S8	456	-6	44	X
S9	432	0	44	X
S10	408	0	44	X
S11	384	0	44	X
S12	360	0	44	X
S13	336	0	44	X
S14	312	0	44	X
S15	600	7	32	X
S16	600	5	24	X
S17	600	5	16	X
S18	504	7	32	X
S19	504	5	24	X
S20	504	5	16	X
S21	456	7	32	X
S22	456	5	24	X
S23	456	5	16	X
S24	408	7	32	X
S25	408	5	24	X

Instrument	X (in.)	Y (in.)	Z (in.)	Orientation
S26	408	5	16	X
S27	312	7	32	X
S28	312	5	24	X
S29	312	5	16	X
S30	600	0	0	X
S31	576	0	0	X
S32	552	0	0	X
S33	528	0	0	X
S34	504	0	0	X
S35	480	0	0	X
S36	456	0	0	X
S37	432	0	0	X
S38	408	0	0	X
S39	384	0	0	X
S40	360	0	0	X
S41	336	0	0	X
S42	312	0	0	X
LC1	0	0	23.5	X

Instrument	Start			End		
	X (in.)	Y (in.)	Z (in.)	X (in.)	Y (in.)	Z (in.)
FOS1	336	-12	43	576	-12	43
FOS2	420	-7	32	492	-7	32
FOS3	420	-5	24	492	-5	24
FOS4	420	-5	16	492	-5	16
FOS5	336	-2	0	459	-2	0
FOS6	576	2	0	453	2	0

Instrument	X (in.)	Y (in.)	Z (in.)	Orientation	Strand
V1	456	-4	3	X	3
V2	456	4	3	X	2

Cross Section B - B

Key:

D — Laser displacement transducer

S — 60-mm concrete strain gage

RS — 5-mm rebar strain gage

V — Vibrating wire strain gage

FOS — Fiber optic sensor

LC — 850-kip Geokon load cell

Top View

Elevation View (East)

Bottom View

Cross Section A - A

Cross Section B - B

Key:

Laser displacement transducer (D)

60-mm concrete strain gage (S)

5-mm rebar strain gage (RS)

Vibrating wire strain gage (V)

Fiber optic sensor (FOS)

850-kip Geokon load cell (LC)

16

Top View

17'-0" — 6 @ 2' = 12'-0" — 17'-0"

6"

S5

11" — 1'-10"

6"

S1 S2 S3 S4 S6 S7 S8

B

Load

Elevation View (West)

S9 S12 S15 S18 S21
S10 S13 S16 S19 S22
S11 S14 S17 S20 S23

4'-0" — 2'-0" — 2'-0" — 4'-0"

B

Bottom View

11" — 1'-10"

S24 S25 S26 S27 S28 S29 S30

17'-1" — 6 @ 2' = 12'-0" — 17'-1"

Cross Section B - B

Load

6" 6"

S4 S5

4"

S15

7"

S16

$9\frac{1}{2}$"

S17

$3\frac{1}{2}$"

S27

11"

Key:

Laser displacement transducer (D)

60-mm concrete strain gage (S)

5-mm rebar strain gage (RS)

Vibrating wire strain gage (V)

Fiber optic sensor (FOS)

850-kip Geokon load cell (LC)

261

Top View

Elevation View (East)

DAQ - FOS1
DAQ - FOS2
DAQ - FOS3
DAQ - FOS4

B

21'-3"
17'-0"
3'-6"
Load
21'-3"
17'-0"

12'-0"

Bottom View

DAQ - FOS5
DAQ - FOS6

16'-11 1/4"
6'-4 3/4"
6'-3"
17'-1"

Cross Section B - B

Load

1"
FOS1
4"
FOS2
2 @ 8" = 1'-4"
FOS3
FOS4
4"
4"
FOS6
9"
9"
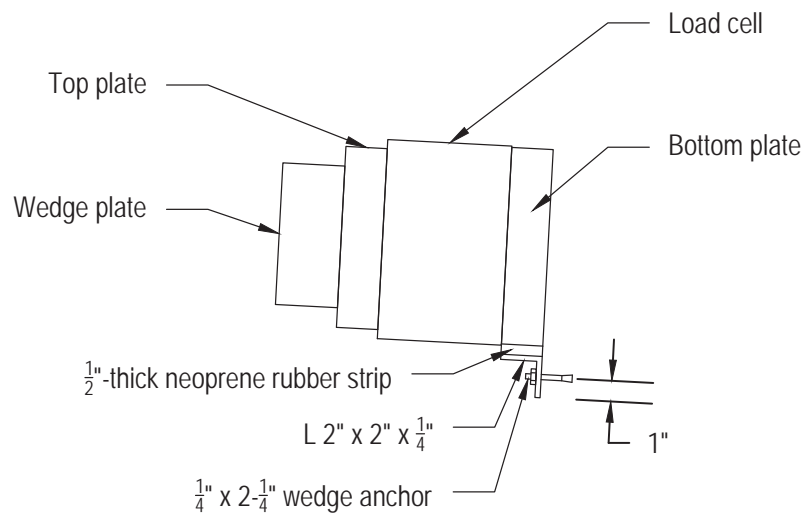FOS5

Key:

Laser displacement transducer (D)

60-mm concrete strain gage (S)

5-mm rebar strain gage (RS)

Vibrating wire strain gage (V)

Fiber optic sensor (FOS)

850-kip Geokon load cell (LC)

Top View

B
Load

Elevation View (East)

V1, V2   3"

B

7"   V1

V2   7"

23'-1"   23'-1"

Bottom View

Load

V2   V1

Cross Section B - B

Key:

	Laser displacement transducer (D)
	60-mm concrete strain gage (S)
	5-mm rebar strain gage (RS)
	Vibrating wire strain gage (V)
	Fiber optic sensor (FOS)
	850-kip Geokon load cell (LC)

263

Section C - C
(Refer to sheet 16)

1'-10"

3'-8"

1'-11"

5" 1'-0" 5"

Section D - D

3'-0"

Precast section

1'-11"

1'-5¾"

3'-1"

Post-tensioned tendons:

1 PT tendon - (4) 0.6" diam. strands

Jacking force = 0.8 f_{pu} = 187.5 kip

3
4
1
2

Strand pattern and wedge plate orientation

Endblock Dimensions

3'-0"

1'-0¼"

1'-6 1/16"

3'-8"

1'-1¾"

3'-1"

20

46'-0"

LC1

Top View

B

23'-0"

Load

Enerpac
RR-40018

Steel plate - 20" x 10" x 2"
Bearing pad - 20" x 10" x 2"

LC1

Bearing pad - 24" x 10" x 2¼"
Steel I-beam - W14x370

B

Bearing pad - 24" x 10" x 2¼"
Steel I-beam - W14x370

22'-6"

45'-0"
46'-2"

22'-6"

Elevation View (East)

LC1

Bottom View

Load

Cross Section B - B

Key:

Laser displacement transducer (D)

60-mm concrete strain gage (S)

5-mm rebar strain gage (RS)

Vibrating wire strain gage (V)

Fiber optic sensor (FOS)

850-kip Geokon load cell (LC)

FDOT Research
Flexural capacity of concrete elements
with unbonded and bonded prestressing
BDV31-977-93

University of Florida
Dept. of Civil and Coastal Engineering
787.201.6874

Task 3: Experimental Test Plan
Specimen SS-3: Test setup
Sheet 21 of 62
Scale: 1/4" = 1'

21

265

Instrument	X (in.)	Y (in.)	Z (in.)	Orientation
S1	348	0	44	X
S2	324	0	44	X
S3	300	0	44	X
S4	276	6	44	X
S5	276	-6	44	X
S6	252	0	44	X
S7	228	0	44	X
S8	204	0	44	X
S9	348	7	32	X
S10	348	5	24	X
S11	348	5	15.75	X
S12	300	7	32	X
S13	300	5	24	X
S14	300	5	15.5	X
S15	276	7	32	X
S16	276	5	25	X
S17	276	5	15.5	X
S18	252	7	32	X
S19	252	5	24.125	X
S20	252	5	15	X
S21	204	7	32	X
S22	204	5	24	X
S23	204	5	16	X
S24	348	0	0	X
S25	324	0	0	X
S26	300	0	0	X
S27	276	0	0	X
S28	252	0	0	X
S29	228	0	0	X
S30	204	0	0	X

Instrument	X (in.)	Y (in.)	Z (in.)	Orientation
D1	6.25	0	44	Z
D2	546	0	44	Z
D3	276	-14.5	44	Z
D4	276	14.5	44	Z
D5	156	0	44	Z
D6	186	0	44	Z
D7	216	0	44	Z
D8	246	0	44	Z
D9	306	0	44	Z
D10	336	0	44	Z
D11	366	0	44	Z
D12	396	0	44	Z
LC1	0	0	23	X

Instrument	Start			End		
	X (in.)	Y (in.)	Z (in.)	X (in.)	Y (in.)	Z (in.)
FOS1	204	-12	43	348	-12	43
FOS2	255	-7	32	297	-7	32
FOS3	255	-5	24	297	-5	24
FOS4	255	-5	16	297	-5	16
FOS5	202.25	-2	0	279	-2	0
FOS6	348	2	0	273	2	0

Instrument	X (in.)	Y (in.)	Z (in.)	Orientation	Strand
V1	276	-4	3	X	2
V2	276	4	3	X	1

Cross Section B - B

Key:

D — Laser displacement transducer

S — 60-mm concrete strain gage

RS — 5-mm rebar strain gage

V — Vibrating wire strain gage

FOS — Fiber optic sensor

LC — 850-kip Geokon load cell

Top View

Elevation View (East)

Bottom View

Cross Section A - A

Cross Section B - B

Key:

Laser displacement transducer (D)

60-mm concrete strain gage (S)

5-mm rebar strain gage (RS)

Vibrating wire strain gage (V)

Fiber optic sensor (FOS)

850-kip Geokon load cell (LC)

Top View

S5 — 6"
S1 S2 S3 S4 S6 S7 S8

17'-0" 6 @ 2' = 12'-0" 17'-0"

1'-10" 11"

B Load

Elevation View (West)

S9 S12 S15 S18 S21
S10 S13 S16 S19 S22
S11 S14 S17 S20 S23

17'-0½" 4'-0" 2'-0" 2'-0" 4'-0"

B

Bottom View

S24 S25 S26 S27 S28 S29 S30

17'-1" 6 @ 2' = 12'-0" 17'-1"

1'-10" 11"

Cross Section B - B

Load
6" 6"
S4 S5
S15
S16 4"
S17 2 @ 8" = 1'-4"
S27 4"
11"

Key:

▌● Laser displacement transducer (D)

▬ 60-mm concrete strain gage (S)

▬ 5-mm rebar strain gage (RS)

▨ Vibrating wire strain gage (V)

▲● Fiber optic sensor (FOS)

■ 850-kip Geokon load cell (LC)

268

Top View

Elevation View (East)

Bottom View

Cross Section B - B

21'-2³⁄₄"

16'-11³⁄₄"

3'-6"
Load

21'-3¹⁄₄"
17'-0³⁄₄"

DAQ - FOS1

DAQ - FOS2
DAQ - FOS3
DAQ - FOS4

B

B

12'-0"

16'-11"

6'-5"

DAQ - FOS5

DAQ - FOS6

6'-4"

17'-0"

Load

1"

FOS1

4"

FOS2

2 @ 8" = 1'-4"

FOS3

FOS4

4"

FOS6

FOS5

9"

9"

Key:

Laser displacement transducer (D)

60-mm concrete strain gage (S)

5-mm rebar strain gage (RS)

Vibrating wire strain gage (V)

Fiber optic sensor (FOS)

850-kip Geokon load cell (LC)

Top View

B
Load

V1, V2 ⌐ 3"

B
Elevation View (East)

7" ⌐ V1

V2 ⌐ 7"

⟵ 23'-1" ⟶ ⟵ 23'-1" ⟶

Bottom View

Load

V2   V1

Cross Section B - B

Key:

▮ ● Laser displacement transducer (D)

▬ 60-mm concrete strain gage (S)

▬ 5-mm rebar strain gage (RS)

▨ Vibrating wire strain gage (V)

▲● Fiber optic sensor (FOS)

◼ 850-kip Geokon load cell (LC)

Section C - C
(Refer to sheet 23)

1'-10"

3'-8"

1'-11"

5" 1'-0" 5"

D

D

Section D - D

3'-0"

Precast section

1'-11"

1'-5$\frac{3}{4}$"

3'-1"

Post-tensioned tendons:

1 PT tendon - (6) 0.6" diam. strands

Jacking force = 0.8 f_{pu} = 281.2 kip

Strand pattern and wedge plate orientation

6
4 5
1 2 3

Endblock Dimensions

3'-0"

1'-0$\frac{1}{4}$"

1'-6$\frac{1}{16}$"

3'-8"

1'-1$\frac{3}{4}$"

3'-1"

Top View

46'-0"

LC1

23'-0"

B

Load

Enerpac
RR-40018

Steel plate - 20" x 10" x 2"
Bearing pad - 20" x 10" x 2"

LC1

Bearing pad - 24" x 10" x 2 $\frac{1}{4}$"
Steel I-beam - W14x370

B

Bearing pad - 24" x 10" x 2 $\frac{1}{4}$"
Steel I-beam - W14x370

22'-6"

22'-6"

45'-0"

46'-2"

Elevation View (East)

LC1

Bottom View

Load

Cross Section B - B

Key:

Laser displacement transducer (D)

60-mm concrete strain gage (S)

5-mm rebar strain gage (RS)

Vibrating wire strain gage (V)

Fiber optic sensor (FOS)

850-kip Geokon load cell (LC)

272

Z
X

Instrument	X (in.)	Y (in.)	Z (in.)	Orientation
S1	348	0	44	X
S2	324	0	44	X
S3	300	0	44	X
S4	276	6	44	X
S5	276	-6	44	X
S6	252	0	44	X
S7	228	0	44	X
S8	204	0	44	X
S9	347.5	7	32	X
S10	347.5	5	24	X
S11	347.5	5	16	X
S12	299.5	7	32	X
S13	299.5	5	24	X
S14	299.5	5	16	X
S15	275.5	7	32	X
S16	275.5	5	24	X
S17	275.5	5	16	X
S18	251.5	7	32	X
S19	251.5	5	24	X
S20	251.5	5	16	X
S21	203.5	7	32	X
S22	203.5	5	24	X
S23	203.5	5	16	X
S24	348	0	0	X
S25	324	0	0	X
S26	300	0	0	X
S27	276	0	0	X
S28	252	0	0	X
S29	228	0	0	X
S30	204	0	0	X

Instrument	X (in.)	Y (in.)	Z (in.)	Orientation
D1	6	0	44	Z
D2	546	0	44	Z
D3	276	-14.5	44	Z
D4	276	14.5	44	Z
D5	156	0	44	Z
D6	186	0	44	Z
D7	216	0	44	Z
D8	246	0	44	Z
D9	306	0	44	Z
D10	336	0	44	Z
D11	366	0	44	Z
D12	396	0	44	Z
LC1	0	0	23	X

Instrument	Start			End		
	X (in.)	Y (in.)	Z (in.)	X (in.)	Y (in.)	Z (in.)
FOS1	203.75	-12	43	347.25	-12	43
FOS2	254.75	-7	32	296.75	-7	32
FOS3	254.75	-5	24	296.75	-5	24
FOS4	254.75	-5	16	296.75	-5	16
FOS5	202	-2	0	279	-2	0
FOS6	349	2	0	273	2	0

Instrument	X (in.)	Y (in.)	Z (in.)	Orientation	Strand
V1	276	-4	3	X	2
V2	276	4	3	X	1

Key:

D — Laser displacement transducer

S — 60-mm concrete strain gage

RS — 5-mm rebar strain gage

V — Vibrating wire strain gage

FOS — Fiber optic sensor

LC — 850-kip Geokon load cell

Cross Section B - B

Top View

Elevation View (East)

Bottom View

Load

Cross Section A - A

Cross Section B - B

Key:

Laser displacement transducer (D)

60-mm concrete strain gage (S)

5-mm rebar strain gage (RS)

Vibrating wire strain gage (V)

Fiber optic sensor (FOS)

850-kip Geokon load cell (LC)

B ← Load

S9 S12 S15 S18 S21
S10 S13 S16 S19 S22
S11 S14 S17 S20 S23

11'-0 3/4" | 3'-0" | 3'-0"

2 @ 18" = 3'-0"

B ←

Elevation View (West)

10"

S24 — S25 — S26 — S27 — S28 — S29 — S30

11'-1" | 6 @ 18" = 9'-0" | 11'-1"

Bottom View

Load

4" | 4"

S4   S5
     5 7/8"
S15
     5"
S16
     4 3/4"
S17
     8 3/8"
S27

10"

Cross Section B - B

Key:

| | Laser displacement transducer (D) |

| | 60-mm concrete strain gage (S) |

| | 5-mm rebar strain gage (RS) |

| | Vibrating wire strain gage (V) |

| | Fiber optic sensor (FOS) |

| | 850-kip Geokon load cell (LC) |

Top View

B
Load

RS1, RS2, RS3, | RS5, RS6, RS7,
RS8 RS9 RS10 | RS12 RS13 RS14

RS4,
RS11

B

Elevation View (East)

RS1 RS2 RS3 RS4 RS5 RS6 RS7

RS8 RS9 RS10 RS11 RS12 RS13 RS14

11'-4"   11'-4"

2 @ 18" = 3'-0"   1'-3"   1'-3"   2 @ 18" = 3'-0"

Bottom View

Load

RS11   RS4

$3\frac{1}{4}$" $3\frac{1}{4}$"

3 @ $4\frac{1}{2}$" = 1'-1$\frac{1}{2}$"

Cross Section B - B

Key:

|● Laser displacement transducer (D)

▬ 60-mm concrete strain gage (S)

▪ 5-mm rebar strain gage (RS)

▨ Vibrating wire strain gage (V)

▲—● Fiber optic sensor (FOS)

■ 850-kip Geokon load cell (LC)

276

Top View

14'-3$\frac{1}{4}$"

11'-6$\frac{1}{4}$"

DAQ - FOS1

B

2'-5$\frac{3}{4}$"

Load

14'-3"

11'-6"

DAQ - FOS2
DAQ - FOS3
DAQ - FOS4

B

8'-0"

Elevation View (East)

11'-7"

4'-3"

DAQ - FOS5

DAQ - FOS6

4'-1$\frac{3}{4}$"

11'-8$\frac{1}{4}$"

Bottom View

Load

1"

2 @ 5" = 10"

4$\frac{1}{2}$"

8$\frac{1}{2}$"

FOS1
FOS2
FOS3
FOS4

FOS6

FOS5

4$\frac{1}{2}$"

4$\frac{1}{2}$"

Cross Section B - B

Key:

Laser displacement transducer (D)	
60-mm concrete strain gage (S)	
5-mm rebar strain gage (RS)	
Vibrating wire strain gage (V)	
Fiber optic sensor (FOS)	
850-kip Geokon load cell (LC)	

277

Top View

DAQ
FOS1

Load

B

11'-1" 9'-0" 11'-1"

Elevation View (East)

FOS instrumentation provided by FDOT Structures Lab

DAQ - FOS7

DAQ - FOS8

Bottom View

Load

FOS8 FOS7

$7\frac{3}{4}$" $7\frac{3}{4}$"

Cross Section B - B

Key:

Laser displacement transducer (D)

60-mm concrete strain gage (S)

5-mm rebar strain gage (RS)

Vibrating wire strain gage (V)

Fiber optic sensor (FOS)

850-kip Geokon load cell (LC)

Task 3: Experimental Test Plan
Specimen SS-5: Additional fiber-optic sensors on rebar
Sheet 34 of 62
Scale: 1/4" = 1'

34

Section C - C
(Refer to sheet 30)

Section D - D

2'-0"
1'-2"
1'-8"
D
D

3'-0"
1'-2"
8¾"
3'-1"

Post-tensioned tendons:

1 PT tendon - (12) 0.6" diam. strands

Jacking force = 0.8 f_{pu} = 562.5 kip

10 11 12
6   7   8   9
3   4   5
1   2

Strand pattern and wedge plate orientation

3'-0"
3¾"
1'-4 11⁄16"
2'-0"
3⅝"
3'-1"

Endblock Dimensions

31'-0"

LC1

Top View

15'-6"

B

Load

Enerpac
RR-40018

Steel plate - 20" x 10" x 2"

Bearing pad - 20" x 10" x 2"

LC1

Bearing pad - 32" x 10" x 2 $\frac{1}{4}$"
Steel I-beam - W14x370

B

Bearing pad - 32" x 10" x 2 $\frac{1}{4}$"
Steel I-beam - W14x370

15'-0"

15'-0"

30'-0"

31'-2"

Elevation View (East)

LC1

Bottom View

Load

Cross Section B - B

Key:

Laser displacement transducer (D)

60-mm concrete strain gage (S)

5-mm rebar strain gage (RS)

Vibrating wire strain gage (V)

Fiber optic sensor (FOS)

850-kip Geokon load cell (LC)

280

FDOT Research
Flexural capacity of concrete elements with unbonded and bonded prestressing
BDV31-977-93

University of Florida
Dept. of Civil and Coastal Engineering
787.201.6874

Task 3: Experimental Test Plan
Specimen SS-5: Instrumentation Coordinates
Sheet 37 of 62
Scale: 1/4" = 1'

37
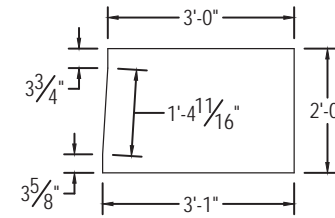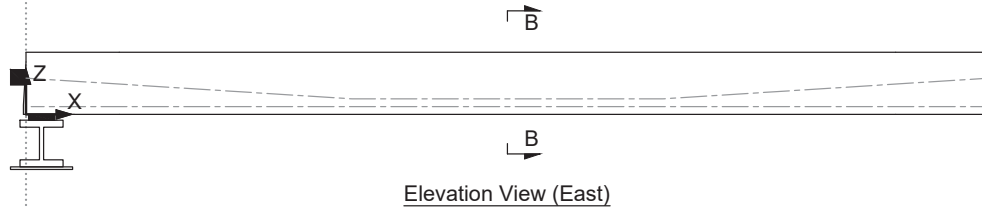
Elevation View (East)

Instrument	X (in.)	Y (in.)	Z (in.)	Orientation
S1	240	0	24	X
S2	222	0	24	X
S3	204	0	24	X
S4	186	6	24	X
S5	186	-6	24	X
S6	168	0	24	X
S7	150	0	24	X
S8	132	0	24	X
S9	239.75	10	17.75	X
S10	239.75	10	13	X
S11	239.75	10	8	X
S12	203.75	10	18.25	X
S13	203.75	10	13.25	X
S14	203.75	10	8	X
S15	185.75	10	18.125	X
S16	185.75	10	13.125	X
S17	185.75	10	8.375	X
S18	167.75	10	18.25	X
S19	167.75	10	13.25	X
S20	167.75	10	8	X
S21	131.75	10	17.5	X
S22	131.75	10	13	X
S23	131.75	10	7.875	X
S24	240	0	0	X
S25	222	0	0	X
S26	204	0	0	X
S27	186	0	0	X
S28	168	0	0	X
S29	150	0	0	X
S30	132	0	0	X

Instrument	X (in.)	Y (in.)	Z (in.)	Orientation	Bar
RS1	135	-6.75	3	X	6L-4
RS2	153	-6.75	3	X	6L-4
RS3	171	-6.75	3	X	6L-4
RS4	186	-6.75	3	X	6L-4
RS5	201	-6.75	3	X	6L-4
RS6	219	-6.75	3	X	6L-4
RS7	237	-6.75	3	X	6L-4
RS8	135	6.75	3	X	6L-1
RS9	153	6.75	3	X	6L-1
RS10	171	6.75	3	X	6L-1
RS11	186	6.75	3	X	6L-1
RS12	201	6.75	3	X	6L-1
RS13	219	6.75	3	X	6L-1
RS14	237	6.75	3	X	6L-1

Instrument	Start			End		
	X (in.)	Y (in.)	Z (in.)	X (in.)	Y (in.)	Z (in.)
FOS1	138.25	-10	23	234	-10	23
FOS2	171.25	-10	18	201.25	-10	18
FOS3	171.25	-10	13	201.25	-10	13
FOS4	171.25	-10	8.5	201.25	-10	8.5
FOS5	138	-5.5	0	189	-5.5	0
FOS6	232.75	5.5	0	183	5.5	0
FOS7	132	-2.25	3	240	-2.25	3
FOS8	132	2.25	3	240	2.25	3

Instrument	X (in.)	Y (in.)	Z (in.)	Orientation
D1	6	0	24	Z
D2	366	0	24	Z
D3	186	-14.5	24	Z
D4	186	14.5	24	Z
D5	126	0	24	Z
D6	146	0	24	Z
D7	146	0	24	Z
D8	166	0	24	Z
D9	206	0	24	Z
D10	226	0	24	Z
D11	246	0	24	Z
D12	266	0	24	Z
LC1	0	0	14	X

Load

Cross Section B - B

Key:

D — Laser displacement transducer

S — 60-mm concrete strain gage

RS — 5-mm rebar strain gage

V — Vibrating wire strain gage

FOS — Fiber optic sensor

LC — 850-kip Geokon load cell

Top View

Elevation View (East)

Bottom View

Cross Section A - A

Cross Section B - B

Key:

- Laser displacement transducer (D)
- 60-mm concrete strain gage (S)
- 5-mm rebar strain gage (RS)
- Vibrating wire strain gage (V)
- Fiber optic sensor (FOS)
- 850-kip Geokon load cell (LC)

12'-1" | 6 @ 18" = 9'-0" | 12'-1"

11" | 1'-10"

S1 S2 S3 S4 S5 S6 S7

Top View

B

A 2 @ 18" = 3'-0"

Load

3'-0" | 3'-0"

S8 S11 S14 S17 S20
S9 S12 S15 S18 S21
S10 S13 S16 S19 S22

S30

B A

Elevation View (West)

S23 S24 S25 S26 S27 S28

11'-11" | 11'-11"

2 @ 18" = 3'-0" Bottom View 2 @ 18" = 3'-0"

Cross Section A - A

1'-0" 1'-0"

S4

S14 4"

S15 2 @ 8" = 1'-4"

S16

4"

S30 S29

1½"

Key:

Laser displacement transducer (D)

60-mm concrete strain gage (S)

5-mm rebar strain gage (RS)

Vibrating wire strain gage (V)

Fiber optic sensor (FOS)

850-kip Geokon load cell (LC)

283

6 @ 18" = 9'-0"

12'-1"   12'-1"

RS8 RS9 RS10 RS11 RS12 RS13 RS14

RS1 RS2 RS3 RS4 RS5 RS6 RS7

Top View

A

Load

RS1, RS2, RS3, RS4, RS5, RS6, RS7,
RS8   RS9   RS10 RS11 RS12 RS13 RS14

A

Elevation View (East)

Bottom View

9" 6" 9"

RS11   RS4

Cross Section A - A

Key:

Laser displacement transducer (D)

60-mm concrete strain gage (S)

5-mm rebar strain gage (RS)

Vibrating wire strain gage (V)

Fiber optic sensor (FOS)

850-kip Geokon load cell (LC)

Top View

Elevation View (West)

Elevation View (East)

Bottom View

Cross Section A - A

Key:

Laser displacement transducer (D)

60-mm concrete strain gage (S)

5-mm rebar strain gage (RS)

Vibrating wire strain gage (V)

Fiber optic sensor (FOS)

850-kip Geokon load cell (LC)

FDOT Research
Flexural capacity of concrete elements
with unbonded and bonded prestressing
BDV31-977-93

University of Florida
Dept. of Civil and Coastal Engineering
787.201.6874

Task 3: Experimental Test Plan
Specimen NB-1: Fiber-optic sensors
Sheet 41 of 62
Scale: 1/4" = 1'

41

17'-7"

15'-7"

V1 V2

4" 6" 10"

Top View

Load

C A D

V1 V2 2"

V3

C A D

Elevation View (East)

V3

16'-6"

Bottom View

Cross Section A - A

V3

Cross Section C - C

V1

Cross Section D - D

V2

Key:

Laser displacement transducer (D)

60-mm concrete strain gage (S)

5-mm rebar strain gage (RS)

Vibrating wire strain gage (V)

Fiber optic sensor (FOS)

850-kip Geokon load cell (LC)

1'-10"

3'-8"

1'-10$\frac{1}{8}$"

5" 1'-0" 5"

F

F

Section E - E
(Refer to sheet 38)

3'-1"

Precast section

1'-10$\frac{1}{8}$"

1'-4$\frac{3}{4}$"

2" Cover

3'-0"

Section F - F

Post-tensioned tendons:

1 PT tendon - (12) 0.6" diam. strands

Jacking force = 0.8 f_{pu} = 562.5 kip

10 11 12

6 7 8 9

3 4 5

1 2

Strand pattern and wedge plate orientation

3'-1"

1'-1$\frac{3}{4}$"

1'-6$\frac{1}{16}$"

3'-8"

1'-0$\frac{1}{4}$"

3'-0"

Endblock Dimensions

Task 3: Experimental Test Plan
Specimen NB-1: Load cell assembly
Sheet 43 of 62
Scale: 1/2" = 1'

43

33'-2"

LC1

Top View

B

1'-7"

Load
Enerpac
RR-40018

Tie down

R14 (C12x30 (x2))

Steel plate - 20" x 10" x 2"

Bearing pad - 20" x 10" x 2"

R33 (W16x100)

LC1

1'-6"

Bearing pad - 24" x 10" x 2$\frac{1}{4}$"

Steel Load blocks

3'-0"   3'-0"   12'-0"   15'-0"

B

15'-0"

16'-6"

33'-0"

Elevation View (East)

LC1

Bottom View

Load

Cross Section B - B

Key:

	Laser displacement transducer (D)
	60-mm concrete strain gage (S)
	5-mm rebar strain gage (RS)
	Vibrating wire strain gage (V)
	Fiber optic sensor (FOS)
	850-kip Geokon load cell (LC)

Instrument	X (in.)	Y (in.)	Z (in.)	Orientation
S1	252	0	44	X
S2	234	0	44	X
S3	216	0	44	X
S4	198	0	44	X
S5	180	0	44	X
S6	162	0	44	X
S7	144	0	44	X
S8	252	7	32	X
S9	252	5	24	X
S10	252	5	16	X
S11	216	7	32	X
S12	216	5	24	X
S13	216	5	16	X
S14	198	7	32	X
S15	198	5	24	X
S16	198	5	16	X
S17	180	7	32	X
S18	180	5	24	X
S19	180	5	16	X
S20	144	7	32	X
S21	144	5	24	X
S22	144	5	16	X
S23	253	0	0	X
S24	235	0	0	X
S25	217	0	0	X
S26	179	0	0	X
S27	161	0	0	X
S28	143	0	0	X
S29	198	-11	1.5	X
S30	198	11	1.5	X

Instrument	X (in.)	Y (in.)	Z (in.)	Orientation	Bar
RS1	144	-3	41.125	X	4A-3
RS2	162	-3	41.125	X	4A-3
RS3	180	-3	41.125	X	4A-3
RS4	198	-3	41.125	X	4A-3
RS5	216	-3	41.125	X	4A-3
RS6	234	-3	41.125	X	4A-3
RS7	252	-3	41.125	X	4A-3
RS8	144	3	41.125	X	4A-2
RS9	162	3	41.125	X	4A-2
RS10	180	3	41.125	X	4A-2
RS11	198	3	41.125	X	4A-2
RS12	216	3	41.125	X	4A-2
RS13	234	3	41.125	X	4A-2
RS14	252	3	41.125	X	4A-2

Instrument	Start			End		
	X (in.)	Y (in.)	Z (in.)	X (in.)	Y (in.)	Z (in.)
FOS1	150	-12	43	201	-12	43
FOS2	150	12	42	195	12	42
FOS3	183	-7	32	213	-7	32
FOS4	183	-5	24	213	-5	24
FOS5	183	-5	16	213	-5	16
FOS6	149	-2	0	185	-2	0
FOS7	247	-2	0	211	-2	0
FOS8	243.25	12	43	195.25	12	43

Instrument	X (in.)	Y (in.)	Z (in.)	Orientation	Strand
V1	186	-1	34	X	12
V2	210	1	34	X	11
V3	198	-4	3	X	2

Instrument	X (in.)	Y (in.)	Z (in.)	Orientation
D1	29	0	44	Z
D2	378	-12.5	44	Z
D3	378	12.5	44	Z
D4	198	0	44	Z
D5	118	0	44	Z
D6	138	0	44	Z
D7	158	0	44	Z
D8	178	0	44	Z
D9	218	0	44	Z
D10	238	0	44	Z
D11	258	0	44	Z
D12	278	0	44	Z
LC1	0	0	22.125	X

Cross Section A - A

Key:

D	Laser displacement transducer
S	60-mm concrete strain gage
RS	5-mm rebar strain gage
V	Vibrating wire strain gage
FOS	Fiber optic sensor
LC	850-kip Geokon load cell

FDOT Research
Flexural capacity of concrete elements
with unbonded and bonded prestressing
BDV31-977-93

University of Florida
Dept. of Civil and Coastal Engineering
787.201.6874

Task 3: Experimental Test Plan
Specimen NB-1: Instrumentation Coordinates
Sheet 45 of 62
Scale: 1/4" = 1'

45

Top View

Elevation View (East)

Bottom View

Cross Section A - A

Cross Section B - B

Key:

	Laser displacement transducer (D)
	60-mm concrete strain gage (S)
	5-mm rebar strain gage (RS)
	Vibrating wire strain gage (V)
	Fiber optic sensor (FOS)
	850-kip Geokon load cell (LC)

Top View

Elevation View (West)

Bottom View

Cross Section A - A

Key:

Laser displacement transducer (D)

60-mm concrete strain gage (S)

5-mm rebar strain gage (RS)

Vibrating wire strain gage (V)

Fiber optic sensor (FOS)

850-kip Geokon load cell (LC)

12'-1⅜"   6 @ 18" = 9'-0"   12'-1⅜"

RS8 RS9 RS10 RS11 RS12 RS13 RS14

RS1 RS2 RS3 RS4 RS5 RS6 RS7

Top View

A

Load

RS1, RS2 RS3, RS4, RS5, RS6, RS7,
RS8 RS9 RS10 RS11 RS12 RS13 RS14

A

Elevation View (East)

Bottom View

9" 6" 9"

RS11   RS4

Cross Section A - A

Key:

Laser displacement transducer (D)

60-mm concrete strain gage (S)

5-mm rebar strain gage (RS)

Vibrating wire strain gage (V)

Fiber optic sensor (FOS)

850-kip Geokon load cell (LC)

Top View

Load

4'-3"   12'-6⅞"

A   DAQ
FOS2

Elevation View (West)

15'-4⅜"   15'-4¼"
12'-6⅞"   4'-3"   16'-4⅞"

A   A

DAQ
FOS1   Load

DAQ - FOS3
DAQ - FOS4
DAQ - FOS5

15'-3"   2'-6"   15'-3"

A

Elevation View (East)

12'-4½" 2'-11½"   2'-11¾"   12'-6"
DAQ - FOS6   DAQ - FOS7

2'-2¼"

Bottom View

Cross Section A - A

FOS2
1"   FOS1
4"   FOS3
2 @ 8" = 1'-4"   FOS4
4"   FOS5

Key:

	Laser displacement transducer (D)
	60-mm concrete strain gage (S)
	5-mm rebar strain gage (RS)
	Vibrating wire strain gage (V)
	Fiber optic sensor (FOS)
	850-kip Geokon load cell (LC)

293

17'-7 3/8"

15'-7 3/8"

V1   V2

4"   6"   10"

Top View

Load

C A D

V1   V2   2"

V3

C A D

Elevation View (East)

V3

16'-6"

Bottom View

Key:

Laser displacement transducer (D)

60-mm concrete strain gage (S)

5-mm rebar strain gage (RS)

Vibrating wire strain gage (V)

Fiber optic sensor (FOS)

850-kip Geokon load cell (LC)

V1

V2

V3

Cross Section A - A

Cross Section C - C

Cross Section D - D

294

1'-10"

3'-8"

2'-4⅞"

1'-1½"

5" 1'-0" 5"

F

F

Section E - E
(Refer to sheet 46)

3'-1⅜"

1'-3⅛" 1'-8¼"

Precast section

1'-1½"

8 5/16"

3'-0"

Section F - F

Post-tensioned tendons:

2 PT tendons - (18) 0.6" diam. strands

(9) strands / tendon

Jacking force = 0.8 f_{pu} = 421.8 kip

7 8 9

5 ◯ ◯ 6

3 ◯ 4

1 2

Strand pattern and wedge plate orientation

3'-1⅜"

1'-11¼"

3'-8"

1'-4⅜"

4½"

3'-0"

Endblock Dimensions

51

33'-2³⁄₄"

LC2

Top View

B

1'-7³⁄₈"

Tie down

R14 (C12x30 (x2))

R33 (W16x100)

Bearing pad - 20" x 10" x 2"

Load

Enerpac
RR-40018

Steel plate - 20" x 10" x 2"
Bearing pad - 20" x 10" x 2"

LC2

LC1

Bearing pad - 24" x 10" x 2¼"

Steel Load blocks

1'-6"   3'-0"   12'-0"   15'-0"

15'-0"

16'-6"

33'-0"

B

Elevation View (East)

LC1

Bottom View

Load

Cross Section B - B

Key:

Laser displacement transducer (D)

60-mm concrete strain gage (S)

5-mm rebar strain gage (RS)

Vibrating wire strain gage (V)

Fiber optic sensor (FOS)

850-kip Geokon load cell (LC)

FDOT Research
Flexural capacity of concrete elements
with unbonded and bonded prestressing
BDV31-977-93

University of Florida
Dept. of Civil and Coastal Engineering
787.201.6874

Task 3: Experimental Test Plan
Specimen NB-2: Test setup
Sheet 52 of 62
Scale: 1/4" = 1'

52

296

Instrument	X (in.)	Y (in.)	Z (in.)	Orientation
S1	144	0	44	X
S2	162	0	44	X
S3	180	0	44	X
S4	198	0	44	X
S5	216	0	44	X
S6	234	0	44	X
S7	252	0	44	X
S8	252	7	31	X
S9	252	5	23	X
S10	252	5	16	X
S11	215.75	7	31	X
S12	215.75	5	23	X
S13	215.75	5	16	X
S14	197.75	7	31	X
S15	197.75	5	23	X
S16	197.75	5	16	X
S17	179.75	7	31	X
S18	179.75	5	23	X
S19	179.75	5	16	X
S20	143.625	7	31	X
S21	143.625	5	23	X
S22	143.625	5	16	X
S23	252	0	0	X
S24	234	0	0	X
S25	216	0	0	X
S26	180	0	0	X
S27	162	0	0	X
S28	144	0	0	X

Instrument	X (in.)	Y (in.)	Z (in.)	Orientation	Bar
RS1	144	-3	41.125	X	4A-3
RS2	162	-3	41.125	X	4A-3
RS3	180	-3	41.125	X	4A-3
RS4	198	-3	41.125	X	4A-3
RS5	216	-3	41.125	X	4A-3
RS6	234	-3	41.125	X	4A-3
RS7	252	-3	41.125	X	4A-3
RS8	144	3	41.125	X	4A-2
RS9	162	3	41.125	X	4A-2
RS10	180	3	41.125	X	4A-2
RS11	198	3	41.125	X	4A-2
RS12	216	3	41.125	X	4A-2
RS13	234	3	41.125	X	4A-2
RS14	252	3	41.125	X	4A-2

Instrument	X (in.)	Y (in.)	Z (in.)	Orientation
D1	30	0	44	Z
D2	377.75	-12.375	44	Z
D3	377.75	12.375	44	Z
D4	118	0	44	Z
D5	138	0	44	Z
D6	158	0	44	Z
D7	178	-1	44	Z
D8	198	-1	44	Z
D9	218	-1	44	Z
D10	238	0	44	Z
D11	258	0	44	Z
D12	278	0	44	Z
LC1	0	0	13.5	X
LC2	0	0	28.875	X

Instrument	Start			End		
	X (in.)	Y (in.)	Z (in.)	X (in.)	Y (in.)	Z (in.)
FOS1	149.5	-12	43	200.5	-12	43
FOS2	149.5	12	43	200.5	12	43
FOS3	183	-7	32	213.125	-7	32
FOS4	183	-5	24	213.125	-5	24
FOS5	183	-5	16	213.125	-5	16
FOS6	148.5	-2	0	184	-2	0
FOS7	246	-2	0	210.25	-2	0

Instrument	X (in.)	Y (in.)	Z (in.)	Orientation	Strand
V1	186	-1	34	X	10
V2	210	1	34	X	9
V3	198	-4	3	X	2

Key:

D — Laser displacement transducer

S — 60-mm concrete strain gage

RS — 5-mm rebar strain gage

V — Vibrating wire strain gage

FOS — Fiber optic sensor

LC — 850-kip Geokon load cell

Cross Section A - A

Top View

Elevation View (East)

Bottom View

Cross Section A - A

Cross Section B - B

Key:

Laser displacement transducer (D)

60-mm concrete strain gage (S)

5-mm rebar strain gage (RS)

Vibrating wire strain gage (V)

Fiber optic sensor (FOS)

850-kip Geokon load cell (LC)

FDOT Research
Flexural capacity of concrete elements
with unbonded and bonded prestressing
BDV31-977-93

Task 3: Experimental Test Plan
Specimen NB-3: Foil-type strain gages on concrete surface
Sheet 55 of 62
Scale: 1/4" = 1'

55

Top View

Elevation View (East)

Bottom View

Cross Section A - A

Key:

Laser displacement transducer (D)

60-mm concrete strain gage (S)

5-mm rebar strain gage (RS)

Vibrating wire strain gage (V)

Fiber optic sensor (FOS)

850-kip Geokon load cell (LC)

12'-1⅜" | 6 @ 18" = 9'-0" | 12'-1⅜"

RS8 RS9 RS10 RS11 RS12 RS13 RS14

RS1 RS2 RS3 RS4 RS5 RS6 RS7

Top View

A

Load

RS1, RS2, RS3, RS4, RS5, RS6, RS7,
RS8   RS9   RS10 RS11 RS12 RS13 RS14

A

Elevation View (East)

Bottom View

Cross Section A - A

9" 6" 9"

RS11   RS4

Key:

Laser displacement transducer (D)

60-mm concrete strain gage (S)

5-mm rebar strain gage (RS)

Vibrating wire strain gage (V)

Fiber optic sensor (FOS)

850-kip Geokon load cell (LC)

FDOT Research
Flexural capacity of concrete elements
with unbonded and bonded prestressing
BDV31-977-93

University of Florida
Dept. of Civil and Coastal Engineering
787.201.6874

Task 3: Experimental Test Plan
Specimen NB-3: Foil-type strain gages on mild steel bars
Sheet 56 of 62
Scale: 1/4" = 1'

56

300

Top View

Load

A

4'-3"　　　　　　　　　　12'-6⅞"

DAQ - FOS2

Elevation View (West)

A

A

15'-4⅜"　　　　　　　15'-4⅜"

12'-7"　　　4'-3"　　　16'-4¾"

DAQ - FOS1

Load

DAQ - FOS3
DAQ - FOS4
DAQ - FOS5

15'-3"　　　2'-6"　　　15'-3"

A

Elevation View (East)

A

12'-4¾"　　DAQ - FOS6　　3'-0"　　2'-10½"　　DAQ - FOS7　　12'-4½"

9"

2'-4¼"

Bottom View

Cross Section A - A

FOS2

1"

2¾"

FOS1

FOS3
S14
FOS4
S15
FOS5
S16

9¼"

8¾"

3¼"

S30

S29

Key:

Laser displacement transducer (D)

60-mm concrete strain gage (S)

5-mm rebar strain gage (RS)

Vibrating wire strain gage (V)

Fiber optic sensor (FOS)

850-kip Geokon load cell (LC)

Top View

17'-7³⁄₈"
15'-7³⁄₈"

V1 V2

4" 6" 10"

Elevation View (East)

Load

C A D

V1 V2 2"

V3

C A D

Bottom View

16'-6"

V3

Cross Section A - A

V3

Cross Section C - C

V1

Cross Section D - D

V2

Key:

Laser displacement transducer (D)

60-mm concrete strain gage (S)

5-mm rebar strain gage (RS)

Vibrating wire strain gage (V)

Fiber optic sensor (FOS)

850-kip Geokon load cell (LC)

302

Section E - E
(Refer to sheet 54)

1'-10"

3'-8"

2'-3½"

11"

5" 1'-0" 5"

F

F

Section F - F

3'-1⅜"

Precast section

1'-4½" 1'-9¾"

11"

6½"

3'-0"

Post-tensioned tendons:

2 PT tendons - (24) 0.6" diam. strands

(12) strands / tendon

Jacking force = 0.8 f_{pu} = 562.5 kip

Strand pattern and wedge plate orientation

10 11 12

6 7 8 9

3 4 5

1 2

Endblock Dimensions

3'-1⅜"

1'-11¼"

1'-4⅜"

4½"

3'-0"

3'-8"

33'-2⅜"

LC2

Top View

B

Tie down

R14 (C12x30 (x2))

R33 (W16x100)

LC2

LC1

Load

Enerpac
RR-40018

1'-7⅜"

Steel plate - 20" x 10" x 2"

Bearing pad - 20" x 10" x 2"

Bearing pad - 24" x 10" x 2¼"

Steel Load blocks

1'-6"   3'-0"   12'-0"   15'-0"

15'-0"

16'-6"

33'-0"

B

Elevation View (East)

LC1

Bottom View

Load

Cross Section B - B

Key:

● Laser displacement transducer (D)

▬ 60-mm concrete strain gage (S)

▪ 5-mm rebar strain gage (RS)

▨ Vibrating wire strain gage (V)

▲● Fiber optic sensor (FOS)

■ 850-kip Geokon load cell (LC)

304

Instrument	X (in.)	Y (in.)	Z (in.)	Orientation
S1	252	0	44	X
S2	234	0	44	X
S3	216	0	44	X
S4	198	0	44	X
S5	180	0	44	X
S6	162	0	44	X
S7	144	0	44	X
S8	251.75	-7	31.5	X
S9	251.75	-5	21.75	X
S10	251.75	-5	13	X
S11	218.25	-7	31.5	X
S12	218.25	-5	21.75	X
S13	218.25	-5	13	X
S14	197.75	-7	31.5	X
S15	197.75	-5	21.75	X
S16	197.75	-5	13	X
S17	179.75	-7	31.5	X
S18	179.75	-5	21.75	X
S19	179.75	-5	13	X
S20	142.5	-7	31.5	X
S21	142.5	-5	21.75	X
S22	142.5	-5	13	X
S23	253.75	0	0	X
S24	238	0	0	X
S25	218	0	0	X
S26	178.5	0	0	X
S27	160.5	0	0	X
S28	141.5	0	0	X
S29	198.25	-11	1.75	X
S30	198.25	11	1.75	X

Instrument	X (in.)	Y (in.)	Z (in.)	Orientation	Bar
RS1	144	-3	41.125	X	4A-3
RS2	162	-3	41.125	X	4A-3
RS3	180	-3	41.125	X	4A-3
RS4	198	-3	41.125	X	4A-3
RS5	216	-3	41.125	X	4A-3
RS6	234	-3	41.125	X	4A-3
RS7	252	-3	41.125	X	4A-3
RS8	144	3	41.125	X	4A-2
RS9	162	3	41.125	X	4A-2
RS10	180	3	41.125	X	4A-2
RS11	198	3	41.125	X	4A-2
RS12	216	3	41.125	X	4A-2
RS13	234	3	41.125	X	4A-2
RS14	252	3	41.125	X	4A-2

Instrument	Start			End		
	X (in.)	Y (in.)	Z (in.)	X (in.)	Y (in.)	Z (in.)
FOS1	149.625	-12	43	200.625	-12	43
FOS2	200.5	12	43	149.5	12	43
FOS3	183	-7	33.25	213	-7	33.25
FOS4	183	-5	24	213	-5	24
FOS5	183	-5	15.25	213	-5	15.25
FOS6	148.75	-2	0	184.75	-2	0
FOS7	247.5	-2	0	213	-2	0

Instrument	X (in.)	Y (in.)	Z (in.)	Orientation	Strand
V1	186	-1	34	X	7
V2	210	1	34	X	6
V3	198	-4	3	X	2

Instrument	X (in.)	Y (in.)	Z (in.)	Orientation
D1	29.5	0	44	Z
D2	377.5	-12.5	44	Z
D3	377.5	12.5	44	Z
D4	198	0	44	Z
D5	118	0	44	Z
D6	138	0	44	Z
D7	158	0	44	Z
D8	178	0	44	Z
D9	218	0	44	Z
D10	238	0	44	Z
D11	258	0	44	Z
D12	278	0	44	Z
LC1	0	0	11	X
LC1	0	0	27.5	X
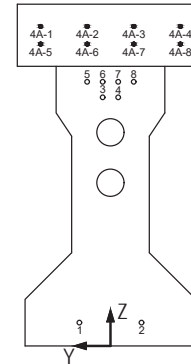
4A-1 4A-2 4A-3 4A-4
4A-5 4A-6 4A-7 4A-8

Cross Section A - A

Key:

D — Laser displacement transducer

S — 60-mm concrete strain gage

RS — 5-mm rebar strain gage

V — Vibrating wire strain gage

FOS — Fiber optic sensor

LC — 850-kip Geokon load cell

Wedge plate

Bottom plate

Load cell

Top plate

$\frac{1}{2}$"-thick neoprene rubber strip

L 2" x 2" x $\frac{1}{4}$"

1"

$\frac{1}{4}$" x 2-$\frac{1}{4}$" wedge anchors

1"

1"

1'-0"

Front view

Top plate

Load cell

Bottom plate

Wedge plate

$\frac{1}{2}$"-thick neoprene rubber strip

L 2" x 2" x $\frac{1}{4}$"

1"

$\frac{1}{4}$" x 2-$\frac{1}{4}$" wedge anchor

Elevation view

Task 3: Experimental Test Plan
Load cell assembly
Sheet 62 of 62
Scale: 2" = 1'

62
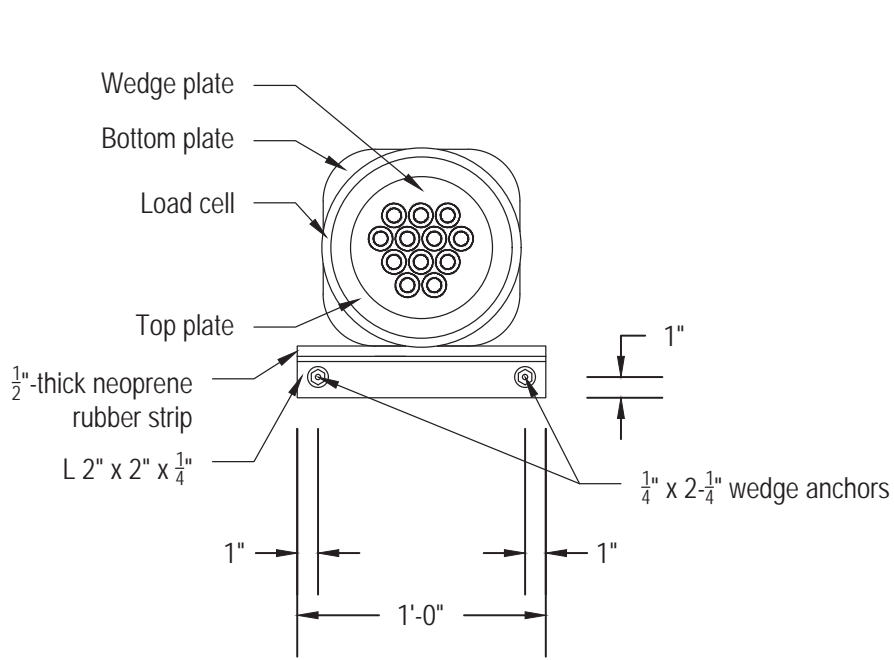
APPENDIX C
Experimental results: Simply-supported precast beam specimens

Beam Specimen SS-1

Summary

(a)

(b)

Figure C.1 Beam specimen SS-1 at end of testing: (a) East side (fiber optic sensors) and (b) West side (foil strain gages)
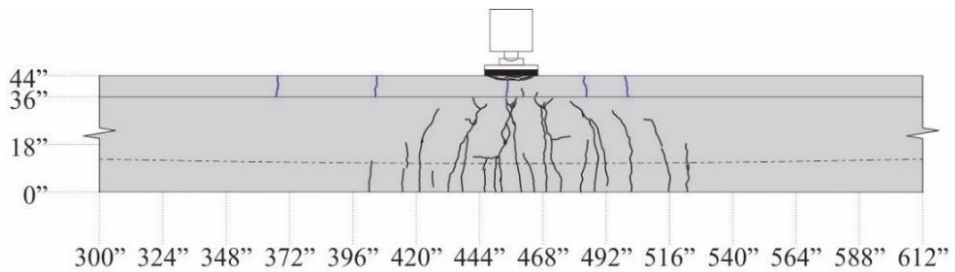
Figure C.2 Beam specimen SS-1 crack pattern: east side
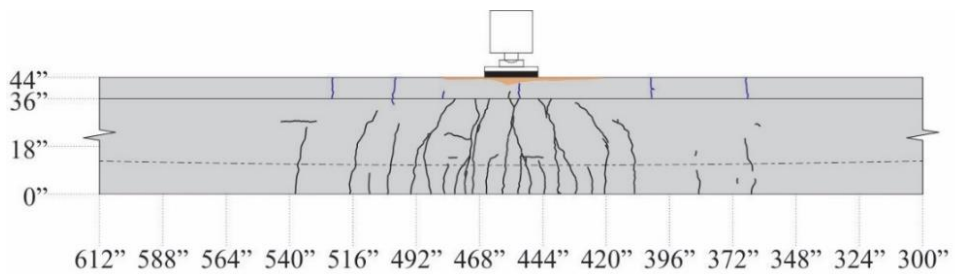
Figure C.3 Beam specimen SS-1 crack pattern: west side
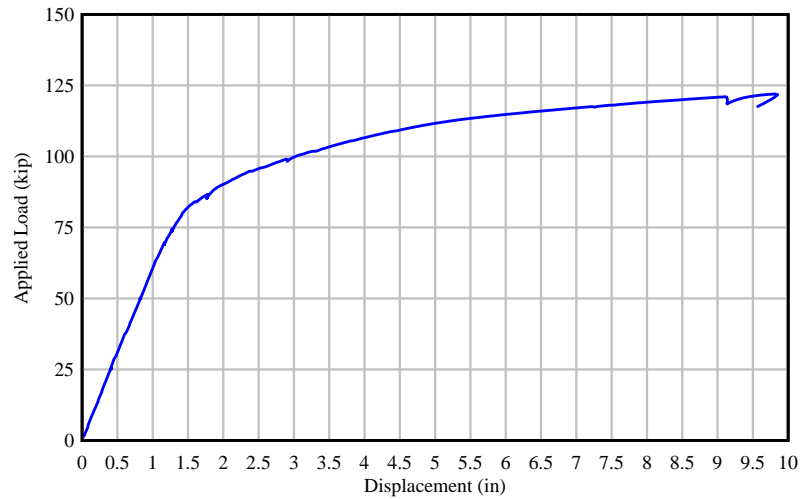
Figure C.4 Beam specimen SS-1: applied force vs. displacement at load point

Specimen Details

The cross-section of beam specimen SS-1 corresponds to a modified AASHTO Type II beam with a web width of 10 in. The girder section was topped with an 8-in. thick concrete deck and rectangular cast-in-place endblocks were added to accommodate post-tensioning anchorage hardware and additional reinforcement. Figure C.5 shows the beam inside the load frame. Key parameters are listed in Table C.1. Concrete cylinders were tested to determine the compressive strength at the time of testing as shown in Table C.2.

Figure C.5 Beam specimen SS-1 inside test frame

Table C.1 Beam specimen SS-1: key parameters

Cross Section	Specimen Length (ft)	L/D	U/T	No. PreT Strands (bottom)	No. PreT Strands (top)	No. PT Strands	PT tendon profile	Longitudinal mild steel bars (deck)
Modified AASHTO Type II	76	25	0.4	10	2	6	F5	8 #4

Table C.2 Beam specimen SS-1: compressive strength results

Description	Cast date	Test date	Test age (days)	Compressive Strength (psi)	Specified Compressive Strength (psi)
Precast girder	2020-01-23	2020-01-24	1	4,720	8,500
		2020-01-27	4	8,595	
		2020-02-20	28	10,698	
		2021-12-06	683	13,404	
Deck	2020-01-27	2020-01-28	1	4,400	8,500
		2020-01-29	2	6,405	
		2020-02-24	28	10,464	
		2021-09-30	612	13,713	
End blocks	2021-11-05	2021-11-19	14	9,563	8,500
		2021-12-03	28	10,035	

Test Procedure

Specimen SS-1 was loaded at a rate of 0.25 kip/sec. Load was held at 25, 49, 69, 74, 87, 99, 120, and 122 kip. This allowed for the beam to be inspected, cracks marked, and VW strain gage readings taken. The first visible cracks were identified and marked at a load of 74 kip (Figure C.6). Fiber optic sensors located on the bottom of the beam recorded the first cracks along the centerline of the beam section at $P = 70$ kip as depicted in Figure C.11. Cracks were marked during loading up until 87 kip, which is 70% of the predicted nominal capacity. Audible indications of damage were heard emanating from concrete in the top of the deck (near midspan, west side). Loading was stopped shortly thereafter at $P = 122$ kip. The beam was then unloaded, cracks were marked, and final VW strain gage readings were taken.
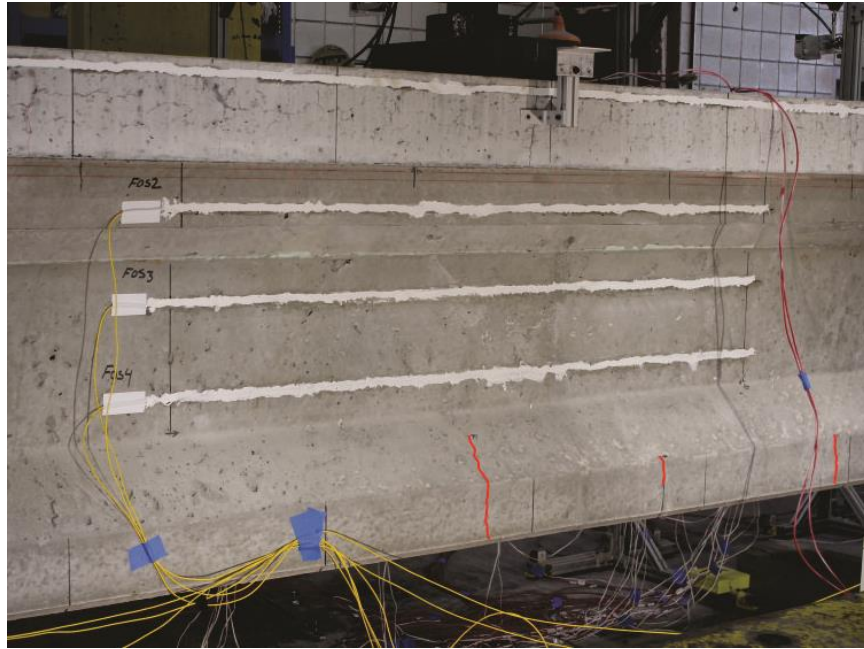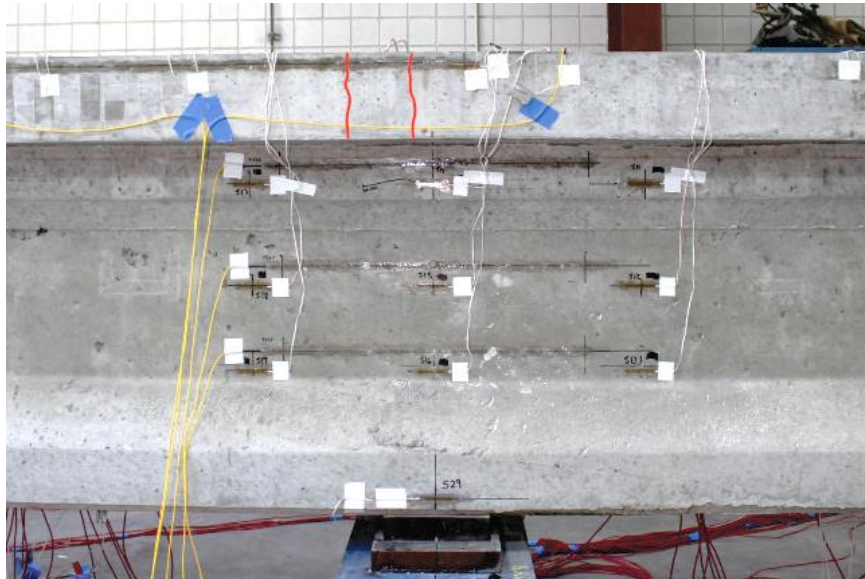
Figure C.6 Specimen SS-1: first observed cracks (marked in red) at P = 74 kip on east side

Detailed Test Results
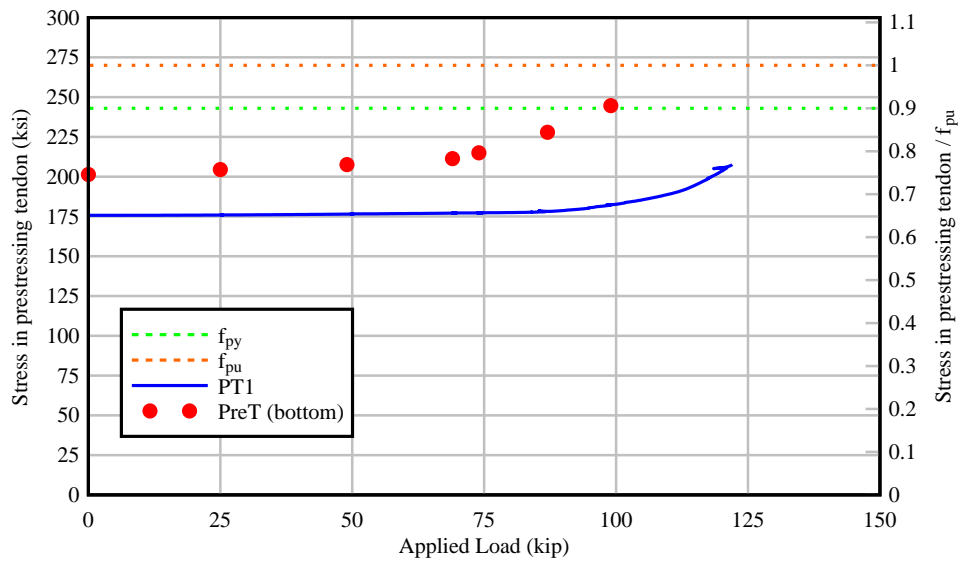
Figure C.7 Specimen SS-1: stress in PT and PreT tendons as a function of applied load
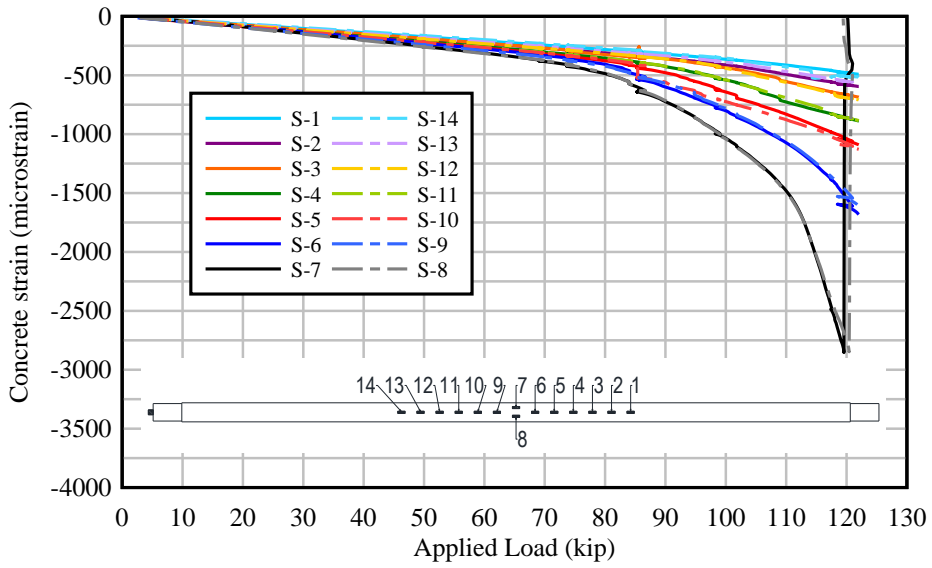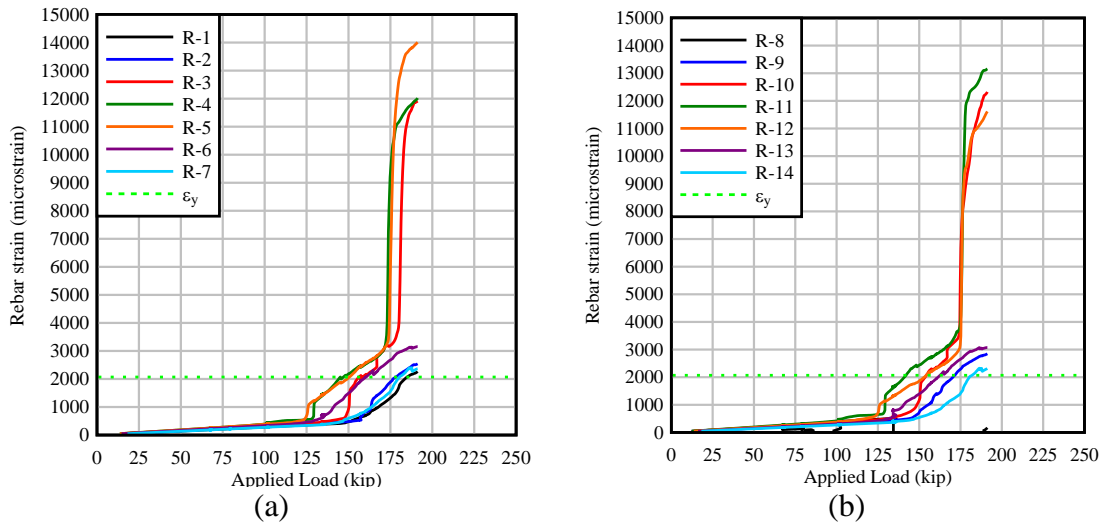
Figure C.8 Specimen SS-1: concrete strain vs. applied load – top of deck
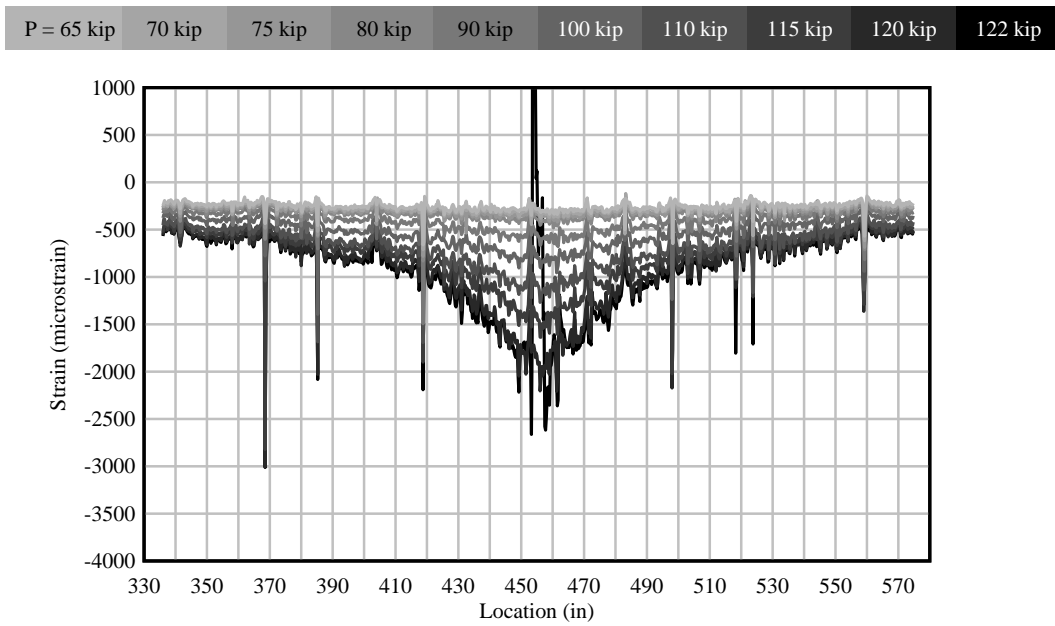
Figure C.9 Specimen SS-1: concrete strain vs. location – top flange (FOS-1)

311

| P = 65 kip | 70 kip | 75 kip | 80 kip | 90 kip | 100 kip | 110 kip | 115 kip | 120 kip | 122 kip |
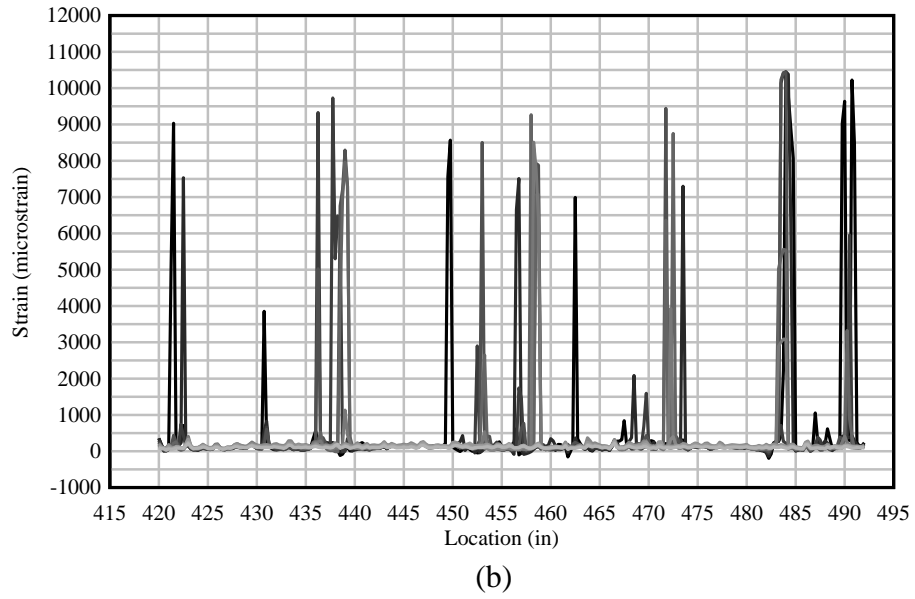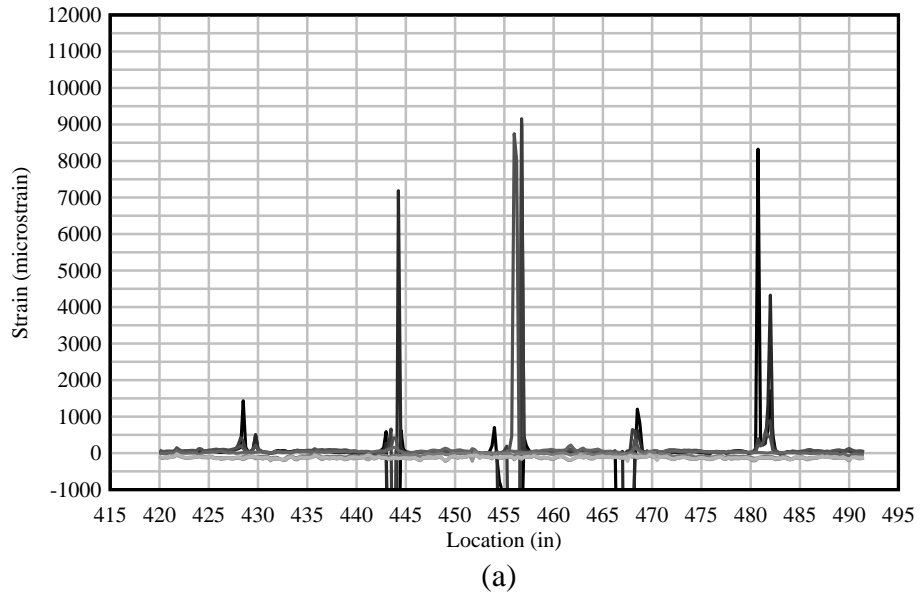
Figure C.10 Specimen SS-1: concrete strain vs. location – beam web: (a) FOS-2 and (b) FOS-4
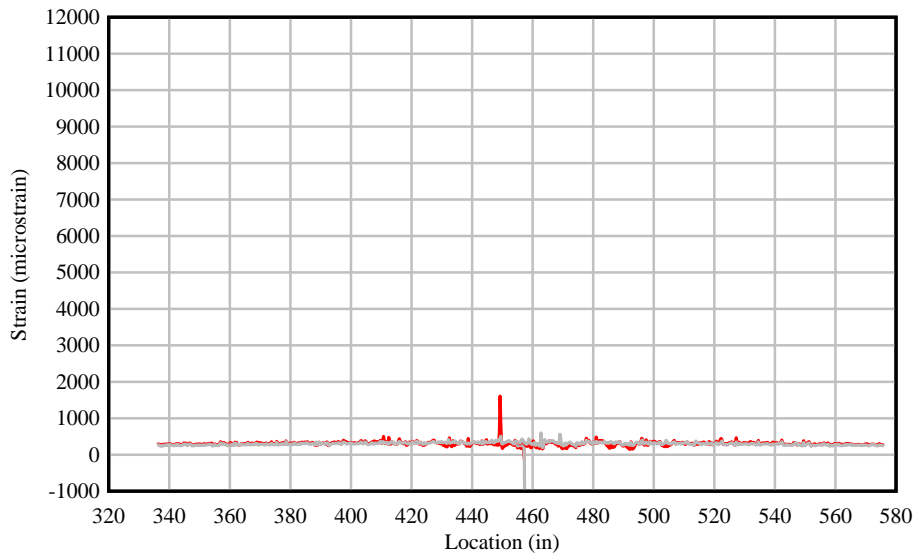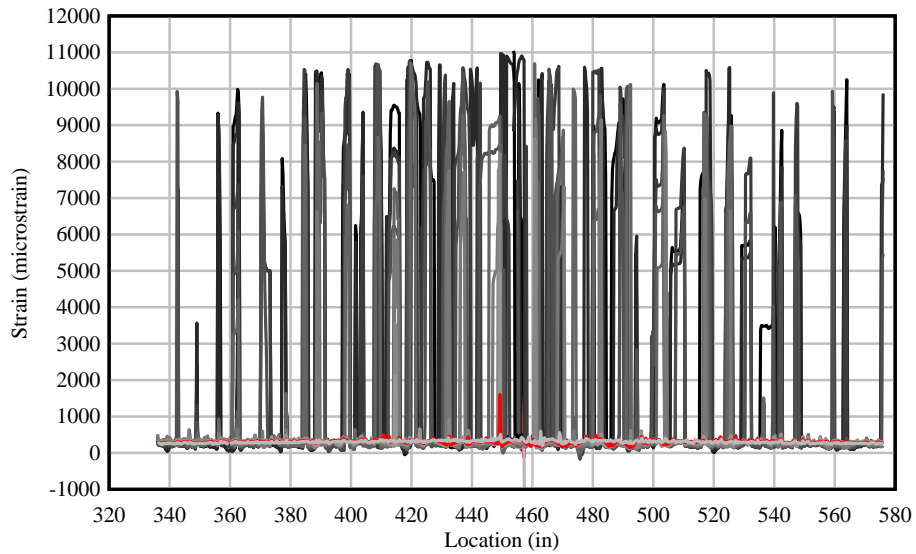
Figure C.11 Specimen SS-1: concrete strain vs. location – bottom of beam (FOS-5, FOS-6, and FOS-7): (a) location of first crack at P = 70 kip, (b) strain at different load levels

Beam Specimen SS-2

Summary

(a)

(b)
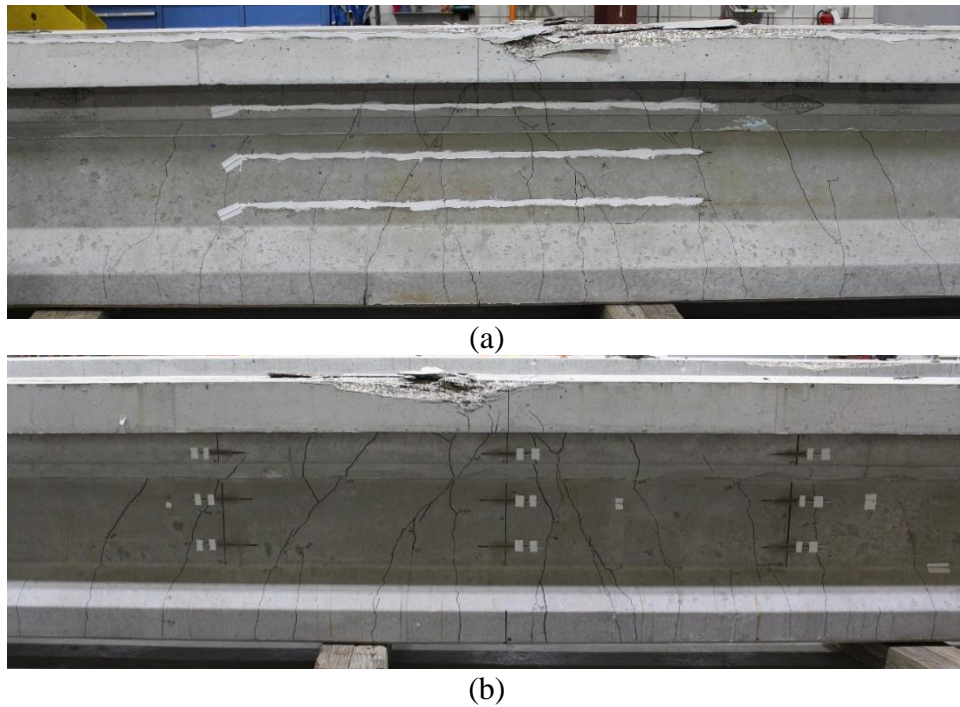
Figure C.12 Beam specimen SS-2 at end of testing: (a) East side (fiber optic sensors) and (b) West side (foil strain gages)
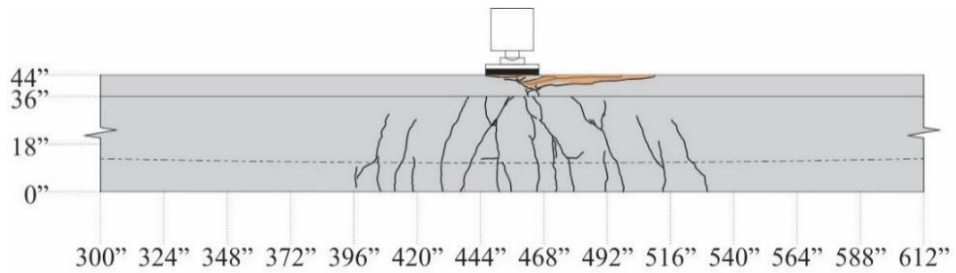
Figure C.13 Beam specimen SS-2 crack pattern: east side
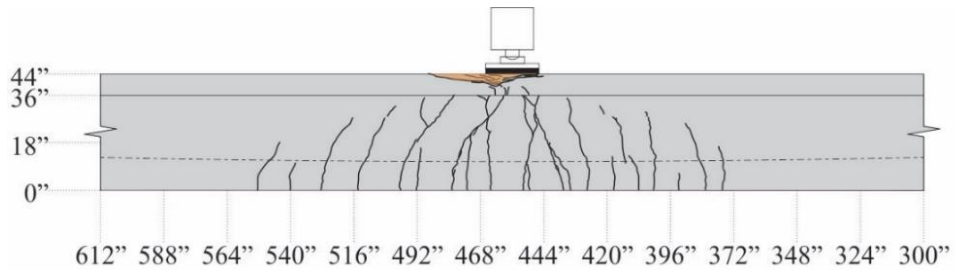
Figure C.14 Beam specimen SS-2 crack pattern: west side

314
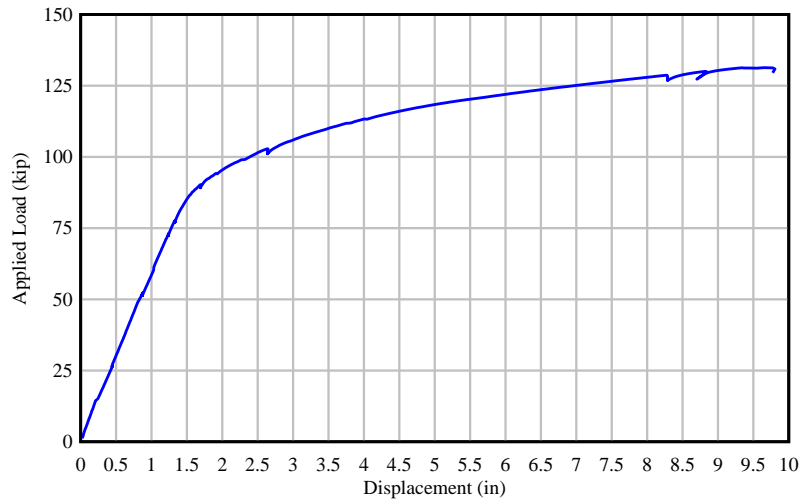
Figure C.15 Beam specimen SS-2: applied force vs. displacement at load point

Specimen Details

The cross-section of beam specimen SS-2 corresponds to a modified AASHTO Type II beam with a web width of 10 in. The girder section was topped with an 8-in. thick concrete deck and rectangular cast-in-place endblocks were added to accommodate post-tensioning anchorage hardware and additional reinforcement. Figure C.16 shows the beam inside the load frame. Key parameters are listed in Table C.3. Concrete cylinders were tested to determine the compressive strength at the time of testing as shown in Table C.4.

Figure C.16 Beam specimen SS-2 inside test frame

Table C.3 Beam specimen SS-2: key parameters

Cross Section	Specimen Length (ft)	L/D	U/T	No. PreT Strands (bottom)	No. PreT Strands (top)	No. PT Strands	PT tendon profile	Longitudinal mild steel bars (deck)
Modified AASHTO Type II	76	25	0.6	8	2	10	F5	8 #4

Table C.4 Beam specimen SS-2: compressive strength results

Description	Cast date	Test date	Test age (days)	Compressive Strength (psi)	Specified Compressive Strength (psi)
Precast girder	2020-01-23	2020-01-24	1	4,720	8,500
		2020-01-27	4	8,595	
		2020-02-20	28	10,698	
		2021-09-30	616	13,578	
		2021-12-06	683	13,222	
		2021-12-15	692	12,380	
Deck	2020-01-28	2020-01-29	1	3,830	8,500
		2020-01-30	2	6,155	
		2020-02-25	28	10,247	
		2021-10-08	619	14,362	
End blocks	2021-11-05	2021-11-19	14	9,563	8,500
		2021-12-03	28	10,035	
		2021-12-06	40	9,856	

Test Procedure

Specimen SS-2 was loaded at a rate of 0.25 kip/sec. Load was held at 26, 51, 73, 77, 90, 103, and 128 kip. This allowed for the beam to be inspected, cracks marked, and VW strain gage readings taken. The first visible cracks were identified and marked at a load of 77 kip (Figure C.17). As depicted in Figure C.22, fiber optic sensors located on the bottom of the beam recorded the first cracks along the centerline of the beam section. Cracks were marked during loading up until 103 kip, which is 80% of the predicted nominal capacity. The concrete in the top of the concrete deck (near midspan, west side) started crushing and loading was stopped at P = 131 kip. The beam was then unloaded, cracks were marked, and final VW strain gage readings were taken.

Figure C.17 Specimen SS-2: first observed cracks (marked in red) at P = 77 kip on east side

Detailed Test Results
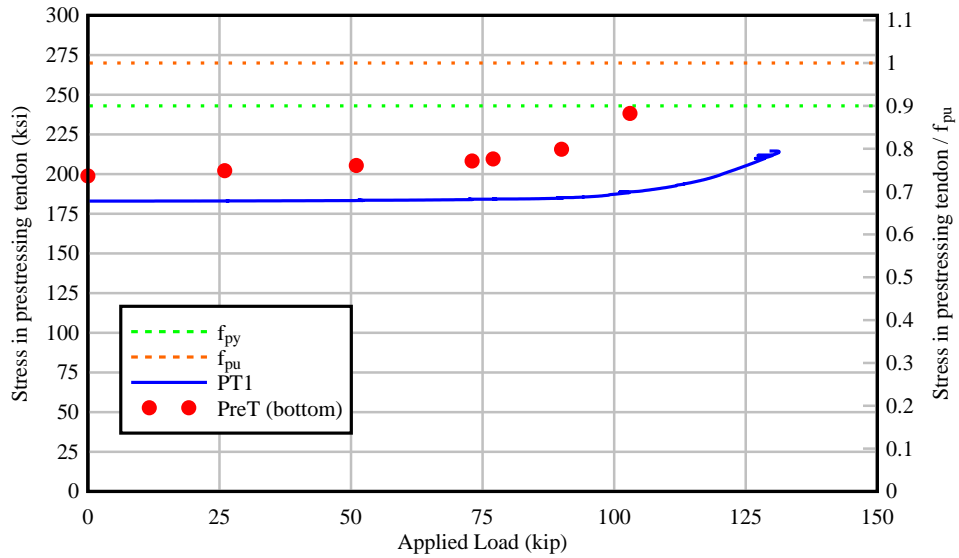
Figure C.18 Specimen SS-2: stress in PT and PreT tendons as a function of applied load
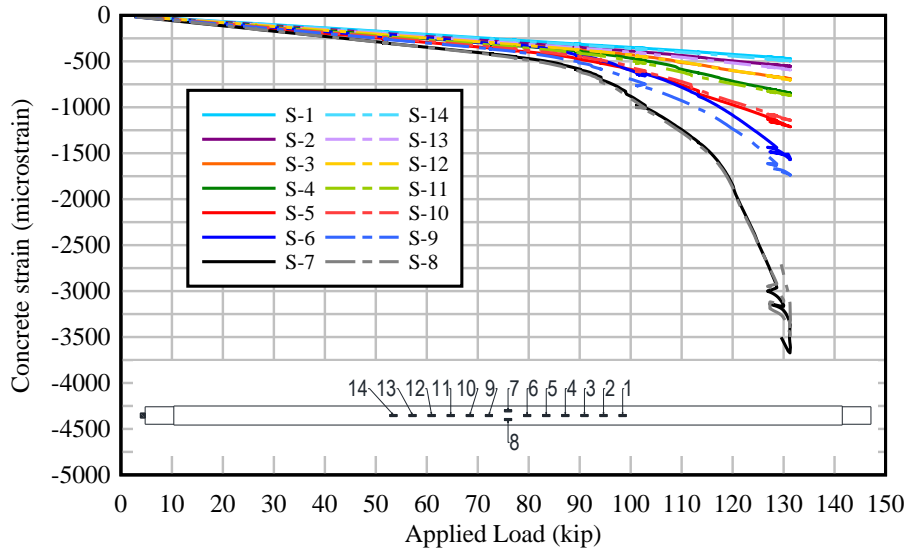
Figure C.19 Specimen SS-2: concrete strain vs. applied load – top of deck

| P = 70 kip | 77 kip | 80 kip | 90 kip | 100 kip | 110 kip | 115 kip | 120 kip | 125 kip | 131 kip |
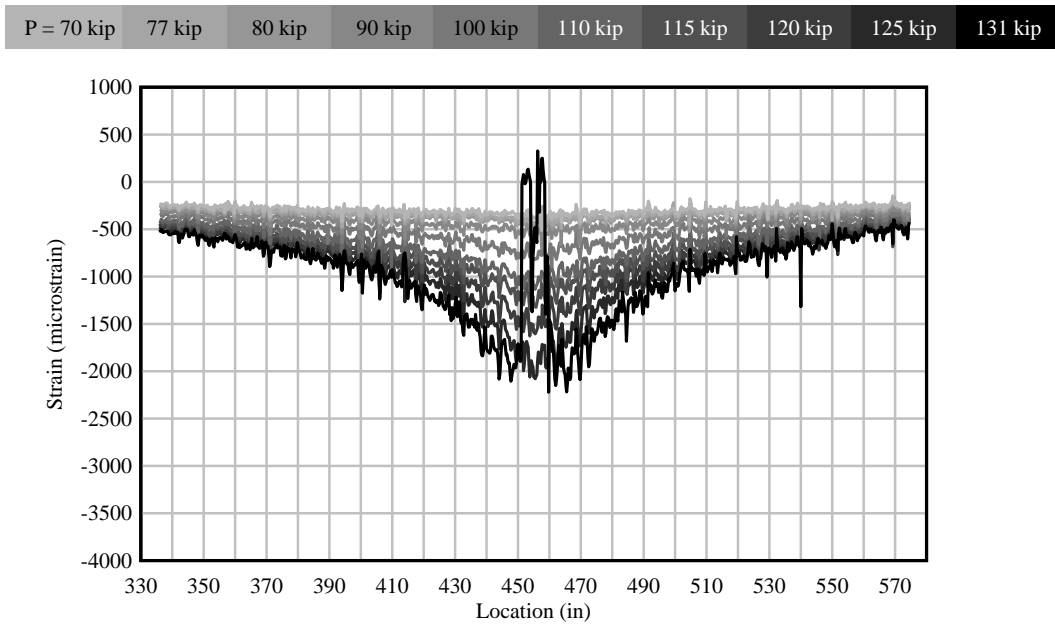
Figure C.20 Specimen SS-2: concrete strain vs. location – top flange (FOS-1)

318

P = 70 kip | 77 kip | 80 kip | 90 kip | 100 kip | 110 kip | 115 kip | 120 kip | 125 kip | 131 kip
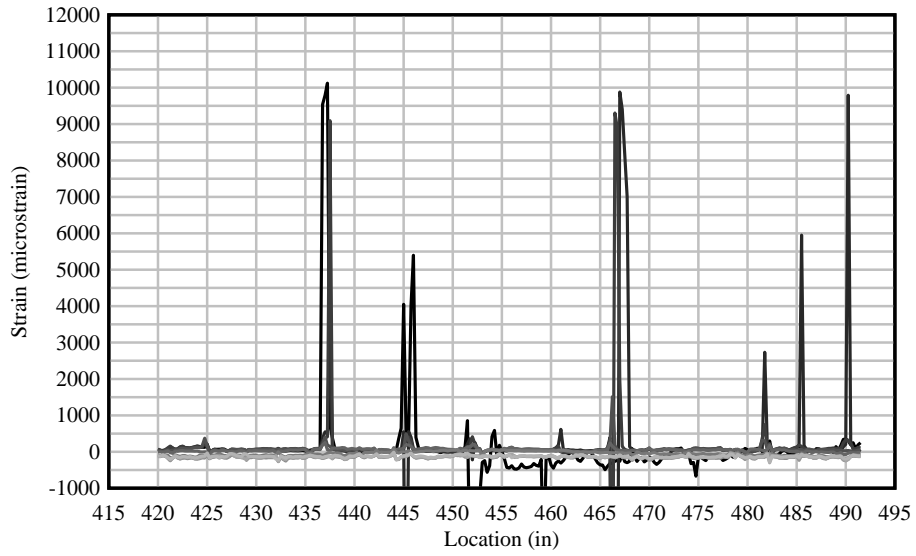
(a)
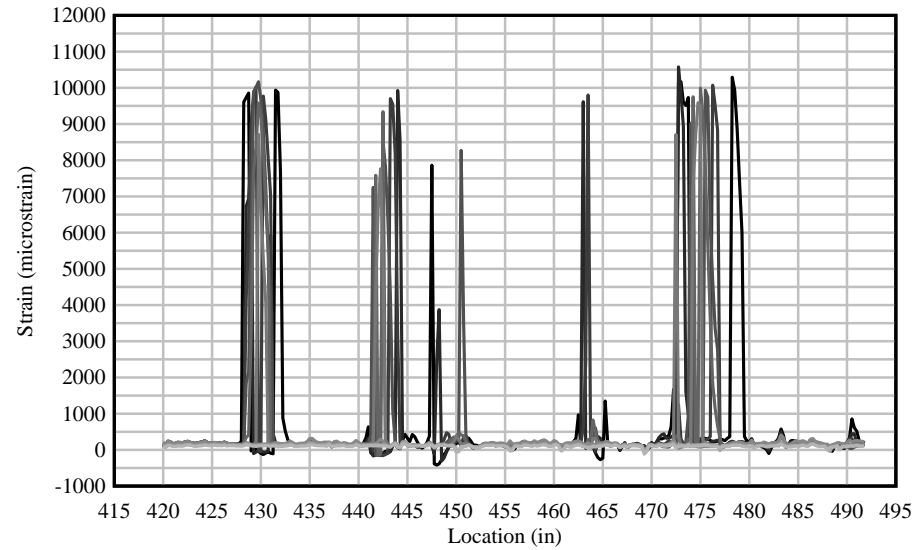
(b)

Figure C.21 Specimen SS-2: concrete strain vs. location – beam web: (a) FOS-2 and (b) FOS-4
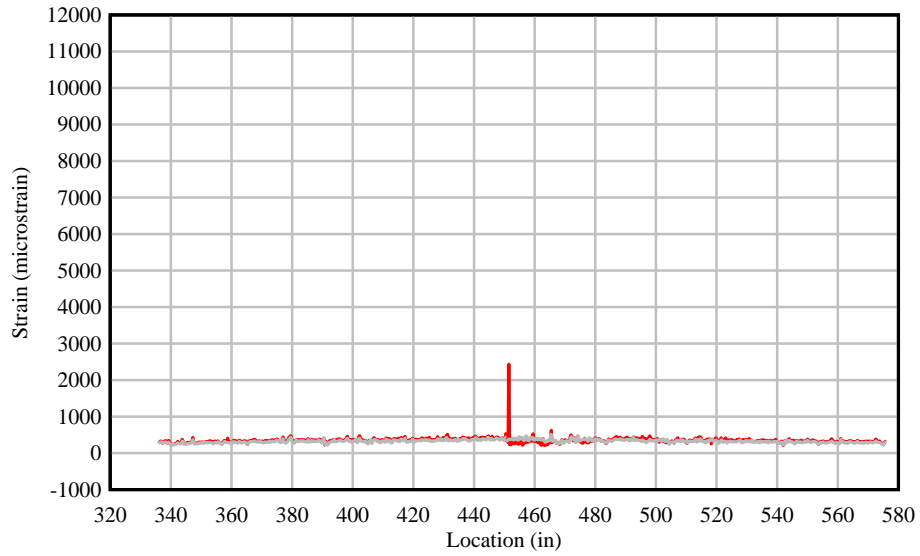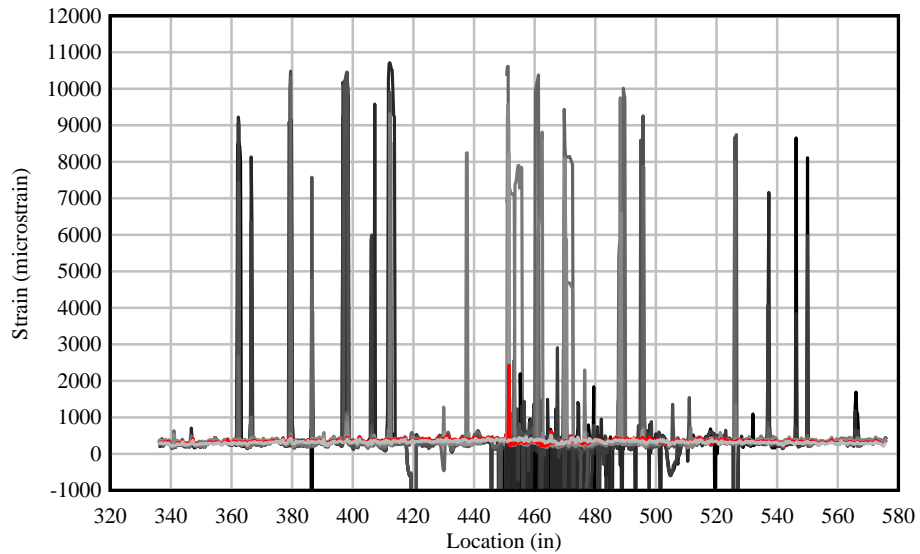
Figure C.22 Specimen SS-2: concrete strain vs. location – bottom of beam (FOS-5 and FOS-6): (a) location of first crack at P = 77 kip, (b) strain at different load levels

Beam Specimen SS-3

Summary

(a)

(b)
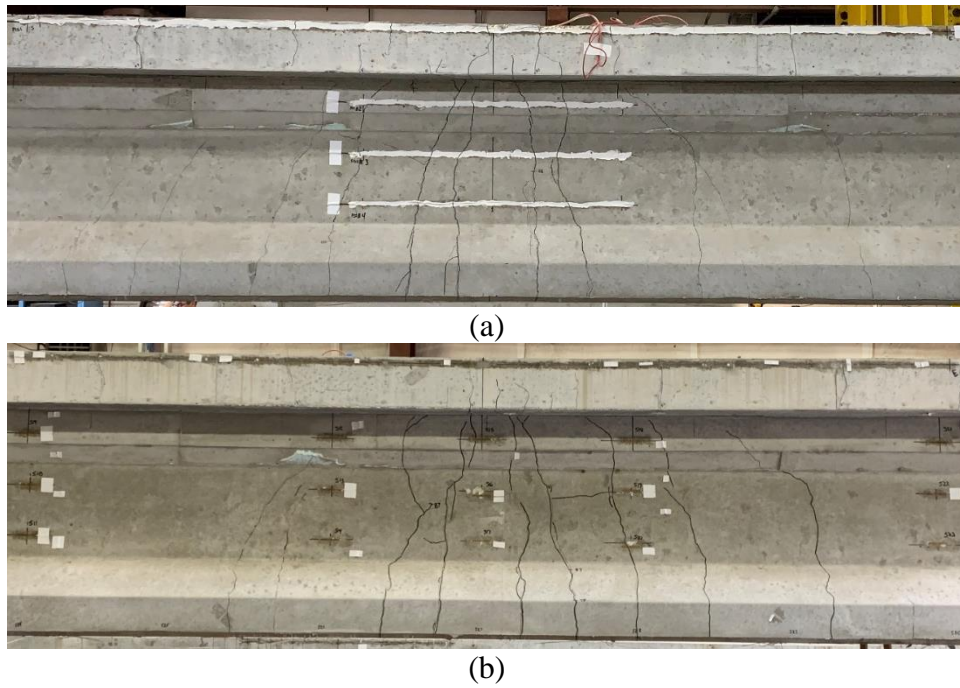
Figure C.23 Beam specimen SS-3 at end of testing: (a) East side (fiber optic sensors) and (b) West side (foil strain gages)
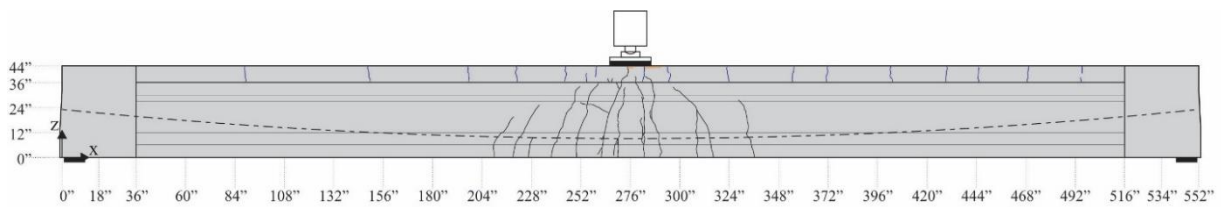
Figure C.24 Beam specimen SS-3 crack pattern: east side
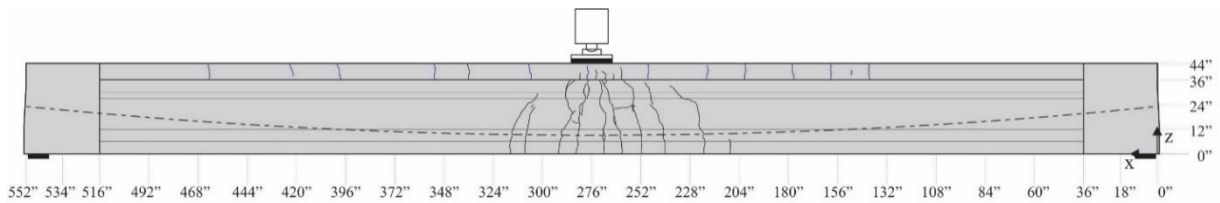
Figure C.25 Beam specimen SS-3 crack pattern: west side
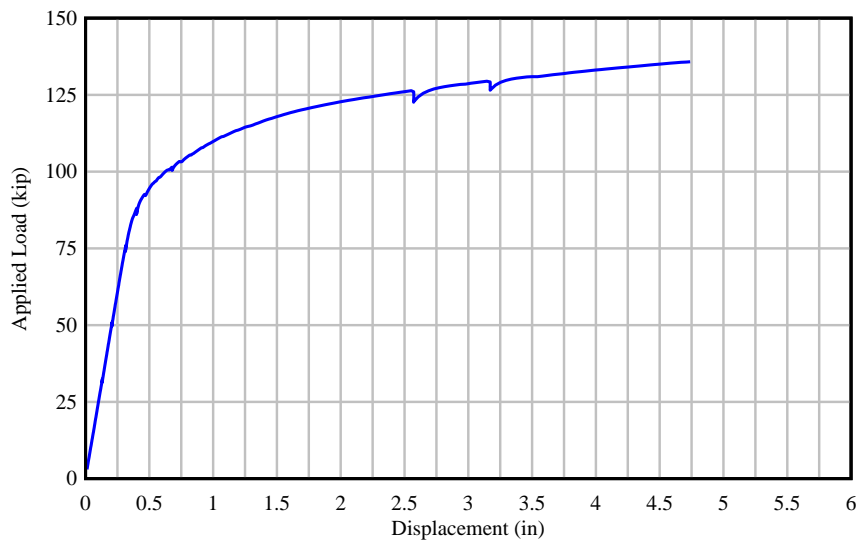
Figure C.26 Beam specimen SS-3: applied force vs. displacement at load point

Specimen Details

The cross-section of beam specimen SS-3 corresponds to a modified AASHTO Type II beam with a web width of 10 in. The girder section was topped with an 8-in. thick concrete deck and rectangular cast-in-place endblocks were added to accommodate post-tensioning anchorage hardware and additional reinforcement. Figure C.27 shows the beam inside the load frame. Key parameters are listed in Table C.5. Concrete cylinders were tested to determine the compressive strength at the time of testing as shown in Table C.6.

Figure C.27 Beam specimen SS-3 inside test frame

Table C.5 Beam specimen SS-3: key parameters

Cross Section	Specimen Length (ft)	L/D	U/T	No. PreT Strands (bottom)	No. PreT Strands (top)	No. PT Strands	PT tendon profile	Longitudinal mild steel bars (deck)
Modified AASHTO Type II	46	15	0.4	6	2	4	F5	8 #4

Table C.6 Beam specimen SS-3: compressive strength results

Description	Cast date	Test date	Test age (days)	Compressive Strength (psi)	Specified Compressive Strength (psi)
Precast girder	2020-01-23	2020-01-24	1	4,720	8,500
		2020-01-27	4	8,595	
		2020-02-20	28	10,698	
		2021-09-30	616	13,578	
Deck	2020-01-27	2020-01-28	1	4,400	8,500
		2020-01-29	2	6,405	
		2020-02-24	28	10,464	
		2021-09-30	612	13,132	
End blocks	2021-08-06	2021-09-13	38	10,285	6,500
		2021-09-20	45	10,992	

Test Procedure

Specimen SS-3 was loaded at a rate of 0.25 kip/sec. Load was held at 32, 51, 75, 88, 101, 126, and 129 kip. This allowed for the beam to be inspected, cracks marked, and VW strain gage readings taken. The first visible crack was identified and marked at a load of 75 kip on the west side of the beam (Figure C.28). Fiber optic sensors located on the bottom of the beam recorded the first cracks along the centerline of the beam section at $P = 85$ kip as depicted in Figure C.33. Cracks were marked during loading up until 88 kip, which is 70% of the predicted nominal capacity. Audible indications of damage were heard emanating from concrete in the top of the deck (near midspan, east side). Loading was stopped shortly thereafter when at $P = 136$ kip, which exceeded the predicted maximum load, and when compressive concrete strain $\varepsilon_c > 0.003$. The beam was then unloaded, cracks were marked, and final VW strain gage readings were taken.
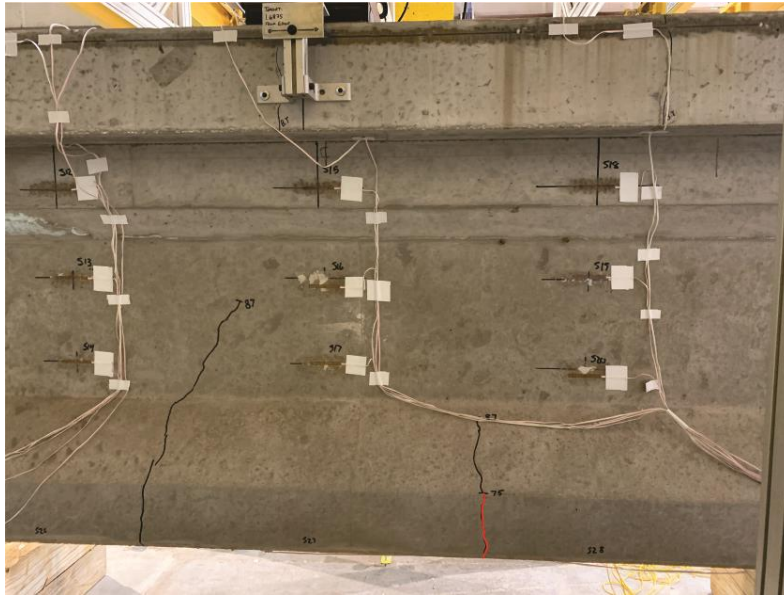
Figure C.28 Specimen SS-3: first observed crack (marked in red) at P = 75 kip on west side

Detailed Test Results
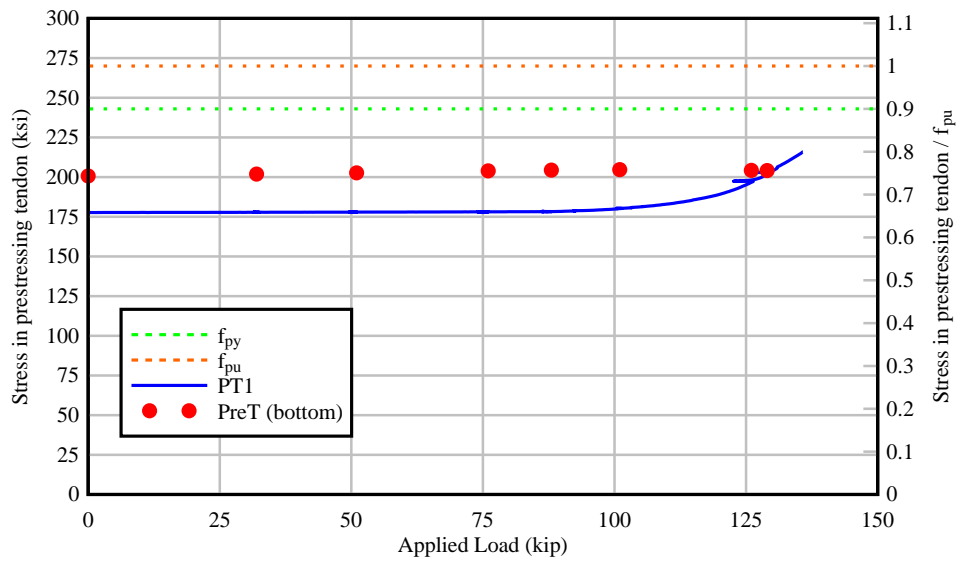
Figure C.29 Specimen SS-3: stress in PT and PreT tendons as a function of applied load
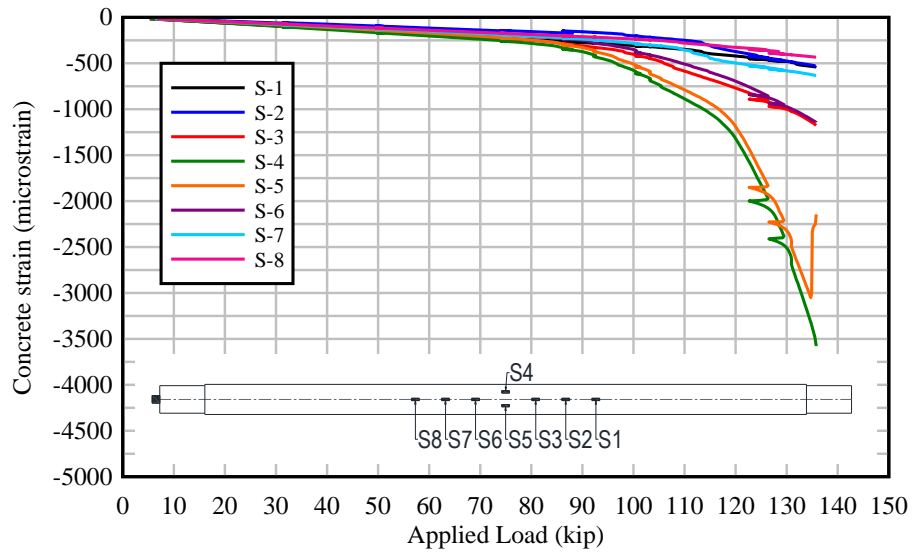
Figure C.30 Specimen SS-3: concrete strain vs. applied load – top of deck
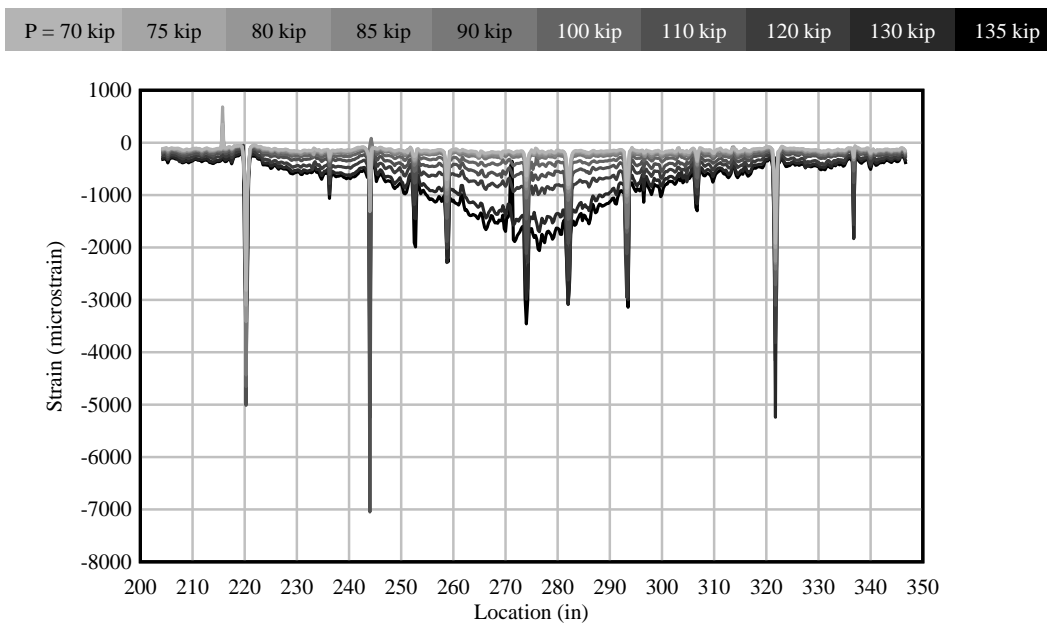
Figure C.31 Specimen SS-3: concrete strain vs. location – top flange (FOS-1)

Figure C.32 Specimen SS-3: concrete strain vs. location – beam web: (a) FOS-2 and (b) FOS-4

326

| P = 75 kip | 80 kip | 85 kip | 90 kip | 100 kip | 110 kip | 114 kip | 120 kip | 130 kip | 135 kip |
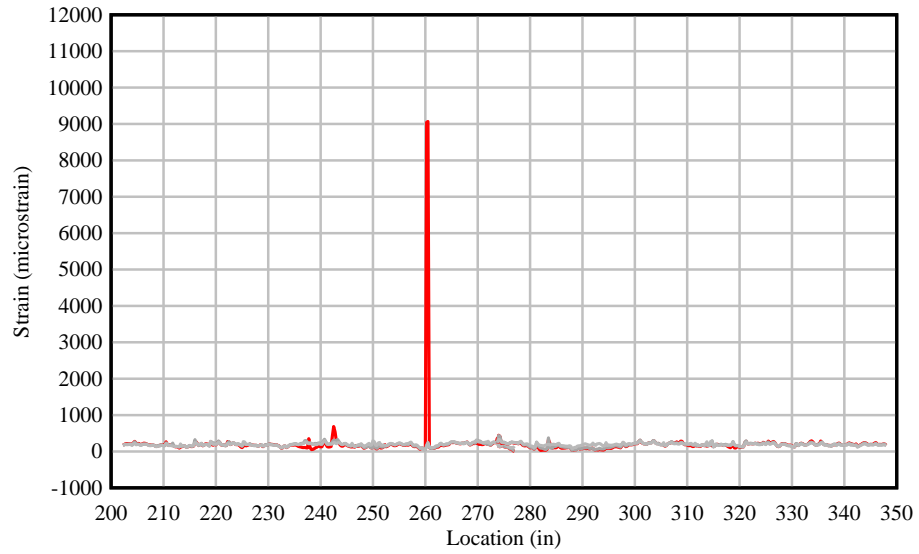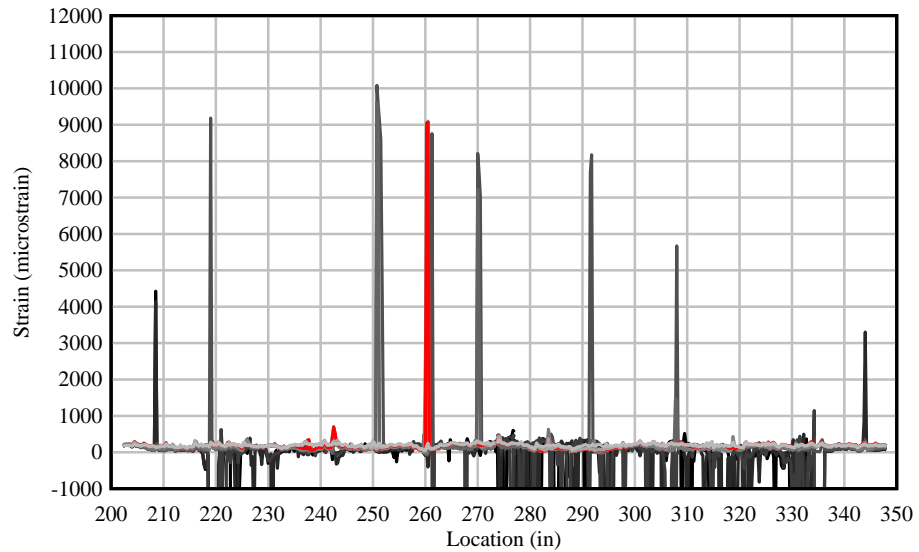
Figure C.33 Specimen SS-3: concrete strain vs. location – bottom of beam (FOS-5 and FOS-6): (a) location of first crack at P = 85 kip, (b) strain at different load levels

Beam Specimen SS-4

Summary
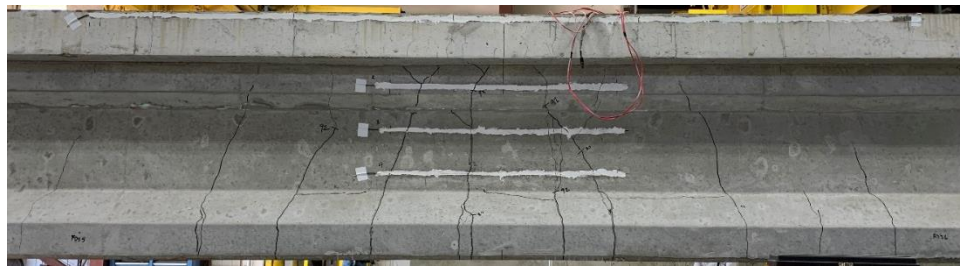
(a)

(b)

Figure C.34 Beam specimen SS-4 at end of testing: (a) East side (fiber optic sensors) and (b) West side (foil strain gages)
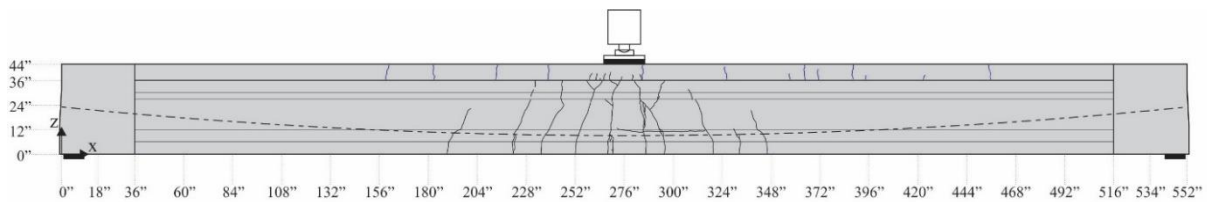
Figure C.35 Beam specimen SS-4 crack pattern: east side
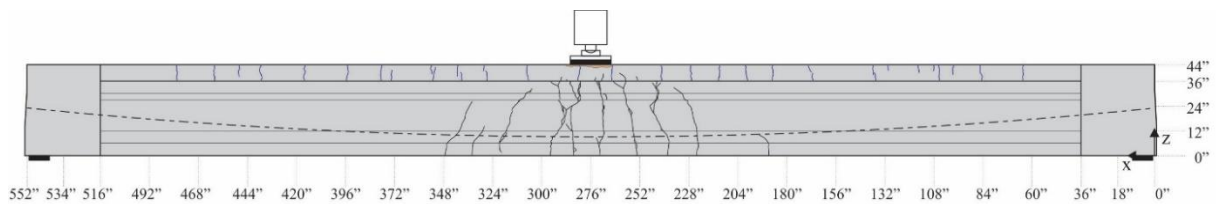
Figure C.36 Beam specimen SS-4 crack pattern: west side
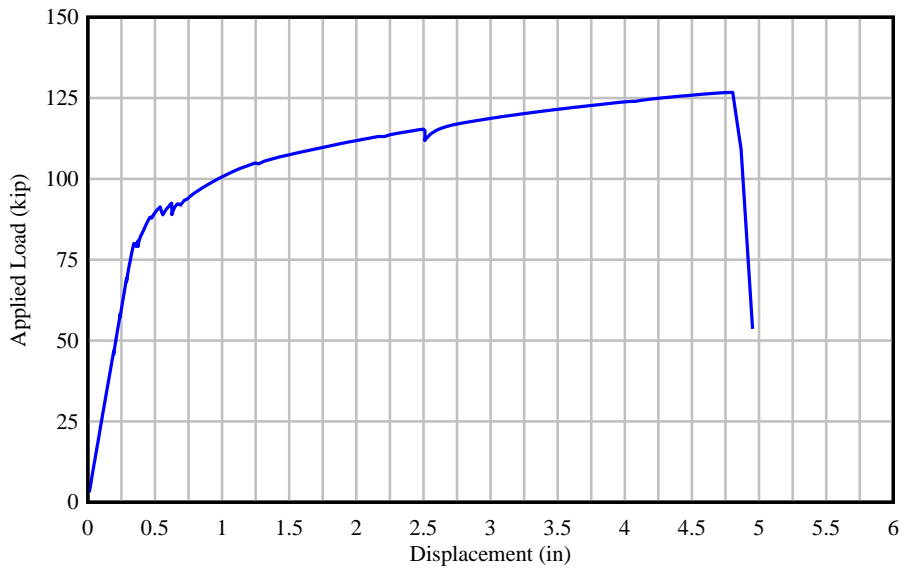
Figure C.37 Beam specimen SS-4: applied force vs. displacement at load point

Specimen Details

The cross-section of beam specimen SS-4 corresponds to a modified AASHTO Type II beam with a web width of 10 in. The girder section was topped with an 8-in. thick concrete deck and rectangular cast-in-place endblocks were added to accommodate post-tensioning anchorage hardware and additional reinforcement. Figure C.38 shows the beam inside the load frame. Key parameters are listed in Table C.7. Concrete cylinders were tested to determine the compressive strength at the time of testing as shown in Table C.8.

Table C.7 Beam specimen SS-4: key parameters

Cross Section	Specimen Length (ft)	L/D	U/T	No. PreT Strands (bottom)	No. PreT Strands (top)	No. PT Strands	PT tendon profile	Longitudinal mild steel bars (deck)
Modified AASHTO Type II	46	15	0.6	4	2	6	F5	8 #4

Figure C.38 Beam specimen SS-4 inside test frame

Table C.8 Beam specimen SS-4: compressive strength results

Description	Cast date	Test date	Test age (days)	Compressive Strength (psi)	Specified Compressive Strength (psi)
Precast girder	2020-01-23	2020-01-24	1	4,720	8,500
		2020-01-27	4	8,595	
		2020-02-20	28	10,698	
		2021-09-30	616	13,859	
		2021-10-08	624	12,120	
Deck	2020-01-28	2020-01-29	1	3,830	8,500
		2020-01-30	2	6,155	
		2020-02-25	28	10,247	
		2021-10-08	619	14,362	
End blocks	2021-08-06	2021-09-13	38	10,285	6,500
		2021-09-20	45	10,992	
		2021-10-08	63	11,167	

Test Procedure

Specimen SS-4 was loaded at a rate of 0.25 kip/sec. Load was held at 46, 58, 69, 80, 92, and 115 kip. This allowed for the beam to be inspected, cracks marked, and VW strain gage readings taken. The first visible cracks were identified and marked at a load of 80 kip on the east side of the beam (Figure C.39). Fiber optic sensors located on the bottom of the beam recorded

the first cracks along the centerline of the beam section at P = 81 kip as depicted in Figure C.45. Cracks were marked during loading up until 92 kip, which is 80% of the predicted nominal capacity. Foil strain gages on the top of the beam exceeded $\varepsilon_c = 0.003$ at P = 124 kip and audible indications of crushing were heard around P = 126 kip. Afterward, concrete in the top of the deck at the load point started crushing. Clearly audible indications of strand ruptures were then heard and a drop in the load-displacement curve was observed. A maximum load of P = 127 kip was recorded. The beam was then unloaded, cracks were marked, and final VW strain gage readings were taken. Partial demolition was conducted afterwards, which confirmed the rupture of all four bonded pretensioned strands as shown in Figure C.40. Note that there were a total of ten pretensioned strands, but six of them were 'debonded'.
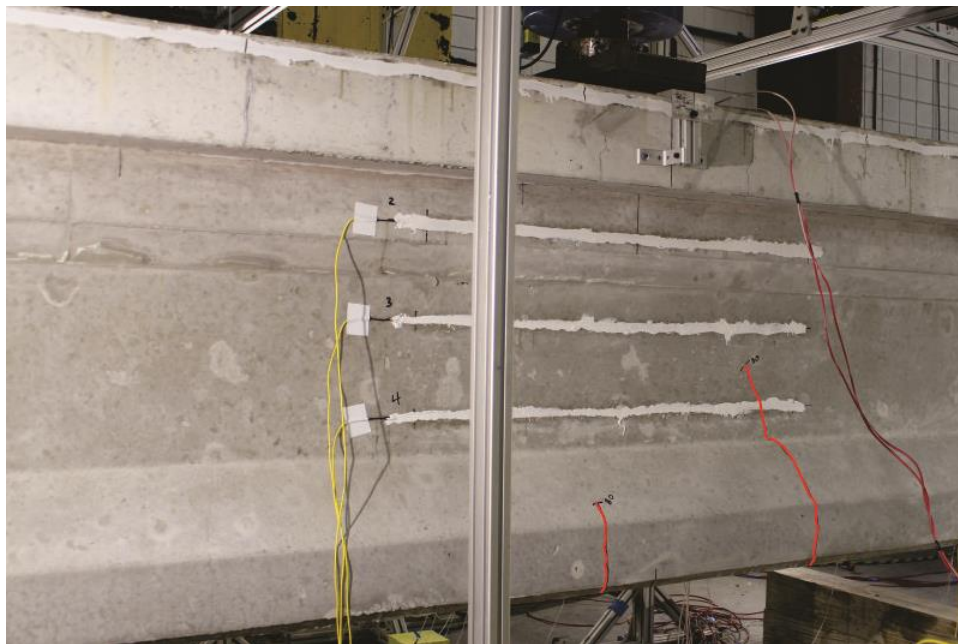
Figure C.39 Specimen SS-4: first observed cracks (marked in red) at P = 80 kip on east side

Figure C.40 Specimen SS-4: Rupture of bonded pretensioned strands (a) View of west side of the beam after partial demolition and (b) close-up view of PreT strands

Detailed Test Results
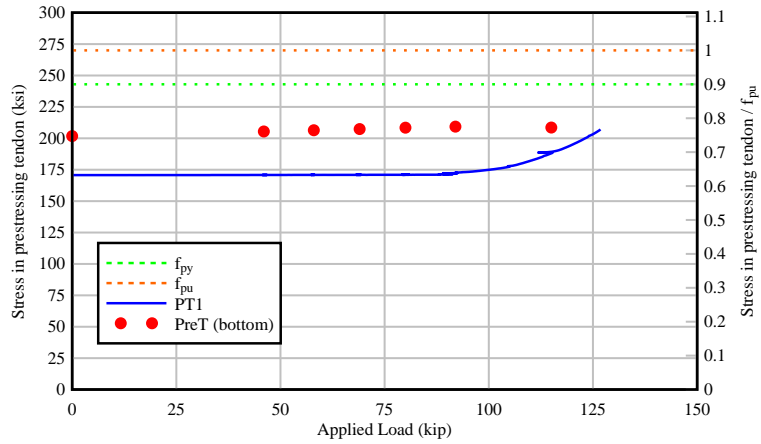
Figure C.41 Specimen SS-4: stress in PT and PreT tendons as a function of applied load
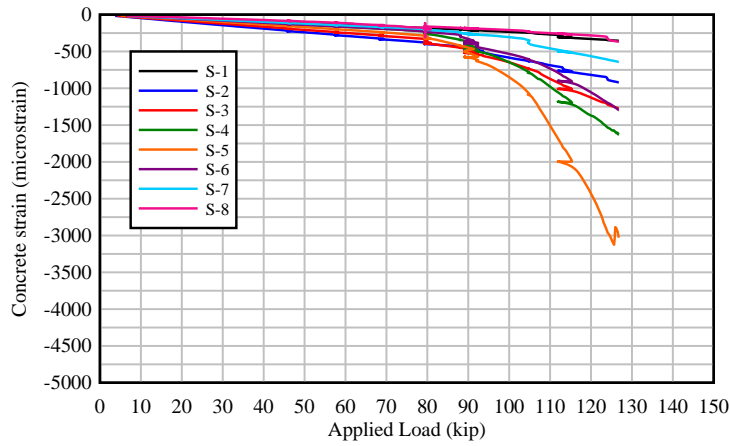
Figure C.42 Specimen SS-4: concrete strain vs. applied load – top of deck
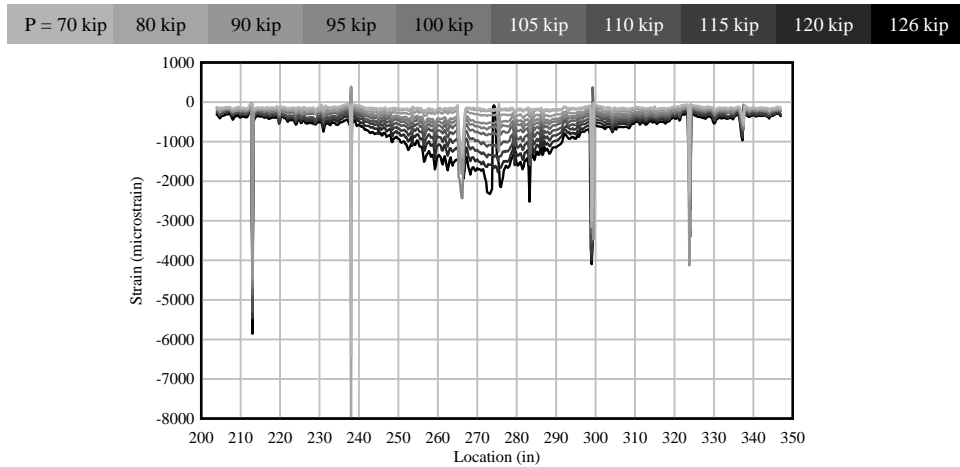
Figure C.43 Specimen SS-4: concrete strain vs. location – top flange (FOS-1)

333

| P = 70 kip | 80 kip | 90 kip | 95 kip | 100 kip | 105 kip | 110 kip | 115 kip | 120 kip | 126 kip |
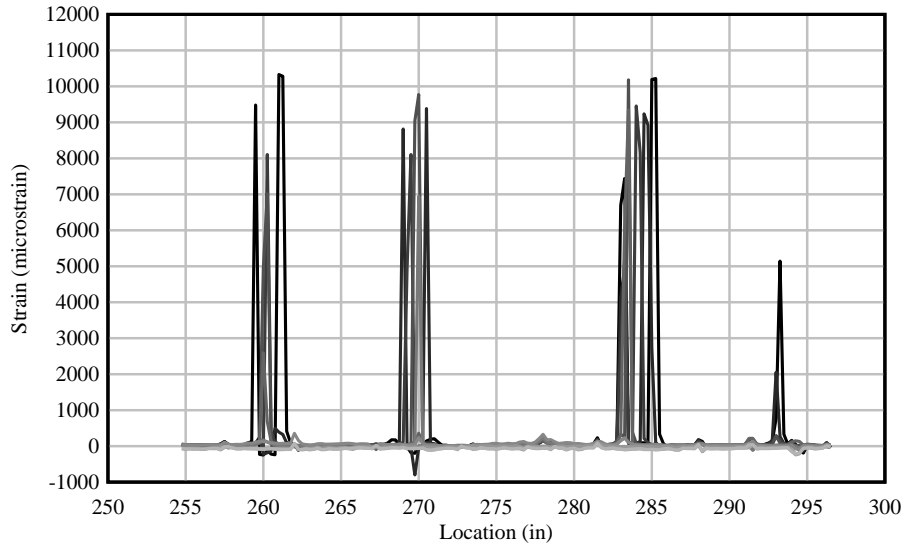
(a)
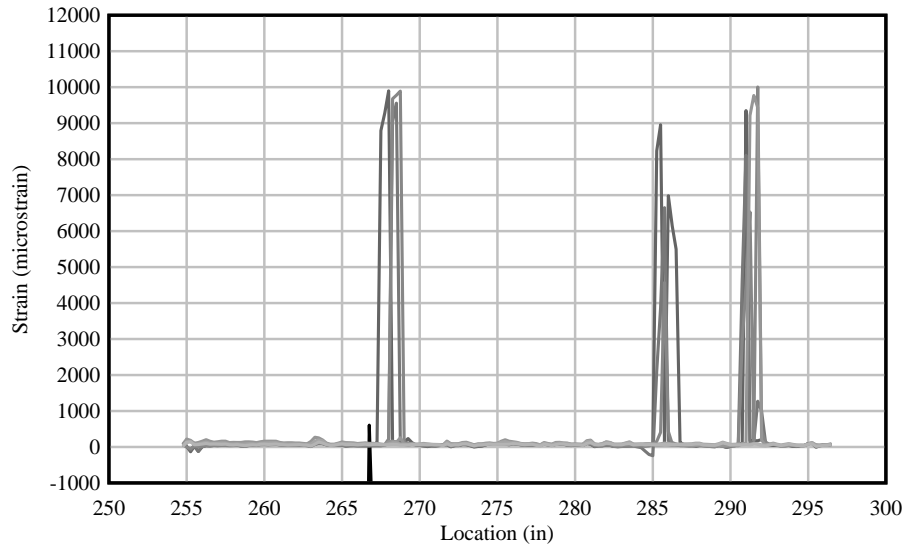
(b)

Figure C.44 Specimen SS-4: concrete strain vs. location – beam web: (a) FOS-2 and (b) FOS-4

334

| P = 70 kip | 81 kip | 90 kip | 95 kip | 100 kip | 105 kip | 110 kip | 115 kip | 120 kip | 126 kip |
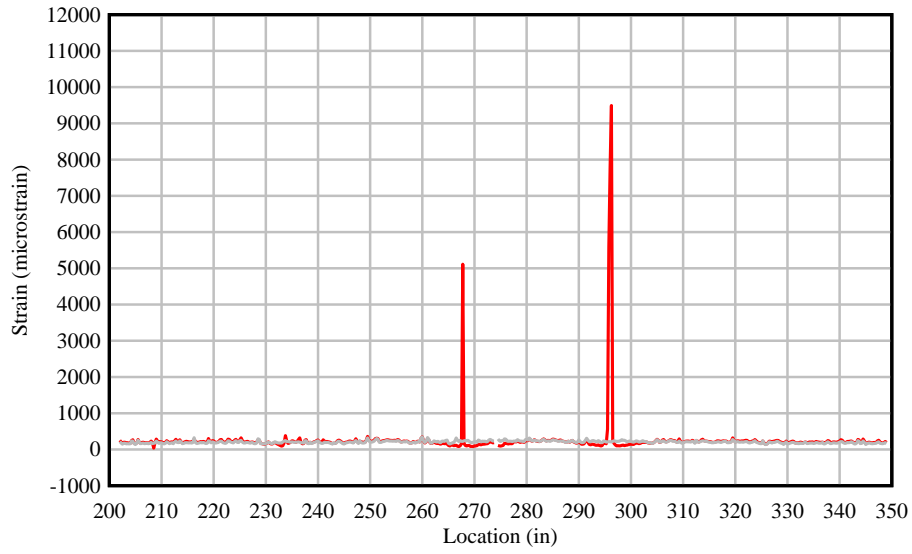
(a)
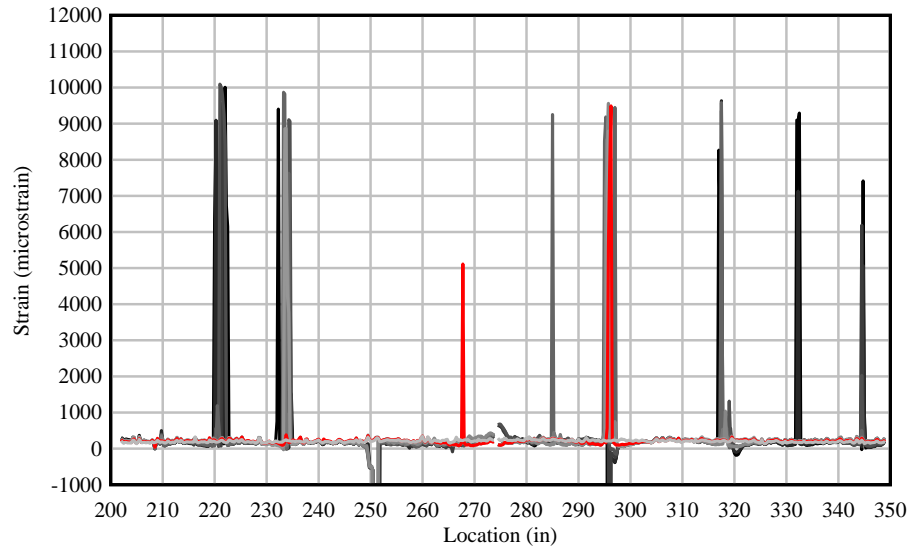
(b)

Figure C.45 Specimen SS-4: concrete strain vs. location – bottom of beam (FOS-5 and FOS-6): (a) location of first cracks at P = 81 kip, (b) strain at different load levels

APPENDIX D
Experimental results: Simply-supported beam specimen (SS-5)

Summary

(a)

(b)
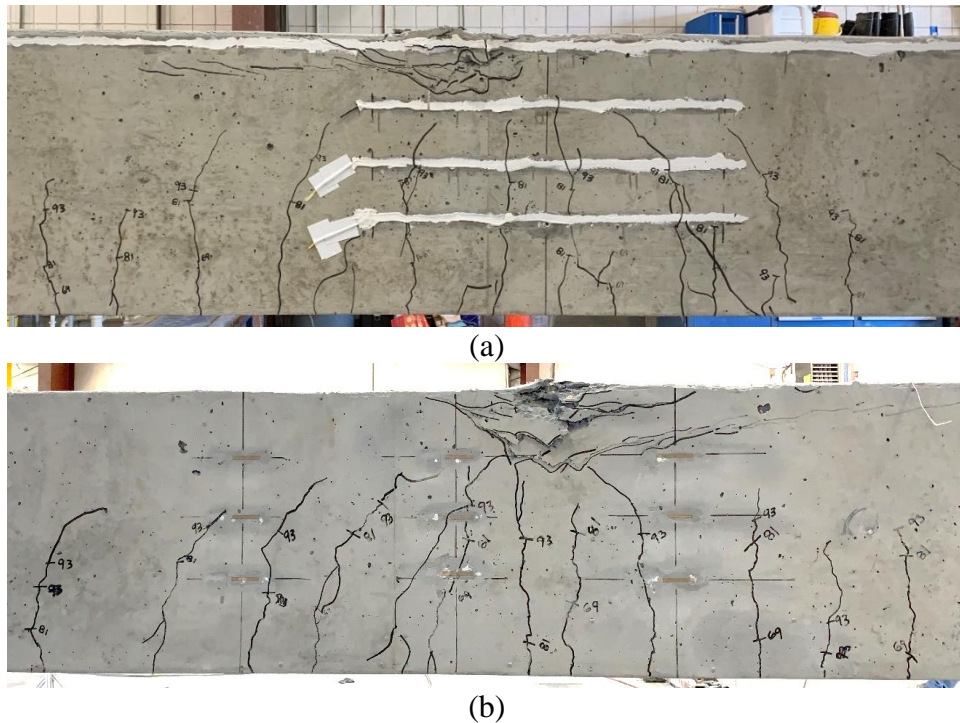
Figure D.1 CIP beam specimen SS-5 at end of testing: (a) East side (fiber optic sensors) and (b) West side (foil strain gages)
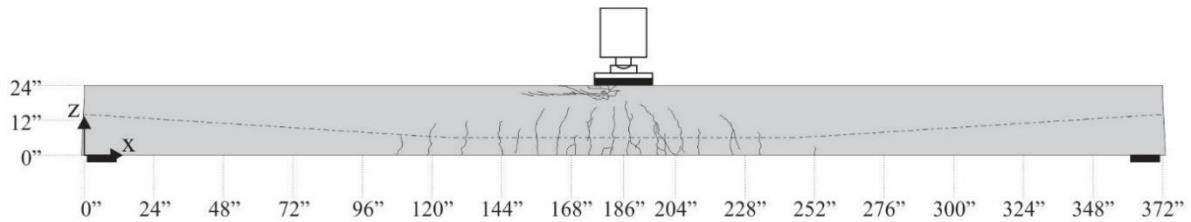
Figure D.2 Beam specimen SS-5 crack pattern: east side
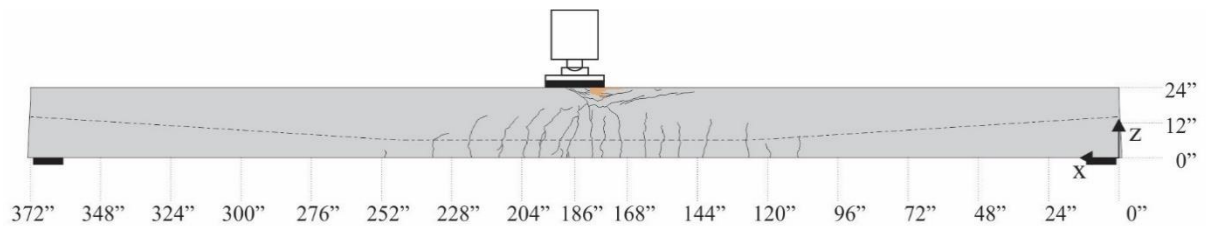
Figure D.3 Beam specimen SS-5 crack pattern: west side
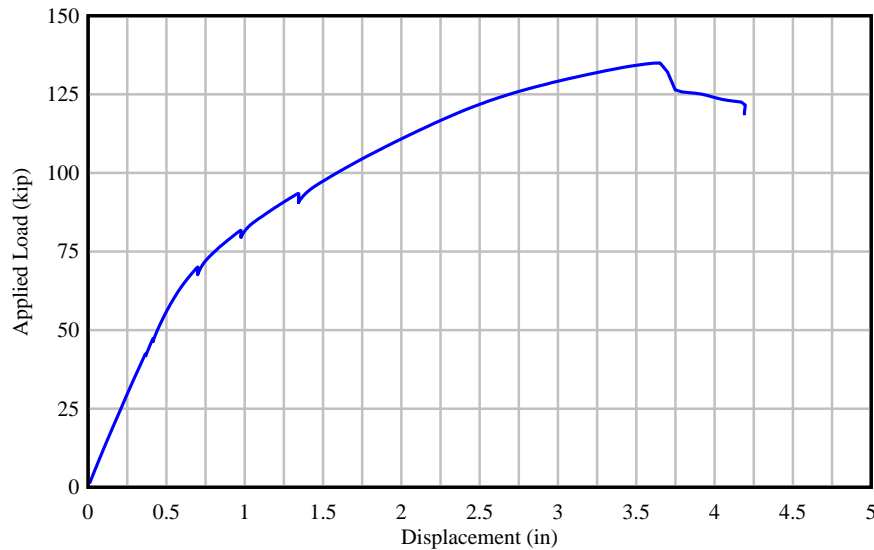
Figure D.4 Beam specimen SS-5: applied force vs. displacement at load point

Specimen Details

Cast-in-place beam specimen SS-5 consisted of a rectangular concrete section

(20 in. x 24 in.). The purpose of this specimen was to investigate the flexural behavior of a beam

simulating a straddle bent arrangement. Figure D.5 shows the beam inside the load frame. Key

parameters are listed in Table D.1. Concrete cylinders were tested to determine the compressive

strength at the time of testing as shown in Table D.2.

Table D.1 Beam specimen SS-5: key parameters

Cross Section	Specimen Length (ft)	L/D	U/T	No. PT Strands	PT tendon profile	Longitudinal mild steel bars (deck)
CIP 20" x 24"	31	15	0.9	12	F11	4 #6

Table D.2 Beam specimen SS-5: compressive strength results

Cast date	Test date	Test age (days)	Compressive Strength (psi)	Specified Compressive Strength (psi)
2021-09-22	2021-10-11	19	7,777	6,500
	2021-10-15	23	8,132	
	2021-10-20	28	8,401	

Figure D.5 Beam specimen SS-5 inside test frame

Test Procedure

Specimen SS-5 was loaded at a rate of 0.25 kip/sec. Load was held at 41, 46, 69, 81,

and 93 kip. This allowed for the beam to be inspected and cracks marked. The first visible cracks

were identified and marked at a load of 69 kip on the east side of the beam (Figure D.6). Fiber

optic sensors located on the bottom of the beam recorded the first cracks along the centerline of

the beam section at $P = 60$ kip as depicted in Figure D.13. Cracks were marked during loading up

until 93 kip, which is 80% of the predicted nominal capacity. The concrete in the top of the beam

(near midspan) started crushing and a drop in the load-displacement curve was observed. A

maximum load of $P = 135$ kip was recorded. The beam was then unloaded and cracks were

marked. As depicted in Figures D.8 and D.9, rebar strain data (from both foil strain gages and

fiber optic sensors) indicated bar yielding.
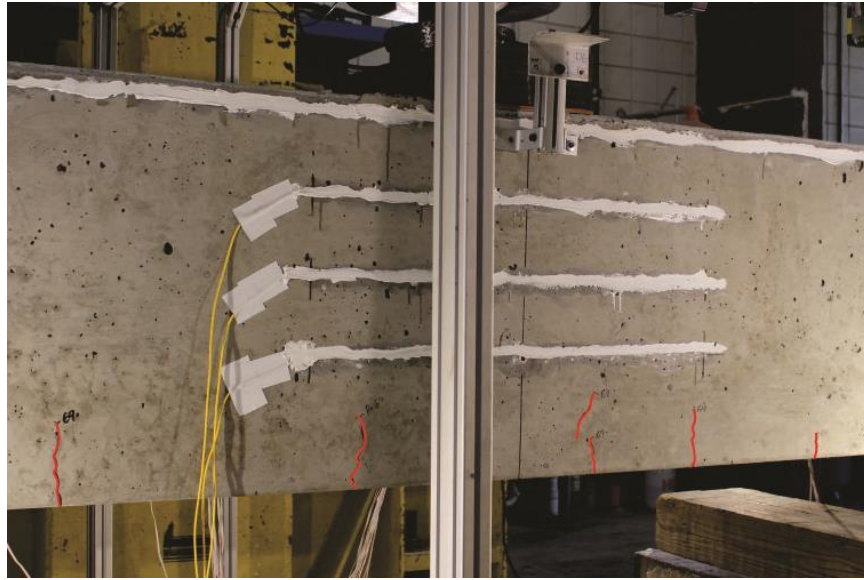
Figure D.6 Specimen SS-5: first observed crack (marked in red) at P = 69 kip on east side

Detailed Test Results
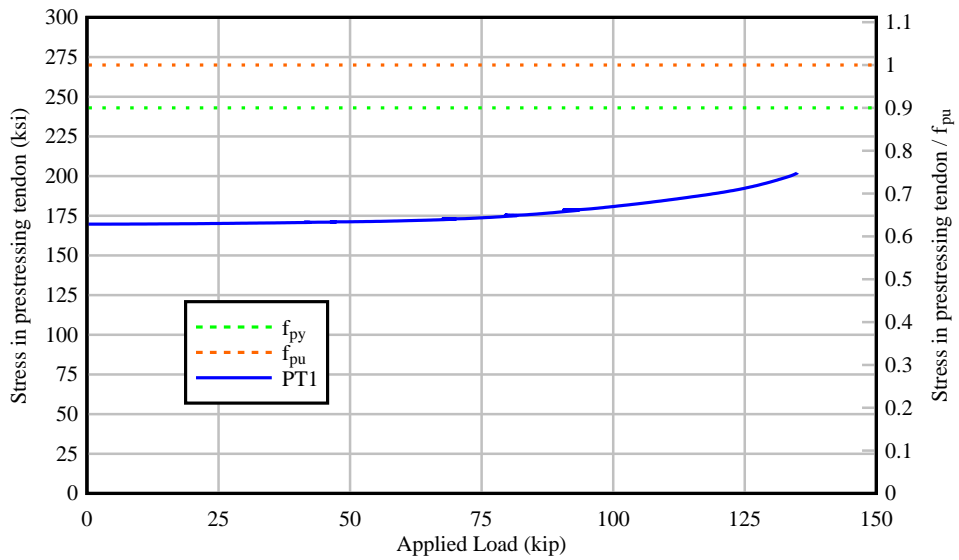
Figure D.7 Specimen SS-5: stress in PT tendon as a function of applied load
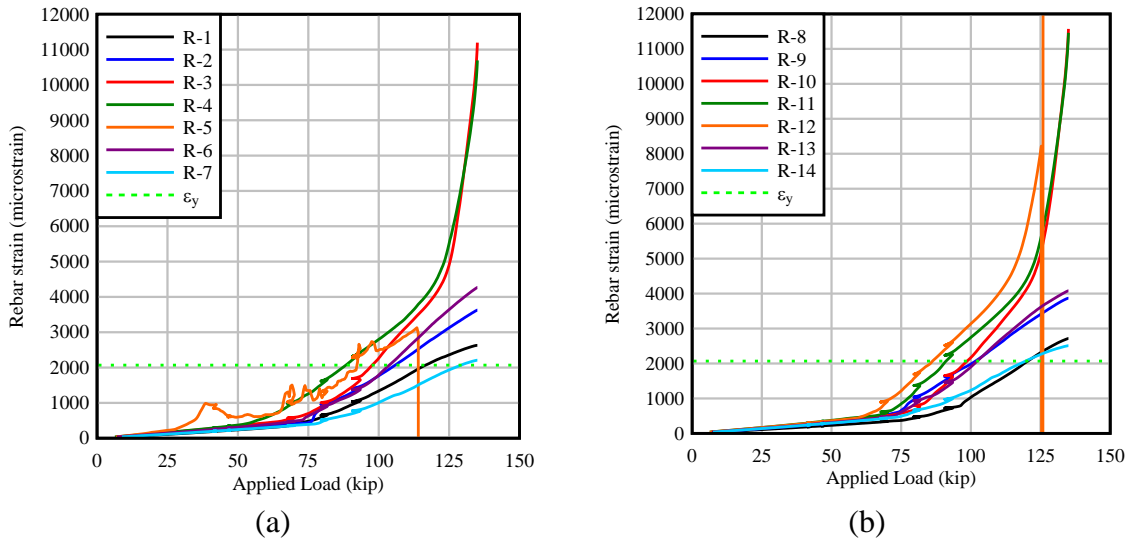
Figure D.8 Specimen SS-5: strain in longitudinal mild steel bars vs. applied load: (a) Bar 6L-4 and (b) Bar 6L-1
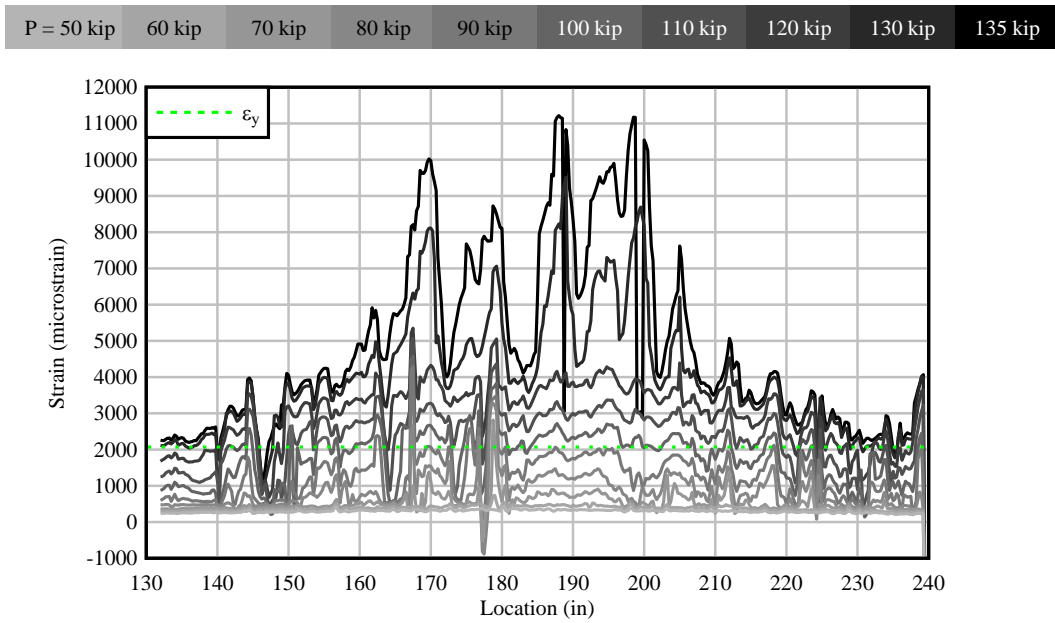
Figure D.9 Specimen SS-5: strain (FOS-7) in longitudinal mild steel bar (6L-3) vs. applied load
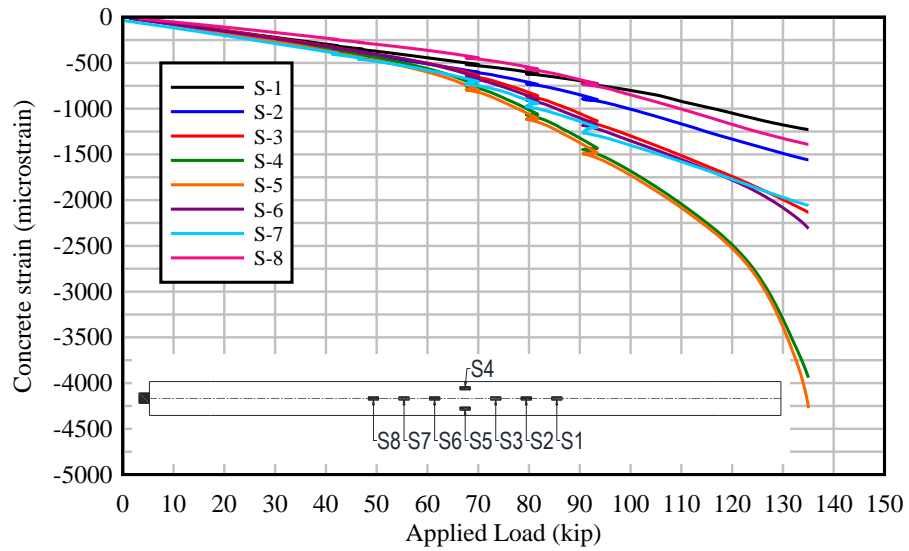
Figure D.10 Specimen SS-5: concrete strain vs. applied load – top of beam
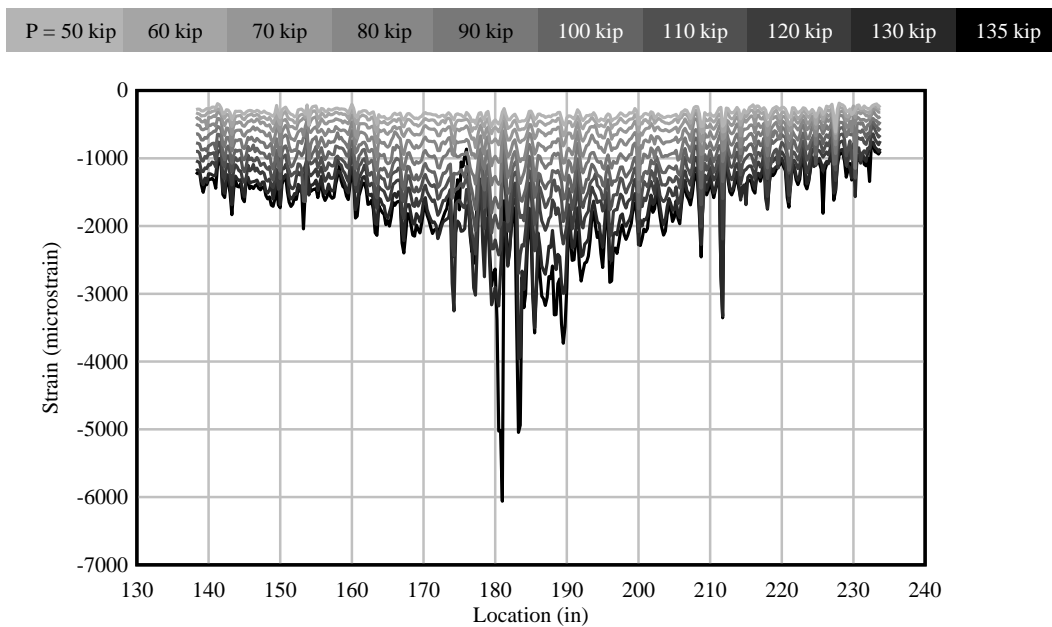
Figure D.11 Specimen SS-5: concrete strain vs location – top of beam, east side (FOS-1)

341
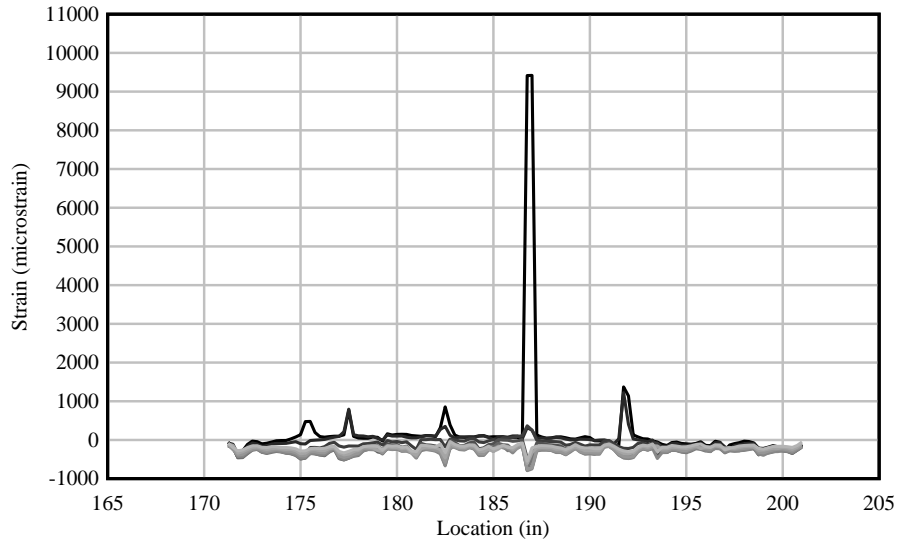
(a)
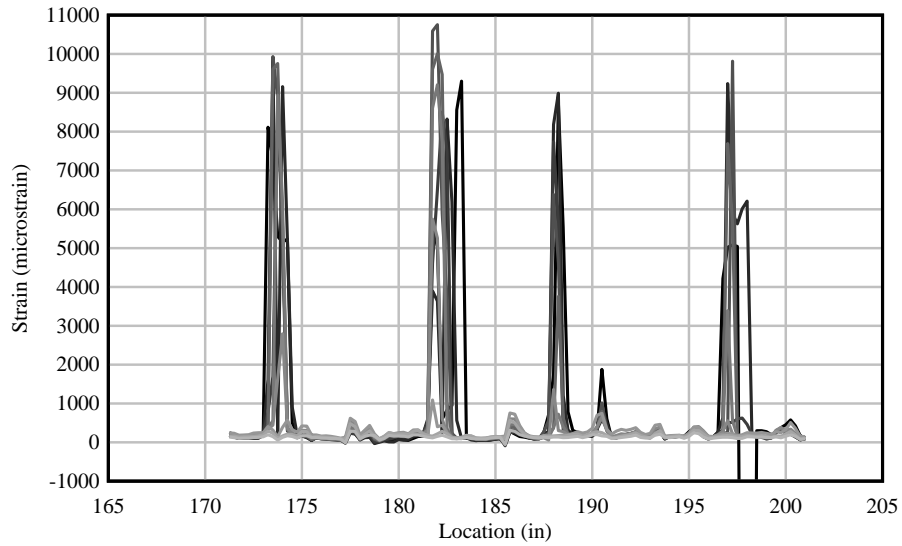
(b)

Figure D.12 Specimen SS-5: concrete strain vs. location – side of beam:
(a) FOS-2 and (b) FOS-4

342
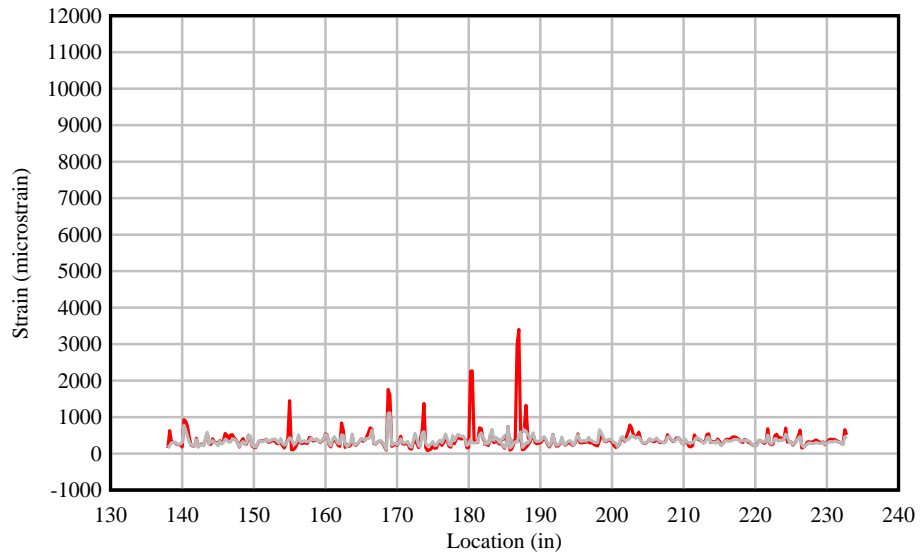
(a)
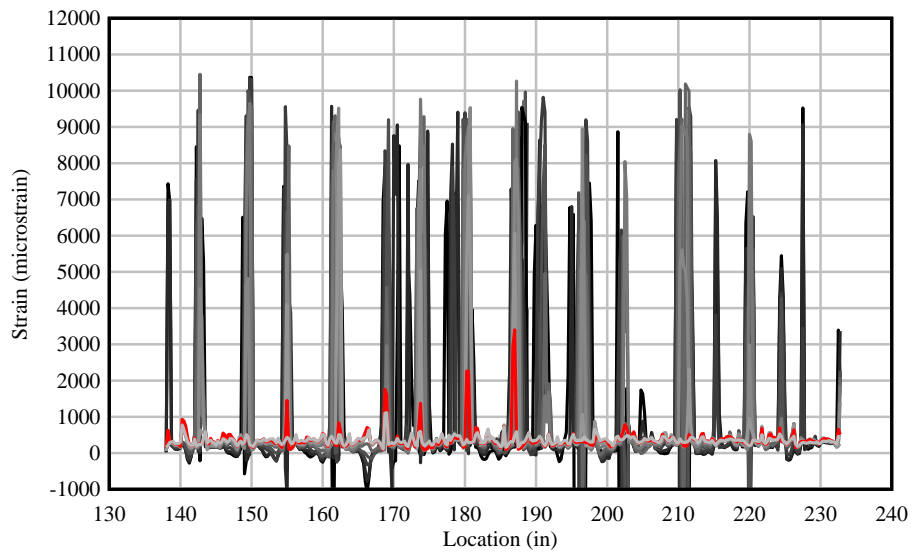
(b)

Figure D.13 Specimen SS-5: concrete strain vs. location – bottom of beam (FOS-5 and FOS-6): (a) location of first cracks at P = 60 kip, (b) strain at different load levels

Beam Specimen NB-1

Summary

Figure E.1 Beam specimen NB-1 at end of testing: (a) East side (fiber optic sensors) and (b) West side (foil strain gages)
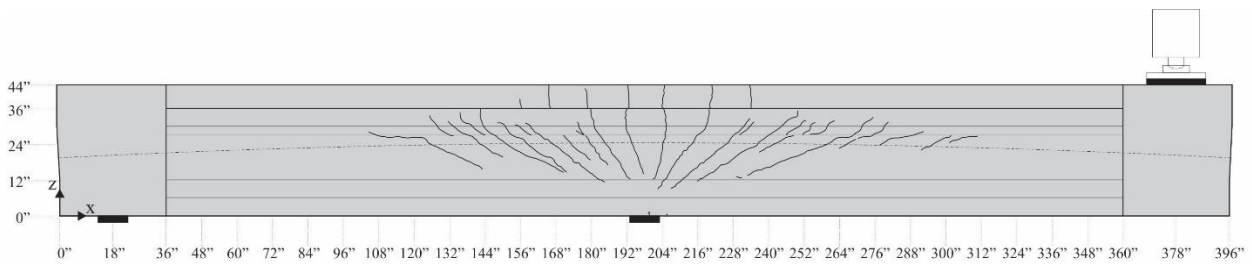
Figure E.2 Beam specimen NB-1 crack pattern: east side
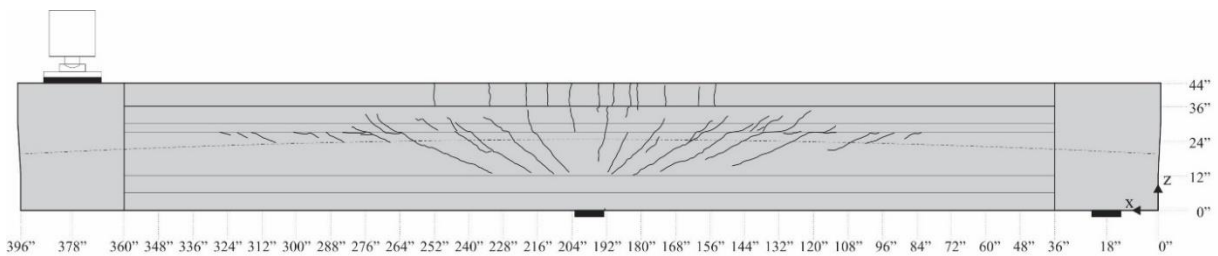
Figure E.3 Beam specimen NB-1 crack pattern: west side
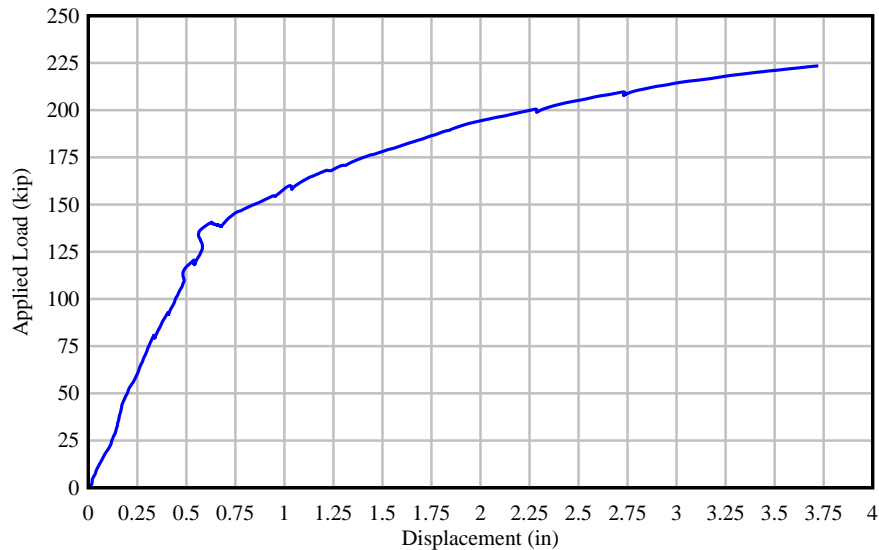
Figure E.4 Beam specimen NB-1: applied force vs. displacement at load point

Specimen Details

The cross-section of beam specimen NB-1 corresponds to a modified AASHTO Type II beam with a web width of 10 in. The girder section was topped with an 8-in. thick concrete deck and rectangular cast-in-place endblocks were added to accommodate post-tensioning anchorage hardware and additional reinforcement. Figure E.5 shows the beam inside the load frame while Figures E.6 and E.7 show the tie down and load point, respectively. Key parameters are listed in Table E.1. Concrete cylinders were tested to determine the compressive strength at the time of testing as shown in Table E.2. Note that some of the cylinders tested at the FDOT Structures Research Center presented significantly lower strengths than cylinders from the same concrete batch previously tested at the precast plant. Additional cylinders were tested at the University of Florida resulting in higher compressive strengths as expected. The problem with the previous FDOT cylinder tests was determined to be related to the use of an excessively worn grinding disk. Concrete cylinders tested after replacing the grinding disk resulted in the expected compressive strengths.

Table E.1 Beam specimen NB-1: key parameters

Cross Section	Specimen Length (ft)	L/D	U/T	No. PreT Strands (bottom)	No. PreT Strands (top)	No. PT Strands	PT tendon profile	Longitudinal mild steel bars (deck)
Modified AASHTO Type II	33	20	0.5	2	12	12	F1	8 #4

Table E.2 Beam specimen NB-1: compressive strength results

Description	Cast date	Test date	Test age (days)	Compressive Strength (psi)	Specified Compressive Strength (psi)
Precast girder	2020-01-23	2020-02-05	1	5,442	8,500
		2020-02-06	2	6,899	
		2020-03-30	28	10,562	
		2021-09-02	576	*8,411	
		2021-09-13	587	**12,537	
Deck	2020-01-27	2020-02-06	1	5,432	8,500
		2020-03-04	28	10,431	
		2021-09-02	575	*9,013	
End blocks	2021-11-05	2021-09-13	38	10,285	6,500
		2021-09-20	45	10,992	

*Cylinders tested at the FDOT Structures Research Center presented significantly lower strengths than those previously tested at the precast plant. It was later determined the disk used to grind the cylinders was worn down. Concrete cylinders tested after replacing the grinding disk resulted in the expected compressive strengths.
**Additional cylinders were tested at the University of Florida, resulting in higher strengths.

Figure E.5 Beam specimen NB-1 inside test frame

(a)   (b)

Figure E.6 Beam specimen NB-1 tie down: (a) South view and (b) East view

Figure E.7 Beam specimen NB-1: load point

Test Procedure

Specimen NB-1 was loaded at a rate of 0.25 kip/sec. Load was held at 80, 92, 120, 140,

160, 200, and 209 kip. This allowed for the beam to be inspected, cracks marked, and VW strain

gage readings taken. The first visible cracks were identified and marked at a load of 120 kip (Figure E.8). However, as shown in Figures E.16 and E.17, the first cracks were recorded by fiber optic sensors at P = 99 kip on the west side and P = 116 kip on the east side of the beam. For safety reasons, cracks were only marked during loading up until 140 kip, which is 70% of the predicted nominal capacity. Loading was stopped once the strains in the bottom flange at the center support exceeded 0.003 in compression. The beam was then unloaded, cracks were marked, and final VW strain gage readings were taken. Figure E.9 shows cracks on the bottom flange near the middle support. Load, displacement, and strains were measured continuously during testing.

Figure E.8 Specimen NB-1: first observed cracks (marked in red) at P = 120 kip on east side

(a)

(b)

Figure E.9 Specimen NB-1: observed cracks near center support: (a) East and (b) West sides

Detailed Test Results
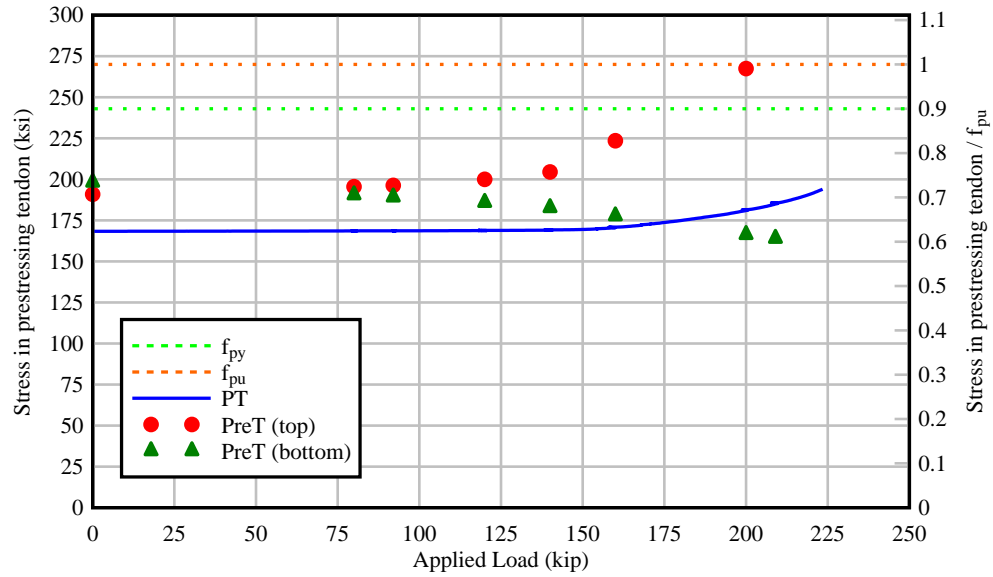
Figure E.10 Specimen NB-1: stress in PT and PreT tendons as a function of applied load
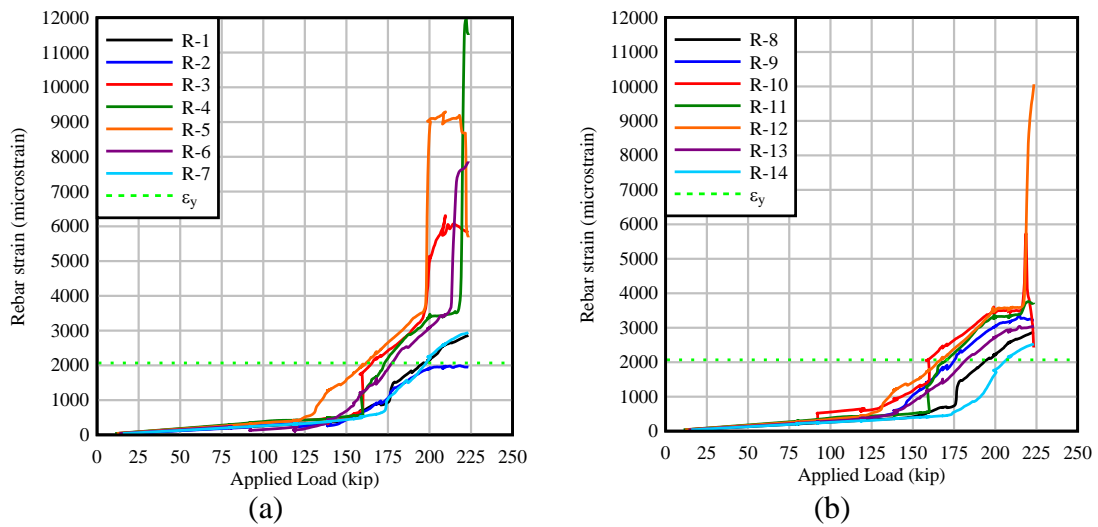
Figure E.11 Specimen NB-1: strain in longitudinal mild steel bars in deck vs. applied load:
(a) Bar 4A-3 and (b) Bar 4A-2
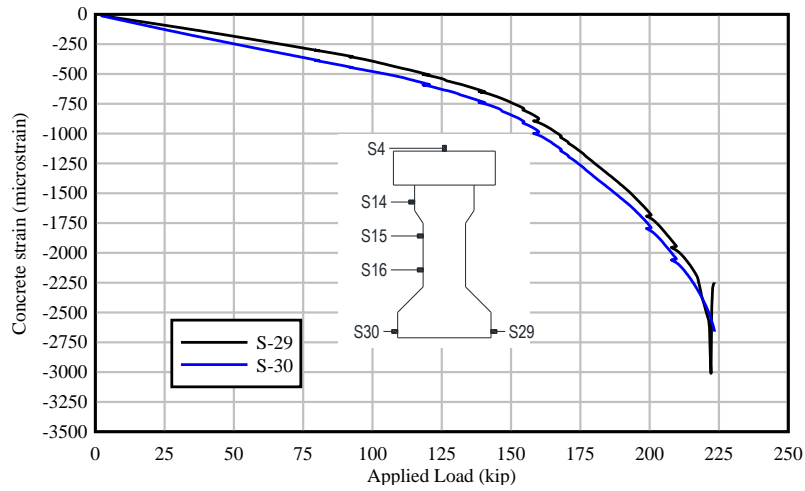
Figure E.12 Specimen NB-1: concrete strain vs. applied load – bottom flange, center support
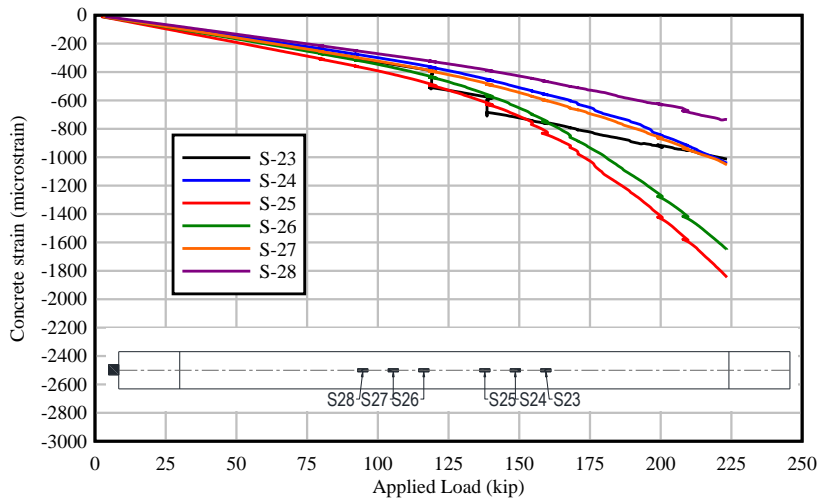
Figure E.13 Specimen NB-1: concrete strain vs. applied load – bottom of beam
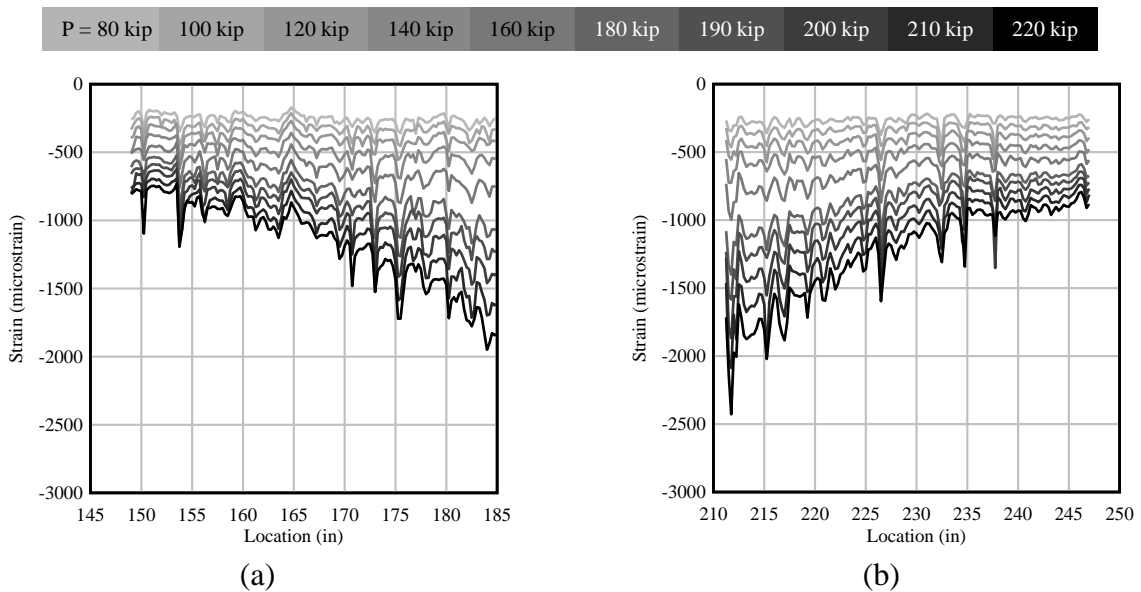
Figure E.14 Specimen NB-1: concrete strain vs. location – bottom of beam: (a) FOS-6 and (b) FOS-7

351

(a)

(b)

Figure E.15 Specimen NB-1: concrete strain vs. location – beam web: (a) FOS-3 and (b) FOS-5

Figure E.16 Specimen NB-1: concrete strain vs. location – top flange (west side): FOS-2
(a) Location of first crack at P = 99 kip, (b) Strain at different load levels

P = 100 kip | 116 kip | 120 kip | 140 kip | 160 kip | 180 kip | 190 kip | 200 kip | 210 kip | 220 kip
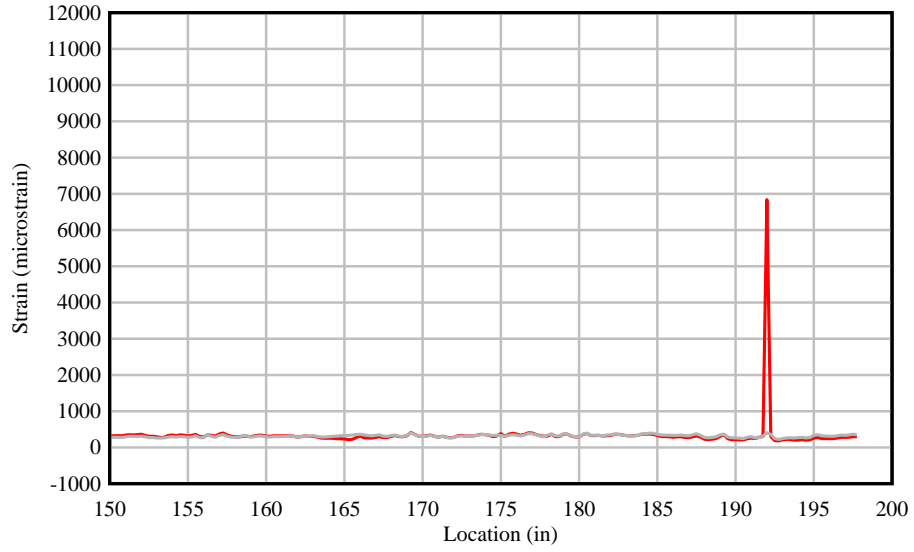
(a)
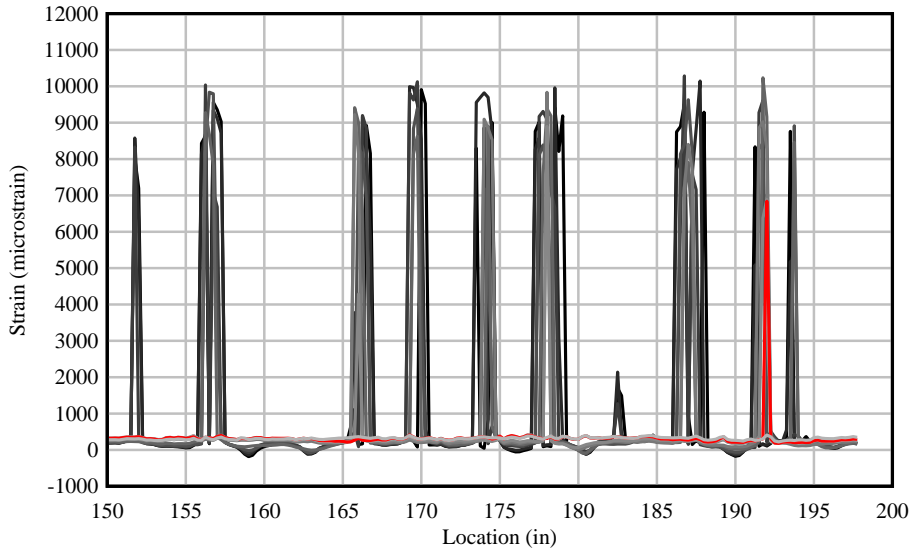
(b)

Figure E.17 Specimen NB-1: concrete strain vs. location – top flange (east side): FOS-1
(a) Location of first crack at P = 116 kip, (b) Strain at different load levels

Beam Specimen NB-2

Summary
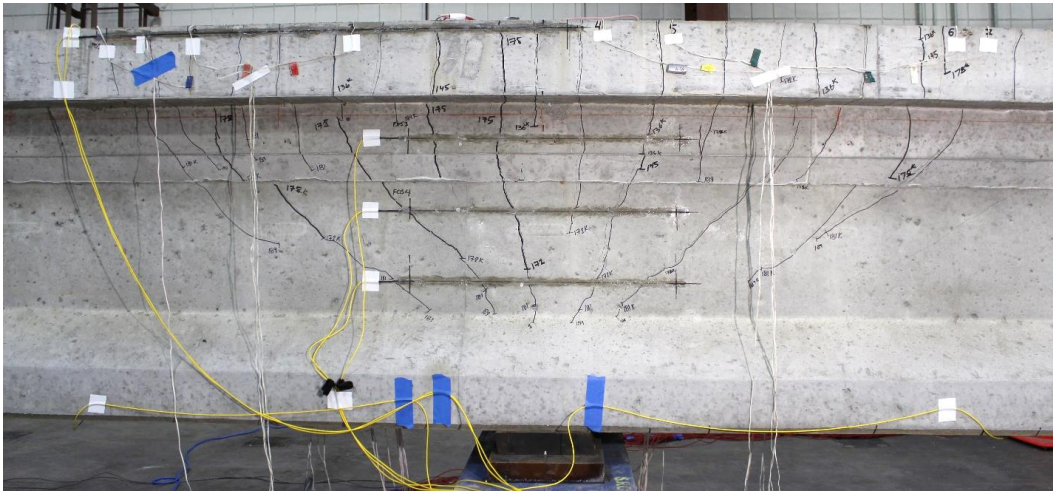
(a)

(b)

Figure E.18 Beam specimen NB-2 during testing: (a) East side (fiber optic sensors) and (b) West side (foil strain gages)

(a)
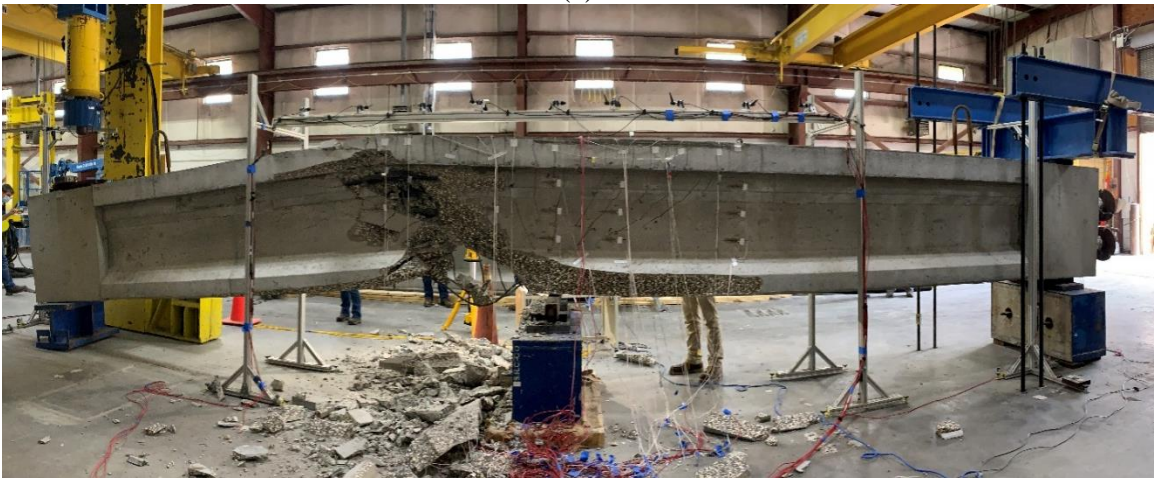
(b)

Figure E.19 Beam specimen NB-2 at end of testing: (a) East side and (b) West side
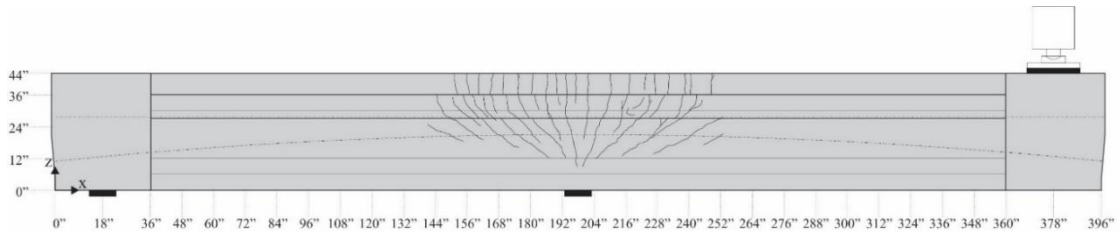
(a)
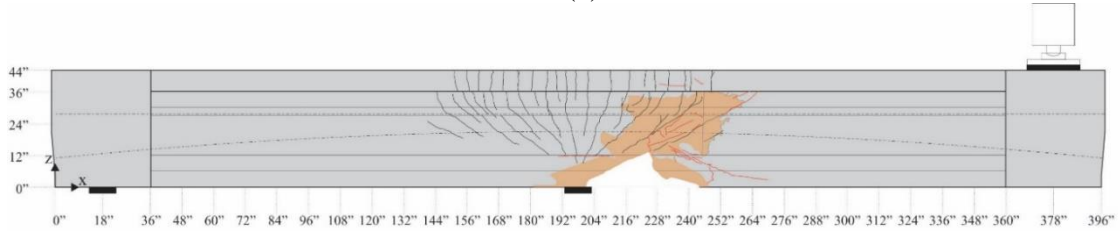
(b)

Figure E.20 Beam specimen NB-2 crack pattern – east side: (a) Before failure and (b) after failure
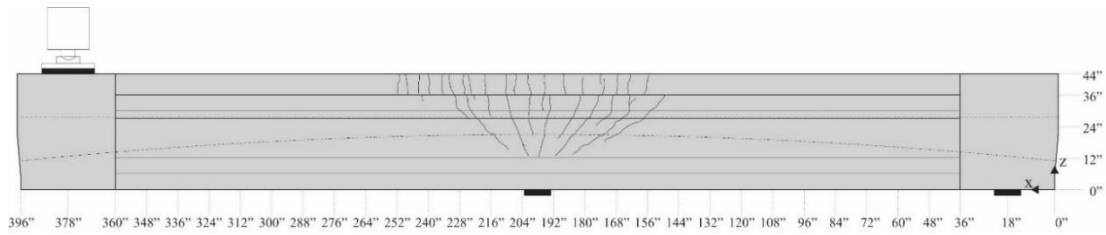
(a)
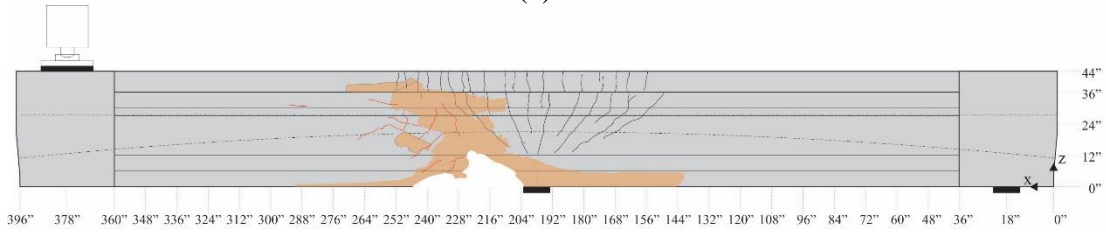
(b)

Figure E.21 Beam specimen NB-2 crack pattern – west side: (a) Before failure and (b) after failure
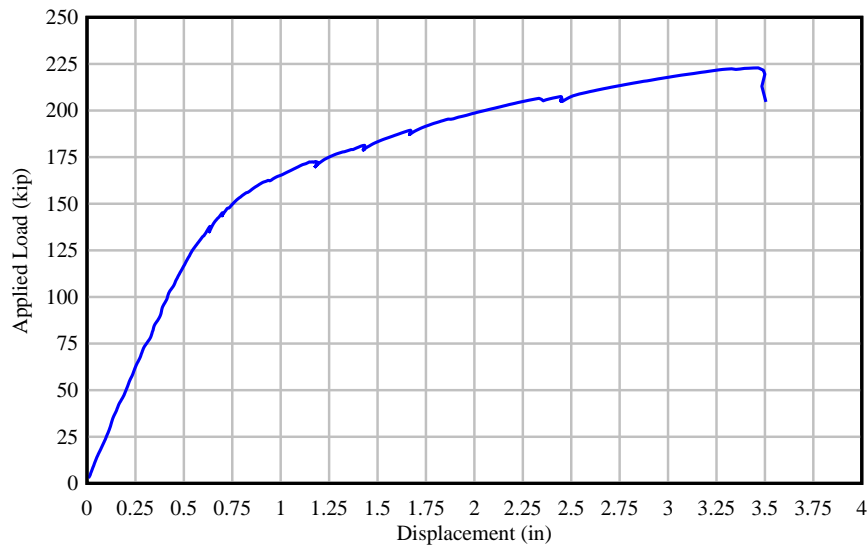
Figure E.22 Beam specimen NB-2: applied force vs. displacement at load point

Specimen Details

The cross-section of beam specimen NB-2 corresponds to a modified AASHTO Type II beam with a web width of 10 in. The girder section was topped with an 8-in. thick concrete deck and rectangular cast-in-place endblocks were added to accommodate post-tensioning anchorage hardware and additional reinforcement. Figure E.23 shows the beam inside the load frame and tie down. Key parameters are listed in Table E.3. Concrete cylinders were tested to determine the compressive strength at the time of testing as shown in Table E.4. Note that some of the cylinders tested at the FDOT Structures Research Center presented significantly lower strengths than cylinders from the same concrete batch previously tested at the precast plant. Additional cylinders were tested at the University of Florida resulting in higher compressive strengths as expected. The problem with the previous FDOT cylinder tests was determined to be related to the use of an excessively worn grinding disk. Concrete cylinders tested after replacing the grinding disk resulted in the expected compressive strengths.

Figure E.23 Beam specimen NB-2 inside test frame and tie-down

Table E.3 Beam specimen NB-2: key parameters

Cross Section	Specimen Length (ft)	L/D	U/T	No. PreT Strands (bottom)	No. PreT Strands (top)	No. PT Strands	PT tendon profile	Longitudinal mild steel bars (deck)
Modified AASHTO Type II	33	20	0.6	2	10	18	F1	8 #4

Table E.4 Beam specimen NB-2: compressive strength results

Description	Cast date	Test date	Test age (days)	Compressive Strength (psi)	Specified Compressive Strength (psi)
Precast girder	2020-01-23	2020-02-05	1	5,442	8,500
		2020-02-06	2	6,899	
		2020-03-30	28	10,562	
		2021-09-02	576	* 8,735	
		2021-09-13	587	** 12,537	
Deck	2020-01-27	2020-02-06	1	5,432	8,500
		2020-03-04	28	10,431	
		2021-09-02	575	* 9,013	
End blocks	2021-07-14	2021-08-11	28	* 7,628	8,500
		2021-09-02	50	* 6,791	
		2021-09-13	61	** 11,223	

*Cylinders tested at the FDOT Structures Research Center presented significantly lower strengths than those previously tested at the precast plant. It was later determined the disk used to grind the cylinders was worn down. Concrete cylinders tested after replacing the grinding disk resulted in the expected compressive strengths.
**Additional cylinders were tested at the University of Florida, resulting in higher strengths.

Test Procedure

Specimen NB-2 was loaded at a rate of 0.25 kip/sec. Load was held at 136, 145, 172, 181, and 189 kip. This allowed for the beam to be inspected, cracks marked, and VW strain gage

359

readings taken. The first visible cracks were identified and marked at a load of 136 kip (Figure E.24). However, as shown in Figures E.30 and E.31, the first cracks were recorded by fiber optic sensors at P = 114 kip on the west side and P = 123 kip on the east side of the beam. Loading was stopped following compression failure in the bottom flange at P = 223 kip. After that, final VW strain gage readings were taken. Load, displacement, and strains were measured continuously during testing.
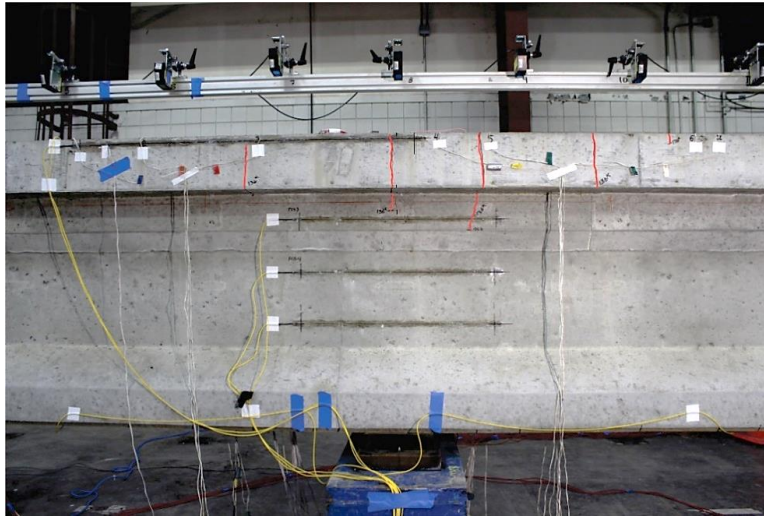
Figure E.24 Specimen NB-2: first observed cracks (marked in red) at P = 136 kip on east side

Detailed Test Results
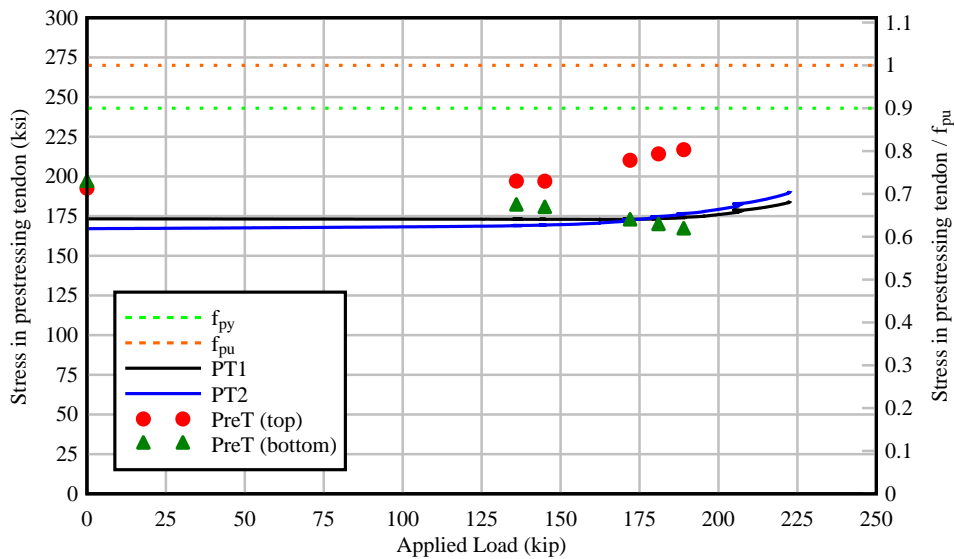
Figure E.25 Specimen NB-2: stress in PT and PreT tendons as a function of applied load
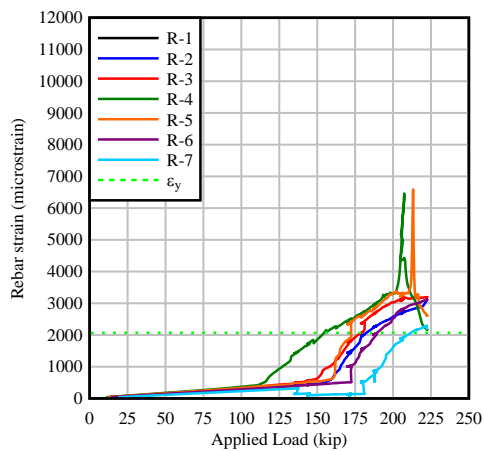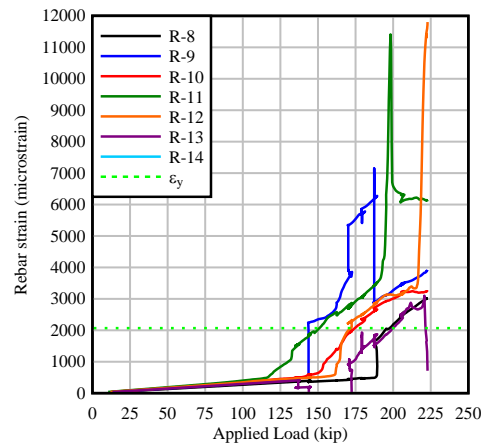
Figure E.26 Specimen NB-2: strain in longitudinal mild steel bars in deck vs. applied load: (a) Bar 4A-3 and (b) Bar 4A-2
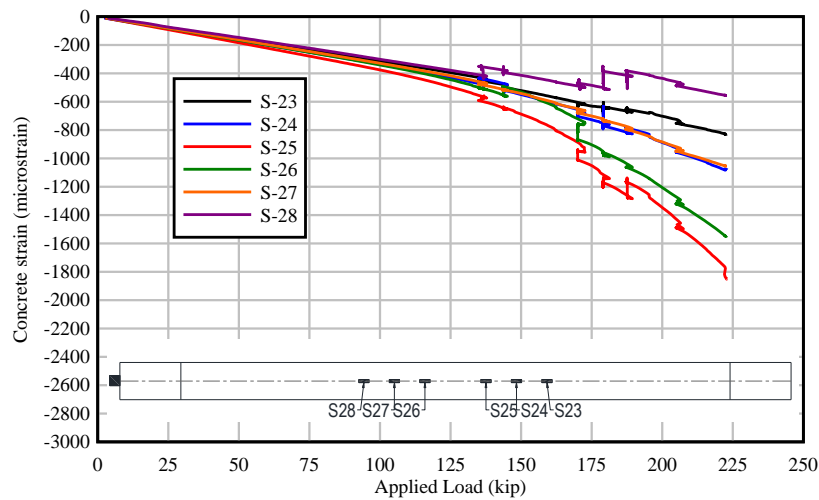
Figure E.27 Specimen NB-2: concrete strain vs. applied load – bottom of beam

Figure E.28 Specimen NB-2: concrete strain vs. location – bottom of beam: (a) FOS-6 and (b) FOS-7

361

(a)

(b)

Figure E.29 Specimen NB-2: concrete strain vs. location – beam web: (a) FOS-3 and (b) FOS-5

(a)

(b)

Figure E.30 Specimen NB-2: concrete strain vs. location – top flange (west side): FOS-2
(a) Location of first crack at P = 114 kip, (b) Strain at different load levels

| P = 100 kip | 120 kip | 123 kip | 136 kip | 140 kip | 160 kip | 180 kip | 200 kip | 220 kip | 222 kip |
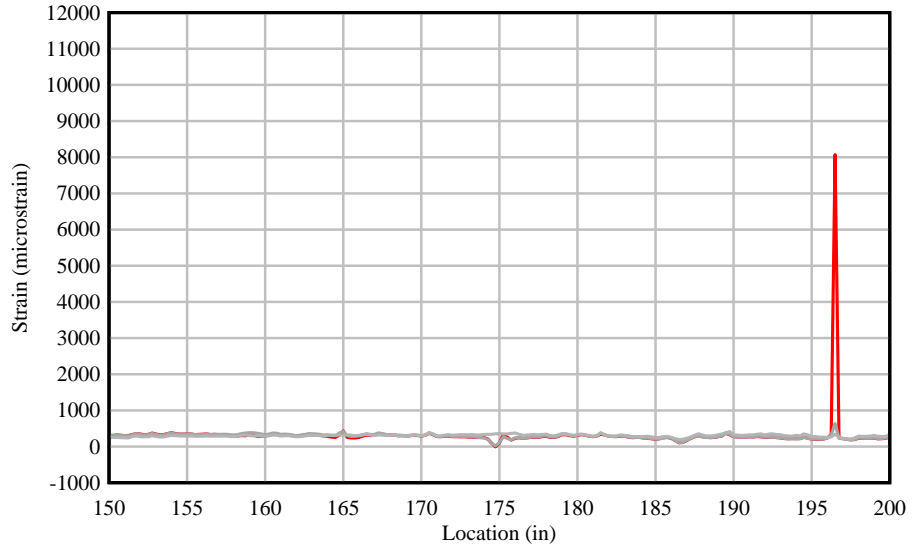
(a)
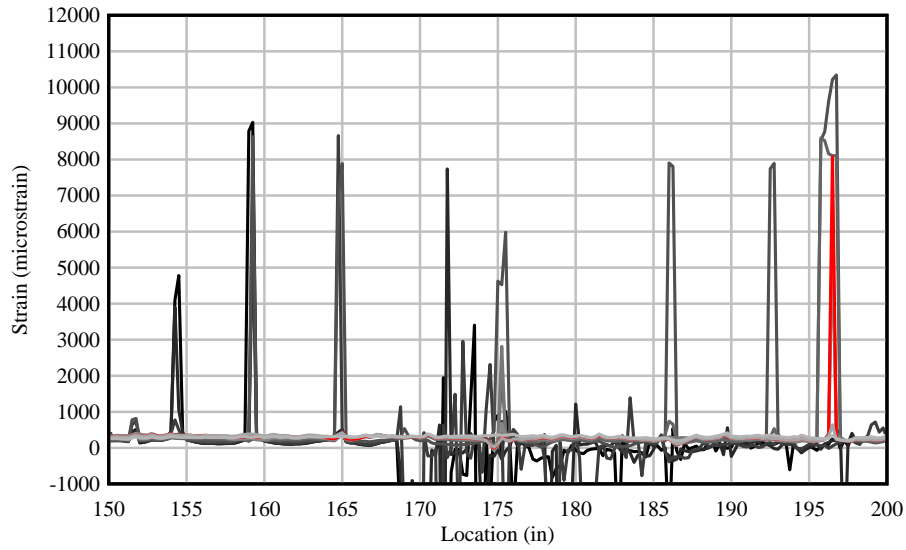
(b)

Figure E.31 Specimen NB-2: concrete strain vs. location – top flange (east side): FOS-1
(a) Location of first crack at P = 123 kip, (b) Strain at different load levels

364

Beam Specimen NB-3

Summary

(a)

(b)

Figure E.32 Beam specimen NB-3 at end of testing: (a) East side (fiber optic sensors) and (b) West side (foil strain gages)
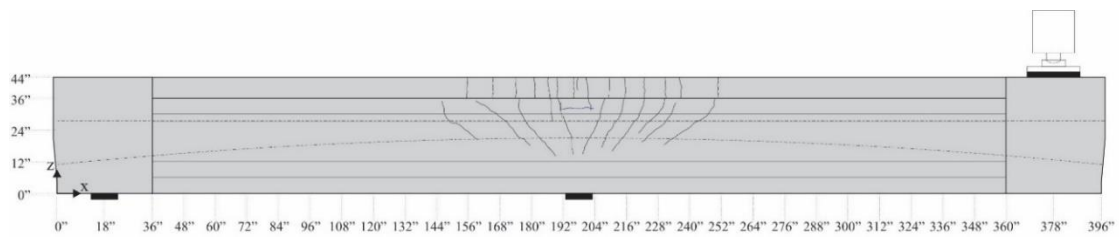
Figure E.33 Beam specimen NB-3 crack pattern: east side
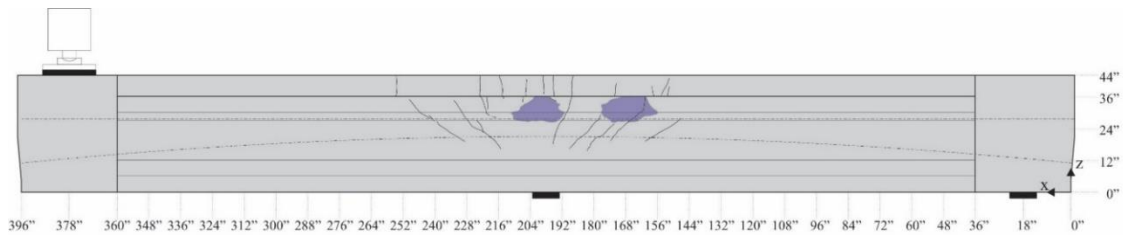
Figure E.34 Beam specimen NB-3 crack pattern: west side (repairs prior to test are shown in light blue)
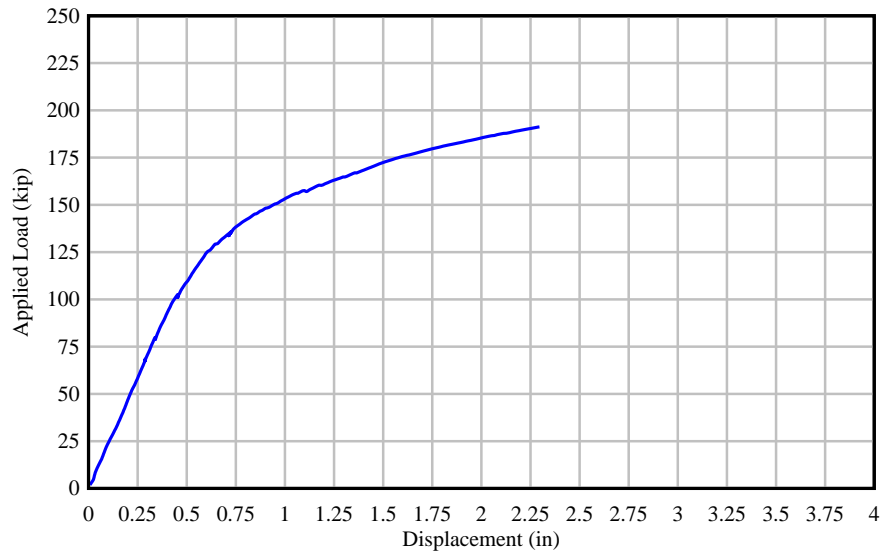
Figure E.35 Beam specimen NB-3: applied force vs. displacement at load point

Specimen Details

The cross-section of beam specimen NB-3 corresponds to a modified AASHTO Type II beam with a web width of 10 in. The girder section was topped with an 8-in. thick concrete deck and rectangular cast-in-place endblocks were added to accommodate post-tensioning anchorage hardware and additional reinforcement. Figure E.36 shows the beam inside the load frame and tie down. Key parameters are listed in Table E.5. Concrete cylinders were tested to determine the compressive strength at the time of testing as shown in Table E.6. Note that some of the cylinders tested at the FDOT Structures Research Center presented significantly lower strengths than cylinders from the same concrete batch previously tested at the precast plant. Additional cylinders were tested at the University of Florida resulting in higher compressive strengths as expected. The problem with the previous FDOT cylinder tests was determined to be related to the use of an excessively worn grinding disk. Concrete cylinders tested after replacing the grinding disk resulted in the expected compressive strengths.

Table E.5 Beam specimen NB-3: key parameters

Cross Section	Specimen Length (ft)	L/D	U/T	No. PreT Strands (bottom)	No. PreT Strands (top)	No. PT Strands	PT tendon profile	Longitudinal mild steel bars (deck)
Modified AASHTO Type II	33	20	0.7	2	6	22	F1	8 #4

Table E.6 Beam specimen NB-3: compressive strength results

Description	Cast date	Test date	Test age (days)	Compressive Strength (psi)	Specified Compressive Strength (psi)
Precast girder	2020-02-04	2020-02-05	1	5,442	8,500
		2020-02-06	2	6,899	
		2020-03-30	28	10,562	
		2021-09-02	576	* 8,735	
		2021-09-10	584	* 10,649	
		2021-09-13	587	** 12,537	
Deck	2020-02-05	2020-02-06	1	5,432	8,500
		2020-03-04	28	10,431	
		2021-09-02	575	* 9,013	
End blocks	2021-07-14	2021-08-11	28	* 7,628	8,500
		2021-09-02	50	* 6,791	
		2021-09-13	61	** 11,223	

*Cylinders tested at the FDOT Structures Research Center presented significantly lower strengths than those previously tested at the precast plant. It was later determined the disk used to grind the cylinders was worn down. Concrete cylinders tested after replacing the grinding disk resulted in the expected compressive strengths.
**Additional cylinders were tested at the University of Florida, resulting in higher strengths.

Figure E.36 Beam specimen NB-3 inside test frame and tie-down

Specimen NB-3 presented spalling on the west side of the beam near the midspan region after detensioning pretensioned strands at the precast plant. Note that although some of the top pretensioned strands were designed as 'debonded', they were still bonded for a distance of 1 ft at midspan. The concrete spalling in this region was attributed to the fact that rapid (dynamic) elastic shortening (from detensioning) of the debonded strands was halted by just 1 ft of bonded length. Prior to post-tensioning of the unbonded tendons, the concrete was sounded with a hammer to determine the extent of areas of delamination. Although the cracks extended for the entire height of the beam top flange, partial demolition on the top flange later revealed that the cracks did not extend through the width of the flange, but instead extended less than 1.5 inches into the flange. Concrete spalling was attributed to the local impact from strand release. The affected area was repaired at the FDOT Structures Research Center using Fast Patch 2 (APL no. 930-011-003), which is an FDOT approved product for concrete repair on predominately vertical surfaces (Figure E.32 B). During testing, no perceptible effect of the repair was evident in the observed flexural behavior of specimen NB-3.

Test Procedure

Specimen NB-3 was loaded at a rate of 0.25 kip/sec. Load was held at 68, 79, 102, and 136 kip. This allowed for the beam to be inspected, cracks marked, and VW strain gage readings taken. The first visible cracks were identified and marked at a load of 102 kip (Figure E.37). However, as shown in Figures E.44 and E.45, the first cracks were recorded by fiber optic sensors at $P = 97$ kip on the east side and $P = 110$ kip on the west side of the beam. Cracks were marked during loading up until 136 kip, which is 80% of the predicted nominal capacity. Audible indications of strand movement in the unbonded post-tensioned tendons were heard at $P = 160$ and 170 kip. Since the prestressing tendons in beam specimen NB-3 were composed of mostly unbonded strands, for safety reasons, loading was stopped at $P = 191$ kip

after exceeding the predicted maximum load. The beam was then unloaded, cracks were marked, and final VW strain gage readings were taken.

Figure E.37 Specimen NB-3: first observed cracks (marked in red) at P = 102 kip on east side

Detailed test results
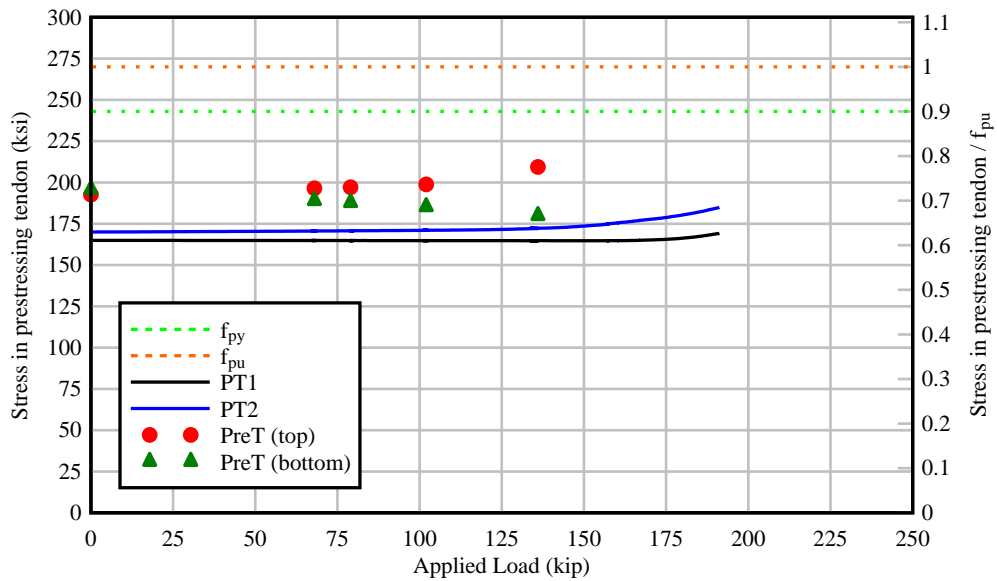
Figure E.38 Specimen NB-3: stress in PT and PreT tendons as a function of applied load

369

Figure E.39 Specimen NB-3: strain in longitudinal mild steel bars in deck vs. applied load: (a) Bar 4A-3 and (b) Bar 4A-2
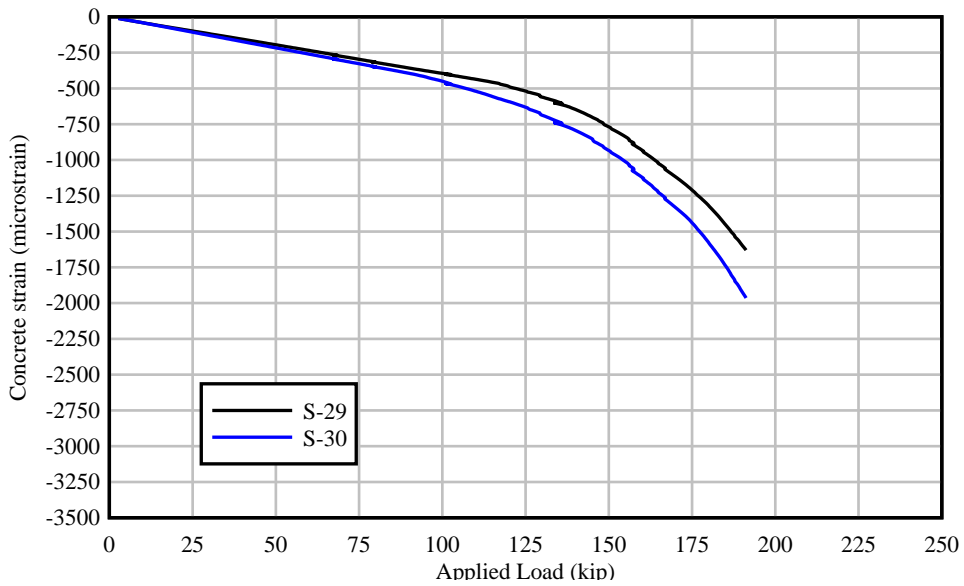
Figure E.40 Specimen NB-3: concrete strain vs. applied load – bottom flange, center support
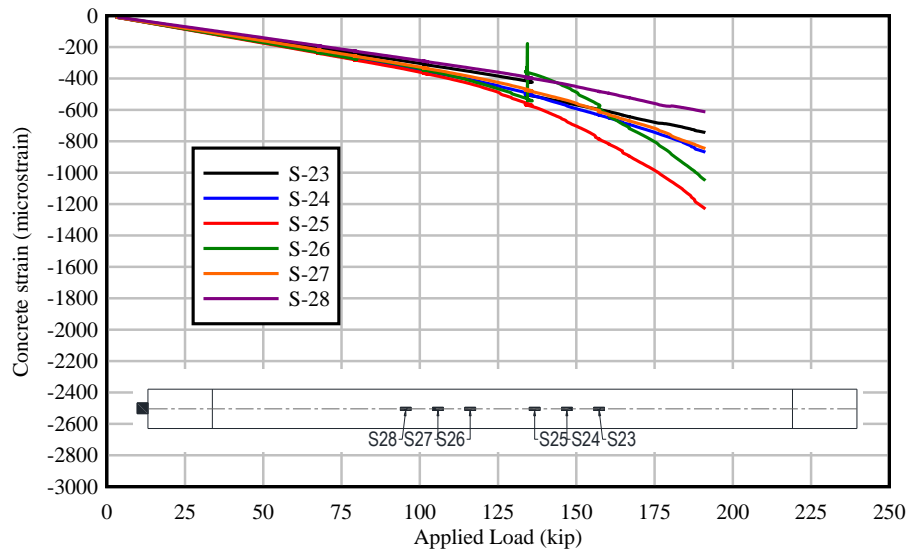
Figure E.41 Specimen NB-3: concrete strain vs. applied load – bottom of beam
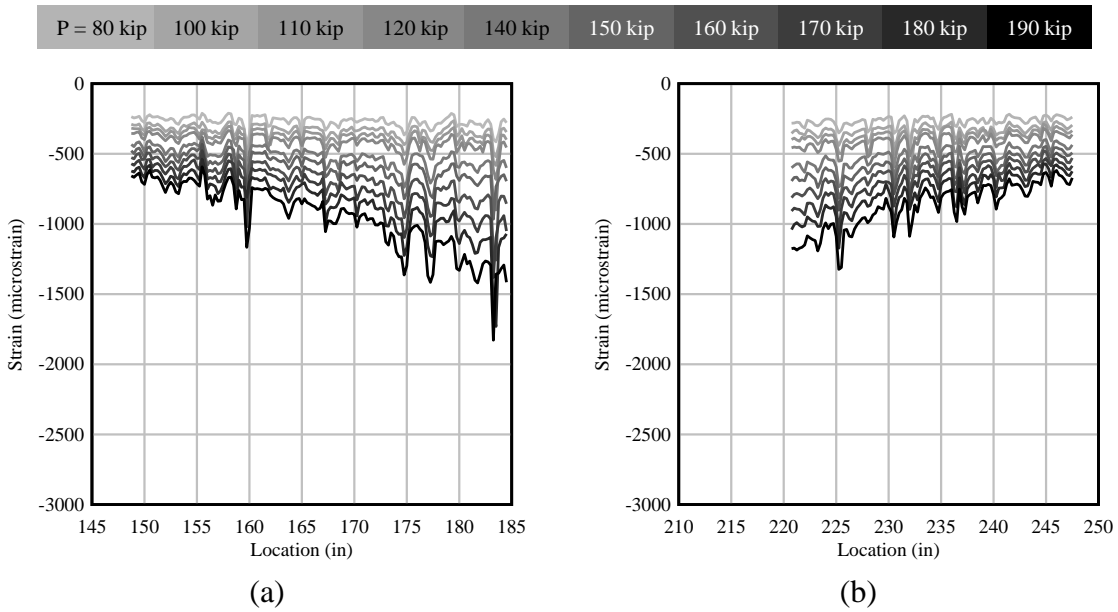
Figure E.42 Specimen NB-3: concrete strain vs. location – bottom of beam: (a) FOS-6 and (b) FOS-7

371
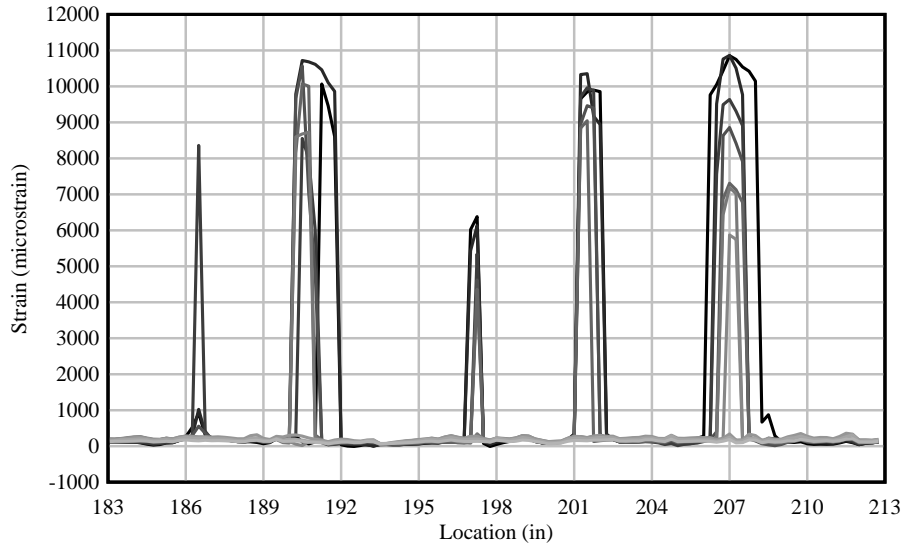
(a)

(b)

Figure E.43 Specimen NB-3: concrete strain vs. location – beam web: (a) FOS-3 and (b) FOS-5

372

Figure E.44 Specimen NB-3: concrete strain vs. location – top flange (east side): FOS-1
(a) Location of first crack at P = 99 kip, (b) Strain at different load levels

| P = 80 kip | 97 kip | 100 kip | 102 kip | 110 kip | 120 kip | 140 kip | 160 kip | 180 kip | 190 kip |
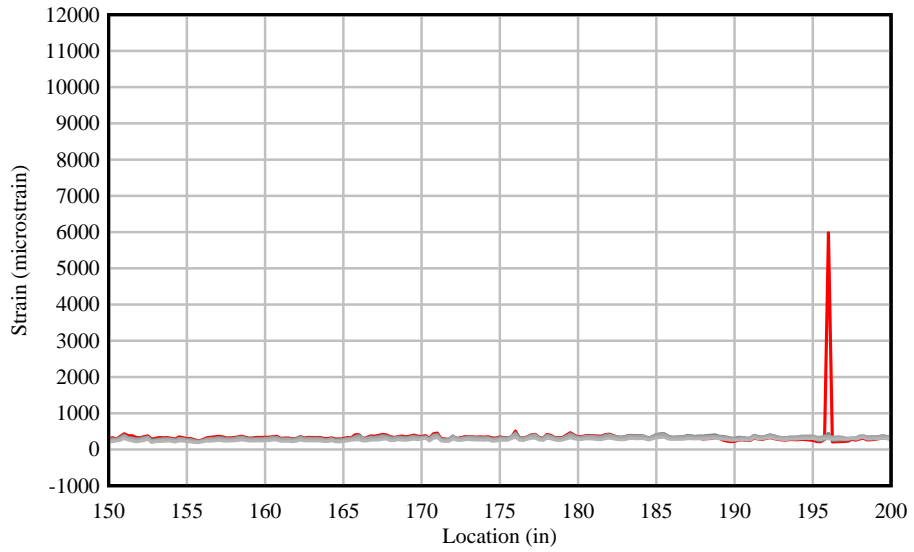
(a)
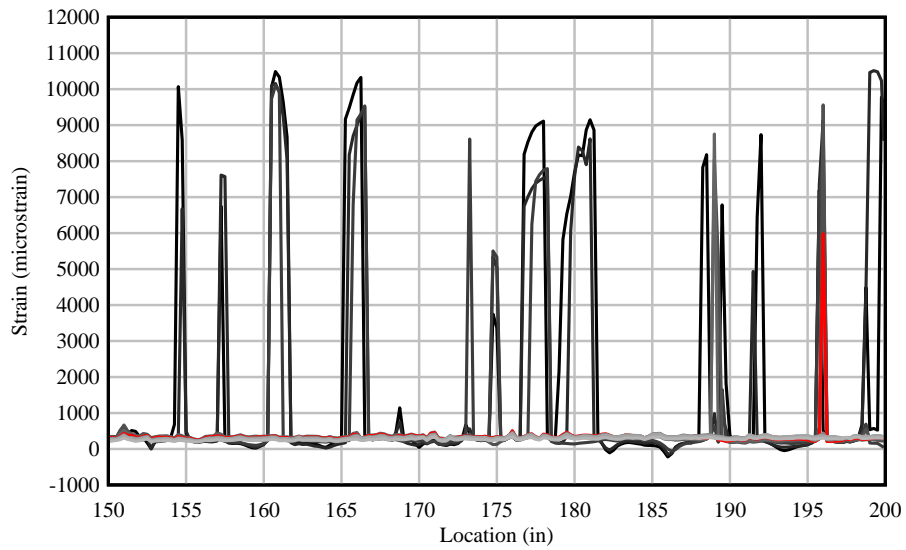
(b)

Figure E.45 Specimen NB-3: concrete strain vs. location – top flange (west side): FOS-2
(a) Location of first crack at P = 110 kip, (b) Strain at different load levels

APPENDIX F
LS-DYNA cards for finite element modeling

Examples of material cards used in the LS-DYNA finite element models are documented in this appendix. Note that all finite element models analyses in this study employed units of kip, in., and seconds.

Concrete

Material card for MAT_CSCM with parameters corresponding to f'c = 12.5 ksi:

```
*MAT_CSCM
       mid          ro       nplot       incre       irate       erode       recov     itretrc
         1     2.24E-7           1           0           0        1.05           0           0
      pred
       0.0
         g           k       alpha       theta       lamda        beta          nh          ch
    2363.0      2588.0       1.833      0.5151       1.524       0.133         1.0           0
    alpha1      theta1      lamda1       beta1      alpha2      theta2      lamda2       beta2
    0.7473    -1.060E-2        0.17     -0.3246        0.66    -1.308E-2        0.16     -0.3246
         r          xd           w          d1          d2
       5.0       20.84        0.05    1.724E-3     1.66E-5
         b         gfc           d         gft         gfs        pwrc        pwrt        pmod
     100.0     0.07223         0.1    7.223E-4    7.223E-4         5.0         1.0           0
     eta0c          nc       eta0t          nt       overc       overt       srate       repow
  9.893E-4        0.78    1.645E-4        0.48       12.31       12.31         1.0         1.0
```

Material card for MAT_ELASTIC with parameters corresponding to f'c = 10.0 ksi:

```
*MAT_ELASTIC
       mid          ro           e          pr          da          db    not used
         3     2.24E-7        6368         0.2           0           0           0
```

Mild steel

Material behavior of mild steel reinforcing bars was represented using the material model MAT_PIECEWISE_LINEAR_PLASTICITY. When a 'load curve' (lcss) is defined in the card for MAT_PIECEWISE_LINEAR_PLASTICITY, it is taken as the true stress versus effective plastic true strain curve and parameters eps1-eps8 and es1-es8 are ignored.

```
*MAT_PIECEWISE_LINEAR_PLASTICITY
       mid          ro           e          pr        sigy        etan        fail        Tdel
       101     7.34E-7       29000        0.33      69.375           0        0.11           0
         c           p        lcss        lcsr          vp         lcf
      40.5         5.0         101           0           0           0
      eps1        eps2        eps3        eps4        eps5        eps6        eps7        eps8
         0           0           0           0           0           0           0           0
       es1         es2         es3         es4         es5         es6         es7         es8
         0           0           0           0           0           0           0           0
```

```
*DEFINE_CURVE_TITLE
      lcid        sidr         sfa         sfo        offa        offo      dattyp       lcint
       101           0           1           1           0           0           0          12
                        a1          o1
                    0.0000     69.3750
                    0.0100     72.0000
                    0.0200     82.2000
                    0.0300     93.0000
                    0.0400    100.5750
                    0.0500    106.3000
                    0.0600    111.0000
                    0.0700    114.7500
                    0.0800    117.2500
                    0.0900    119.2500
                    0.1000    120.5000
                    0.1100    121.0000
```

Prestressing strands

Prestressing strands were represented using the material model MAT_CABLE_DISCRETE_

BEAM. Prestressing of discrete beam elements is achieved by direct specification of the target

prestress force level (f0). Transition length effects at each end of each pretensioned strand were

modeled by increasing (step increments) the prestress force over the elements that fell within the

transition length (Figure 8.8).

Material cards for a pretensioned strand with a target prestressing force of 44.42 kip:

$F_{PreT} = 44.42 \ kip$
```
  *MAT_CABLE_DISCRETE_BEAM
         mid          ro           e        lcid          f0      tmaxf0       tramp       iread
         220     7.344E-7       28500         202       44.42        0.85        0.30           1
      output      tstart      fracl0       mxeps       mxfrc
           1        0.55           0    0.051755         500
```

$F_{PreT} = 0 \ kip \ (transition)$
```
  *MAT_CABLE_DISCRETE_BEAM
         mid          ro           e        lcid          f0      tmaxf0       tramp       iread
         221     7.344E-7       28500         202         0.0        0.85        0.30           1
      output      tstart      fracl0       mxeps       mxfrc
           1        0.55           0    0.051755         500
```

$F_{PreT} = 7.40 \ kip \ (transition)$
```
  *MAT_CABLE_DISCRETE_BEAM
         mid          ro           e        lcid          f0      tmaxf0       tramp       iread
         222     7.344E-7       28500         202        7.40        0.85        0.30           1
      output      tstart      fracl0       mxeps       mxfrc
           1        0.55           0    0.051755         500
```

$F_{PreT} = 14.81 \ kip \ (transition)$
```
  *MAT_CABLE_DISCRETE_BEAM
         mid          ro           e        lcid          f0      tmaxf0       tramp       iread
         223     7.344E-7       28500         202       14.81        0.85        0.30           1
      output      tstart      fracl0       mxeps       mxfrc
           1        0.55           0    0.051755         500
```

F_{PreT} = 22.21 kip (transition)
```
*MAT_CABLE_DISCRETE_BEAM
      mid          ro           e        lcid          f0      tmaxf0       tramp       iread
      224     7.344E-7       28500         202       22.21        0.85        0.30           1
   output      tstart      fracl0       mxeps       mxfrc
        1        0.55           0    0.051755         500
```

F_{PreT} = 29.61 kip (transition)
```
*MAT_CABLE_DISCRETE_BEAM
      mid          ro           e        lcid          f0      tmaxf0       tramp       iread
      225     7.344E-7       28500         202       29.61        0.85        0.30           1
   output      tstart      fracl0       mxeps       mxfrc
        1        0.55           0    0.051755         500
```

F_{PreT} = 37.02 kip (transition)
```
*MAT_CABLE_DISCRETE_BEAM
      mid          ro           e        lcid          f0      tmaxf0       tramp       iread
      226     7.344E-7       28500         202       37.02        0.85        0.30           1
   output      tstart      fracl0       mxeps       mxfrc
        1        0.55           0    0.051755         500
```

PT tendons were modeled using discrete beam elements such that the beam elements had

an area equivalent to the total area of the tendon. Therefore, a prestressing force equivalent to the

total force in the post-tensioned tendon before loading was applied to one end of the tendon.

Material cards for post-tensioned tendons:

Live end
```
*MAT_CABLE_DISCRETE_BEAM
      mid          ro           e        lcid          f0      tmaxf0       tramp       iread
      301     7.344E-7       28500         202       228.7         1.4         0.3           1
   output      tstart      fracl0       mxeps       mxfrc
        1         1.1           0    0.051755        5000
```

All other
```
*MAT_CABLE_DISCRETE_BEAM
      mid          ro           e        lcid          f0      tmaxf0       tramp       iread
      300     7.344E-7       28500         202         0.0         0.0         0.0           1
   output      Tstart      fracl0       mxeps       mxfrc
        1         0.0           0    0.051755        5000
```

```
*DEFINE_CURVE_TITLE
      lcid      sidr       sfa       sfo      offa      offo    dattyp     lcint
       202         0         1         1         0         0         0        41
                              a1        o1
                        0.000000    0.000000
                        0.001126   30.994500
                        0.001443   40.518206
                        0.001792   51.238058
                        0.002167   62.075074
                        0.002558   73.243702
                        0.002964   85.968798
                        0.003378   97.714231
                        0.003805  110.503787
                        0.004235  123.133338
                        0.004670  136.094192
                        0.005112  148.709346
                        0.005556  160.997563
                        0.005997  174.153619
                        0.006447  186.944135
                        0.006894  199.529991
                        0.007345  211.638709
                        0.007798  223.322855
                        0.008244  233.518521
                        0.008693  242.062472
                        0.009154  247.910699
                        0.009622  252.614366
                        0.011156  258.800233
                        0.014119  263.888046
                        0.016809  264.838081
                        0.019498  265.826120
                        0.022185  267.190341
                        0.024874  269.019432
                        0.027562  270.858862
                        0.030250  272.632303
                        0.032938  274.420036
                        0.035626  276.010631
                        0.038315  277.445306
                        0.041002  278.837140
                        0.043690  280.012476
                        0.046378  280.944563
                        0.049066  281.734406
                        0.051755  282.386162
                        0.054443  282.850396
                        0.057131  283.155538
                        0.058632  283.074023
```

APPENDIX G
Parametric study – Florida I-beams (parabolic PT tendons)

Table G.1 Ratios of unbonded reinforcement: SS FIB-72 (parabolic PT tendon)

Bonded PreT	Qty	49 (.6 strands)	30 (.6 strands)	13 (.6 strands)
	Area	10.6 in^2	6.5 in^2	2.8 in^2
	Total force	2870.9 kip	1757.7 kip	761.7 kip
Unbonded PT	PT-tendons	1 (12 strands)	2 (12 strands) & 1 (7 strands)	4 (12 strands)
	Model PT1	1 (6 strands)	1 (15 strands)	1 (24 strands)
	Model PT2	1 (6 strands)	1 (16 strands)	1 (24 strands)
	Qty	12 (.6 strands)	31 (.6 strands)	48 (.6 strands)
	Area	2.6 in^2	6.7 in^2	10.4 in^2
	Total force	703.1 kip	1816.3 kip	2812.3 kip
U_A/T_A		0.20	0.51	0.79
U_F/T_F		0.20	0.51	0.79

Table G.2 Ratios of unbonded reinforcement: NB FIB-72 (parabolic PT tendon)

Mild steel	Qty	#4@12" & #5@6"	#4@12" & #5@6"	#4@12" & #5@6"
	Area	6.56 in^2	6.56 in^2	6.56 in^2
	Total force	393.6 kip	393.6 kip	393.6 kip
Bonded PreT	Qty	24 (.6 strands)	14 (.6 strands)	4 (.6 strands)
	Area	5.208 in^2	3.038 in^2	0.868 in^2
	Total force	1406.16 kip	820.26 kip	234.36 kip
Unbonded PT	PT-tendons	1 (12 strands)	2 (12 strands) & 1 (7 strands)	4 (12 strands)
	Model PT1	1 (6 strands)	1 (15 strands)	1 (24 strands)
	Model PT2	1 (6 strands)	1 (16 strands)	1 (24 strands)
	Qty	12 (.6 strands)	31 (.6 strands)	48 (.6 strands)
	Area	2.604 in^2	6.727 in^2	10.416 in^2
	Total force	703.1 kip	1816.3 kip	2812.3 kip
U_A/T_A		0.18	0.41	0.58
U_F/T_F		0.28	0.60	0.82

U_A/T_A = ratio of unbonded reinforcement area to total reinforcement area
U_F/T_F = ratio of unbonded force to total force
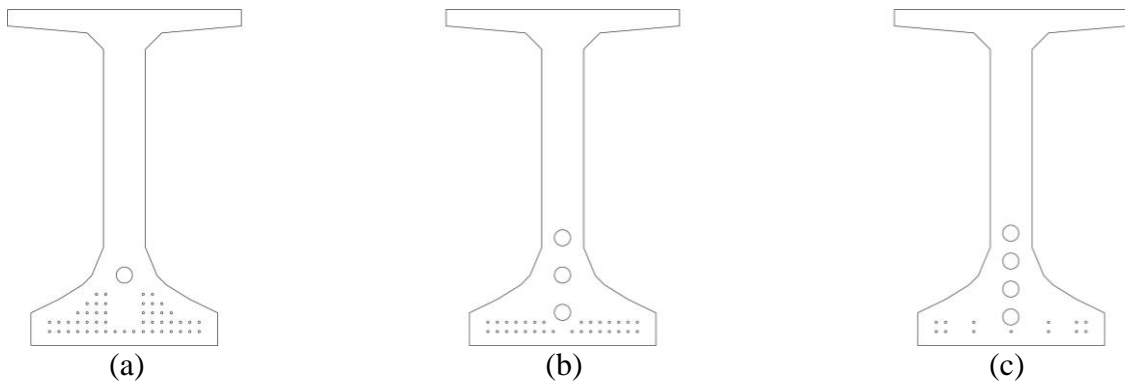
Figure G.1 Ratios of unbonded reinforcement for positive bending (parabolic PT tendon)
(a) $U_A/T_A = 0.2$; (b) $U_A/T_A = 0.5$; (c) $U_A/T_A = 0.8$
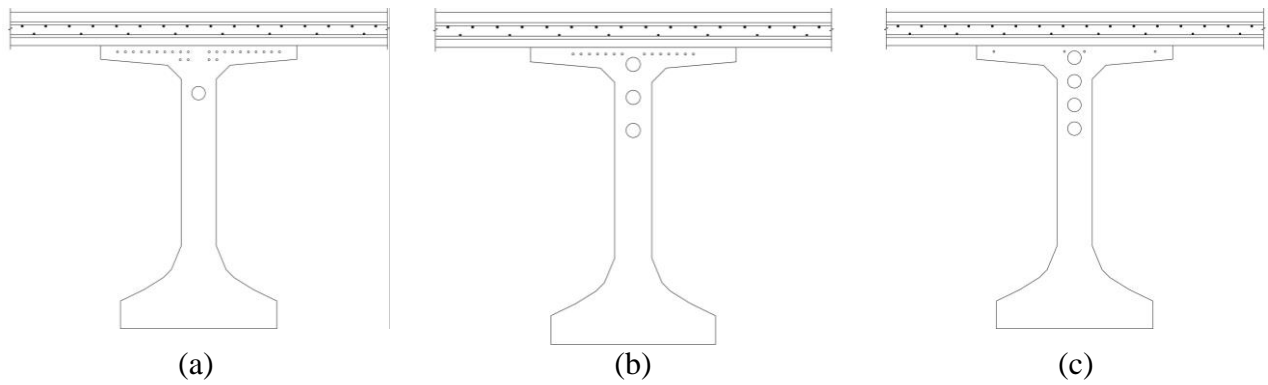
Figure G.2 Ratios of unbonded reinforcement for negative bending (continuous beams)
(a) $U_F/T_F = 0.3$; (b) $U_F/T_F = 0.6$; (c) $U_F/T_F = 0.8$
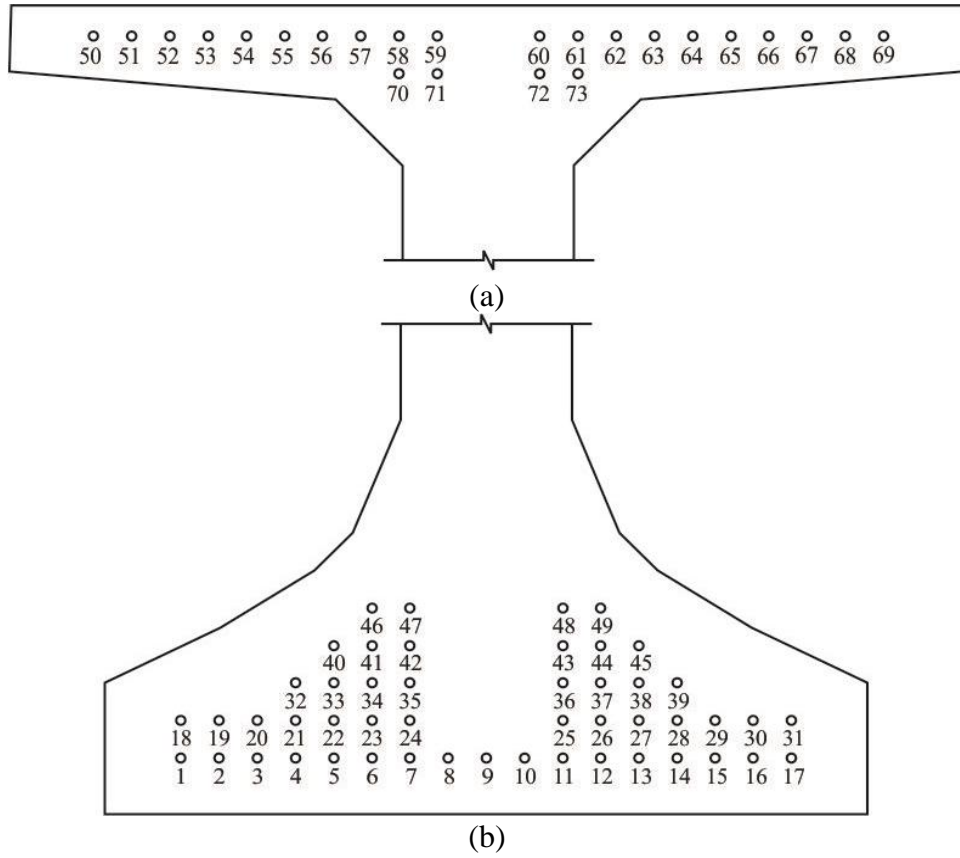
Figure G.3 Pretensioning strands numbering: (a) negative bending and (b) positive bending

Below is a description of the results from simply-supported beam models:

Model No.
FIB72-SS-01

Axial Force vs. Location on Pretensioning Strand

Curvature vs. Location

Moment vs. Curvature
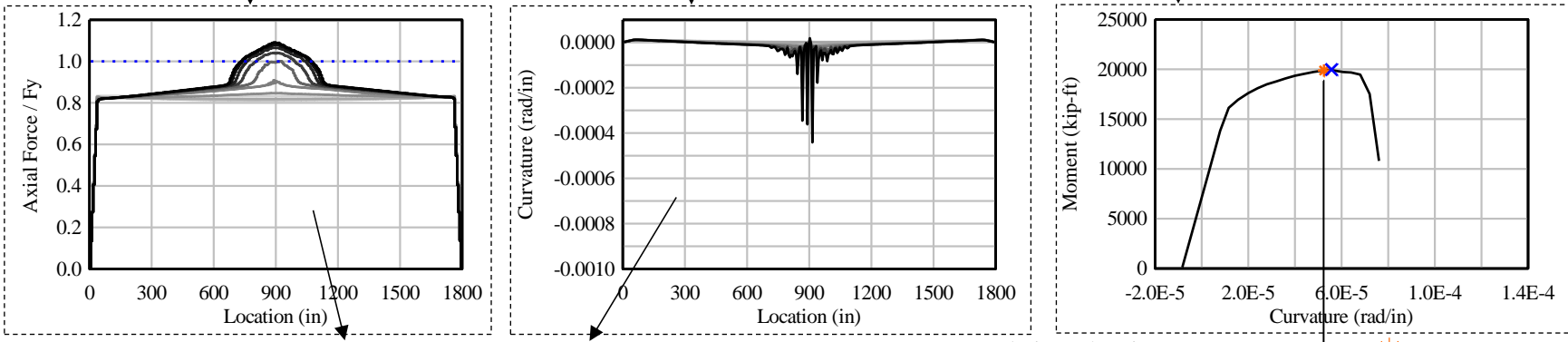
Start of Analysis — Time (*t*) — M_max

Renderings showing damage index at different *t*

✳ M at ε = 0.003
✕ M_max

Elevation View

Bottom View

Damage Index
0   0.1   0.2   0.3   0.4   0.5   0.6   0.7   0.8   0.9   1.0

382

FIB72-SS-01: U/T = 0.2; μ = 0; Point Load

Elevation View

Bottom View

Damage Index

383
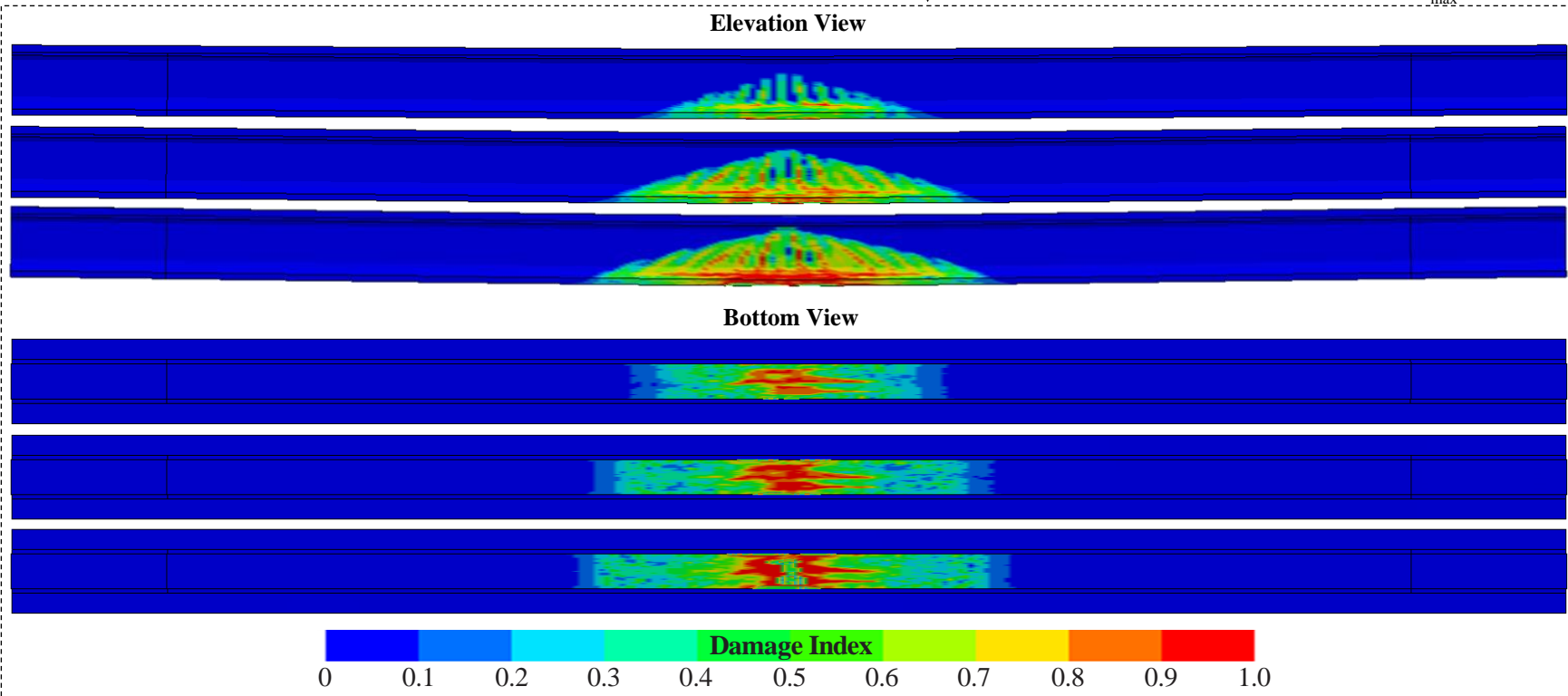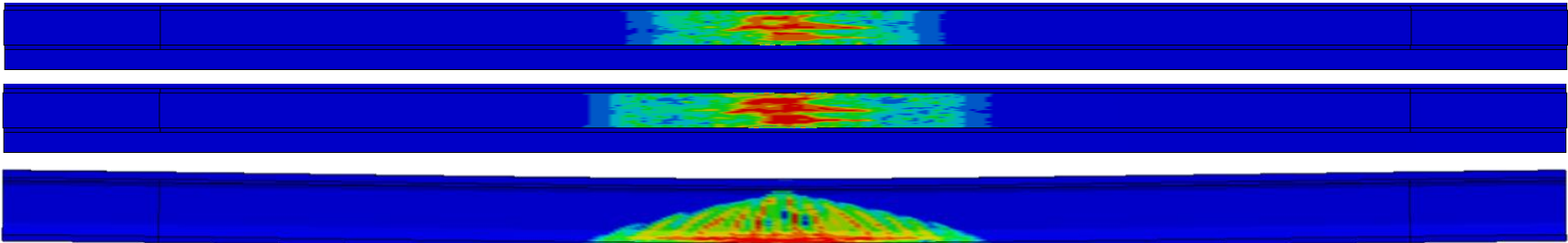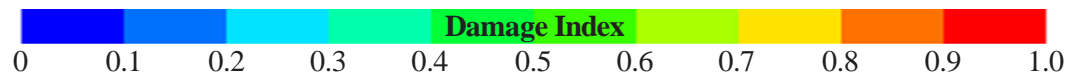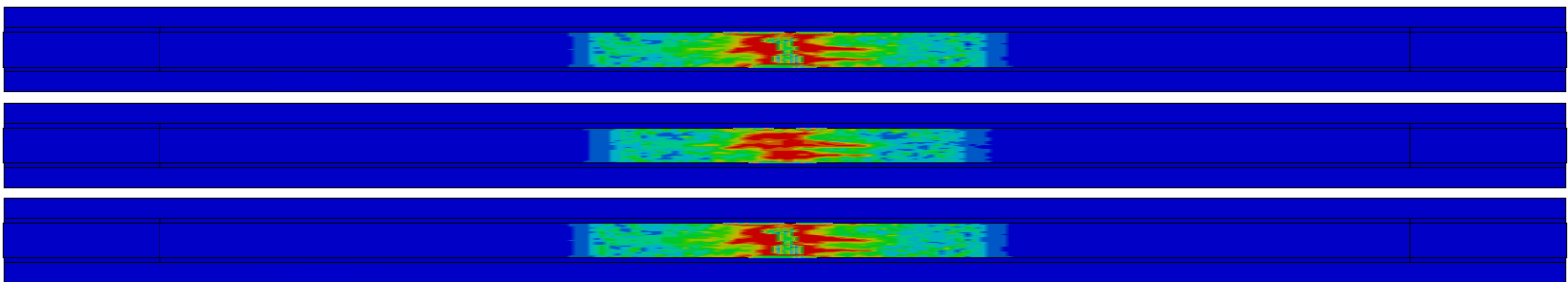
FIB72-SS-02: U/T = 0.5; μ = 0; Point Load

Elevation View

Bottom View

FIB72-SS-03: U/T = 0.8; μ = 0; Point Load

Elevation View

Bottom View

Damage Index

385

FIB72-SS-04: U/T = 0.2; μ = 0; Tandem Load

Elevation View

Bottom View

Damage Index

FIB72-SS-05: U/T = 0.5; μ = 0; Tandem Load

Elevation View

Bottom View

Damage Index

387

FIB72-SS-06: U/T = 0.8; μ = 0; Tandem Load

Elevation View

Bottom View

Damage Index

388

FIB72-SS-07: U/T = 0.2; μ = 0; Uniform Load

Elevation View

Bottom View

Damage Index

FIB72-SS-08: U/T = 0.5; μ = 0; Uniform Load

Elevation View

Bottom View

Damage Index

FIB72-SS-09: U/T = 0.8; μ = 0; Uniform Load

Elevation View

Bottom View

Damage Index

FIB72-SS-10: U/T = 0.5; μ = 0.14; Uniform Load

Elevation View

Bottom View

Damage Index

392

FIB72-SS-11: U/T = 0.5; μ = 0.3; Uniform Load

Elevation View

Bottom View

Damage Index

0   0.1   0.2   0.3   0.4   0.5   0.6   0.7   0.8   0.9   1.0

Below is a description of the results from continuous beam models:

Model No.

↳ **FIB72-NB-01** — Axial Force vs. Location on Bottom Pretensioning Strand: Left Beam Segment

Axial Force vs. Location on Top Pretensioning Strand: Middle Beam Segment

Axial Force vs. Location on Bottom Pretensioning Strand: Right Beam Segment
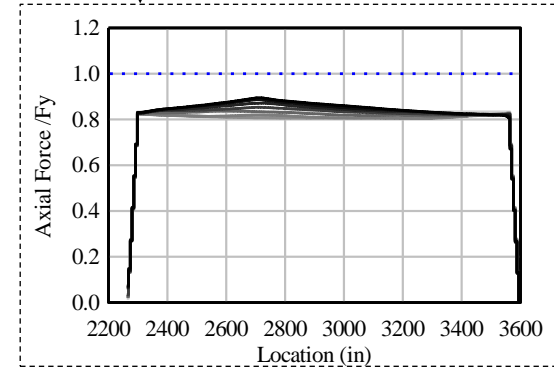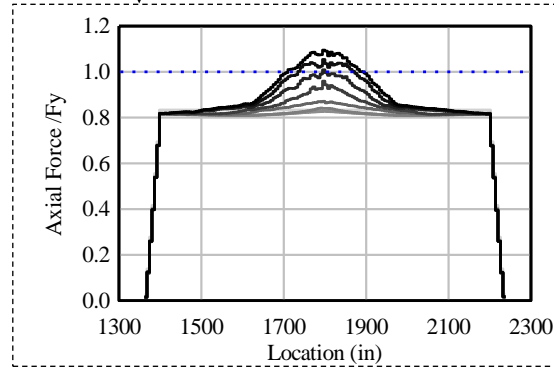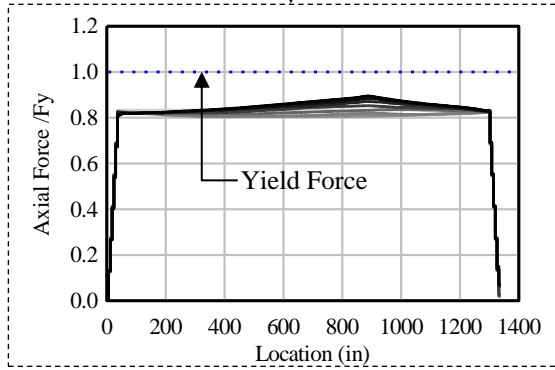
Start of Analysis Time (*t*) M$_{max}$
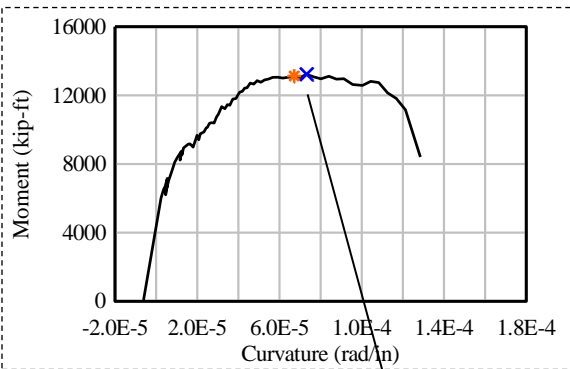
Moment vs. Curvature

M at ε = 0.003

M$_{max}$
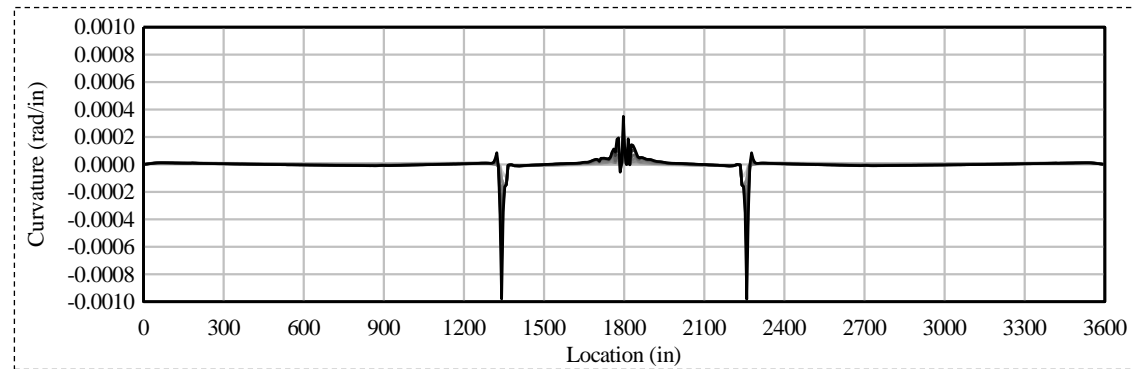
Curvature vs. Location

Renderings showing damage index at different t

Top View

Elevation View

Bottom View

Damage Index

0   0.1   0.2   0.3   0.4   0.5   0.6   0.7   0.8   0.9   1.0

FIB72-NB-01: U/T = 0.3; μ = 0; Point Load

Top View

Elevation View

Bottom View

Damage Index

0   0.1   0.2   0.3   0.4   0.5   0.6   0.7   0.8   0.9   1.0

FIB72-NB-02: U/T = 0.6; μ = 0; Point Load

Top View

Elevation View

Bottom View

Damage Index

| 0 | 0.1 | 0.2 | 0.3 | 0.4 | 0.5 | 0.6 | 0.7 | 0.8 | 0.9 | 1.0 |

FIB72-NB-03: U/T = 0.8; μ = 0; Point Load

Top View

Elevation View

Bottom View

Damage Index

0   0.1   0.2   0.3   0.4   0.5   0.6   0.7   0.8   0.9   1.0

FIB72-NB-04: U/T = 0.3; μ = 0; Tandem Load

Top View

Elevation View

Bottom View

Damage Index

0   0.1   0.2   0.3   0.4   0.5   0.6   0.7   0.8   0.9   1.0

FIB72-NB-05: U/T = 0.6; μ = 0; Tandem Load

Top View

Elevation View

Bottom View

Damage Index

0   0.1   0.2   0.3   0.4   0.5   0.6   0.7   0.8   0.9   1.0

FIB72-NB-06: U/T = 0.8; μ = 0; Tandem Load

Top View

Elevation View

Bottom View

Damage Index

0   0.1   0.2   0.3   0.4   0.5   0.6   0.7   0.8   0.9   1.0

FIB72-NB-07: U/T = 0.3; μ = 0; Uniform Load

Top View

Elevation View

Bottom View

Damage Index

0   0.1   0.2   0.3   0.4   0.5   0.6   0.7   0.8   0.9   1.0

FIB72-NB-08: U/T = 0.6; μ = 0; Uniform Load

Top View

Elevation View

Bottom View

Damage Index

0   0.1   0.2   0.3   0.4   0.5   0.6   0.7   0.8   0.9   1.0

FIB72-NB-09: U/T = 0.8; μ = 0; Uniform Load

Top View

Elevation View

Bottom View

Damage Index

0   0.1   0.2   0.3   0.4   0.5   0.6   0.7   0.8   0.9   1.0

413

FIB72-NB-10: U/T = 0.6; μ = 0.14; Uniform Load

Top View

Elevation View

Bottom View

Damage Index

0   0.1   0.2   0.3   0.4   0.5   0.6   0.7   0.8   0.9   1.0

FIB72-NB-11: U/T = 0.6; μ = 0.3; Uniform Load

Top View

Elevation View

Bottom View

Damage Index
0   0.1   0.2   0.3   0.4   0.5   0.6   0.7   0.8   0.9   1.0

FIB72-NB-12: U/T = 0.6; μ = 0.5; Uniform Load

Top View

Elevation View

Bottom View

Damage Index

0   0.1   0.2   0.3   0.4   0.5   0.6   0.7   0.8   0.9   1.0

Figure H.1 Ratios of unbonded reinforcement for positive bending (straight PT tendon)
(a) $U_A/T_A = 0.95$; (b) $U_A/T_A = 0.90$; (c) $U_A/T_A = 0.80$, (d) $U_A/T_A = 0.70$, (e) $U_A/T_A = 0.50$,
(f) $U_A/T_A = 0.35$, (g) $U_A/T_A = 0.25$, (h) $U_A/T_A = 0.10$, (i) $U_A/T_A = 0$ (bonded)
[unbonded PT tendons shown in orange]

FIB72-SS-12: U/T = 0.95; μ = 0; Point Load

Elevation View

Damage Index

0   0.1   0.2   0.3   0.4   0.5   0.6   0.7   0.8   0.9   1.0

421
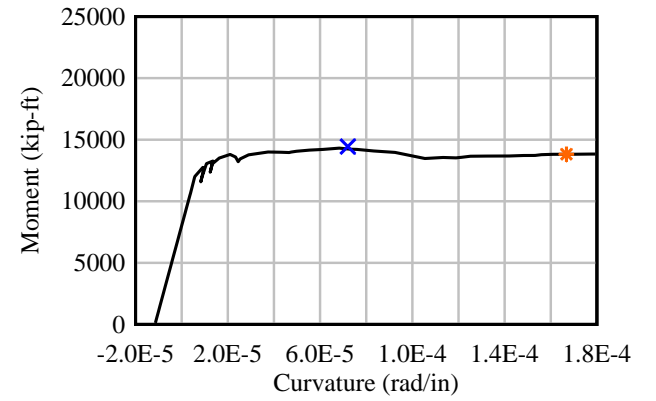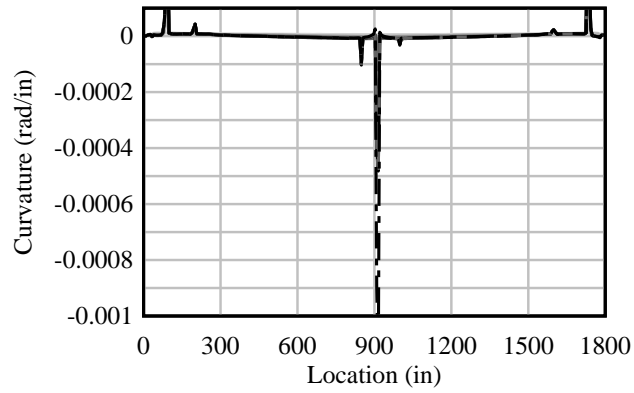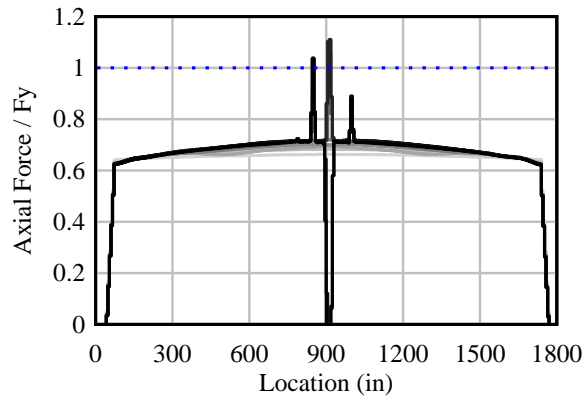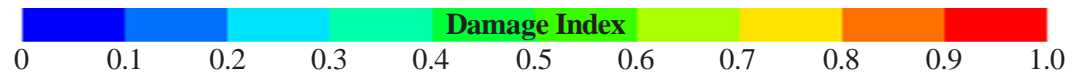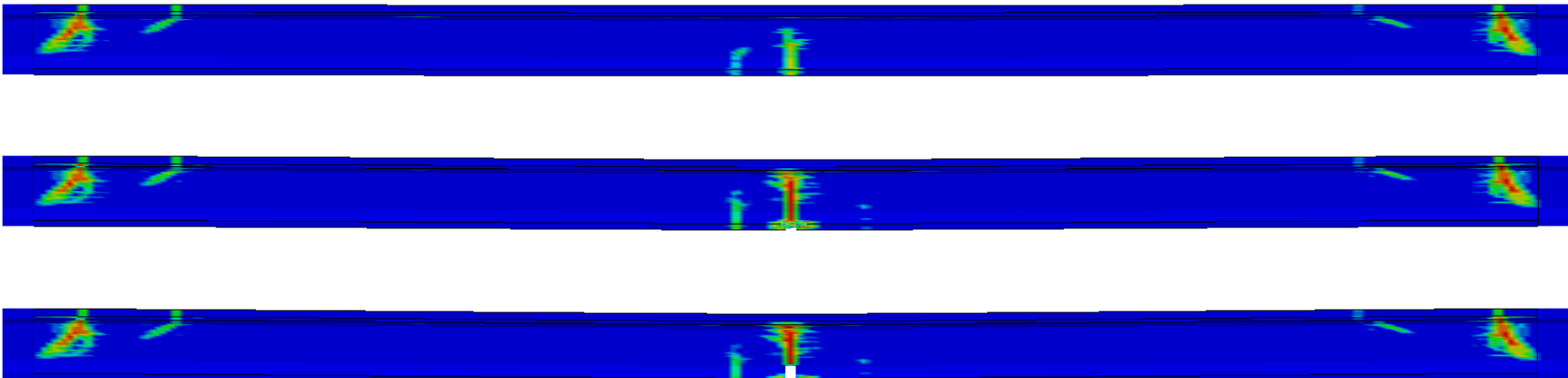
FIB72-SS-13: U/T = 0.90; μ = 0; Point Load
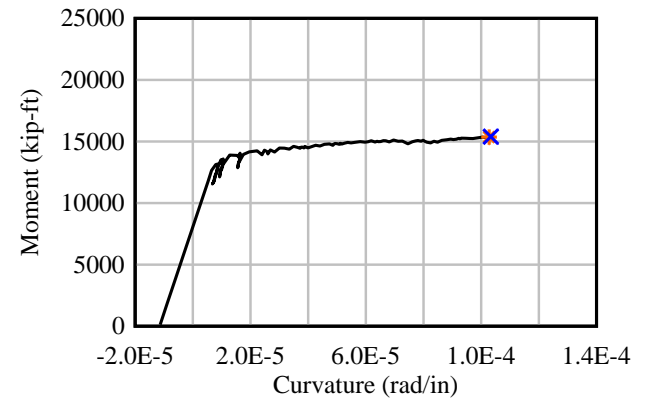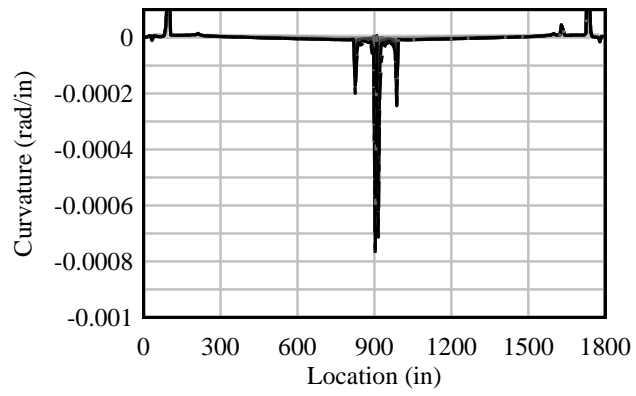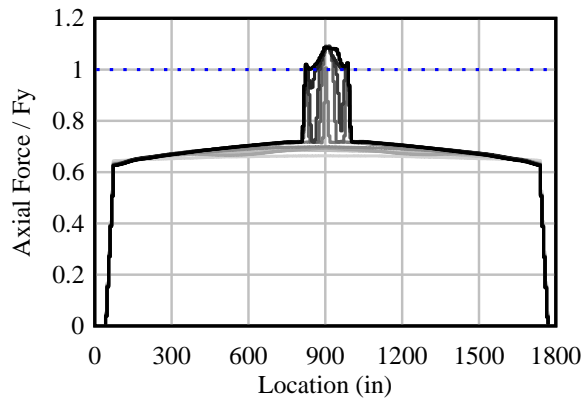
Elevation View

FIB72-SS-14: U/T = 0.90; μ = 0; Tandem Load

Elevation View

Damage Index

0   0.1   0.2   0.3   0.4   0.5   0.6   0.7   0.8   0.9   1.0
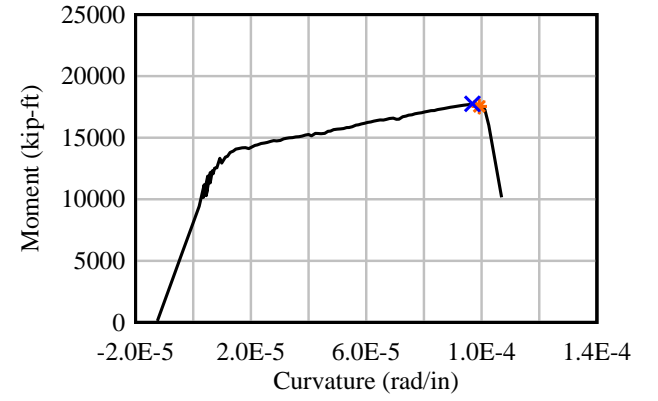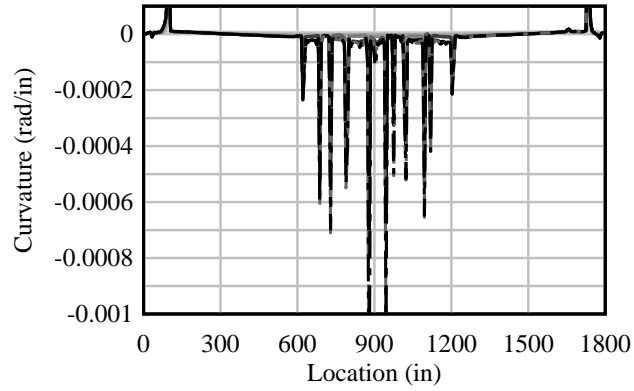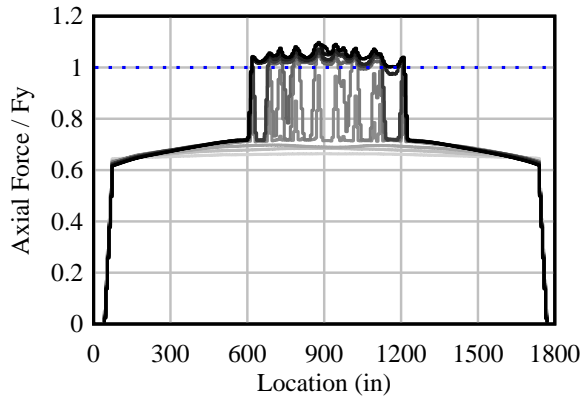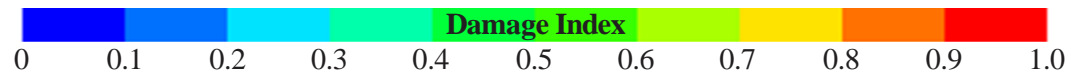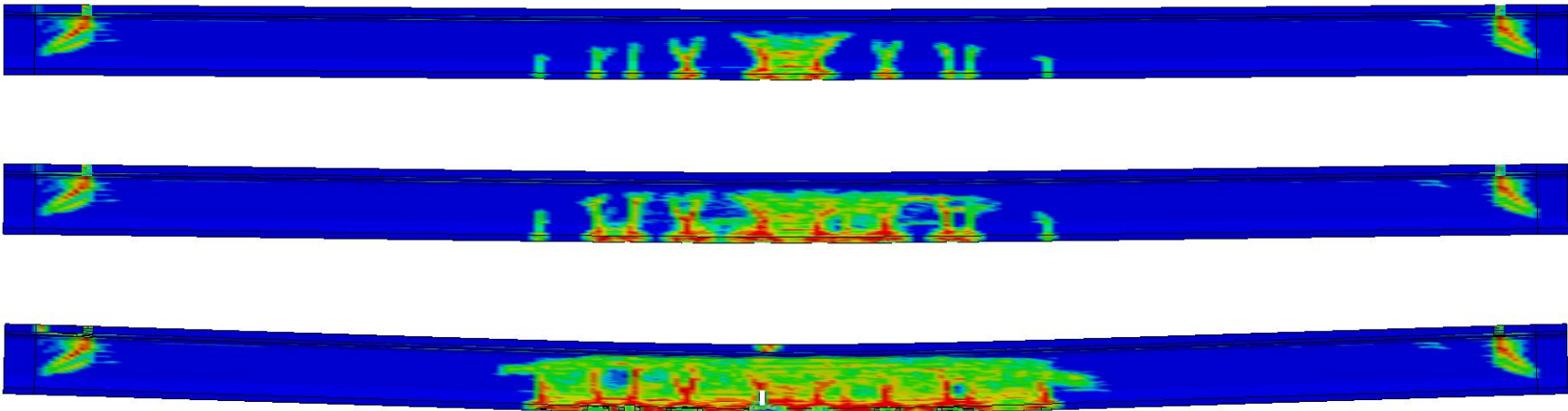
FIB72-SS-15: U/T = 0.90; μ = 0; Uniform Load
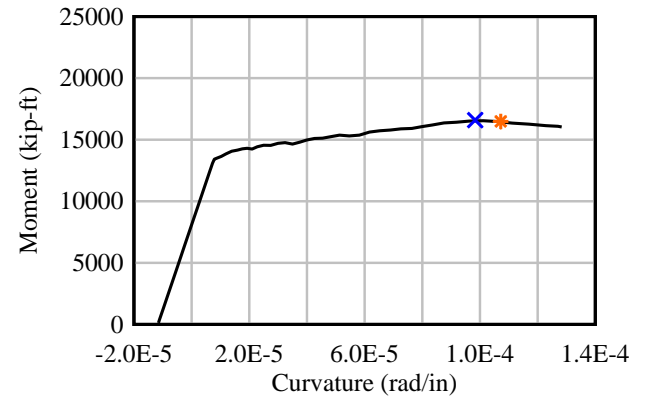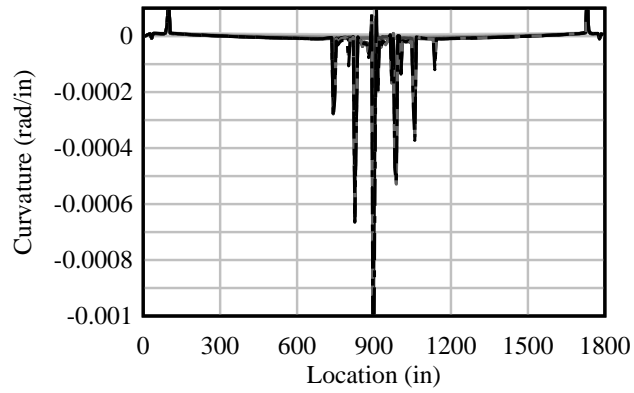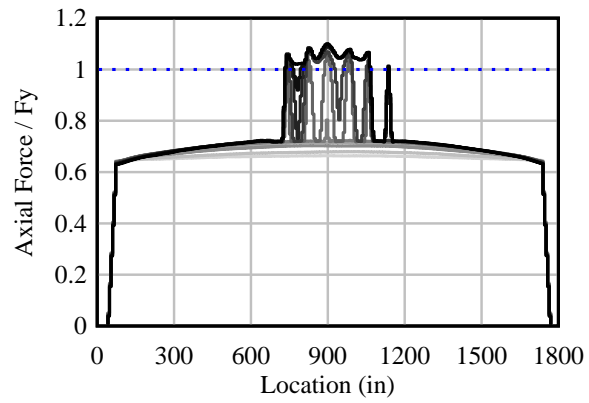
Elevation View

FIB72-SS-16: U/T = 0.80; μ = 0; Point Load

Elevation View

Damage Index

| 0 | 0.1 | 0.2 | 0.3 | 0.4 | 0.5 | 0.6 | 0.7 | 0.8 | 0.9 | 1.0 |

FIB72-SS-17: U/T = 0.80; μ = 0; Tandem Load

Elevation View

Damage Index

0   0.1   0.2   0.3   0.4   0.5   0.6   0.7   0.8   0.9   1.0

FIB72-SS-18: U/T = 0.80; μ = 0; Uniform Load

Elevation View

Damage Index

| 0 | 0.1 | 0.2 | 0.3 | 0.4 | 0.5 | 0.6 | 0.7 | 0.8 | 0.9 | 1.0 |

FIB72-SS-19: U/T = 0.70; μ = 0; Point Load

Elevation View

Damage Index

0   0.1   0.2   0.3   0.4   0.5   0.6   0.7   0.8   0.9   1.0

FIB72-SS-20: U/T = 0.70; μ = 0; Tandem Load

Elevation View

Damage Index

0   0.1   0.2   0.3   0.4   0.5   0.6   0.7   0.8   0.9   1.0

FIB72-SS-21: U/T = 0.70; μ = 0; Uniform Load

Elevation View

Damage Index

0   0.1   0.2   0.3   0.4   0.5   0.6   0.7   0.8   0.9   1.0

FIB72-SS-22: U/T = 0.50; μ = 0; Point Load

Elevation View

Damage Index

0   0.1   0.2   0.3   0.4   0.5   0.6   0.7   0.8   0.9   1.0

FIB72-SS-23: U/T = 0.35; μ = 0; Point Load

Elevation View

Damage Index

| 0 | 0.1 | 0.2 | 0.3 | 0.4 | 0.5 | 0.6 | 0.7 | 0.8 | 0.9 | 1.0 |

FIB72-SS-24: U/T = 0.25; μ = 0; Point Load

Elevation View

Damage Index

0   0.1   0.2   0.3   0.4   0.5   0.6   0.7   0.8   0.9   1.0

433

FIB72-SS-25: U/T = 0.10; μ = 0; Point Load

Elevation View

Damage Index

0   0.1   0.2   0.3   0.4   0.5   0.6   0.7   0.8   0.9   1.0
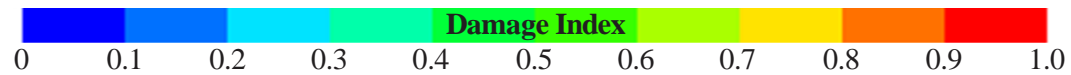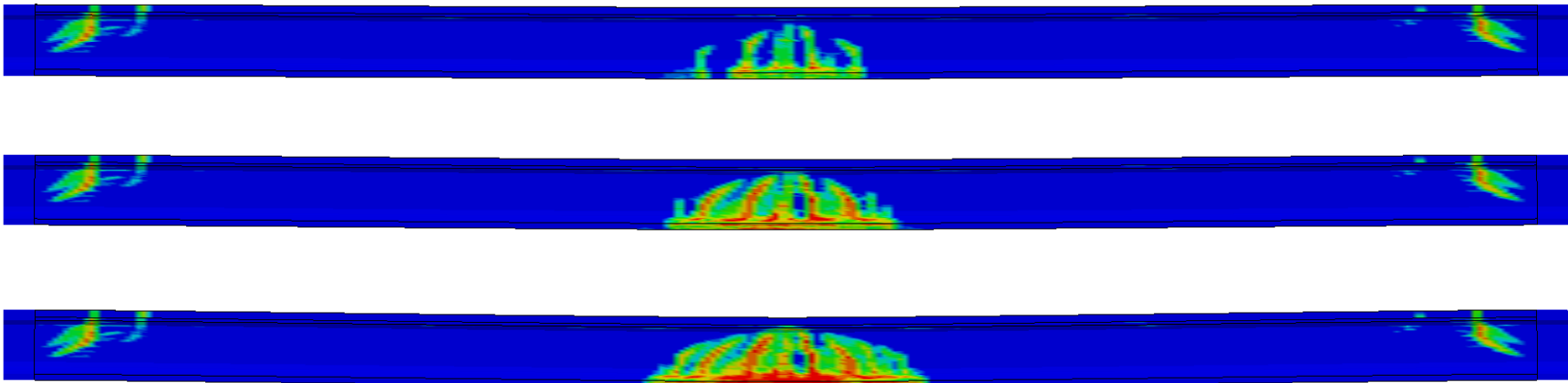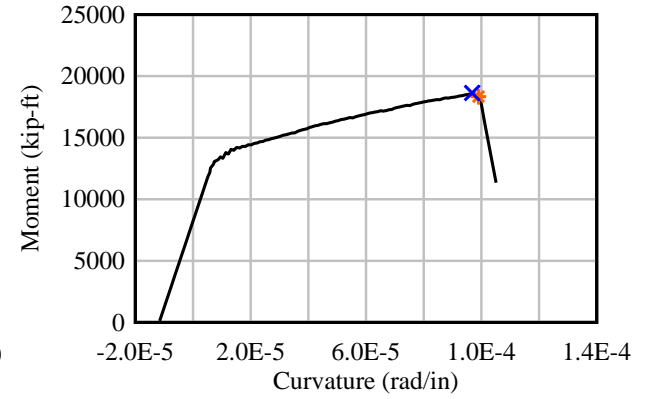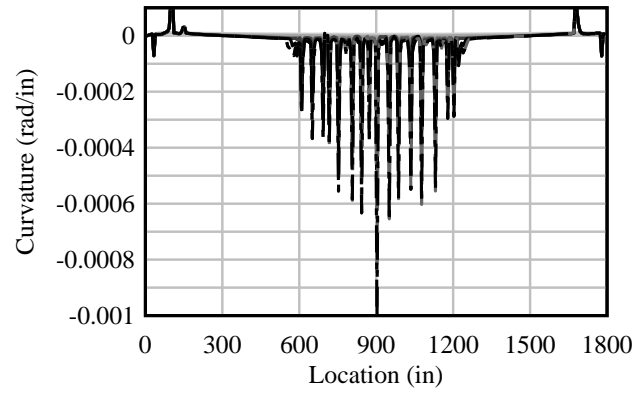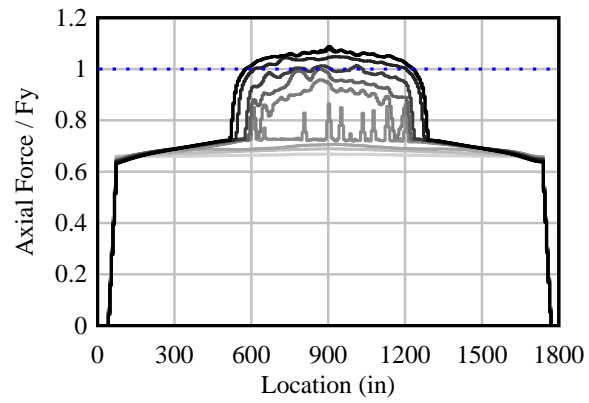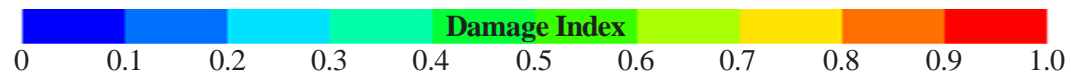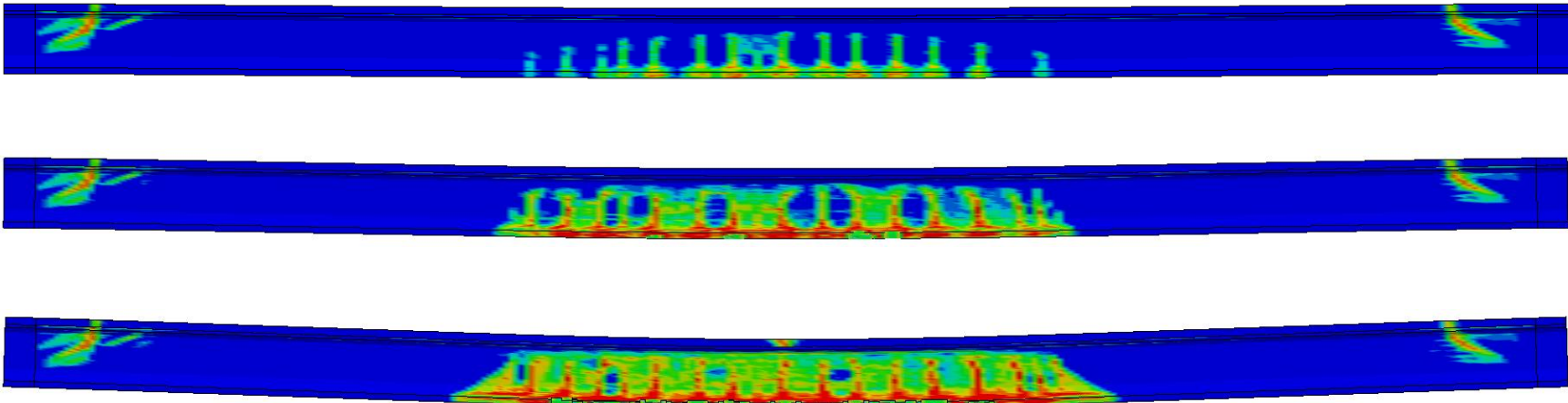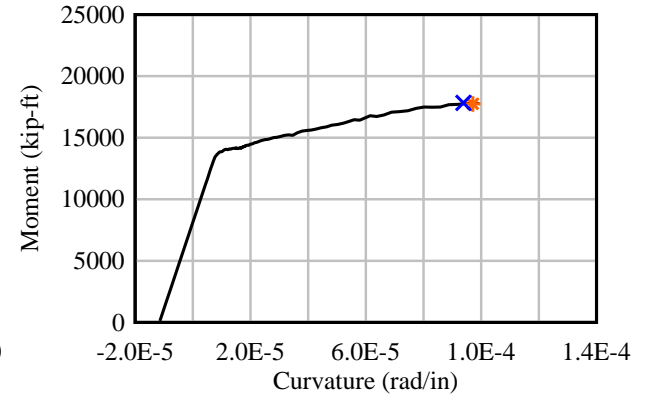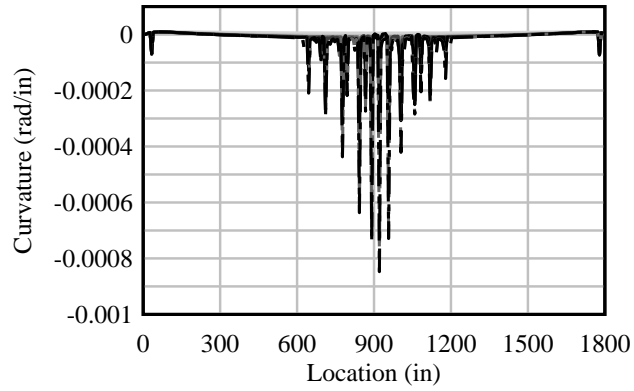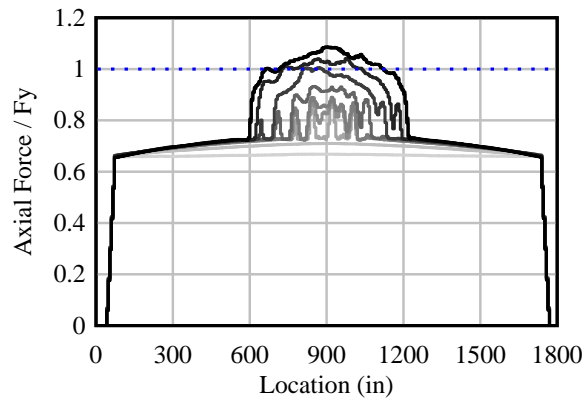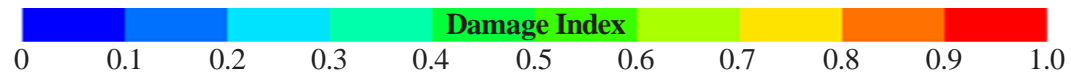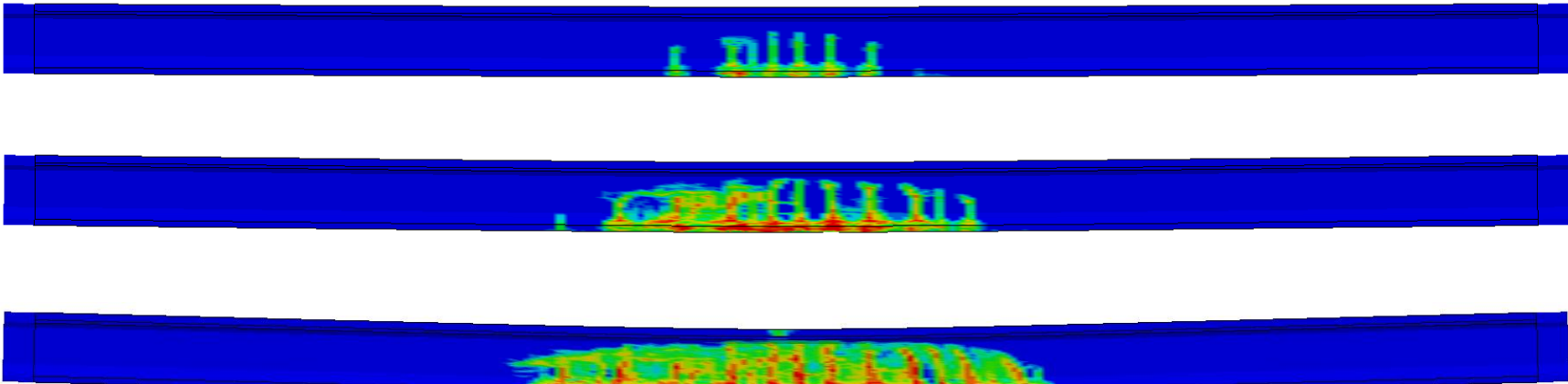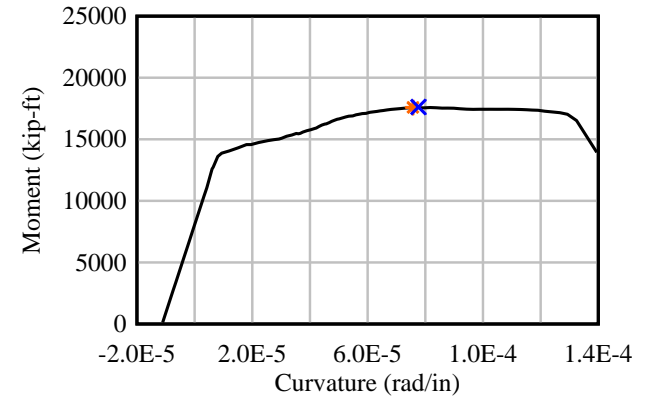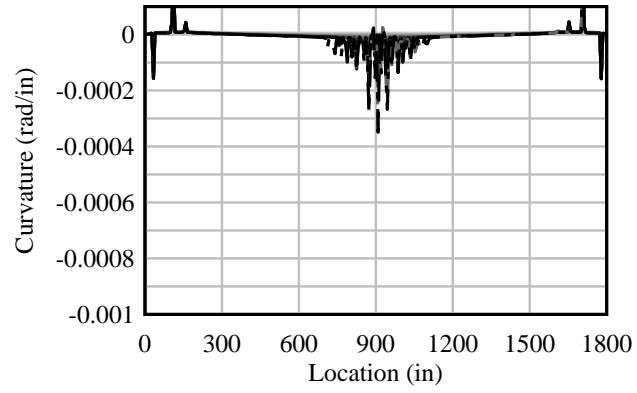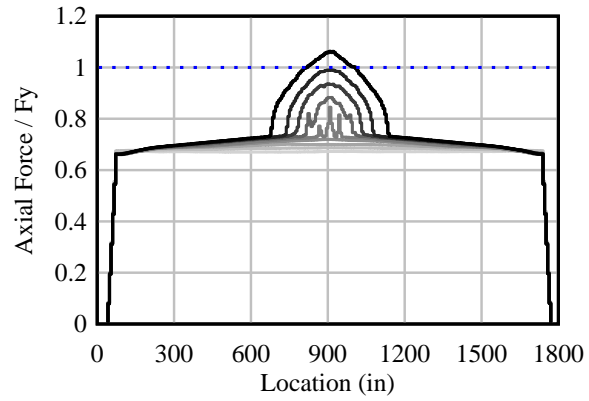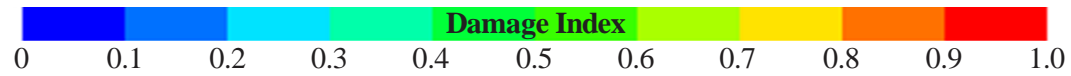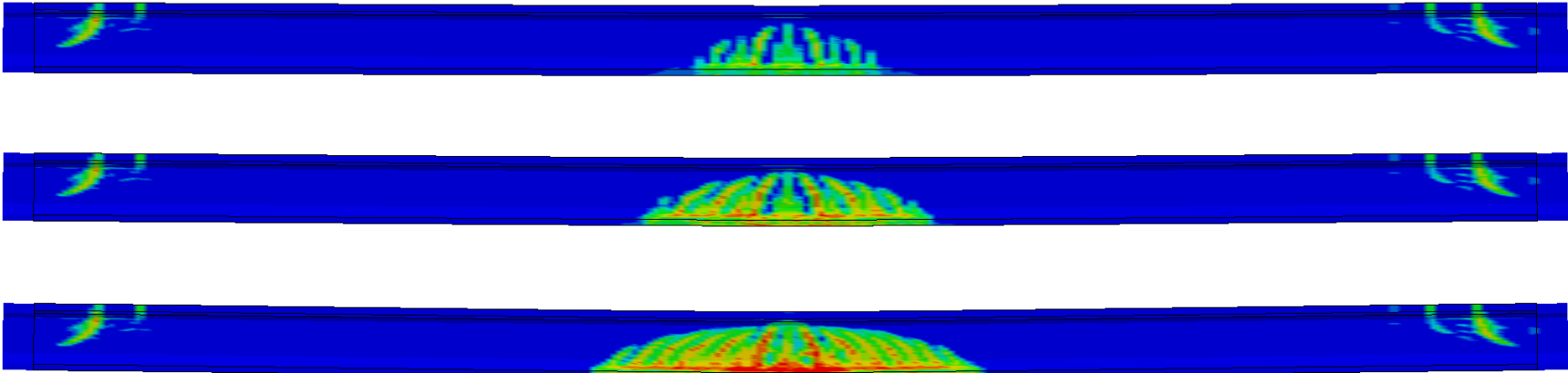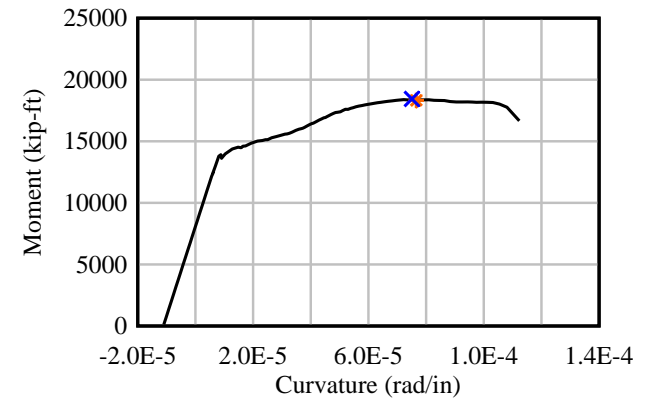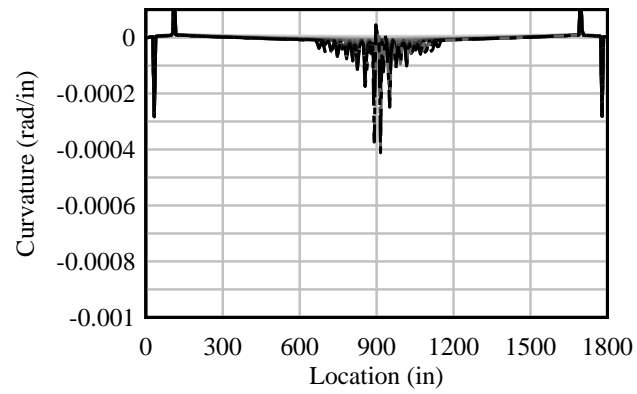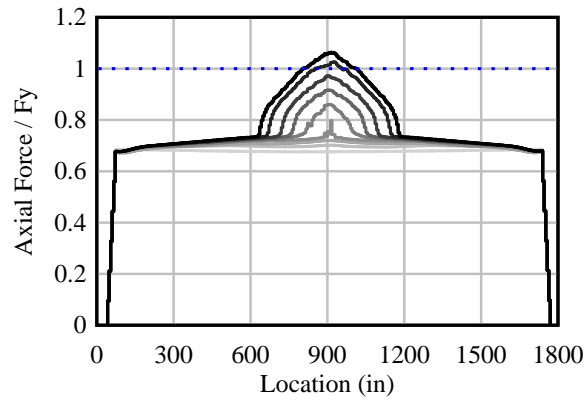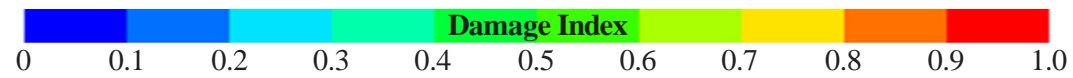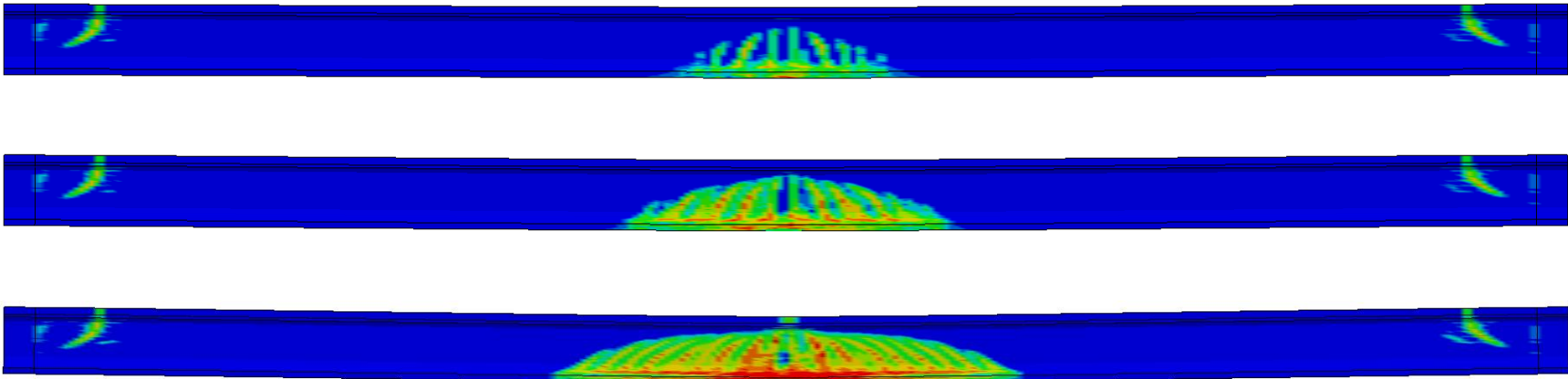
FIB72-SS-26: U/T = 0.00 (bonded); μ = 0; Point Load

Elevation View

Damage Index

| 0 | 0.1 | 0.2 | 0.3 | 0.4 | 0.5 | 0.6 | 0.7 | 0.8 | 0.9 | 1.0 |

435

Figure I.1 Ratios of unbonded reinforcement for positive bending (straight PT tendon)
(a) $U_A/T_A = 0.9$; (b) $U_A/T_A = 0.80$; (c) $U_A/T_A = 0.70$, (d) $U_A/T_A = 0.70$, (e) $U_A/T_A = 0.35$,
(f) $U_A/T_A = 0.25$, (g) $U_A/T_A = 0.10$ [unbonded PT tendons shown in orange]

AASHTO-II-SS-1: U/T = 0.90; μ = 0; Point Load

Elevation View

Damage Index

0   0.1   0.2   0.3   0.4   0.5   0.6   0.7   0.8   0.9   1.0

AASHTO-II-SS-2: U/T = 0.90; μ = 0; Tandem Load

Elevation View

Damage Index

0   0.1   0.2   0.3   0.4   0.5   0.6   0.7   0.8   0.9   1.0
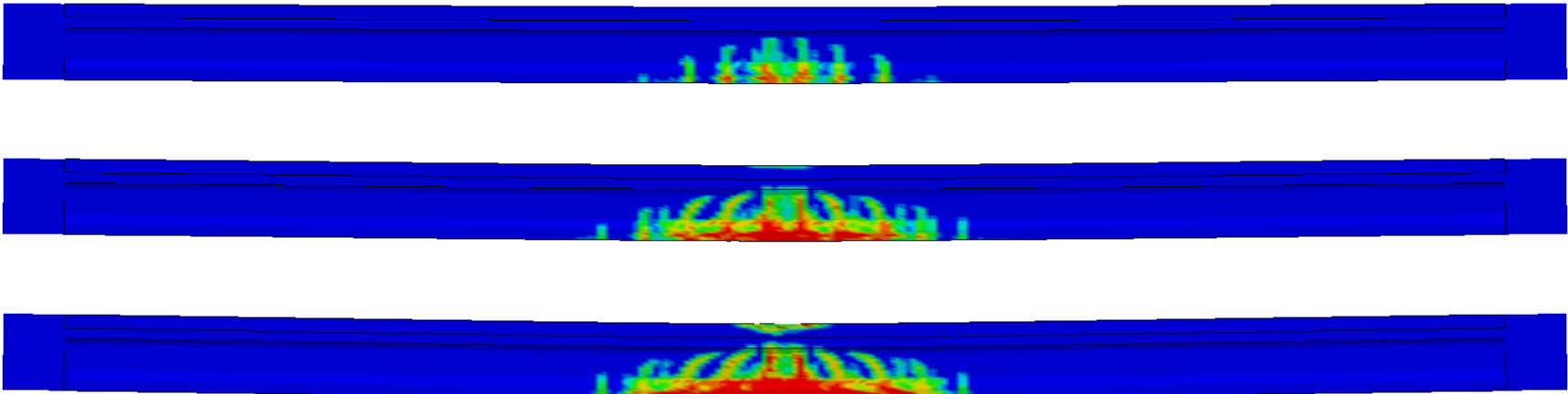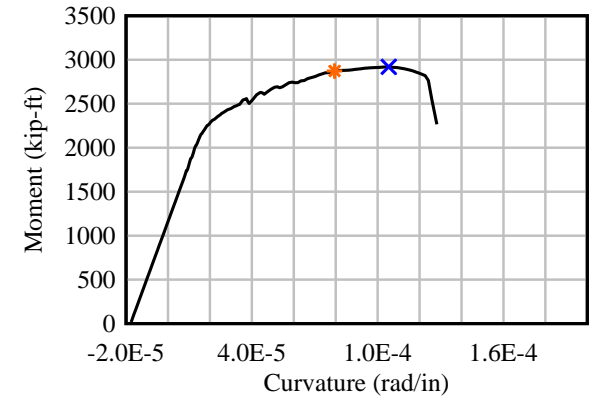
438

AASHTO-II-SS-3: U/T = 0.90; μ = 0; Uniform Load

Elevation View

Damage Index

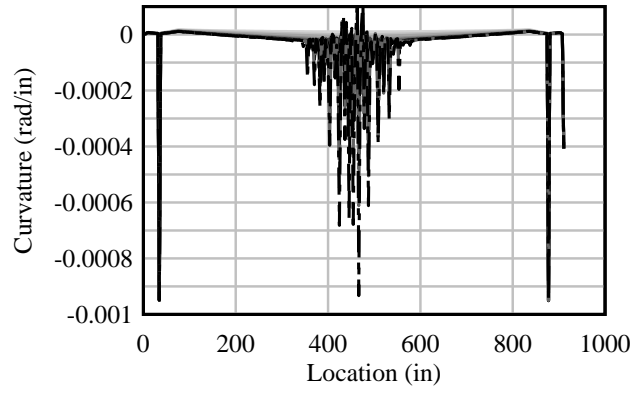0   0.1   0.2   0.3   0.4   0.5   0.6   0.7   0.8   0.9   1.0

AASHTO-II-SS-4: U/T = 0.80; μ = 0; Point Load

Elevation View

Damage Index

0   0.1   0.2   0.3   0.4   0.5   0.6   0.7   0.8   0.9   1.0

AASHTO-II-SS-5: U/T = 0.80; μ = 0; Tandem Load

Elevation View

Damage Index

0   0.1   0.2   0.3   0.4   0.5   0.6   0.7   0.8   0.9   1.0

AASHTO-II-SS-6: U/T = 0.80; μ = 0; Uniform Load

Elevation View

Damage Index

0   0.1   0.2   0.3   0.4   0.5   0.6   0.7   0.8   0.9   1.0
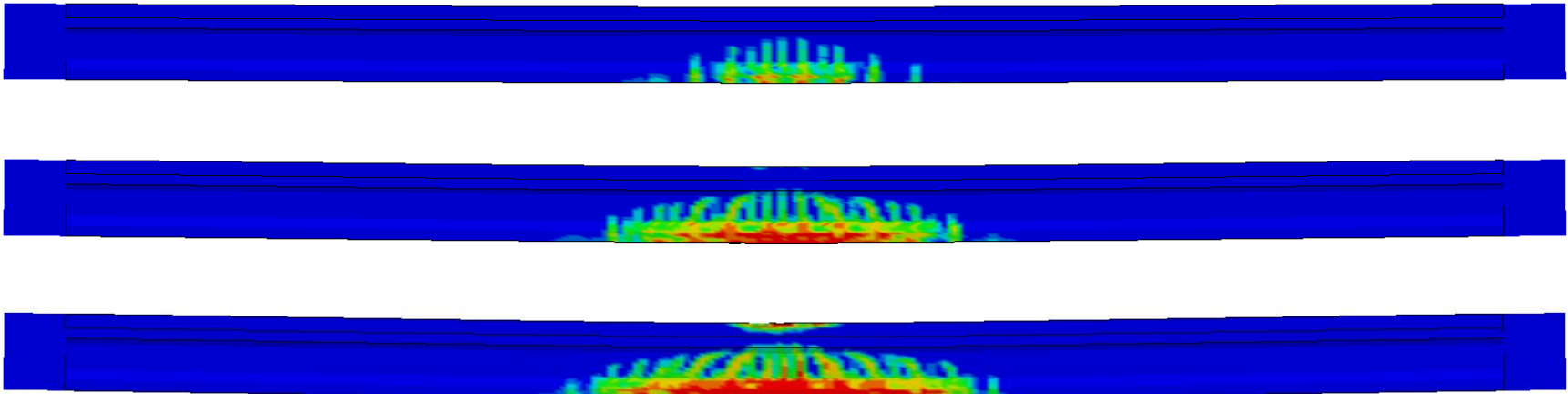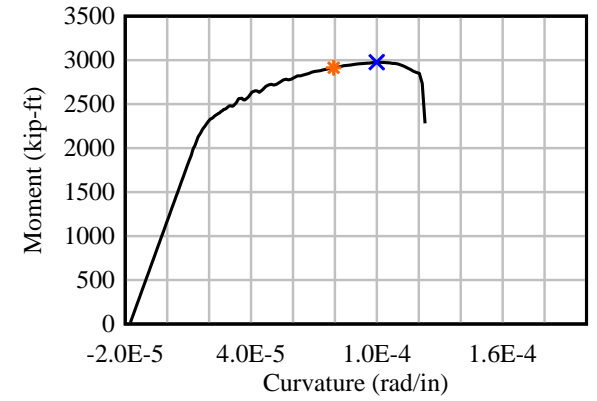
AASHTO-II-SS-7: U/T = 0.70; μ = 0; Point Load

Elevation View

Damage Index

0   0.1   0.2   0.3   0.4   0.5   0.6   0.7   0.8   0.9   1.0

AASHTO-II-SS-8: U/T = 0.70; μ = 0; Tandem Load

Elevation View

Damage Index

AASHTO-II-SS-9: U/T = 0.70; μ = 0; Uniform Load

Elevation View

Damage Index
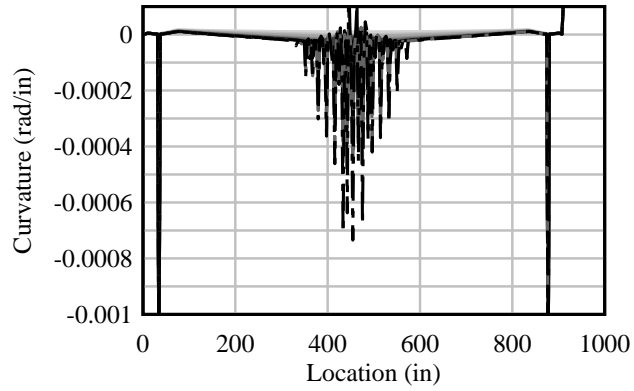
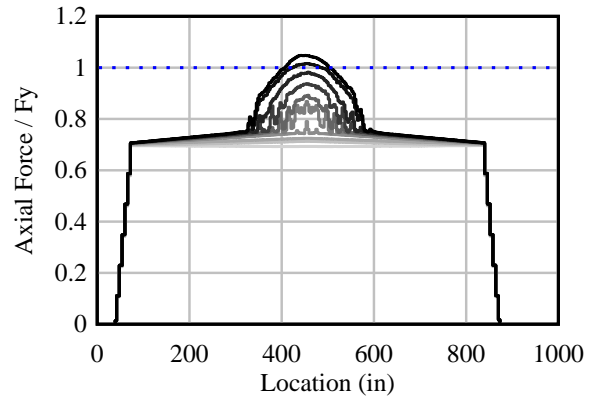**AASHTO-II-SS-10: U/T = 0.50; μ = 0; Point Load**

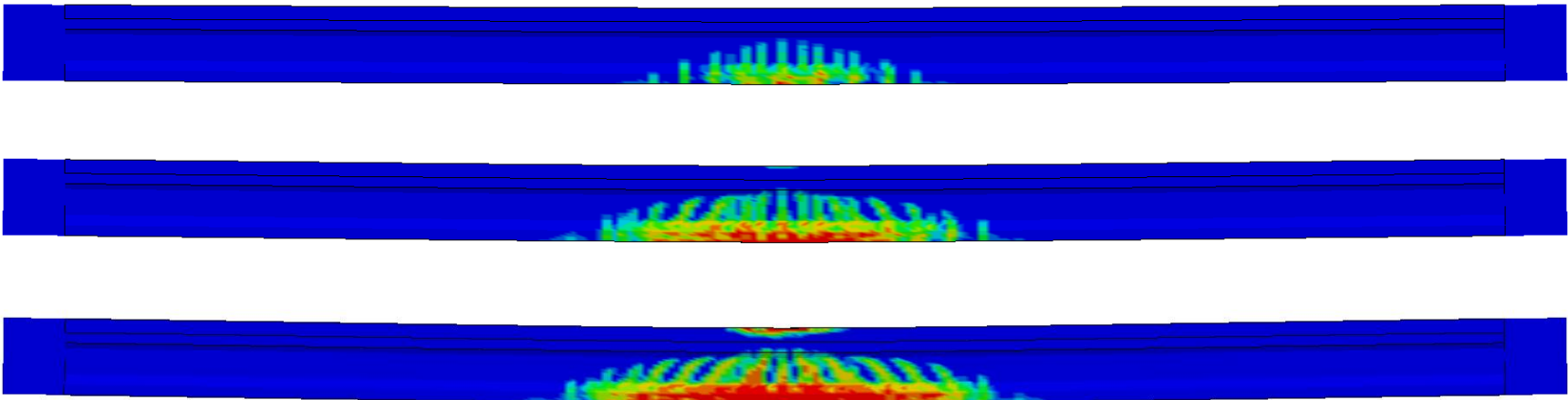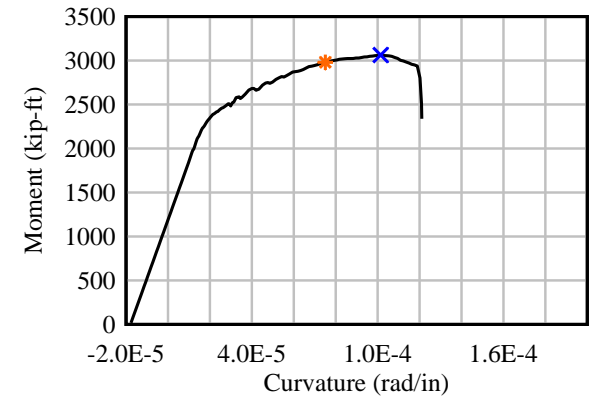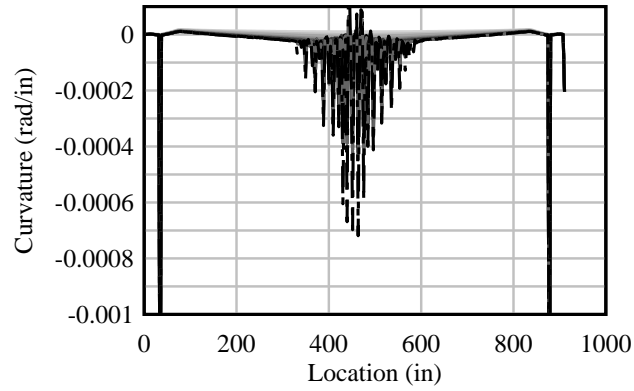

Elevation View
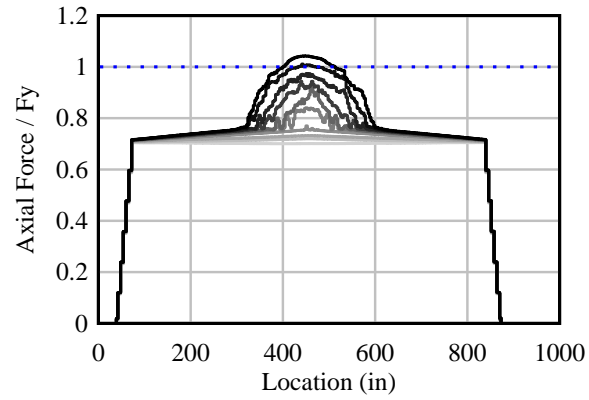
AASHTO-II-SS-11: U/T = 0.35; μ = 0; Point Load

Elevation View

Damage Index

0   0.1   0.2   0.3   0.4   0.5   0.6   0.7   0.8   0.9   1.0

AASHTO-II-SS-12: U/T = 0.25; μ = 0; Point Load

Elevation View

Damage Index

AASHTO-II-SS-13: U/T = 0.10; μ = 0; Point Load

Elevation View

Damage Index

0   0.1   0.2   0.3   0.4   0.5   0.6   0.7   0.8   0.9   1.0

449